Transactions of the ASME®

Transactions of the ASME, Journal of Engineering for Gas Turbines and Power (ISSN 0742-4795) is published quarterly (Jan., Apr., July, Oct.) for $125.00 per year by The American Society of Mechanical Engineers, 345 East 47th Street, New York, NY 10017. Second class postage paid at New York, NY and additional mailing offices. POSTMASTER: Send address changes to Transactions of the ASME, Journal of Engineering for Gas Turbines and Power, c/o THE AMERICAN SOCIETY OF MECHANICAL ENGINEERS, 22 Law Drive, Box 2300, Fairfield, NJ 07007-2300.
CHANGES OF ADDRESS must be received at Society headquarters seven weeks before they are to be effective. Please send old label and new address.
PRICES: To members, $36.00, annually; to nonmembers, $125.00.
Add $15.00 for postage to countries outside the United States and Canada.

INDEXED by Applied Mechanics Reviews and Engineering Information, Inc.
Canadian Goods & Services Tax Registration #126148048

Journal of Engineering for Gas Turbines and Power

Published Quarterly by The American Society of Mechanical Engineers
VOLUME 114 • NUMBER 1 • JANUARY 1992

TECHNICAL PAPERS

(Contents continued on page 7)

Contents (continued)

A Computational Procedure for Diffuser-Combustor Flow Interaction Analysis

K. C. Karki

V. L. Oechsle

H. C. Mongia

Allison Gas Turbine Division,
General Motors Corporation,
Indianapolis, IN 46206

This paper describes a diffuser-combustor flow interaction analysis procedure for gas turbine combustion systems. The method is based on the solution of the Navier-Stokes equations in a generalized nonorthogonal coordinate system. The turbulence effects are modeled via the standard two-equation (k-ϵ) model. The method has been applied to a practical gas turbine combustor-diffuser system that includes support struts and fuel nozzles. Results have been presented for a three-dimensional simulation, as well as for a simplified axisymmetric simulation. The flow exhibits significant three-dimensional behavior. The axisymmetric simulation is shown to predict the static pressure recovery and the total pressure losses reasonably well.

Introduction

In a gas turbine combustion system, the interaction between the diffuser and combustor external flows plays a key role in controlling the pressure loss, airflow distribution around the combustor liner, and the attendant effects on performance, durability, and stability. The diffuser-combustor flow interaction is governed by several geometric and flow parameters. For a dump diffuser system, these include the prediffuser length and area ratio; the dump gap and expansion ratio; the airflow splits between the dome and the inner and outer annuli; and the velocity distribution and turbulence level at the compressor exit. Additional considerations are the locations of support struts, locating pins, and fuel nozzles. These subcomponents should be designed and placed such that they have minimal effect on the pressure recovery and burner exit temperature quality. The diffuser system should be designed such that there are no unnecessary pressure losses. Further, it should lead to uniform air feed to various liner orifices and cooling devices on the combustor walls. The nonuniformities in the pressure distribution can result in an inadequate cooling film at various locations or can even cause reversal of the flow direction with consequent overheating of the combustor liner.

A diffuser design procedure requires as input the various losses in the system. These include the prediffuser momentum losses, flow dumping losses, and the parasitic drag losses of struts, mounts, and fuel nozzles. Currently, these losses are calculated using empirical correlations based on existing experimental data. Such an approach cannot be used effectively for new design concepts. Further, due to the complexity of the geometry and the resulting flow, the choice of the optimum configuration depends upon the selection of a large number of parameters. Evidently, the conventional approach of identifying an optimum combination of a large number of parameters through scale model testing followed by selective full-scale testing is both expensive and time consuming. These difficulties have led to the development of multidimensional computational methods for analyzing the diffuser and combustor external flows.

A prediction procedure for diffuser-combustor flow interaction should be able to predict the pressure loss, velocity profile, and flow distribution around the combustor head and annuli. It should also provide accurate estimates for the cold-side heat transfer coefficients for the combustor walls so that the surface temperature calculations can properly account for the combustor external flow pattern. The flow in a dump diffuser system is comprised of regions of recirculating flow, strong streamline curvature, adverse pressure gradient, developing boundary layers, and impingement flow. Such a flow structure coupled with complex geometric configuration makes the computations of combustor-diffuser flows difficult.

Most of the applications (e.g., McGuirk and Whitelaw, 1984; Shyy, 1985; Ando et al., 1986; Karki and Patankar, 1986) of computational methods to dump diffusers have been restricted to simplified two-dimensional or axisymmetric configurations. These studies have primarily been directed toward the adequacy and applicability of the numerical procedures based on computational fluid dynamics for predicting the diffuser flows. These methods are based on the solution of the Navier-Stokes equations in a body-fitted coordinate system. The turbulence effects are simulated using the two-equation (k-ϵ) turbulence model (Launder and Spalding, 1974). The reported results for the model diffusers indicate that the gross features of the flow can be predicted reasonably well. However, accurate predictions of static pressure recovery and total pressure losses will require improved turbulence models that take into account the anisotropic nature of the flow as well as the effects of adverse pressure gradient.

In spite of the abovementioned limitations, a computational procedure based on a body-fitted coordinate system and the k-ϵ model can be used effectively to study the influence of

Contributed by the International Gas Turbine Institute and presented at the 35th International Gas Turbine and Aeroengine Congress and Exposition, Brussels, Belgium, June 11-14, 1990. Manuscript received by the International Gas Turbine Institute December 21, 1989. Paper No. 90-GT-35.

various parameters on the performance of a diffuser system. In the present paper, we report the details of such a procedure for diffuser-combustor flow interaction studies. The method has been applied to a practical configuration that includes support struts and fuel nozzles. Results have been presented for a full three-dimensional simulation as well as for a simplified axisymmetric simulation. The adequacy of the simplified analysis has been assessed by comparing these results with those from the full simulation and the experimental data. A more complete discussion and analysis of the work reported here may be found from Oechsle et al. (1989).

Mathematical Model

The calculation procedure presented here is based on the solution of the complete form of the equations governing the conservation of mass and momentum in the time-averaged form; using Cartesian tensor notation these can be written as

$$\frac{\partial}{\partial x_i}(\rho U_i) = 0 \tag{1}$$

$$\frac{\partial}{\partial x_j}(\rho U_i U_j) = -\frac{\partial P}{\partial x_i} - \frac{\partial}{\partial x_j}(\rho \overline{u_i u_j}) \tag{2}$$

where the upper case letters represent time mean quantities and lower case letters fluctuating components. For the calculations presented here, the flow is assumed isothermal. The quantities $(\rho \overline{u_i u_j})$ represent the turbulent Reynolds stresses. These stresses are approximated via the high Reynolds number version of the two-equation $(k$–$\epsilon)$ model. The Reynolds stress is related to the mean rate of strain via a turbulent viscosity

$$-\rho \overline{u_i u_j} = \mu_t \left(\frac{\partial U_i}{\partial x_j} + \frac{\partial U_j}{\partial x_i} \right) - \frac{2}{3} \delta_{ij} \rho k \tag{3}$$

In this expression the turbulent viscosity is calculated from

$$\mu_t = C_\mu \rho \frac{k^2}{\epsilon} \tag{4}$$

where k and ϵ are the turbulence kinetic energy and dissipation rate of turbulence energy, respectively, the values of which are obtained from the solution of the modeled transport equations:

$$\frac{\partial}{\partial x_j}(\rho U_j k) = \frac{\partial}{\partial x_j}\left(\frac{\mu_t}{\sigma_k} \frac{\partial k}{\partial x_j} \right) - \rho \overline{u_i u_j} \frac{\partial U_i}{\partial x_j} - \rho e \tag{5}$$

$$\frac{\partial}{\partial x_j}(\rho U_j \epsilon) = \frac{\partial}{\partial x_j}\left(\frac{\mu_t}{\sigma_\epsilon} \frac{\partial \epsilon}{\partial x_j} \right) - C_1 \frac{\epsilon}{k} \rho \overline{u_i u_i} \frac{\partial U_i}{\partial x_j} - C_2 \rho \frac{\epsilon^2}{k} \tag{6}$$

The model constants are assigned the following standard values:

$$C_\mu = 0.09, \quad C_1 = 1.44, \quad C_2 = 1.92, \quad \sigma_k = 1.0, \quad \sigma_\epsilon = 1.3$$

The set of coupled nonlinear equations was solved using the finite-volume procedure developed by Karki and Patankar (1988). The discretization of the equations is performed in a generalized coordinate system. A staggered grid arrangement is used in which the scalar quantities are located at the center of a control volume and the velocity components are displaced along the coordinate directions to lie at the midpoints of the control-volume faces. The momentum equations are written in terms of the covariant (grid-oriented) velocity components. Due to the spatial variation of the base vectors associated with these velocity components, curvature source terms appear in the governing equations. In the procedure of Karki and Patankar (1988), a locally fixed coordinate system is used to derive the discretization equations for the curvilinear velocity components. In this approach (Karki, 1986; Karki and Patankar, 1988), the coordinate axis, in the direction of the velocity component being considered, is fixed at the neighboring grid points. Thus, all velocity components appearing in the discretization equation are parallel and curvature terms do not appear explicitly in the formulation. The coupling between the pressure and velocity fields is handled using the SIMPLER algorithm (Patankar, 1980). The power-law differencing scheme (Patankar, 1980) is used to discretize the combined convection-diffusion terms in the transport equations. This calculation procedure has been applied to a variety of recirculating flows including the flow in an annular dump diffuser (Karki and Patankar, 1986).

Geometric Configuration

An annular diffuser-combustor system, as shown in Fig. 1, was used to measure pressure loss distribution in a full-scale combustor rig. Compressed air flows from a plenum chamber attached to a straight annular section via a bell-mouth nozzle before entering the prediffuser. The diffuser corrected air flow rate at the combustion system design condition is 1.795 kg/s and the corresponding diffuser inlet Mach number based on the inlet annulus geometric area is 0.236. The prediffuser length and expansion ratio are $4.55h$ and 1.29, where h is the prediffuser inlet annulus height. Eight support struts with a thickness to chord ratio of 0.3 are equally spaced circumferentially inside the prediffuser. The strut leading edge is located 22.8 mm downstream of the prediffuser inlet. Of the flow exiting the prediffuser, 32.9 percent is diverted to the inner annulus, 22.3 percent to the combustion liner dome, and 44.8 percent to the outer annulus.

The combustor design consists of a typical film-cooled throughflow annular combustor. The combustor liner side wall orifices are located at the primary zone (PZ), intermediate zone (IZ), and dilution zone (DZ), as shown in Fig. 1(*b*). Sixteen piloted air blast fuel nozzles are inserted through the combustor dome. Each fuel nozzle is surrounded by concentric axial swirlers. A splash-plate/film-cooling technique is used for the dome wall.

Results and Discussion

In this section results from two sets of calculations have been presented. In the first, the flow is assumed to be axisymmetric. The effects of various blockages are incorporated in the simplified geometry. This is followed by the results of the three-dimensional simulation. For each case, the details of modeled geometry, computational grid, and boundary conditions are presented in the subsequent subsections.

Axisymmetric Simulation

Modeled Geometry and Grid. For the axisymmetric simulation, computations are made only for a median plane. The

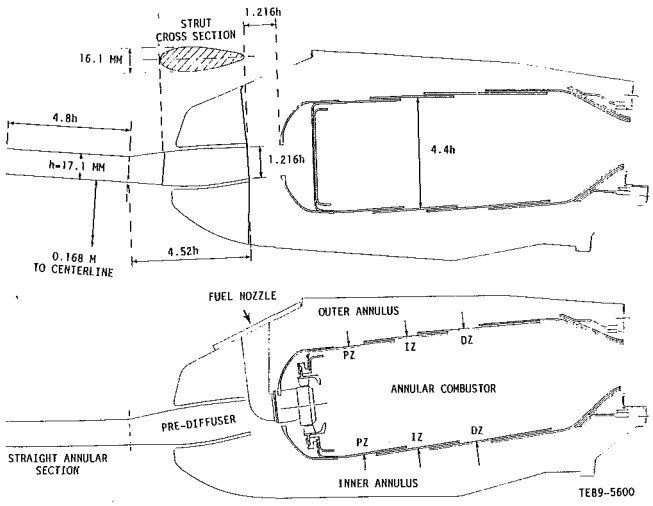

Fig. 1 Combustor-diffuser configuration

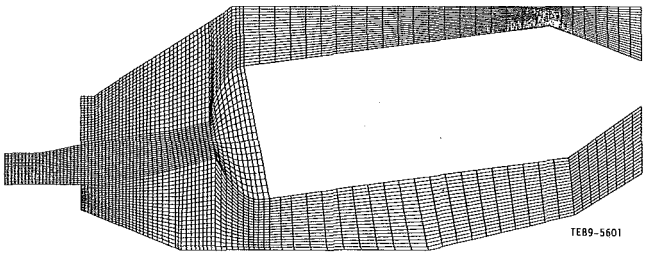

Fig. 2 Computational grid for axisymmetric simulation

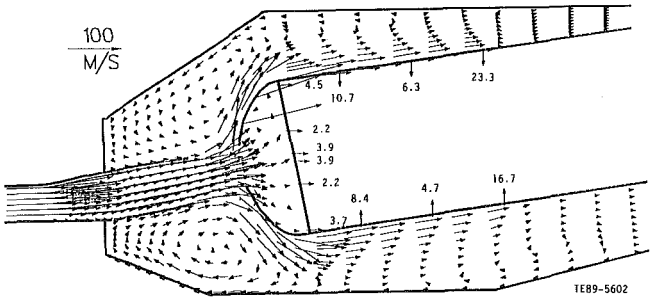

Fig. 3 Flow field and air flow distribution from axisymmetric simulation

geometry is, however, modified to reflect the presence of various blockages. The flows entering the combustor are considered as mass sinks at appropriate locations.

The computational grid for the axisymmetric simulation is shown in Fig. 2. This grid was generated algebraically by nondimensionalizing the distances between prominent boundaries in the configuration. The results presented here were obtained using a 96 × 64 (x–r) grid. To assess the numerical accuracy, calculations were also repeated using a coarser 51 × 44 grid. The predicted static pressure recovery and the total pressure losses from these two sets of calculations differed by less than 2 percent.

Boundary Conditions. At the prediffuser inlet, profiles for all dependent variables are prescribed. The prescribed streamwise velocity profile was deduced from measured total pressure and static pressure distributions at the inlet. For this condition, the blocked area fraction B defined as

$$B = 1 - \frac{1}{A}\int \left(\frac{u}{U_{\max}}\right) dA \tag{7}$$

is 0.06. The design point blocked Mach number and mass averaged dynamic head at the inlet are 0.251 and 0.0534 MPa, respectively. The cross-stream velocity components were assumed zero. The inlet turbulence intensity level was taken as 5 percent. The values for inlet energy dissipation were calculated by assuming a length scale equal to 3 percent of the annulus height. The near-wall regions were treated following the conventional wall function approach (Launder and Spalding, 1974). At the outflow boundaries, the axial diffusion was neglected and the normal velocity components were adjusted to ensure that the specified amount of flow exited from each annulus.

In addition to the boundary conditions described above, the computational scheme also requires the specification of either the mass flow rate through or the total pressure loss up to various combustor air entry points. The pressure loss can usually be prescribed in terms of an empirical loss coefficient. In the present procedure, mass flow rate (as a sink) is specified at each combustor entry point. These mass flow rates are iteratively updated in conjunction with a simplified annulus flow model. The calculation cycle proceeds as follows. The axisymmetric flow calculations are performed with a guessed combustor liner airflow distribution (mass sinks). This solution

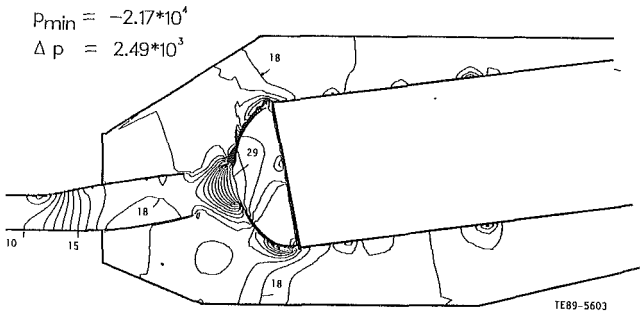

Fig. 4 Static pressure distribution from axisymmetric simulation

provides total pressure losses and static pressure recovery coefficients in each passage of the diffuser-combustor system. These estimates for the pressure losses are used as inputs in the annulus flow calculations to provide a new airflow distribution around the combustor. The diffuser flow calculations are now repeated with the new mass sinks. This iterative procedure typically requires three or four cycles for convergence.

Results. Figure 3 shows the predicted flow field along with the associated airflow distribution. The mass flow rates have been presented as percentage of the flow entering the prediffuser. After being discharged from the prediffuser, the flow is split into three branches: two streams that feed the inner and outer combustor annuli and a third that supplies air to the combustor dome. As a result of the flow expansion, two recirculation zones form at the corners in the dump region. The lower recirculation zone is stronger than the upper one. There is strong flow acceleration around the cowls. Further, there is a substantial nonuniformity in the velocity distributions in the annuli.

The static pressure distribution in the form of constant pressure contours is presented in Fig. 4. The pressure levels have been calculated with reference to the lowermost grid point at the inlet. The minimum pressure and the increment for the isopleths (in Pascal) have been indicated on this figure. This pressure increment corresponds to 4.7 percent of inlet dynamic head. Some prominent contour lines have been identified by numerals, which designate the corresponding pressure levels in terms of the number of increments above the minimum value indicated. For example, the contour marked 29 at the cowling inlet corresponds to a pressure rise of 0.05 MPa above the reference point. The static pressure rises in the prediffuser; high pressures are encountered within the combustor dome; and regions of low pressure form around the cowls due to flow acceleration. On the combustor walls, the presence of various sinks results in pockets of low pressure in their vicinity.

The predicted pressure recoveries in various passages of the diffuser system are of interest from design considerations. For the present system some typical values are now presented as percentage of the inlet dynamic head. The static pressure recovery in the prediffuser section is 38 percent. The pressure recovery from inlet to the primary jet location on the outer annulus is 39 percent; the corresponding value for the inner annulus is 48 percent. There is very small pressure rise in the annuli beyond the primary jet locations. These values are 3.2 and 1.5 percent for the outer and inner annuli, respectively. The calculations show that the pressure recovery in the dome region is almost 100 percent. In conjunction with the annulus flow model, the static pressure drop across the primary orifices is estimated to be 64 percent for the inner wall and 70 percent for the outer wall.

The predicted and measured static pressure recovery coefficients along the inner and outer walls of the prediffuser and combustor casing are presented in Fig. 5. Pressure measurements were made at selected axial locations. In the azimuthal direction, the ease of placement of the pressure taps was the

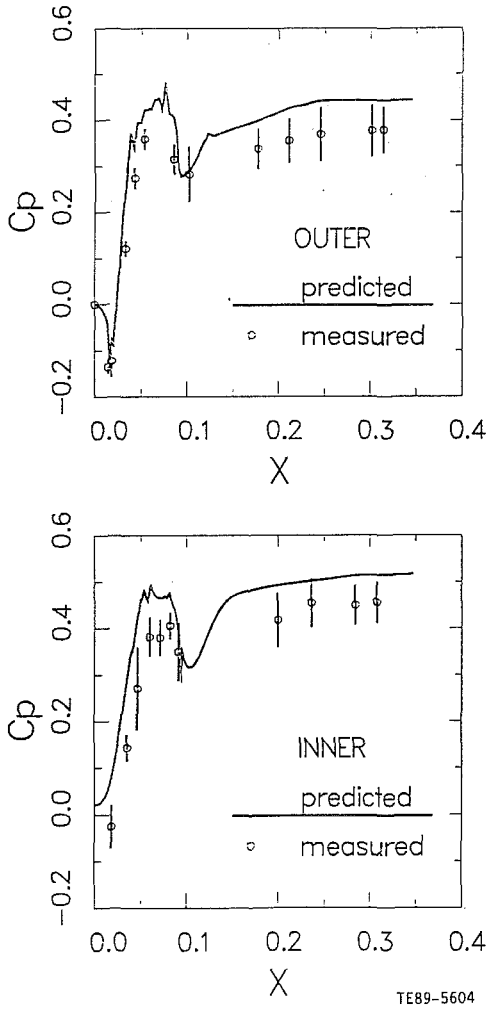

Fig. 5 Comparison of predicted and measured static pressure recovery coefficients

primary consideration in the selection of the measurement locations. Consequently, the measurement points do not lie along a line; instead, the angular location varies from point to point. The error bars about the measurement points represent the value of 2 σ (i.e., two standard deviations). The standard deviation was calculated from nine sets of data points. The predicted static pressure values closely follow the experimentally observed trend. The predicted asymptotic pressure recovery is within 10 to 15 percent of the experimental value. Considering the three-dimensional nature of the flow and the known limitations (e.g., Rodi and Scheuerer, 1986) of the k–ϵ model for flows with separation and adverse pressure gradient, the theory/data agreement is considered satisfactory.

Three-Dimensional Simulation. The axisymmetric simulation presented above cannot account for the circumferential nonuniformities introduced by struts, fuel nozzles, and support pins. The results of the full three-dimensional simulation presented here help in understanding the complex flow within the diffuser. In addition, these calculations form a basis for assessing the adequacy of the simplified analysis.

Modeled Geometry and Grid. The flow and geometric periodic repeatability of the configuration considered allow the computations to be restricted to a sector formed by a 45-deg slice comprised of a load-bearing support strut and two fuel nozzles. The computational grid for three-dimensional calculations was obtained by rotating the grid in an axial (x–r) plane about the axis of the combustor. For the results reported here, a 37 × 38 × 32 (x–r–θ) grid was used. The strut and

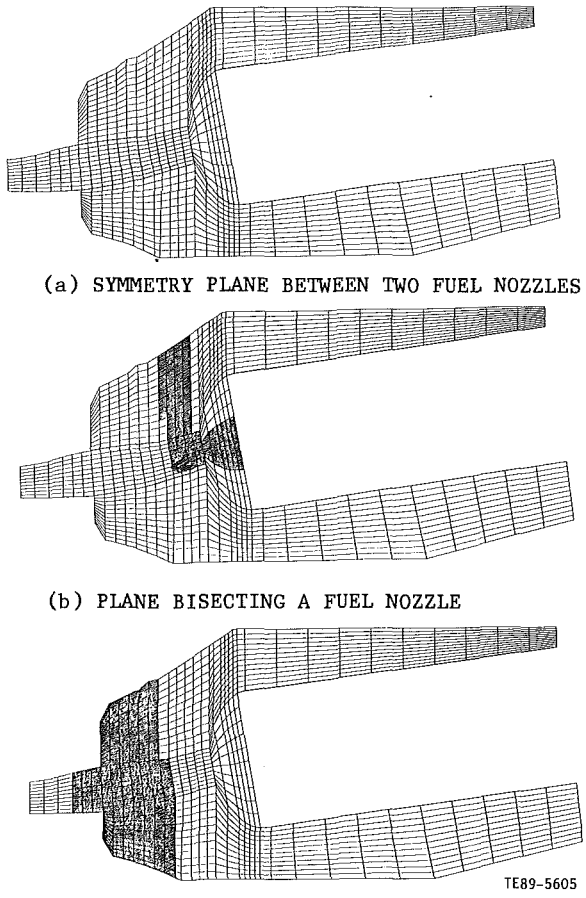

Fig. 6 Computational grid for three-dimensional simulation

the fuel nozzles were simulated as blocked-off regions in the computational grid. Figure 6(a) shows the grid in the axial plane midway between the fuel nozzles. The modeled descriptions of the fuel nozzle and the strut in the axial planes bisecting these components are shown in Figs. 6(b) and 6(c), respectively.

The boundary conditions for the three-dimensional calculations are similar to those described above for the axisymmetric simulation. The only added feature is the incorporation of symmetry conditions at the boundaries in the azimuthal direction. The three-dimensional calculations reported here were made with the air flow distribution obtained from the axisymmetric simulation. Attention was focused primarily on the region between the inlet to the prediffuser and a section downstream of the primary jets. Consequently, the dilution and intermediate zone orifices were not simulated; the corresponding flows were considered part of the turbine cooling streams. The main objective of these calculations is to highlight the three-dimensional nature of the flow under consideration. These features are presented via the velocity vectors and static pressure distribution on selected axial (x–r) and tangential (r–θ) planes.

Flow Field. The predicted flow patterns in the form of velocity vectors on three representative axial planes are presented in Fig. 7. Figure 7(a) corresponds to the x–r plane midway between the fuel nozzles. The flow pattern in this plane is qualitatively very similar to that predicted by the axisymmetric simulation in the median plane discussed earlier. The presence of obstacles in the domain, however, causes a reduction in the strength of corner recirculation zones compared to the axisymmetric simulation. Also, the velocities in the dome are higher in the three-dimensional simulation.

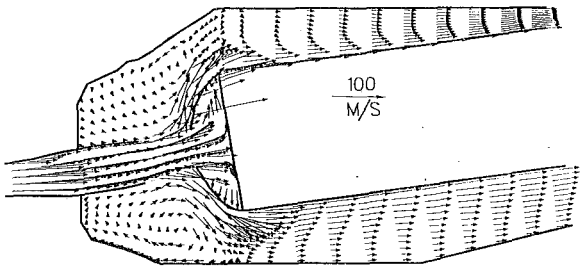

(a) SYMMETRY PLANE BETWEEN TWO FUEL NOZZLES

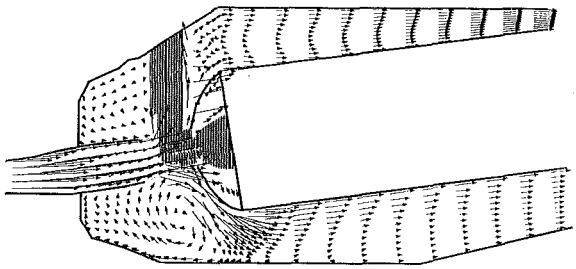

(b) PLANE BISECTING A FUEL NOZZLE

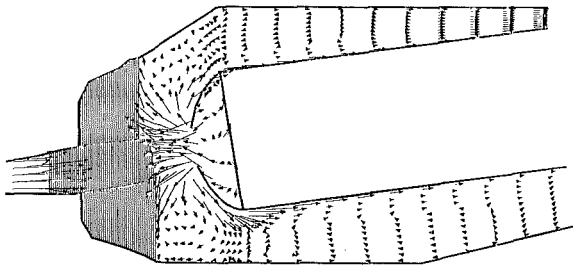

(c) PLANE BISECTING A STRUT

Fig. 7 Flow patterns in axial planes

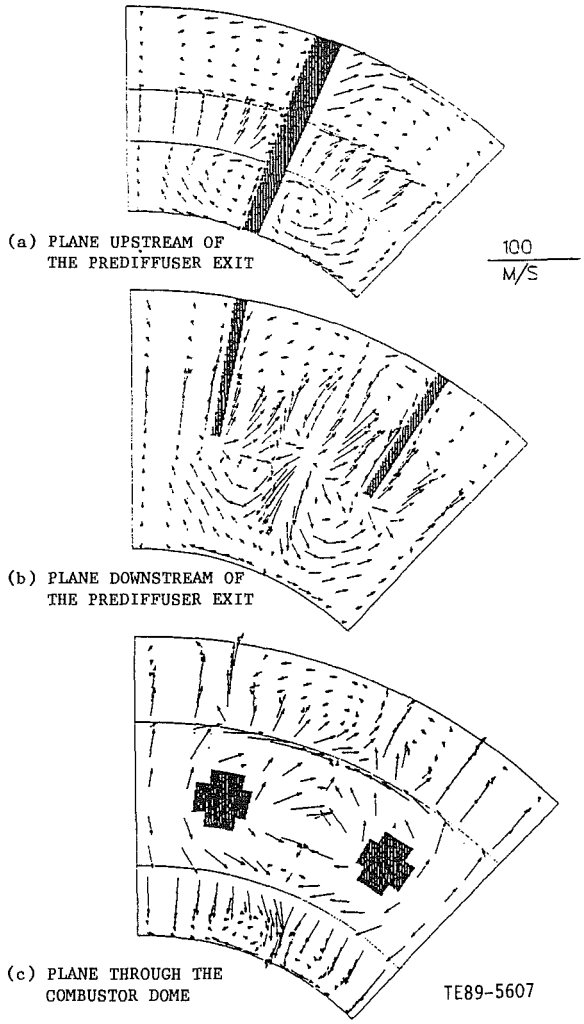

Fig. 8 Flow patterns in azimuthal planes

The velocity vectors in the $(x\text{-}r)$ plane bisecting a fuel nozzle are presented in Fig. 7(b). In contrast to the plane between the fuel nozzles, the presence of the fuel nozzle stem and tip causes a significant slow down of the flow exiting the prediffuser. Further, there is a severe change in the flow direction as the flow approaches the stem. In this plane, the upper recirculation zone is considerably weaker than the lower one.

The flow pattern in a plane through the strut is shown in Fig. 7(c). The behavior in this plane is markedly different from that observed in the other two planes discussed above. At the trailing edge of the strut, wakes are formed that extend up to the dome region. This back flow causes the development of weak recirculation regions within the dome.

It is of interest to note that the velocities coming out of the dome region are quite large. The back flow along with the presence of the strut nearly eliminates the recirculation region in the upper corner. However, a weak back-flow region still prevails in the lower corner of the dump region.

A comparison of the flow patterns in the combustor annuli in the three planes considered clearly shows the three-dimensional nature of the flow. In the symmetry plane between the fuel nozzles, the flow acceleration around the cowls results in larger velocities near the combustor walls in both annuli. In the other two planes, similar behavior is observed in the inner annulus. However, as a result of the flow redistribution caused by the presence of various blockages, lower liner cold-side scrubbing velocities are encountered in the outer annulus.

The three-dimensional nature of the flow is more clearly evident from secondary flow patterns in various azimuthal $(r\text{-}\theta)$ planes. Figure 8(a) shows the flow pattern in a plane, through the strut, slightly upstream of the prediffuser exit. The flow within the prediffuser is primarily directed radially outward. In the upper dump region, the flow is directed outward near the strut and inward along the symmetry lines. The trend is reversed in the lower dump region. Also, the secondary flow is stronger in the lower dump region than in the upper one.

Figure 8(b) shows the crossflow pattern in an $(r\text{-}\theta)$ plane downstream of the prediffuser exit. This particular plane contains the fuel nozzle stems. The flow in this plane is predominantly radial. Near the lower part of the stem, the flow is directed radially outward. The fluid has a tendency to rush toward the gap originally occupied by the strut at the upstream locations. As the flow proceeds downstream, a similar pattern is also noticed in the regions occupied by the fuel nozzle stems.

The flow pattern in a representative plane through the combustor dome is presented in Fig. 8(c). The blocked-off regions in this plane correspond to the fuel nozzle tips. Globally, the fluid still has a tendency to flow toward the center region. This is a residual effect of the motion created upstream to fill the void created by the removal of the strut. A similar flow pattern caused by the presence of the fuel nozzle stems is evident in the outer annulus.

Static Pressure Distribution. In this section static pressure distributions on some representative planes are presented in the form of constant pressure contours. In each plot, the minimum value of the static pressure and the increment in the pressure levels, in Pascals, are indicated. The pressure levels are calculated with reference to the lowermost grid point at

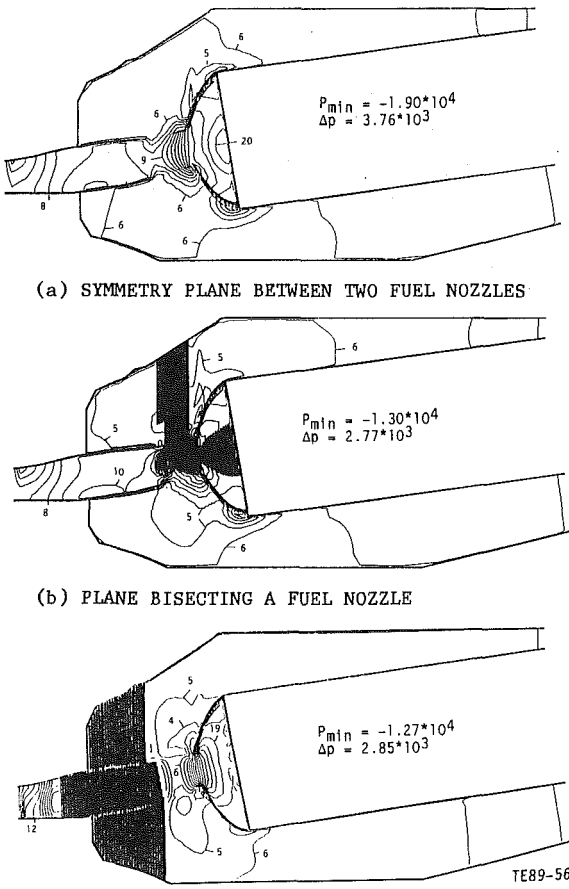

Fig. 9 Static pressure distributions in axial planes

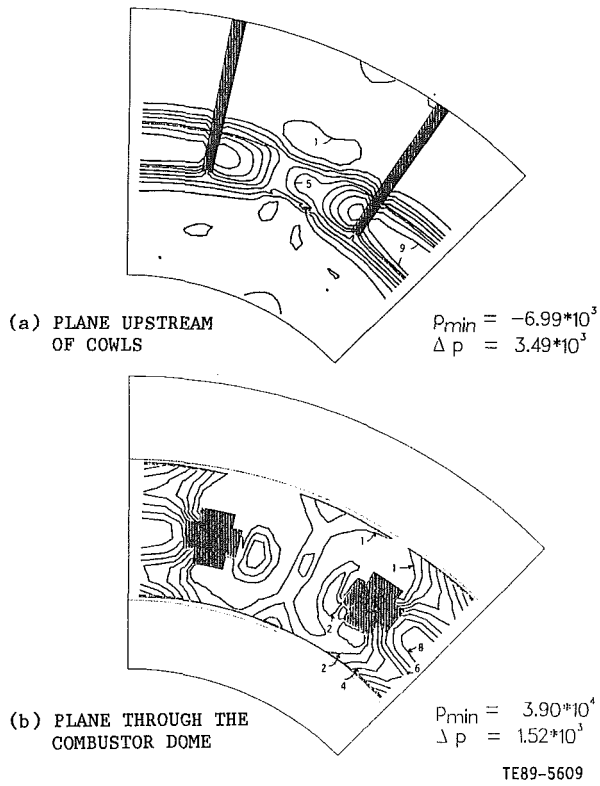

Fig. 10 Static pressure distributions in azimuthal planes

the prediffuser inlet. In the subsequent figures, the numeral associated with a contour line designates the number of pressure increments above the minimum level indicated.

Figure 9(*a*) shows the static pressure distribution on a plane midway between two fuel nozzles. In conformance with the flow field characteristics, the pressure distribution on this plane is also very similar to that predicted by the axisymmetric simulation. In the prediffuser, however, there is significant pressure variation in the radial direction; lower pressure recoveries are predicted along the region near the upper wall.

The static pressure distribution on the (x–r) plane bisecting the fuel nozzle is shown in Fig. 9(*b*). The predicted behavior in the prediffuser is only slightly different from that observed in the plane between the fuel nozzles. A region of high pressure is created upstream of the fuel nozzle stem as the flow experiences deceleration. The presence of the stem also modifies the pressure distribution around the cowling.

Figure 9(*c*) shows the pressure distribution on the axial plane bisecting the strut. The wake region behind the strut represents an area of low pressure. The pressure levels in the dome for the plane containing the strut are lower than those predicted in the plane midway between the fuel nozzles. The pressure in the prediffuser is nearly uniform in the radial direction. However, there is a substantial circumferential nonuniformity in pressure caused by the presence of the strut. A stagnation region is formed at its leading edge and the effect is propagated upstream. Also, wakes are formed at the trailing edge of the strut that will lead to further nonuniformities in pressure. The presence of fuel nozzles has similar effect on the pressure distribution. A better understanding of the circumferential variation of pressure can be obtained by discussing the pressure distributions in various azimuthal (r–θ) planes.

Figure 10(*a*) shows the pressure variation on an (r–θ) plane just upstream of the cowls. This particular plane contains the fuel nozzle stems. The low-pressure region midway between the stems is caused by the strut wake. In this plane, the pressure nonuniformity in the circumferential direction is equivalent to 65 percent of the inlet dynamic head.

Figure 10(*b*) shows the pressure distribution on a plane just upstream of the combustor dome. The blocked-off regions in this plane simulate the fuel nozzle tips. The calculations reveal that the circumferential pressure variation is about 25 percent of the inlet dynamic head. It should be noted that one half (180-deg sector) of the fuel nozzle is subjected to low pressures, while the other half is exposed to a region of high pressure. The resulting nonuniform airflow distribution through the fuel nozzles and dome swirlers can significantly affect the combustor exit temperature quality. Specifically, this dome pressure distribution is expected to give eight local high-temperature peaks corresponding to each of the eight support struts.

Adequacy of the Axisymmetric Simulation. The results of the full three-dimensional simulation presented above provide a basis for assessing the validity of the simplified axisymmetric approach for combustor diffuser flow analysis.

The flow characteristics from the axisymmetric simulation are qualitatively similar to those predicted by the three-dimensional analysis on the plane midway between the fuel nozzles. The inclusion of various blockages in the three-dimensional simulation causes a reduction in the strength and extent of the recirculation zones in the dump region as compared to the axisymmetric case. The axisymmetric simulation cannot predict the circumferential variation in the flow field. The three-dimensional simulation reveals that struts and fuel nozzles modify the flow field significantly. The nonaxisymmetric effects are prominent in the region downstream of the struts and in the annuli. Such behavior has important implications regarding the liner hot streaks and burner exit temperature profile.

The estimates provided by the simplified model for static pressure recovery and total pressure losses are within 10 to 15 percent of the experimental data. The uncertainty in the predicted airflow distribution around the combustor is expected to be less than 10 percent. The pressure nonuniformity in the circumferential direction leads to uneven airflow rates through the liner air orifices, swirlers, and cooling slots/configurations. Although the axisymmetric diffuser-combustor analysis is adequate for most applications, full simulation is necessary for accurate predictions of three-dimensional processes including hot streaks and pattern factor.

Concluding Remarks

In this paper, a computational procedure for diffuser-combustor flow interaction analysis has been presented. The procedure is based on the solution of the Navier–Stokes equations on a body-conforming grid. The turbulence effects are simulated using the high Reynolds number form of the k–ϵ model. The calculation method has been applied to a practical configuration that includes support struts and fuel nozzles. Results have been reported for a simplified axisymmetric simulation and a full three-dimensional simulation. The simplified analysis, restricted to a median plane, provides a flow structure that is a good representation of the three-dimensional flow. The resulting estimates for the static pressure recovery agree with the experimental data to within 15 percent.

The results of the full simulation provide an insight into the three-dimensional nature of the flow. The presence of struts and fuel nozzles results in significant nonaxisymmetric effects in the flow. For the configuration considered in this paper, the calculations indicate that the primary orifices operate properly, but the flow distribution through the dome swirlers is nonuniform.

References

Ando, Y., Kawai, M., Sato, Y., and Toh, H., 1986, "Numerical Calculations of Turbulent Flows in a Dump Diffuser," AIAA Paper No. 86-1656.

Karki, K. C., 1986; "A Calculation Procedure for Viscous Flows at All Speeds in Complex Geometries," Ph.D. thesis, Department of Mechanical Engineering, University of Minnesota, Minneapolis, MN.

Karki, K. C., and Patankar, S. V., 1986, "Use of Subdomains for Flow Computations in Complex Geometries," in: *Numerical Methods in Heat Transfer*, J. L. S. Chen and K. Vafai, eds., ASME, New York, pp. 7-12.

Karki, K. C., and Patankar, S. V., 1988, "Calculation Procedure for Viscous Incompressible Flows in Complex Geometries," *Numerical Heat Transfer*, Vol. 14, pp. 295–307.

Launder, B. E., and Spalding, D. B., 1974, "The Numerical Computation of Turbulent Flows," *Computer Methods in Applied Mechanics and Engineering*, Vol. 3, pp. 269–289.

McGuirk, J. J., and Whitelaw, J. H., 1984, "Internal Flows of Relevance to Gas Turbines," in: *Computation of Internal Flows: Methods and Applications*, P. M. Sockol and K. N. Ghia, eds., ASME, New York, pp. 37–52.

Oechsle, V. L., Mongia, H. C., and Karki, K. C., 1989, "A Design Methodology for Dump Diffusers," Internal Report, Allison Gas Turbine Division, General Motors Corporation, Indianapolis, IN.

Patankar, S. V., 1980, *Numerical Heat Transfer and Fluid Flow*, Hemisphere, Washington, DC.

Rodi, W., and Scheuerer, G., 1986, "Scrutinizing the k–ϵ Turbulence Model Under Adverse Pressure Gradient Conditions," ASME *Journal of Fluids Engineering*, Vol. 108, pp. 174–179.

Shyy, W., 1985, "A Numerical Study of Annular Dump Diffuser Flows," *Computer Methods in Applied Mechanics and Engineering*, Vol. 53, pp. 47–65.

R. C. Adkins

M. H. Wardle

School of Mechanical Engineering,
Cranfield Institute of Technology,
Cranfield, Bedfordshire, United Kingdom

A Method for the Design of Optimum Annular Diffusers of Canted Configuration

A simple method is presented for the design of annular diffusers that can take into account the effects of compressibility and of canted configurations by use of the area bisector line. No complex boundary layer calculations are required.

Preliminary Diffuser Design

Two situations occur during engine design when it is essential to have diffuser dimensions and contours close to their optimum. The first arises during the process of initial layout of the engine when an accurate assessment of diffuser dimensions helps to ensure that a practical configuration is reached. The second occurs during the final stages of design when a near-optimized diffuser design considerably speeds up any iterations made using computational fluid dynamics (CFD) analysis. It is unlikely that the designer will be fortunate in finding an appropriate diffuser chart to assist him with these tasks due to the infinite variation in configurations of annular diffusers.

A simple method of diffuser design that addressed these problems was presented by Adkins (1983) following experimental verification by Sherras (1980) and Guidicelli and Vuillot (1981). More recently, however, combustors with high inlet Mach numbers and canted axes in which the general flow direction is no longer parallel to the engine axis have become more commonplace. These developments have thus prompted this update of the original method.

Summary of Basic Design Method

In order to ensure simplicity, the original design method uses a one-dimensional approach and avoids boundary layer calculations by the introduction of a nondimensional parameter, termed the "G" parameter. This parameter is defined as the ratio of local pressure gradients, namely the streamwise adverse gradient of static pressure and the transverse gradient of dynamic pressure. The former is the cause of diffuser failure due to flow separation whereas the latter motivates the flow of energy to the wall and hence serves to inhibit the separation of flow. As such it will be appreciated that a correct balance between these two gradients (and hence value of G) will produce an optimum diffuser.

The G parameter can be defined in mathematical terms as follows:

$$G = (dp/dx)/(q/y) \tag{1}$$

where: p = static pressure; x = streamwise distance; q = dynamic pressure in the free stream; y = distance between free stream and wall.

A number of simplifying assumptions were made in order to evaluate optimum values of G. Firstly it was argued that diffusers in gas turbine engines operate at such high flow rates that they avoid Reynolds number dependence. In these circumstances boundary layer thickness, y, will be almost completely dependent upon geometric configuration and so is directly proportional to the local hydraulic diameter, Dh, defined as:

$$Dh = 4 \cdot \frac{\text{cross-sectional area}}{\text{wetted perimeter}}$$

It was further argued that the term, dp/q, is in essence the static pressure coefficient of a local element of the diffuser. It can therefore be represented by the theoretically ideal value of $d(Cpi)$, where for incompressible flow:

$$d(Cpi) = 1 - (A_n/A_{n+1})^2 \tag{2}$$

where A_{n+1}/A_n is the area ratio of the element. The parameter, G, can now be expressed in a simpler form as:

$$G = Dh \cdot d(Cpi)/dx \tag{3}$$

Here, the right-hand side of the equation is entirely a function of geometry.

Conical diffusers are widely recognized as being the most aerodynamically efficient form of straight-walled diffuser. Furthermore they are peculiar in that the value of G remains constant down their length and this is at a value of:

$$G = 8 \cdot \tan(\phi) \tag{4}$$

where ϕ is the half angle of the cone.

The relationship between G and area ratio for annular diffusers is more complex and depends upon the angles made between both walls and the major axis and upon the local ratio of inner to outer diameter, r.

$$G = \frac{8 \cdot (\tan \phi_o - r \cdot \tan \phi_i)}{1 + r} \tag{5}$$

Here ϕ_o denotes the half angle of the outer wall; ϕ_i denotes the half angle of the inner wall.

Contributed by the International Gas Turbine Institute and presented at the 35th International Gas Turbine and Aeroengine Congress and Exposition, Brussels, Belgium, June 11–14, 1990. Manuscript received by the International Gas Turbine Institute January 10, 1990. Paper No. 90-GT-52.

Basically the design procedure is used to develop the streamwise wall profiles of an annular diffuser by maintaining the value of G at some optimum constant value.

The value for G depends, to some extent, upon the application. Typical of these is the requirement in gas turbine engines to keep diffuser length to a minimum while producing the maximum level of static pressure recovery within that length. Such diffusers are called *Cp* diffusers and one of their features is that the divergence angle between walls is an inverse and complex function of overall area ratio.

The value of nondimensional pressure gradient for *Cp** diffusers have accordingly been denoted by G^*. From the paragraphs above it follows that a similar relationship exists between G^* and area ratio as that between divergence angle and area ratio. This relationship was determined using standard charts derived from conical diffuser tests using incompressible flow and was given (Adkins, 1983) as:

$$G^* = [0.915(AR_o)^{1.424} - 1]^{-0.5} \qquad (6a)$$

An alternative equation has recently been developed by Wardle (1989) that is more accurate and is applicable over the range $1 < AR_o < 6$; this is given as:

$$G^* = 0.1487 \cdot [\tan((6 - AR_o) \cdot \pi/10)]^{0.987} + 0.36 \qquad (6b)$$

Both Eqs. (*6a*) and (*6b*) make use of empirical data to relate the ideal performance of the diffuser to the actual one and so make the necessary adjustments for real effects, such as boundary layer growth, without the need for complex calculations.

Having obtained the relevant value of G^* from either of Eqs. (6), it was shown how this can be used to design the diffuser. The flow was considered as one dimensional and incompressible and it was assumed that any inclination to the major axis would only be slight. It was necessary to define either the inner or outer wall of the diffuser, the unknown wall then being derived using a step by step routine. The simplest category of design was when the overall area ratio could be specified, then G^* could be obtained directly from Eq. (6). Alternatively, if the overall length was specified, then an estimate of area ratio was necessary, followed by an iterative procedure, which converged when a compatible combination of area ratio and length was obtained.

The Effects of Compressibility

Some confusion exists on the influence of compressibility due to conflicting experimental data taken from a straight-walled, conical diffuser. Dolan and Runstadler (1973) showed that values of pressure recovery increased with Mach number until well into the transonic flow regime. Livesey and Odukwe (1973), on the other hand, showed that values of *Cp* only increase until a Mach number of around 0.65 is achieved. After this there is a progressively rapid and significant deterioration in diffuser performance with an apparent onset of choking at a Mach number of less than unity.

It is suggested here that this major difference in findings arises from Dolan and Runstadler's use of an aerodynamic throat as the datum from which they assessed pressure recovery. This datum shifted along the axis according to inlet conditions and would have been at the trough of a depression created by the diffuser in its inlet region or just downstream. Assessment of pressure rise from this trough would therefore have resulted in highly optimistic values of pressure recovery coefficient. Livesey and Odukwe, in their experiments, made use of the more conventional pressure datum, which was located just upstream of the diffuser and would thus have avoided any misleading effect arising from depressions in the inlet region.

The following arguments are suggested by the present authors in support of Livesey and Odukwe's findings:

From continuity of mass flow it can be shown that:

$$v = \frac{m}{\rho \cdot A}$$

With compressible flow both area, A, and density, ρ, increase with passage down the diffuser so that the reduction in velocity, v, will be greater than in the case of incompressible flow where only the cross-sectional area increases. It therefore follows that the pressure recovery coefficient should also be greater. A potentially detrimental effect arises from this because the corresponding increase in adverse pressure gradient will not be supported by an increase in transverse energy gradient and so G, the ratio of the two gradients, increases. The diffuser then becomes more susceptible to flow separation.

The effect of inlet Mach number upon ideal values of *Cp* (i.e., *Cpi*) has been computed and the results are shown in Fig. 1. Here it is shown that the rate of increase in values of *Cp* is not rapid until Mach numbers of 0.6 have been exceeded and then the effect is most pronounced when area ratios are low. These low area ratios correspond to the diffuser inlet region and flow separation would therefore occur here as a result of the predicted increase in adverse pressure gradient caused by the higher subsonic inlet Mach numbers, thereby supporting the Livesey and Odukwe data.

Furthermore, this onset of flow separation at diffuser inlet would cause the flow stream to accelerate and so deepen the level of depression at the aerodynamic throat, thereby supporting the hypothesis that the data of Dolan and Runstadler could be misleading.

From the above argument it follows that two modifications should be made to diffusers if they are to operate at high subsonic Mach numbers. First, for a given geometric area ratio, they must be made longer than the lengths suggested by diffuser charts derived from tests using incompressible flow. This modification is necessary because of the enhancement in overall static pressure recovery. It can be implemented by the derivation of an equivalent area ratio, *Ae*, that would have been necessary to produce an identical value of *Cpi* if the flow had been incompressible. This value, *Ae*, is also used for determining the value of G^* from Eq. (6).

Second, the wall divergence angle must be reduced in order

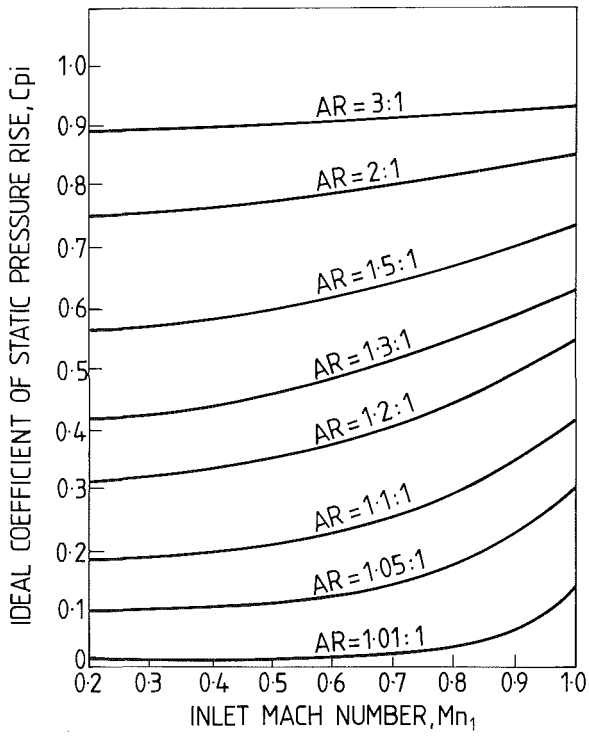

Fig. 1 Relationship between *Cpi* and Mach number

to counteract the effects of compressibility in increasing the adverse pressure gradient. This is of particular importance at diffuser inlet if the Mach number in this region is likely to exceed 0.60. Diffusers taking account of this effect would therefore adopt a trumpet shape. The design procedure relating to these two modifications is given in the following paragraphs.

The Overall Effect of Compressibility

For the purpose of simplicity it is necessary to assume that the flow is both isentropic and adiabatic; this enables direct use of the two equations for ideal compressible flow, viz.:

$$P/p = [1 + M^2 \cdot (\gamma - 1)/2]^{\gamma/(\gamma-1)} \tag{7}$$

$$A/A^* = M \cdot \left[\frac{[1 + (\gamma - 1)/2]}{[1 + M^2 \cdot (\gamma - 1)/2]}\right]^{(\gamma+1)/2/(\gamma-1)} \tag{8}$$

where M = Mach number; γ = ratio of specific heats.

Equation (8) can be used to derive an expression for the exit Mach number, say at plane 2, where:

$$M_2 = \frac{M1}{AR} \cdot \left[\frac{1 + M2^2 \cdot (\gamma - 1)/2}{1 + M1^2 \cdot (\gamma - 1)/2}\right]^{(\gamma+1)/2/(\gamma-1)} \tag{9}$$

(n.b.: Equation (9) is solved by iteration.)

The definition for *Cp* in compressible flow can be written as:

$$Cp_{\text{compressible}} = \frac{p_2 - p_1}{P_1 - p_1}$$

Ideally the flow would be isentropic so that *P* remains constant down the diffuser (i.e., $P_1 = P_2$); then dividing both numerator and denominator by *P* gives:

$$Cpi_{\text{compressible}} = \frac{(P/p_2)^{-1} - (P/p_1)^{-1}}{1 - (P/p_1)^{-1}} \tag{10}$$

This can be determined when the inlet Mach number, M_1, and area ratio, *AR*, are given. The two pressure ratios, namely P/p_1 and P/p_2, can then be obtained from Eqs. (7) and (9) as appropriate, enabling use of Eq. (10) to calculate *Cpi*. For incompressible flow the ideal value of *Cp* is a simple function of area ratio where:

$$Cpi_{\text{incompressible}} = 1 - (AR)^{-2} \tag{11}$$

Equating Eqs. (10) and (11) for *Cp* in order to evaluate the equivalent area ratio, AR_e, for incompressible flow gives:

$$AR_e = (1 - Cpi_{\text{compressible}})^{-0.5} \tag{12}$$

This equivalent, incompressible area ratio is used in conjunction with Eq. (6) to obtain the value of G^*, which is to be used for the compressible flow design. It can also be used to obtain a first estimate of diffuser length from standard diffuser charts, which are based upon incompressible flow.

Effect of Compressibility Upon Wall Design

As previously discussed, the design of diffuser walls is achieved by using a step-by-step or "marching" method where small elements of diffuser are considered in sequence. It was recommended that the length of each element, *s*, should be on the order of 2 percent of the hydraulic diameter when assessed at diffuser inlet.

The area ratio of each element, in turn, is obtained from the use of Eq. (3) after replacing the term, *dx*, by the finite length, *s*. After rearrangement this equation then gives an expression for ideal pressure recovery generalized by considering the *n*th element along the diffuser, where:

$$(Cpi)_n = G^* \cdot s/Dh_n \tag{13}$$

Here all the terms on the right-hand side are known so that the ideal pressure recovery of the element can be determined. Following this a rearrangement of Eq. (10) gives an expression for the pressure ratio at diffuser exit, viz.:

$$(P/p_2)^{-1} = Cp \cdot [1 - (P/p_1)^{-1}] + (P/p_1)^{-1} \tag{14}$$

The theoretical Mach number at exit of the diffuser element can then be calculated from a rearranged version of Eq. (7) where:

$$M_2 = \{[(P/p_2)^{(\gamma-1)/\gamma} - 1] \cdot 2/(\gamma -)\}^{0.5} \tag{15}$$

An expression for area ratio of this element of diffuser can now be derived by applying Eq. (9) to both the inlet and exit of the elemental diffuser and taking their ratio, viz.:

$$AR_{\text{element}} = \frac{M_2}{M_1} \cdot \left[\frac{1 + M_1^2 \cdot (\gamma - 1)/2}{1 + M_2^2 \cdot (\gamma - 1)/2}\right]^{(\gamma+1)/2/(\gamma-1)} \tag{16}$$

By knowing the dimensions at inlet to the element, it is thus possible to calculate those at its exit, and hence proceed to the next element.

Use of the Area Bisector for Canted Diffusers

In the original design method the *G* parameter was used in conjunction with a known diffuser wall in order to generate the profile of the second wall. In canted diffusers, however, divergence angles and wall curvatures can become significantly larger so that the assumption of one-dimensional flow is invalidated. The situation can be much improved, however, by using the area bisector of the annular passage instead of one of the walls. If the flow velocity is uniform across the duct, then there would be no flow crossing this area bisector line, and so the flow would be quasi-one-dimensional in this region. Furthermore, since the angle made between the area bisecting line and each wall is around one-half that made between the walls themselves then any deviation from one dimensionality will be significantly reduced.

Although specification of the area mean streamline may be thought of as an unusual requirement, knowledge of its position is advantageous to the combustor designer to control air distribution between inner and outer liner feed passages.

At diffuser inlet it is usual to know the radii of both the outer and inner casings, Ro_1 and Ri_1, respectively, as these will coincide with the exit dimensions of the engine component (compressor) located immediately upstream. The radius of the area bisecting line, *Rm*, at this section 1, with reference to the engine axis, is then given by:

$$Rm_1 = [(Ro_1^2 + Ri_1^2)/2]^{0.5} \tag{17}$$

The local streamwise radius of curvature of this area bisector, Rc_1, together with its center of curvature, will either be given or can be calculated from the form of the profile. It is unlikely that this radius will be subtended from the engine axis. Figure 2 illustrates such an arrangement where the center of curvature is at a distance, e_1, below the engine axis, here:

$$e_1 = Ro_1 - Rm_1$$

and

$$Dh_1 = 2 \cdot (Ro_1 - Ri_1)$$

Use can then be made of Eqs. (18)–(21), which were derived from the generalized elements *n* shown in Fig. 3, which are described as follows:

Flow area, A_n, through annular section subtending angle θ_n to the perpendicular through the engine axis:

$$A_n = \frac{2 \cdot \pi}{\cos \theta_n} \int_{Ri}^{Ro} r \cdot dr = \frac{\pi}{\cos \theta_n} \cdot [Ro_n^2 - Ri_n^2] \tag{18}$$

For half of the annular cross-sectional area:

$$A_n/2 = \frac{2 \cdot \pi}{\cos \theta_n} \int_{Ri}^{Ro} r \cdot dr = \frac{\pi}{\cos \theta_n} \cdot [Ro_n^2 - Rm_n^2] \tag{19}$$

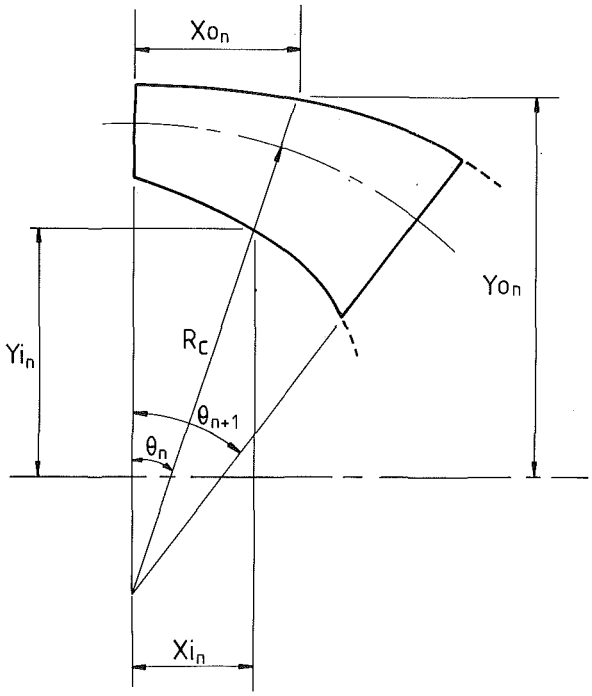

Fig. 2 Geometry at diffuser inlet

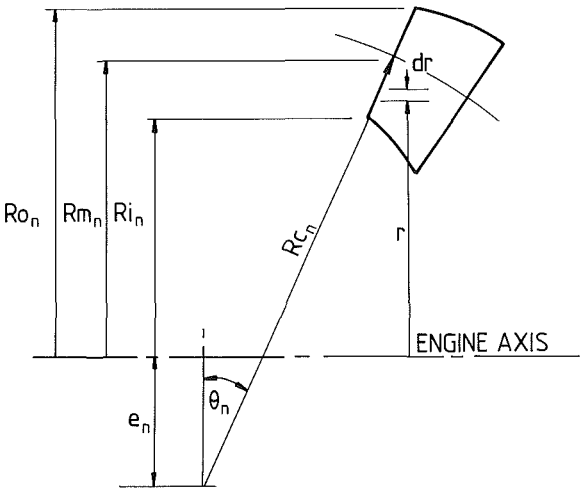

Fig. 3 Geometry at *n*th element

From (19):

$$Ro_n = \left[\frac{A_n \cdot \cos\theta_n}{2 \cdot \pi} + Rm_n^2 \right]^{0.5} \tag{20}$$

From (18):

$$Ri_n = (Ro_n^2 - A_n \cdot \cos\theta_n / \pi)^{0.5} \tag{21}$$

Coordinate geometry can then be used directly in order to determine the Cartesian coordinates of both the inner and outer walls. By way of an example these are given for a typical case, when the streamwise profile of the area bisector generator follows a circular arc, as sketched in Fig. 4.

In this particular instance:

$$Xo_n = Rc \cdot \sin\theta_n + [Ro_n - Rc \cdot \cos\theta_n - e] \cdot \tan\theta_n$$

$$Yo_n = Ro_n$$

$$Xi_n = Rc \cdot \sin\theta_n - [Rc \cdot \cos\theta_n - e - Ri_n] \cdot \tan\theta_n$$

$$Yi_n = Ri_n$$

Other configurations are likely to require a greater manipulation of the coordinate geometry and are not included in the scope of the present paper.

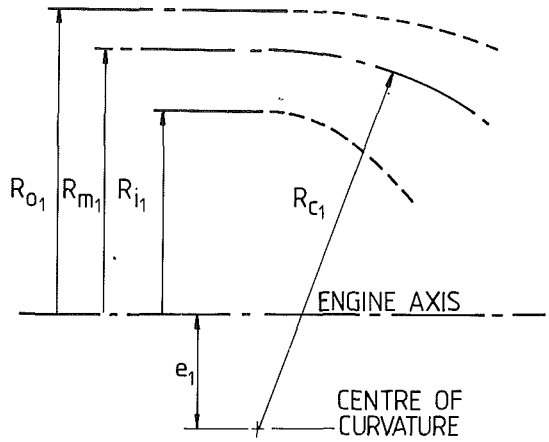

Fig. 4 Area bisector of constant curvature *Rc*

The hydraulic diameter is given by:

$$Dh_n = 2 \cdot A_n / \{\pi \cdot (Ro_n + Ri_n)\} \tag{22}$$

The angle at the inlet to the next element is then given by:

$$\theta_{n+1} = \frac{s}{Rc} + \theta_n \tag{23}$$

The new local radius of curvature, together with the position for the center of curvature, must be obtained from knowledge of the profile of the area dividing line.

Limitations of the Design Method

As previously intimated, the method can only be considered as approximate. In addition to the deviation from one dimensionality there are other important factors to be considered with respect to boundary layer development.

The empirical relationships of Eqs. (6) were derived from data taken from straight-walled, conical diffusers. As such, the wall circumference increased with distance along the diffuser and thereby produced a thinning influence on the boundary layer. This is not always the situation in annular diffusers. In particular, when annular diffusers are canted toward the engine axis, the circumference of the inner wall decreases and this has a thickening rather than a thinning influence on the boundary layer.

Wall curvature is also known to influence boundary layer development. Convex curvature on the inner annular wall will "stabilize" the boundary layer such that it tends toward relaminarization. Such a boundary layer is less able to compete against an adverse pressure gradient. On an outer wall with concave curvature, however, boundary layer adhesion is likely to be improved by the presence of Gortler-type vortices.

It is common for convex curvature on the inner wall to increase with distance along the diffuser. This will have the effect of reducing the static pressure recovery near this wall and a problem could arise at the diffuser exit. If the pressure recovery here is significantly less than that on the outer wall then flow separation could result.

It is apparent that although the proposed method is useful for initial and intermediate stages of design, full three-dimensional computational flow analysis should be used as a final stage, particularly in cases where curvature is severe.

References

Adkins, R. C., 1983, "A Simple Method for Designing Optimum Annular Diffusers," ASME Paper No. 83-GT-42.

Dolan, F., and Runstadler, P., 1973, "Pressure Recovery Performance of Conical Diffusers at High Subsonic Mach Numbers," NASA CR-2299.

Guidicelli, A., and Vuillot, F., 1991, "Design of Minimum Length Diffusers,"

Report from School of Mechanical Engineering, Cranfield Institute of Technology/Ecole Nationale Superieure de l'Aeronautique et de l'Espace, Toulouse, France.

Livesey, J., and Odukwe, A., 1973, "Some Effect of Pipe Flow Generated Entry Conditions on the Performance of Straight Walled Conical Diffusers With High Subsonic Entry Mach Number," *Israel Journal of Tech.*, Vol. 11, No. 4.

Sherras, B. R., 1980, "An Investigation of the G Parameter for Design of Annular Diffusers," M.Sc. Thesis, School of Mechanical Engineering, Cranfield Institute of Technology, United Kingdom.

Wardle, M., 1989, "A Simple Design Method for Annular and Radial Diffusers," M.Sc. Thesis, School of Mechanical Engineering, Cranfield Institute of Technology, United Kingdom.

G. J. Sturgess

D. G. Sloan

Pratt & Whitney,
East Hartford, CT 06108

A. L. Lesmerises
WRDC/POSF,
Wright-Patterson AFB, OH 45433

S. P. Heneghan

D. R. Ballal

University of Dayton,
Dayton, OH 45429

Design and Development of a Research Combustor for Lean Blow-Out Studies

In a modern aircraft gas turbine combustor, the phenomenon of lean blow-out (LBO) is of major concern. To understand the physical processes involved in LBO, a research combustor was designed and developed specifically to reproduce recirculation patterns and LBO processes that occur in a real gas turbine combustor. A total of eight leading design criteria were established for the research combustor. This paper discusses the combustor design constraints, aerothermochemical design, choice of combustor configurations, combustor sizing, mechanical design, combustor light-off, and combustor acoustic considerations that went into the final design and fabrication. Tests on this combustor reveal a complex sequence of events such as flame lift-off, intermittency, and onset of axial flame instability leading to lean blowout. The combustor operates satisfactorily and is yielding benchmark quality data for validating and refining computer models for predicting LBO in real engine combustors.

Introduction

The provision of adequate stability in aircraft gas turbine combustors is a long-term problem that is exacerbated by several current design trends. Of particular concern is the phenomenon of lean blow-out (LBO). The solution to this problem is made difficult by deficiencies in present calculation methods and by conflicting design criteria. A joint U.S. Air Force, industry, and university research program is being carried out to improve the understanding of the physical processes involved in LBO and also the calculation procedures used. Recently, Sturgess et al. (1989) have provided a broad description of this overall program.

In a modern annular gas turbine combustor, flame is stabilized by producing a recirculation zone in the flow field. This zone is generated by a combination of *three* mechanisms, namely: an axial swirling air jet associated with each fuel introduction, sudden expansion of the axial swirling jets as they enter the primary zone, and back-pressure provided by an array of radial air jets at the end of the primary zone. The recirculation zone itself serves a *triple* purpose of: (*i*) producing a region of low velocity, (*ii*) providing high residence time for the flame to propagate into the incoming fresh mixture, and (*iii*) serving as a source of continuous ignition for the combustible fuel–air mixture.

To obtain low exhaust emissions, Pratt & Whitney currently tailors the combustor flow control mechanisms to produce an "inside-out" recirculation pattern, illustrated in Fig. 1. Therefore, the research combustor was required to reproduce this type of recirculation pattern. At the same time, it had to provide stable combustion over a wide variation in its loading, be geometrically simple for ease of experimentation and computation, and provide adequate optical access for measurements.

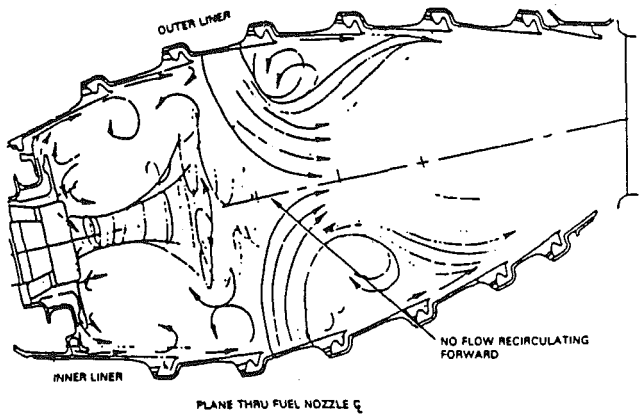

Fig. 1 Flow patterns in a modern annular combustor showing swirl and recirculation dominating the "inside-out" primary zone

Design Criteria

The following were established as the leading criteria to satisfy the above design requirements:

1 Introduce fuel and air separately to produce a turbulent diffusion flame.

2 Have geometric simplicity so that accuracy of CFD modeling is not affected by the combustor shape representation.

Contributed by the International Gas Turbine Institute and presented at the 35th International Gas Turbine and Aeroengine Congress and Exposition, Brussels, Belgium, June 11–14, 1990. Manuscript received by the International Gas Turbine Institute January 16, 1990. Paper No. 90-GT-143.

3 Be two-dimensional to minimize the cost of CFD modeling, and to simplify measurements and their interpretation.

4 Have well-defined boundary conditions so these may be correctly represented in CFD modeling.

5 Contain the flame fully near blow-out conditions for all loadings that should be achieved without recourse to exotic operating conditions.

6 Avoid flow field interference and nonstationary behavior due to acoustic resonance.

7 Provide good optical access for flow visualization and laser diagnostics.

8 Be inexpensive to manufacture and operate, but have structural robustness and durability.

These criteria contain several potential conflicts and indeed, simultaneous satisfaction of all criteria without some compromises proved not to be possible.

Design Constraints

The research combustor was to be operated in the Fundamental Combustion Laboratory of the U.S. Air Force, Wright Research and Development Center, Aero Propulsion and Power Laboratory, W-PAFB, Ohio. A layout and a detailed description of this laboratory are given by Ballal et al. (1987).

The research combustor was mounted vertically on the laboratory burner, which is bolted to a traverse platform capable of a vertical movement of 61 cm and a horizontal movement of 23 cm in each of the other two directions. An exhaust hood is located directly above the combustor exit section. A three-component LDA system for velocity measurements and a CARS system for flame temperature measurements are arranged on two separate 1.22 m × 2.44 m optics tables on either side of the combustor. By moving the combustor relative to the fixed optical diagnostics, the complexity of the optical arrangement is minimized. Of course, this imposes constraints on the combustor design. For example, the combustor dimensions must be chosen such that the scale of events of interest taking place inside the combustor is within the traverse distance of the platform. Similarly, the requirement to have the base of the combustor in line with the height of the laser beams above the optics table and the location of the exhaust hood above the optics table places a restriction on the maximum length of the combustor. Finally, the combustor has to pass through a 40 cm × 40 cm square cut-out in the breadboard optical bench that carries the LDA-CARS optics and also binds the other two optics tables.

Air was supplied to the combustor in the 510 kg/h to 4900 kg/h range at atmospheric pressure. The combustion laboratory provides gaseous propane and methane fuels. For propane, flow rates beyond 20 kg/h are difficult to obtain due to limitations of the facility. This fuel flow rate limit imposes additional constraints on the combustor design.

Aerothermochemical Design

At the outset, use of swirl generators was ruled out for establishing a recirculating flow field because Sturgess et al. (1986) found that they produce complex inlet boundary conditions for CFD codes and current turbulence modeling calculates swirling flows inaccurately (Sturgess and Syed, 1985). Also, Gupta et al. (1984) observe that a strongly swirling central jet induces exit flow into a combustor and produces precessing vortex cores. Therefore, jet expansion was used to generate the inside-out recirculation.

The jet expansion arrangement consists of a central gaseous fuel jet surrounded by a coflowing annular air jet. Both jets suddenly expand into a confinement that is symmetric about the jet axes. This configuration, which can be either planar or axisymmetric, represents a single sector of a practical annular combustor rather well. The back-pressure effects produced by the transverse air jets in a real combustor had to be considered for the research combustor as well. Individual air jets are three dimensional and do not provide the required uniformity. Therefore, the back-pressure effect was simulated by restricting the outlet from the research combustor by means of an orifice plate. This restriction was sufficiently far downstream from the sudden expansion that the step-recirculation zones were not affected.

In this research combustor, gaseous hydrocarbon fuel was burned because its chemistry resembles that of vaporized JP fuels. The choice between propane and methane was made based upon their peak flame temperatures, transition Reynolds numbers, flame lengths, lift-off heights, and blow-out characteristics.

Peak flame temperatures were important because the annealing temperature limit for fused quartz window is approximately 1450 K. Since, heat release would be confined to the central portion of the combustor, it seemed feasible to operate the combustor at 1700 K corresponding to $\phi = 0.6$ for propane–air mixture. This value of ϕ represents LBO conditions similar to well-stirred reactor performance (see Clarke et al., 1958).

Since the research combustor must operate in the fully developed turbulent region, the critical transitional Reynolds numbers for propane and methane fuel jets were obtained from Hottell and Hawthorne (1949) as 10,000 and 3000, respectively. Flame length is important because the combustor must confine the flame. For enclosed flames, Beer and Chigier (1972) and Lenze (1982) have shown that the flame length depends on the Thring–Newby criterion θ, and the excess air ratio, λ. Figure 2 shows a plot of flame length ratio L/L_f versus $1/\theta$.

Now, for $\phi = 0.6$, and $\lambda = 1.7$, the maximum flame length $L/L_f = 1.3$ occurs for zero recirculation (i.e., when $\theta < 1$). This condition determines maximum combustor length = 200 and 296 fuel jet passage heights for propane and methane respectively.

When conditions for critical Reynolds numbers, maximum propane flow rate, and maximum flame length are combined, the required combustor length for both fuels exceeds the available space in the facility. Therefore, recirculation ($1/\theta > 1.0$) becomes a prerequisite. At $\phi = 0.6$, less recirculation is re-

Nomenclature

B = blockage ratio
D = flameholder diameter
d = diameter
h = height
L = length
$\dot{m}$ = mass flow
p = pressure
r = radius
T = temperature
Tu = mainstream turbulence intensity
U = mean velocity
x, y, z = directions
θ = Thring–Newby parameter
λ = excess air ratio
ρ = density
ϕ = equivalence ratio

Subscripts

a = air, annulus
c = combustor
f = flame, fuel tube
FAR = fuel air ratio
i = equivalent fuel–air supply passage
LBO = lean blow-out
s = step, air passage radius

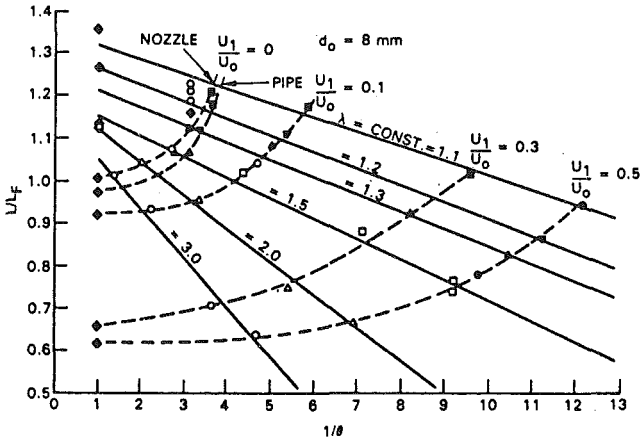

Fig. 2 Flame length ratio as a function of reciprocal Thring-Newby criterion for various values of excess air ratio for an enclosed, natural gas flame (Lenze, 1982)

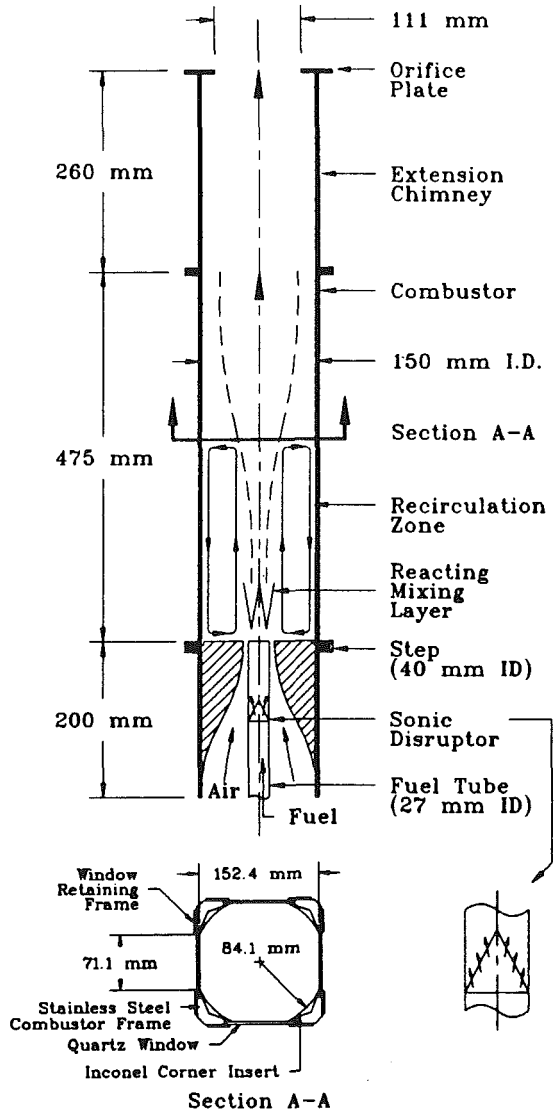

Fig. 3 Schematic diagram of the final configuration of the research combustor mounted on the burner (inset shows "sonic disruptor")

quired for a propane flame of the requisite length than is required for methane.

As the LBO condition is approached, the attached diffusion flame lifts from the fuel tube and is stabilized slightly downstream. This is the region of most interest and relevance to the present study. Thus, the combustor has to be long enough to contain the lifted flame region; and this region has to fall within the traverse window. Both Kalghatgi (1987) and Dahm and Dibble (1988) have shown that propane has less lift-off height than methane. Considering both flame length and lift-off heights, the choice of gaseous propane yields smaller combustor length.

Choice of Configuration

For easy optical access, the most ideal configuration for the research combustor was a planar cross section. However, experimentally it is extremely difficult to establish planar flows that are truly symmetric about the jet axes. In addition, the aspect ratio considerations for a planar rig resulted in propane flow rates that exceeded the capacity of the facility. Therefore, an axisymmetric jet arrangement was preferred.

A jet discharging into a quartz cylindrical working section provides an ideal axisymmetric configuration, but poses severe problems for optical measurements through curved glass surfaces. Corrective lens techniques have been developed by Durrett et al. (1985). However, these are too complex and immature for the advanced laser diagnostics (three-dimensional LDA and CARS) used in this program. A box-section combustor with corner fillets to reduce vorticity concentration and eliminate its effect on the bulk flow field in the combustor was an attractive alternative. CFD calculations made using Pratt & Whitney's 3D-TEACH computer code indicated, in agreement with Brundett and Baines (1964), that a single, linear corner fillet in a square-section duct reduces the peak vorticity by half. Therefore, corner fillets were provided for the research combustor.

Figure 3 shows a schematic of the final agreement for the research combustor. It consists of a central fuel tube surrounded by a co-annular air jet. This jet system supplies unmixed reactants at the exit to a dump-step inside the combustor. The burner contains the jet system and also supports the combustor vertically. The combustor is comprised of *two* separate sections. The first section holds windows (quartz or instrumented metal panels) on all four sides, and the second one is a short extension Inconel chimney. On the top of this chimney, orifice plates of specific blockage ratios can be fitted.

Combustor Sizing

To decide step height, the stability expression of Ballal and Lefebvre (1979) was used:

$$\phi_{\mathrm{LBO}} = \left[\frac{2.25(1+0.4U_m[1+0.1Tu])}{p^{0.25}T_0\exp(T_0/150)D_b(1-B)}\right]^{0.16} \quad (1)$$

In the present context, $B = (D_b/D_c)^2$, where D_b is an effective diameter representing an orifice plate closed area.

Preliminary estimates made by assuming d_f = 13.2 mm, ϕ = 0.6, and $U_a/U_f > 1$, had yielded a value of 40 mm for an equivalent premixed passage diameter at the combustor inlet. Equation (1) was then used to generate the parametric curve of blow-out velocity versus step height for this value of passage diameter. Figure 4 shows plots of these calculations. From these data a step height of 55 mm was found appropriate for ϕ = 0.6. This value of step height with a 40 mm inlet gives a combustor diameter of 150 mm. This step will generate a symmetric recirculation zone with a reattachment point plane that depends on the step height, inlet Reynolds number, and equivalence ratio as is evident, for example, in the work of Morrison et al. (1987). Figure 5 shows reattachment lengths for reacting and nonreacting laminar and turbulent flows. For ϕ = 0.6 and Re = 10^4, the reattachment plane is about five step-heights downstream of the step. To accommodate this recirculation zone, and the one formed due to flow stagnation

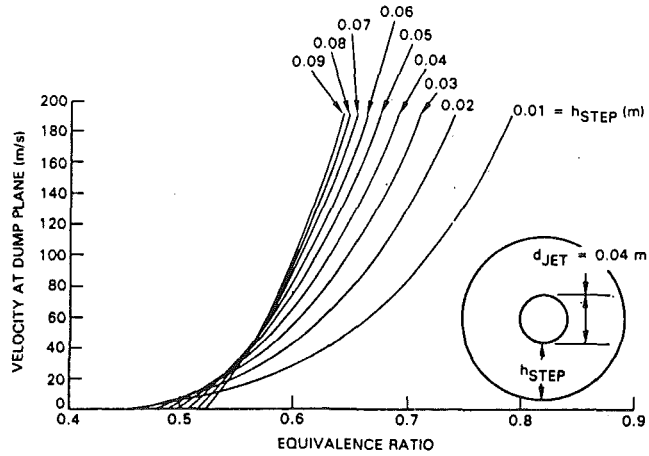

Fig. 4 Blowout velocity versus equivalence ratio for various values of step height as calculated by Ballal and Lefebvre (1979) correlation

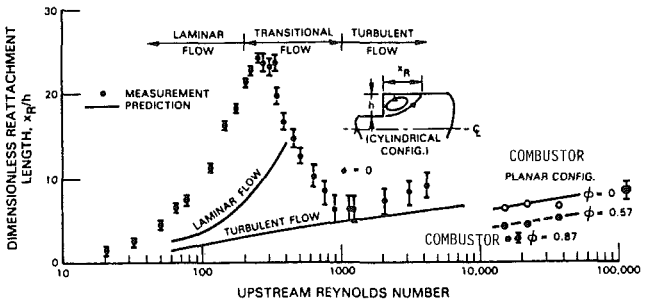

Fig. 5 Recirculation zone length for nonreacting and reacting cylindrical and planar flows

on the orifice plate at exit, a combustor length 2–3 times the reattachment length is required to avoid interference between the two zones, i.e., combustor length = 825 mm approximately.

Since the reactants are not premixed the velocity ratio should be high, e.g., $U_a/U_f > 10$, to provide good mixing. Also, the temperature of the combustion products in the step recirculation zone should be high enough to guarantee continuous ignition of fresh reactants when the flame is in lifted condition. For propane–air mixtures, Sturgess (1979) has shown, and CFD analysis for $\phi = 0.6$ suggests, that auto-ignition times become short and temperatures of 400–800 K exist in the shear layer when the gas temperature at reattachment was around 1000 K. Therefore, recirculation zone rettachment plane gas temperature at the combustor wall should not be less than 1000 K for continuous ignition of a lifted flame.

A CFD code was used to obtain the relationship between reattachment plane temperature and the Thring–Newby parameter, θ, for a duct with sudden expansion, namely:

$$\theta = \left(1 + \frac{1}{\text{FAR}}\right)(\rho_f/\rho_a)^{0.5}(r_i'/r_c) \tag{2}$$

where

$$r_i' = \frac{(\dot{m}_f + \dot{m}_a)}{\sqrt{\pi\bar{\rho}}\,(\dot{m}_f U_f + \dot{m}_a U_a)^{0.5}} \tag{3}$$

$$\bar{\rho} = (\dot{m}_a\rho_a + \dot{m}_f\rho_f)/(\dot{m}_a + \dot{m}_f) \tag{4}$$

Results of these calculations are plotted in Fig. 6. In this figure each data point represents a separate calculation and the line drawn through them serves as a design curve.

Based on manipulation of Fig. 6 and Eqs. (2)–(4), Fig. 7 plots the reattachment plane gas temperature in the 150 mm

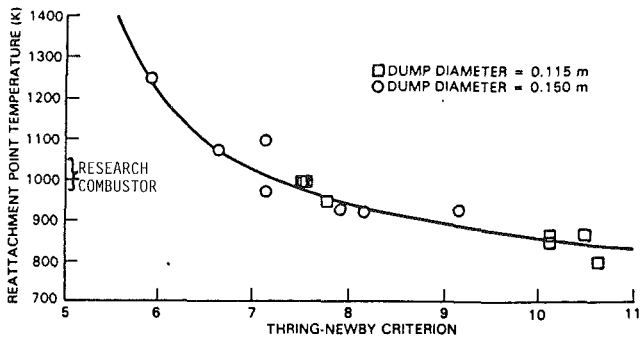

Fig. 6 Correlation of 2D-PREACH results for the stagnation temperature in terms of the Thring–Newby criterion

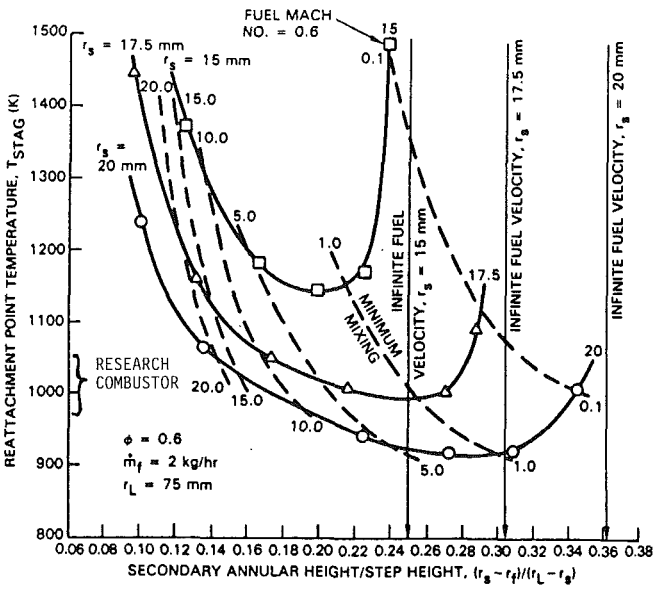

Fig. 7 Plots of reattachment point temperature versus annular/step height ratio for a 150 mm i.d. combustor

i.d. combustor versus the ratio of annular height to step height for the various secondary passage radii, r_s. The reattachment temperature has two asymptotes; one corresponding to choking in the air passage, and the other due to choking of the fuel passage. For each r_s, the reattachment temperature exhibits a minimum corresponding to $U_a/U_f = 1$. The left-hand side of the plot represents the strongly recirculated step flames of interest for this combustor. The position of minimum temperature occurs at lower values of the abscissa as r_s is decreased. This may be explained in two ways: First, as r_s gets smaller, the step height gets bigger in a fixed combustor and the reattachment plane moves downstream into the regions of increasing gas temperature. Second, as r_s gets smaller so does the air passage annular height for a fixed fuel passage. Therefore, the fuel source is relatively closer to the shear layer associated with the recirculation bubble at the step. Thus, for a given rate of jet expansion, higher temperature gases are delivered at the reattachment plane. For a given r_s, the annular/step height ratio is also changed by changing the fuel passage size. Then, the temperature changes because the jet velocity ratio and hence the rates of mixing jet expansion, are also changed. Plots similar to Fig. 7 can be produced at every equivalence ratio. For a given r_s, increasing the equivalence ratio increases the reattachment temperature at all velocity ratios.

From Fig. 7, geometric relationships may be found for specified mixing conditions or specified temperature conditions. This relationship is shown in Fig. 8 for $\phi = 0.6$, minimum

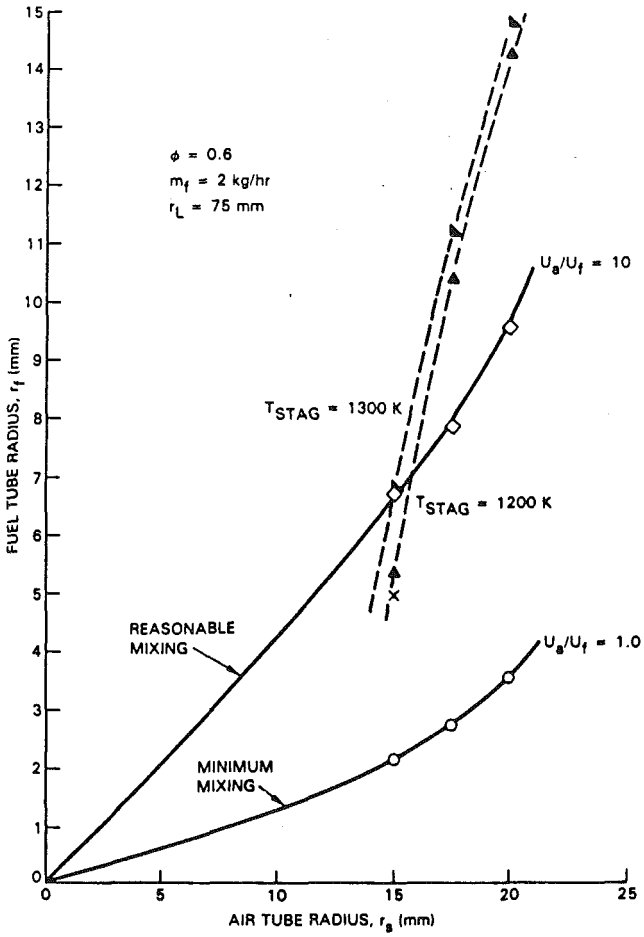

Fig. 8 Relationship between reactant supply tube dimensions, mixing, and stagnation point temperature in a 150-mm i.d. combustor

and moderately strong mixing (U_a/U_f = 1.0 and 10.0, respectively), and reattachment temperatures of 1200 K and 1300 K. Figure 8 indicates that for r_s = 20 mm, the fuel tube needs to be at least 12.5 mm radius to provide the desirable minimum reattachment plane temperature of 1000 K. Allowing for heat losses from the combustor, the fuel tube radius was increased to 13.5 mm. For this radius, Fig. 8 indicates that the reattachment plane temperature would be somewhat over 1100 K. In this way, combustor sizing is completed. The final combustor dimensions are given in Fig. 3.

Mechanical Design

The combustor frame establishes reference planes for the quartz windows. These reference planes ensure that windows on opposite sides of the combustor remain flat and parallel as the combustor is moved. Thus, the combustor frame had to be dimensionally stable, despite frequent and extreme thermal cycling. A thorough heat treatment, for stress relief, was performed on the combustor frame prior to final machining. This proved to be effective since follow-up inspection revealed that deviations from design dimensions were less than 0.25 mm.

The windows are spring-loaded against the window retaining frames by means of Inconel corner inserts. These inserts also form the corner fillets needed to minimize vortex formation. Inconel was used because of its high melting temperature, resistance to oxidation, and its better spring constant at high temperature. The corner insert concept has several advantages. The step discontinuity, where the insert meets the glass, is quite small since the inserts are only 0.81 mm thick. Thus, the combustor frame required less intricate machining. Also, the window can float between the lightly spring-loaded inserts and the frame, thus permitting its independent expansion and contraction.

The windows for this combustor had to meet several design requirements, such as a need to overlap LDA and CARS beams, a desire for cylindrical symmetry, the ability to withstand vibration and high temperature, optical clarity even under laser power approaching 1 GW/cm^2, the preclusion of beam steering as the combustor is moved, and the cost of high-quality quartz glass.

Quartz windows, while expensive, have proven to be quite durable, exhibiting lifetimes on the order of hundreds of hours. The quartz windows used in this combustor are only 3.2 mm thick and this keeps thermal stresses between inner and outer window surfaces to a minimum. Further, thermal shock to the windows was minimized by devising a proper light-off procedure for the combustor. Finally, the windows were designed such that they could easily be replaced, for example, with stainless steel plates equipped with thermocouples and pressure taps.

Window durability with the high-power CARS laser operation has been good except for where soot accumulates. A new short focal length lens is being incorporated in the CARS system to reduce laser power density incident on the window surface by a factor of 4. Insertion of plane windows in the path of the laser beams still causes the probe volume of both the CARS and LDS systems to move. Therefore, the overlap volume must be determined after the windows are in place. The window width was established to allow adequate probe distance perpendicular to the laser propagation direction, and still maintain sufficient cylindrical symmetry.

As illustrated in Fig. 3, the shape of the annular air passage is dictated by the inner contour of the combustor step. Early step designs exhibited poor flow characteristics because of too sudden a contraction. Also, the fuel tube was not concentric with the step. Eventually, a new step was designed, which produced uniform and symmetric annular air velocity profiles.

An Inconel extension is fitted to the downstream end of the research combustor. Prior to the combustor fabrication, it was recognized that the metal walls of the extension piece would get rather hot. This Inconel extension provides a passage with the same cross-sectional profile as the lower portion of the combustor and conveys the combustion products to the exhaust hood directly above the combustor. It may be equipped with either a top-hat restriction (available in various sizes), no restriction at all, or what is preferred, a simple orifice plate.

Combustor Light-Off

Several techniques for igniting the combustor were tested. These include:

Lighting at the exit plane
Lighting through a 6.3 mm hole in the step
Lighting in recirculating zone, 25 mm above the step, through a hole in the side plane.

Only the last of these gave smooth, successful, and reproducible ignition. Ignition in the recirculation zone has been satisfactorily accomplished with a small propane torch igniter attached to the side plate fitting. Normal light-off is accomplished by first establishing an airflow of 300 SLPM, then lighting the torch igniter, and finally admitting about 10 SLPM of fuel in the combustor. Upon successful ignition, air and fuel flows are increased, taking care to maintain constant fuel/air ratio, until the air flow reaches about 900 SLPM. At this flow rate, the flame is very stable, exhibiting lean blow-out at ϕ = 0.5. The only major problem is that at these ignition conditions there is a tendency for significant sooting on the

upper portion of the windows. Attempts to initiate combustion at lower equivalence ratios or higher initial flow rates were not successful. After a light-off is successful, the torch ignitor is removed and the fitting is capped.

Combustion Characteristics

Before performing combustion tests, acoustic characteristics of this research combustor were investigated because it was feared that eddy-shedding off the step might result in satisfying the Rayleigh criterion, and this may set up resonance in the combustor and fuel supply tube. A breadboard version of the combustor was tested and it revealed noisy combustion and flame flicker. Also, mechanical vibrations shortened the window life. Therefore, and after some development work, a "sonic disruptor" (see Fig. 3, inset), which can pass LDA seed particles but is acoustically closed, was introduced into the fuel tube. This device and the redesign of the annular air passage reduced pressure fluctuations in the combustor significantly. These developments are fully described by Heneghan et al. (1989).

Combustion tests revealed that the combustor operates as designed, with the reactants being ignited in the shear layer formed between the fuel and air jets. The shear layer flame appears removed from the confluence of the jets. In agreement with results shown in Figs. 6 and 7, reattachment point temperatures around 1000 K were obtained from the measurements of combustor wall temperatures. Also, in Fig. 5, we show measurements of flame recirculation zone length for Re = 20,000, ϕ = 0.87, and isothermal recirculation zone length for Re = 110,000 obtained by using an LDA instrument. These values are consistent with other isothermal and combusting flow data from the literature.

Figure 9 illustrates the sequence of events leading to lean blow-out in our research combustor for a variety of Reynolds numbers (based on fuel and air flows) and air loading parameters. As the overall equivalence ratio is reduced below unity, the luminosity of the recirculation zone vanishes and the shear-layer *attached* flame moves farther downstream into the combustor in a characteristic *lifted flame* position and form. Continuing reduction in the equivalence ratio produces an onset of flow instability in the lifted flame, increase in the amplitude of the instability, onset of intermittency, severe intermittency, and finally, an onset of strong axial flame instability. At this point, a slight increase in equivalence ratio results in an *attached* flame, while a slight decrease produces a *lean blow-out*. Provided the air jet is always turbulent and the velocity ratio u_a/u_f is sufficiently large, the above sequence of events was the same whether equivalence ratio is decreased by reducing fuel flow rate or by increasing air flow rate. This sequence of events leading to flame-out clearly highlights the complexity of the lean blow-out mechanism in a modern annular gas turbine combustor.

Figure 10 shows the LBO performance of our research combustor. It appears that the combustion characteristics of our research combustion are more similar to those of well-stirred reactors than those of the practical combustor designs of the past. Since high-performance annular combustors of the future will approach the combustion characteristics of the well-stirred reactors, it is reasonable to conclude that our research combustor correctly reproduces the LBO processes of a real gas turbine combustor.

Conclusions

A research combustor that simulates the "inside-out" recirculation pattern and LBO processes of a modern annular aircraft gas turbine combustor was designed and fabricated. This was accomplished using CFD-generated design curves and data available in the literature.

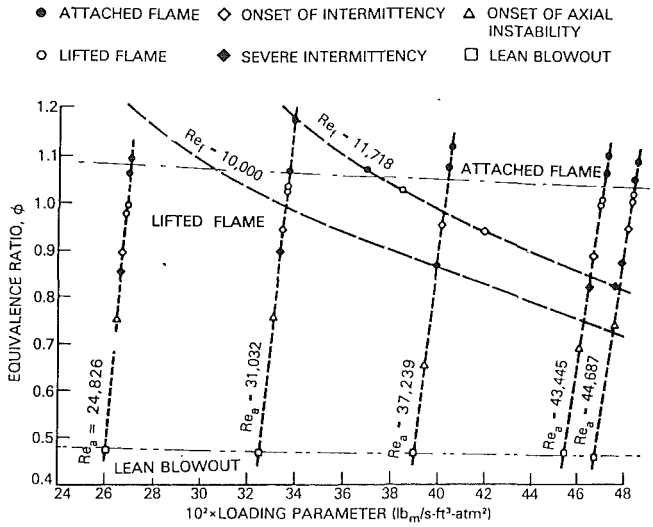

Fig. 9 Flame characteristics in the research combustor

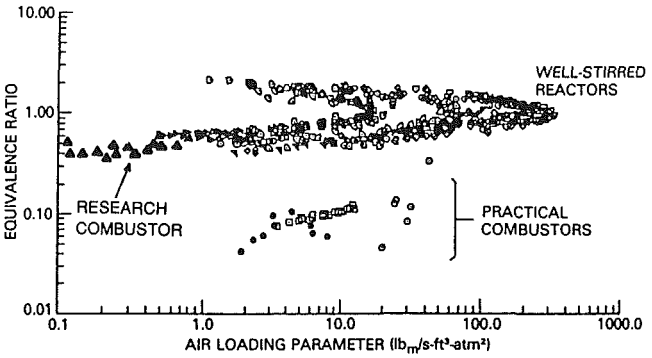

Fig. 10 Lean Blow-out (LBO) performance of the research combustor

It was found that the existing test facility, optics capabilities, and limit on fuel flow rate due to safety considerations imposed dimensional constraints on combustor length and shape. The requirement of simple inlet boundary conditions and two-dimensional flow field for CFD codes made it undesirable to use swirl for improved mixing and reduced flame length. Peak flame temperatures of 1700 K inside the combustor were dictated by the temperature limit of fused quartz.

An axisymmetric arrangement of fuel and air jets, 27 mm and 40 mm diameter, respectively, dumping unmixed reactants at a 55 mm wide step, emerged as the final preferred configuration of this combustor. The combustor is 735 mm long, has 150 mm square cross section with rounded corner fillets of 84 mm radius, and is fitted with an Inconel extension chimney with an orifice plate as its exit.

It was found that the combustor operates in a stable and predictable manner over a range of loadings. Measurements revealed a complex sequence of events such as flame lift-off, intermittency, and onset of axial flame instability eventually leading to lean blow-out. Also, the LBO performance of the research combustor was similar to that of well-stirred reactor. These tests confirmed the soundness of the combustor design for the intended purpose. This combustor is now making possible acquisition of more benchmark quality data on LBO.

Acknowledgments

This research was sponsored by the U.S. Air Force, Wright Research and Development Center, Aero Propulsion and Power

Laboratory, under Contract No. F33615-87-C-2822 to Pratt and Whitney, East Hartford, CT (Contract Monitor: 1Lt. A. L. Lesmerises) and Contract No. F33615-87-C-2767 to University of Dayton, Dayton, OH (Contract Monitor: Dr. W. M. Roquemore).

References

Ballal, D. R., Lightman, A. J., and Yaney, P. P., 1987, "Development of Test Facility and Optical Instrumentation for Turbulent Combustion Research," *AIAA Journal of Propulsion and Power*, Vol. 3, pp. 97–104.

Ballal, D. R., and Lefebvre, A. H., 1979, "Weak Extinction Limits of Turbulent Flowing Mixtures," ASME JOURNAL OF ENGINEERING FOR GAS TURBINES AND POWER, Vol. 101, pp. 343–348.

Beer, J. M., and Chigier, N. A., 1972, *Combustion Aerodynamics*, Wiley, New York.

Brundrett, E., and Baines, W. M., 1964, "The Production and Diffusion of Vorticity in Duct Flow," *Journal of Fluid Mechanics*, Vol. 19, pp. 375–394.

Clarke, A. E., Harrison, A. J., and Odgers, J., 1958, "Combustion Instability in a Spherical Combustor," *Seventh Symposium (International) on Combustion*, Butterworths Scientific Publications, London, pp. 664–673.

Dahm, W. J. A., and Dibble, R. W., 1988, "Combustion Stability Limits of Coflowing Turbulent Jet Diffusion Flames," AIAA Paper No. 88-0538.

Durrett, R. P., Gould, R. D., Stevenson, W. H., and Thompson, H. D., 1985, "A Correction Lens for Laser Doppler Velocimeter Measurements in a Cylindrical Tube," *AIAA Journal*, Vol. 23, pp. 1387–1391.

Gupta, A. K., Lilley, D. G., and Syred, N., 1984, *Swirl Flows*, Abacus Press, London, United Kingdom.

Heneghan, S. P., Vangsness, M. L., Ballal, D. R., Lesmerises, A. L., and Sturgess, G. J., 1989, "Acoustic Characteristics of a Model Step Combustor," in preparation.

Hottel, H. C., and Hawthorne, W. R., 1949, "Diffusion in Laminar Flame Jets," *Third Symposium (International) on Combustion, Flame, and Explosion Phenomena*, The Williams and Wilkins Co., Baltimore, MD, pp. 254–266.

Kalghatgi, G. T., 1987, "Lift-Off Heights and Visible Lengths of Vertical Turbulent Jet Diffusion Flames in Still Air," *Combustion Science and Technology*, Vol. 41, pp. 17–29.

Lenze, B., 1982, "The Influence of Recirculation and Excess Air on Enclosed Turbulent Diffusion Flames," *Nineteenth Symposium (International) on Combustion*, The Combustion Institute, Pittsburgh, PA, pp. 565–572.

Morrison, G. L., Tatterson, G. B., and Long, M. W., 1987, "A 3-D Laser Velocimeter Investigation of Turbulent, Incompressible Flow in an Axisymmetric Sudden Expansion," AIAA Paper No. 87-0119.

Sturgess, G. J., 1979, "Premixed Prevaporized Combustor Technology Forum," NASA Report CP-2078.

Sturgess, G. J., and Syed, S. A., 1985, "Calculation of Confined Swirling Flows," AIAA Paper No. 85-0060.

Sturgess, G. J., Syed, S. A., and McManus, K. R., 1986, "Importance of Inlet Boundary Conditions for Numerical Simulation of Combustor Flows," *International Journal of Turbo & Jet Engines*, Vol. 3, pp. 43–55.

Sturgess, G. J., Roquemore, W. M., and Lesmerises, A. L., 1989, "Enhancement of Computer Simulation as a Combustor Design Tool Through a Lean Blow Out Research Program," in preparation.

The Role of Primary Jets in the Dome Region Aerodynamics of a Model Can Combustor

C. D. Richards

G. S. Samuelsen

UCI Combustion Laboratory,
Institute of Combustion and
Propulsion Science and Technology,
University of California,
Irvine, CA 92717

The role of the primary jets in the aerothermal behavior and overall performance of a gas turbine combustor is explored through an experimental study. The study is performed in a model laboratory combustor that possesses the essential features of practical combustors. The test bed is designed to accommodate optical access for laser diagnostics and overall flow visualization, and is capable of incorporating variable inlet geometries. In the present case, the combustor is operated on JP-4 at atmospheric pressure. A parametric variation in the number of jets per row and axial location of the jet row is performed. The aerodynamic and thermal fields are characterized using laser anemometry and a thermocouple probe, respectively. Species concentrations are acquired via extractive probe sampling. The results demonstrate the importance of primary jet location with respect to the dome swirler. The percent mass recirculated into the dome region, as well as the overall uniformity of mixing and combustion efficiency, are substantially influenced by jet row location. The momentum ratio of the incoming primary jet stream to that of the approaching crossflow of reacting dome gases has a direct impact on the mixing patterns as well. An increase in the number of primary jets leads, in the present case, to more uniform mixing.

Introduction

Substantial interest is now directed to gas turbine combustion as a result of (1) a goal to double gas turbine engine performance, (2) the need to create combustor nozzle systems that are fuel flexible, and (3) the initiative to expand combustor technology in support of hypersonic flight.

The design of gas turbine combustors is today predicated on empirical data associated with the overall combustion performance of the system. Although experimental research has been conducted in both laboratory bench-scale and full-scale hardware (Brum and Samuelsen, 1987; Gouldin et al., 1985; Lilley, 1985; Bicen and Jones, 1986), little is understood about the detailed aerodynamics, the detailed mixing of fuel and air, and the relationship of these processes to the overall system performance. The reasons are associated with (1) the absence of model reactors with optical access and clean boundary conditions in combination with the necessary features representative of practical systems, (2) key voids in diagnostic capability, and (3) the lack of data to develop and validate numerical codes for complex, two-phase flows.

The present program addresses all three of these voids. First, a model laboratory can combustor is employed with optical access and the essential features of gas turbine combustors (including spray injection, swirl stabilized dome aerodynamics, and wall jet injection). Second, nonintrusive optical diagnostics such as laser anemometry (LA) and phase Doppler interferometry are used for probing of the flow field. Third, data are acquired for use in the development and validation of numerical codes.

The penetration of the primary jets and subsequent mixing likely play a dominant role in fuel-air mixing in the dome region of gas turbine combustors. The primary jets penetrate the flow field to interact with the swirl-induced recirculation zone and provide additional air to the dome region as well as to the intermediate or "secondary" zone. In this paper the focus is on the role of the primary jets in dome region aerodynamics and fuel-air mixing.

Background

The combustors used in this study are based on a model combustor dubbed the Wall Jet Can Combustor, WJCC, developed at the UCI Combustion Laboratory (Rudoff, 1986). This combustor features dome swirl and two rows of discrete wall jets. Each row of jets consists of four individual jets with an injection angle of 90 deg. The original combustor was constructed of stainless steel with two windows along the length of the combustor for optical access. A schematic of this combustor is shown in Fig. 1(*a*). In previous work this combustor was characterized via detailed spatial maps of velocity, temperature, and droplet field statistics (Cameron et al., 1989a, 1986b), and found to produce an overall flow field and combustor performance that is representative of a gas turbine can combustor.

Contributed by the International Gas Turbine Institute and presented at the 35th International Gas Turbine and Aeroengine Congress and Exposition, Brussels, Belgium, June 11–14, 1990. Manuscript received by the International Gas Turbine Institute January 16, 1990. Paper No. 90-GT-142.

a) The Wall Jet Can Combustor (WJCC).

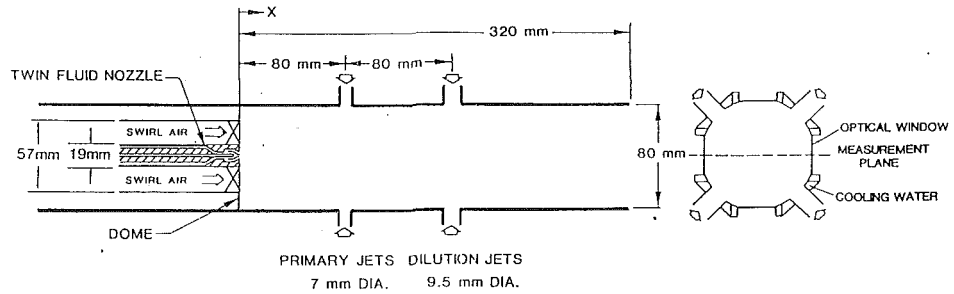

b) Module 1.

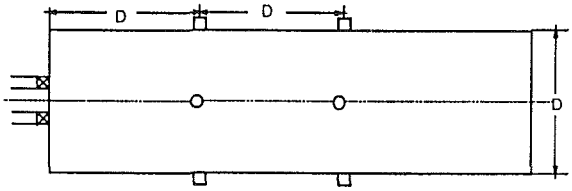

c) Module 2.

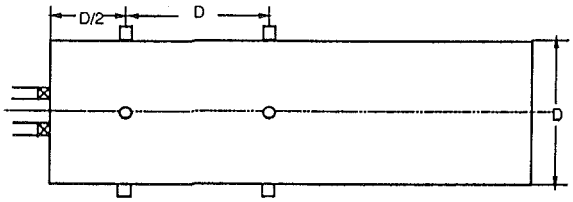

d) Module 3.

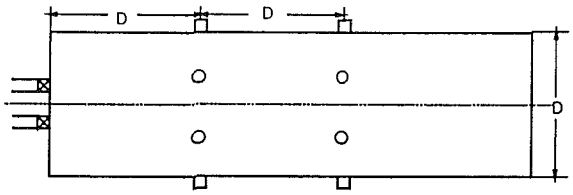

Fig. 1 Model combustors

The combustor modules used in this study feature the same general characteristics; namely, dome swirl and two rows of discrete wall jets. The new modules, however, are manufactured from quartz and thus provide full optical access to the highly three-dimensional flow field present in these reactors. In addition, three modules were manufactured so that a parametric variation of number of jets per row and axial position of jet row can be performed.

In the present study the role of the primary jets is evaluated through an experimental investigation. The goals of the study are to explore (1) the relative importance of primary jet location relative to the dome swirler, and (2) the effect of the number of jets in the primary row to the swirl-stabilized dome region aerodynamics.

Experiment

Approach. The approach is to characterize the aerodynamic field of the combustor. Measurements of velocity are made across the diameter of the combustor in increments of 4 mm at selected axial locations as well as along the centerline. A thermocouple probe is used to obtain the average temperature at the same locations. An extractive probe and gas analyzers are used to determine species concentrations at an axial location 2.5 duct diameters downstream of the nozzle inlet plane.

a)

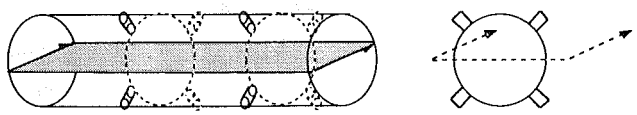

b)

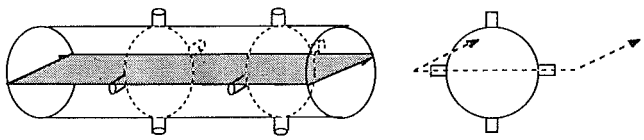

c)

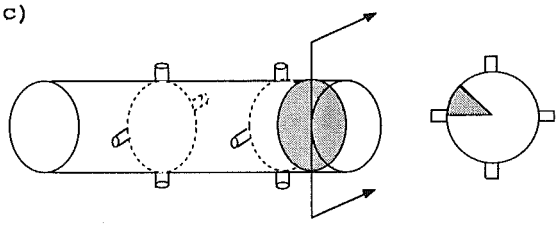

Fig. 2 Measurement locations

a) The thermal field in the plane of the jets.

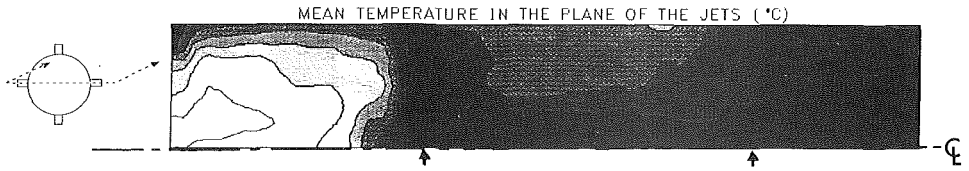

b) The thermal field in the plane of symmetry.

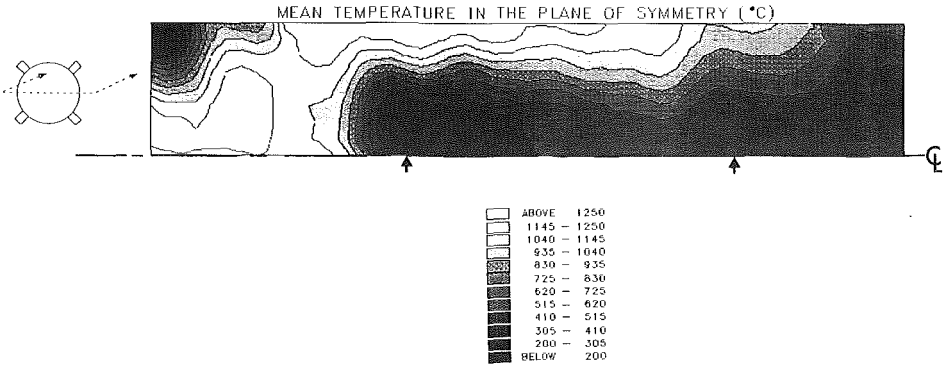

c) Radial profiles of mean axial velocity.

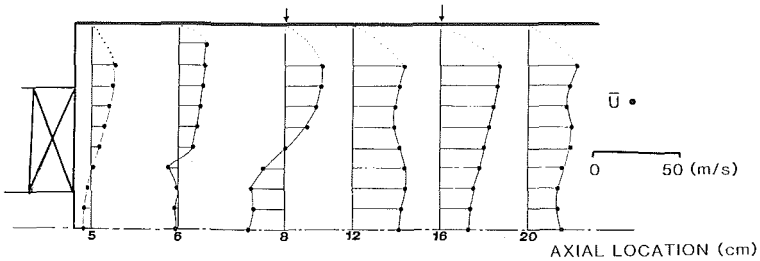

d) Emissions profiles at the exit plane.

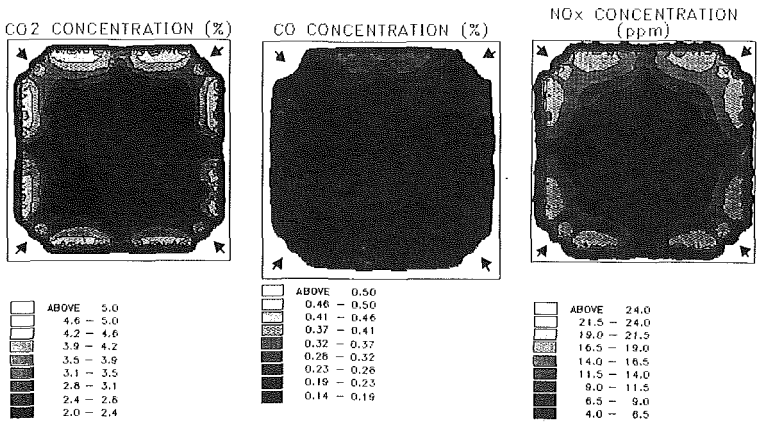

Fig. 3 Module 1 results

Test Bed. The combustor modules, as shown in Fig. 1, are 80 mm quartz circular ducts with an operating length of 32 cm. Air flow to the combustor is split into three separate lines delineated as the dome swirl, primary jets, and dilution jets. Each line is separately metered and controlled so that the flow splits may be varied. The swirl air enters the combustor at the inlet plane through a 34-mm-dia, 100 percent blockage, 45 deg swirler. Each of the wall jet lines is further split into six lines, which are individually controlled and metered. These lines feed the discrete wall jets.

A 19 mm o.d. centrally positioned fuel delivery assembly is sized to house a twin-fluid air-assist atomizer. The dome swirl vanes are concentrically positioned around the fuel delivery assembly as shown in Fig. 1(*a*).

Each combustor module features two rows of discrete wall jets. The number of jets per row and the axial position of the jet rows vary between the modules. Module 1, the baseline case, consists of four jets per row positioned one and two duct diameters downstream from the inlet, as shown in Fig. 1(*b*). Module 2, shown in Fig. 1(*c*), also features four jets per row

but they are positioned 1/2 and 3/2 duct diameters downstream from the inlet. Module 3 features six jets per row positioned one and two duct diameters downstream of the inlet, as shown in Figure 1(*d*).

Diagnostics

Laser Anemometer. A single component laser anemometer (LA) system is used to characterize the flow field velocities. The LA system is described in detail elsewhere (Brum and Samuelsen, 1987). To eliminate directional ambiguity, frequency shifting is provided by a Bragg cell. All flows are uniformly seeded with nominally 1 μm alumina powder to scatter light while passing through the probe volume.

Measurements of mean and rms axial velocities are acquired in the plane of symmetry between the jets as shown in Fig. 2(*a*).

Thermocouple Probe. The thermal field is established using a Type R thermocouple probe mounted on a three-axis positioning traverse. The data are presented uncorrected for radiation loss.

Temperature measurements are obtained in the plane of symmetry between the jets as well as in the plane of symmetry through the jets (as shown in Fig. 2*b*), across the radius of the combustor in 5 mm increments at 11 axial locations along the length of the combustor.

Species Measurement. Exit plane species concentrations are determined with a water-cooled extractive probe mounted on a three-axis positioning traverse. Concentrations of oxygen, carbon dioxide, carbon monoxide, and nitric oxide and nitrogen dioxide are acquired using a Beckman Model 755 O_2 analyzer, Horiba PIR 2000 analyzers for CO and CO_2, and a TECO Model 10 analyzer for NO_x concentrations.

Species concentrations are obtained at an axial plane 2.5 duct diameters downstream of the inlet plane in a slice defined by the two planes of symmetry as shown in Fig. 2(*c*). The probe was traversed along radial lines in 5 mm increments. The axial plane was selected to be near the end but within the combustor duct.

Test Conditions. The swirl, primary jet and dilution jet flows comprise 26, 30, and 39 percent, respectively of the total

a) The thermal field in the plane of the jets.

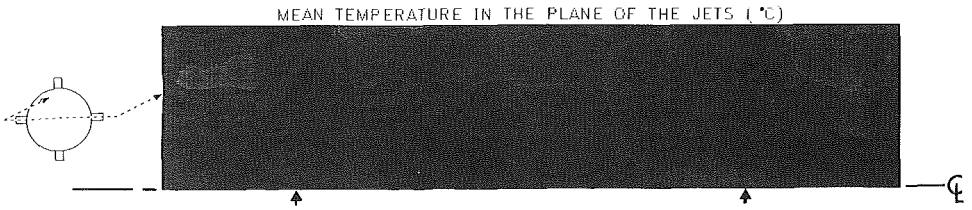

b) The thermal field in the plane of symmetry.

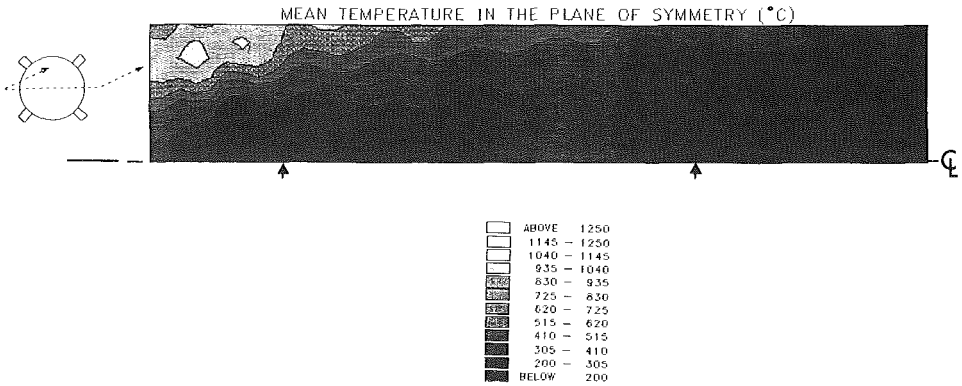

c) Emissions profiles at the exit plane.

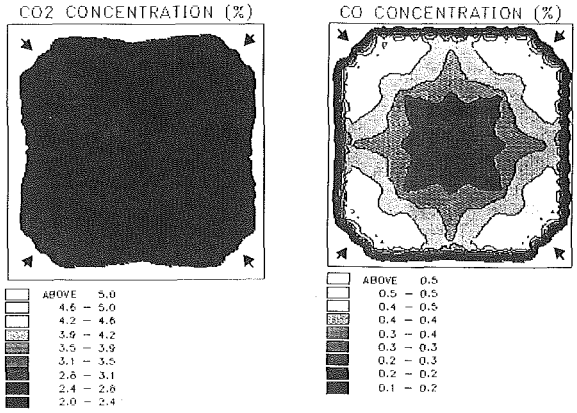

Fig. 4 Module 2 results

flow. The atomizing air in the nozzle circuit accounts for the remaining 5 percent. The swirl air plus the atomizing air alone are sufficient to provide a near-stoichiometric ($\phi = 0.95$) mixture. Lean combustion is desirable in this combustor due to the thermal limitations of the quartz. These flow split conditions are based on previous studies (Cameron et al., 1989a, 1986b; Richards and Samuelsen, 1990).

The combustor is operated at atmospheric pressure. The bulk flow rate of air is 163 kg/h. Under reacting conditions, the combustor is operated on a petroleum-derived JP-4 at a fuel flow rate of 3.27 kg/h (which corresponds to an overall equivalence ratio of 0.3) and a nozzle atomizing air to fuel mass ratio of 3.0.

Results and Discussion

Baseline Condition. The mean temperature field in the plane of the jets for Module 1 is shown in Fig. 3(*a*). The trajectory of the jets is evident, and the containment of the dome region reaction by the penetration of the primary jets to the centerline can be clearly deduced. In contrast, the dilution jets are more diffuse and their penetration is not as well defined.

In Fig. 3(*b*), the mean temperature field in the plane of symmetry between the jets is shown. A cold region occurs at the front corner of the combustor. This is a zone of recirculation due to the step expansion from the swirler to the duct and, because of the heat sink provided by the walls (and likelihood of a lean mixture as well), a reaction cannot be sustained.

The influence of the jets can be seen in the cold regions along the centerline as well. The hot reacting gases in the dome region move around the jets and are directed toward the wall in the secondary region between the jets as a result of the air injected to the centerline. The core of the combustor remains relatively cool beyond the primary jets.

Radial profiles of mean velocity data for this condition are shown in Fig. 3(*c*). At the first two axial locations ($x = 5$, 6 cm), the profiles are characteristic of the recirculation zone induced by the aerodynamic swirler. At the location $x = 8$ cm (corresponding to the primary jet location), the influence of the jet penetration is clearly detectable. Negative velocities are increased at the centerline. High velocities near the wall result from diversion of the hot gases to the wall. At $x = 16$ cm (the axial location of the dilution jets), evidence of the dilution jet penetration is seen in a slight deficit near the centerline, and a modest increase in the centerline mean velocity downstream of the dilution jets at $x = 20$ cm.

Emissions data are presented in Fig. 3(*d*). The data acquired have been rotated through 360 deg to provide a full cross-sectional view. The jet positions are marked for reference by arrows. In general CO, CO_2, and NO_x emissions are depressed at the centerline and increase toward the wall and correspondingly O_2 profiles exhibit the reverse behavior. O_2 profiles are not presented for brevity. This is in agreement with the trend observed in the temperature profiles for the dome region effluent to move around the jets toward the wall regions. NO_x concentrations tend to be highest on the wall at the circumferential locations that correspond to the jet locations. Conversely CO_2 and CO concentrations are highest between the jets.

Parametric Variations

Module 2. In this module the jet rows are located closer to the inlet plane. As shown in Fig. 1(*c*), the primary jets are one half duct diameter from the swirler exit. The air flow rates and fuel loading are identical to those run in Module 1.

The mean temperature field in the plane of the jets, shown in Fig. 4(*a*), reveals overall lower temperatures. The substantially cooler temperatures in the dome region, for example, indicate a much larger air contribution from the jets and, as a consequence, leaner combustion than in Module 1. The temperature profiles in the plane of symmetry between the jets show that reaction takes place along the walls and that the cold core provided by the jets results in substantial quenching.

Emissions data are presented in Fig. 4(*c*). The levels of CO and CO_2 are high and low, respectively, compared to Module 1, an indication of relatively degraded combustion performance. CO_2 concentrations range from 2.2 to 3.1 percent compared to 2.4 to 5.1 percent in Module 1. Temperatures in this condition were not sufficiently high to produce a significant level of NO_x.

The centerline profile of mean axial velocity is shown in Fig. 5(*a*). The negative velocity at the position of the jets for Module 2 (at $x = 4$ cm) is close to that in Module 1 (at $x = 8$ cm). In Fig. 5(*b*), a radial profile of mean axial velocity acquired at the axial position of the primary jets is shown. Again the profiles are similar to those of Module 1. These data indicate that the penetration of the jets in the two cases is not substantially different.

Although the aerodynamic field near the jets is similar, the thermal fields and effluent are substantially different. This is attributed to the way in which the jets interact with the swirl induced recirculation zone. In Module 2, the primary jet axial location corresponds to approximately the middle of the extent of the recirculation zone. The jets penetrate to the centerline, impact, and feed directly into the swirl-induced recirculation bubble, providing a substantial amount of cold air to the reaction. In Module 1, the primary jets are close to the end of

a) Centerline profiles of mean axial velocity.

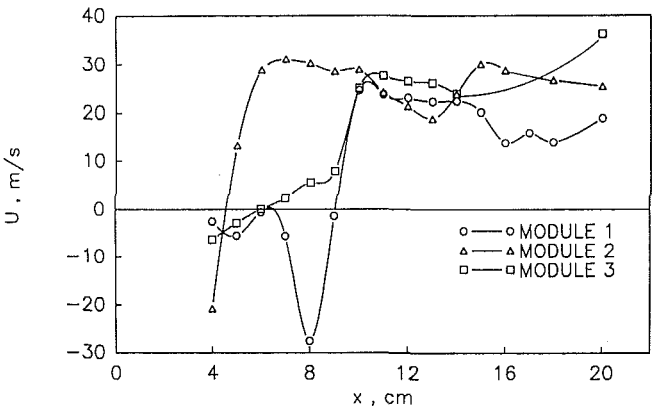

b) Radial profiles of mean axial velocity.

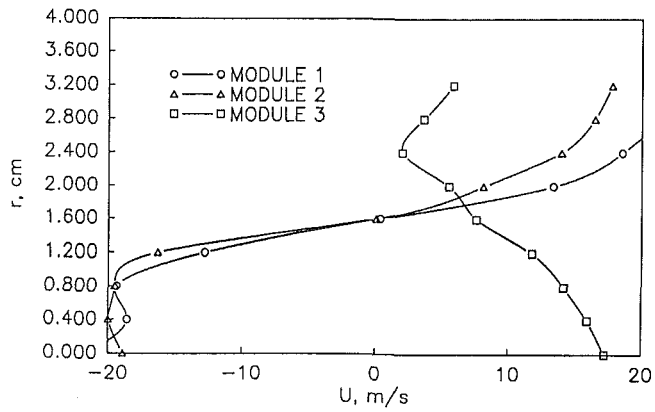

Fig. 5 Comparison of mean axial velocities

the recirculation bubble and, although backflow is produced by the impact of the jets, very little of the cold air is recirculated into the dome region.

Module 3. In this module, the primary jets are positioned one duct diameter downstream of the swirler (as in module 1) but, instead of four jets per row, the number of jets is increased to six. Air flows and fuel loading are kept the same in this case as well. It is important to note, however, that because the same flow must now be divided among six jets instead of four, the jet injection velocity is reduced. In Module 1, the primary jet velocity is 60.7 m/s, whereas in Module 3, the jet velocity is reduced to 40.5 m/s.

The ratio of the primary jet momentum to the approaching crossflow momentum is important to the resulting penetration and trajectory of the jets. In this case, because the momentum ratio has been reduced, the jets do not penetrate as deeply. This is demonstrated by the mean temperature in the plane of the jets (Fig. 6*a*).

The dome region temperature map of Module 3 is similar to that of Module 1; the reaction is contained in the central region of the combustor and a small cold corner is present. In contrast to Module 1, temperatures are substantially higher and the high-temperature region extends into the region downstream of the jets. Although it is clear the jets are deflected by the approaching crossflow, the presence of steep thermal gradients near the centerline in the axial region of the primary jets indicate cooling is influenced by the jets. The mean temperature profiles in the plane of symmetry, Fig. 6(*b*), also show this effect. Relative to the other modules, the hot gases from the dome region flow are not preferentially directed to the wall region. Instead, the hot gases are more uniformly mixed in the secondary region (between the primary and dilution jets) and the core of the combustor is, as a result, relatively hot.

Emissions data for this combustor are shown in Fig. 6(*c*). In general the pattern for this combustor is reversed from the other two modules. Levels of CO_2 and NO_x are high at the central core and drop off near the walls, except very near the walls where levels are again high. In contrast CO levels are low in the core and rise toward the wall.

The mean axial velocity profile along the centerline is shown in Fig. 5(*a*). The end of the swirl-induced recirculation zone is located approximately 2 cm upstream of the primary jets. The radial profile of axial velocity at $x = 8$ cm (corresponding

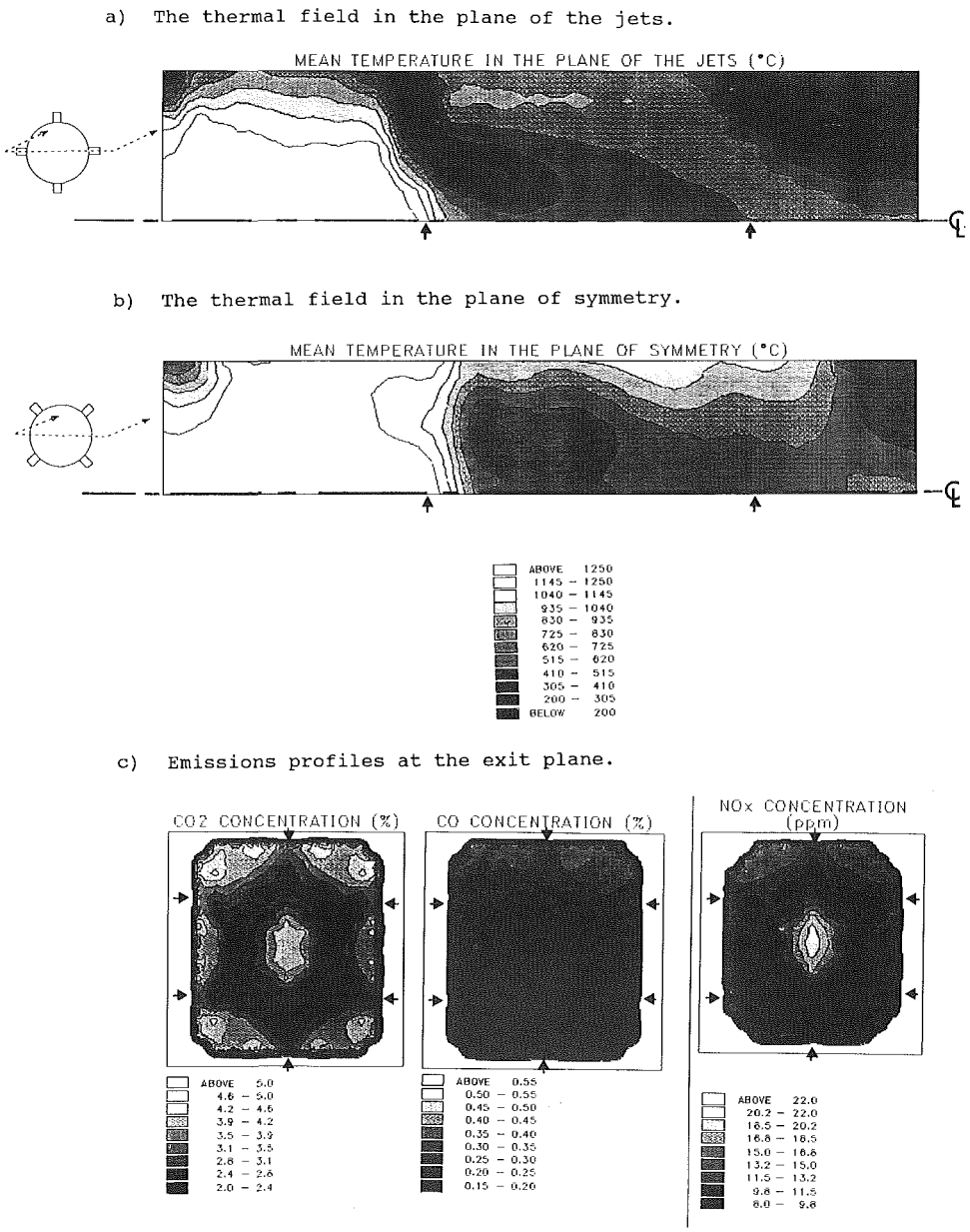

Fig. 6 Module 3 results

to the axial position of the primary jets) in Fig. 5(*b*) shows no evidence of jet penetration to the centerline. The slight deficit off centerline at $r = 0.8$ cm is probably an indication of where the primary jets penetrate to the plane of symmetry between the jets. Because the jets do not penetrate to the centerline, the jets do not contribute to the air mass entering the recirculation zone. Thus the dome region mixture ratio in this case is close to the stoichiometric conditions dictated by the ratio of fuel and swirl air injected, and the dome region temperatures are correspondingly higher.

Summary and Conclusions

This study delineates the importance and complexities associated with the primary jets in controlling combustor aerothermal behavior, and the overall performance.

The relative position of the primary jets to the swirl injection plane is of paramount importance. Although the two cases produce similar primary jet trajectories into the combustor core, the percent mass recirculated into the dome region is substantially different. This is attributed to the way in which the primary jets feed into the recirculation zone. In this study the location of the feed point was found to influence the mass recirculated. In parallel isothermal studies (Richards and Samuelsen, 1990), increasing the jet to crossflow ratio is found to produce a similar effect for primary jets located one duct diameter downstream of the swirler.

The number of primary jets also impacts the combustor aerothermal behavior in two ways. First, for the case in which fuel loading and equivalence ratio are maintained constant, increasing the number of jets per row results in decreased jet injection velocities. Second, the increased number of jets spread the mixing more uniformly about the duct circumference. Hence Module 3, with six jets per row, produces exit temperature and emissions profiles that are more uniform than those produced by the four jet combustors.

The next series of tests will explore the impact of jet to crossflow momentum and its relative impact compared to primary jet location and number. Experiments at elevated pressure are planned as well.

The conclusions of the present study are as follows:

- Years of combustor design, combustor development, and combustor research have demonstrated that the location and number and size of the primary jets are important to combustor performance. The present work is able to contribute the measurements and data presentation formats that quantify these empirically and intuitively held perceptions. In addition, the data base established should prove useful for the validation and development of the three-dimensional codes developed for can and annular combustor design.
- The percent mass recirculated into the dome region, as well as the overall uniformity of mixing and combustion efficiency, is substantially influenced by jet row location. The momentum ratio of the incoming primary jet stream to that of the approaching crossflow of reacting dome gases has a direct impact on the mixing patterns as well. An increase in the number of primary jets leads, in the present case, to more uniform mixing due to a reduced penetration and a more uniform distribution of mixing about the duct circumference.

Acknowledgments

This study is supported by the Air Force Engineering and Services Center, Research and Development Directorate, Environics Division (Air Force Contract F08635-86-C-0309) with Captain Wayne Chepren as the contract monitor. The program is also supported by the Naval Air Propulsion Center with Mr. Anthony Klarman as the project liaison. The United States government is authorized to reproduce and distribute reprints for governmental contracts notwithstanding any copyright notation hereon. The authors gratefully acknowledge the assistance of Brian Bissel, Mark Baskovitch, Li Chen, Jay Pang, and Fayad Khatid for the collection and presentation of the data.

References

Bicen, A. F., and Jones, W. P., 1986, "Velocity Characteristics of Isothermal and Combusting Flows in a Model Combustor," *Combust. Sci. Tech.*, Vol. 49, pp. 1–15.

Brum, R. D., and Samuelson, G. S., 1987, "Two Component Laser Anemometry Measurements of Non-reacting and Reacting Complex Flows in a Swirl Stabilized Model Combustor," *Experiments in Fluids*, Vol. 5, pp. 95–102.

Cameron, C. D., Brouwer, J., and Samuelsen, G. S., 1989a, "A Detailed Characterization of the Velocity and Thermal Fields in a Model Can Combustor With Wall Jet Injection," ASME *Journal of Engineering for Gas Turbines and Power*, Vol. 111, pp. 31–35.

Cameron, C. D., Brouwer, J., and Samuelsen, G. S., 1989b, "A Model Gas Turbine Combustor With Wall Jets and Optical Access for Turbulent Mixing, Fuel Effects, and Spray Studies," *Twenty-Second International Symposium on Combustion*, the Combustion Institute, pp. 465–475.

Gouldin, F. C., Depsky, J. S., and Lee, S. L., 1985, "Velocity Field Characteristics of a Swirling Flow Combustor," *AIAA Journal*, Vol. 23, p. 95.

Lilley, D. G., 1985, "Investigations of Flowfields Found in Typical Combustor Geometries," NASA Contractor Report 3869.

Richards, C. D., and Samuelsen, G. S., 1990, "The Interaction of Primary Jets With a Swirl-Induced Recirculation Zone, Paper No. AIAA-90-0455.

Rudoff, R. C., 1986, "Design, Evaluation, and Characterization of a Gas Turbine Model Laboratory Combustor With Discrete Wall Injection," Masters Thesis, UCI Combustion Laboratory Report UCI-ARTR-86-1, Department of Mechanical Engineering, University of California, Irvine, CA, 92717.

Full Annular Rig Development of the FT8 Gas Turbine Combustor

T. G. Fox

B. C. Schlein

Pratt and Whitney Aircraft,
Division of United Technologies,
East Hartford, CT 06108

The results of developmental testing in a high-pressure, full annular combustion section of the FT8 industrial gas turbine are presented. Base power conditions were simulated at approximately 60 percent of burner pressure. All aspects of combustion performance with liquid fuel were investigated, including starting, blowout, exit temperature signature, emissions, smoke, and liner wall temperature. Configurational change were made to improve liner cooling, reduce emissions, adjust pressure loss, and modify exit temperature profile. The effects of water injection on emissions and performance were evaluated in the final test run. Satisfactory performance in all areas was demonstrated with further refinements to be carried out during developmental engine testing.

Introduction

The FT8 industrial/marine gas turbine is currently under development for introduction into service by late 1990. Although this gas turbine is a derivative of the widely used JT8D aircraft jet engine, the combustion system will have significantly different operational requirements. A new fuel injector, capable of employing either liquid or gaseous fuels, water or steam injection for NO_x control, or any combination thereof, has been under development in a single-segment rig [1]. The basic JT8D combustion chamber was modified to accept the new larger injector.

Prior to introduction into an actual FT8 engine, further testing was required in a full annular combustor rig to verify measurements made in the single-segment rig and develop combustor performance qualities such as exit temperature signature and flame propagation, which are not measurable in a single-segment rig. Like the JT8D, the FT8 combustion system has nine fuel injectors and nine individual can-type combustors situated in an annular combustion case. The full annular rig as described in the following section fully simulated this arrangement, as well as all the geometry and aerodynamics of the combustion section from the diffuser inlet to the burner exit. The test program was accomplished in four runs. Use of split configurations (four adjacent combustors of one configuration and five of another) in the final three tests allowed a total of seven configurations to be evaluated.

Although the full annular rig is primarily a tool for exit temperature signature development, opportunity was taken to modify the burner front end combustion airflow addition schedule for reduced NO_x emissions. Due to the lack of gas fuel storage and handling facilities at the test stand, only liquid fuel and water were evaluated.

Test Facility

The test facility, described schematically in Fig. 1, has high-pressure airflow supplied to the inlet by two series-mounted compressors driven by an FT4A gas turbine. Rig inlet air is preheated to combustor inlet conditions in two indirectly fired, nonvitiating preheaters operating in parallel. Airflow capacity of up to 45.5 kg/s (100 pps) with inlet temperatures and pressures up to 923°K (1200°F) and 4.14 MPa (600 psia), respectively, is available.

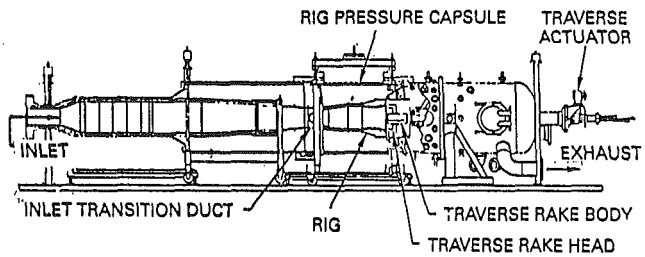

Fig. 1 High-pressure combustion test facility

Redundant airflow measurements are made both upstream and downstream of the preheaters. The primary measurement is made upstream of each preheater with a pair of sonic orifices with measurement accuracy of within 0.5 percent. The test section is installed in a breech-locked tank, which is pressurized above rig operating pressure to minimize burst loads. The rig inlet air duct provides an accelerating flow field in the transition from cylindrical to annular cross section.

The rig test section itself is comprised of full annular diffuser and burner cases in which are mounted nine fuel injectors and nine can combustors. The rear end of each combustor fits into a porthole in the face of an annular transition duct. Calibrated holes at the rear of the burner case allow shroud air to bypass the burner at a rate equal to the engine turbine cooling air requirements.

The fuel system consists of a single fuel feed pipe, which feeds a single flow divider. This valve has nine ports, supplying nine fuel manifolds, one to feed each fuel nozzle.

Contributed by the International Gas Turbine Institute and presented at the 35th International Gas Turbine and Aeroengine Congress and Exposition, Brussels, Belgium, June 11–14, 1990. Manuscript received by the International Gas Turbine Institute December 27, 1989. Paper No. 90-GT-29.

Circumferentially traversing combustor discharge rakes are mounted on a shaft rotating about the centerline of the combustor annulus. The traverse shaft extends through the rear wall of the exhaust chamber and is turned by an externally mounted actuator.

The pressure level in the test rig is regulated by a water-cooled back-pressure valve. Combustion exhaust gas is quenched by a water spray prior to atmospheric discharge through a silencer pit.

The data acquisition system incorporates, in addition to the standard pressure and temperature instrumentation, instrumentation for emissions and smoke measurements consistent with those specified by the latest EPA requirements. Steam-traced emission sampling lines are routed to the emission console located in the control room, where they can be manifolded as required.

Instrumentation

Figure 2 shows the fixed diffuser and burner case instrumentation. Three multihead Kiel-type total pressure rakes and two multihead total temperature rakes are spaced circumferentially at the diffuser inlet. Each rake has four radially spaced sensors. Burner case static pressures are located at five axial positions along the inner case and four axial locations along the outer case. At each of these locations probes are located at three circumferential positions.

Kiel-type total pressure probes are located at three circumferential positions at the rear of both cases. Static pressure taps are situated at the exit of the bypass air bleed holes to calculate the simulated turbine cooling air flow.

In order to detect lightoffs and blowouts, a total of 18 thermocouples, two per fuel injector, are installed in the wall of the transition duct.

Exit temperature measurements are made with two multihead rakes mounted on the rotating traverse. These were composed of six radially spaced thermocouples each. Similarly, exit pressure measurements and exhaust smoke and emissions sampling were accomplished by a multihead rake comprised of four Kiel-type heads mounted on the rotating traverse mechanism.

A Kulite-type sensing probe was inserted into the burner case to measure pressure oscillations.

Test Program

Hardware. The production dual fuel nozzle as shown in Fig. 3 is externally a more compact version of the experimental nozzle described in [1], but employs the same fuel injection philosophy. The liquid fuel is atomized by the air blast method whereby a swirling thin liquid film encounters high-velocity airflow on either side. This system produces a good circumferential spray pattern, even at low pressure drop, and allows for the large turndown ratio necessary when water injection for NO_x control is passed through the same passage. Swirl is induced in both inner and outer air passages by angled vanes. Gaseous fuel injection would ordinarily take place from slots in the exit of an annular passage wrapped around the liquid fuel nozzle. The nozzle used in the annular rig was devoid of this feature for ease of manufacturing early in the program since gas was not employed in this test series.

The initial combustor configuration was a basic JT8D reduced emissions can-type combustion chamber modified to accept the larger diameter of the dual fuel injector, as in the single-segment rig testing. The initial combustor airflow ad-

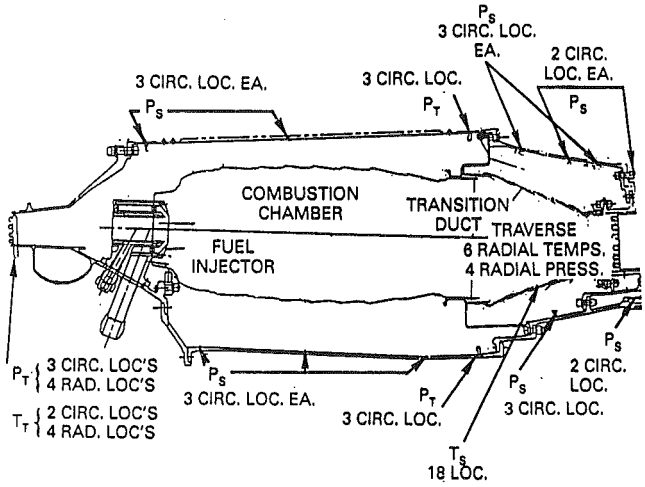

Fig. 2 Full annular combustion section with instrumentation

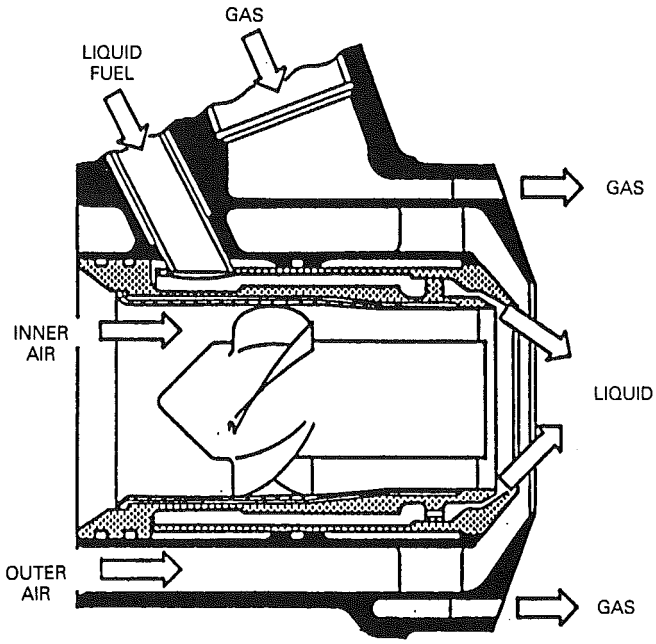

Fig. 3 Dual fuel injector (gas system not incorporated in full annular rig injector)

Nomenclature

ALP = Air Loading Parameter
b, c = constants in ALP equation
CO = carbon monoxide
ER = equivalence ratio, fuel–air/stoichiometric fuel–air
LBO = lean blowout fuel–air ratio
NO_x = oxides of nitrogen
PF = pattern factor; nondimensional peak exit gas temperature (Eq. (3))
ppm = parts per million by volume
P_{in} = Burner section inlet pressure, psia
R_{nox} = ratio of wet NO_x to dry NO_x
SN = SAE smoke number
T_{in} = burner section inlet temperature, R
V = burner volume, cubic feet
VBR = Von Brand Reflectance
W_a = burner section air flow, pps
W_f = fuel flow, pph
W/F = water-to-fuel ratio

Table 1 Test objectives

Run No.	Scheme	NOx Reduction	Exit Temp. Profile	Cooling	Pressure Loss
1	2A	----------BASELINE----------			
2	4C	X		X	X
2	5C	X		X	X
3	6D	X		X	X
3	7D	X		X	X
4	8D		X		X
4	9D	X	X		X

Table 2 Full annular rig operating points

Point	Pin psia	Tin °F	Wa pps	Wfuel pph	ALP
Start	16.0	66	10.9	500-700	
LBO	34.4	238	34.2		2.1
LBO	39.7	269	34.2		1.5
LBO	66.0	300	50.4		1.0
LBO	100.0	395	51.3		0.3
Base	159.3	838	100.0	6350	

dition schedule was similar to that of the JT8D reduced emissions combustor, which had been optimized for low idle emissions with its hybrid fuel injector [2]. The industrial engine goal of reduced NO_x at high power required a new airflow addition optimization, which was pursued in the present test program through modifications to the combustor hole pattern. After the initial baseline test of scheme 2A, schemes 4C through 9D were tested at the rate of two configurations per run while adjustments were made for pressure loss, exit temperature profile, cooling flow, and NO_x emissions as listed in Table 1. The axial air flow distributions are presented in Figs. 4 and 5.

Fuel. Standard Jet A aviation fuel was readily available at the test site and was employed throughout the program. Although this fuel is somewhat more volatile than the diesel fuel used in industrial gas turbines, both the literature [3] and our single-segment rig testing had indicated that the differences would be small. Diesel fuel would be expected to produce slightly higher smoke and NO_x and to require longer starting time. There should be no effect on exit temperature profile.

Test Conditions. Data were aquired at starting, snap decelerations (decel), and simulated base power conditions. The start and decel points are representative of steady-state points along engine transients and fully simulate the engine temperature, pressure, and airflow at the burner inlet. The blowout testing (Table 2) was performed over a range of air loading parameters (ALP) to define a blowout boundary. The facility had an airflow limitation below that of the engine; therefore the base (100 percent) power point had to be simulated by duplicating burner inlet and exit temperatures and burner inlet flow parameter. The simulated conditions for base power are given in Table 2.

Combustor Development

Starting and Propagation. Both starting and flame propagation were relatively fast for an industrial engine. Thermocouples behind each burner can indicated a three second elapsed time between fuel entering the combustors and the initial lightoff. Flame propagation took another 0.2 to 4.5 seconds. The starting and propagation times were independent of fuel flow rate over the range tested.

Section Pressure Loss. Target section pressure loss was 6 percent of burner inlet pressure (P_{in}). The initial test configuration produced a section pressure loss within 0.1 percent P_{in}

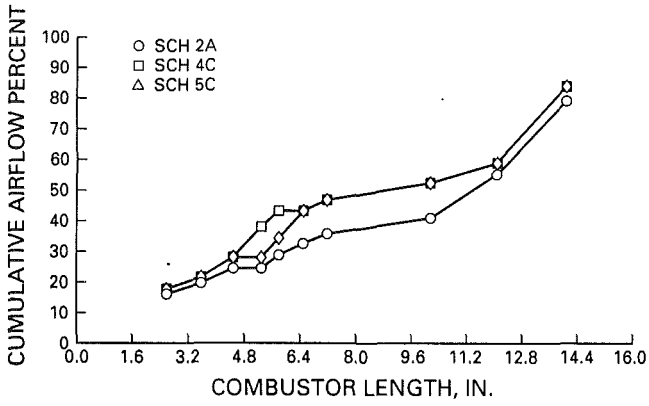

Fig. 4 Combustor airflow distribution

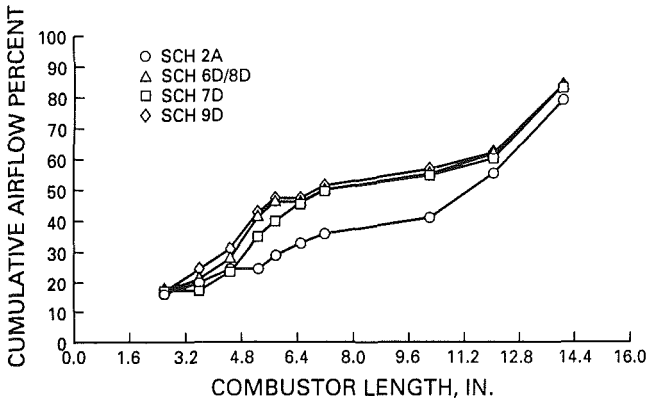

Fig. 5 Combustor airflow distribution

of the target. However, inspection of the exit temperature isotherms indicated spikes of cold air at both span edges. These spikes were traced to leakage between the burner aft end seals. The leakage was corrected for the final three runs. With minor modifications in each run the final configuration was 0.15 percent P_{in} above goal. This left some margin for future modifications to the cooling flow in engine development without having to compensate by adjusting the combustion and dilution holes.

Lean Blowout. Lean blowout (LBO) is the fuel-air ratio below which combustion cannot be sustained for a given burner inlet condition. LBO data is generally correlated against a combustor air loading parameter (ALP) such as that suggested by Lefebvre and Greenbough [4]:

$$\text{ALP} \propto \frac{W_a}{P_{IN}^{1.8} V e^{T_{in}/b}} \tag{1}$$

The authors state that the factor b is a function of combustor equivalence ratio, but in practice the local stoichiometry in the flame stabilization region is not known so that b is set to a constant. Blowout occurrences in the full annular rig are measured with the same exit thermocouples behind each combustor as employed as startup indicators. Data for the last two runs are plotted versus the air loading parameter in Fig. 6. The difference between the two runs is negligible. Run 2 LBO data, not shown, were 10 percent higher than runs 3 and 4. That configuration had a high pressure loss, which would have increased front end air flow sufficiently to explain the discrepancy. Comparison of the final run (run 4) data versus the calculated engine drop load decel path indicates sufficient margin exists to prevent combustor blowout.

Exit Temperature Profile and Pattern Factor. An intentional effort to adjust the exit temperature profile was made

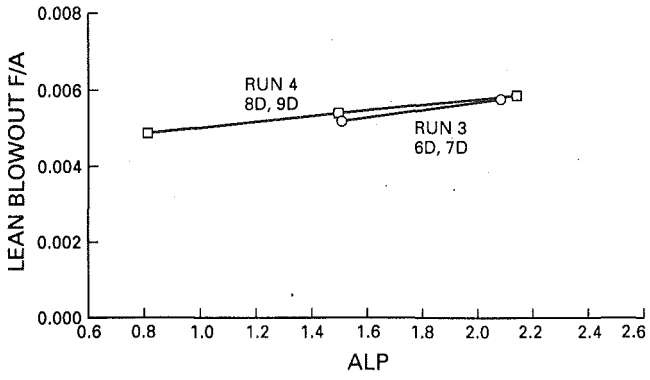

Fig. 6 Full annular rig lean blowout versus air loading parameter

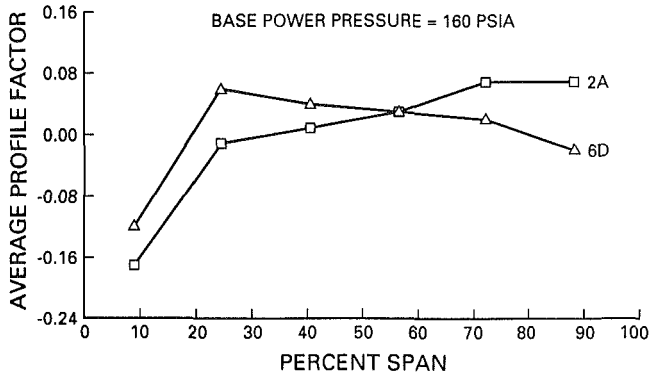

Fig. 7 Comparison of exit temperature radial profiles

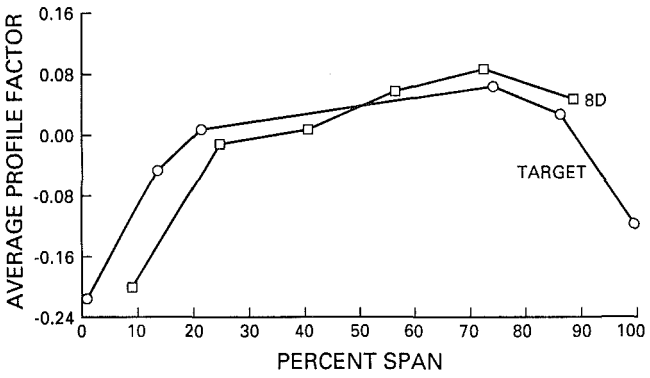

Fig. 8 Dry exit temperature radial profile versus target

only in the final run. Adjustments of front end air flow made in runs 2 and 3 for emissions reductions had significant effects on the exit profile. The baseline scheme 2A configuration had a profile that peaked in the outer span (73–88 percent span) as shown in Fig. 7. Profile factor is defined as:

$$\text{PROFILE FACTOR} = \frac{T_{\text{MAX AVG}} - T_{\text{AVG}}}{T_{\text{AVG}} - T_{IN}} \qquad (2)$$

The successful front end combustion hole adjustment, which resulted in reduced NO_x scheme 6D of run 3, shifted the profile peak to the inner (24 percent) span. Adjustment of the combustion rear end dilution hole pattern was made for scheme 8D to shift the profile to the outer span as shown in Fig. 8 versus the target profile. The match was considered more than acceptable for initial engine testing. Water injection had little effect on the exit profile. Figure 9 compares the scheme 8D profile dry and at water to fuel ratios of 0.5, 1.0, and 1.5. They are essentially the same.

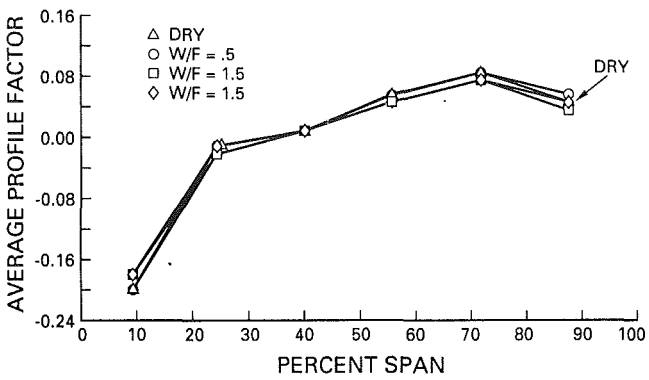

Fig. 9 Effect of water on average exit radial temperature profile

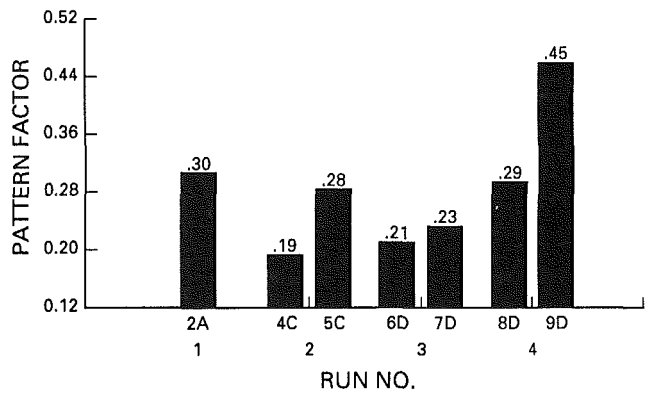

Fig. 10 Pattern factor comparison

Where exit profile is a measure of the average gas signature, pattern factor is a measure of the peak exit temperature:

$$PF = \frac{T_{\text{MAX}} - T_{\text{AVG}}}{T_{\text{AVG}} - T_{IN}} \qquad (3)$$

Like the profile, the pattern factor was affected by front end air flow. Scheme 6D, which shifted the profile toward the inner diameter, also reduced the pattern factor by 0.09 relative to the baseline. The final configuration, scheme 8D, had an acceptable pattern factor that was only 0.01 lower than the baseline. Apparently the very low pattern factor of scheme 6D was associated with the inner peaked profile. The pattern factors for the various combustor configurations are summarized in Fig. 10.

As with profile factor, water injection had no effect on pattern factor, indicating that the combustion-dilution hole pattern obtained for dry running is also suitable for wet application.

Emissions. Industrial gas turbines must meet strict NO_x emissions regulations while controlling unburned hydrocarbons and carbon monoxide. When water injection is employed as the NO_x control method, the combustor must have a relatively low dry NO_x level and an effective reduction (R_{nox}) at a given water/fuel ratio. The initial test showed the dry NO_x level of the baseline scheme to be too high at 325 ppm (all emissions levels reported are on a dry basis corrected to 15 percent oxygen) at simulated base power condition. When corrected to actual engine pressure by the standard factor of $P_{in}^{0.5}$, a dry NO_x level of approximately 425 ppm would be expected. The high NO_x level of the baseline configuration was not entirely unexpected because of the significant difference in performance requirements, and fuel injection technique between the JT8D, from which the baseline was derived, and the FT8.

An analysis of the fuel-air schedule for the initial scheme

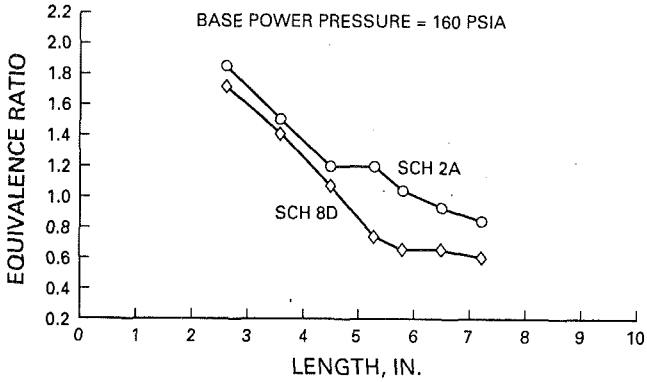

Fig. 11 Equivalence ratio versus burner length

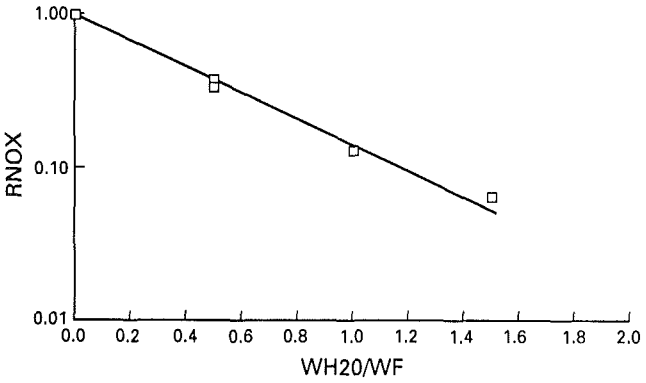

Fig. 12 NO_x reduction ratio (R_{NOX}) versus water/fuel, for liquid fuel and water

2A combustor showed that at base power, an equivalence ratio between 0.8 and 1.2 was maintained for a considerable length of the combustor, as shown in Fig. 11. This combination of long residence time at high temperature promotes NO_x formation.

Subsequent schemes were devised to add quench air at the end of the primary zone to reduce the time spent at high temperature. This technique was generally successful. For example, schemes 6D and 8D (identical except for dilution holes), which followed the quick quench stoichiometric schedule also shown in Fig. 11, had measured NO_x levels of 243 and 239 ppm, respectively, a reduction of 26 percent from the 2A baseline. Scaling for pressure to actual engine base power produces an estimated 315 ppm of NO_x. This was within published levels for other aeroderivative engines of the FT8 class [5].

While the simple one-dimensional analysis of combustor stoichiometry shown in Fig. 11 was useful in obtaining significant NO_x reductions, the limitations of this type of analysis were demonstrated by scheme 9D, where NO_x levels were 50 ppm higher than scheme 8D despite additional midcombustor air addition. It is surmised that the additional air overpenetrated the two-dimensional midcombustor flame zone or else recirculated back into the primary.

Water injection testing with the scheme 8D demonstrated excellent NO_x reduction efficiency. R_{nox} shown in Fig. 12 is consistent with published data [6].

Carbon monoxide and unburned hydrocarbons were not a problem with water injection. Hydrocarbons never rose above 3.6 ppm. Carbon monoxide was less than 15 ppmv below a 1.2 water–fuel ratio, increasing to 54 ppmv at a 1.5 water–fuel ratio. At the 1.2 ratio NO_x was less than 30 ppmv even after correcting for pressure while an acceptable CO level of 15 was maintained. The effect of increased pressure at actual engine conditions would be to reduce the measured levels of both hydrocarbons and carbon monoxide.

Table 3 Full annular rig smoke levels

Run No.	Scheme	SAE SMOKE NO.
1	2A	13.2
4	8D	9.5
4	9D	8.5

Smoke. Smoke data were acquired by means of a sampling traverse at the combustor exit. The dry smoke number (SAE units) for the initial scheme 2A and the final two configurations, 8D and 9D, of run 4 are listed in Table 3.

Schemes 8D and 9D had progressively more midcombustor air addition for NO_x reduction relative to the 2A baseline and the trend of decreasing smoke indicated that these modifications were also beneficial to smoke.

The effect of water addition on smoke levels is shown in Fig. 13 where smoke number is shown versus water–fuel ratio for schemes 8D and 9D. Smoke decreases to very low levels at water–fuel ratios above 1.0. It can be concluded that if dry smoke levels are satisfactory, wet levels will be even more so.

Industrial engine smoke requirements are typically quoted in Von Brand Reflectance (VBR) units, where 100 VBR is perfectly clean and 0 is perfectly black. The relationship between SAE and VBR smoke levels is described in Fig. 14. An SAE 13 smoke level is approximately 95 VBR. Although smoke visibility depends on many factors, the smoke demonstrated by schemes 8D and 9D should be invisible.

No pressure correction to actual engine conditions was made since none was indicated by testing in full pressure single segment rig testing. Smoke regulations are enforced at the exhaust stack rather than the burner exit. Clean air from turbine cooling added between the burner exit and the stack should reduce smoke sufficiently to compensate for the increasing smoke effect of diesel fuel relative to Jet A.

Burner Efficiency. In dry operation, the FT8 combustor system operated at over 99.9 percent burner efficiency at all high-power conditions. This level was retained even up to 1.5 water/fuel ratio on wet operation. Burner efficiency was lower during idle operation, as expected. Measurements made during run 3 indicated a 96.5 percent level for scheme 6D which has the same front end as the 8D. This level is considered satisfactory since it should be sufficient to prevent visible "white smoke" often seen in the exhaust at these conditions.

Liner Durability. Combustor cans of each configuration were coated with temperature sensitive paint on both the hot and cold surfaces to assess wall temperatures and potential durability. Thermal barrier coating, which is bill-of-material on production combustors, was not employed on the test cans.

On the basis of the paint results, cooling patterns evolved from the "A" to "C" to "D" schemes and liner hot spots were eliminated. Adding front end air for NO_x quenching cooled the rear liner walls as flame temperature decreased. In some configurations (5C and 7D) where the front end hole pattern was more radically altered, new hot spots appeared that would have required further development had these configurations shown promise as low-NO_x candidates.

Burner Noise. Combustor noise levels that increase with increasing water injection rates and increasing fuel–air ratios have been reported in the literature [7]. These trends were observed in the full annular rig by instrument and human ear. Levels of concern were observed only for water–fuel ratios above 1.5. Experience has shown that stand geometry, specifically the length of the exhaust duct, has an influence on resonant frequencies such that rig-generated noise may not appear in the engine. Combustor noise will be fully monitored in engine water injection tests.

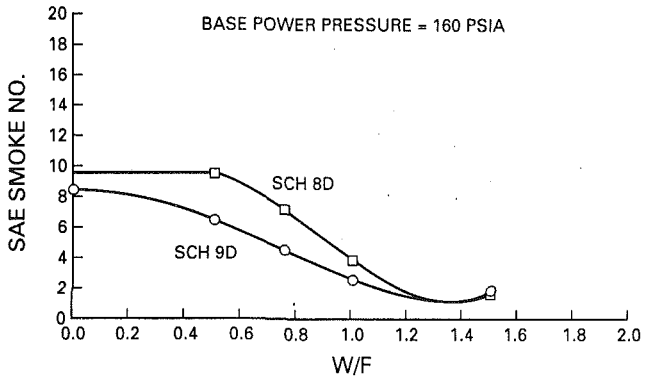

Fig. 13 Effect of water on SAE smoke number

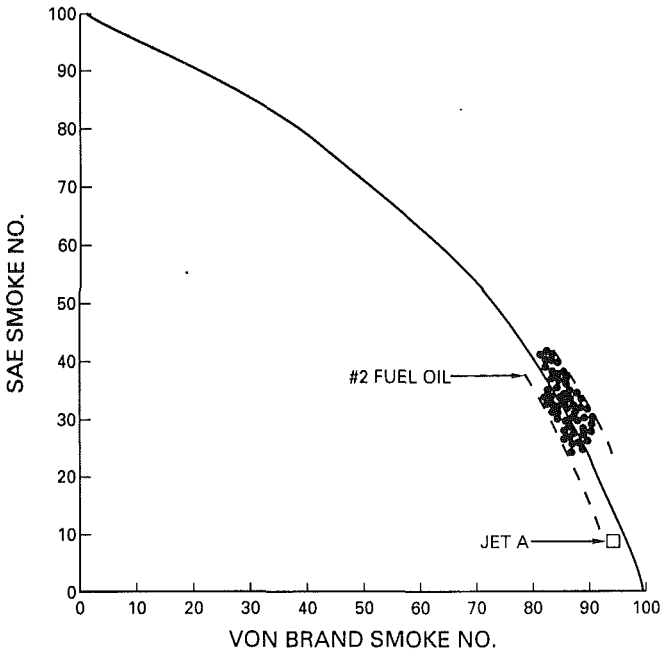

Fig. 14 Correlation of SAE and Von Brand smoke numbers

Conclusions

A combustor configuration (scheme 8D) was developed in the full annular rig that fully satisfied all goals for initial engine testing with liquid fuel and water for NO_x abatement. Dry NO_x emissions were reduced by 26 percent from the initial configuration. Target exit temperature signatures and section pressure loss were obtained. Adequate starting characteristics, blowout, smoke, and potential liner durability were demonstrated. Both dry NO_x and NO_x reduction effectiveness with water should produce competitive NO_x levels. Water injection reduced smoke levels and had no effect on exit temperature pattern.

References

1 Schlein, B. C., Fox, T. G., and Puma, C. J., "Development of a Dual Fuel Injector for a Gas Turbine Combustor," ASME Paper No. 89-GT-25, 1989.

2 Zeisser, M. H., and Fox, T. G., "A JT8D Low Emissions Combustor by Radial Zoning," presented at the AIAA/SAE/ASME 19th Joint Propulsion Conference, June 27-29, 1983, Seattle, WA.

3 Butz, H. F., and Smith, A. L., "Effect of Fuel Properties on Performance of a Single Aircraft Turbojet Combustor at Simulated Idle, Cruise and Takeoff Conditions," NASA TM-73780, Sept. 1977.

4 Lefebvre, A. H., and Greenbough, W. V., "Some Applications of Combustion Theory to Gas Turbine Development," Sixth Symposium (International) on Combustion, Reinhold Publishing, New York, 1957, p. 858.

5 Smith, S. S., "Aeroderivative Gas Turbine Performance, Emissions and STIG," Turbomachinery International, Jan.-Feb. 1989, pp. 21-31.

6 Bahr, D. W., and Lyon, T. E., "NO_x Abatement via Water Injection in Aircraft-Derivative Turbine Engines," ASME Paper No. 84-GT-103, 1984.

7 Hilt, M. B., and Waslo, J., "Evolution of NO_x Abatement Techniques Through Combustor Design for Heavy-Duty Gas Turbines," ASME JOURNAL OF ENGINEERING FOR GAS TURBINES AND POWER, Vol. 106, 1984, pp. 825-832.

Turbulent Combustion Properties Behind a Confined Conical Stabilizer

J. C. Pan

W. J. Schmoll

D. R. Ballal

University of Dayton,
Dayton, OH 45469

Turbulence properties were investigated in and around the recirculation zone produced by a 45 deg conical flame stabilizer of 25 percent blockage ratio confined in a pipe supplied with a turbulent premixed methane–air mixture at a Reynolds number of 5.7×10^4. A three-component LDA system was used for measuring mean velocities, turbulence intensities, Reynolds stresses, skewness, kurtosis, and turbulent kinetic energy. It was found that wall confinement elongates the recirculation zone by accelerating the flow and narrows it by preventing mean streamline curvature. For confined flames, turbulence production is mainly due to shear stress–mean strain interaction. In the region of maximum recirculation zone width and around the stagnation point, the outer stretched flame resembles a normal mixing layer and gradient-diffusion closure for velocity holds. However, and in the absence of turbulent heat flux data, countergradient diffusion cannot be ruled out. Finally, and because of the suppression of mean streamline curvature by confinement, in combusting flow, the production of turbulence is only up to 33 percent of its damping due to dilatation and dissipation.

Introduction

Bluff body flame holders are widely used in afterburners and other practical combustion systems to stabilize a flame. They produce a recirculation zone in the flow field. This zone serves a triple purpose: (*i*) producing a region of low velocity, (*ii*) providing long residence time for the flame to propagate into the incoming fresh mixture, and (*iii*) serving as a source of continuous ignition for the incoming fuel–air mixture. Thus, a steady flame is stabilized and propagates downstream into the combustor.

Many different geometric shapes of bluff bodies, such as a cylinder, cone, disk, vee-gutter, or sphere, can be used as flame stabilizers. The recirculation zone produced by each bluff body is affected by its geometry (aerodynamic effect), the type of fuel and equivalence ratio (chemical effect), and its confinement (pressure-gradient effect) in the combustor. Thus, a complex aerodynamics-chemistry-pressure gradient interaction is present in reactive recirculatory flow fields. This fact, together with its existence in many practical combustor configurations, such as gas turbine combustors, dump combustors, and backward-facing step combustors, makes any investigation of this type of flow field of considerable practical significance.

Numerous studies report measurements of mean and turbulent cold flow properties behind bluff bodies; for example, see the review paper by Griffin (1985). In contrast, very little information is available on the turbulent combustion properties behind bluff bodies. The work of Winterfeld (1965) describes effects of recirculation zone geometry on exchange coefficients and mean residence time, that of Ballal and Lefebvre (1979) discusses weak extinction limits, and that of Rao and Lefebvre (1982) analyzes flame blowout. Recently, Heitor and Whitelaw (1986) and Sivasegaram and Whitelaw (1987) have presented measurements of stability limit in a small gas turbine combustor, and discussed the suppression of combustion instability. Finally, Ballal et al. (1989) report data on turbulent flow properties, but in an *open* turbulent premixed flame.

In this paper, we provide turbulence properties in the practically more interesting case of a *confined* turbulent recirculatory flame. Measurements of turbulent velocity fluctuations such as mean and rms values, skewness and flatness factors, Reynolds shear stresses, and axial mean pressure gradients are reported with and without combustion. Then these data are interpreted to elucidate the recirculation zone structure, effects of flow confinement, and the role of combustion-generated turbulence.

Experimental Work

1 Test Facility. Figure 1 shows the test facility we used for these experiments. A machined stainless steel conical flame stabilizer of base diameter, $d = 4.44$ cm (1.75 in.), apex angle $\theta = 45$ deg, and $BR = 25$ percent was mounted coaxially inside a pipe of 8-cm nominal dimension and which has cut-outs for four optical quality glass windows. This pipe is supplied with high-velocity, premixed methane–air combustible mixture from a vertical combustion tunnel mounted on a three-axis traversing platform described by Ballal et al. (1987). A torch igniter was used to ignite the turbulent combustible mixture. Measure-

Contributed by the International Gas Turbine Institute and presented at the 35th International Gas Turbine and Aeroengine Congress and Exposition, Brussels, Belgium, June 11–14, 1990. Manuscript received by the International Gas Turbine Institute January 10, 1990. Paper No. 90-GT-51.

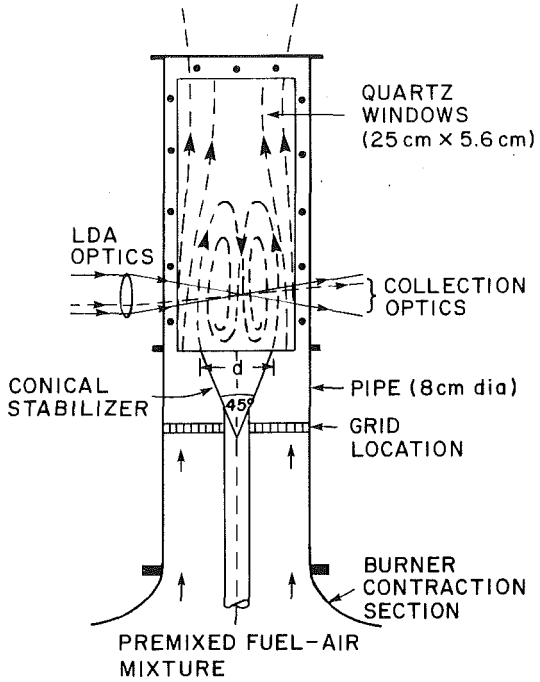

Fig. 1 Schematic diagram of the confined flame stabilizer test facility

ments of turbulence quantities and mean wall-static pressure were performed downstream of the confined conical stabilizer by using a three-component laser-Doppler Anemometer (LDA) and precision micromanometer, respectively.

2 Test Condition. Zukoski and Marble (1955) have pointed out that the bluff body wake region becomes fully turbulent when $\mathrm{Re}_d \geq 10^4$. Therefore, all our experiments were performed at $U_a = 20$ m/s or $\mathrm{Re}_d = U_a d/\nu = 5.7 \times 10^4$, and approach turbulence level $u'/U_a = 4$ percent, and $v'/U_a = 2.8$ percent. Thus, conditions of fully developed turbulence existed in our recirculatory flow field. Also, limitations posed by the test facility maximum fuel flow rate, capability of the LDA seed particle generator, and safety considerations related to flame flashback, all combined to restrict the maximum annular mixture velocity to the above stated value. Tests were performed at three different equivalence ratios, $\phi = 0.65$, 0.80, and 1.0, of methane–air mixture, corresponding to $T_f = 1755$ K, 1996 K, and 2226 K, respectively, at room temperature and pressure. The measurement locations ranged in axial direction from $x/d = 0.05$ to 4.5 and in radial direction from $r/d = -0.55$ to $+0.55$.

3 LDA Instrumentation. A three-component LDA system was used for all velocity measurements. Essentially, this instrument is an upgraded and refined version of the two-component LDA system used by Ballal et al. (1989). It uses the green (514.5 nm) and blue (488 nm) lines of 15-W, argon-ion laser as a source. Two measurement channels of this LDA system are separated by polarization, whereas the third channel uses the blue beam. Principally, this instrument incorporates Bragg cell frequency shifting for measurements in a recirculatory flow, a unique three-channel coincidence circuit for rapid acquisition of valid data (a feature necessary for integrating LDA with CARS, Raman, or Rayleigh spectroscopic techniques), software to filter spurious signals, for example, due to seed agglomeration, and a correction subroutine to account for the LDA signal biasing effect in combusting flows. The third-channel optics of the LDA is set up normal to the two-channel optics, and the scattered signal is collected in a forward direction 10 deg off axis. A fluidized bed seeder is used to inject submicron sized Al_2O_3 seed particles into the flowing combustible mixture. The effective LDA measurement volume dimensions were $50\ \mu m \times 500\ \mu m \times 1000\ \mu m$. Scattered signals were detected by TSI Counter Processors (CP) and processed by our custom-designed software to yield intensity, shear stress, higher moments (skewness and kurtosis), and pdfs. Typical sampling rates for LDA measurements exceeded 1 kHz for both isothermal and combusting flows. For a three-component system with a relatively small measurement volume, these sampling rates (particularly in combusting flows) were considered satisfactory.

4 Error Analysis. Both the fuel flow and airflow were monitored by separate TYLAN electronic flow control units to within 1 percent. Also, mass conservation balance in the plane of the bluff body base provided an additional cross-check against flow meter readings. The primary source of error in LDA measurement is the statistical bias of the final measured velocity toward higher mass flux (velocity × density) when number-weighted averages are used to calculate stationary statistics. Chen and Lightman (1985) and Glass and Bilger (1978) have discussed bias correction schemes. After allowing for this bias, we estimated that for the single-stream seeding and relatively high sampling rates of our experiments, the uncertainty in the measurement of mean velocity was 1 percent, for rms velocity 5 percent, and for skewness and flatness 7 percent. Near the flame front, where intermittency would be much higher, the uncertainty in rms velocity could be greater than 7 percent. The long-term repeatability of measurements was found to be within 5 percent for turbulence quantities.

Nomenclature

a = ratio of $(\overline{uv}/q)$
BR = blockage ratio
C_p = static pressure coefficient $= \Delta P/0.5\ \rho U_a^2$
d = base diameter of conical stabilizer
D_t = turbulent eddy diffusivity
K = kurtosis
L = length of the recirculation zone
$\dot{m}$ = mass flow rate
P = pressure
q = turbulent kinetic energy (TKE)
r = radial direction
R = pipe radius
S = skewness
T = temperature
U, V = mean velocities in axial and radial directions
u, v = fluctuating velocities in axial and radial directions
$\overline{uv}$ = Reynolds shear stress
$\overline{uT}, \overline{vT}$ = axial and radial turbulent heat flux
W = recirculation zone maximum width
x = axial direction
θ = cone apex angle
ν = kinematic viscosity
ρ = density
τ = heat release parameter
ϕ = equivalence ratio
ψ = mean stream function

Superscripts

$\bar{}$ = mean value
$'$ = rms value

Subscripts

a = annular flow
b, u = burned and unburned
c, f = combusting flow, flame
r = reverse direction
t = total, turbulent

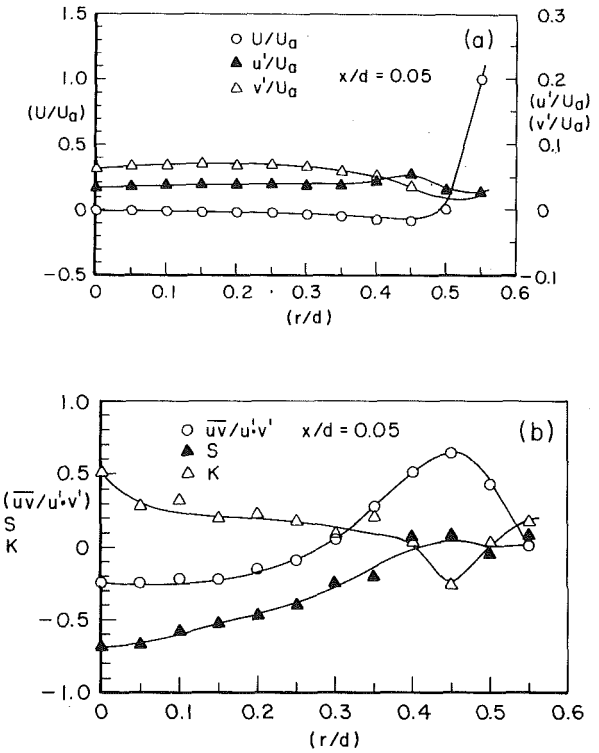

Fig. 2 Measurements of inlet boundary flow conditions at $U_a = 20$ m/s, $\phi = 0.65$, and $(x/d) = 0.05$: (*a*) profiles of mean and rms turbulence velocities; (*b*) profiles of Reynolds shear stress, skewness and kurtosis.

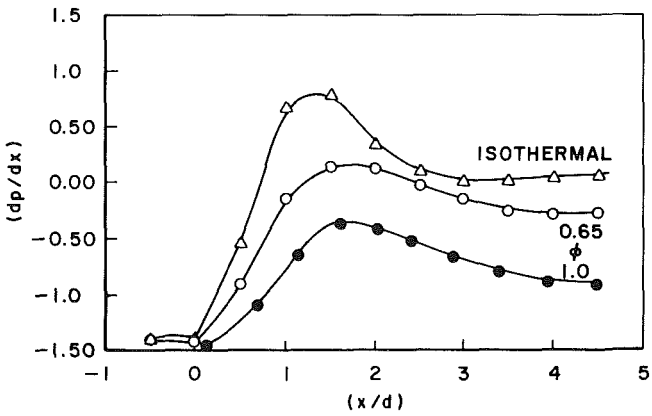

Fig. 3 Combustor wall pressure gradients at $U_a = 10$ m/s in confined isothermal and combusting flows

Results and Discussion

Recently, it has been recognized that *chaotic* systems such as turbulent flows are extremely sensitive to inlet boundary conditions. Also, as suggested by Strahle and Lekoudis (1985), modeling codes require the specifications of inlet or starting conditions to initiate predictions of flow development downstream. Finally, the importance of inlet boundary conditions to numerical simulation of combustor flows is very elegantly demonstrated by Sturgess et al. (1983). For these reasons, we begin by providing turbulence properties in the inlet plane of the conical bluff body. Lack of space precludes our presenting all our data. Therefore, only selected data that are relevant to the discussion of recirculation zone structure, effect of confinement and combustion generated turbulence are presented.

1 Inlet Boundary Conditions. Figures 2(*a*) and 2(*b*) show radial profiles of mean and turbulence quantities in the axial plane $x/d = 0.05$ ($x = 2.25$ mm), respectively. This plane is so close to the base of the bluff body that, as seen in Fig. 2(*a*), the axial mean velocity is negligibly small in the recirculation zone ($r/d < 0.5$) and rises rapidly to $U/U_a = 1$ beyond $r/d > 0.5$. Also, the axial turbulence intensity has value close to approach turbulence value of $u'/U_a = 4$ percent, but the radial turbulence intensity v'/U_a is significantly higher and dominates.

Figure 2(*b*) shows the radial profiles of Reynolds shear stress, skewness $S = u^3/(u'^2)^{3/2}$ and kurtosis $K = u^4/(u'^2)^2 - 3$ of axial velocity fluctuations. The Reynolds shear stress reaches a maximum value in the mixing region around the conical stabilizer. Values of S and K were respectively *lower* than and *higher* than zero in the hot recirculatory flow, but tend to zero in the annular stream because of the small-scale structure of the incoming free-stream turbulence. Note that for this confined flame, no narrow peaks or transient dips could be observed, as was the case for the open flame (see Ballal et al., 1989, Figs. 3*a* and 3*b*).

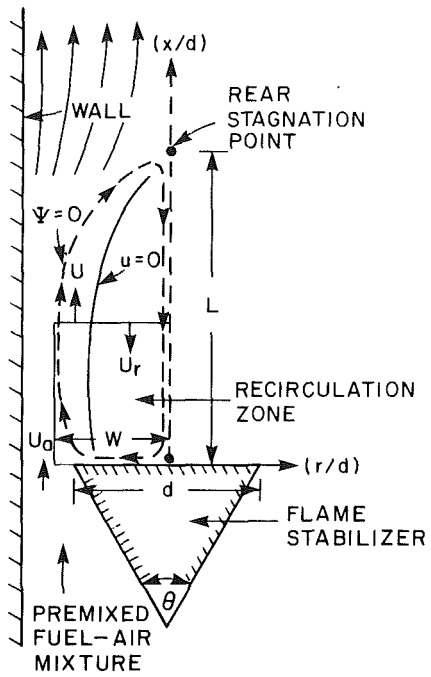

Fig. 4 Sketch of the recirculation zone in a confined combusting flow

2 Axial Pressure Distribution. When the combustion process is confined, it accelerates the incoming isothermal flow and decreases wall static pressure. Figure 3 shows the measured axial wall pressure gradient dP/dx in our combustor for isothermal and combusting cases. A negative value of dP/dx suggests flow acceleration and this is found to be the case for combusting flows. For isothermal flow, deceleration sets in beyond $x/d = 0.7$, which corresponds to a minimum value of C_p or the location of maximum recirculation zone width. Finally, the maximum positive value of dP/dx is generally associated with the location of the rear stagnation point. Therefore, the data presented in Fig. 3 give the recirculation zone length as $1.5d$, $1.7d$, and $1.6d$ for isothermal, confined lean-combusting ($\phi = 0.65$), and confined stoichiometic-combusting ($\phi = 1$) flows, respectively.

3 Recirculation Zone Parameters. The size, shape, and mean flow structure of the recirculation zone may be determined by calculating the spatial distribution of the mean stream function ψ from the equation

$$\psi = \int_0^r \rho U r dr \tag{1}$$

Table 1 Recirculation zone parameters

Conical Stabilizer

$\theta = 45^0$, BR = 25%, $\phi = 0.65$, $Re_d = 5.7 \times 10^4$

	Confined Cold Flow	Confined Flame	Open Flame
(L/d)	1.5	1.70	1.85
(W/d)	0.55	0.58	0.65
$(U_r/U_a)^*$	-0.24	-0.40	-0.30
$(\dot{m}_r/\dot{m}_t)$	0.20	0.13	0.10
(u'/U_a)	0.3	0.24	0.32
(v'/U_a)	0.26	0.17	0.28
(q_c/q)	1.0	0.64	1.12

* at x/d = 0.8, r/d = 0.3

Also, knowing the value of $C_{p,\min}$, we can derive the maximum width W of the recirculation zone as:

$$W = R[1 - \{(1 - BR)/(1 - C_{p,\min})^{1/2}\}]^{1/2} \quad (2)$$

From Eq. (1), the ratio of reverse to total mass flow rate $\dot{m}_r/\dot{m}_t$ was calculated. This ratio represents the recirculation strength. Figure 4 shows a sketch of the recirculation zone which appears similar to an ellipsoid of revolution. Table 1 lists the various recirculation zone parameters for confined cold flow, confined flame, and open flame, respectively.

In Table 1, the recirculation zone is more elongated in combusting as opposed to isothermal flows. This is consistent with the findings of Winterfeld (1965). A physical explanation is that acceleration of flow throughout the combustor together with prevention of mean streamline curvature by the confining walls causes the flow to overcome the adverse pressure gradients, thereby producing an elongated recirculation zone. On the other hand, confined combustion always produces a certain positive back pressure and this keeps the length of the recirculation zone somewhat shorter in confined than in open flames. Large mean streamline curvature and turbulent dilatation in open flames produce the widest recirculation zone. The recirculation strength of the cold confined flow is highest principally because of higher gas density, even though the reverse mean flow velocity is highest in confined flame. Finally, in an open flame, large streamline curvature more than compensates for any damping of turbulence by dilatation and generates larger axial and radial turbulence intensities and turbulent kinetic energy as compared to confined flows.

4 Turbulence Properties. As illustrated in Fig. 4, the recirculation zone causes flame stretching in the axial plane corresponding to its maximum width and in the vicinity of the rear stagnation point. For our confined flame, these two locations are at $x/d = 0.8$ and 1.7, respectively. Therefore, we present and discuss data on turbulence properties at these locations.

(*a*) *Region of Maximum Recirculation Zone Width.* Figure 5(*a*) shows profiles of centerline mean and rms velocity fluctuations. Note that the mean reverse velocity and axial turbulence intensity have maximum values in the axial plane corresponding to the first location of the flame stretch. At the stagnation point, $U/U_a = 0$ and both axial and radial turbulence intensities are significant as expected.

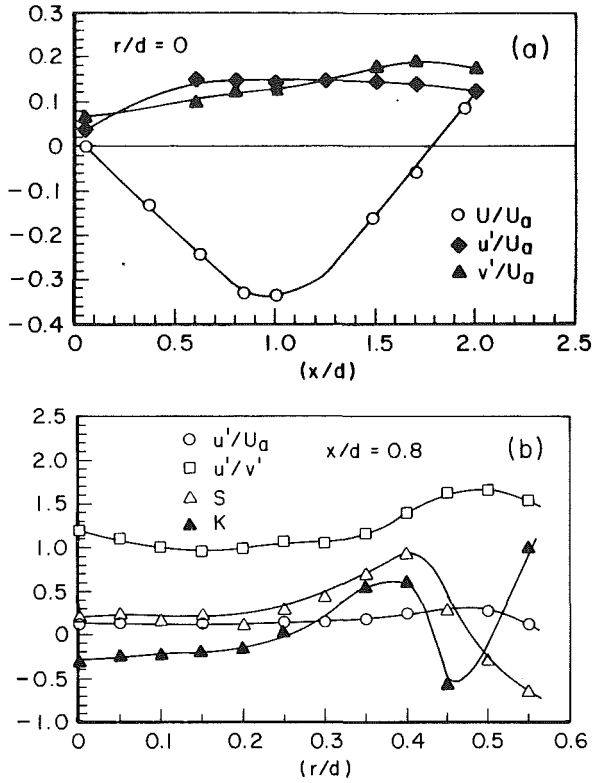

Fig. 5 Measurements of turbulence properties at $U_a = 20$ m/s, $\phi = 0.65$, in the region of maximum recirculation zone width ($x/d = 0.8$: (*a*) centerline profiles of mean and rms velocity fluctuations; (*b*) radial profiles of axial turbulence intensity, anisotropy, skewness, and kurtosis

Figure 5(*b*) shows radial profiles of u'/U_a, u'/v', S, and K in the axial plane of maximum recirculation zone width, $x/d = 0.8$. It is observed that axial turbulence intensity is fairly constant within the recirculation zone and reaches a maximum value of 28 percent at $r/d = 0.45$, very close to the stretched flame surrounding the recirculation zone. Close to this location, the reactive flow has a highly skewed turbulence structure (note: $S = 0.8$ and $K = -0.7$), presumably due to the presence of a large-scale eddy formed in the mixing layer around the highly strained flame region. Also, note that the axial turbulence intensity dominates in the flame region.

(*b*) *Stagnation Point Region.* The exact location of a stagnation point is very difficult to assess. This is a small region in which the flow direction is quickly reversed, the fluid parcels are stretched, and strong gradients of mean and turbulence quantities are present. A simple way to ascertain the location of the stagnation point is to seek a common location at which axial and radial velocity profiles cross and change sign. However, a more definitive way to establish the location of the stagnation point is to seek the maximum local value of u'/U. These criteria were combined to pinpoint the exact *mean* location of the stagnation point at $x/d = 1.7$ and $r/d = 0$.

Figures 6(*a*) and 6(*b*) show turbulence properties in the vicinity of the stagnation point. In Fig. 6(*a*), positive axial velocity is found beyond $r/d = 0.3$. This suggests, and visual observations confirm, the necking down of the flame in the vicinity of the stagnation point. The axial turbulence intensity has a peak value of almost 25 percent at $r/d = 0.3$ in this second flame stretch region. Finally, and as would be expected, the

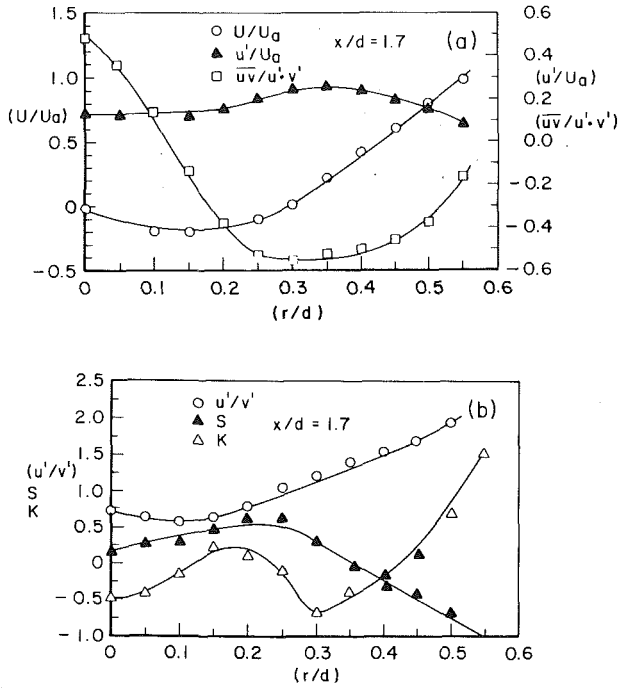

Fig. 6 Turbulence properties for $U_a = 20$ m/s, $\phi = 0.65$, in the rear stagnation point region ($x/d = 1.7$: (*a*) profiles of mean and rms velocities, and Reynolds shear stresses; (*b*) profiles of anisotropy, skewness, and kurtosis

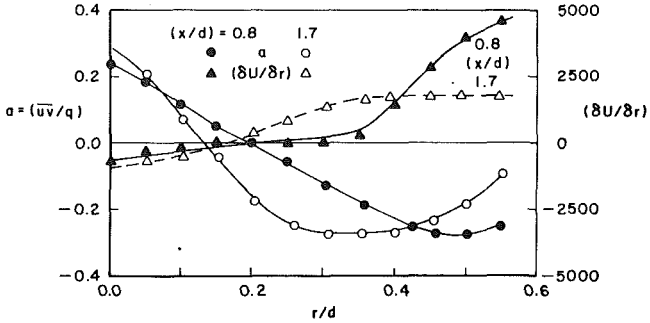

Fig. 7 Radial profiles of $(\overline{uv}/q)$ and $\delta U/\delta r$ at $U_a = 20$ m/s, $\phi = 0.65$, illustrating the validity of the gradient-diffusion relationship in turbulent combusting flows

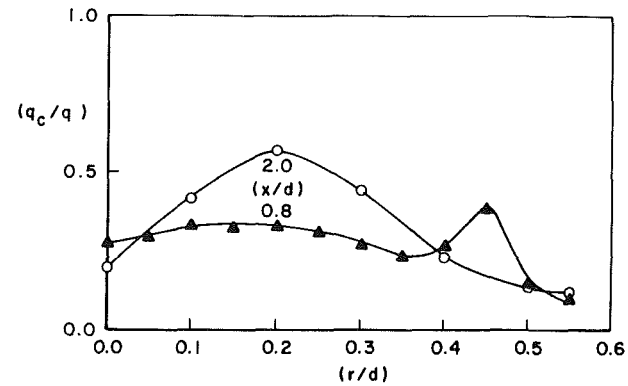

Fig. 8 Radial profiles of (q_c/q) at $U_a = 10$ m/s, $\phi = 0.65$, illustrating the influence of combustion on turbulent kinetic energy in a confined recirculatory flow

Reynolds shear stresses change sign about half-way (at $r/d = 0.15$) between the centerline and the flame necking-down location.

Figure 6(*b*) illustrates the nature of turbulent flow in the vicinity of the stagnation point via plots of u'/v', S, and K. Inspection of (u'/v') data immediately reveals that marked anisotropy of turbulence prevails in the region around the stagnation point. Moreover, the radial turbulence component is dominant in the zone between the centerline and the flame necking-down region, i.e, $r/d = 0$ to 0.3. Also, peaks in skewness and kurtosis profiles are evident around $r/d = 0.3$. Such peaks can also arise due to flow unsteadiness, and spectral analysis may be required. Nevertheless, it is apparent that the turbulence structure is distorted in the combusting flow. This observation differs from the experiments of Starner and Bilger (1980) who found that the structure parameters were essentially the same for both isothermal and reacting flows for a jet diffusion flame with axial pressure gradient.

Further Discussion

In this section, we briefly discuss three issues: (*i*) the effect of wall confinement, (*ii*) the nature of the flame reaction zone, and (*iii*) combustion-generated turbulence.

(i) Influence of Wall Confinement. A bluff body confined in a pipe not only produces a geometric blockage, but also an aerodynamic blockage corresponding to the deflection of the mean separation streamline from its trailing edge. Wall confinement prevents any significant deflection of mean flow streamlines and also produces flow acceleration to elongate the recirculation zone. Consequently, in confined flames, the production of TKE is by the interaction of Reynolds stress and shear strain, i.e., via the term $\overline{uv}\,\partial U/\partial r$, and therefore restricted to the shear layer surrounding the maximum width of the recirculation zone. If the wall confinement is removed, only turbulent dilatation and mean pressure gradients (i.e., normal and not Reynolds stresses) would contribute to TKE production. An increase in aerodynamic blockage (say by increasing geometric blockage) decreases the angles of the streamline at the baffle trailing edge. It also brings streamlines closer to the walls. Both these effects contribute to decreasing streamline curvature and, as shown by Winterfeld (1965), produce increased length and decreased width of the recirculation zone.

(ii) Turbulent Flame Region. It is important to examine the flame region surrounding the recirculation zone particularly in a confined flame. This is because this region produces both TKE and heat release. Accordingly, Fig. 7 shows plots of the ratio turbulent shear stress to kinetic energy, $a = \overline{uv}/q$, and values of $\delta U/\delta r$ at each location. It is observed that (*a*) both positive and negative values of Reynolds stresses can be found in the combusting recirculation zone, (*b*) values of coefficient a lie between -0.3 and 0.3, and therefore are close to values expected in "normal" shear layers as suggested by Bradshaw et al. (1967) and Harsha and Lee (1970), (*c*) in almost all of the flow field, the Reynolds stresses (or a) have sign opposite to that of $\delta U/\delta r$, i.e., the conventional *gradient-diffusion* turbulence modeling, which employs the eddy viscosity closure assumption $-\rho\overline{uv} = D_t\,\partial U/\partial r$, may be successful to the extent of predicting velocity flow field.

In confined turbulent reactive flow, Shepherd et al. (1982) have reported countergradient diffusion of turbulent heat fluxes. In confined flows involving significant heat release and large density fluctuations, countergradient diffusion arises because low-density, fully burned products of combustion are preferentially accelerated by the pressure gradient in comparison with high-density unburned reactants. Thus, turbulent transport is influenced by preferential diffusion in addition to conventional eddy diffusion. Now, in a confined recirculatory reactive flow, this situation is further complicated because the mean axial pressure gradient is favorable in the outer flame zone ($r/d > 0.5$) but adverse inside the recirculation region ($r/d < 0.5$). Therefore, detailed measurements of turbulent heat fluxes $\overline{uT}$ and $\overline{vT}$, and mean temperature gradients $\partial T/\partial x$ and $\partial T/\partial r$ are required to examine this flow field fully.

(iii) Combustion-Generated Turbulence. Combustion affects the turbulent flow field in a variety of ways. Ballal (1988) has stated that turbulent dilatation and viscous dissipation processes suppress flame turbulence, whereas turbulent advection and shear-generated turbulence will augment flame turbulence. Depending upon which processes dominate, combustion will either produce additional so-called combustion-generated turbulence or damp existing isothermal turbulence.

Figure 8 shows radial variation of ratio (q_c/q) at two different axial locations. Clearly, the TKE is lower by as much as 70 percent in the combusting flow than in cold flow. This result suggests that a minimum shear-generated turbulence is produced because wall confinement prevents deflection of mean flow streamlines and produces extremely low streamline curvature. In the absence of this strong turbulent production mechanism, the processes of turbulent dilatation and viscous dissipation take over to damp cold flow turbulence significantly. We believe that an oblique flame of fast burning mixtures, e.g., H_2, or stoichiometric combustion when confined in a duct, may generate enough shear to overcome the damping of the turbulence. In Fig. 8 note that where shear is prominent, e.g., at $r/d=0.45$, and 0.2 for $x/d=0.8$ and 2 respectively, the TKE ratio does increase.

From his studies of combustion-generated turbulence, Ballal (1986) derived simple formulae to estimate the magnitudes of shear-generated turbulence, turbulence dilatation, viscous dissipation and turbulent advection. For the confined flame studied here, $T_f=1755$ K and $T_u=295$ K, so $\tau=(T_f-T_u)/T_u\approx 5.0$. So, we can calculate that the magnitude of suppression due to turbulent dilatation = 55 percent and that due to viscous dissipation = 24 percent, i.e., total suppression = 79 percent. However, in Fig. 8, at $x/d=0.8$, the TKE in the combusting flow is lower by 70 percent in the recirculation zone $(r/d<0.4)$ and lower by 60 percent in the vicinity of the flame front. Thus, the total turbulence production (shear-generated turbulence + turbulent advection) in these two regions can be estimated to be about 9 and 19 percent, respectively. Likewise, at $x/d=2$, the total turbulence production is up to 26 percent downstream of the rear stagnation point. These estimates show that the ratio of production/suppression of turbulence varies between 12 and 33 percent in our fuel-lean $(\phi=0.65)$ high-speed confined flame.

Concluding Remarks

The following observations summarize our studies of turbulent combustion properties:

1 Combustor wall confinement elongates the recirculation zone by 13 percent over cold flow and narrows it by 12 percent over an open flame. Also, mean reverse flow velocity and hence also the recirculated mass flow increase by 30 percent over their corresponding value in open flame.

2 Flame confinement prevents mean streamline curvature. In such flows, turbulence production is principally due to shear stress-strain interaction. In contrast, for open flames, normal stresses and dilatation dominate.

3 Two regions of highly strained flames—one in the axial plane of maximum recirculation zone width and other around the stagnation point—are observed. A significant distortion of turbulent flow structure, as shown by high values of skewness and kurtosis, was evident in these regions.

4 The flow enveloping the recirculation zone resembles a normal mixing layer, i.e., $a=+0.3$ to -0.3 and gradient-diffusion closure for velocity holds. However, and in the absence of turbulent heat flux data, countergradient diffusion cannot be ruled out.

5 Finally, and principally due to suppression of mean streamline curvature by confinement, in combusting flow, the production of turbulence is only up to 33 percent of its damping due to dilatation and dissipation.

Acknowledgments

This research was sponsored by the U.S. Air Force, Wright Research and Development Center, Aero Propulsion and Power Laboratories, under Contract No. F33615-87-C-2767. The authors are indebted to Dr. W. M. Roquemore, the Air Force Technical Monitor, for his interest and helpful discussion during the course of this work.

References

Ballal, D. R., and Lefebvre, A. H., 1979, "Weak Extinction Limits of Turbulent Flowing Mixtures," ASME JOURNAL OF ENGINEERING FOR POWER, Vol. 101, pp. 343–348.

Ballal, D. R., 1986, "Studies of Turbulent Flow-Flame Interaction," *AIAA Journal*, Vol. 24, pp. 1148–1154.

Ballal, D. R., Lightman, A. J., and Yaney, P. P., 1987, "Development of Test Facility and Optical Instrumentation for Turbulent Combustion Research," *AIAA Journal of Propulsion and Power*, Vol. 3, pp. 97–104.

Ballal, D. R., 1988, "Combustion-Generated Turbulence in Practical Combustors," *AIAA Journal of Propulsion and Power*, Vol. 4, pp. 123–134.

Ballal, D. R., Chen, T. H., and Schmoll, W. J., 1989, "Fluid Dynamics of a Conical Flame Stabilizer," ASME JOURNAL OF ENGINEERING FOR GAS TURBINES AND POWER, Vol. 111, pp. 97–102.

Bradshaw, P., Ferriss, D. H., and Atwell, N. P., 1967, "Calculation of Boundary Layer Development Using Turbulent Energy Equation," *Journal of Fluid Mechanics*, Vol. 28, pp. 593–616.

Chen, T. H., and Lightman, A. J., 1985, "Effects of Particle Arrival Statistics on Laser Anemometer Measurements," ASME FED-Vol. 33, pp. 172–176.

Glass, M., and Bilger, R. W., 1978, "The Turbulent Jet Diffusion Flame in Coflowing Stream-Some Velocity Measurements," *Combustion Science and Technology*, Vol. 18, pp. 165–177.

Griffin, O. M., 1985, "Vortex Shedding From Bluff Bodies in a Shear Flow: A Review," ASME *Journal of Fluids Engineering*, Vol. 107, pp. 298–306.

Harsha, P. T., and Lee, S. C., 1970, "Correlation Between Shear Stress and Turbulent Kinetic Energy," *AIAA Journal*, Vol. 8, pp. 1508–1512.

Heitor, M. V., and Whitelaw, J. H., 1986, "Velocity, Temperature, and Species Characteristics of the Flow in a Gas Turbine Combustor," *Combustion and Flame*, Vol. 64, pp. 1–32.

Rao, K. V. L., and Lefebvre, A. H., 1982, "Flame Blowoff Studies Using Large-Scale Flameholders," ASME JOURNAL OF ENGINEERING FOR POWER, Vol. 104, pp. 853–857.

Shepherd, I. G., Moss, J. B., and Bray, K. N. C., 1982, "Turbulent Transport in a Confined Premixed Flame," *Nineteenth Symposium (International) on Combustion*, The Combustion Institute, pp. 423–431.

Sivasegaram, S., and Whitelaw, J. H., 1987, "Suppression of Oscillations in Confined Disk-Stabilized Flames," *AIAA Journal of Propulsion and Power*, Vol. 3, pp. 291–295.

Starner, S. H., and Bilger, R. W., 1980, "LDA Measurements in a Turbulent Diffusion Flame with Axial Pressure Gradients," *Combustion Science and Technology*, Vol. 21, pp. 259–270.

Strahle, W. C., and Lekoudis, S. G., 1985, "Evaluation of Data on Simple Turbulent Reacting Flows," Technical Report TR-85-0880, Air Force Office of Scientific Research, Bolling Air Force Base, Washington DC.

Sturgess, G. J., Syed, S. A., and McManus, K. R., 1983, "Importance of Inlet Boundary Conditions for Numerical Simulation of Combustion Flows," AIAA Paper No. 83-1263.

Winterfeld, G., 1965, "On Processes of Turbulent Exchange Behind Flame Holders," *Tenth Symposium (International) on Combustion*, The Combustion Institute, Pittsburgh, PA, pp. 1265–1275.

Zukoski, E. E., and Marble, F. E., 1955, "The Role of Wake Transition in the Process of Flame Stabilization on Bluff Bodies," *AGARD Combustion Researches and Reviews*, A. H. Lefebvre et al., eds., Butterworths Publishing Co., London, pp. 167–180.

An Experimental Study of the Effects of Liquid Properties on the Breakup of a Two-Dimensional Liquid Sheet

B. E. Stapper

W. A. Sowa

G. S. Samuelsen

UCI Combustion Laboratory,
Institute of Combustion and Propulsion
Science and Technology,
University of California,
Irvine, CA 92717

The breakup of a liquid sheet is of fundamental interest in the atomization of liquid fuels. The present study explores the breakup of a two-dimensional liquid sheet in the presence of co-flow air with emphasis on the extent to which liquid properties affect breakup. Three liquids, selected with varying values of viscosity and surface tension, are introduced through a twin-fluid, two-dimensional nozzle. A pulsed laser imaging system is used to determine the sheet structure at breakup, the distance and time to breakup, and the character of the ligaments and droplets formed. Experiments are conducted at two liquid flow rates with five flow rates of co-flowing air. Liquid properties affect the residence time required to initiate sheet breakup, and alter the time and length scales in the breakup mechanism.

Introduction

Liquid atomization is used for a wide variety of applications, including agricultural sprays, spray coatings, rapid solidification of metals, and combustion and propulsion systems. In many of these systems, a twin-fluid atomizer is employed. In gas turbine engine combustors, for example, the liquid fuel is most often introduced through an annular orifice and exits under relatively low pressure in the form of an annular sheet. High-velocity air is passed along either or both sides of the liquid sheet to produce a shear force at the air–liquid interface. While increasing relative air/liquid velocity has been shown to produce smaller droplets, the mechanism for breakup is not clearly established. The common notion is that (1) the shear causes spanwise waves to form on the surface of the sheet, and (2) the waves grow and separate from the sheet in the form of ligaments, which subsequently fragment into droplets.

The first studies of the instabilities and breakup of liquids were theoretical and focused on jets. Castleman (1930), for example, applied the analysis of Rayleigh (1878) to the breakup of a liquid jet in an air stream, and postulated that the formulation of ligaments was a necessary intermediate in the breakup mechanism. Squire (1953) followed with an analysis of a moving liquid film, in which he determined that two modes of wave instability were possible. The first mode was symmetric about the central plane of the film, and the second mode was axisymmetric. These results have also been verified using nonlinear vortex discretion theory (Rangel and Sirignano, 1988).

In a related theoretical study, Inoue (1989) has applied a three-dimensional vortex method to the growth of a two-dimensional turbulent homogeneous mixing layer. The results show that the streamwise vortices (1) are produced through an amplification of initial disturbances, (2) counterrotate in pairs as a result of the stretching and rotation of the spanwise vortices, and (3) are equal in magnitude to the spanwise vortices.

Because the geometry of an air blast atomizer is somewhat complex, a planar liquid sheet has been used in most of the experiments conducted to study atomization. Researchers at Imperial College, for example, first used fan sprays in quiescent environments to obtain photographs of the breakup of liquid sheets (Fraser, 1956; Dombrowski and Hooper, 1962; Dombrowski and Johns, 1963) and Rizk and Lefebvre (1980) later used a pair of atomizers (Fig. 1) in which a plane sheet of liquid is sheared by air streams on the upper and lower surfaces. The first design is for a prefilming atomizer, while the second design injects a liquid sheet from a wedge surrounded by co-flowing, shearing air streams.

Most sheet disintegration research (Arai and Hashimoto, 1985; Sattelmayer and Wittig, 1986; Beck et al., 1989; Stapper and Samuelsen, 1990) has since been performed on nozzles similar to those of Rizk and Lefebvre (1980). The focus of the research previously cited has been to assess the manner by which the final droplet size distribution is affected by (1) air and liquid properties, and (2) the geometry of the nozzle. The general conclusions are that SMD decreases with increasing relative air/liquid velocity, increasing liquid density, and decreasing surface tension. Viscosity is found to have little or no effect, and sheet thickness, while not playing a role in the prefilming atomizer, can have an effect in the wedge design depending on the relative angle of injection between the liquid and co-flowing air streams. Little emphasis has been placed on the instabilities in the liquid sheet itself, other than to suggest that (1) spanwise waves are the dominant instability, (2) the waves are periodic and a function of air velocity, and (3) the relative strength of the spanwise and streamwise vortical waves

Contributed by the International Gas Turbine Institute and presented at the 35th International Gas Turbine and Aeroengine Congress and Exposition, Brussels, Belgium, June 11–14, 1990. Manuscript received by the International Gas Turbine Institute January 16, 1990. Paper No. 90-GT-265.

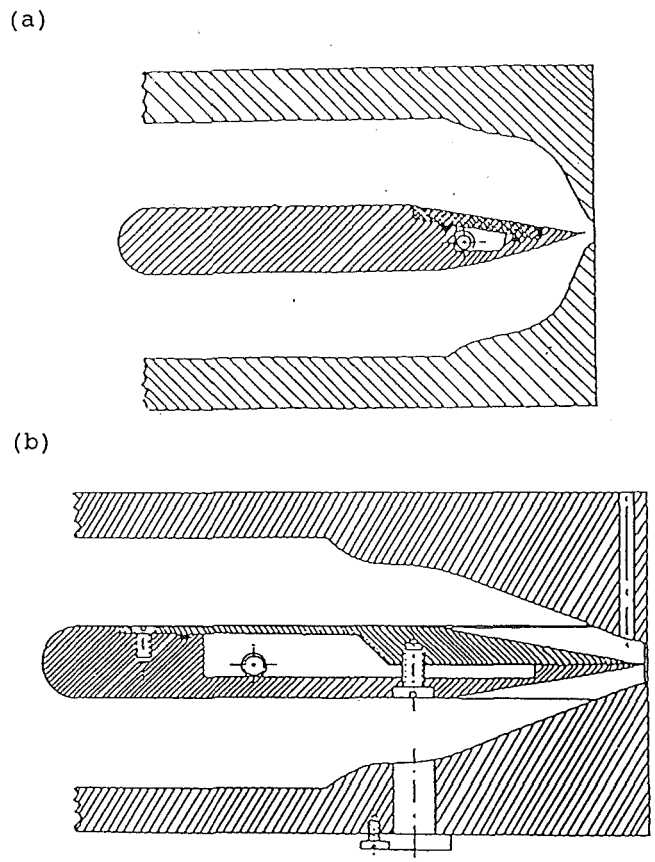

Fig. 1 Two-dimensional air blast atomizers: (*a*) prefilming atomizer, (*b*) fixed sheet thickness atomizer (Rizk and Lefebvre, 1980)

in the sheet is a controlling factor in the breakup mechanism (Sattelmayer and Wittig, 1986; Stapper and Samuelsen, 1990; Hagerty and Shea, 1955; Asare et al., 1981).

Even less attention has been directed to the transitional breakup regime of the spray beginning with the formation of ligaments and ending with their breakup. To explore this area of interest, we have recently examined the role of air and liquid velocities on the formation, size, and lifetime of ligaments using water as the test liquid (Stapper and Samuelsen, 1990). This study revealed that (1) the relative air/liquid velocity is a primary factor in the ligament formation and breakup, (2) the breakup is a complex three-dimensional interaction of spanwise and streamwise waves, between which are stretched thin film membranes, (3) the relative velocity establishes the relative importance of the spanwise and streamwise waves, and (4) an increase in relative velocity leads to further stretching of both the liquid membranes and streamwise ligaments, both of which lead to smaller droplets and, hence, lower SMDs. The present paper addresses the effects of liquid properties on the mechanisms of breakup.

Approach

Three liquids were selected that would demonstrate the differences in viscosity and surface tension effects on the breakup mechanisms. A two-dimensional nozzle was employed in combination with a nonintrusive pulsed laser imaging system to obtain images of the spray elements in sharp focus. Emphasis was placed on the breakup mechanisms of the liquid sheet at the various conditions, and the time required for the sheet to break up into ligaments.

Experimental Apparatus

The experimental apparatus, described in detail elsewhere

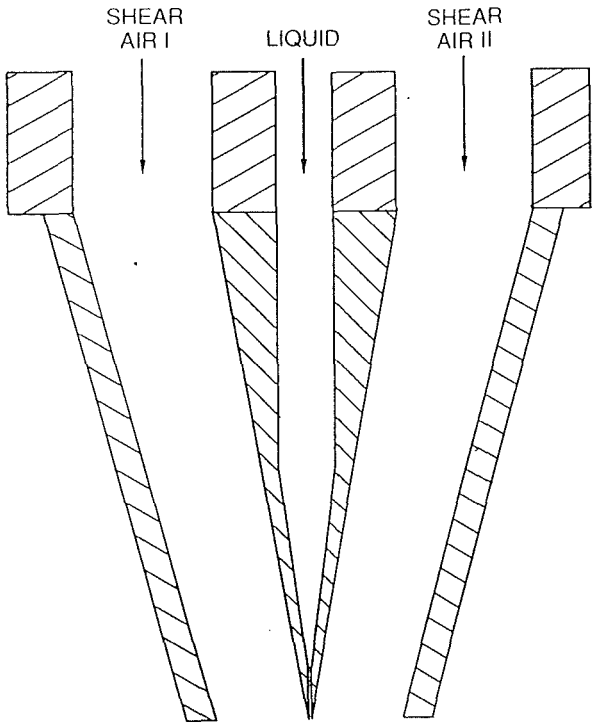

Fig. 2 Two-dimensional parallel flow plane sheet atomizer

(Stapper and Samuelsen, 1990), consists of a test fixture and a supporting facility. By way of summary, the test fixture is a two-dimensional parallel flow plane sheet nozzle, similar to the second design of Rizk and Lefebvre (1980). As shown in Fig. 2, the nozzle consists of a pair of triangular wedges, which are separated by shims to achieve the desired thickness for the liquid sheet. The sheet that is produced is 4.7 cm wide and 508 μm thick. A plexiglass plenum surrounds the wedges to contain the shear air as it passes on either side of the sheet. The air plenum converges slightly as it approaches the nozzle tip to maintain straight flow.

The flow preparation upstream of the injection can affect the vorticity generated by the liquid feed in the nozzle. The liquid enters the nozzle in a central reservoir from which it is forced under pressure to the injection plane of the nozzle. The liquid passes through a section of constant channel height for a distance of 13 channel heights before exiting the nozzle. To assess the effect of boundary conditions internal to the nozzle on the results, tests were conducted for a wide range of surface roughness, and a variety of screens in the central reservoir. No effect on the results reported was observed. For the results reported here, screens were not used and the internal surfaces were unpolished.

The nozzle is down-fired and the liquid is driven through the system by a gear pump with a maximum capacity of 157 g/s at 1.72 MPa. The two shear air lines can each deliver 0.126 kg/s.

To image the atomization of the liquid sheet properly, a nonintrusive method for measuring the dimensions of the spray elements was created. A pulsed nitrogen laser (PRA Model LN1000) was used to backlight the sheet. The short duration of the laser pulse (1 ns) allows the rapidly moving small structures in the breakup mechanism to be visualized in sharp focus, a marked benefit in comparison to previously reported exposure times (e.g., 0.8 μs; Arai and Hashimoto, 1985). The UV laser pulse was expanded and directed to impinge on a sheet of paper behind the liquid sheet. The fluorescence of the paper created visible backlighting. The results were documented using a 35 mm camera (Pentax Superprogram) and

Table 1 Liquid properties

Liquid	Viscosity ($mN \cdot s/m^2$)	Surface Tension (mN/m)	Density (kg/m^3)	Re_{ch}
Water (H_2O)	0.89	72	998	561
Ethanol (C_2H_6O)	1.39	22	789	284
Ethylene Glycol ($C_2H_6O_2$)	14.72	48	1114	38

Table 2 Experimental test matrix

Case	Velocity (m/sec)		
	Liquid	Air I	Air II
11	5	0	0
12	5	20	20
13	5	30	30
14	5	40	40
15	5	50	50
16	5	60	60
21	1	0	0
22	1	20	20
23	1	30	30
24	1	40	40
25	1	50	50
26	1	60	60

Professional Ektachrome film (P800/1600). Developing was pushed two stops.

Test Matrix

The properties of the liquids used for the evaluation of the viscosity and surface tension effects on ligament formation and breakup are given in Table 1. Three different liquids with widely varying physical properties (e.g., viscosity and surface tension) were chosen to examine the influence of liquid properties on sheet breakup. The Reynolds number based on the channel height of the nozzle exit is given for the liquids at 1 m/s.

The test matrix for the experiment is given in Table 2. The shear air velocity of the sheet was varied from 0 to 60 m/s, with the same velocity on both sides of the sheet. The liquid velocity was set at one of two values: 1 or 5 m/s.

Results

Liquid Sheet Breakup. An example is first provided to describe the general behavior and structure of the liquid sheet for a representative operating condition. This is followed by a description of the two mechanisms observed for breakup. A schematic of the face and side views of the structures that form during the breakup of a sheet is provided in Fig. 3 to assist the reader in the interpretation of the figures.

Example. An example of a water sheet with no co-flow air (Case 11) is shown in Fig. 4(*a*). Spanwise vorticity is generated as a result of the shear between the liquid velocity and quiescent surroundings. The spanwise vortical waves extend to the edges of the sheet and propagate in the streamwise direction. Less

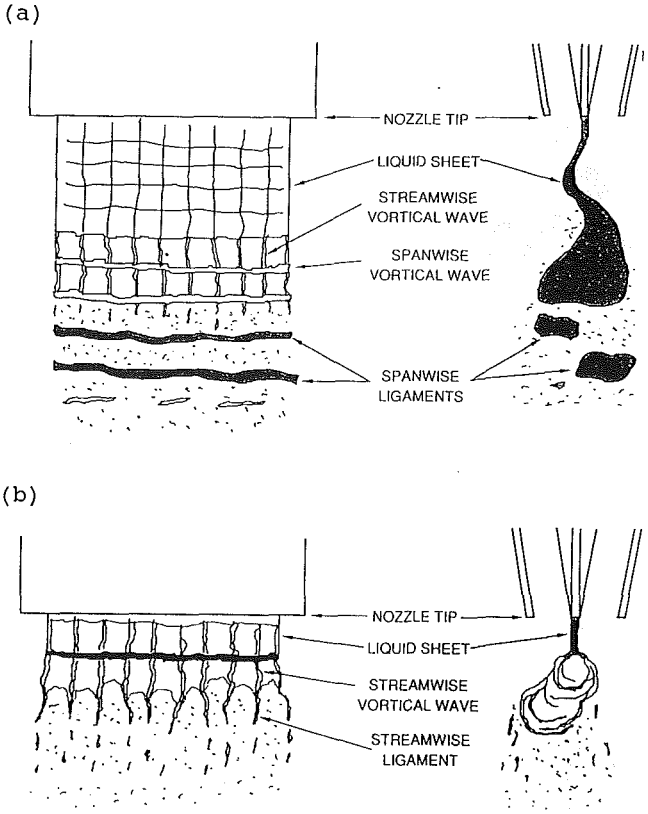

Fig. 3 Schematic of face and side views detailing the structures in the breakup of a liquid sheet for (*a*) cellular breakup, and (*b*) stretched streamwise ligament breakup (Stapper and Samuelsen, 1990)

noticeable on the liquid sheet, but important to the eventual breakup, are streamwise waves that are present at the nozzle tip and extend through the length of the sheet at a fixed spanwise location. These streamwise striations are attributed to counterrotating streamwise vortices generated by background disturbances and amplified by the close coupling with the spanwise vortices as described by Inoue (1989).

Figure 4(*b*) shows the water sheet with 40 m/s co-flow shear air (Case 14). In this case, spanwise waves again form on the sheet due to the relative velocity of the air and liquid flows, but the presence and role of the streamwise striations become more pronounced. In particular, the combination of the streamwise and spanwise vortical waves produces a cellular structure embodied by thin film membranes. The sheet is stretched by the shear air until the membranes burst into relatively small droplets, and the waves separate as ligaments. These ligaments then become unstable and fragment into droplets.

Sheet Breakup Mechanisms. Two mechanisms of sheet breakup have been identified in the experiments conducted to data (Stapper and Samuelsen, 1990). The first of these, labeled in this study as "cellular breakup," occurs at higher relative air-to-liquid velocities, but where the breakup is well displaced from the nozzle tip. This breakup mechanism, illustrated in Fig. 4(*b*), is characterized by the presence of spanwise vortical waves that are approximately equal in strength to the streamwise vortical waves. As the sheet is extruded by the shearing action of the air, the membranes stretch between the spanwise and streamwise vortical waves, forming cell-like structures. Eventually, the sheet is stretched to the point where (1) the streamwise vortical waves and connecting membranes burst, and (2) the spanwise vortical waves separate into spanwise ligaments. The small droplets in the resultant spray distribution originate from the bursting membranes. Larger droplets are

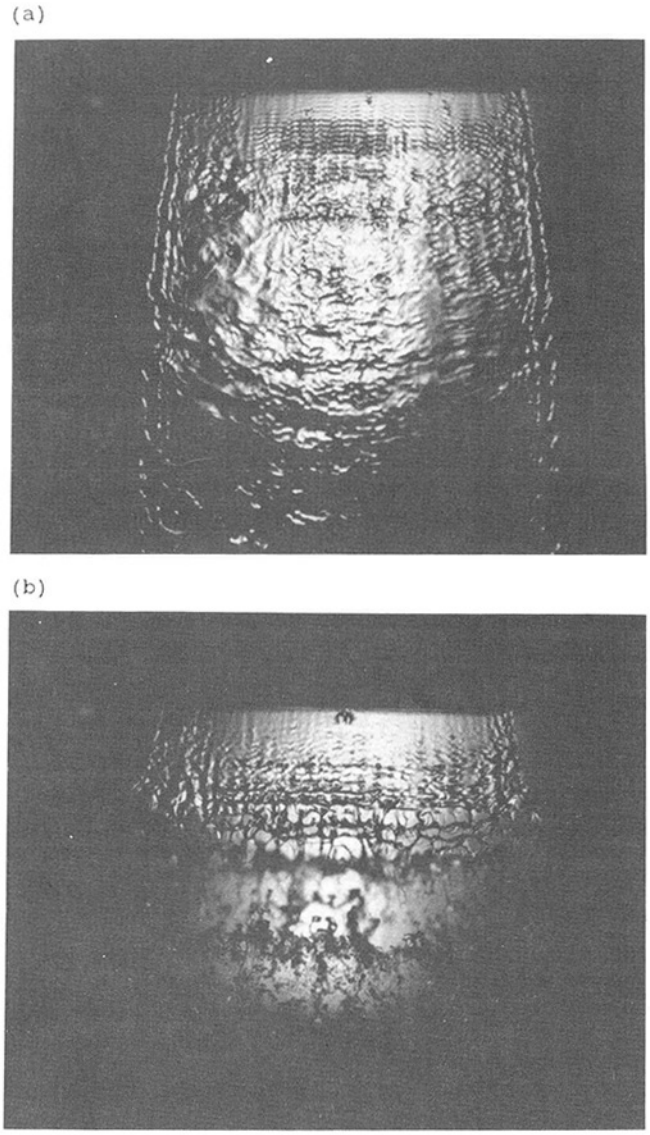

Fig. 4 "Cellular breakup" (Stapper and Samuelsen, 1990): water sheet at 5 m/s with (*a*) no co-flow air, (*b*) 40 m/s co-flow air

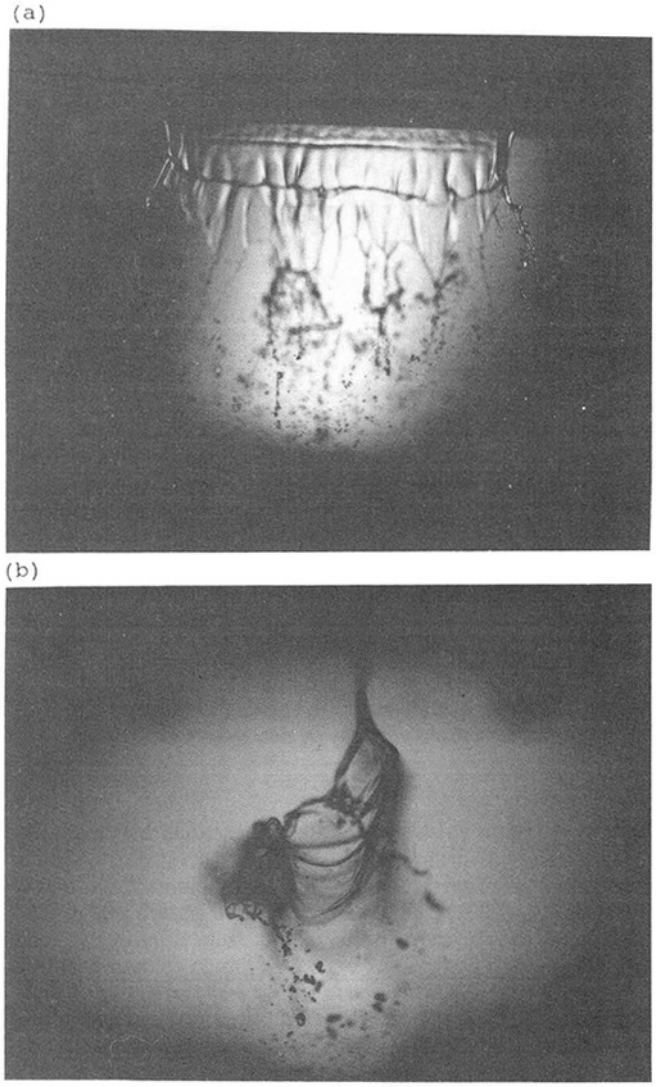

Fig. 5 "Stretched streamwise ligament breakup" (Stapper and Samuelsen, 1990): water sheet at 1 m/s with 20 m/s co-flow air: (*a*) face view, (*b*) side view

associated with the breakup of the streamwise waves. The largest droplets are associated with the fragmentation of the spanwise ligaments.

The second breakup mechanism, referred to as "stretched streamwise ligament breakup," occurs at low liquid velocities. As shown in Fig. 5(*a*) for Case 22, this mechanism is dominated by the streamwise vortical waves in the breakup process. As the sheet is stretched by the co-flowing air, the streamwise vortices amplify with thin liquid membranes stretched between. The sheet is a corrugated structure with the membranes stretched sinusoidally about the plane of the sheet. A side view of this process is presented in Fig. 5(*b*). As a result, the membranes are stretched by the counterrotation of the bounding vortices. When the membranes burst, the liquid film forms small drops, while the vortical waves form streamwise ligaments. These ligaments are then stretched by the shearing action of the air and transition to higher rotating velocities, and finally fragment into relatively large drops when the surface tension forces can no longer keep the ligaments intact.

Liquid Property Effects. The variation in the liquid properties considered did not alter the general character of the two breakup mechanisms. However, the change in liquid properties had a pronounced effect on the time and length scales. Results are presented first for the influence of liquid properties on sheet breakup length and sheet breakup time. This provides a global perspective. Secondly, an examination of the effect of liquid properties is presented for both the cellular breakup, and for the stretched streamwise ligament breakup mechanisms. For the latter, select conditions are presented where the photographs are most illustrative of the effects.

Although the liquid properties of the three liquids vary, the liquids were selected for their substantial variation in viscosity and surface tension: Water has relatively high surface tension and relatively low viscosity, ethanol has a threefold lower surface tension and a slightly higher viscosity (~ 50 percent) than water, and ethylene glycol has a viscosity much greater than water while its surface tension is slightly lower (~ 30 percent).

While it is likely that the liquid property effects presented are dominated by the differences in surface tension and viscosity, the variation in other physical properties and the limited number of fluids considered preclude an unequivocal determination of the precise role of viscosity and surface tension. As a consequence, the results are presented in terms of the generic names of the liquids with a parenthetical note of the relative values of surface tension and viscosity.

Sheet Breakup Time. Measurements were made of the length from the nozzle tip to the point at which the thin film membranes fragment. The results, presented in Fig. 6(*a*), reveal

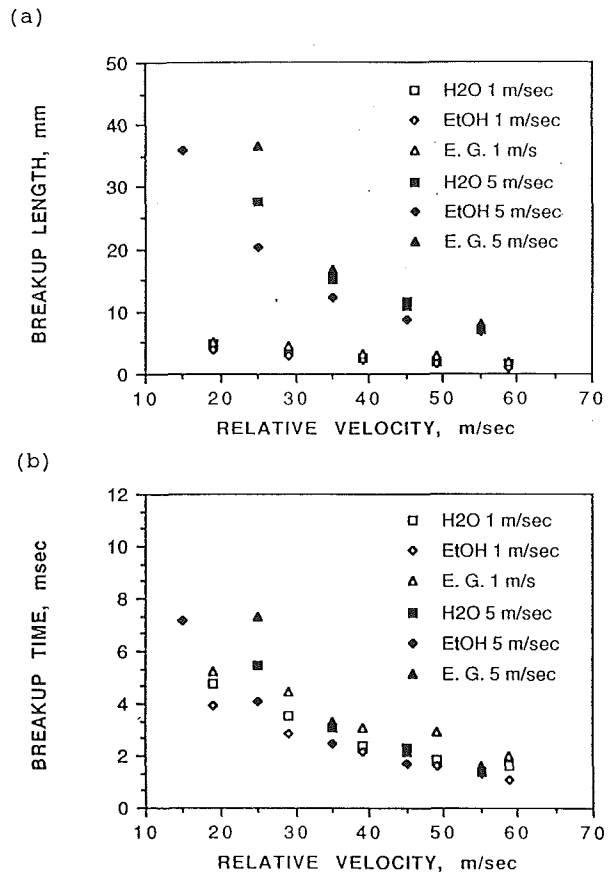

Fig. 6 Effect of relative velocity on: (*a*) sheet breakup length, (*b*) sheet breakup time

that the higher liquid velocity leads to longer sheet breakup lengths. The breakup lengths were strongly correlated with the liquid sheet–air residence time of interaction. In Fig. 6(*b*), the data are replotted in terms of interaction time and air-to-liquid relative velocity, where interaction time is defined as the breakup length divided by the liquid velocity at the nozzle tip. Based on these data, it is apparent that the liquid properties have a notable effect on the required air-liquid interaction time to breakup. The required interaction time of the ethanol is the shortest, while the ethylene glycol generally has the longest required time. The former is the lowest in surface tension of the three liquids, while the latter is the highest in viscosity. It should also be noted that the sheet breakup time correlates well with the liquid density as would be expected due to conservation of momentum. The lowest density liquid (ethanol) has the shortest breakup time, while the highest density liquid (ethylene glycol) has the longest.

Cellular Breakup. The effect of liquid properties on the cellular breakup mechanism is presented in Fig. 7(*a*) by comparing the face view of sheets of water and ethanol for Case 13. Spanwise vortical waves are formed closer to the injector inlet for ethanol (the lower surface tension liquid), and the cellular structures that form are smaller than those of water. It is also noteworthy that the streamwise ligaments fragment into droplets at the point the spanwise ligament breaks off, while in the case of water, the streamwise ligaments persist well downstream of the sheet breakup. The rapid breakup of the ethanol is illustrated effectively by a side view of sheets of water and ethanol (Fig. 7*b*, Case 26).

Figure 7(*c*) demonstrates the characteristics of ethylene glycol relative to the cellular breakup mechanism (Case 14). The high viscosity of the ethylene glycol dampens out the small-scale structures in the sheet that are generated by the shear layer instabilities. The spanwise vortical waves develop in a

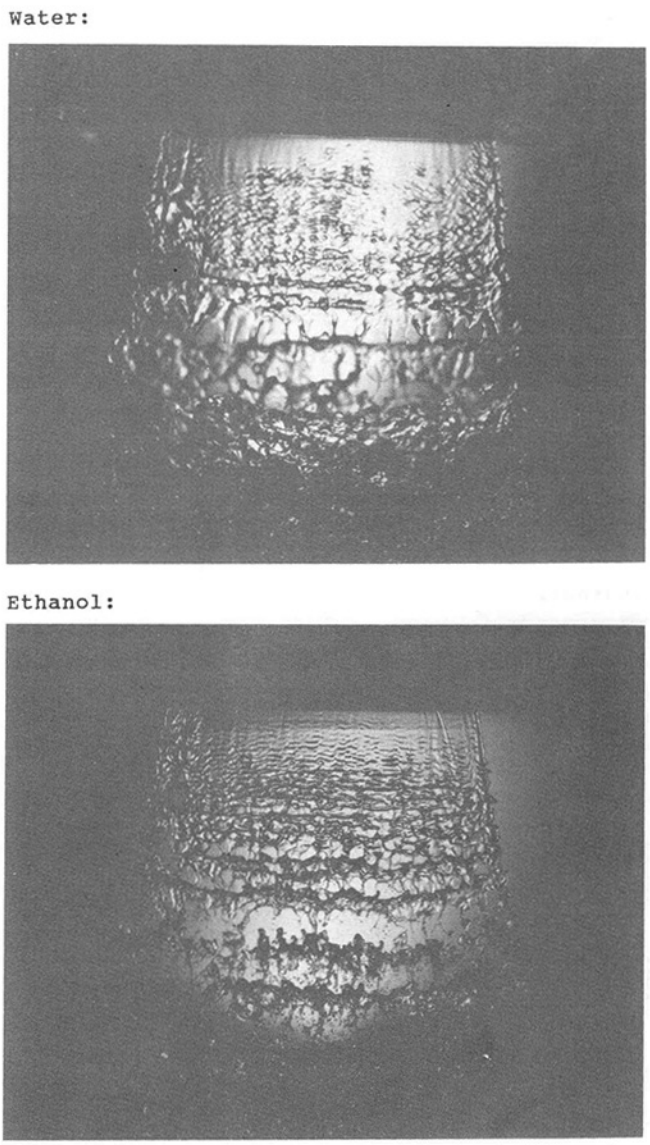

Fig. 7(*a*) Effect of liquid properties on "cellular breakup": face view, water and ethanol (Case 13)

shorter time, and appear more dominant than the streamwise vortical waves. The cellular structure in the ethylene glycol sheet is not as uniform as in the water sheet. After the spanwise ligaments break off the sheet, the streamwise ligaments formed by the ethylene glycol (higher viscosity fluid) remain intact for a longer time than those formed by the water.

Stretched Streamwise Ligament Breakup. The stretched streamwise ligament breakup mechanism is also affected by the liquid properties. Figure 8 is a face view of the three liquids at a low liquid flow condition (Case 22). The membrane formed between the streamwise vortical waves is broken up rapidly into small drops in the case of the lower surface tension liquid (ethanol). The streamwise ligaments of the water break off and form globules and then break up farther downstream into drops. The ethylene glycol stretches farther and the streamwise ligaments persist longer than those for either water or ethanol.

Conclusions

The breakup of a liquid sheet in a field of co-flow shearing air, and the effects of liquid properties on the breakup have been studied in a two-dimensional nozzle. Two mechanisms of breakup are identified. The first, termed "cellular breakup," exhibits vortical waves of equal strength in the streamwise and

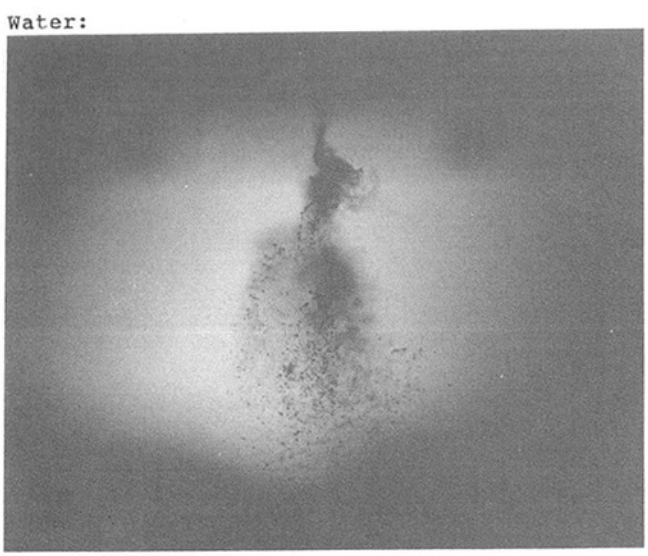

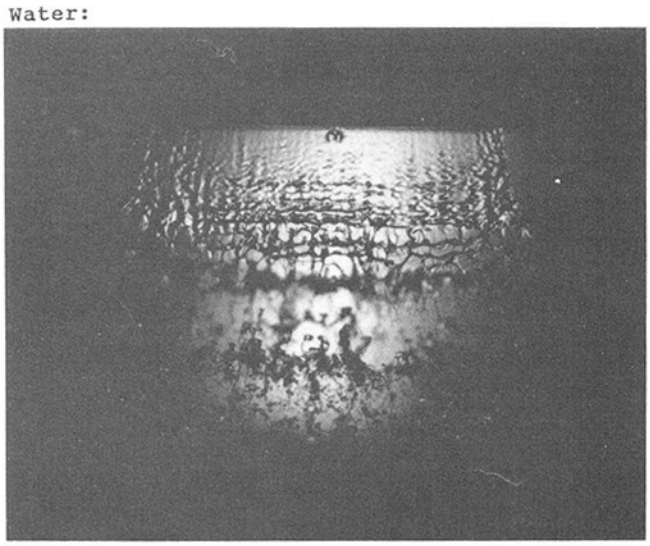

Fig. 7(*b*) Effect of liquid properties on "cellular breakup": side view, water and ethanol (Case 26)

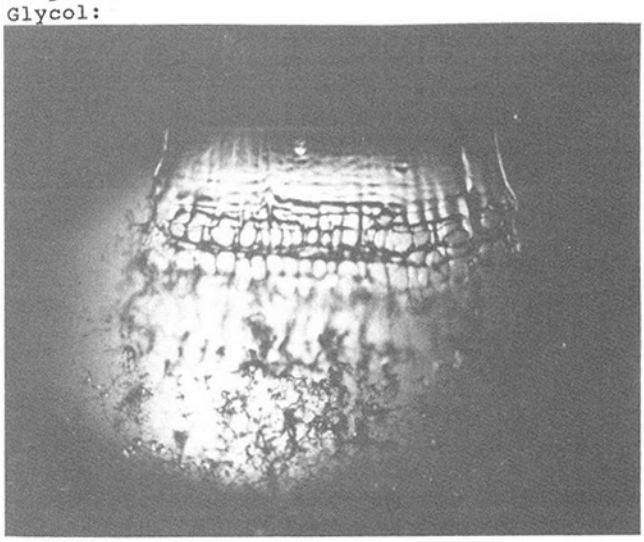

Fig. 7(*c*) Effect of liquid properties on "cellular breakup": face view, water and ethylene glycol (Case 14)

spanwise directions, with membranes stretched between. In this case, the streamwise vortical waves are broken off the sheet, forming spanwise ligaments downstream of the sheet. The second, termed "streamwise ligament stretching breakup," occurs at low liquid and air flow conditions. It is dominated by streamwise ligaments with thin membranes of liquid stretched between.

The liquid properties in the range evaluated do not change the breakup mechanisms, but do contribute to an altered form of the breakup in terms of the time and length scales. The ethanol (lower surface tension compared to water and ethylene glycol) displays smaller scale structures on the sheet, and a greater tendency to break up into droplets rather than form streamwise ligaments. The ethylene glycol (higher viscosity compared to water and ethanol) stretches farther before breakup, which results in the streamwise ligaments reaching smaller diameters before fragmenting into drops.

The breakup time of the sheet is dependent on liquid properties and relative velocity of the liquid and air. The ethanol (lower surface tension and density) demonstrates decreased breakup time, while the ethylene glycol (higher viscosity and density) exhibits increased breakup time relative to water.

The relationship of these events to the ultimate distribution of the droplets formed is the subject of present inquiry.

For the conditions and liquid properties examined, the following conclusions can be made:

- Liquid properties, especially excursions in surface tension and viscosity, do not appreciably change the basic mechanisms of cellular and stretched streamwise ligament breakup.
- Liquid properties can affect, however, the structural details of the sheet, leading to a notable change in the characteristic time and length scales associated with breakup.

Acknowledgments

This research was supported by the Air Force Office of Scientific Research Air Force Systems Command, USAF, under Grant AFOSR #86-0016D, with Dr. Julian Tishkoff as technical monitor. The U. S. Government is authorized to reproduce and distribute reprints for Governmental purposes notwithstanding any copyright notation thereon. The authors thank Dr. Roger Rangel for his contributions to the data analysis. We also thank Brian Bissell and Howard Crum for their technical assistance.

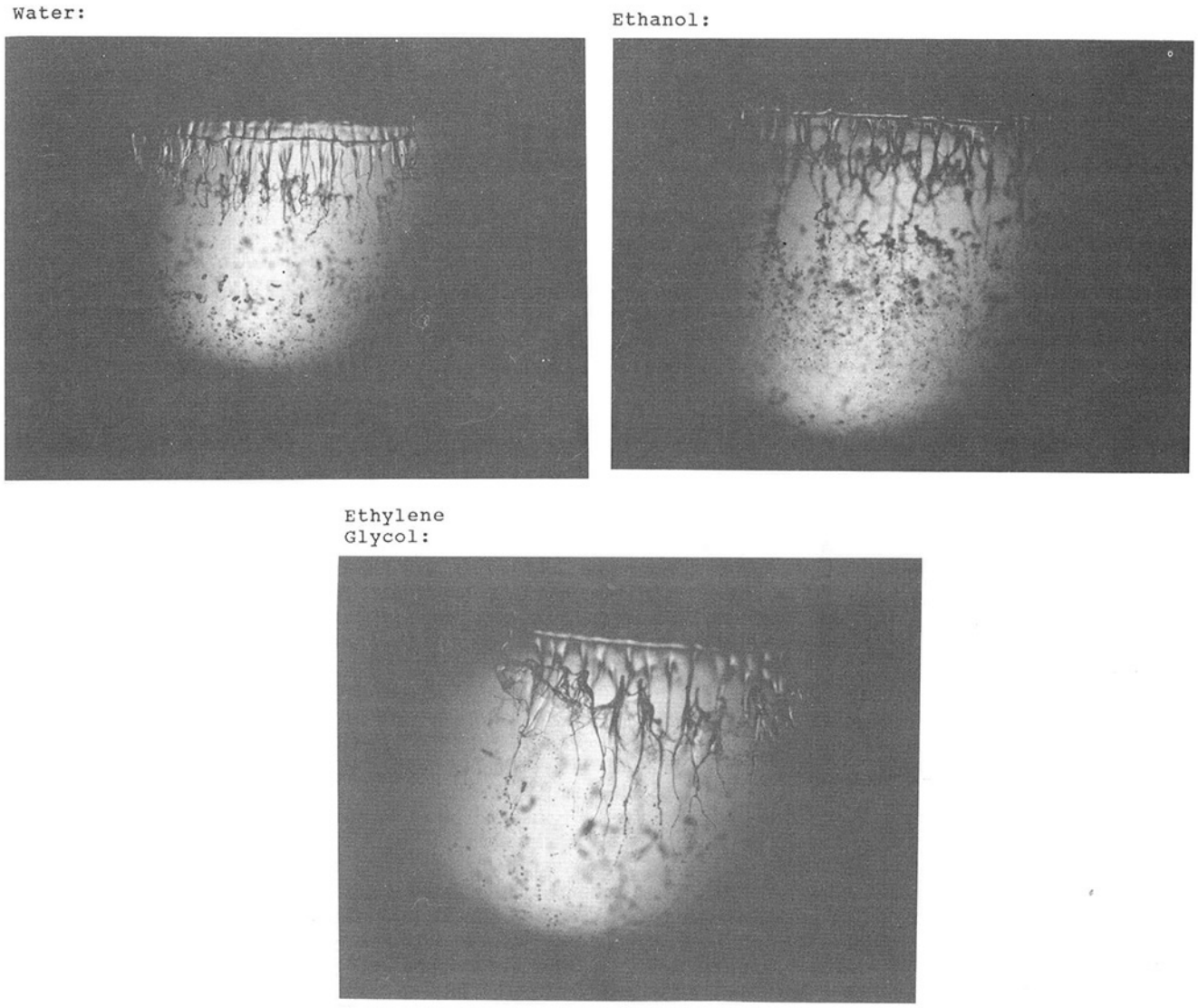

Fig. 8 Effect of liquid properties on "stretched streamwise ligament breakup" (Case 22): (*a*) water, (*b*) ethanol, (*c*) ethylene glycol

References

Arai, T., and Hashimoto, H., 1985, "Behavior of Gas–Liquid Interface on a Liquid Film Jet," *Bulletin of JSME*, Vol. 28, No. 245, pp. 2652–2659.

Asare, H. R., Takehashi, R. K., and Hoffman, M. A., 1981, "Liquid Sheet Jet Experiments: Comparison With Linear Theory," ASME *Journal of Fluids Engineering*, Vol. 103, pp. 595–604.

Beck, J., Lefebvre, A. H., and Koblish, T., 1989, "Air Blast Atomization at Conditions of Low Air Velocity," Paper No. AIAA 89-0217.

Castleman, R. A., Jr., 1930, "The Mechanism of the Atomization of Liquids," *Bureau of Standards Journal of Research*, Vol. 6, pp. 369–376.

Dombrowski, N., and Hooper, P. C., 1962, "The Effect of Ambient Density on Drop Formation in Sprays," *Chemical Engineering Science*, Vol. 17, pp. 291–305.

Dombrowski, N., and Johns, W. R., 1963, "The Aerodynamic Instability and Disintegration of Viscous Liquid Sheets," *Chemical Engineering Science*, Vol. 18, pp. 203–214.

Fraser, R. P., 1956, "Liquid Fuel Atomization," *6th Symposium (International) on Combustion*, pp. 687–701.

Hagerty, W. W., and Shea, J. F., 1955, "A Study of the Stability of Plane Fluid Sheets," ASME *Journal of Applied Mechanics*, Vol. 22, pp. 509–514; Paper No. 55-APM-21.

Inoue, O., 1989, "Vortex Simulation of Spatially Growing Three-Dimensional Mixing Layers," *AIAA Journal*, Vol. 27, No. 11, pp. 1517–1523.

Rangel, R. H., and Sirignano, W. A., 1988, "Non-linear Growth of Kelvin-Helmholz Instability: Effect of Surface Tension and Density Ratio," *Physics of Fluids*, Vol. 31, pp. 1845–1855.

Rayleigh, L., 1878, "On the Instability of Jets," *Proceedings of the London Mathematical Society*, Vol. 10, pp. 4–13.

Rizk, N. K., and Lefebvre, A. H., 1980, "The Influence of Liquid Film Thickness on Air Blast Atomization," ASME JOURNAL OF ENGINEERING FOR POWER, Vol. 102, pp. 706–710.

Sattelmayer, T., and Wittig, S., 1986, "Internal Flow Effects in Prefilming Airblast Atomizers: Mechanisms of Atomization and Droplet Spectra," ASME JOURNAL OF ENGINEERING FOR GAS TURBINES AND POWER, Vol. 108, pp. 465–472.

Squire, M. A., 1953, "Investigation of the Instability of a Moving Liquid Film," *British Journal of Applied Physics*, Vol. 4, pp. 167–169.

Stapper, B. E., and Samuelsen, G. S., 1990, "An Experimental Study of the Breakup of a Two-Dimensional Liquid Sheet in the Presence of Co-flow Air Shear," presented at the 28th AIAA Aerospace Sciences Meeting, Reno, NV, Paper No. AIAA-89-0461.

Mixing of an Acoustically Excited Air Jet With a Confined Hot Crossflow

P. J. Vermeulen
Professor.
Mem. ASME

P. Grabinski
Graduate Student.

V. Ramesh
Research Associate.

The University of Calgary,
Department of Mechanical Engineering,
Calgary, Alberta, Canada T2N 1N4

The mixing of an acoustically pulsed air jet with a confined hot crossflow has been assessed by temperature profile measurements. These novel experiments were designed to examine the effects of acoustic driver power and Strouhal number on jet structure, penetration, and mixing. The results showed that excitation produced strong changes in the measured temperature profiles. This resulted in significant increases in mixing zone size, penetration (at least 100 percent increase), and mixing, and the length to achieve a given mixed state was shortened by at least 70 percent. There was strong modification to the jet-wake region. The increase in jet penetration and mixing was saturating near 90 W, the largest driving power tested. The jet response as determined by penetration and mixing was optimum at a Strouhal number of 0.27. Overall, pulsating the jet flow significantly improved the jet mixing processes in a controllable manner.

Introduction

The mixing of steady free gaseous jets and steady gaseous jets mixing with a confined crossflow have been extensively studied. These investigations were broadened, fairly recently, when Crow and Champagne [1] and later workers [2–4] indirectly showed that jet entrainment was significantly increased by exciting the jet flow. The first direct measurement of the entrainment rate of acoustically excited free air jets was made by Vermeulen et al. [5], and showed for the fully developed region that entrainment may be increased up to about six times. The mixing of an excited jet is therefore also significantly increased. A technical application to a gas turbine combustor has been made [6, 7], where acoustic control of dilution-air mixing was shown to be beneficial to the exit plane temperature distribution.

The performance of a gas turbine combustor depends fundamentally on jet flow mixing and in particular on the mixing of air jets with a confined hot crossflow. Therefore, an experimental study into the mixing of an acoustically pulsed air jet with a confined cold crossflow was recently carried out [8]. This showed that acoustically pulsing the jet flow caused significant increases in jet spread, penetration, and mixing. A strong reduction in the length to achieve a given mixed state was also measured. Toroidal vortices shedding from the jet orifice produced profound changes in the jet structure. The entraining action of the traveling torodial vortices is the primary mechanism of the acoustically augmented penetration and mixing process. Since this previous work inferred improvement in mixing from measured mean velocity and turbulence profiles, it has been extended by an experimental investigation into the mixing of an acoustically pulsed air jet with a confined hot crossflow. This therefore allows the mixing to be more directly assessed, and acoustic improvements confirmed, by temperature profile measurements and was the main motivation for the study to be reported here. These novel experiments were designed to examine the affects of acoustic driver power and Strouhal number on jet structure, penetration, and mixing, and to show the potential for combustor improvement by application of acoustically augmented jet flows.

Experimental

Apparatus for Acoustically Pulsed Air Jets in a Confined Hot Crossflow. The experimental equipment (Fig. 1) is the same as that used in [8] except for the provision of a combustor upstream of the test section to heat the crossflow, and the inclusion of a bank of 17 chromel-alumel thermocouples to make temperature traverses in selected planes in the test section. The fuel used was natural gas burning in air supplied by a 56 kW blower. The fuel mass flow rate was measured by a choked nozzle meter.

Up to five pairs of multiply opposed air jets (in the test section floor and ceiling) may be injected into the confined hot uniform crossflow. However, because of the need to keep the flow field simple, in order to develop a basic understanding, only a single jet from the center of the test section floor has been investigated so far. As shown, the jet was pulsed by a 200 W loudspeaker driver. The air for the jet flow was diverted from the main flow by a valve, and an orifice resistance plate was mounted downstream of the diversion branches in order to assist in controlling the jet/crossflow velocity ratio. Good quality jets and crossflow were ensured by settling chambers with screens and an exit contraction. The mass flow rates of

Contributed by the International Gas Turbine Institute and presented at the 35th International Gas Turbine and Aeroengine Congress and Exposition, Brussels, Belgium, June 11–14, 1990. Manuscript received by the International Gas Turbine Institute December 30, 1989. Paper No. 90-GT-28.

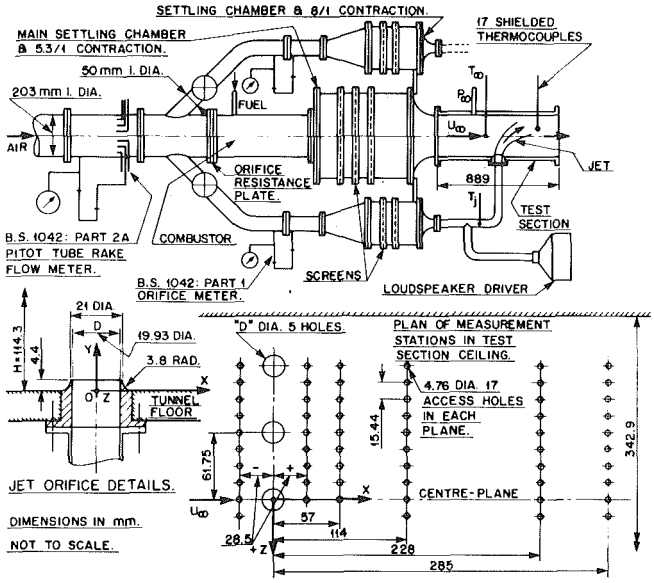

Fig. 1 Apparatus for acoustically pulsed air jets in a confined hot crossflow

jet and crossflow were measured by standard flow meters conforming to B.S. 1042. The 114 mm × 343 mm (inside dimensions) × 889 mm test section had pyrex glass windows in the side walls, and steel plates formed the floor and ceiling. Through the ceiling a pattern of holes (plugged when not in use) (Fig. 1) positioned the 17 thermocouples so that temperature profiles could be measured. A traversing mechanism and gantry (not shown) positioned the thermocouples in parallel array so that accurate, vertical, simultaneous traverses could be made to determine the mean temperature profiles in a particular plane. The thermocouple array was moved in 9.53 mm steps to give 12 different vertical positions, i.e., a total of 12 × 17 = 204 temperature measurements. The thermocouples were shielded assemblies of standard design for measuring stagnation temperature, and had an o.d. of 3.26 mm. This instrumentation enabled the pulsed jet mixing to be assessed by temperature profile measurements made on five planes downstream of the jet orifice for the range X/D = 1.43 to 14.30. The jet orifice, shown in Fig. 1, had a lip outside geometry corresponding to that of the dilution air holes of the combustor used in [6].

Power at the loudspeaker driver $\dot{W}$ was measured by an a-c voltmeter and ammeter, ignoring the power factor correction since previous work had shown it to be small [5]. The acoustic excitation pulses the jet flow at the orifice exit, causing the jet flow to develop wave motion growing into a train of toroidal vortices [4, 8, 9]. Since the driving system is the same as that calibrated previously [8] only a check was made of the frequency for strongest excitation of the jet. This was determined (as before) by means of dual channel FFT analysis at zero flow conditions, and found to be 204 Hz, in close agreement with 208 Hz of the former work. Thus, the jet relative pulsation strength V_e/V_j versus power number $\dot{W}/\rho_j D^2 V_j^3$ calibration, i.e.,

$$\left[\frac{V_e}{V_j}\right]^2 = F\left[\frac{\dot{W}}{\rho_j D^2 V_j^3}\right] \tag{1}$$

at a particular frequency, and almost a linear function, was taken to be the same as that given in [8]. This equation can also be written as

$$\frac{V_e}{V_j} = F_1\left[\frac{\sqrt{\dot{W}}}{V_j\sqrt{\dot{M}_j}}\right] \tag{2}$$

and therefore, a constant excitation can be maintained by keeping $\sqrt{\dot{W}}/V_j\sqrt{\dot{M}_j}$ constant. The jet flow response also depends on the Strouhal number St, and was shown to be optimum for penetration and mixing at about St = 0.22 by the cold flow study. This is therefore an important reference value for this new work.

The main variables affecting the mixing behavior are the jet flow/crossflow momentum flux ratio J, the jet relative pulsation strength V_e/V_j, the axial distance X downstream from the orifice exit plane, and the jet Strouhal number. Temperature profile measurements were made at average conditions of St = 0.223, J = 3.17, a power range of 0 to 90 W, and for a crossflow Mach number of 0.03. These test conditions

Nomenclature

a = jet thermal axis, point where $\theta = \theta_{max}$
D = jet orifice diameter
f = driving frequency
F, F_1 = functions
H = tunnel height
j = approximate boundary of the jet-wake zone
J = momentum flux ratio $\rho_j V_j^2/\rho_\infty U_\infty^2$
$\dot{M}_j$ = constant average mass flow rate through the jet orifice
$\dot{M}_\infty$ = constant average crossflow mass flow rate
n = number of data points
p_∞ = crossflow static pressure at $X/D = -2.23$
Re_j = Reynolds number of jet at the orifice
Re_∞ = Reynolds number of crossflow based on hydraulic diameter
S_m = standard deviation for mixing effectiveness
St = jet Strouhal number at the orifice = fD/V_j
T = local mean stagnation temperature, which because of low velocity is close to static temperature and the distinction can be ignored
T_j = temperature of the jet flow at orifice exit plane
T_m = average temperature in a particular transverse plane
T_∞ = crossflow local mean temperature in the reference transverse plane at $X/D = -1.43$
$\bar{T}_\infty$ = reference plane average temperature
U_∞ = average crossflow velocity at $X/D = -2.23$ cross section
V_e = jet velocity excitation pulsation amplitude, or pulsation strength, at the orifice exit plane centre (unsteady flow)
V_j = steady mean jet velocity at the orifice exit plane
$\dot{W}$ = power at acoustic driver
X, Y, Z = rectangular coordinates; see Fig. 1 for origin location
Y_o = jet penetration without acoustic drive at a particular X location; see Fig. 7
ΔY = change in jet penetration, caused by acoustic excitation, at a particular X location
θ = dimensionless temperature difference ratio
θ_m = dimensionless relative temperature or mixing parameter
θ_{max} = maximum value of θ
ρ_j = density of the jet flow at orifice exit plane
ρ_∞ = crossflow density at $X/D = -2.23$

were close to those of the main tests of [8], with the Mach number selected at the low end of the range of the reference combustor [6] in order that the jet velocity used could be effectively pulsed by the driver power available. The maximum power used was restricted to 90 W (140 W was possible) because of increasing interference by the tunnel ceiling on the jet mixing behavior. Finally, a series of tests for an St range of 0.187 to 0.352, $X/D = 2.86$, average $J = 3.02$, and constant $\sqrt{\dot{W}}/V_j\sqrt{\dot{M}_j}$ (excitation) were performed in order to assess the effect of Strouhal number on the jet flow response.

Crossflow Calibrations. The pitot tube total air mass flow rate meter was calibrated over the full operation range (diversion branches closed) and referred to the tunnel reference velocity measured by a pitot tube-static tube pair, at $X/D = -2.23$, $Y/H = 0.50$, $Z/D = +3.10$ to avoid interference from the jet flow. Hence, the test section crossflow mass flow rate was conveniently calibrated (linearly) against density × velocity at the reference pitot-static tubes. Also the total air mass flow rate was referred to a meter pitot tube nearest the meter centerline to provide another convenient density × velocity versus mass flow rate calibration.

Mean temperature profile measurements in the test section were made on transverse planes $X/D = -1.43$, 1.43, 2.86, and 14.30 for a crossflow velocity U_∞ range, spanning the main tests, of 8.6 to 15.4 m/s. This was for no jet flow, and the tunnel walls had been made flush by appropriate sealing plugs. The conditions were steady throughout the measurements, and the resulting mean temperature contour maps showed that the test section flow was uniform to within ± 10 percent outside the boundary layers, which was considered to be acceptable.

Experimental Results—Mean Temperature Profiles and Contour Maps. Figure 2 presents typical mean temperature vertical profiles on the centerplane ($Z/D = 0$), for a good penetration and mixing response Strouhal number, and for zero and medium (75 W) excitation. The data are given in terms of the dimensionless relative temperature or mixing parameter

$$\theta_m = \frac{T - T_m}{T_m - T_j} \tag{3}$$

where T is the local mean temperature, and T_m is the average temperature in a particular transverse plane (the average of 204 local mean temperatures) and approximates the value that would be reached by perfect mixing in that plane. The corresponding contour maps are shown in Fig. 3. It is conventional [10] to present the data in terms of the dimensionless temperature difference ratio

$$\theta = \frac{T_\infty - T}{\overline{T}_\infty - T_j} \tag{4}$$

where T_∞ is the mean temperature of the undisturbed crossflow. However, here, in order to eliminate the boundary layers, T_∞ is the crossflow local mean temperature (average of 25 readings over 0.017 s) in the reference transverse plane at $X/D = -1.43$, and $\overline{T}_\infty$ is the reference plane average temperature, i.e., the average of 204 local mean temperatures. In this form Fig. 4 presents the center-plane profiles and Fig. 5 the corresponding contour maps. Since $T_\infty > T_j$, θ is maximized in the coolest regions of the flow, i.e., in the jet flow.

Because the temperature distribution in the transverse reference plane is nearly the same as that in all the transverse measurement planes without the jet flow, the definition of θ eliminates the crossflow temperature field for all practical purposes. Thus, the θ profiles and contours show largely the jet flow temperature field, with small residual values outside this field due to the small temperature differences between the crossflow reference plane and the measurement plane. This, of course, demonstrates that the temperature fields of the reference plane and the measurement planes without the jet flow are nearly the same, and it is unnecessary to measure separately the temperature fields in the downstream planes without the jet flow.

The boundary of the jet zone, point "j," is defined when $\theta = 0$ ($T = T_\infty$); however, because of the residual errors in the flow field outside of the jet zone, the $\theta = 0$ contour is unreliable. Thus, the jet zone was estimated from the vertical profile as it becomes nearly tangent to $\theta = 0$ (Fig. 4), and from the $\theta = 0.05$ contour (Fig. 5). The thermal axis of the jet is commonly taken to be defined by θ being a maximum [10], point "a," and hence the locus of point "a" is the centerplane thermal jet trajectory. Thus, the center-plane structure of the jet in crossflow can be estimated, and is shown by Fig. 6 for a good penetration and mixing response Strouhal number and for zero and medium (75 W) excitation. For the "no-drive" condition the jet zone upper boundary is well defined, but because of mixing of jet and crossflow fluids in the wake region beneath the jet, indicated by assymetry in the θ (also

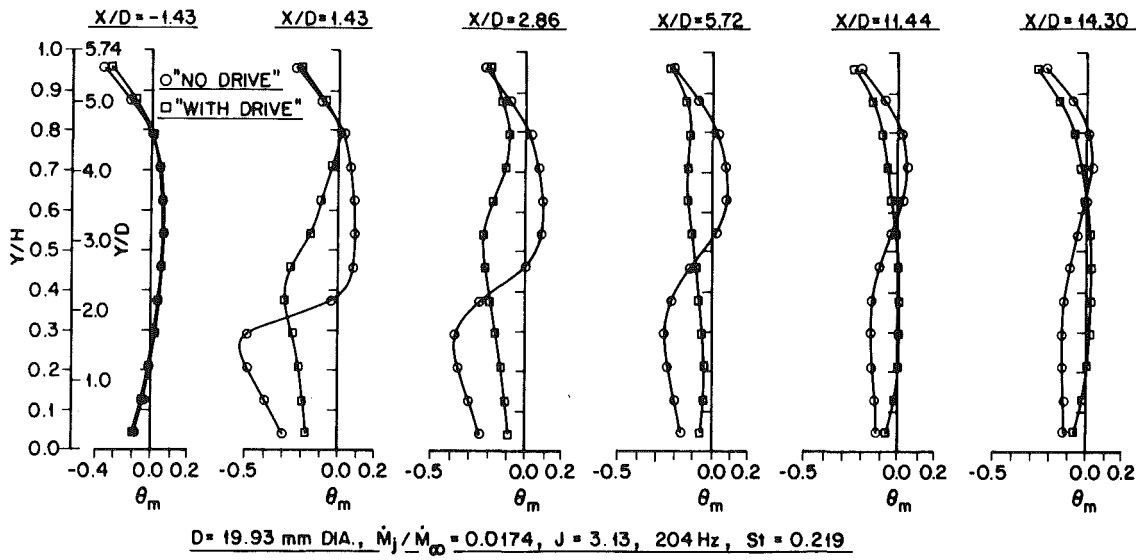

Fig. 2 Center-plane typical mean temperature vertical profiles for zero and medium (75 W) powers; average conditions: V_j = 18.5 m/s, V_j/U_∞ = 1.44, V_e/V_j = 1.16, T_j = 41.5°C, $\overline{T}_\infty$ = 195.3°C, ρ_j = 0.989 kg/m^3, ρ_∞ = 0.653 kg/m^3, Re_j = 19,002, Re_∞ = 56,781

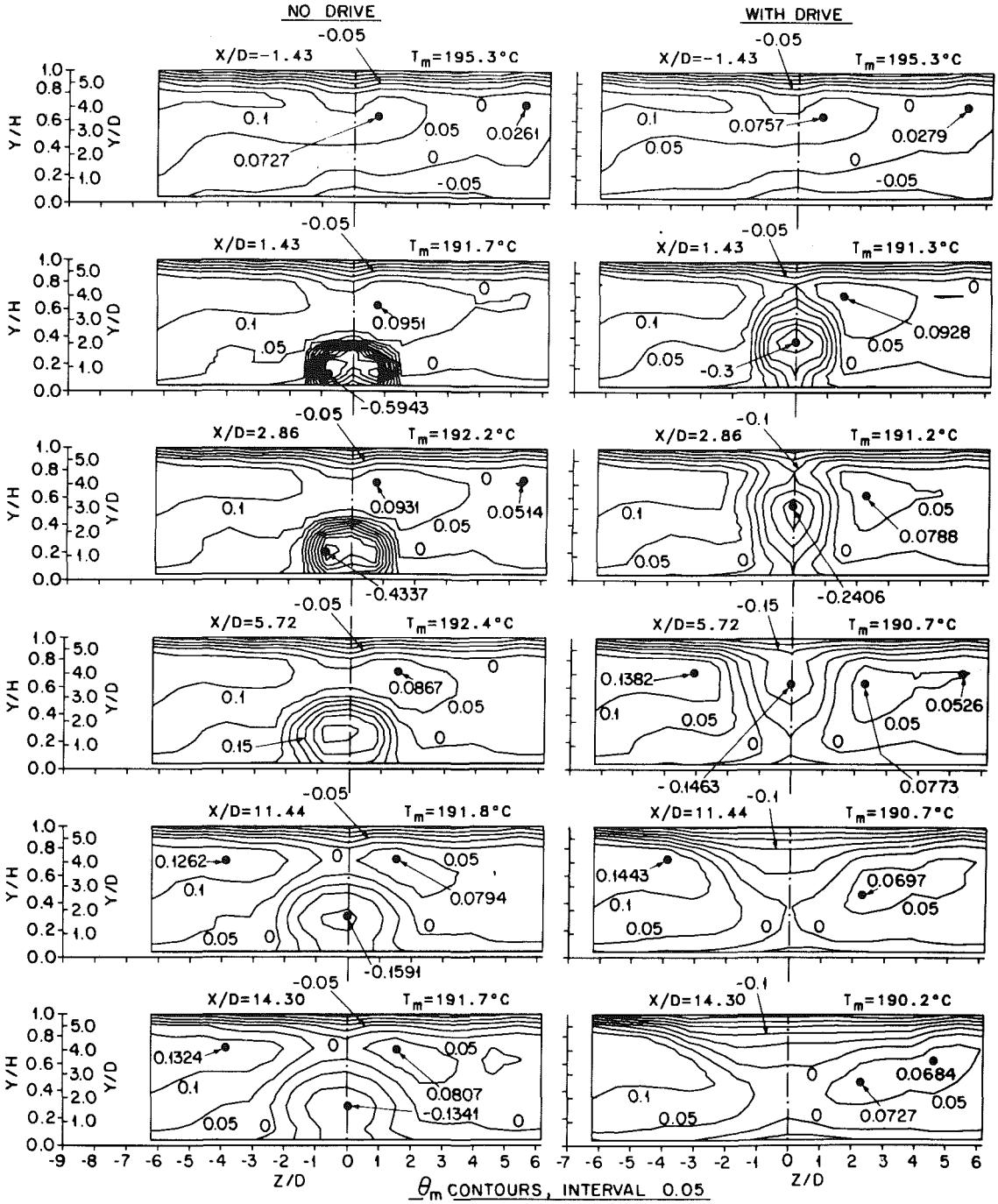

Fig. 3 Typical mean temperature contour maps for zero and medium (75 W) powers; 19.93-mm-dia orifice, J = 3.13, 204 Hz, St = 0.219, V_e/V_j = 1.16; see Fig. 2 for other data

θ_m) profile, the jet zone and the wake region cannot be separated. Effectively, for the centerplane, the region between the tunnel floor and the boundary "$j-j$" is composed of jet fluid and fluid entrained from the crossflow. "With-drive" the situation is less clear cut because of interference from the tunnel ceiling, and because of apparatus restraints profiles could not be obtained at X/D = 0.0. A lower boundary for the jet-wake region, separate from the tunnel floor, has appeared.

Test Results "Without Acoustic Drive". Referring to the θ_m and θ "no-drive" data of Figs. 2, 3, 4, and 5, the jet-wake zone is plainly visible, and in the transverse planes at X/D = 1.43 and 2.86 the characteristic kidney-shaped jet cross section [11] due to the bound vortices can be recognized. By X/D = 11.44 the influence of the bound vortices has disappeared. The general nature of the crossflow temperature field (Fig. 3) was revealed with a cool layer at the tunnel ceiling being noticeable. As mixing proceeded the temperature field outside the cool layer, and over the jet-wake zone width, became uniform to within ± 13.5 percent of perfect mixing by X/D = 14.30. The data also show, for the range covered, that the whole jet-wake region is bounded by the tunnel floor (Fig. 6). However, the θ data indicate that for $X/D \geq 5.72$ wake effects became weaker and a round cross-sectional jet zone was emerging. Also, the cross-sectional area of the jet-wake zone increased as turbulent entrainment and mixing with the crossflow fluid proceeded. The jet had good symmetry about the centerplane and the thermal axis of the jet coincided closely with the cen-

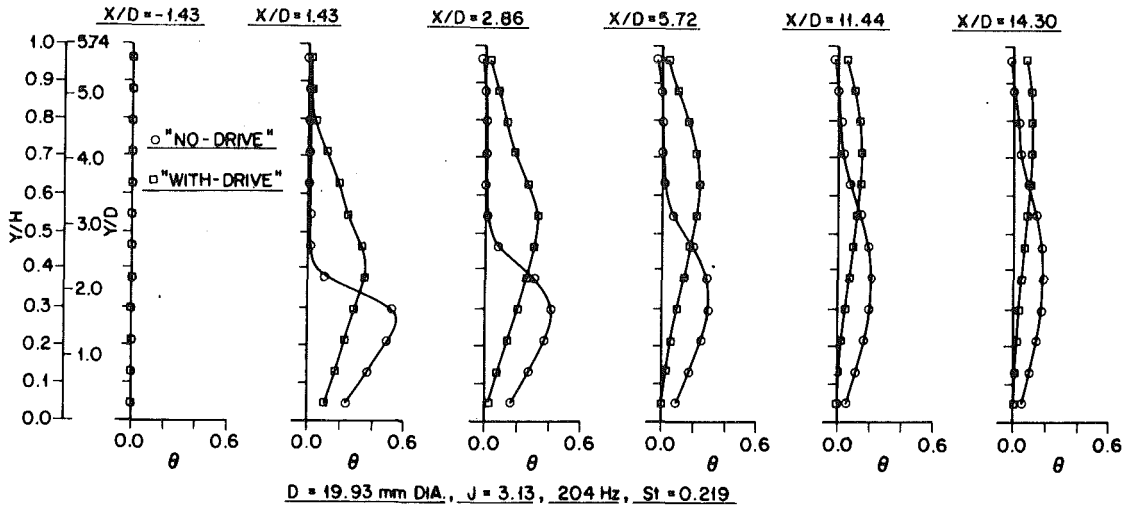

Fig. 4 Typical center-plane θ vertical profiles for zero and medium (75 W) powers, $V_e/V_j = 1.16$, see Fig. 2 for other data

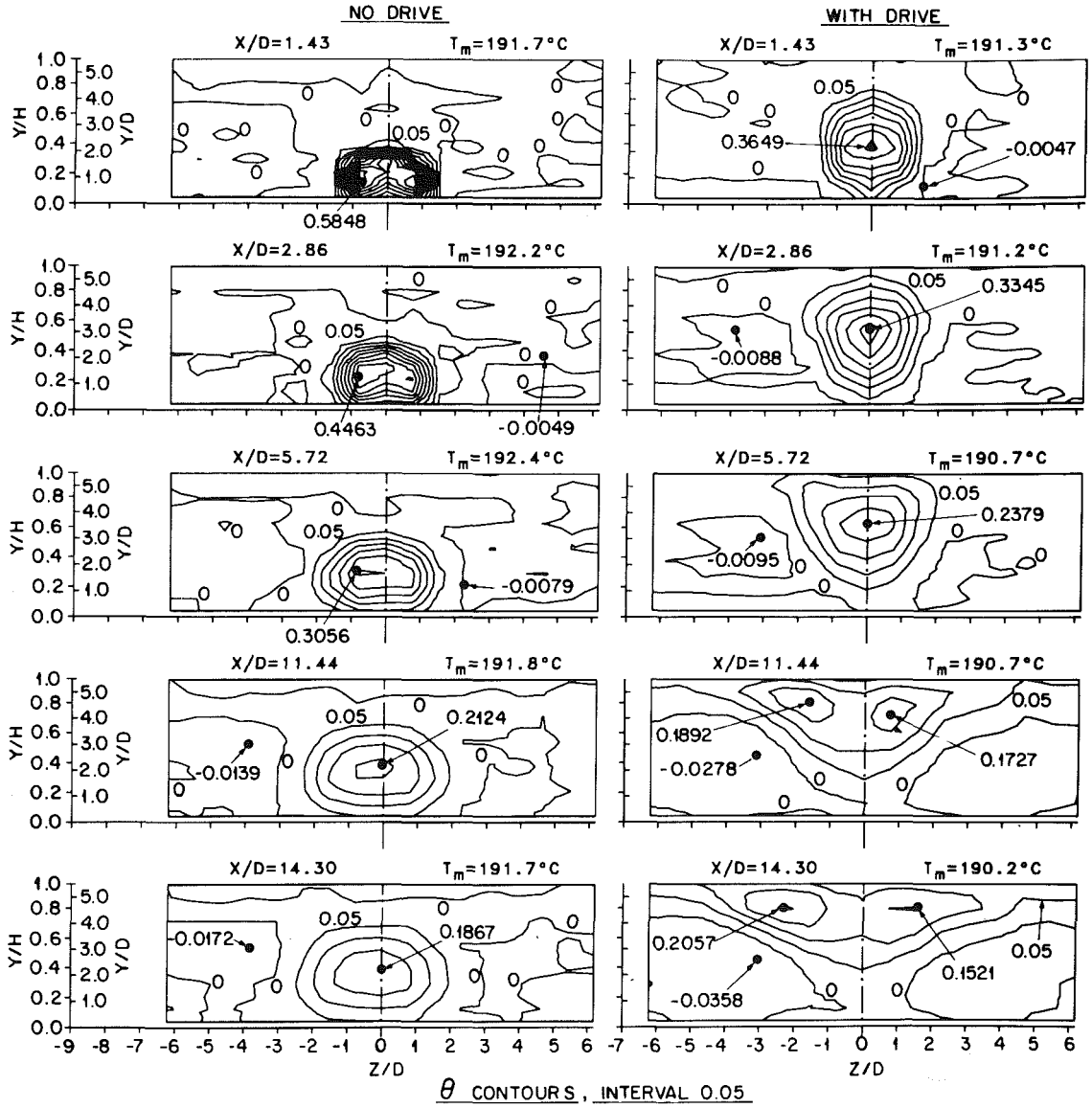

Fig. 5 Typical θ contour maps for zero and medium (75 W) powers; 19.93-mm-dia orifice, $J = 3.13$, 204 Hz, St = 0.219, $V_e/V_j = 1.16$, see Fig. 2 for other data

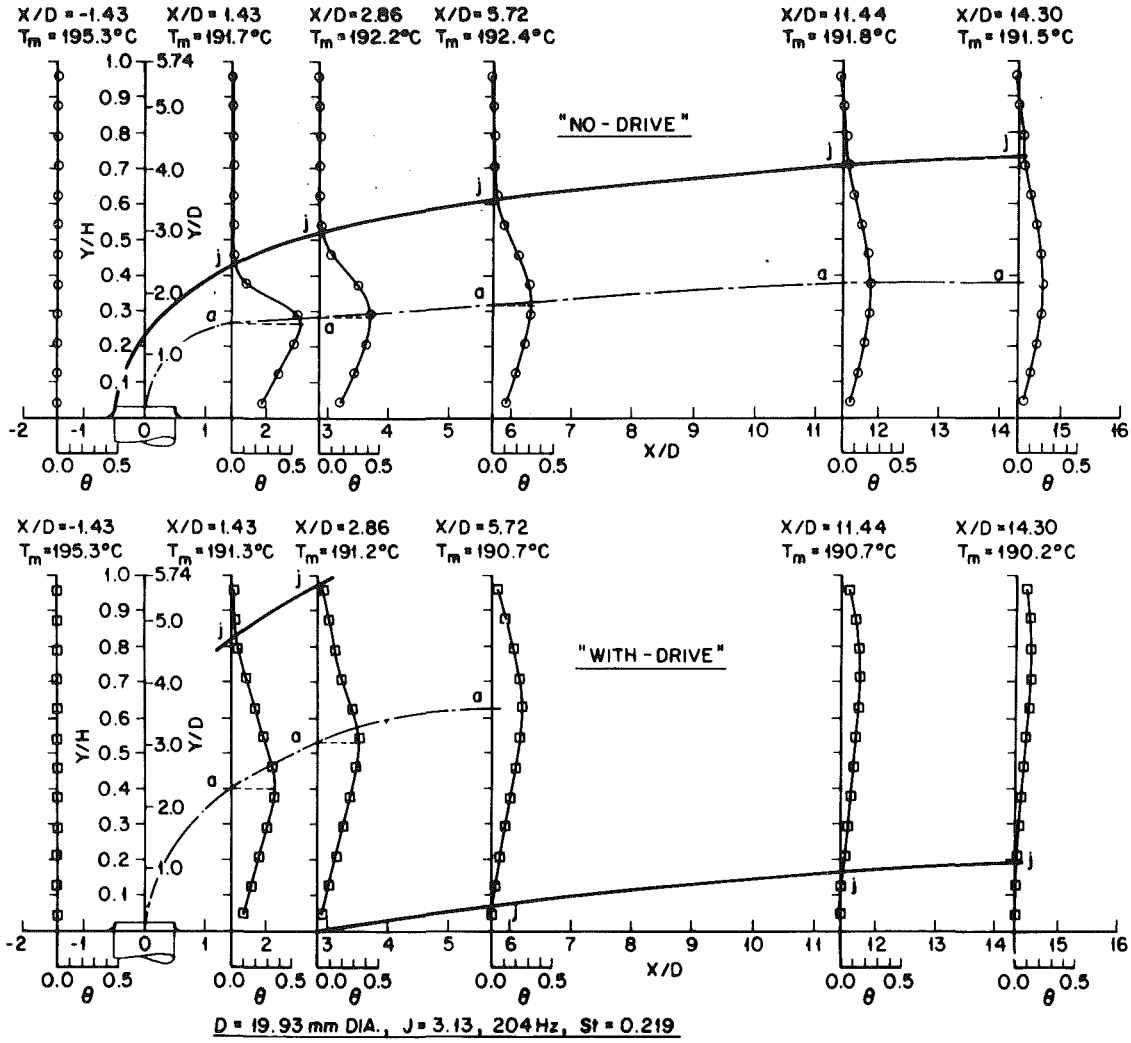

Fig. 6 Center-plane jet-crossflow structure corresponding to the θ profiles of Fig. 4, zero and medium (75 W) powers, V_a/V_j = 1.16

terplane. The general features of the jet-crossflow are consistent with the literature [10, 11], were repeatable, and therefore indicate that the behavior was stable and normal.

Test Results "With Acoustic Drive." First consider the center-plane vertical profiles of Figs. 2 and 4 together with the jet in crossflow structure of Fig. 6. The changes produced by acoustic excitation are most pronounced in that the jet penetration as defined by the thermal jet trajectory, and the depth of the jet-wake region, were significantly increased. The profiles are in general much flatter, with temperature minima much reduced, therefore demonstrating that the acoustic drive has strongly increased entrainment and mixing. The inflection in the upper portion of the profile at X/D = 1.43 (and X/D = 2.86 θ profile) may be due to the action of the toroidal vortices [8]. The more symmetric θ profile shows that the wake region has undergone strong modification. By X/D = 5.72 the mixing achieved is about the same as that for "no-drive" at X/D = 11.44; also, for "with-drive" the mixing zone occupies 92 percent of the tunnel flow height whereas for "no-drive" (X/D = 11.44) it only occupies 71 percent. This indicates the mixing zone was increased and in a much shorter length.

Turning now to the contour maps of Figs. 3 and 5, the increased acoustic excitation obviously increased the penetration and transformed the kidney-shaped cross section to an oval cross section. For $X/D \geq 2.86$ the wake region beneath the jet has become fully merged with the jet flow and the total flow has separated from the tunnel floor. Beyond X/D = 5.72 interference by the tunnel ceiling was strong and the remaining jet flow has separated into two small zones traveling along the ceiling wall as shown by the θ contours, perhaps the remaining effects of the bound vortices? This results in a much thickened cool ceiling layer shown by the θ_m contours. Excluding the plots much distorted by the ceiling ($X/D \geq 11.44$) acoustic drive has about doubled the depth of the combined jet-wake zone (little change in width), the temperature has been significantly increased and is more uniform, demonstrating that entrainment and mixing were strongly increased. By X/D = 14.30 the θ_m contour plot (Fig. 3), indicates that a relatively flat temperature distribution (within ± 5 percent, over the jet-wake zone width) has been achieved, except for the thickened cool ceiling layer, and the average temperature was reduced by 5.1°C because of jet mixing. This indicates that mixing was nearly complete, in contrast to the "no-drive" situation.

Discussion

Jet Penetration. The center-plane structure of the jet in hot crossflow of Fig. 6, when compared with that for the cold flow study of [8], shows about 34 percent less penetration at X/D = 2.86 for the hot crossflow "no-drive" and "with-drive." This difference between the thermal and velocity jet trajectories has been previously observed and discussed by Kamotani and Greber [12] and Ramsey and Goldstein [13]. The difference may also be due in part to buoyancy effects,

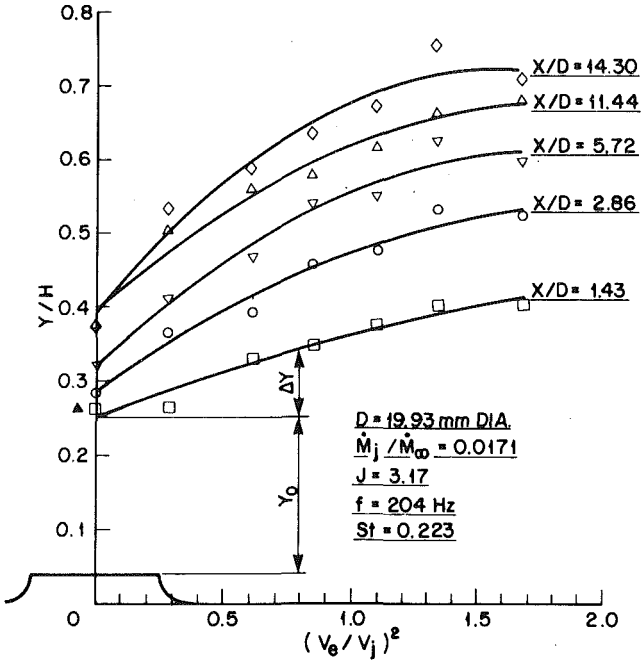

Fig. 7 Center-plane jet penetration versus relative pulsation strength, for 0-90 W powers; average conditions, V_j = 18.2 m/s, V_j/U_∞ = 1.53, T_j = 42.2°C, T_∞ = 195.0°C, ρ_j = 0.985 kg/m^3, ρ_∞ = 0.700 kg/m^3, Re_j = 18,701, Re_∞ = 57,639

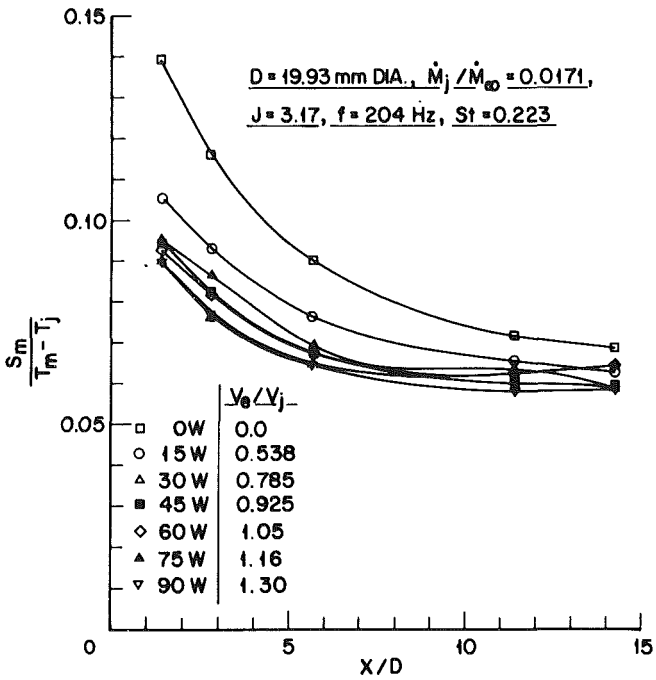

Fig. 8 Relative mixing effectiveness versus downstream distance, for 0-90 W powers; average conditions, V_j = 18.2 m/s, V_j/U_∞ = 1.53, T_j = 42.2°C, T_∞ = 195.0°C, ρ_j = 0.985 kg/m^3, ρ_∞ = 0.700 kg/m^3, Re_j = 18,701, Re_∞ = 57,639

i.e., ρ_j/ρ_∞ of 1.52 for the hot crossflow versus 1.04 for the cold flow study.

The center-plane thermal jet trajectories allow the increase in jet penetration with relative pulsation strength V_e/V_j to be determined. Using the relative pulsation strength power number calibration, the data are presented in Fig. 7 as a function of $(V_e/V_j)^2$, for various downstream locations, and for a good penetration and mixing response Strouhal number. The increased jet penetration with acoustic drive is strong; however, for $X/D \geq 5.72$ the tunnel ceiling suppresses the penetration. At X/D = 1.43 and 2.86 there is no tunnel ceiling interference, therefore the nonlinear behavior indicates that penetration cannot be increased indefinitely. Thus, further gains in penetration by increasing the excitation beyond $(V_e/V_j)^2 \geq 1.70$ (90 W) are small, and the maximum increase in penetration is therefore not less than 100 percent at X/D = 2.86. This agrees with the findings of [8] from velocity profiles, and the saturation effect may be due to excitation of the toroidal vibration mode of the torodial vortices shedding from the orifice, as speculated in the mixing and entrainment studies of [4, 5].

Length to Achieve a Given Mixed State. The overall mixing effectiveness for a particular transverse plane may be assessed by the standard deviation

$$S_m = \left[\frac{\sum_{i=1}^{n} (T - T_m)_i^2}{n-1} \right]^{1/2} \quad (5)$$

This parameter when normalized as $S_m/(T_m - T_j)$ may be termed the relative mixing effectiveness. Figure 8 plots the relative mixing effectiveness versus X/D for the data set encompassing the data of Figs. 2, 3, 4, and 5, i.e., for St = 0.223. The calculations were only performed for a width between 125 mm and 217 mm, and for a height from 4.8 mm to 81 mm, in order to eliminate masking by the temperature field outside this acoustically active zone, essentially a signal-to-noise problem. When mixing is perfect $T = T_m$, and the relative mixing effectiveness becomes zero. Therefore, as mixing proceeds with X/D this parameter tends to zero, as shown by Fig. 8, and also tends to zero as V_e/V_j is increased. However, because the temperature distribution in the reference plane, just upstream of the jet orifice, is not uniform (S_m not zero) the relative mixing effectiveness reduces as mixing proceeds to an asymptotic value determined by the upstream temperature distribution. Also, for powers greater than 30 W, the jet penetrates into the cold ceiling layer by about X/D = 11.44 and the asymptotic value is reached. Thus, the "no-drive" mixed state at X/D = 14.30 is achieved at X/D = 4.3 for an acoustic excitation of V_e/V_j = 1.30 (90 W), or the superior mixed state at X/D = 14.30 (near the asymptotic value) has been attained by acoustic excitation. The length to achieve a given mixed state has therefore been shortened by 70 percent, in this case, and the mixing has been significantly increased by acoustic excitation, which is in agreement with [8]. It will also be noticed from Fig. 8 that the improvement in mixing showed saturation taking place as V_e/V_j was increased, which again agrees with [8]. Some further small improvement in mixing and reduction in length to reach a given mixed state may therefore be expected for powers greater than 90 W (V_e/V_j = 1.30). Since mixing is directly related to entrainment, and Vermeulen et al. [5] found that the increase in entrainment mass flow rate saturated with acoustic drive, it is not surprising that mixing also saturates and for the same reason.

Strouhal Number Effect. Keeping $\sqrt{\dot{W}}/V_j\sqrt{\dot{M}_j}$ constant for X/D = 2.86, and for J = 3.02 while varying the Strouhal number, ΔY, the change in jet penetration, was obtained from the center-plane vertical θ profiles. The available data normalized in the form $\Delta Y/Y_o$ are plotted against Strouhal number in Fig. 9. Very clearly the optimum penetration occurs at St = 0.29, hence for a given acoustic excitation maximum penetration will be obtained at this Strouhal number. It is possible that this optimum will depend on the excitation; however, V_e/V_j could not be significantly changed because as $\dot{W}$ is increased the jet flow decreases, requiring the branch flow valve to be opened in order to maintain V_j. Thus, at the lowest St (highest V_j), the valve was fully open for a driver power of 45 W, hence

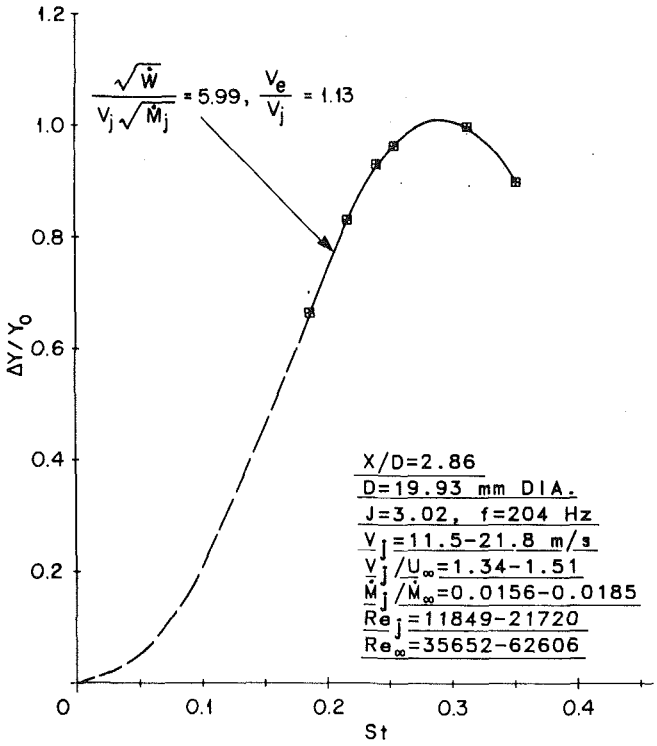

Fig. 9 Relative change in jet penetration versus Strouhal number; average conditions T_j = 40°C, T_∞ = 190°C, ρ_j = 0.985 kg/m^3, ρ_∞ = 0.644 kg/m^3

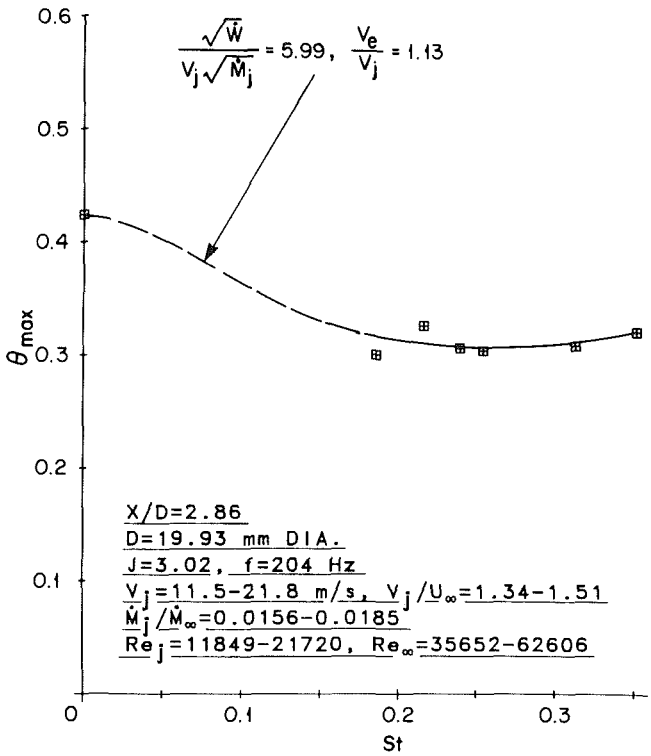

Fig. 10 θ_{max} versus Strouhal number; see Fig. 9 for other data

even though up to 140 W was available such powers could not be used because the required Strouhal number range (jet velocities) could not be maintained.

The maximum value of θ, θ_{max}, is well defined and should therefore be an effective indicator of Strouhal number effect. This is presented in Fig. 10 where the minimum value indicates

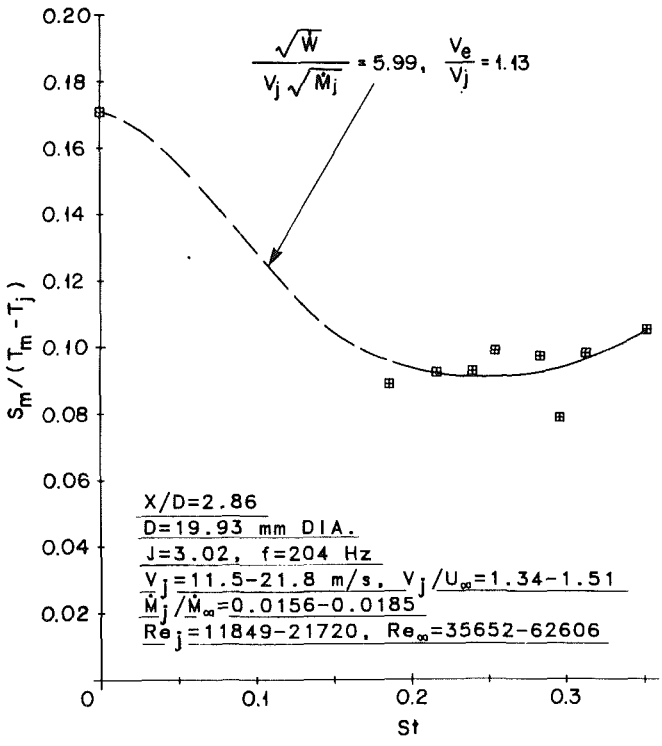

Fig. 11 Relative mixing effectiveness versus Strouhal number; see Fig. 9 for other data

the optimum St (θ_{max} minimizes as $T \to T_m$ "with-drive"). The optimum Strouhal number by this approach is therefore St = 0.27. The Strouhal number effect may also be assessed by the relative mixing effectiveness from the same test data as established the optimum by jet penetration and θ_{max}, except that two extra test points may be included, which had to be excluded for ΔY and θ_{max} because of profile distortion. The distortion was caused by the action of the traveling torodial vortices, which were very strong due to these tests being close to the optimum St. The data are presented in Fig. 11, where the minimum value indicates the most effective mixing, and therefore the optimum Strouhal number is St = 0.25, in fair agreement with that found from penetration and θ_{max}.

The average optimum Strouhal number is therefore 0.27 as determined by penetration and mixing. This is 24 percent greater than that found from the cold flow work [8], St = 0.22. However, an optimum St = 0.25 for the entrainment rate and mixing found for a free jet [4, 5] agrees with the St range established by this new work. The optimum St established by the cold flow work is understandably low because of data limitations. There is good agreement with the maximum turbulence optimum St = 0.30 obtained by Crow and Champagne [1] for free jet centerline turbulence measurements, which supports an optimum Strouhal number of 0.27 for mixing and penetration.

Excitation Method. The use of a loudspeaker driver to pulse the jet flow is very convenient for laboratory experiments. However, for engine applications a more reliable excitation method is required and must be developed. In this context it should be noted that mechanical devices have been successfully employed, for example, a reciprocating piston by Binder and Favre-Marinet [2] and a rotating disk valve by Seno et al. [14].

Conclusions

The experimental investigation into the mixing of an acoustically excited air jet with a confined hot crossflow showed that the excitation produced strong changes in the measured

temperature profiles. This resulted in significant increases in mixing zone size, penetration (at least 100 percent increase), and mixing, and the length to achieve a given mixed state was shortened by at least 70 percent. There was strong modification to the jet-wake region. The increase in jet penetration and mixing was saturating near 90 W, the largest driving power tested. The jet response as determined by penetration and mixing was optimum at a Strouhal number of 0.27. Overall, pulsating the jet flow significantly improved the jet mixing processes in a controllable manner.

Acknowledgments

The authors are indebted to Mr. R. Bechtold, Chief Technical Supervisor; Mr. R. W. Gustafson, and Mr. B. Sanders, Research Technicians; and particularly to Technicians Mr. W. Crews, Mr. G. East, and Mr. A. Moehrle, for their careful work in the building and operation of the test rig. Also our gratitude is extended to Mr. L. Raciborski, Research Associate, for valuable help with data acquisition and computer programming. Canadian Western Natural Gas. Co., Ltd., generously supplied the natural gas for operation of the test rig. The work was supported financially by the Natural Sciences and Engineering Research Council of Canada, under Grant No. A7801.

References

1 Crow, S. C., and Champagne, F. H., "Orderly Structure in Jet Turbulence," *Journal of Fluid Mechanics*, Vol. 48, 1971, pp. 547–591.

2 Binder, G., and Favre-Marinet, M., "Mixing Improvement in Puslating Turbulent Jets," ASME Symposium on Fluid Mechanics of Mixing, Georgia Institute of Technology, Atlanta, GA, June 20–22, 1973, pp. 167–172.

3 Hill, W. G., and Greene, P. R., "Increased Turbulent Jet Mixing Rates Obtained by Self-Excited Acoustic Oscillations," *Journal of Fluids Engineering*, Vol. 99, No. 3, 1977, pp. 520–525.

4 Vermeulen, P. J., and Yu, Wai Keung, "An Experimental Study of the Mixing by an Acoustically Pulsed Axisymmetrical Air-Jet," *International Journal of Turbo & Jet-Engines*, Vol. 4, Nos. 3–4, 1987, pp. 225–237.

5 Vermeulen, P. J., Ramesh, V., and Yu, Wai Keung, "Measurements of Entrainment by Acoustically Pulsed Axisymmetric Air Jets," ASME JOURNAL OF ENGINEERING FOR GAS TURBINES AND POWER, Vol. 108, No. 3, 1986, pp. 479–484.

6 Vermeulen, P. J., Odgers, J., and Rasmeh, V., "Acoustic Control of Dilution-Air Mixing in a Gas Turbine Combustor," ASME JOURNAL OF ENGINEERING FOR POWER, Vol. 104, No. 4, 1982, pp. 844–852.

7 Vermeulen, P. J., Odgers, J., and Ramesh, V., "Full Load Operation of a Gas Turbine Combustor With Acoustically Controlled Dilution-Air Mixing," *International Journal of Turbo & Jet-Engines*, Vol. 4, Nos. 1–2, 1987, pp. 139–147.

8 Vermeulen, P. J., Chin, Ching-Fatt, and Yu, Wai Keung, "An Experimental Study of the Mixing Behaviour of an Acoustically Pulsed Air Jet With a Confined Crossflow," AIAA Paper No. 88-3296, 1988.

9 Ho, Chih-Ming, and Huerre, P., "Perturbed Free Shear Layers," *Annual Reviews of Fluid Mechanics*, Vol. 16, 1984, pp. 365–424.

10 Holdeman, J. D., and Walker, R. E., "Mixing of a Row of Jets With a Confined Crossflow," *AIAA Journal*, Vol. 15, 1977, pp. 243–249.

11 Moussa, Z. M., Trischka, J. W., and Eskinazi, S., "The Near Field in the Mixing of a Round Jet With a Cross Stream," *Journal of Fluid Mechanics*, Vol. 80, 1977, pp. 49–80.

12 Kamotani, Y., and Greber, I., "Experiments on a Turbulent Jet in a Cross Flow," *AIAA Journal*, Vol. 10, No. 11, 1972, pp. 1425–1429.

13 Ramsey, J. W., and Goldstein, R. J., "Interaction of a Heated Jet With a Deflecting Stream," ASME *Journal of Heat Transfer*, Vol. 93, 1971, pp. 365–372.

14 Seno, T., Kageyama, S., and Ito, R., "Effect of Controlled Pulsation on Axisymmetric Jet Behaviour," *Journal of Chemical Engineering of Japan*, Vol. 20, No. 2, 1987, pp. 128–133.

A. F. Ali Al-Shaikhly

G. E. Andrews

C. O. Aniagolu

Department of Fuel and Energy,
The University of Leeds,
Leeds, LS2 9JT, United Kingdom

Jet Shear Layer Turbulent Diffusion Flames for Ultralow NO_x Emissions

Direct fueling of each shear layer generated by an array of holes in a grid plate was shown to have ultralow NO_x emissions combined with a good flame stability, compared with a premixed system. Two methods of fuel injection were investigated that had opposite NO_x/stability characteristics. Four shear layers in a 76-mm combustor were used at gas turbine primary zone operating conditions with 60 percent simulated primary zone air at one bar pressure. The fuels used were propane and natural gas and a minimum NO_x emission of 2.5 ppm at 15 percent oxygen, compatible with a 0.1 percent inefficiency, was demonstrated for natural gas with a reasonable stability margin. These designs have the potential for a dry NO_x solution to any current or proposed gas turbine NO_x regulation for natural gas.

1 Introduction

Gas turbine combustion chambers are characterized by a series of discrete holes in a combustor liner, which generate jet shear layers and hence turbulence. There has generally been little relationship between the fuel injection and the jet shear layer configuration. A single central fuel injector is usually used with the jet shear layers relatively remote from the fuel injector. This results in a good flame stability and ignition characteristic, due to poor mixing, with combustion occurring mainly in the recirculation zones between shear layers. This results in very large temperature gradients, as shown in the internal gas composition traverses of Heitor and Whitelaw (1986) and Bicen et al. (1988), which generate large NO_x concentrations and high smoke emissions. The authors have previously shown that if fuel injection is arranged such that the fuel is injected into the base of jet shear layers, then simultaneous mixing and flame stabilization can be achieved within the jet shear layer (Al Dabagh and Andrews, 1983; Al Dabagh et al., 1984, 1989). The locally rich mixtures were confined to the shear layers, which ensured a wide stability range, but mixing was nearly complete by the end of the shear layers and the downstream combustion achieved low NO_x emissions by minimizing the thermal NO_x in the lean primary zone. Further development of this concept, as the basis of an ultralow NO_x combustor, is presented in this work.

The aim of the present work was the development of a lean primary zone gas turbine combustor with low NO_x emissions, without using fully premixed fuel and air. For industrial gas turbines, NO_x legislation exists in several countries that can only be met by using water or steam injection, with an associated performance penalty. The current worldwide concern over NO_x emissions is already reflected in renewed interest in low NO_x aero-engines. It is well known that NO_x emissions can be reduced by using lean well-mixed primary zones, but the level of reduction is closely related to the quality of the improved fuel and air mixing. Future higher turbine entry temperature gas turbines will also require more air in the primary zone with better fuel and air mixing.

Premixed fuel and air systems offer the lowest NO_x emissions but involve major practical problems (Sotheran et al., 1985). One of these problems is that of flame stability. Andrews et al. (1988) have developed a range of techniques for low NO_x gas turbine primary zones with good flame stability, all of which use fuel injection into the base of jet shear layers. Low NO_x emissions have been demonstrated for nonswirling jet shear layer systems for both gas and liquid fuels (Abdul Aziz

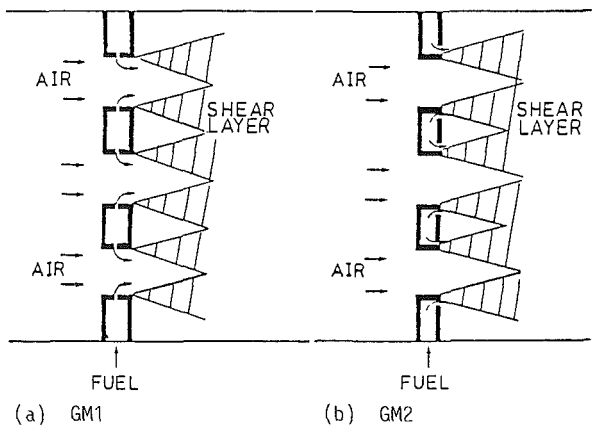

Fig. 1 Grid mix fuel injection, radial injection GM1, and annular ring axial injection GM2

Contributed by the International Gas Turbine Institute and presented at the 35th International Gas Turbine and Aeroengine Congress and Exposition, Brussels, Belgium, June 11–14, 1990. Manuscript received by the International Gas Turbine Institute January 20, 1990. Paper No. 90-GT-144.

Table 1 Four-hole grid mix designs

GM	Dia.mm	Cd	Blockage	M	ΔP/P%
GM1A	22.1	0.93	66.3	0.047	1.6
GM1AA	19.7*	1.0	73.2	0.047	2.05
GM1B	18.0	0.84	77.6	0.047	4.8
GM1C	16.3	0.81	81.7	0.047	6.9
				0.038	4.35
				0.030	2.7
GM2A	19.6	0.97	73.3	0.047	2.4
GM2AA	17.1*	0.98	80.0	0.047	3.9
GM2AB	16.5*	1.0	81.2	0.047	3.9
				0.032	1.9

* - A hole restriction insert into the previous stabiliser was used.

et al., 1987; Abdul Hussain et al., 1988) and for swirl-stabilized systems (Alkabie et al., 1988; Alkabie and Andrews, 1989). The Grid Mix technique of directly fueling an array of shear layers was shown to have low NO_x characteristics (Al Dabagh and Andrews, 1983; Al Dabagh et al., 1985, 1989) and the present work investigates techniques to produce further reductions in NO_x emissions using lower primary zone air flows for enhanced overall combustor stability.

2 Grid Mix Shear Layer Flame Stabilizers

Two flat plate stabilizers, termed Grid Mix, with four equal diameter holes in a 76-mm-diam combustor, were investigated. Two methods were used for direct gaseous fuel injection into the base of the shear layers generated by the air flow through the holes. These two methods of fuel injection, termed Grid Mix 1 (GM1) and Grid Mix 2 (GM2), are shown in Fig. 1. Grid Mix 1 had radial fuel injection jets at the base of the shear layer into the high-velocity air jets. This was designed to give the fastest mixing, as some premixing of the fuel and air would occur prior to interaction with the shear layer and the radial fuel jet would also generate vortices that would enhance the shear layer mixing. Grid Mix 2 had an annular fuel feed into the outer part of the shear layer and hence into the low velocity interjet recirculation zone. This was designed to give slower mixing with larger shear layer residence times, to give better flame stability. This design is also the basis of a commercial process heater burner. Al Dabagh et al. (1989) have shown that direct fueling of each shear layer gives much lower NO_x emissions than a central fuel injector of the same array of shear layers. Internal traverses showed that with central fuel injection of the four shear layers there was a poor fuel distribution with rich regions created on the outer part of the shear layers.

The shear layer jet velocities and pressure loss are set by the blockage of the stabilizer and air mass flow through it. It was the objective of the present work to investigate the influence of the air mass flow or primary zone Mach number at a constant pressure loss and this involved a variation of the blockage or hole diameter of the stabilizer. The Grid Mix geometries used and the test Mach numbers and pressure loss are shown in Table 1. For the Grid Mix 1 design different stabilizers were manufactured with different hole diameters, as used by Al Dabagh and Andrews (1983). The highest blockage of these was used in the present work at reduced Mach numbers of 0.03 and 0.038. To increase the pressure loss of the lowest pressure loss design an insert was placed in the hole with large side holes to allow the passage of the fuel jets. This insert could affect the shear layer as it changed the hole entrance shape. However, it is considered that the recess in the insert around the radial fuel injection holes would have the greatest effect by promoting fuel and air mixing by recirculation within the recess. The results show lower NO_x and hence better mixing with the insert in place.

Table 2 Weak extinction equivalence ratio results at 600 K

GM	M	ΔP/P%	Fuel	EqR
GM1A	0.047	1.6	P	0.22
GM1AA	0.047	2.05	P	0.27
			Premix	0.45
GM1B	0.047	4.8	P	0.27
			Premix	0.51
GM1C	0.047	6.9	P	0.31
	0.038	4.35	P	0.24
	0.030	2.7	P	0.27
	0.030	2.7	NG	0.33
GM2A	0.047	2.4	P	0.18
GM2AA	0.047	3.9	P	0.24
GM2AB	0.047	3.9	P	0.22
	0.032	1.9	NG	0.22

For the Grid Mix 2 design an insert into the four holes was manufactured to achieve the reduction in the hole diameter. This also altered the distance between the fuel annulus and the air jet, but this was not considered to have a major impact on the mixing. This is supported by the experimental results, with similar weak extinction with the insert in place and lower NO_x emissions due to the higher pressure loss in spite of the deterioration in mixing due to the greater fuel separation from the air jet.

3 Experimental Equipment

The atmospheric pressure test facility consisted of an air supply fan, venturi flow metering, electrical air preheater, 1.5-m-long, 76-mm-dia approach pipe, flame stabilizer, 330-mm-long, 76-mm-dia uncooled combustor, mean gas sample probe, 152-mm water-cooled exhaust pipe with an observation window on the combustor centerline of a 90 deg bend. The air and fuel flow rate metering accuracy was ±2 percent for the air flow and 5 percent for the fuel flow. The 76-mm combustor was a practical annular combustor depth and hence equivalent to single burner rig. The combustor was instrumented with wall static pressure tappings and thermocouples so that axial profiles of temperature and static pressure could be measured. These were used to determine the recirculation zone size and the axial location of the main heat release zone.

The atmospheric pressure testing used in the present work is a rapid relatively cheap technique for the evaluation of combustor performance. It is particularly suitable for the evaluation of low NO_x combustor designs, as systems that have high NO_x emissions at one bar must have even higher NO_x emissions at higher pressures. Thus a low NO_x design at one bar pressure, with adequate air preheat, is a firm basis for

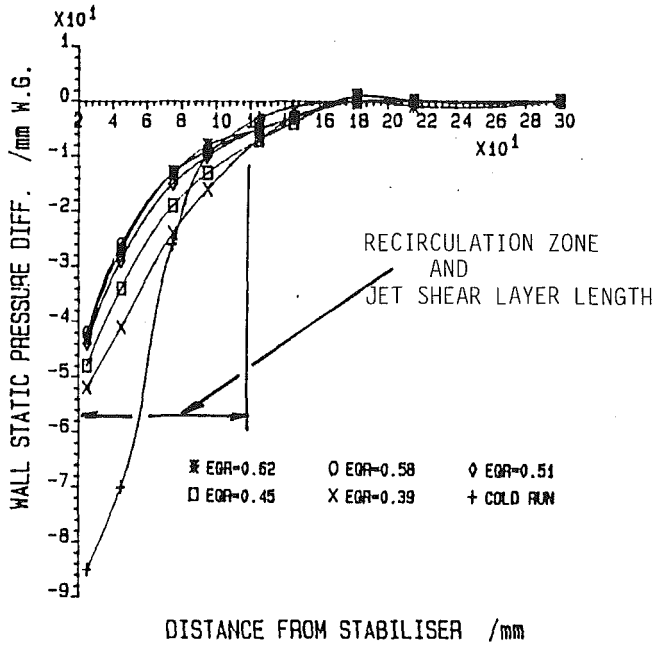

Fig. 2 Axial variation of the wall static pressure relative to the static pressure at 300 mm for GM1C at 600 K and M = 0.03; comparison of the isothermal profiles with those for natural gas combustion over the equivalence ratio range of 0.39–0.62

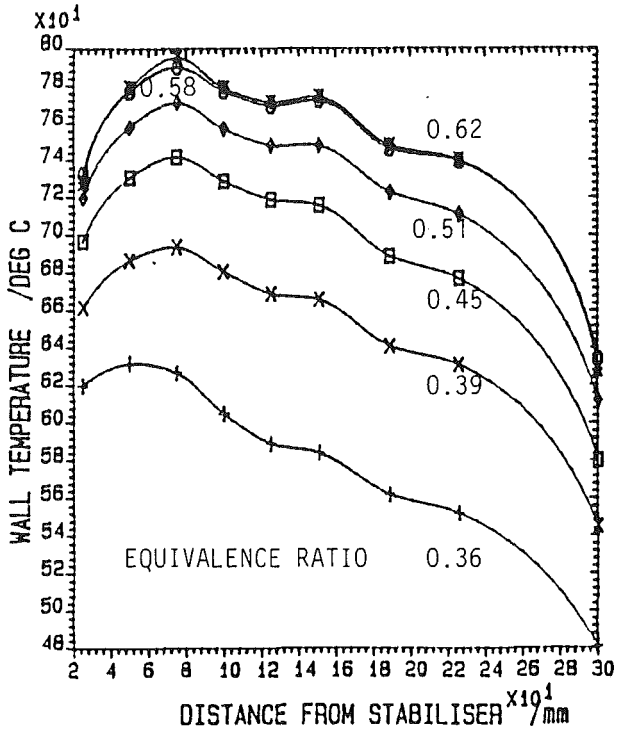

Fig. 3 Axial variation of the uncooled combustor wall temperatures for GM1C at 600 K and M = 0.03

testing at full pressure providing there is a high combustion efficiency with the low NO_x emissions at one bar. If 99.9 percent combustion efficiency can be achieved at one bar, then pressure cannot significantly improve on this. The NO_x emissions can then be reasonably reliably scaled to higher pressures using the conventional square root dependence on pressure.

Mean exhaust plane gas samples were obtained using a 20 hole water cooled **X** configuration probe. The sample gases were passed into a heated sample line and on through a heated filter and pump to a heated gas analysis system. The gas analysis results were computer processed to provide air-to-fuel ratio, combustion efficiency, mean adiabatic flame temperature, and various pollution parameters. For the same calibration gases the test to test repeatability was better than 5 percent on all the gases analyzed, including NO_x. All calibration gases for NO_x were calibrated using the same 1 percent accurate reference NO_x standard in a BOC Spectroseal gas cylinder.

An inlet temperature of 600 K was used to simulate high power operation and 400 K to simulate low power operation. Propane was supplied from a bank of six liquefied propane cylinders. The composition of the propane was analyzed by gas chromatography and this composition was used in the gas analysis computations. Natural gas was also used to compare with propane and was supplied from the mains using a 1 bar boost pressure. This was also analyzed by gas chromatography and the composition used in the gas analysis computations.

4 Weak Extinction Results

At a constant mean velocity and inlet temperature the fuel flow was gradually reduced until visual observation, through the 100 mm window in the exhaust, showed the flame to go out. The extinction process was also detectable from the gas analysis by a sudden increase in UHC emissions. The weak extinction results were repeatable to ± 0.02 equivalence ratio and are summarized in Table 2.

The weak extinction results show that the annular fuel injection of the GM2 design had a better stability than GM1 for both propane and natural gas. The differences were not large at 600 K although larger differences were found at 400 K (0.44 and 0.25 for GM1C and GM2AB, respectively, at M = 0.03 for natural gas). There was a better than twofold improvement in the premixed flame stability for both of the designs. For a similar pressure loss there was no influence of the Mach number on the weak extinction. This indicates that the weak extinction is controlled by the pressure loss or turbulence rather than the Mach number. This is because the pressure loss governs the fuel and air mixing, which has the greatest influence on the stability. For a fixed hole size the influence of Mach number on the weak extinction was to decrease it as the Mach number and pressure loss increased. This was because the increased pressure loss improved the mixing, which reduced the stability. For the GM1 design natural gas had a slightly worse weak extinction than for propane, but there was little difference for the GM2 design. For the GM1 design the natural gas used the same fuel hole sizes and would have a higher penetration than for propane due to the higher injection dynamic pressure, as the injected flow was similar for the two fuels at the same equivalence ratio. This would lead to slightly more mixing prior to the shear layers and hence a worse stability, as shown in Table 2.

5 Wall Static Pressure and Temperature Profiles

The wall static pressure profiles for GM1C at M = 0.03 and 600 K are shown in Fig. 2 for a range of natural gas equivalence ratios and for no combustion. The aerodynamics was simply that of an expanding jet and similar to that of the classical orifice plate used in flow metering. Figure 2 shows that the interjet recirculation zone length was approximately one third of the combustor length, with little influence of combustion on this length. The wall temperature profiles in Fig. 3 show that the heat release was well established in this shear layer region with peak wall temperatures before the end of the shear layer recirculation zone. Similar results were obtained for propane and at 400 K.

The decrease in the negative static pressure in the shear layer region with combustion was due to the density difference be-

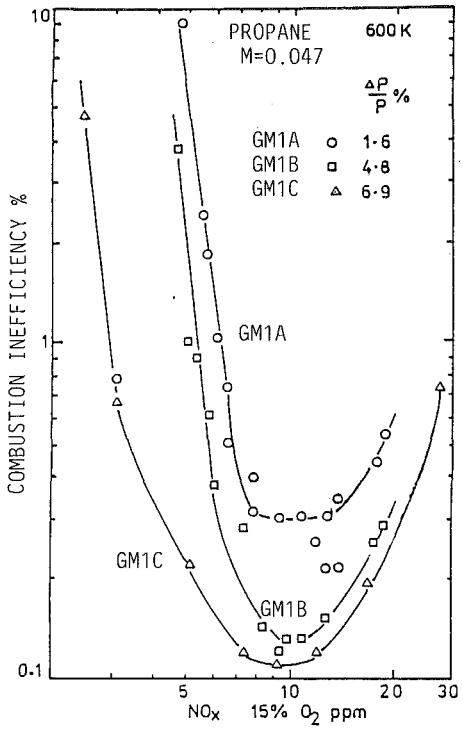

Fig. 4 Influence of the Grid Mix 1 pressure loss at M = 0.047 and 600 K on the relationship between the combustion inefficiency and NO_x corrected to 15 percent oxygen

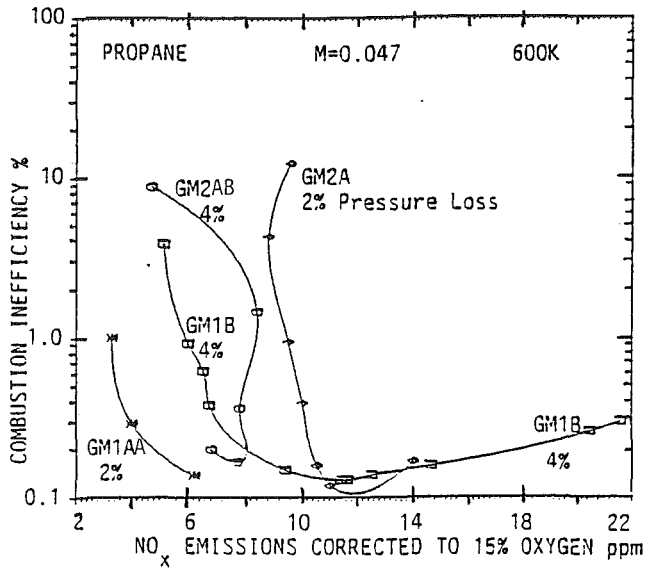

Fig. 5 The influence of the Grid Mix flame stabilizer blockage or pressure loss at 600 K and M = 0.047 on the corrected NO_x emissions and combustion inefficiency for two methods of shear layer fueling, GM1 and GM2

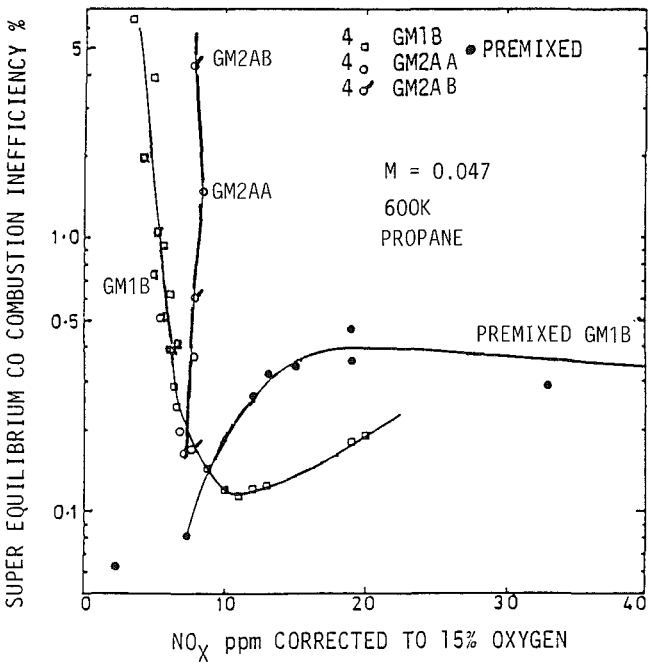

Fig. 6 Comparison of the radial fuel injection GM1 design with the annular axial fuel injection on the periphery of each shear layer jet, GM2, and with premixed combustion; correlation of combustion inefficiency corrected for equilibrium CO and NO_x corrected to 15 percent oxygen

tween the unburned jet shear layer and the burned gas recirculation region. The velocity difference between the shear layer jet and the downstream high-velocity burned gases was reduced relative to the constant density situation and hence the wall static pressure difference between the downstream and shear layer region was reduced. The reduction increased as the equivalence ratio increased due to the greater velocity difference between the shear layer and the downstream burned gases.

6 Influence of Pressure Loss at Constant Mach Number

Al Dabagh and Andrews (1983) and Al Dabagh et al. (1984) have shown that increasing the pressure loss at a constant Mach number, by increasing the stabilizer blockage, produces an increase in the turbulence fuel and air mixing. The turbulent velocity was proportional to the square root of the fractional pressure loss and the turbulence dissipation energy that governs the molecular mixing was proportional to the pressure loss to the 1.5 power. The improvement in the combustion inefficiency and NO_x corrected to 15 percent oxygen relationship as a function of the pressure loss is shown in Fig. 4. These results were obtained at a 0.047 Mach number with propane and a 600 K inlet temperature using the radial fuel injection into the air jets with stabilizers GM1A, GM1B, and GM1C.

Figure 4 shows that both the combustion inefficiency and the NO_x emissions were improved by increasing the pressure loss. For a constant inefficiency of 0.3 percent the NO_x was reduced from 8 to 4 ppm as the pressure loss was increased from 1.6 to 6.9 percent. All the NO_x emissions were ultralow levels of NO_x and would scale for the lowest pressure drop to below 32 ppm at 16 bar pressure using the square root pressure dependence of thermal NO_x, with less than 20 ppm possible at the higher pressure loss. The optimum primary zone equivalence ratio to achieve these low NO_x emissions with the 0.3 percent combustion inefficiency was 0.46, 0.43, and 0.40 for the three pressure losses 1.6, 4.8 and 6.9 percent, respectively. Table 2 shows that there was a substantial stability margin between these optimum primary zone equivalence ratios and the weak extinction. However, the margin decreased to achieve the lower NO_x emissions of the higher pressure loss designs. The optimum equivalence ratio was also outside the operational stability range of a premixed system. Equivalent NO_x emissions to these could only be obtained with a premixed system by operating at an equivalence ratio of 0.5, which was very close to the weak extinction (Al Dabagh and Andrews, 1983).

The difference in the pressure loss between GM1A and GM1B was rather large. To establish data at an intermediate pressure a restriction insert was placed in the holes of GM1A to achieve

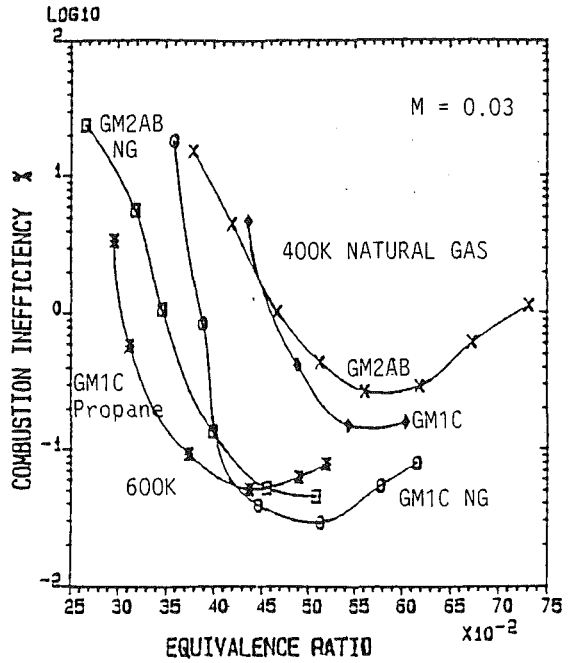

Fig. 7 Comparison of the GM1 and GM2 designs at M = 0.03 for natural gas and propane at 400 K and 600 K; combustion inefficiency as a function of equivalence ratio

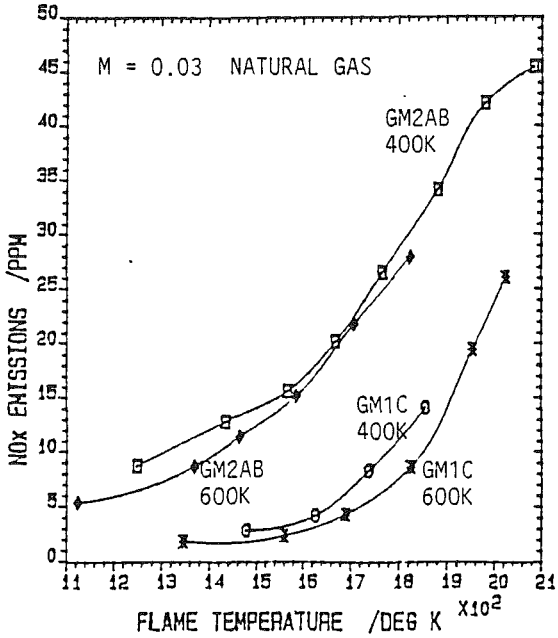

Fig. 8 Comparison of the GM1 and GM2 designs at M = 0.03 for natural gas at 600 K and 400 K; mean NO_x emissions as a function of the mean adiabatic flame temperature based on the rig metered A/F and the combustion efficiency

an increased blockage, as detailed in Table 1. A pressure loss of 2.05 percent was achieved at the 0.047 Mach number for this GM1AA design. This insert had large (3 mm) holes in the wall to line up with the fuel injection holes. These may have influenced the local fuel and air jet mixing. Figure 5 shows that GM1AA had lower NO_x emissions than the higher pressure loss GM1B. It is considered that the reason for this was the presence of the recess by the fuel hole outlet. This would cause a small recirculation zone in the recess, which would accelerate the fuel and air mixing. The NO_x emissions for GM1AA were very low at 4 ppm corrected to 15 percent oxygen for a 0.3 percent combustion inefficiency and were achieved with a much better weak extinction than for the GM1C results with similar NO_x emissions.

Figure 5 also includes the results for the influence of pressure loss on the annular fuel injection stabilizers, GM2A and GM2AB. The pressure loss was varied by inserting a restrictor into the holes in the GM2A stabilizer. The influence of pressure loss was to decrease the NO_x emissions as the pressure loss and blockage were increased. This was due to the increased fuel and air mixing within the shear layer as the turbulence increased with the pressure loss, as for the GM1 design in Fig. 4. At the higher pressure loss the NO_x emissions were close to those for GM1B with a similar pressure loss and equivalence ratio of 0.41. As the pressure loss increased, the shear layer fuel and air mixing would increase to overcome any differences in initial mixing caused by the location of the fuel injection relative to the shear layer.

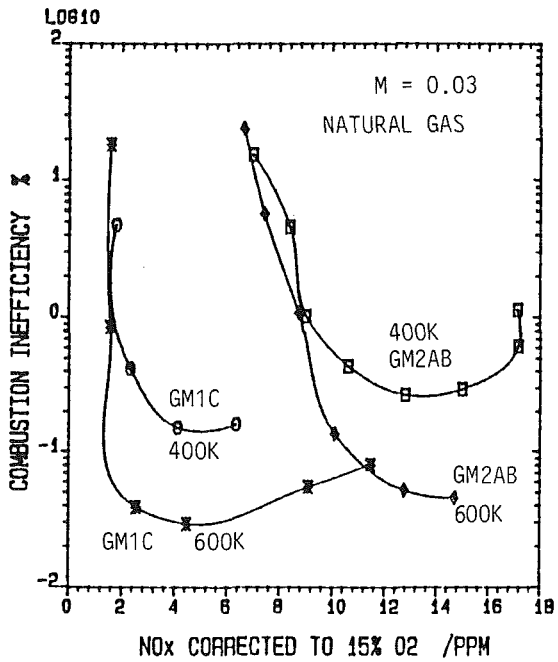

Fig. 9 Comparison of the GM1 and GM2 designs for natural gas at M = 0.03 for 600 K and 400 K; combustion inefficiency as a function of NO_x corrected to 15 percent oxygen

7 Comparison of the Two Methods of Fuel Injection

The combustion inefficiency as a function of NO_x corrected to 15 percent oxygen is shown in Fig. 6 for the GM1 and GM2 methods of fuel injection. This shows that at a high pressure loss the two designs had little difference. These results at M = 0.047 and 3.9 percent pressure loss are compared with the same stabilizers operated premixed in Fig. 6. This shows that premixed systems only exhibit low NO_x emissions very close to the weak extinction and hence the present shear layer stabilized diffusion flame designs are preferable, as the stability margin is much wider. Figure 6 also compares the stabilizers GM2AA and GM2AB, which have a different hole diameter but the same pressure loss. The results are identical and illustrate that the pressure loss rather than the blockage or hole diameter is the most important parameter that determines the NO_x emissions. The optimum primary zone operating condition for a minimum NO_x with an acceptable inefficiency of better than 0.3 percent is 7 ppm for both the GM1 and GM2 designs and this occurred at a 0.4 primary zone equivalence ratio for both stabilizers. This represents a primary zone temperature of 1550 K at 600 K inlet temperature. This compares

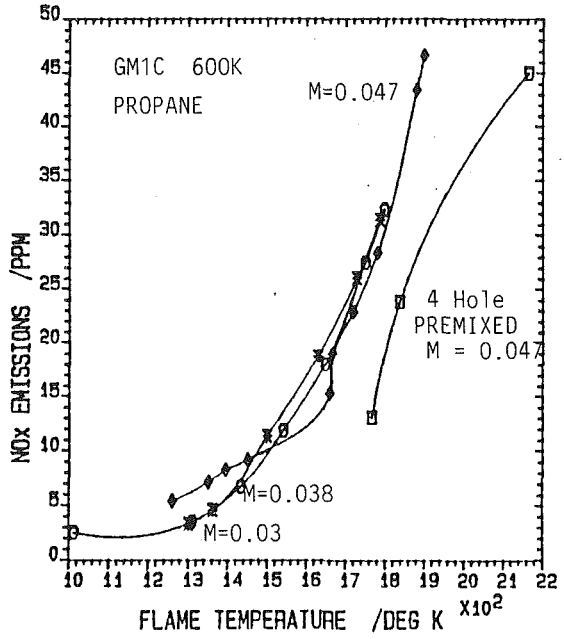

Fig. 10 Influence of Mach number or residence time on the NO_x emissions as a function of mean adiabatic flame temperature calculated from the rig metered A/F and the combustion efficiency; comparison with the equivalent premixed results

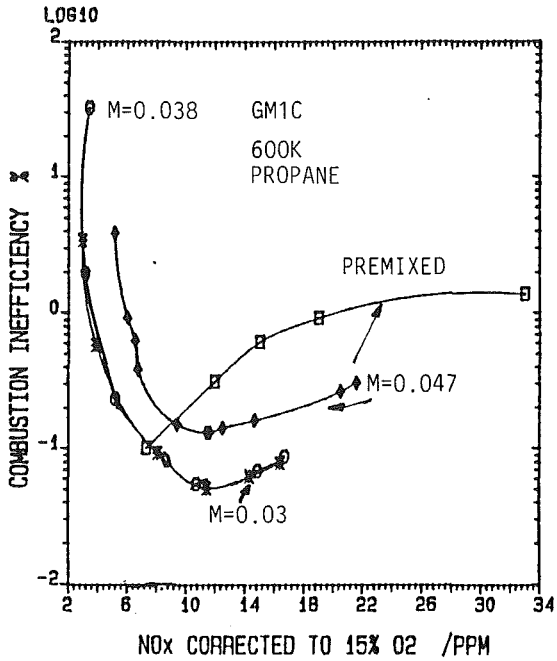

Fig. 11 Influence of the Mach number or residence time on the GM1C combustion inefficiency correlation with NO_x emissions corrected to 15 percent oxygen

with an equivalence ratio of 0.5 for NO_x emissions of 7 ppm with a premixed system, which is very close to the weak extinction compared with a factor of 2 stability margin for the shear layer fuel injection Grid Mix designs.

This optimum equivalence ratio is richer than the overall, but the 0.047 test Mach number assumes that all the combustion air passed through the primary zone. A 60 percent air flow in the primary zone is required to achieve a 0.4 equivalence ratio at typical overall operating conditions. This is equivalent to a 0.03 Mach number in the present work. Figure 7 shows the comparison of the combustion inefficiency as a function of equivalence ratio for the GM1C and GM2AB designs at a 0.03 Mach number using natural gas at 600 K and 400 K air inlet temperatures. There was a small difference in the pressure loss between these designs, as shown in Table 1, 2.7 percent for GMIC compared with 1.9 percent for GM2AB.

Figure 7 shows that at both 400 and 600 K the radial fuel injection of GM1C produced a slightly lower inefficiency. Both designs had the minimum inefficiency at the same equivalence ratio, but the annular fuel injection design was more efficient for mixtures leaner than the minimum inefficiency, as expected from the wider flame stability. The minimum inefficiency was lower than at the 0.047 Mach number in Fig. 6 due to the higher residence time. The simulated low-power 400 K inefficiencies were well below 1 percent over a wide range of equivalence ratios, but required a richer primary zone of 0.55 equivalence ratio. As the overall equivalence ratio is leaner at low power, this requires either a variable area or a variable fuel combustor design if the primary zone is to be at the optimum at both low and high power.

The NO_x emissions as a function of the primary zone mean temperature are shown in Fig. 8 for GM1C and GM2A2 at a 0.03 Mach number for natural gas at 400 K and 600 K. This shows that the radial fuel injection GM1 design had substantial reductions in NO_x emissions compared with the GM2 annular fuel injection. Figure 9 shows the combustion inefficiency as a function of NO_x corrected to 15 percent oxygen and this demonstrates a difference in NO_x between the two designs similar to that at a 2 percent pressure loss in Fig. 5 for the 0.047 Mach number. For the same flame temperature the inlet

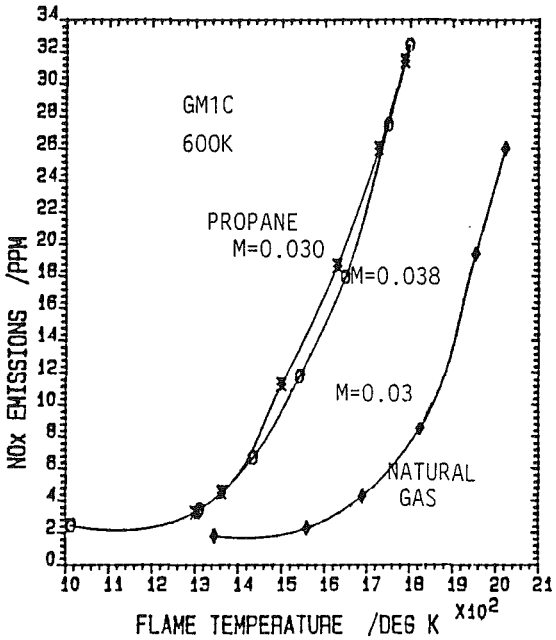

Fig. 12 Comparison of propane and natural gas NO_x emissions as a function of the mean adiabatic flame temperature corrected for the combustion inefficiency for GM1C at M = 0.03 and 600 K

temperature had little influence on the NO_x emissions with slightly lower NO_x for the higher inlet temperature, as shown in Fig. 8. This indicates that the mixing was good, as any zones with a near-stoichiometric mixture would have generated higher NO_x emissions at the higher inlet temperature.

Figure 9 shows that although both fuel injection methods achieved low NO_x emissions, the radial fuel injection method, GM1, achieved ultralow NO_x emissions. The minimum NO_x emissions corrected to 15 percent oxygen compatible with a 0.1 percent inefficiency at 600 K was 2.5 ppm for GM1C and 10 ppm for GM2AB. These NO_x emissions were achieved at

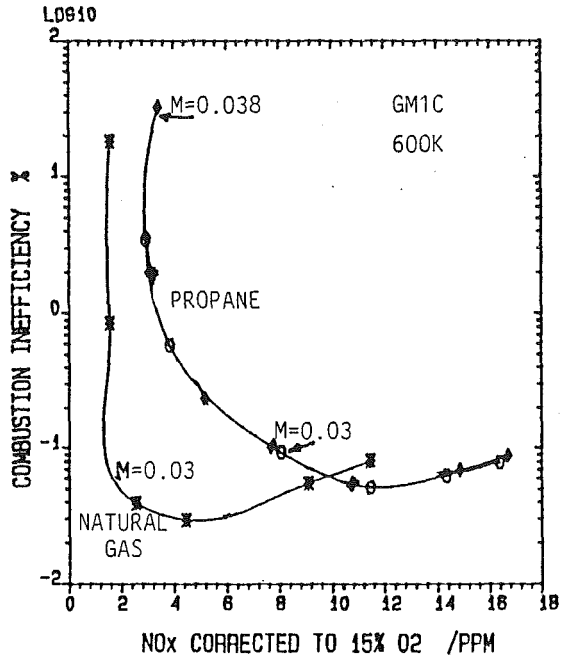

Fig. 13 Comparison of propane and natural gas NO_x emissions corrected to 15 percent oxygen as a function of the combustion inefficiency for GM1C at M = 0.03 and 600 K inlet temperature

a primary zone equivalence ratio of 0.45 for GM1C and 0.4 for GM2AB. However, the wider stability of the GM2 design gave a better stability margin compared with GM1C. The ultralow NO_x emissions for GM1C scale to 10 ppm at 16 bar using a square root pressure dependence for thermal NO_x. This indicates the possibility of meeting most of the current stringent NO_x emissions regulations without using steam or water injection or catalytic techniques.

8 The Influence of the Combustor Mach Number

The optimum equivalence ratio that was found for minimum NO_x emissions with an acceptable efficiency was approximately 0.4–0.45. This was considerably richer than current industrial gas turbines operate, where a 0.25 equivalence ratio is typical. To achieve a 0.43 equivalence ratio in the primary zone requires only 60 percent of the total air flow. This will reduce the mean combustor unburned gas Mach number from 0.047 to 0.03. The increased residence time at lower Mach numbers may increase the thermal NO_x emissions. The radial fuel GC1C injector was investigated at three Mach numbers with propane and a 600 K inlet temperature.

The NO_x emissions are shown as a function of the mean primary zone temperature in Fig. 10. There was little difference in the NO_x emissions, except in the low-temperature region where the highest Mach number results were higher. Between 1500 and 1700 K there was a small increase in NO_x emissions as the residence time increased.

The combustion inefficiency is shown as a function of the NO_x corrected to 15 percent oxygen in Fig. 11. The results at a Mach number of 0.047 have a worse inefficiency than the higher residence time lower Mach number results. Thus, for the same inefficiency a higher optimum NO_x will occur at the 0.047 Mach number. For a 0.1 percent inefficiency a 0.45 equivalence ratio was required for the 0.047 condition compared with 0.4 for the lower Mach numbers. A 0.5 equivalence ratio was required for premixed combustion and the ultralow NO_x emissions of the GM1C design could not be achieved, as weak extinction occurred below 0.5.

These results show that the NO_x did not increase with the residence time, in spite of the reduction in pressure loss and hence fuel and air mixing intensity. Both of these effects should have increased the NO_x if thermal NO_x was important. The reduction in achievable NO_x emissions at the lower Mach numbers indicates that thermal NO_x may not be important near the optimum low-NO_x conditions. The flame temperatures are well below the 1800 K condition where thermal NO_x production becomes rapid and hence most NO_x may be generated by a prompt NO_x mechanism. This may result in the assumed square root NO_x dependence being an inappropriate scaling factor as this is for thermal NO_x. However, there is no agreement on the pressure effect on prompt NO_x, but it may be lower than a 0.5 exponent.

9 The Comparison Between Propane and Natural Gas

Figure 7 shows that the combustion inefficiency for propane was better than that for natural gas for equivalence ratios less than 0.45. This was due to the better stability for propane. However, at the minimum inefficiency condition there was little difference between the two fuels. A comparison of the NO_x emissions for propane and natural gas is made in Fig. 12 for the GM1C radial fuel injector at the 0.03 Mach number. The small effect of the Mach number on the propane NO_x emissions is shown to contrast with the very large difference in the NO_x emissions between the two fuels, with much lower NO_x emissions for natural gas. At 1700 K the difference is a factor of 4.

The combustion inefficiency as a function of the NO_x corrected to 15 percent oxygen is shown in Fig. 13. This shows that for the 0.03 Mach number the optimum NO_x was 2.5 ppm for natural gas and 8 ppm for propane for a 0.1 percent inefficiency. The optimum primary zone equivalence ratio was 0.37 for propane and 0.45 for natural gas. Thus, natural gas achieved lower NO_x emissions in spite of a richer optimum primary zone. It is considered that the lower NO_x emissions for natural gas were due mainly to lower prompt NO_x, as thermal NO_x should be small for temperatures below 1800 K. Prompt NO_x is due to reactions of hydrocarbon intermediate species, which are more numerous for propane.

10 Conclusions

10.1 The direct injection of gaseous fuel into simple jet shear layers formed by a grid plate has a good flame stability compared with a premixed system with lower NO_x emissions than can be achieved by premixed combustion.

10.2 Two methods of fuel injection into the jet shear layers were used. Radial injection into the air jets (GM1) gave the lowest NO_x emissions but with an inferior flame stability compared with annular fuel injection around the jet hole (GM2). However, this design had higher NO_x emissions, but sufficiently low to offer a possible 50 percent reduction on the 75 ppm EPA NO_x regulation. The GM1 design with NO_x emissions as low as 2.5 ppm could potentially meet any current NO_x regulation.

10.3 A 0.03 Mach number was shown to give reduced optimum NO_x emissions for the same combustion inefficiency compared with a 0.047 Mach number operation. Thus operation with a portion of the combustion air flow in the primary zone is beneficial in terms of NO_x and has the advantage of a greater overall stability. The present M = 0.03 primary zone condition corresponds to a 60 percent primary zone air flow.

10.4 Natural gas gave substantially lower NO_x emissions than for propane. This difference was considered to be due to less prompt NO_x with natural gas.

Acknowledgments

This work was supported by internal Departmental funds

but the test facilities were developed with a series of SERC grants. Some work on the Grid Mix program was supported by a contact from Ruston Gas Turbines. R. A. Boreham operated the test facility and commissioned the equipment.

References

Abdul Aziz, M. M., Abdul Hussain, U. S., Al Dabagh, N. A., Andrews, G. E., and Shahabadi, A. R., 1987, "Lean Primary Zones: Pressure Loss and Residence Time Influences on Combustion Performance and NO_x Emissions," *1987 Tokyo International Gas Turbine Congress*, Vol. III, pp. 89–96.

Abdul Hussain, U. S., Andrews, G. E., Cheung, W. G., and Shahabadi, A. R., 1988, "Low NO_x Primary Zones Using Jet Mixing Shear Layer Combustion," ASME Paper No. 88-GT-308.

Al Dabagh, N. A., and Andrews, G. E., 1983, "The Influence of Flame Stabiliser Pressure Loss on Mixing, Combustion Performance and Flame Stability," *Sixth International Symposium on Air Breathing Engines*, Paris, AIAA, pp. 172–181.

Al Dabagh, N. A., Andrews, G. E., and Manoharan, R., 1984, "Shear Layer Mixing for Low Emission Gas Turbine Primary Zones," ASME Paper No. 84-GT-13; *Int. J. Turbo Jet Engines*, Vol. 2, 1985, pp. 227–239.

Al Dabagh, N. A., Al-Shaikhly, A. F. A., Andrews, G. E., Aniagolu, C. O., and Manoharan, R., 1989, "Shear Layer Combustion: Influence of the Method of Fuel Injection on Stability and Emissions," *The Ninth International Symposium on Air Breathing Engines*, Athens, AIAA, pp. 325–332.

Alkabie, H. S., Andrews, G. E., and Ahmad, N. T., 1988; "Lean Low NO_x Primary Zones Using Radial Swirlers," ASME Paper No. 88-GT-245.

Alkabie, H. S., and Andrews, G. E., 1989, "Ultra Low NO_x Emissions for Gas and Liquid Fuels Using Radial Swirlers," ASME Paper No. 89-GT-322.

Andrews, G. E., Abdul Aziz, M. M., Abdul Hussain, U. S., Al Dabagh, N. A., Ahmad, N. A., Ali, A. F., Al-Shaikhly, A. F., Alkabie, H. S., Kowkabi, M., and Shahabadi, A. R., 1988, "High Intensity Burners With Low NO_x Emissions," British Flame Days 1988, *Furnace Combustion Research and Its Applications*, The Institute of Energy.

Bicen, A. F., Tse, D., and Whitelaw, J. H., 1988, "Flow and Combustion Characteristics of an Annular Combustor," *Combustion and Flame*, Vol. 72, pp. 175–186.

Heitor, M., and Whitelaw, J. H., 1986, "Velocity, Temperature and Species Characteristics of the Flow in a Gas Turbine Combustor," *Combustion and Flame*, Vol. 64, pp. 1–32.

Sotheran, A., Pearce, D. E., and Overton, D. L., 1985, "Some Practical Aspects of Staged Premixed, Low Emissions Combustors," ASME JOURNAL OF ENGINEERING FOR GAS TURBINES AND POWER, Vol. 107, pp. 2–9.

Experimental Measurement of the Vortex Development Downstream of a Lobed Forced Mixer

W. A. Eckerle
Fluids Metrology,
Cummins Engine Co., Inc.,
Columbus, IN 47202

H. Sheibani

J. Awad

MIE Department,
Clarkson University,
Potsdam, NY 13676

An experimental study was conducted to investigate the mixing processes downstream of a forced mixer. A forced mixer generates large-scale, axial (stirring) vorticity, which causes the primary and secondary flow to mix rapidly with low loss. These devices have been successfully used in the past where enhanced mixing of two streams was a requirement. Unfortunately, details of the mixing process associated with these lobed forced mixers are not well understood. Performance sensitivity to design variables has not been documented. An experiment was set up to investigate the mixing processes downstream of a mixer. Air flow was independently supplied to each side of the forced mixer by separate centrifugal blowers. Pressures were measured at the entrance to the lobes with a pitot-static probe to document the characteristics of the approaching boundary layer. Interior mean and fluctuating velocities were nonintrusively measured using a two-component laser-Doppler velocimetry (LDV) system for velocity ratios of 1:1 and 2:1. The wake structure is shown to display a three-step process where initially secondary flow was generated by the mixer lobes, the secondary flow created counterrotating vortices with a diameter on the order of the convolute width, and then the vortices broke down resulting in a significant increase in turbulent mixing. The results show that the mean secondary motion induced by the lobes effectively circulated the flow passing through the lobes. This motion, however, did not homogeneously mix the two streams. Turbulent mixing in the third step of the mixing process appears to be an important element in the enhanced mixing that has been observed with forced mixers. The length required for the flow to reach this third step is a function of the velocity ratio across the mixer. The results of this investigation indicate that both the mean secondary motion and the turbulent mixing occurring after vortex breakdown need to be considered for prediction of forced mixer performance.

Introduction

In general, mixing of multiple flows is an important factor in determining the length of devices. A forced mixer promotes rapid mixing by creating streamwise vorticity, as shown in Fig. 1. These devices employ a splitter plate, which is highly convoluted at the trailing edge to form lobes where the streams to be mixed initially merge. The lobes generate significant secondary flows that lead to the formation of large-scale vortices whose axes are aligned in the streamwise direction. The enhanced mixing of these devices is believed to be directly attributable to the large mixing scales generated by the vortices. These mixers are also more attractive for enhancing mixing than devices that generate shear mixing because the mixing is accomplished with low total pressure loss. Consequently, forced mixers have a variety of applications such as ejectors, afterburners, vortex generators, combustors, and heat exchangers.

Forced mixers of the type tested in this experiment have been used in turbofan engines to mix the hot inner and the cold outer flows rapidly. In this application, the mixer was a splitter plate (the surface separating the outer fan stream and the inner core engine stream), which was convoluted at the trailing edge

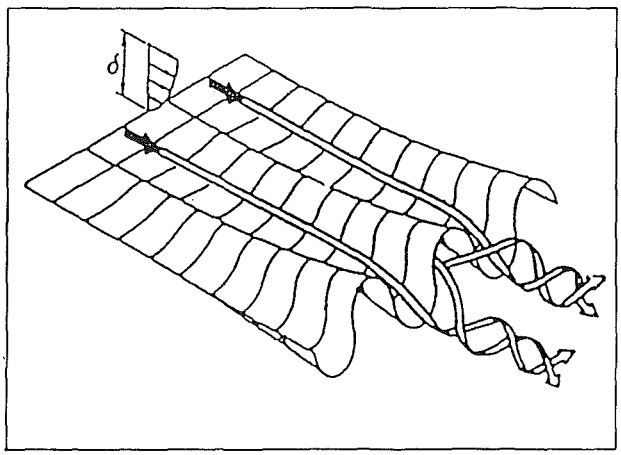

Fig. 1 Streamwise vorticity generated by a forced mixer

Contributed by the International Gas Turbine Institute and presented at the 35th International Gas Turbine and Aeroengine Congress and Exposition, Brussels, Belgium, June 11-14, 1990. Manuscript received by the International Gas Turbine Institute December 30, 1989. Paper No. 90-GT-27.

where the two streams initially merged. By proper tailoring of the splitter surfaces, high levels of flow uniformity were achieved in very short distances. Reports by Kozlowski and Kraft (1980) and Head et al. (1984) summarize the guidelines developed from their work for designing the surfaces of the forced mixing nozzles. These guidelines were based on the gross performance of the mixing nozzles. Details of the flow field were not measured, so a basic understanding of the flow mechanisms associated with the rapid mixing was not understood. Paterson (1982a, 1982b) provided the first detailed data in the mixing region downstream of the mixing nozzles. Results from that test effort showed strong secondary flows in the mixing region. Axially oriented vortices having scales on the order of the mixer lobe width were measured. These vortices were believed to have been created by the lobe geometry and the trailing edge Kutta condition, i.e., an inviscid effect.

Skebe et al. (1988) acquired detailed measurements just downstream of a two-dimensional segment of three different forced mixer geometries. The primary variables were the lobe shape (sinusoidal versus parallel side walls) and lobe penetration. The tests were conducted in a low-speed wind tunnel at a test section velocity of 37 m/s. The tests involved laser-Doppler velocimeter (LDV) measurements of the interior fluid and total pressure measurements of the mixer boundary layers just downstream of the mixer exit. The boundary layer measurements indicate that low-momentum flow tended to collect in the lobe troughs. Thin boundary layers were measured on the lobe crests. The accumulation of low-momentum flow in the lobe troughs was due to pressure gradients inviscidly generated by the lobe surface curvature. This accumulation impacts the mixer design because the low-momentum flow effectively reduces the lobe peak-to-peak amplitude and causes a corresponding drop in magnitude of the secondary velocities generated by the mixer. Since these secondary velocities are an important element of the mixing process, high-performance mixers must have relatively large lobe amplitudes. In addition, the data measured with sinusoidal shaped lobes showed that the lobe sidewall boundary layers merged in the lobe troughs, further reducing the mixer effectiveness. Higher mixer performance is achieved, then, with the lobe sidewalls parallel. The LDV measurements near the mixer exit showed strong secondary flow generated by the lobe shape. The authors concluded that the generation of axial vortices in the mixing region was due to this secondary flow and, therefore, that the vortices were inviscidly generated. The implication of this conclusion is that forced mixers can be designed based on inviscid analyses and that the circulation generated by the mixer is the most important parameter representing the mixing strength of a forced mixer. The authors performed an inviscid analysis and showed that the circulation is proportional to the product of the lobe amplitude and the lobe inclination angle. This analysis, then, also shows the importance of large lobe amplitudes in generating effective mixing.

Presz et al. (1986, 1987) have studied the effect of lobe shape on forced mixer performance in low-pressure-ratio ejector systems. This is a generic application for a forced mixer since ejector performance depends on low-loss mixing of the primary and secondary streams. Pressure and velocity traverses were acquired in the mixing region to determine the ejector performance associated with the various mixers. The test results identified lobe shapes that mixed the flows well in a very short ejector duct length. The best performance was measured with lobes having parallel sidewalls and a penetration of at least 60 percent. Lobe inclination angles as large as 25 deg were used without the flow separating from the lobe surface. Their results indicate that low-pressure-ratio ejector pumping with a forced mixer can be improved over conventional designs by over 300 percent. These tests, then, clearly show the dramatic effect that forced mixers have on the mixing process.

Recent efforts by Werle et al. (1987) have been particularly concerned with the flow behavior mechanism downstream of the mixer. One aspect of this study involved injecting dye into the boundary layer on the upper and lower surface of the mixer lobe in a water tunnel. Mixing of the dyes was observed for both a laminar and a turbulent approaching boundary layer on the mixer. The flow appeared to be dominated by the presence of large-scale axial vorticity in the mixing region. Downstream of the splitter three regions of mixing were defined. The first region was characterized by large-scale circulation due to the secondary flow inviscidly generated by the lobes. In the second region, the secondary flow generated fully developed vortex cells that appeared to intensify as they were transported downstream. In the third region, the vortices started to break down and disappear. They observed that the most intense mixing seemed to occur in region three. While this development process is primarily based on observations with a laminar approaching boundary layer, visualizations with a turbulent approaching boundary layer qualitatively agree with laminar boundary layer results. The implication here is that even though the axial vortices are possibly formed via an inviscid process, the turbulence generated as the vortices break down may be a very important contributor to the mixing process.

In summary, forced mixers mix streams together quite efficiently. However, only a few references in the literature report on the details of the physical structure in the mixing region downstream of a forced mixer. The information available strongly indicates that axial vortices are generated due to the inviscid effects created by the lobe shape. There is also an indication that turbulence is an important parameter, and that viscous effects must be included in analyses that predict forced mixer performance. However, there are no published results that contain detailed measurements in the mixing region to quantify the effects of flow turbulence on the mixing process. The objective of this study was to acquire detailed LDV measurements in the mixing region downstream of a forced mixer to quantify the formation process of the streamwise vortices and the flow properties of the vortices themselves.

Experimental Setup

Wind Tunnel. The wind tunnel constructed for this study is located in the fluid dynamics laboratory in the Mechanical and Industrial Engineering department at Clarkson University. Figure 2(*a*) is a schematic representation of the wind tunnel. Separate airflows were supplied to the test section by two

Nomenclature

C_f = local skin friction coefficient
h = lobe width = 1.9 cm
l = lobe peak-to-peak amplitude = 3.8 cm
Re_θ = Reynolds number based on momentum thickness
u = horizontal mean velocity, m/s
u' = horizontal rms velocity in the x direction, m/s
$\overline{\hat{u}'\hat{v}'}$ = Reynolds shear stress, m^2/s^2
v = vertical mean velocity, m/s
v' = vertical rms velocity in the y direction, m/s
w = axial mean velocity, m/s
x, y, z = Cartesian coordinate system, Fig. 2(*b*)
δ = boundary layer thickness
δ^* = boundary layer displacement thickness
θ = boundary layer momentum thickness

a) Wind Tunnel Schematic

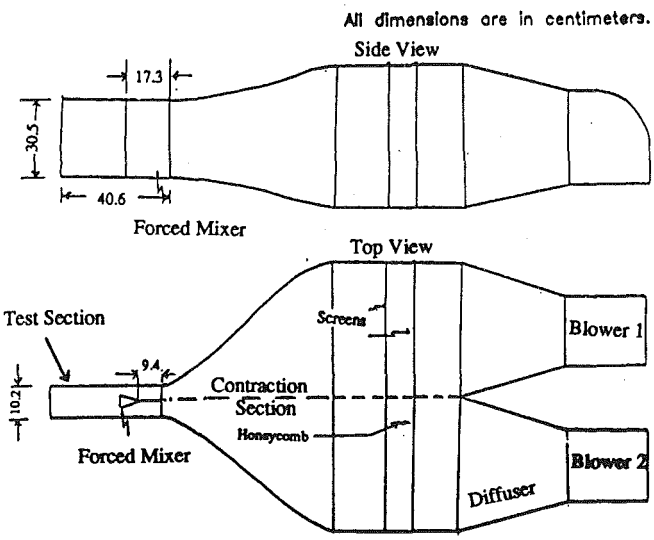

b) Mixer exit Geometry

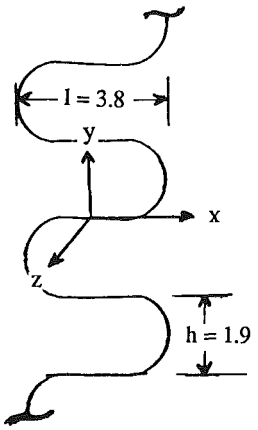

Fig. 2 Experimental setup

centrifugal blowers. Each blower was powered by a 3 hp motor and controlled with a variable speed controller. Each blower provided velocities up to 47 m/s to the corresponding side of the forced mixer in the test section. Each flow first entered a three-dimensional diffuser with a wall divergence angle of 6.6 deg. The diffusers, with an entrance of 34.9 cm by 23.2 cm and an exit of 48.3 cm by 48.3 cm, slowed the flow prior to the conditioning section in order to reduce the pressure drop through the conditioning section containing honeycomb sandwiched between fine mesh screens. After passing through the constant-area flow conditioning section, the flow entered a three-dimensional contraction section with a contraction ratio of 15. This large ratio provided a uniform core flow to the test section entrance. The test section was a rectangular box 10.16 cm wide by 30.48 cm high by 40.64 cm long. The test section, fabricated from 12.7-mm-thick plexiglass, held the forced mixer and provided a mixing region downstream of the mixer of 20.95 cm.

The forced mixer was made of 1.3-mm-thick fiberglass. The flat leading edge of the mixer was joined to the splitter plate in the contraction section as shown in Fig. 2(*a*). The flat plate was formed into 15 full lobes, 8 on one side and 7 on the other, and one half lobe on each end. The mixer was fixed to the test section by gluing a portion of each half lobe into a slot machined into each end of the test section. The lobe exit geometry is shown in Fig. 2(*b*). The lobes had parallel sides with a peak-to-peak amplitude of 3.8 cm and an equal wavelength. The lobe penetration was 37.5 percent with an included divergence angle of 27 deg. The coordinate system used to present the test measurements is shown in Fig. 2(*b*).

Instrumentation. The flow conditions at the inlet to the test section were documented with pitot-static probes. The output from the probes was translated into voltage readings via ±1.2 kPa pressure transducers. 100 samples acquired over a one-minute period were averaged for each data point.

Interior velocity measurements were acquired using a two-component laser-Doppler velocimetry (LDV) system. A water-cooled 4-W argon-ion laser was used with the system operated in the backscatter mode. The laser beam was transmitted into modular optics and split into three beams with different colors: green, blue, and cyan. The beams were transmitted to the test section through mirror units and either a 600 or 300 mm focal length lens. The 600 mm lens was used in the system when the beams were sent through the exit of the test section to measure the secondary velocities. The 300 mm lens was used to measure axial velocities with the beams entering through the side of the test section. The probe volume created at the intersection of the three beams was of an ellipsoid shape with a minor axis of 0.134 mm and a major axis of 3.362 mm and a minor axis of 0.067 mm and a major axis of 0.843 mm for the 600 and 300 mm lenses, respectively. The mirror and lens units were placed on an automated three-axis traversing system that was computer controlled for data acquisition. Bragg shifting was used to eliminate directional ambiguity. The Doppler signals were sensed by a photodetector whose output was processed by a counter-type processor.

Fine oil droplets created by a commercially available fogger were used to seed the wind tunnel flow. The size of the fog droplets was measured with a droplet-sizing interferometer. The majority of the droplets were less than one micron. The ability of the seed particles to follow the flow was checked by Awad (1989) by comparing the velocity profile of the core flow approaching a cylinder at midspan in the plane of symmetry measured with the LDV system to the prediction of the potential flow theory. Excellent agreement between the measured velocities and the potential flow distribution indicates that the seed particles followed the strong deceleration approaching the cylinder and, therefore, also tracked the smaller gradients generated by the forced mixer.

The accuracy of the probe measurement data was calculated using the uncertainty analysis of Kline and McClintock (1953), with the uncertainty intervals being calculated based on 20 to 1 odds. The probable errors in mean and fluctuating velocities were calculated at a 95 percent confidence level based on the uncertainty analysis method of Patrick (1985).

Results and Discussion

Inlet Conditions. The flow field at the test section entrance was documented with a pitot-static probe. Velocity profiles were acquired across the width and the height of the test section with and without the mixer mounted in the test section to check the uniformity of the flow entering the test section. Variations in the core flow velocity were less than 2 percent of the mean value. The boundary layers on the flat section of the forced mixer were characterized with pitot-static probe traverses acquired 7.2 cm downstream of the test section entrance. This location is slightly upstream of the start of the splitter convolution into lobes. The correlation developed by Burton (1964) was used to fill in the velocity profile near the wall where data could not be acquired due to the probe thickness. The boundary layer parameters for both profiles are shown in Table 1. δ, δ^*, θ, C_f, and Re_θ are the boundary layer thickness, displacement thickness, and momentum thickness, the local skin friction coefficient, and Reynolds number based on the momentum thickness, respectively. The parameters indicate that the two boundary layers were very similar. The values of Re_θ and the

Table 1 Boundary layer parameters on the forced mixer flat section (uncertainty in $\delta = \pm 0.13$ mm, $\delta^* = \pm 0.0025$ mm, $\theta = \pm 0.0028$ mm, $\delta^*/\theta = \pm 0.0299$, $Re_\theta = \pm 12$, and $C_f = \pm 0.0002$ at 20:1 odds)

	δ (mm)	δ^* (mm)	θ (mm)	δ^*/θ	Re_θ	C_f
BLOWER1	3.07	0.27	0.41	1.49	598	0.0049
BLOWER2	3.07	0.24	0.39	1.51	529	0.0051

shape factor, δ^*/θ, both indicate that the boundary layers approaching the lobes were turbulent (Kays and Crawford, 1980; White, 1974). The technique developed by Clauser (1953) was used to determine the local skin friction coefficient. These values are also typical of a two-dimensional turbulent boundary layer.

Core flow turbulence was documented on each side of the forced mixer at the same streamwise location using a hot-film probe. The turbulence intensity of the core flow was less than 1 percent on both sides of the mixer.

LDV Measurements at a Velocity Ratio of 1:1. Velocity components were measured for a matched approach velocity on each side of the mixer of 36 m/s. Data were acquired in the projected area corresponding to four lobes. Only secondary fluctuating and mean velocities are shown to demonstrate the vortex development. These data were gathered with the laser beams passed through the exit of the test section.

The horizontal and vertical mean velocities, u and v, are presented in the form of velocity vector arrows with the arrow base located at the measurement point. The vertical and horizontal velocities were combined to calculate the angle and magnitude of the vector. The outline of the forced mixer exit plane is included with the figures to aid in interpreting these results.

The velocity vector plot at $z/h = 2.6$ is shown in Fig. 3(a). Large vortices are not indicated by the vector plot, though significant secondary flow is indicated by the vectors. The seed for vortex formation is evident near the projected lobe horizontal lines. Oblong regions containing a vortical pattern can be discerned in the region that corresponds with the shear layer that formed in the wake of the forced mixer. The area between the oblong regions contains reasonably uniform secondary flow. A similar pattern was measured at $z/h = 1.3$.

Velocity components of $z/h = 5.3$ are presented in Fig. 3(b). The velocity vectors indicate the presence of four fully developed and nearly equally spaced vortices. The vortices are approximately centered about a vertical line at $x = 0$. Adjacent vortices are counterrotating and located near the lobe projected horizontal lines. The vortex size is on the order of the lobe width h. The vortices have a velocity profile like a forced vortex.

At $z/h = 7.9$, the velocity vectors indicate horizontally stretched but fully developed vortices compared to the previous location. The vortex centers were located slightly to the left of their location at $z/h = 5.3$. The vortices were approximately evenly spaced but displaced slightly downward from the projected lobe horizontal portion of the contour.

Velocity components at $z/h = 10.5$ (Fig. 3(c)) indicate that the vortices are not as strong, in the mean sense, when compared to the previous locations. Strong secondary velocities between the vortices are still indicated by the vector plot, however. The locations of the vortex centers are nearly the same as those at $z/h = 7.9$.

The velocity vectors indicate a mean flow pattern like the pattern described by Werle et al. (1987). Near the mixer, vortices were not present. Rather, only a strong secondary flow with the rudiments of vortices in the mixer wake shear layer is indicated by the mean velocity vectors at $z/h = 1.3$ and 2.6. The secondary flow developed into well-formed vortices between $z/h = 2.6$ and 5.3. These vortices remained intact

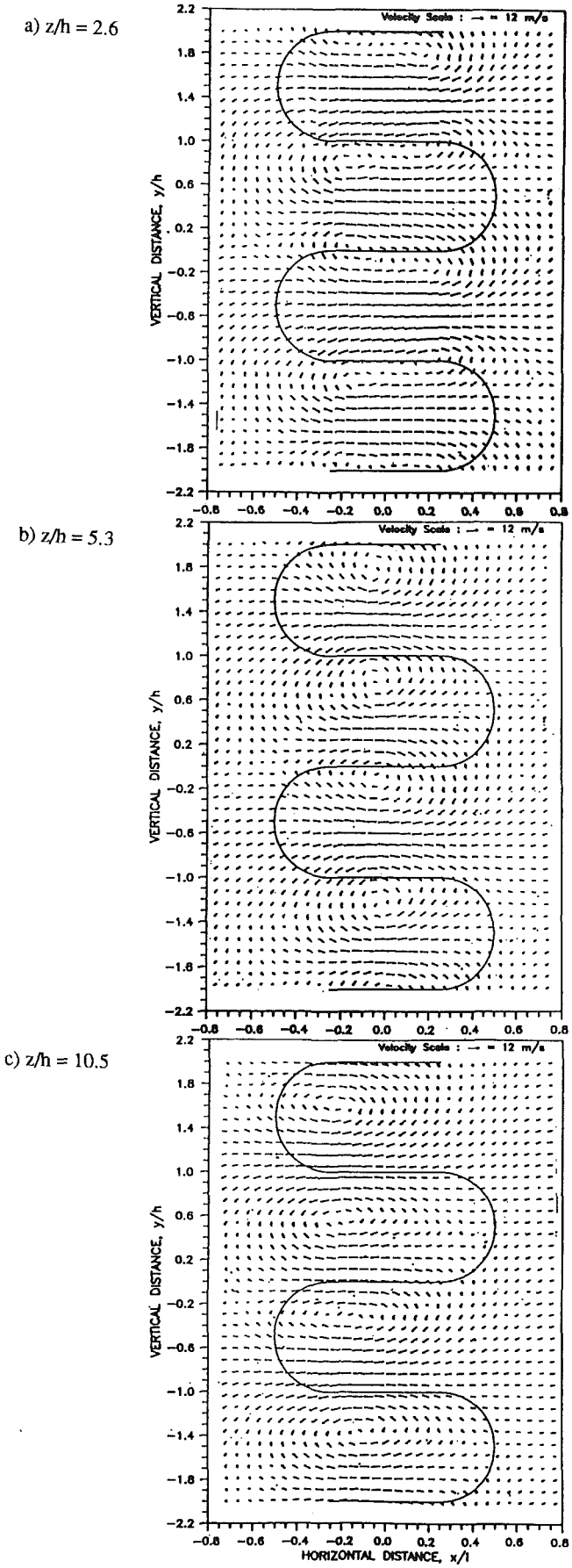

Fig. 3 Secondary mean velocity vectors for a velocity ratio of 1:1 (uncertainty in $x/l = \pm 0.003$, and $y/h = \pm 0.005$; maximum uncertainty in $u = \pm 0.170$ m/s, and $v = \pm 0.113$ m/s)

a) Horizontal RMS Velocities (m/s)

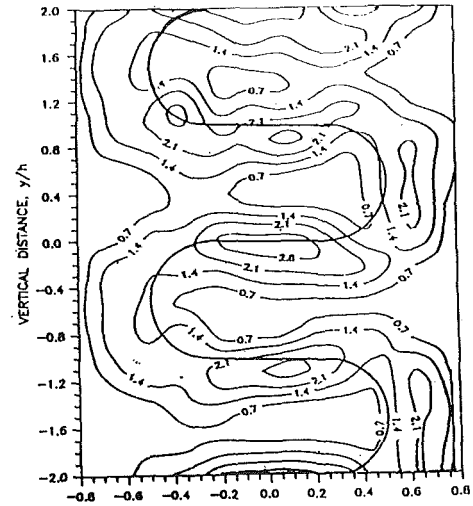

b) Reynolds Shear Stresses (m^2/s^2)

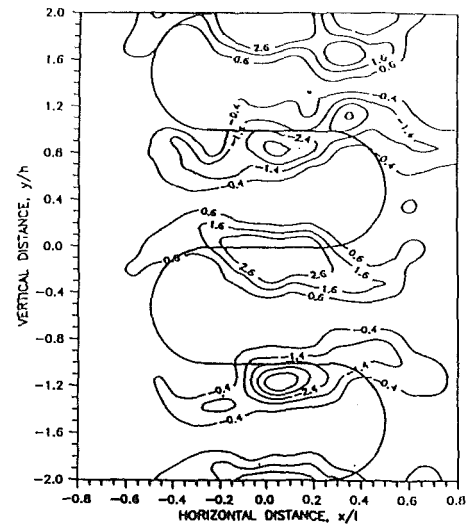

Fig. 4 Turbulence parameters at z/h = 2.6 for a velocity ratio of 1:1 (uncertainty in x/l = ±0.003, and y/h = ±0.005; maximum uncertainty in u' = ±0.140 m/s, in $\overline{u'v'}$ = ±0.204 m^2/s^2)

a) Horizonal RMS Velocities (m/s)

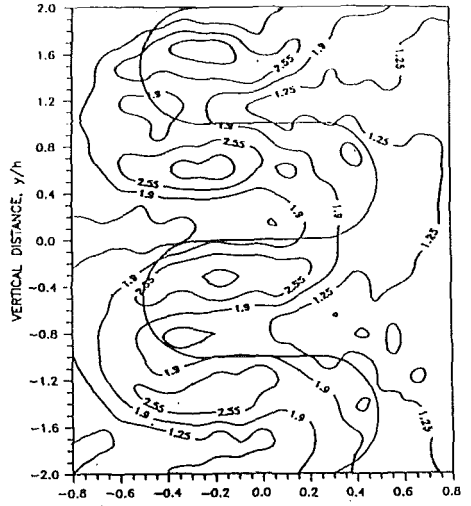

b) Reynolds Shear Stresses (m^2/s^2)

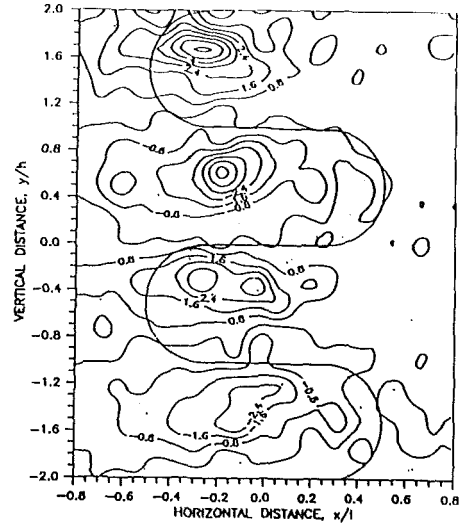

Fig. 5 Turbulence parameters at z/h = 10.5 for a velocity ratio of 1:1 (uncertainty in x/l = ±0.003, and y/h = ±0.005; maximum uncertainty in u' = ±0.126 m/s, in $\overline{u'v'}$ = ±0.178 m^2/s^2)

through the remaining test area, though the mean strength of the vortices was reduced at z/h = 10.5. The velocity vectors indicate that the locations of the vortices migrated as the vortices traveled downstream.

The root-mean-square (rms) velocities, u' and v', as well as the Reynolds shear stresses, $\overline{u'v'}$, were also measured downstream of the forced mixer at a velocity ratio of 1:1. Results are presented in the form of contour maps. Contours for v' are not shown because the trends displayed by these data are similar to the trends developed below with the u' data.

Figure 4(a) contains contours for the u' data acquired at z/h = 2.6. The contours indicate that the fluctuating velocities are low throughout the cross section. The highest values form closed contours in the locations corresponding to the oblong regions of vortical flow indicated by the velocity vector plot. Between the closed contours, large regions with low fluctuating velocity are shown. These regions correspond with the strong secondary velocities shown in the velocity vector plot. The remaining contours outline the forced mixer wake region.

The Reynolds shear stress contours for z/h = 2.6 are contained in Fig. 4(b). The sign convention is: Positive values of shear stress indicate clockwise vortical flow, and negative values indicate counterclockwise vortical flow. The stresses are highest in the horizontal shear layer regions between the streams. The stresses are low in the regions aligned with the lobe peaks and in the regions with large secondary flow.

As the flow moved downstream, the peak magnitudes of the rms velocities and shear stresses did not significantly increase, but the turbulence generated in the shear layer tended to diffuse through the flow that passed through the lobes. The rms velocities and shear stresses at z/h = 10.5 are shown in Fig. 5. The regions of low turbulence between the shear layers are no longer present. The regions of highest turbulence values correspond to the vortices identified in the velocity vector plots. The gradients in the shear stresses are quite strong in the vicinity of the vortices. The lines of constant u' take on the shape of the lobes. This characteristic indicates that little mixing occurred with the flow that did not pass through or near the lobes. The shear stress data also indicate that only small turbulent fluctuations were measured in the regions outside of the projection of the lobes.

In general, even though the peak turbulence levels did not increase significantly as the flow moved downstream, the average turbulence levels across the cross section started to increase as the vortices started to break down between z/h = 7.9 and 10.5. Figure 6 shows the streamwise variation of the area-averaged root-mean-square (rms) velocities and the area-averaged magnitude of the Reynolds shear stresses. The values

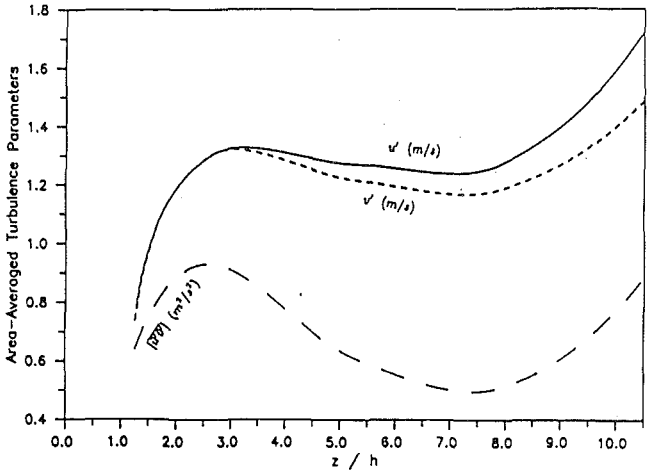

Fig. 6 Average rms velocity and Reynolds shear stress variation in the streamwise direction for a velocity ratio of 1:1 (maximum uncertainty in $z/h = \pm 0.005$, $u' = \pm 0.085$ m/s, $v' = \pm 0.070$ m/s, and $\overline{u'v'} = \pm 0.064$ m^2/s^2)

shown represent the average value over the area bounded by $-0.6 < x/l < 0.6$ and $0.0 < y/h < 2.0$. The average was calculated, then, in the projected region downstream of the top two lobes. The area-averaged rms velocities increase sharply between the lobe exit and $z/h = 2.6$, but level off between $2.6 < z/h < 7.9$. The initial rise is due to the mixer shear layer spreading. The leveling off is associated with the organized secondary flow structure set up as the vortices developed in this region. Downstream of $z/h = 7.9$, the averaged rms velocity increases rapidly again. This increase is associated with a breakdown of the vortices in the mean sense, as shown by the velocity vector plots. In effect, the energy associated with mean circulation of the vortices cascaded into turbulent kinetic energy. The combined effect of these small-scale turbulent fluctuations superimposed on the mean secondary motion still present in the mixing region is believed to enhance mixing significantly. This conclusion is consistent with the observations of Werle et al. (1987) that significant mixing occurs as the mean strength of the vortices breaks down in the third mixing region.

The averaged Reynolds stress also increased between the lobe exit and $z/h = 2.6$. After the vortices formed, the averaged Reynolds stress decreased in this organized flow region between $z/h = 2.6$ and 7.9. As the vortices' mean strength decreased downstream of $z/h = 7.9$, the averaged Reynolds stress increased in this region characterized by turbulent mixing. Though not shown, the streamwise rms velocities were nearly constant in the measured region.

In summary, the forced mixer generated large-scale secondary flows that led to the formation of streamwise vortices with a diameter on the order of the lobe width. The vortices were not fully formed until between approximately three and five lobe widths downstream of the exit plane. The vortices formed around lobe wake shear layer. This phenomenon indicates that although the secondary flows were inviscidly generated by the lobes, the viscous forces in the shear layer affect the vortex formation process. Between approximately five and eight lobe widths, the counterrotating vortices created an organized secondary flow pattern with low turbulence levels between the vortices. The vortices were of the forced vortex type with the highest turbulence levels measured in the vicinity of the vortices. Beyond approximately eight lobe widths downstream of the mixer, the vortices appear to have started breaking down, in the mean sense. The measured rms and shear stress levels started to increase dramatically as the mean strength of the vortices decreased. These larger turbulence levels superimposed on the mean circulation still present in the secondary flow are

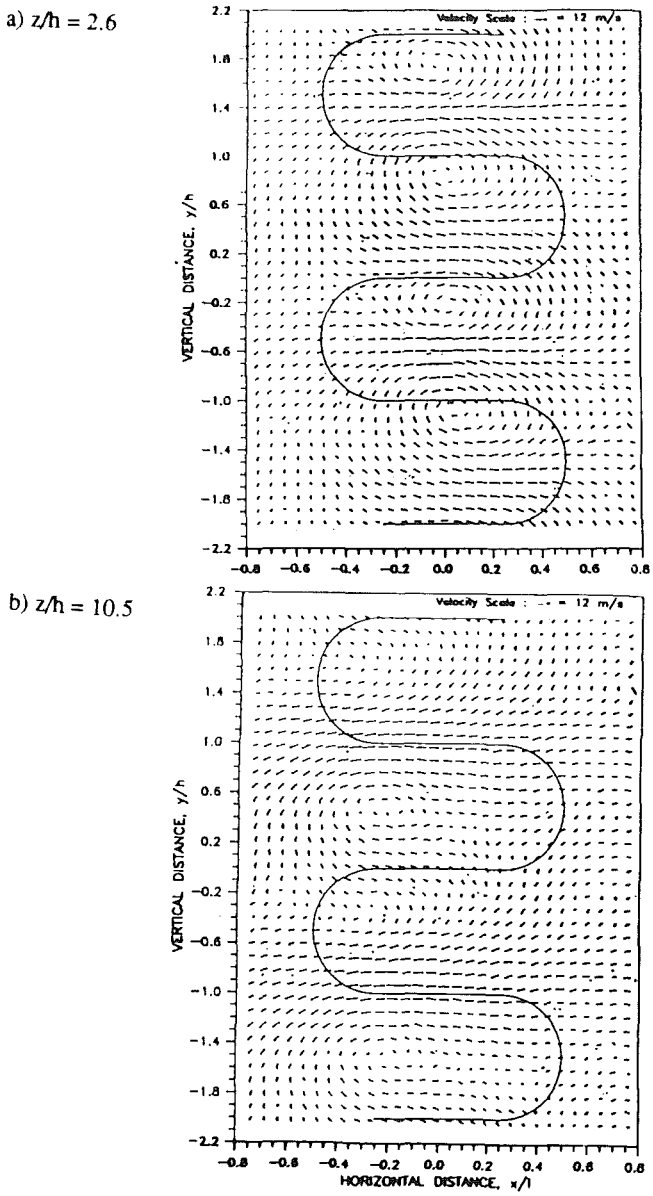

Fig. 7 Secondary mean velocity vectors for a velocity ratio of 2:1 (uncertainty in $x/l = \pm 0.003$, and $y/h = \pm 0.005$; maximum uncertainty in $u = \pm 0.314$ m/s, and $v = \pm 0.221$ m/s)

expected to enhance mixing significantly between the two streams. The flow outside of the projected lobe exit outline was not involved in the secondary flow to an appreciable extent. Only negligible secondary velocities were measured beyond approximately one half of a lobe width on either side of the outline. This result documents the importance of having high lobe penetration to mix the streams passing around the mixer uniformly.

LDV Measurements at a Velocity Ratio of 2:1. The vertical, horizontal, and axial velocities were measured at $z/h = 2.6$, 7.9, and 10.5 for a velocity ratio of 2:1. The approach velocities created by blower 1 and blower 2 were 46 m/s and 23 m/s, respectively. Data were acquired downstream of the same four lobes where data at a velocity ratio of 1:1 were obtained.

Figure 7(*a*) shows the velocity vectors measured at $z/h = 2.6$. In contrast to the matched velocity tests, the velocity vectors indicate that four fully developed vortices were formed in this plane. Fully formed vortices were measured in the matched velocity tests downstream of this plane. The centers

of these vortices were located along a vertical line at $x = 0$ and near the projected lobe horizontal lines. The diameter of the vortices in this plane is approximately one lobe width. However, the vortices were not of equal strength. The second and fourth vortices, from the top of the figure, were stronger than the first and third vortices. The mean secondary velocities on the left side of the first and third vortices were lower. The vectors indicate that the flow on the bottom portion of these vortices tended to be entrained by the higher velocity flow on the left side (from blower 1) instead of following the vortical path of the vortex. Even though the approaching axial velocity ratio across the mixer was two, the secondary flow strength was nearly the same downstream of both the high-speed and the low-speed lobes.

The breakdown of the vortices is quite apparent in the results measured at $z/h = 7.9$. The first and third vortices are much less defined in this plane. The second and fourth vortices also started to weaken near this plane. The secondary velocities measured at $z/h = 10.6$ are shown Fig. 7(b). The first and third vortices are barely discernible, and the second and fourth vortices were also weaker.

These vector plots indicate that the vortex development occurred closer on the trailing edge of the mixer with the velocity mismatch. The vortices became fully formed upstream of $z/h = 2.6$, and the mean circulation associated with two of the vortices was nearly completely dissipated 10 lobe widths downstream of the mixer. These plots also indicate that the demarcations of the mixing regions discussed previously are not as clear as with matched velocities since the vortices started to dissipate at different streamwise locations.

The rms velocities associated with this vortex development for a velocity mismatch are more difficult to interpret than with matched velocities. In the matched velocity case, higher rms velocities characterized the vortices and the remaining contour lines had a pattern similar to the exit plane of the lobes. Vortex locations could be identified from the closed contours in the rms contour maps. Much larger rms velocities were measured with mismatched velocities, and the rms velocities associated with the vortices do not stand out in the contour maps. The flow asymmetry is emphasized by matching groups of closed contours near the lobe tips and troughs. Closed contours do not correspond to the vortex locations. Evidently, the rms velocities generated in the shear layers between the streams and transported by the secondary flow mask the rms velocities generated by the vortices. The average magnitude of the rms values is approximately three times larger than the value for the matched velocity case. With the exception of low values near the lobe peaks, the variation of rms velocity inside the lobe projection is approximately the same level as measured at matched velocities.

The shear stress variation was strongly affected by the vortices. Closed contours are quite evident at the vortex positions. The strongest stresses were created by the first and third vortices, whose mean circulation was decaying faster as indicated by the velocity data. This trend is consistent with the matched velocity data that showed significant increases in flow turbulence as the mean circulation of the vortices decreased.

The axial rms velocities measured at $z/h = 10.5$ (Fig. 8(a)) displayed less variation in the mixing region than at upstream locations. Evidently, the flow was more uniformly mixed resulting in more uniform rms velocities. The shear stress variation, however, was still markedly influenced by the vortices as shown in Fig. 8(b). The largest shear stresses were again measured in the regions associated with the first and third vortices. The shear stresses generated by the second and fourth vortices were larger than those in previous planes. This increase is expected since the mean circulation of these vortices dissipated between the measurement locations.

The variation of the averaged secondary rms velocities and shear stresses, averaged over the same two lobe-region as for

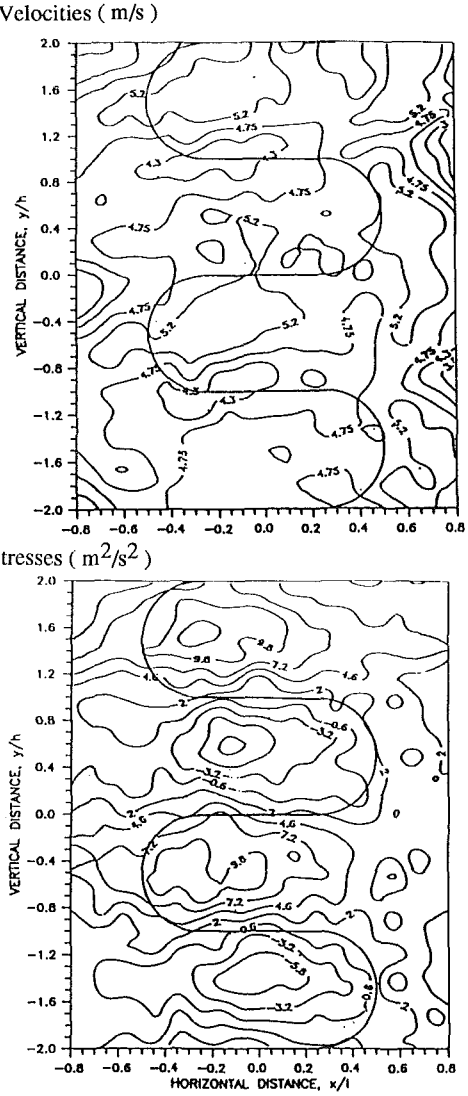

Fig. 8 Turbulence parameters at $z/h = 10.5$ for a velocity ratio of 2:1 (uncertainty in $x/l = \pm 0.003$, and $y/h = \pm 0.005$; maximum uncertainty in $u' = \pm 0.262$ m/s, in $\overline{u'v'} = \pm 0.562$ m²/s²)

the matched velocity tests, is shown in Fig. 9. In contrast to the matched velocity case, these turbulence parameters increased throughout the mixing region. This is again consistent with the observed trend that these parameters increase as the mean strength of the vortices dissipates. Since these terms contribute to the turbulent kinetic energy of the flow, the turbulent kinetic energy, which significantly impacts mixing rates, also increased throughout the mixing region. The average values of the turbulence parameters are approximately three times the values measured at corresponding planes with the velocity of the two streams matched. The mixing rates for the velocity ratio of two tests, then, are expected to be significantly larger than for the matched velocity tests. Since the mean velocity data show that vortex breakdown occurred closer to the mixer for the tests with a velocity mismatch, this result is consistent with the conclusion of Werle et al. (1987) that extensive mixing occurs when the vortices break down.

Throughout the discussion of test results, the trend of turbulence production, because of its impact on mixing, has been indicated. Evidence of the importance of turbulent mixing to achieve a homogeneous mixture of the two flows around the forced mixer is contained in the axial velocity measurements. Figure 10 contains axial velocity distributions for the top two lobes in the measurement region for $z/h = 2.6$, 7.9, and 10.5.

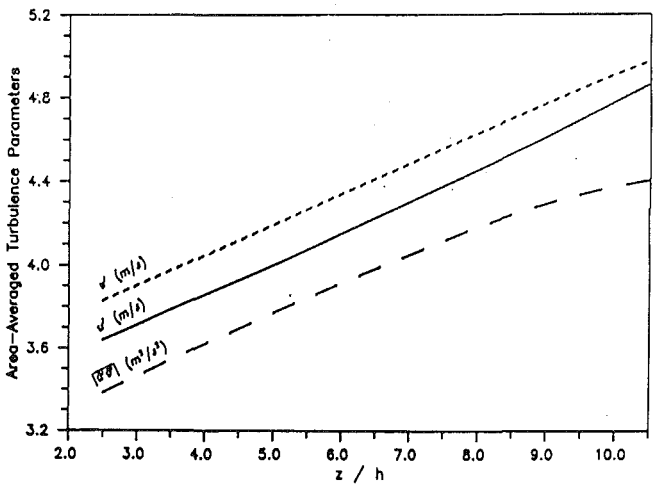

Fig. 9 Average rms velocity and Reynolds shear stress variation in the streamwise direction for a velocity ratio of 2:1 (maximum uncertainty in $z/h = \pm 0.005$, $u' = \pm 0.235$ m/s, $v' = \pm 0.245$ m/s, and $\overline{u'v'} = \pm 0.440$ m^2/s^2)

At $z/h = 2.6$, fully formed vortices were measured. The data in Fig. 10(a) show that little mixing between the streams occurred upstream of this plane. Sharp velocity gradients existed between the two streams in this plane. The localized effect of the vortices can be seen in this plot rotation as the narrowing of the "core" portion of the high velocity lobe (the second lobe) in the vicinity of the vortex location (Fig. 7).

The measurements at 7.9 lobe widths downstream of the mixer show that although significantly more mixing of the flows occurred between the measurement locations, sharp velocity gradients in the vertical direction still existed in this plane. The ability of the secondary flow to transport flow is dramatically illustrated in Fig. 10(b). The axial velocity in the region downstream of the first lobe is higher than the axial velocity in the second lobe in this plane. Based on calculations with the measured axial and secondary mean velocities, the flow rotated 1.5 times between the measurement planes at $z/h = 2.6$ and 7.9. The implication here is that the mean circulation associated with the vortices circulates the flow so that the two streams intertwine, but this motion does not provide for rapid homogeneous mixing of the streams. Rapid mixing occurs due to the superposition of turbulent mixing, generated as the vortices break up, on the mean rotation of the secondary flow.

The axial distribution at $z/h = 10.5$ indicates the two streams were more mixed in this plane. Note that the axial distance between the planes shown in Figs. 10(b) and 10(c) is one half the distance between the planes shown in Figs. 10(a) and 10(b). The higher rates of mixing can be attributed to the higher turbulence levels. The dips in the distribution are in the locations where the vortices were formed and the shear stress concentrations were measured.

This axial velocity distribution indicates another important point. Even though the streams were mixing in the projected area downstream of the forced mixer, little mixing occurred in the flow outside of this region. This effect is indicated by the low velocities at $x/l = 0.8$ in Fig. 10(c). This result again indicates that high lobe penetration is required to mix the two streams approaching a mixer homogeneously.

Summary and Conclusions

Separate airflows were supplied by two centrifugal blowers to a forced mixer mounted vertically in the test section. Interior mean velocity measurements as well as the turbulence parameters were nonintrusively acquired downstream of the forced mixer using a two-component laser-Doppler velocimetry (LDV) system for two velocity ratios.

a) z/h = 2.6

b) z/h = 7.9

c) z/h = 10.5

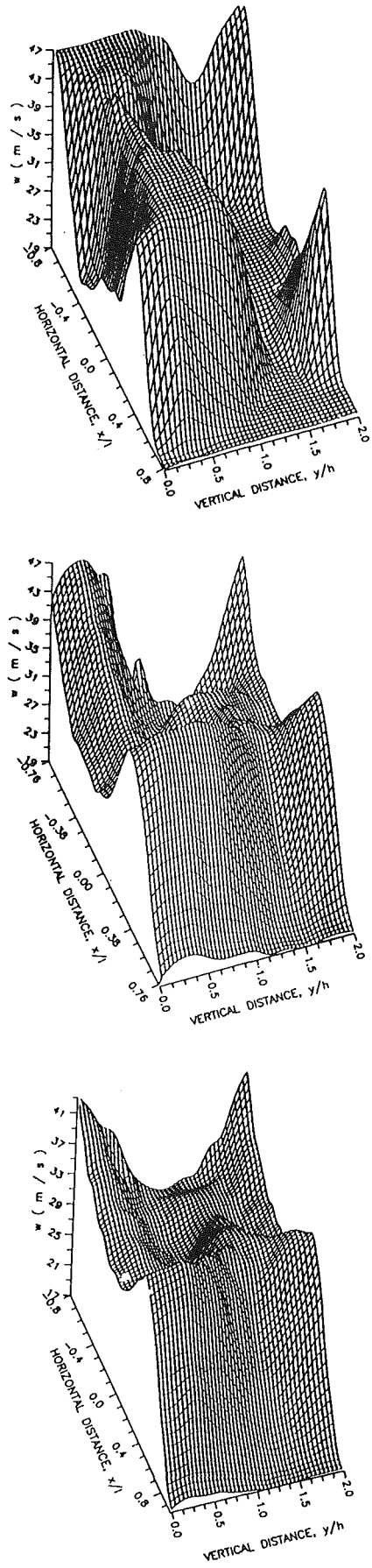

Fig. 10 Axial velocity distributions for a velocity ratio of 2:1 (uncertainty in $x/l = \pm 0.003$, $y/h = \pm 0.005$; maximum uncertainty in $w = \pm 0.615$ m/s)

This study indicated three regions of vortex development in the mixing region downstream of the forced mixer. In the first stage, secondary motion was generated in the flow passing through the lobes. The second stage involved formation of counterrotating vortices by the secondary flow around the shear layer region formed in the wake of the lobes. These vortices, whose size was on the order of the width of one lobe convolute, effectively circulated the flow in the vicinity of the vortices. The third stage had the largest impact on mixing. During this stage, the vortices broke down, resulting in a significant increase in turbulent mixing. The turbulent mixing superimposed on the circulation induced by the vortices was an essential part of mixing the two streams together.

The mixing regions identified above were located closer to the mixer and the demarcation of the regions not as well defined for a velocity ratio of two. With the approaching velocities matched, fully formed vortices were not measured in the plane 2.6 lobe widths downstream of the mixer. Fully formed vortices were measured in this plane with a velocity ratio of two. In addition, the vortices created by the secondary flow for the velocity ratio of two case were not of equal strength. The counterclockwise rotating vortices were stronger than those rotating in the clockwise direction. This asymmetry in vortex strength was due to the approaching flow asymmetry. The result of the asymmetry in vortex strength was that the weaker vortices broke down closer to the mixer, and increases in flow turbulence were measured throughout the mixing region.

The location of vortex formation depends on the velocity ratio across the mixer. The mechanism for this parameter to affect the vortex formation is its effect on the lobe wake shear layer that the vortices form around. This result indicates that flow properties that alter the shear layer, such as the velocity ratio of the two streams, are important in the vortex formation process.

The results of these tests also indicate that turbulent mixing is important to achieve a homogeneously mixed flow. The large-scale secondary motion created by the lobe contour leads to formation of the vortices and transportation of fluid from stream to stream but does not homogeneously mix two streams together. Smaller scale turbulence, superimposed on this mean motion, is required to mix two flows together homogeneously.

A general conclusion of this work is that the viscous effects are important in the mixing process downstream of lobed forced mixers, and that viscous effects must be included in analyses that predict forced mixer performance.

Acknowledgments

The authors gratefully acknowledge program manager R. S. Tuthill of Pratt and Whitney Aircraft Company, Commercial Business, for supporting this work.

References

Awad, J., 1989, "Cooling of Endwall Region Upstream of a Cylinder," Ph.D. Thesis, Clarkson University, Potsdam, NY.

Burton, R. A., 1964, "A Simple Universal Velocity Profile Equation," *AIAA Journal*, Vol. 3, No. 4.

Clauser, F. H., 1953, "Turbulent Boundary Layer in Adverse Pressure Gradients," *Journal of the Aeronautical Sciences*, Vol. 21, pp. 91-108.

Head, V. L., Povinelli, L. A., and Getstenmaier, W. H., 1984, "Hot-Flow Test of a Series of 10-Percent-Scale Turbofan Forced Mixing Nozzles," NASA TP-2268.

Kays, M. W., and Crawford, E. M., 1980, *Convective Heat and Mass Transfer*, McGraw-Hill, New York, pp. 161-163.

Kline, S. J., and McClintock, F. A., 1953, "Describing Uncertainties in Single-Sample Experiments," *Mechanical Engineering*, p. 3.

Kozlowski, H., and Kraft, G., 1980, "Experimental Evaluation of Exhaust Mixers for an Energy Efficient Engine," AIAA Paper No. 80-1088.

Paterson, R. W., 1982a, "Turbofan Forced Mixer-Nozzle Internal Flowfield, Part I—A Benchmark Experimental Study," NASA CR-3492.

Paterson, R. W., 1982b, "Turbofan Mixer Nozzle Flowfield—A Benchmark Experimental Study," ASME JOURNAL OF ENGINEERING FOR GAS TURBINES AND POWER, Vol. 106, pp. 692-698.

Patrick, W. P., 1985, "Error Analysis for Benchmark Fluid Dynamic Experiments, Part I: Error Analysis Methodology and the Quantification of Laser Velocimetry Error Sources," United Technologies Research Center Report R85-151772.

Presz, W., Gousy, R., and Morin, B., 1986, "Forced Mixer Lobes in Ejector Designs," AIAA Paper No. 86-1614.

Presz, W., Blinn, R. F., and Morin, B., 1987, "Short Efficient Ejector Systems," AIAA Paper No. 87-1837.

Skebe, S. A., Paterson, R. W., and Barber, T. J., 1988, "Experimental Investigation of Three-Dimensional Forced Mixer Lobe Flow Fields," United Technologies Research Center Report 88-3785-CP.

Werle, M. J., Presz, W., and Paterson, R. W., 1987, "Flow Structure in a Periodic Axial Vortex Array," AIAA Paper No. 87-0610.

White, F. M., 1974, *Fluid Mechanics*, McGraw-Hill, New York, pp. 400-403.

The Effect of Swirl on the Velocity and Turbulence Fields of a Liquid Spray

A. Breña de la Rosa

G. Wang

W. D. Bachalo

Aerometrics, Inc.,
Sunnyvale, CA 94086

The work reports an experimental study of the effect of swirl on the structure of a liquid spray, i.e., on the behavior of drops and their interaction with the gaseous phase, and on the velocity and turbulence fields of the spray in the swirling flow. Three vane-type swirlers having low, medium, and high swirl numbers were used in the tests. The swirlers were placed on the liquid supply tube of a pressure atomizer and tested in the wind tunnel under specified conditions. Properties of the dispersed phase such as velocity and size distributions, particle number density, and volume flux were measured at several locations within the swirling flow field. In addition, mean velocity and turbulence properties were obtained for the gas phase. The results show that flow reversal of the drops is present at the high swirl number within the recirculation region. The spatial distribution of drops reveals a widening of the spray with increasing swirl strength while the concentration of large drops is shown to increase near the core of the swirling field with increasing swirl number. Plots of the turbulence kinetic energy, normal Reynolds stresses, and Reynolds shear stresses show double-peak radial distributions, which indicate regions in the flow where high energy content, mean velocity gradients, and large shear forces are present. The decay of turbulence velocities in the axial direction was observed to be very fast, an indication of high diffusion and dissipation rates of the kinetic energy of turbulence. The significance of the turbulence measurements is that these double-peak profiles indicate a deviation of the swirling spray from isotropy. This information should be relevant to researchers modeling these complex flows.

Introduction

The important effects of swirl in reacting and nonreacting flows have been known for some time. In combustion systems swirl generation is, undoubtedly, the most extensively used mechanism for stabilizing the flame and for controlling the efficiency and generation of pollutants (Gupta et al., 1984). While swirl burners have been used widely in combustion, a major effort has been put recently to elucidate the basic mechanisms that govern swirl flows (Sislian and Cusworth, 1986; Cameron et al., 1989). In the application of swirl combustion devices to utility and industrial gas turbine systems, special emphasis has been placed in understanding the mechanism of formation and emission of pollutants such as CO, unburned hydrocarbons (UHC), NO_x, and soot; especially when it is recognized that measures customarily taken to reduce, for example, CO, UHC, and soot tended to increase the emission of NO_x.

An important aspect in the design of combustion systems is the ability to predict and control their performance and efficiency. Both innovative diagnostic techniques and analytical/numerical studies are needed in the study of practical swirl combustion systems to control the emission of pollutants and increase their efficiency.

One of the major obstacles in the study of swirl flows has been the difficulty in obtaining turbulence data, mainly because of the limited instrumentation available for the analysis of these highly complex flows. Most of the research done with swirl flows has dealt with gaseous fuels under both isothermal and reactive conditions. Because of the inherent complexity of having a liquid phase in the form of small drops coupled to the gaseous phase, liquid swirling flows have been studied less comprehensively.

The present work is a first attempt to study the effect of swirl on the structure and on the velocity and turbulence fields of a liquid spray. For this purpose, the dynamic properties of the air and the spray have been measured for three vane swirlers producing low, medium, and high swirl numbers. The investigation shall focus on the influence that swirl has on the velocity and turbulence fields of the gaseous phase, and on its overall effect on the properties of the liquid spray, i.e., on the spatial distribution of the drops over its size and velocity, on the number density and on the liquid volume flux. Preliminary work by Breña de la Rosa et al. (1989) focused on the differences between a spray in coflowing air and that in a low swirling field. The present investigation is a continuation of that work

Contributed by the International Gas Turbine Institute and presented at the 35th International Gas Turbine Aeroengine Congress and Exposition, Brussels, Belgium, June 11–14, 1990. Manuscript received by the International Gas Turbine Institute December 23, 1989. Paper No. 90-GT-32.

and constitutes the first phase of an effort to investigate the effect of swirl on the structure of liquid spray flames, the stability of the flame, and its effect on the emission of pollutants such as NO_x, and CO.

Experimental Setup

The experiments were carried out in a 46×46 cm^2 wind tunnel using a vane-type swirler fitted to the liquid supply tube (12.5 mm i.d.) of the atomizer. The nozzle used was a Hago 45 deg. solid cone, pressure swirl atomizer of 3.0 gph (11.36 lph) nominal flow rate, which atomized water at a pressure of $P_a = 415$ kPa. Liquid flow rate to the nozzle was kept constant for the sprays atomizing in the swirling field of the three swirlers tested in this work. The swirler/atomizer assembly was positioned at a downstream distance where the flow conditioner and screens produced a homogeneous flow over the cross-sectional area of the wind tunnel. The wind tunnel free-stream velocity was set at $U_{fs} = 20$ m/s in all the experiments reported here.

The three swirlers tested were manufactured of stainless steel and consisted each of a hub of 19 mm i.d. and eight straight vanes welded equidistantly to it and forming angles of 20, 30, and 60 deg, respectively, with the longitudinal axis of the swirler. The design of the swirlers followed the general guidelines depicted by Beer and Chigier (1983). The set of vanes and hub were placed inside a tube of 76 mm i.d. and 250 mm in length and the whole assembly fitted to the atomizer supply tube; see Fig. 1. The length of the swirl vanes varied according to their angle of inclination, but they blocked all the cross-sectional area of the swirl housing, such that it was not possible to see through the swirl assembly. The 20, 30, and 60 deg vane swirlers gave nominal swirl numbers of $S = 0.26$, $S = 0.40$, and $S = 1.23$, respectively. The swirl number of an annular swirler, such as the one used in the present study, with constant vane angle α can be determined from an expression given by Beer and Chigier (1983),

$$S = \frac{G\psi}{G_x' R_s} = \frac{2}{3}\left\{\frac{1-(R_h/R_s)^3}{1-(R_h/R_s)^2}\right\} \tan \alpha \qquad (1)$$

where $G_x' = \pi\rho U_0^2 (R_s^2 - R_h^2)$ is the linear momentum, U_0 is the velocity at the outer edge of the swirler, R_h and R_s are the radii of the hub and of the swirl vane assembly, respectively.

The measurements were obtained with an Aerometrics two-component Phase Doppler Particle Analyzer (PDPA) whose principle of operation is given by Bachalo and Houser (1984). The system consists of a 3 W argon-ion laser, however, the power used in the present experiments was 50 mW. The PDPA was configured in the 30 deg off-axis forward scatter, where the scattering of light by refraction is the dominant mode and yields a linear relationship of particle size versus phase between the photodetectors over the detectable size range of the instrument. Particle sizing is done with the 0.5145 μm green beam, which also gives the first component of velocity, while the 0.488 μm blue beam provided the second orthogonal component of velocity. Frequency shifting was provided by a rotating grating, which for these experiments varied, approximately, from 1.0 to 2.6 MHz. The optical components selected to obtain the turbulence data were an $f = 300$ mm collimating lens and an $f = 200$ mm transmitter lens which gave an effective particle detection range of 0.5 to 40 μm in diameter. For the spray data an $f = 160$ mm collimating lens and an $f = 500$ mm transmitter lens yielded a particle detection range of 4.0 to 300 μm in diameter.

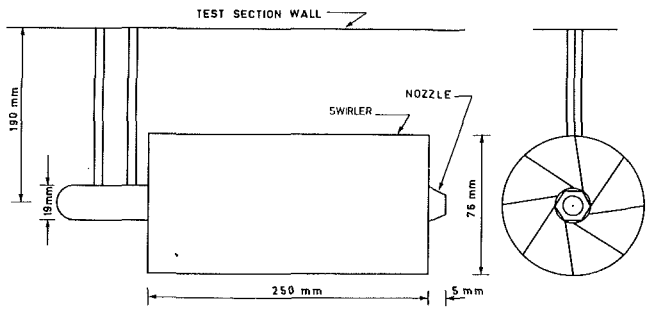

Fig. 1 Schematic of the swirl vane assembly fitted to the liquid supply tube of the atomizer inside the wind tunnel test section

The axial, radial, and tangential velocity components of the swirling field were evaluated for three different conditions, namely, with the airflow seeded with micron size particles only, with the seed particles and the liquid spray simultaneously in the flow, and with the spray alone in the swirling field. The seed particles were produced by a vaporizer, which yielded a size distribution having a linear mean of $D_{10} = 1.8$ μm and Sauter mean diameter $D_{32} = 3.9$ μm. Ten thousand particles were measured at each location to yield the velocity, size, and turbulence information for every experiment.

The experiments consisted of radial scans of the flow field, which were obtained at six different axial locations, namely, $X = 10$, 20, 50, 100, 150, and 200 mm downstream from the face of the atomizer to evaluate the velocity and turbulence fields. At these same positions (except at $X = 10$ mm where only velocity information was taken), measurements of drop size, drop velocity, size-velocity correlations, number density, and volume flux were obtained for a water spray in the swirling field. At each axial position the radial measurements were taken at 2-mm intervals from the centerline of the nozzle to the periphery of the flow field.

Results and Discussion

In order to investigate the symmetry of the velocity field produced by the three vane swirlers, a diametral scan of the mean and rms air velocities in the three orthogonal directions was obtained, in the absence of liquid injection, at an axial distance of $X = 10$ mm from the face of the atomizer and with the flow seeded with particles only. Symmetry of the spray alone with no swirl air was also performed to check the atomization of the nozzle and was found to be satisfactory.

Figure 2 gives the radial distribution of the mean axial $\bar{u}$

Nomenclature

D_s = internal diameter of swirl vane assembly
N_d = particle number density
Q_f = liquid volume flux
R = radial position
S = degree of swirl
u', v', w' = fluctuating axial, radial, and tangential components of velocity
$\overline{u'^2}, \overline{v'^2}, \overline{w'^2}$ = normal Reynolds streses
$\overline{u'v'}, \overline{u'w'}, \overline{v'w'}$ = shear stresses
$\bar{u}, \bar{v}, \bar{w}$ = mean axial, radial and tangential components of velocity
u, v, w = instantaneous axial, radial, and tangential components of velocity
X = axial distance from nozzle

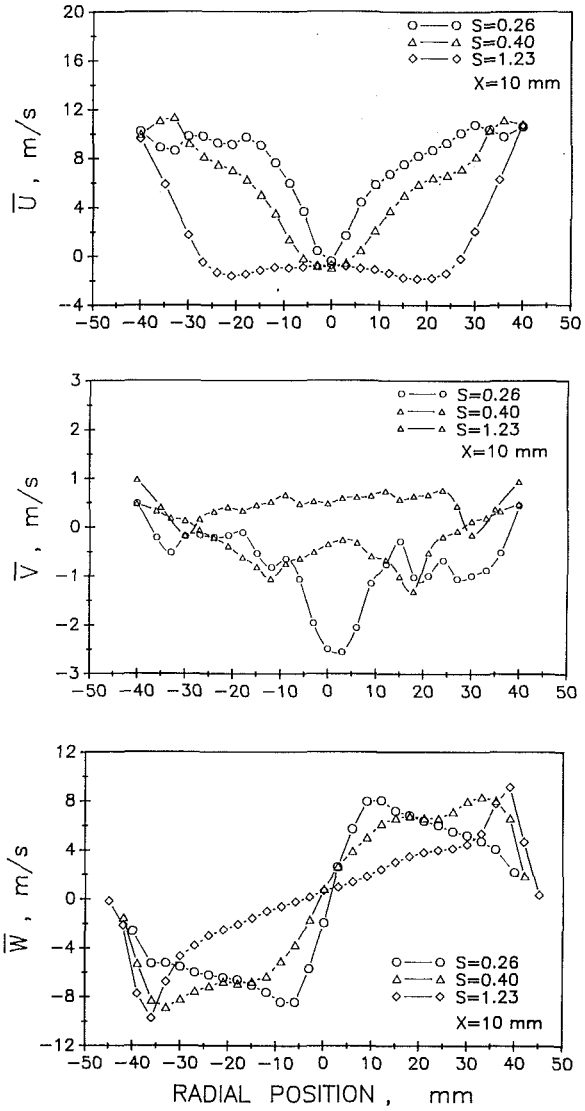

Fig. 2 Mean axial $\bar{u}$, radial $\bar{v}$, and tangential $\bar{w}$ velocities of the air as a function of radial position for the three swirlers at a distance of X = 10 mm from the nozzle

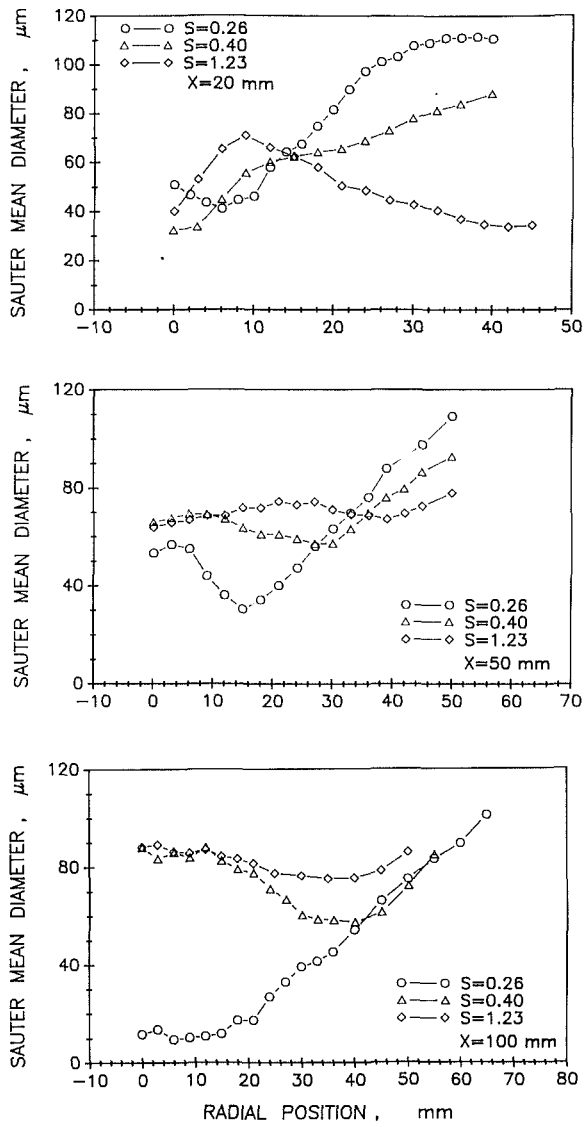

Fig. 3 Radial distribution of ($\bar{D}_{32}$) for the three swirlers at three axial locations from the nozzle

(top), radial $\bar{v}$ (center), and tangential $\bar{w}$ (bottom) velocities of the air, respectively, obtained for the three swirlers at X = 10 mm from the face of the atomizer. Good symmetry was obtained for the axial and tangential mean velocities; however, some asymmetry is evident in the radial velocity profiles. At the edge of the swirl vane assembly, i.e., at R = 40 mm, the velocity of the air for the three swirlers attained the same value. It is interesting to note in Fig. 2 that the gradients of the tangential velocity at low swirl numbers are larger than those for the stronger swirling field. The explanation for this may be that at low swirl, the circumferential velocity of the flow increases rapidly with increasing radial distance; however, at $S \geq 0.60$ a recirculation zone is set up and this impedes the acceleration of the air flow with increasing R. Notice also that the rapid acceleration of the air at low swirl is followed by a negative gradient of velocity, caused by the effect of the external air flow field, which yields tangential air velocities close to zero at the edge of the swirler.

Average Mean Diameters. The local drop size distribution within the swirling field was different for the three swirlers. For the low swirl condition S = 0.26, the radial distribution of particle sizes is not much different from that obtained from an atomizer spraying into quiescent air. However, as the swirling effect on the drops increases, a vigorous mixing is established and the radial distribution of the Sauter mean diameter (D_{32}) peaks within the swirling field and subsequently decreases toward the periphery of the spray. Figure 3 shows the radial distribution of (D_{32}) for the three swirlers at three axial locations. Other mean diameters such as the linear mean D_{10}, and the volume mean D_{30} were obtained; their radial distribution followed a similar pattern to that exhibited by the D_{32}.

Velocity Profiles. One of the parameters that is of utmost importance for combustion spray modeling is the velocity of the drops, since drag coefficients and angle of trajectory can be determined from that information. Because of the complex interaction between the dispersed phase and the gas phase, velocity and angle of trajectory are difficult to model. It is of interest, then, to show how the swirling field changes the velocity of the drops and its effect on discrete drop sizes.

The axial, radial, and tangential components of velocity for discrete drop diameters were measured with the PDPA. Figure 4 is a comparison between the mean axial air velocity and the mean axial velocity obtained for 10, 20, 30, and 50 μm drops at X = 20 mm for the three swirlers.

Focusing our attention on the velocity of the drops (the air-liquid interaction is discussed below), two different effects are

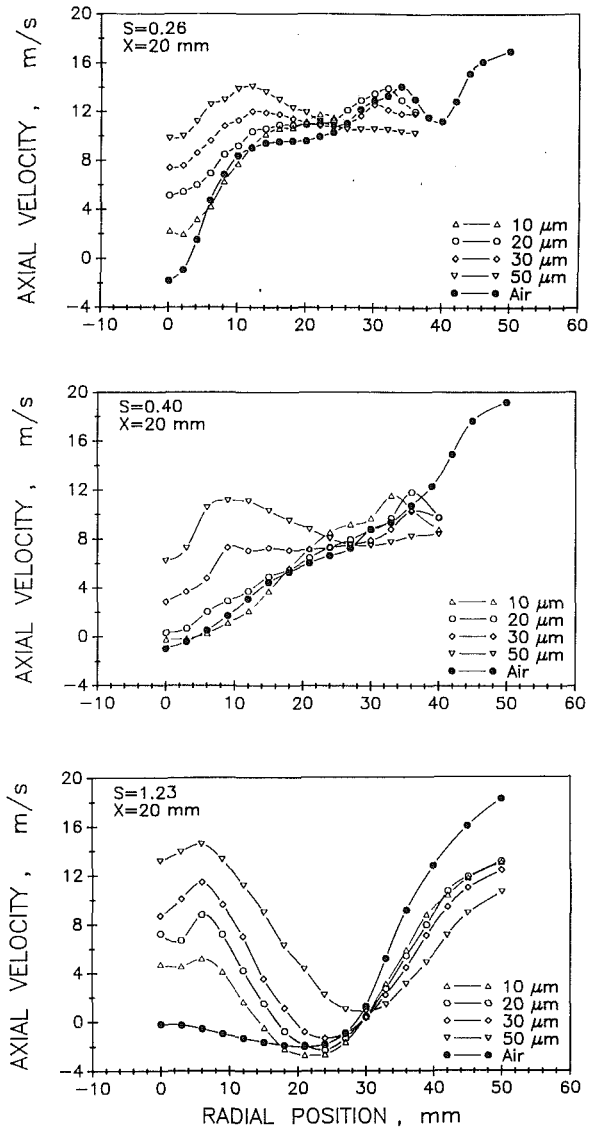

Fig. 4 Comparison of mean axial air velocity with the velocity of discrete drop diameters for the three swirlers at a distance of X = 20 mm from the nozzle

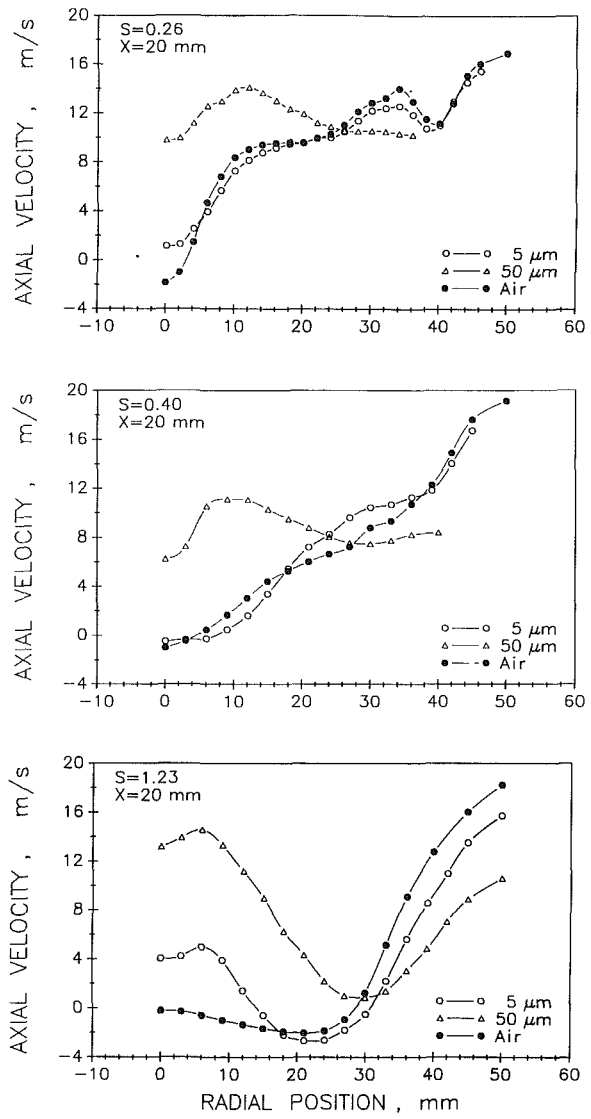

Fig. 5 Comparison of mean axial air velocity with the velocity of 5 μm and 50 μm drops for the three swirlers at a distance of X = 20 mm from the nozzle

appreciable, (top of Fig. 4). First, from the centerline to about $R = 24$ mm, the mean velocity of the drops increases with particle size, as one would expect, the predominant effect being the velocity of atomization. However, from this radial position to the periphery of the swirling field the effect of the external air flow is greater and it is the small drops that respond to the higher fluctuations in the flow and attain higher velocities. A similar behavior is observed for the 30 deg ($S = 0.40$) vane swirler. A critical swirl number is attained at S = 0.60: An adverse pressure gradient is set in the flow that cannot be overcome by the axial velocity and a recirculation zone in the form of a toroidal vortex is established in the core of the swirling field. The effect of this recirculation region is evident in Fig. 4 (bottom), where the drops exhibit a negative velocity in the core; however, outside of it the effect of the external air flow is felt by the drops, which increase their velocity toward the periphery of the swirling field.

Figure 5 is a plot similar to Fig. 4, but the profile of the velocity of 5 μm drops has been included. It was observed that, in general, drops as large as 5 μm in diameter responded well to the fluctuations of the air velocity about its mean velocity values. Larger differences in the velocity between the air and the 5 μm drops were observed for the 60 deg vane swirler close to the centerline, (bottom of Fig. 4).

Interaction of the Liquid Phase and the Gaseous Phase. The dynamic interaction of the liquid drops and the gaseous phase is intimately related with the performance of any combustion system. The knowledge of the spatial distribution of drop sizes, their number density, and their response to the air flow pattern in the combustion zone is important, since drop evaporization rates determine fuel concentration regions in the combustor that have an effect on the flame, sooting characteristics, and emission of products of combustion.

Figures 4, 5, and 6 show a comparison of the mean axial air velocity with the axial velocity of discrete drop sizes at $X = 20$ and $X = 50$ mm from the nozzle for the three swirlers, respectively. It is interesting to see in Fig. 4 the 10 μm drops having velocities that are similar to the air velocities, except at $S = 1.23$, where the reverse flow conditions in the core of the swirling field yield negative velocities from the centerline to about $R = 28$ mm. Notice also the steep velocity gradient experienced by the 10 μm drops from $R = 6$ mm to about $R = 28$ mm, which is the boundary of the recirculation region for the swirler $S = 1.23$.

Farther downstream at $X = 50$ mm and $X = 100$ mm (not

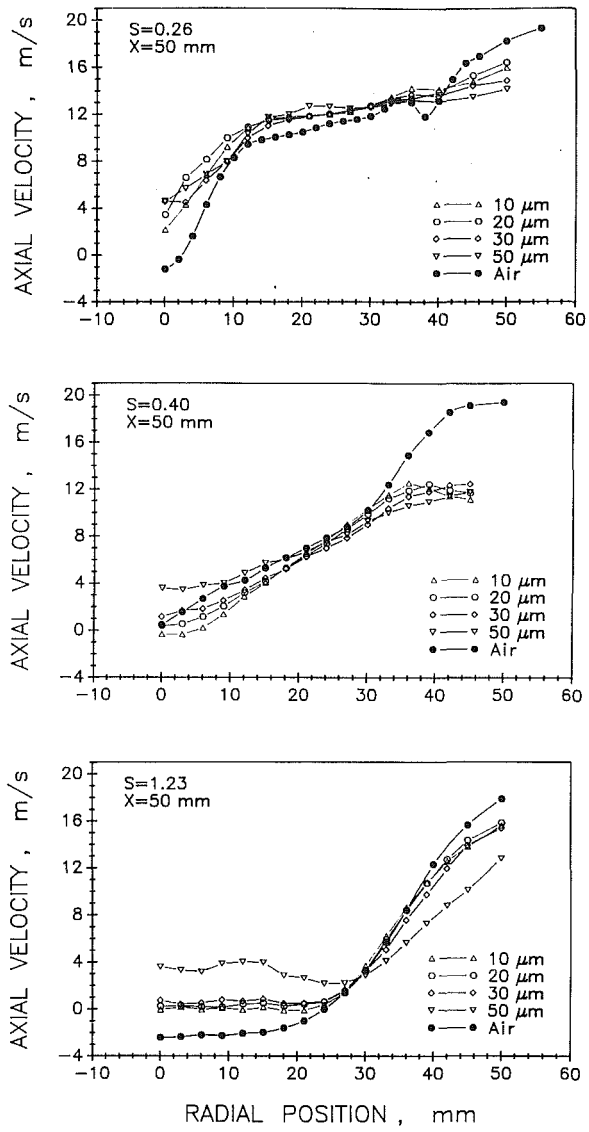

Fig. 6 Comparison of mean axial air velocity with the velocity of discrete drop diameters for the three swirlers at a distance of X = 50 mm from the nozzle

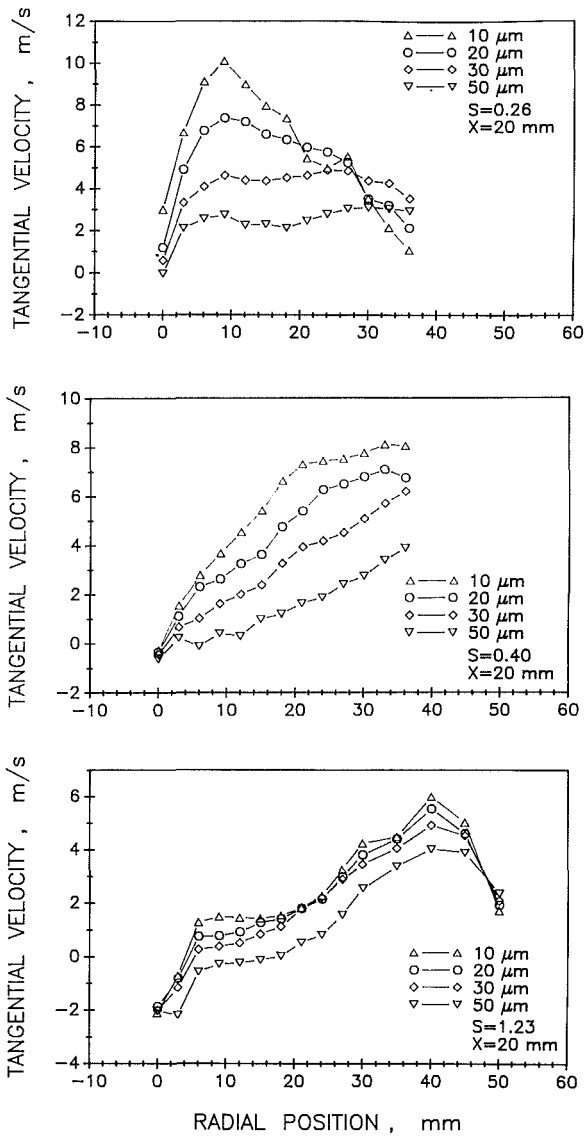

Fig. 7 Mean tangential velocity of discrete drop sizes as a function of radial position for the three swirlers at a distance of X = 20 mm from the nozzle

shown), the weaker effect of the swirl yields velocities of the smaller drops, which are similar to the air velocity. In Fig. 6 the strong effect of the swirl $S=1.23$ produces negative air velocities to about $R=24$ mm. The much larger momentum of the 50 μm drops is evident with velocities at the centerline, which are roughly four times larger than the velocities of other sizes. At large axial locations and $S=0.26$ the swirl is weak and only the small drops are found in the core. Those drops with larger momentum overcome the swirling field strength and are found only at larger radial distances.

At axial locations of $X=50$ mm (Fig. 6) away from the strong effect of the swirling flow, the velocity profiles of these discrete drop sizes are similar. Outside of the recirculation region and farther away from the nozzle, i.e., at $X=100$ mm (not shown) the same discrete drops sizes exhibit velocity profiles that are similar to each other, having low values at the centerline and higher ones at the periphery of the swirler.

The profiles of the mean radial velocity of the drops (not shown) indicate that, for all conditions of swirl, larger drops attain higher radial velocities within the swirling field, but due to the external air flow, this velocity decreases near the edge of the swirling spray.

The mean tangential velocity of the drops for discrete drop sizes is shown in Fig. 7 at an axial distance of $X=20$ mm for the three swirlers. The behavior of the radial profiles of the tangential velocity is very different for the three degrees of swirl. At $S=0.26$ the swirl effect is not strong enough to overcome the external air field and the tangential velocity, after a steep gradient near the core, either decreases or remains almost constant to the edge of the swirling field. At $S=0.40$ and $S=1.23$, the tangential velocity of the drops increases monotonically to the boundaries of the swirling field. Farther downstream, at $X=50$ mm and $X=100$ mm (not shown), the tangential velocity profiles of the three swirlers do not differ greatly among themselves and resemble those depicted in Fig. 7 for the 20 deg swirler, $S=0.26$.

The angle of trajectory of discrete drop sizes was also determined using the mean orthogonal velocities of the different size bins in the velocity histogram. These results will not be presented due to space limitations but clearly reflect the widening of the spray with increasing swirl number, with the larger drops attaining large angles and moving radially outward.

Turbulence intensity values were obtained for these discrete drop sizes and compared to those of air. The important conclusion from this calculation is that turbulence intensity for the 5 μm drops and for the air particles differs only slightly.

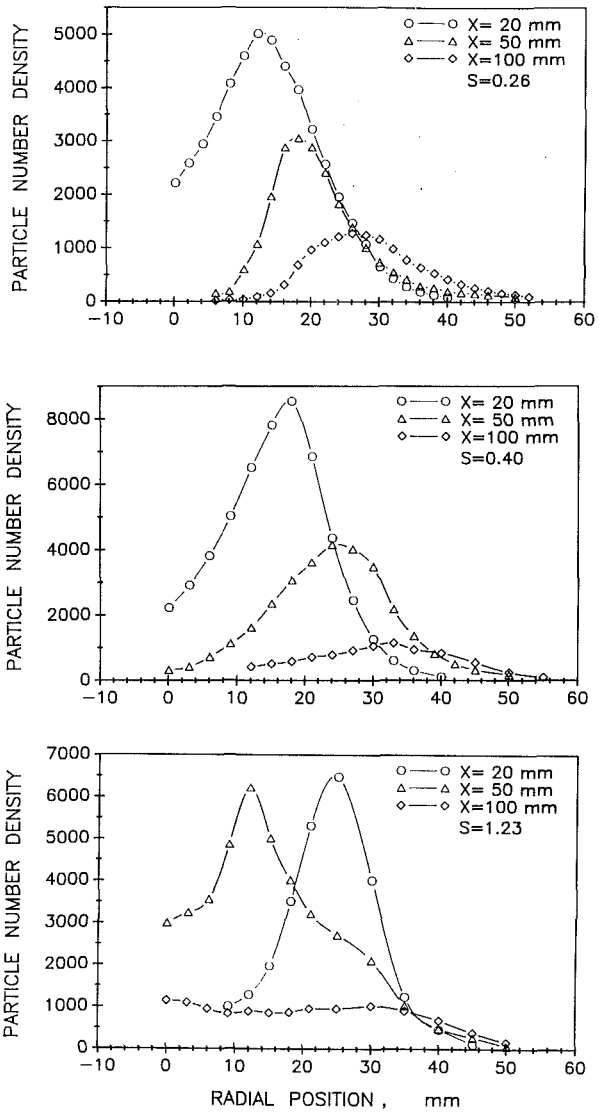

Fig. 8 Radial distribution of particle number density at three axial positions for the three conditions of swirl

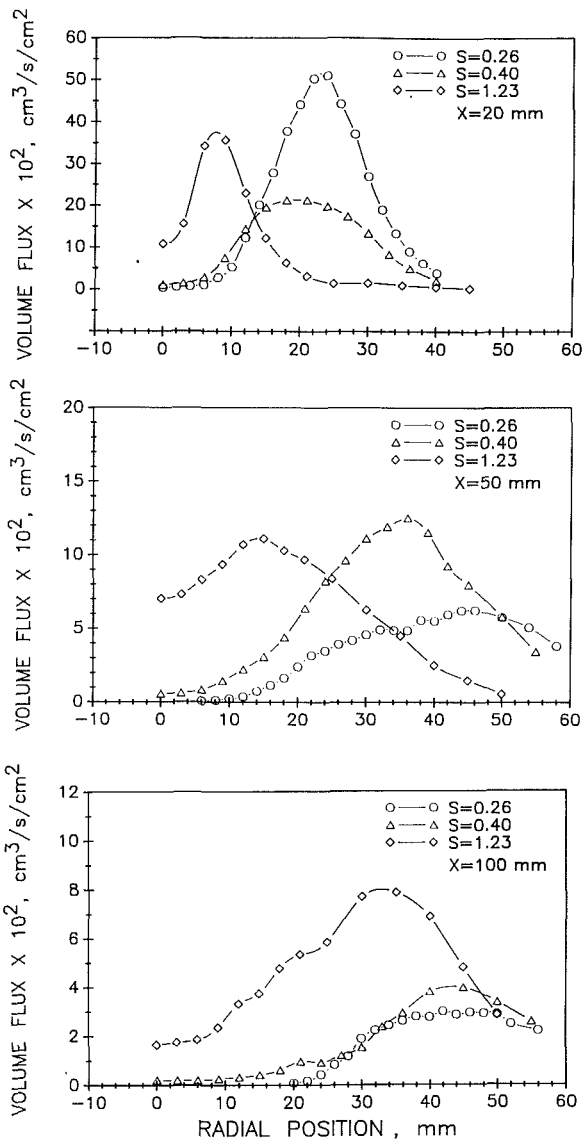

Fig. 9 Radial distribution of liquid volume flux at three axial positions for the three conditions of swirl

This information is valuable since it was previously stated that drops of less than 5 μm can follow the air motion reasonably well.

Particle Number Density and Liquid Volume Flux. Paramount to the calculation of particle number density, N_d, and liquid volume flux, Q_f, is the accurate determination of the sampling cross section, sampling statistics, and the theoretical description of the light intensity distribution in the sampling cross section. The relative merits these parameters have in the determination of N_d and Q_f have been discussed in detail by Bachalo et al. (1988a) and will not be repeated here.

Particle number density was obtained for the liquid spray for the three conditions of swirl. The expression used to calculate the particle number density is given by

$$N_d = \sum_{i=1}^{50} \frac{1}{|v_i|} \sum_{j=1}^{50} n_{ij} \left(A_j \sum_{k=2}^{n_{ij}} \Delta t_{ijk} \right)^{-1} \quad (2)$$

where v_i is the velocity of the ith bin in the velocity histogram composed of 50 bins, A_j is the probe area of the jth size bin, n_{ij} is the total number of particles of size j in the ith velocity bin, and Δt_{ijk} is the interarrival time between the kth and $(k-1)$th particles of size j within the ith velocity bin.

Figure 8 is a plot of the radial distribution of particle number density at three axial positions for the three swirlers. The profiles of N_d show that the spray spreads slightly radially outward as swirl increases and that the concentration of particles peaks toward the periphery as axial distance increases. In the case of the high swirl number, the vigorous mixing and the presence of a recirculation region causes the spray to have a higher concentration of particles closer to the core at $X = 50$ mm. Outside of the recirculation region the particle number density attains a uniform value across the flow. Notice also that N_d is higher by about 20 percent and peaks farther out when the number density profiles of the 60 and 20 deg swirlers are compared closest to the nozzle.

Figure 9 shows the radial distribution of liquid volume flux for the three swirlers at three axial locations, namely, $X = 20$, $X = 50$, and $X = 100$ mm. Those values obtained at other axial stations are not plotted in these figures to facilitate the reading of the curves. The effect of increasing swirl number on the volume flux is to produce a radial distribution that peaks closer to the centerline. This behavior is observed at all axial stations, although the differences for the low and intermediate swirl are

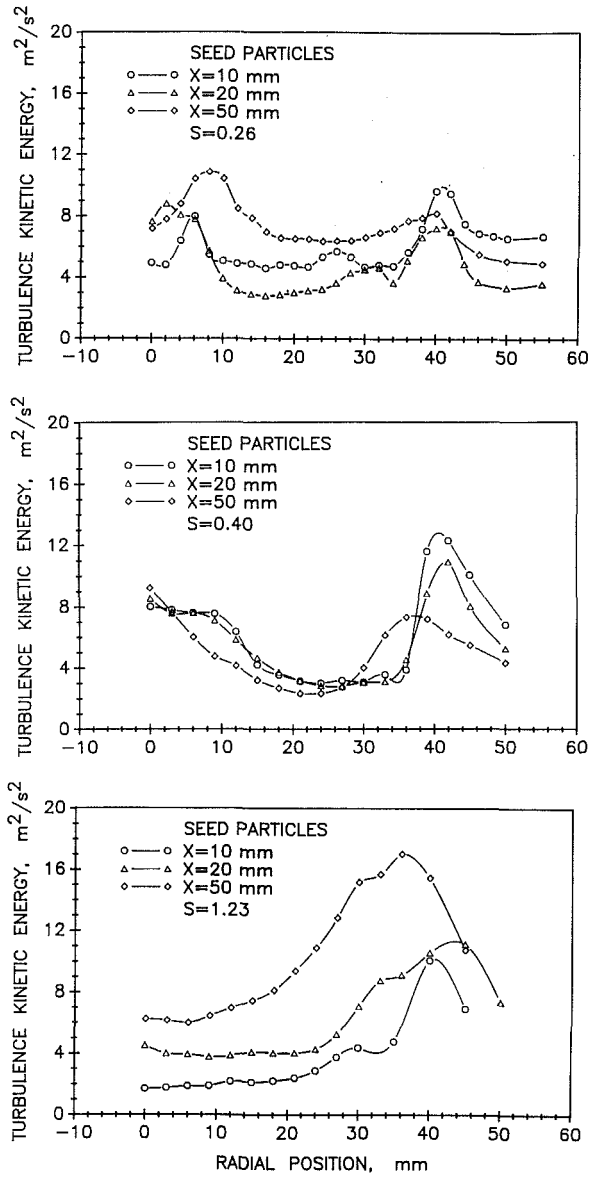

Fig. 10 Radial distribution of turbulence kinetic energy at three axial locations for the 20, 30, and 60 deg swirlers

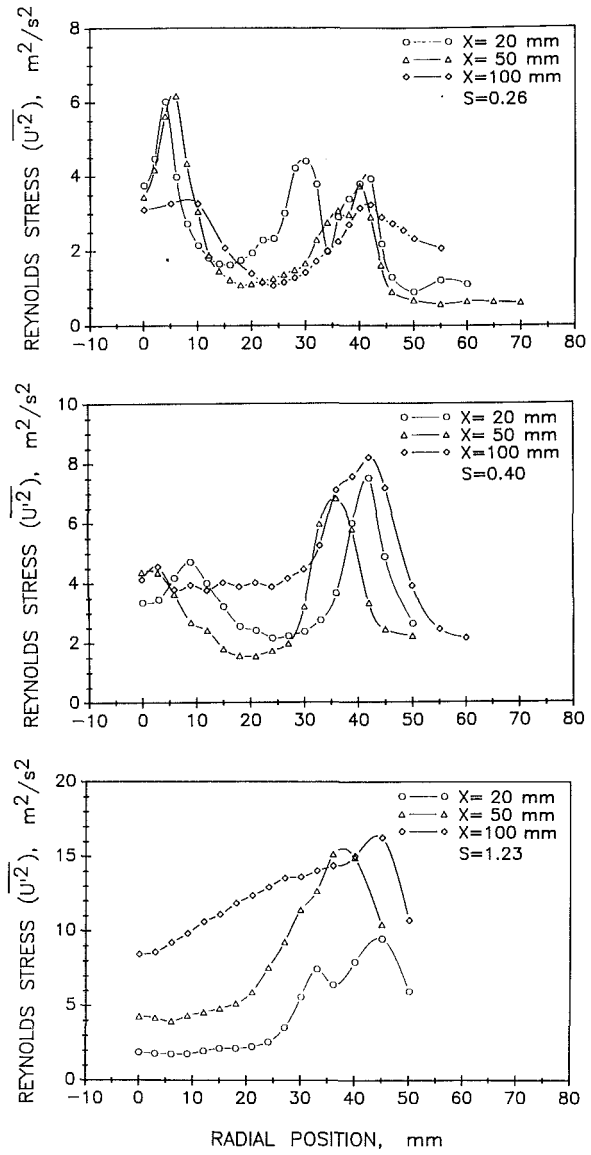

Fig. 11 Normal Reynolds stresses $\overline{u'^2}$ as a function of radial position for the three vane swirlers at axial locations of X = 20, X = 50, and X = 100 mm from the nozzle

not as large far away from the swirler. It is noted that liquid volume flux is proportional to D_{30}^3, therefore, large drops have a strong effect on Q_f.

Comparisons of liquid volume fluxes obtained with the PDPA with patternator data or comparisons of integrated values of Q_f across the cross-sectional area of the spray obtained with the PDPA with flow rates to the nozzle were not attempted in this study because the accuracy of these type of measurements has already been assessed for a quiescent spray, (Bachalo et al., 1988b). It is believed that the accuracy of liquid volume flux calculations in the present measurements remains unaltered, i.e., within ±15 percent.

Turbulence Properties of the Spray. Turbulence properties were obtained of the swirling field with the seed particles in the flow at axial locations of X = 10, 20, 50, 100, 150, and 200 mm from the atomizer. Radial traverses consisted of measurements taken at 2-mm intervals at X = 10, 20, and 50 mm and at 5-mm intervals at X = 100, 150, and 200 mm.

Figure 10 shows the radial profiles of the turbulence kinetic energy plotted at three axial stations for the three conditions of swirl number. The results are very different for the three swirlers. In the case of low swirl S = 0.26, double-peak profiles are appreciable, showing the core and the boundary with the external air flow field to be the regions of high energy content. At S = 0.40 the field surrounding the core shows a low kinetic energy region; this energy subsequently increases at the boundary with the external air. At S = 1.23, Fig. 10 shows a somewhat unexpected result: The flow does not exhibit a high energy content in the shear region surrounding the core. At this condition of high swirl number, S = 1.23, a recirculation region in the form of a toroidal vortex is predicted in the core; however, these results show a low kinetic energy region in the core that sharply increases at the edge of the swirling field. From the profiles of the kinetic energy of turbulence it was found that it decays rapidly in the axial and radial directions as the swirling field expands rapidly into the external air flow field.

Turbulence intensity was also calculated for the three swirling flows at five axial locations (not shown). The reference velocity for these calculations was considered the mean velocity of the air at each particular location. The three swirlers showed high turbulence intensities near the centerline, and surprisingly at S = 0.26 and S = 0.40 there are no peaks in the intensity profile in the shear layer with the external flow. At S = 1.23

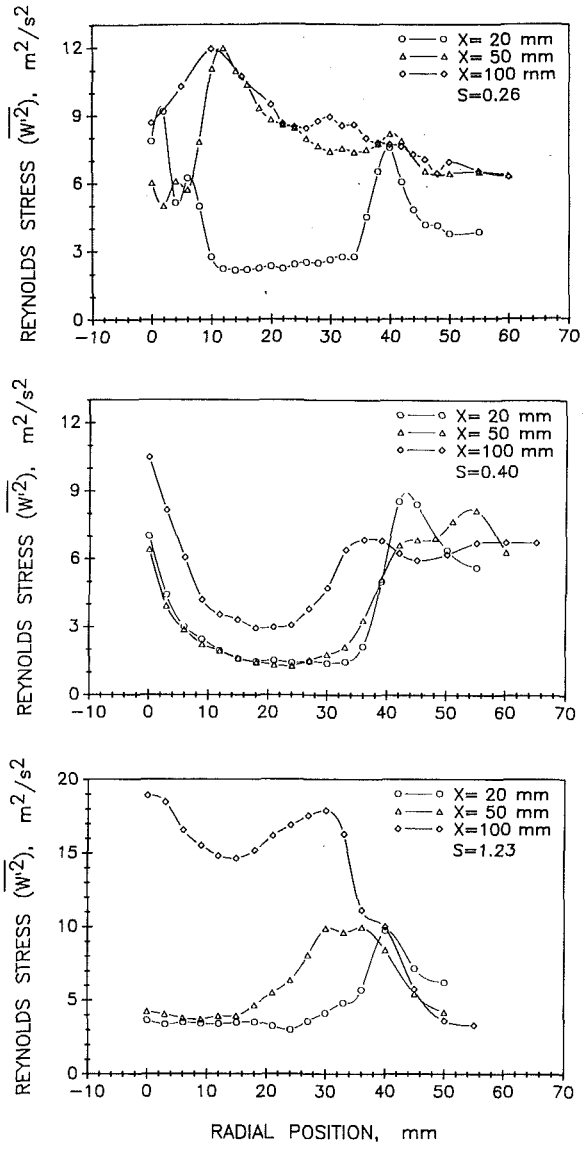

Fig. 12 Normal Reynolds stresses $\overline{w'^2}$ as a function of radial position for the three vane swirlers at axial locations of X = 20, X = 50, and X = 100 mm from the nozzle

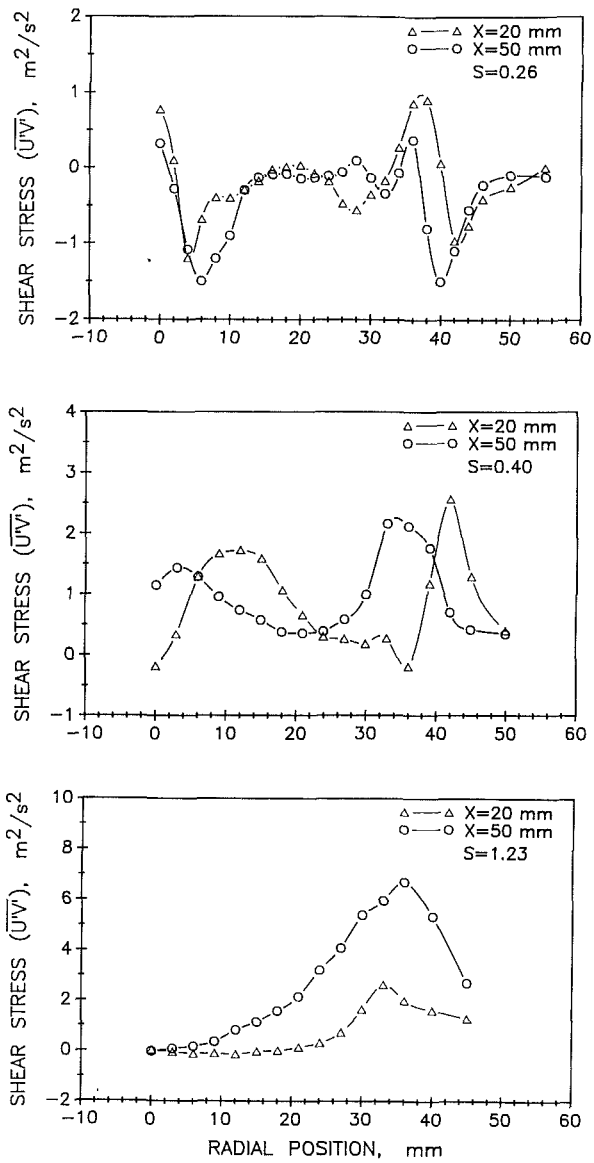

Fig. 13 Radial distribution of Reynolds shear stresses $\overline{u'v'}$ for the three vane swirlers at a distance of X = 20 and X = 50 mm from the nozzle

very high turbulence levels are seen in this region. For the low conditions of swirl the turbulence intensity was virtually uniform throughout the field, yielding values of approximately 20 percent. In comparison, at $S=1.23$ and closest to the nozzle $X=10$ mm, the turbulence intensity resulted in values ranging from 100 to 150 percent for $-20\le R\le 20$ mm. It is noted that for the three conditions of swirl, axial velocities very close to zero near the centerline resulted in the very high values of turbulence intensity.

The normal Reynolds stresses $\overline{u'^2}$, $\overline{v'^2}$, and $\overline{w'^2}$ were obtained as a function of radial position at five axial locations for the 20, 30, and 60 deg vane swirlers, respectively. Figures 11 and 12 show the radial profiles of u'^2 and w'^2. Noteworthy of these data are the double peak profiles, which indicate regions in the flow where high gradients of mean velocity exist. Also of interest is the unexpected result that at $S=1.23$ (Fig. 11), the profile does not indicate a region of high gradients of mean velocity in the boundary of the recirculation region in the core of the flow. However, at $S=1.23$ within the recirculation region, the values of the Reynolds stress w'^2 are much higher than those depicted at low and medium swirl numbers (Fig. 12).

Shear stresses $\overline{u'v'}$ and $\overline{u'w'}$ have been plotted in Figs. 13 and 14 at two axial locations for the three swirlers. The profiles at other axial stations have been omitted for the sake of clarity in interpreting the data. High Reynolds stresses are observed for the low and medium swirl numbers in the shear layer near the centerline and in the boundary with the external air flow resulting in double peak profiles. The reason could be that at these conditions the flow maintains a stronger vortex core farther downstream than that maintained at $S=1.23$. High shear stresses at the edge of the vortex core are an indication of strong shear forces between the vortex core and the external air flow. The 60 deg swirler showed, however, much higher shear stresses at the boundary with the external air flow (bottom of Figs. 13 and 14). The profiles of the shear stresses are consistent with the profiles of the normal stresses, i.e., double-peak curves are present at $S=0.26$ and $S=0.40$ but are absent at $S=1.23$. The profiles of the shear stresses for the three conditions of swirl at other axial stations are similar to the ones exhibited in Figs. 13 and 14 for the corresponding conditions, except that farther downstream, $X\ge 150$ mm, the shearing energy of the flow has decreased substantially and double peak profiles are not observed.

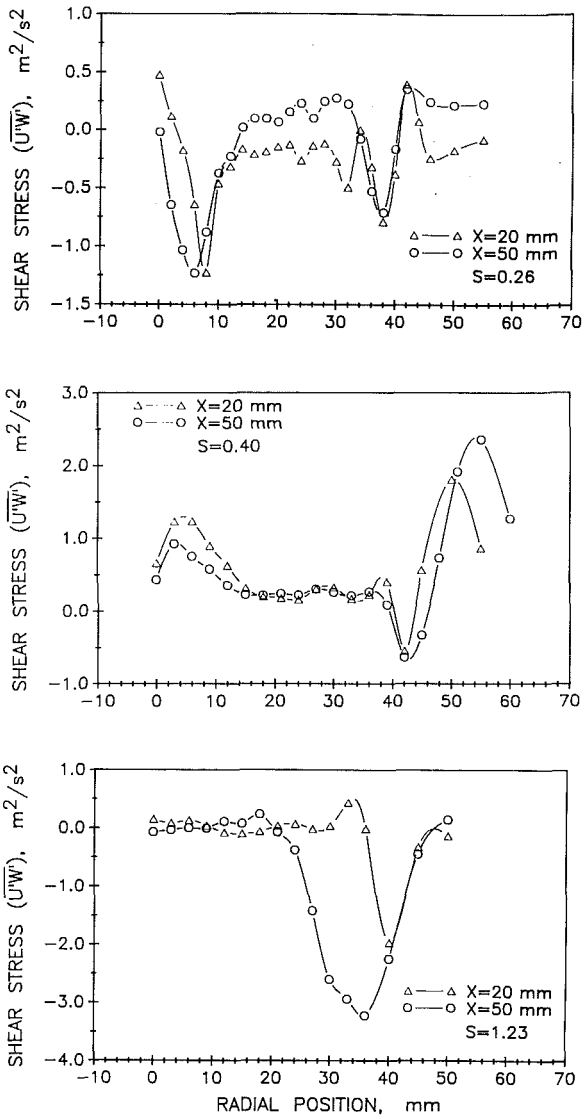

Fig. 14 Radial distribution of Reynolds shear stresses $\overline{u'''w'''}$ for the three vane swirlers at a distance of X = 20 and X = 50 mm from the nozzle

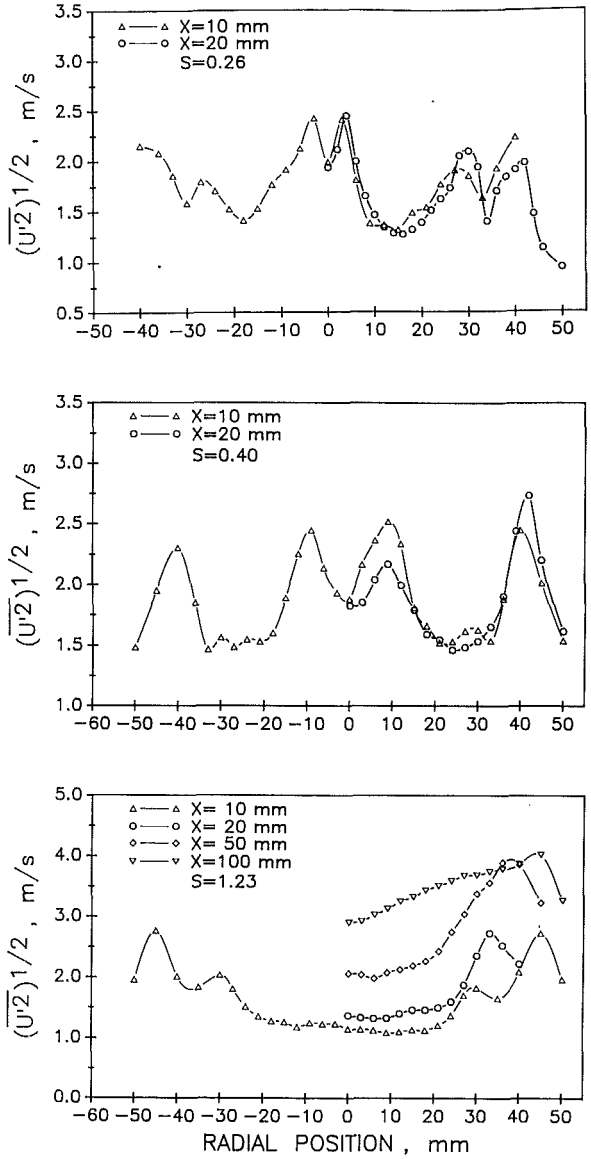

Fig. 15 Radial distribution of the rms of the velocity fluctuations for the three vane swirlers at several axial positions

Double peak values of turbulence kinetic energy, normal Reynolds stresses, and shear stresses, which are evident in Figs. 11–14, have also been observed by Sislian and Cusworth (1986) and Fuji et al. (1981) in a free isothermal swirling jet. These peaks, as already mentioned, are produced in regions with high gradients of mean velocity. The outer peak values are due to the shear layer at the edge of the air flow. What these profiles indicate is a substantial deviation of the flow from isotropy. In the present study the normal stresses were also found to be significantly larger than the Reynolds shear stresses, which indicates the need to consider the three normal stresses in any turbulence model of such flows.

Figure 15 depicts the radial distribution of the rms of the axial velocity fluctuations at four axial positions for the three swirlers. These radial distributions also show for $S=0.26$ and $S=0.40$ double-peak profiles where large fluctuations of the axial velocity occur in the core and in the shear layer with the external flow. At $S=1.23$, the axial velocity fluctuations show almost a constant value, even within the boundaries of the recirculation region; however, large fluctuations are present in the shear layer with the external air flow. This result is consistent with the profiles obtained for the turbulence intensity (not shown). The decay of turbulence velocities in the axial direction was also observed to be very fast, which, as has been previously mentioned, is an indication of high diffusion and dissipation rates of the kinetic energy of turbulence. This is in agreement with experiments performed by Nejad et al. (1989) in a dump combustor at isothermal conditions.

Conclusions

This investigation has dealt with the study of the dynamic behavior of a liquid isothermal spray under the influence of a swirling field. The experimental conditions were carefully designed such that the adequate selection of three vane swirlers with swirl intensities of S = 0.26, S = 0.40, and S = 1.23 produced distinctive effects on the liquid sprays. The measurement of turbulence properties confirmed that the three swirlers gave very different results of the turbulence field, thus being able to draw conclusions of the effect of swirl on the spatial distribution of the spray over its size, velocity, liquid volume flux, and particle number density. The conclusions of the work can be summarized as follows:

- The spatial distribution of sizes and velocities, particle number density, and liquid volume flux of the spray are strongly

influenced by the dynamics imposed by the swirling field. Most notable is the effect of flow reversal experienced by the liquid drops in the core of the recirculation region under the effect of a high swirl number (Figs. 4 and 5). Also evident at this high swirl number is a more homogeneous distribution of mean drop sizes, which clearly reflects a vigorous mixing induced by a higher turbulence intensity.

- Detailed plots of the orthogonal components of mean velocity of the drops for discrete drop sizes and of the air together with the trajectories of drops provide a more complete picture of the interaction of the gas and the dispersed phase.
- The presence of an adverse pressure gradient and, therefore, the conditions of a recirculation region in the core of the swirling field were not present at the low $S = 0.26$ or at the medium $S = 0.40$ swirl intensity, but were identified at the high condition of swirl $S = 1.23$.
- The measurement of the velocity and turbulence parameters of the swirling field using seed particles was also performed. Air velocities were compared with the velocities of drops 1–50 μm in diameter. The results show that drops as large as 5 μm follow the air motion reasonably well. In addition, turbulence intensity values obtained for the 1 μm seed particles and for the 5 μm liquid drops were found to differ only slightly.
- Plots of the turbulence kinetic energy, normal Reynolds stresses, and Reynolds shear stresses show double-peak radial distributions indicating regions in the flow with high energy content, or where high mean velocity gradients or large shear forces in the shear region of two flows exist. These double peak distributions deteriorate and decay, obviously, with increasing downstream distance.
- The importance of the turbulence measurements is that these double-peak profiles indicate a significant deviation of the flow from isotropy. The normal Reynolds stresses were also found to be significantly larger than the Reynolds shear stresses, indicating the need to consider the three normal stresses in any turbulence model of swirling sprays. This information is relevant and should be available to researchers working in numerical modeling of liquid spray combustion processes.

The authors realize the shortcomings of the present investigation such as the atomization at low pressures, using water as the liquid, and performing the experiments in a wind tunnel. It is felt, however, that the fundamental fluid mechanics of the problem has been retained and that the necessary preliminary investigation has been covered before the reactive condition is addressed.

Phase II of this investigation, currently under way at Aerometrics, shall consider tests in gas turbine combustor geometries in both isothermal and reacting flows at conditions that reflect more closely those present in gas turbine environments.

Acknowledgments

The authors gratefully acknowledge the support of this work by the National Science Foundation, Contract No. ISI-8860783. The authors would also like to express their thanks to Mr. Mark Yoneyama, Mr. Martin Holladay, and Mr. Robert Kennedy for their assistance at various stages of this investigation.

References

Bachalo, W. D., and Houser, M. J., 1984, "Phase/Doppler Spray Analyzer for Simultaneous Measurements of Drop Size and Velocity Distributions," *Optical Engineering*, Vol. 23, No. 5, p. 583.

Bachalo, W. D., Breña de la Rosa, A., and Rudoff, R. C., 1988a, "Advances in Diagnostics for Complete Spray Characterization," *Proceedings of the 4th International Conference on Liquid Atomization and Spray Systems*, Sendai, Japan, Aug. 22–24.

Bachalo, W. D., Rudoff, R. C., and Breña de la Rosa, A., 1988b, "Mass Flux Measurements of a High Number Density Spray System Using the Phase Doppler Particle Analyzer," Paper No. AIAA-88-0236.

Barbella, R., Beretta, F., Ciajolo, A., D'Alessio, A., Pratti, M. V., and Tamai, R., 1988, "Spray-Swirl Interaction and Early Pyrolysis of Kerosene and Light Oils Spray Flames Produced by Simplex Pressure Atomizer," presented at the 22nd Symposium International on Combustion, Seattle, WA, Aug. 14–19.

Beer, J. M., and Chigier, N. A., 1983, *Combustion Aerodynamics*, Robert E. Krieger Publishing Company, p. 111.

Breña de la Rosa, A., Bachalo, W. D., and Rudoff, R. C., 1989, "Spray Characterization and Turbulence Properties in an Isothermal Spray With Swirl," ASME Paper No. 89-GT-273.

Cameron, C. D., Brouwer, J., Wood, C. P., and Samuelsen, G. S., 1989, "A Detailed Characterization of the Velocity and Thermal Fields in a Model Can Combustor With Wall Jet Injection," ASME JOURNAL OF ENGINEERING FOR GAS TURBINES AND POWER, Vol. 111, pp. 31–35.

Fujii, S., Eguchi, K., and Gomi, M., 1981, "Swirling Jets With and Without Combustion," *AIAA Journal*, Vol. 19, No. 11, pp. 1438–1442.

Gouldin, F. C., Depsky, J. S., and Lee, S-L., 1985, "Velocity Field Characteristics of a Swirling Flow Combustor," *AIAA Journal*, Vol. 23, No. 1., pp. 95–102.

Gupta, A. K., Lilley, D. G., and Syred, N., 1984, *Swirl Flows*, Abacus Press.

Lilley, D. G., 1988, "Lateral Jet Injection Into Swirling Combustor Flowfields," AIAA Paper No. AIAA-88-3183.

Nejad, A. S., Vanka, S. P., Favaloro, S. C., Samimy, M., and Langenfeld, C., 1989, "Application of Laser Velocimetry for Characterization of Confined Swirling Flow," ASME JOURNAL OF ENGINEERING FOR GAS TURBINES AND POWER, Vol. 111, pp. 36–45.

Sislian, J. P., and Cusworth, R. A., 1986, "Measurements of Mean Velocity and Turbulence Intensities in a Free Isothermal Swirling Jet," *AIAA Journal*, Vol. 24, No. 2, pp. 303–309.

Experimental Study of the Effect of Dense Spray on Drop Size Measurement by Light Scattering Technology

Ju Shan Chin
Visiting Professor,
Purdue University,
West Lafayette, IN 47907

Wei Ming Li

Yan Zhang

Beijing University of Aeronautics
and Astronautics,
Beijing, People's Republic of China

The effect of dense spray on drop size measurement by light scattering technology was studied using a Malvern instrument with five duplicated internal mixing airblast atomizers aligned with a laser beam. The correction factor data for multiple scattering were obtained. By regression analysis, an empirical equation was obtained that correlated the correction factor as a function of obscuration (OBS), Sauter mean diameter under dilute spray condition (SMD_0), and drop size distribution parameter for Rosin-Rammler distribution under dilute spray conditions (N_0). The experimental data showed definitely that the correction factor is not only a function of OBS and SMD_0, as proposed by Dodge, but also is a function of N_0. The correlation fits the experimental data very well, and can be used for practical purposes to correct the data from the Malvern drop sizer at high obscuration conditions.

Introduction

A Malvern drop sizer has been used widely for spray characteristics measurement, which is based on light scattering technology. The instrument was designed on the assumption that a laser light beam is scattered only once. If the particle number density is high, which for liquid spray is called dense spray, multiple scattering will occur. This will cause measurement error in a systematic way. Dodge conducted an experimental study (1984), which showed that at high obscuration conditions, the measured spray characteristics will always be different from the true value. The measured SMD and N values are always less than they should be (see Fig. 1) and a correction factor may be introduced as follows:

$$(CF)_{\mathrm{SMD}} = \frac{\mathrm{SMD}_m}{\mathrm{SMD}_0}$$

$$= 1. - 0.9456\exp(-3.811T)\exp(-0.0204\mathrm{SMD}_0) \quad (1)$$

$$(CF)_N = \frac{N_m}{N_0}$$

$$= 1 - 0.4264\exp(-3.672T)\exp(-0.0130\mathrm{SMD}_0) \quad (2)$$

where $(CF)_{\mathrm{SMD}}$ = correction factor for SMD
$(CF)_N$ = correction factor for N
SMD = Sauter mean diameter
N = drop size distribution parameter in Rosin-Rammler distribution
T = light transmission

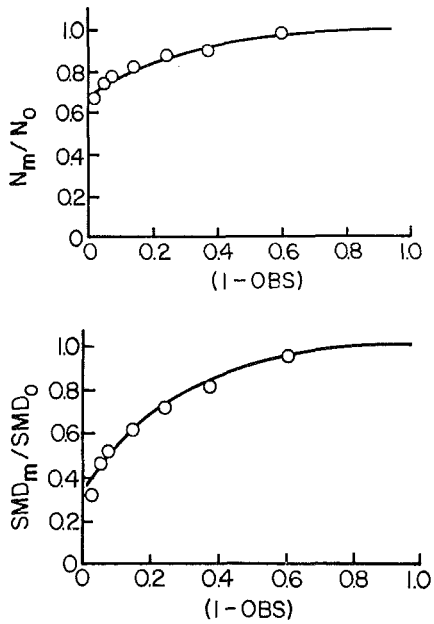

Fig. 1 Effect of obscuration on drop size measurement by light scattering technology (Dodge, 1984)

The subscript m means measured and o means dilute spray.

Dodge used a number of duplicated pressure swirl atomizers. When he varied the pressure drop across the atomizer, he obtained different $(\mathrm{SMD})_0$ values, but basically the same N_0 values for his experiments. Thus he could not take into account the effect of N_0 on correction factor. His data range was SMD_0 = 20–60 μm, $N_o \approx 2.0$.

Contributed by the International Gas Turbine Institute and presented at the 35th International Gas Turbine and Aeroengine Congress and Exposition, Brussels, Belgium, June 11–14, 1990. Manuscript received by the International Gas Turbine Institute December 13, 1989. Paper No. 90-GT-1.

Later Felton et al. (1985) conducted a theoretical analysis. Based on their calculated results, they obtained a correlation as follows:

$$(CF)_x = \frac{\overline{X}_0}{\overline{X}_m} = 1.0 + [0.036 + 0.4947(\mathrm{OBS})^{8.997}] \cdot N_m^{[1.9 - 3.437(\mathrm{OBS})]} \quad (3)$$

$$(CF)_N = \frac{X_0}{X_m} = 1.0 + [0.035 + 0.1099(\mathrm{OBS})^{8.65}] \cdot N_m^{[0.35 + 1.45(\mathrm{OBS})]} \quad (4)$$

where $\overline{X}$ = characteristic drop diameter in Rosin–Rammler distribution

OBS = obscuration of laser beam, which related to transmission as OBS = 1 − T

The Rosin–Rammler distribution is expressed as follows:

$$Q = 1 - \exp\left[- \left(\frac{D}{\overline{X}} \right)^N \right] \quad (5)$$

where Q = volume fraction contained in droplets less than D

D = drop diameter

Obviously in Felton's equation, (CF) is a function of OBS and N_m, but not a function of (SMD) or $\overline{X}_0(\overline{X})$, which is in contradiction with Dodge's result.

The present authors are sure that the correction factor should be a function of OBS, SMD_0, and N_0. The purpose of this study is to prove this argument by experiments and to obtain an empirical correlation based on the measured experimental data.

The correction for the effect of dense spray on drop size measurement by light scattering technology is a very practical problem for atomization research and atomizer design, development, and even production. We know from previous experimental work that for aero gas turbine engines (except small ones), only under idle condition, the spray from the atomizer can be considered as dilute. Otherwise there is always a need to take into account the effect of dense spray on drop size measurement. Roughly speaking, for measured SMD less than 50 μm, when the fuel flow rate is higher than 30 g/s, the measured drop size data will always be obtained at obscuration higher than 40 percent. That is, such drop size measurements should be corrected.

In order to investigate the effect of OBS, SMD_0, and N_0 on the correction factor, it is necessary that we use the same type of atomizer to change SMD and N separately. This means we may have, for the same atomizer, different SMD but the same N values or different N values but same SMD. That is impossible to achieve by pressure swirl atomizer and only possible with an air blast atomizer. In this case, we have separate control over air velocity and air–liquid ratio, changing SMD (or N) while keeping N (or SMD) constant. We follow the same method as Dodge, who also used duplicated atomizers aligned with the laser beam to increase the obscuration, until the maximum obscuration exceeds 90 percent.

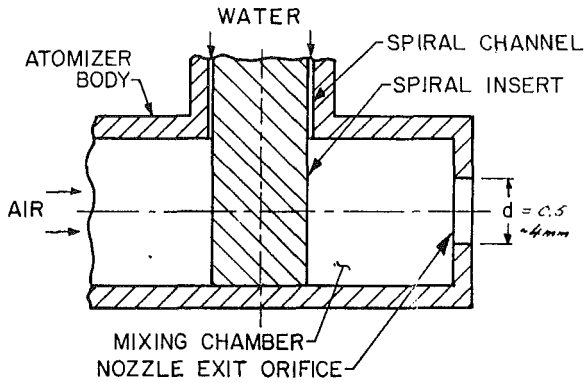

Fig. 2 Atomizer

Atomizers and Experimental Method

The atomizers used in this study are internal mixing air blast atomizers, as shown in Fig. 2. Water was used as the working fluid. The fluid passed a spiral channel flowing into a mixing chamber to mix with air. The water supply pressure, water flow rate, air supply pressure, air flow rate, and thus the pressure in the mixing chamber can all be controlled separately.

By changing air flow velocity, air–liquid ratio, and nozzle exit hole diameter we are able to obtain sprays with a series of different SMD_0 with the same N_0 value or a series of different N_0 with the same SMD_0 under the condition that the obscuration for single atomizer is less than 42 percent. By aligning five atomizers with the laser beam and turning on or turning off these atomizers in different combinations, we may have the obscuration of measured spray varying from 25 to 92 percent. The key features of these experimental atomizers are that they are very simple and cheap, and it is very easy to change their dimensions and control their operational parameters to have SMD and N values suitable for the study. The spray characteristics measured for one atomizer (of which the obscuration is less than 42 percent and may be considered as a dilute spray) are shown in Fig. 3. It is obvious that by controlling air pressure drop and liquid flow rate, we will be able to have desirable SMD_0 and N_0 within the range $\mathrm{SMD}_0 \approx 10 \sim 80$ μm, $N_0 \approx 1.2 \sim 1.9$. The possible data points we may choose are shown in Fig. 4. Dotted lines show the ranges of SMD_0 and N_0 that are possible to obtain from one single atomizer.

The experimental setup is shown in Fig. 5. If we turn on two, three, or four atomizers (with different combinations) obscuration will be within the range of 50–70 percent, 70–80 percent, 83–89 percent, respectively; for five atomizers (only one combination), 92 percent.

The present study is an empirical scheme rather than one based on theoretical analysis.

The experimental setup needs some special attention. The sprays from different atomizers shall not impinge or intersect each other; they should not be placed too far apart as they must be within approximately one focal length of the receiver

Nomenclature

A = cross-sectional area
CF = correction factor
d = orifice diameter
I = light intensity
l = beam length
$\dot{m}_w$ = water flow rate
n = droplet number density
N = drop size distribution parameter in Rosin–Rammler distribution
OBS = obscuration = 1 − T
ΔP_a = air pressure drop across the atomizer
Q = volume fraction contained in droplets less than D
SMD = Sauter mean diameter
T = transmission
$\overline{X}$ = characteristic drop diameter in Rosin–Rammler distribution
Δ = data fitting error

Subscripts

o = dilute spray or initial condition
m = measured
C = correlation

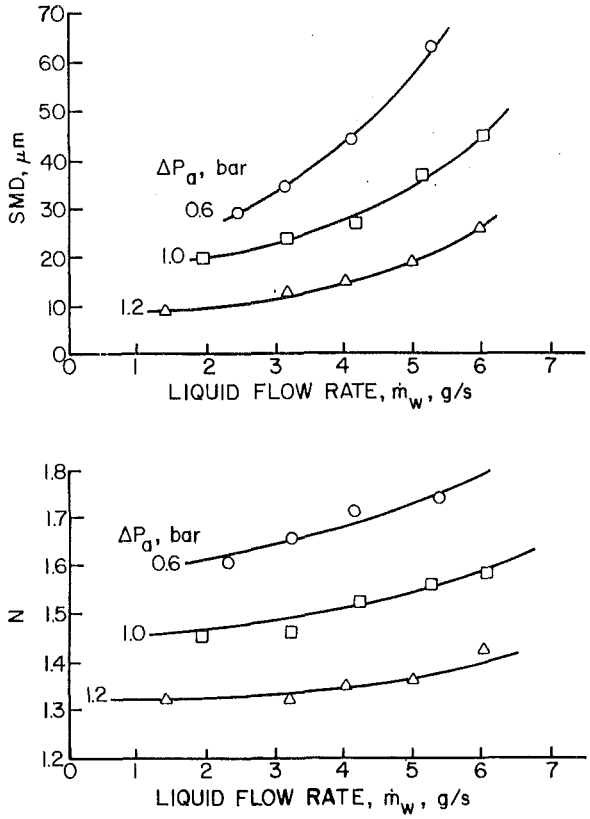

Fig. 3 Spray characteristics changing with liquid flow rate and air pressure drop

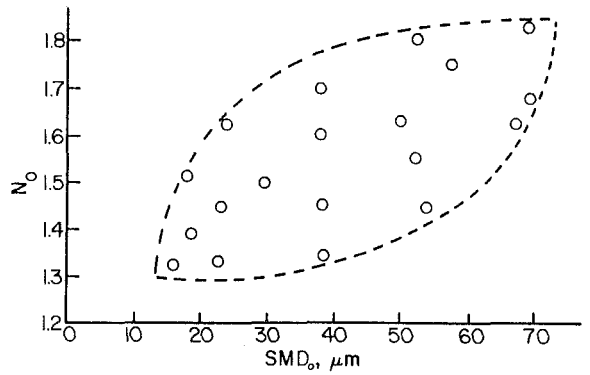

Fig. 4 Spray characteristic data points for single atomizer (dilute spray)

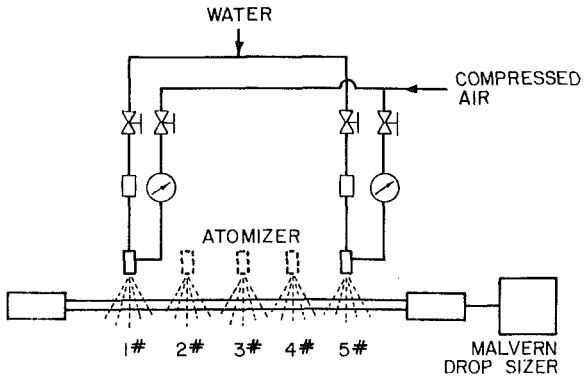

Fig. 5 Experimental setup

lens. The central lines of these sprays shall be perpendicular to the laser light beam. In order to have as close as possible the same SMD_0 and N_0 for these five duplicated atomizers,

Table 1 Spray characteristics

	Atomizer No.						
	1	2	3	4	5	ave.	difference
$SMD_0 \mu m$	38.94	37.22	36.80	38.37	38.84	38.03	+3.2% −2.4%
N_0	1.62	1.63	1.60	1.59	1.59	1.606	±1.5%
OBS	0.248	0.246	0.252	0.418	0.421	–	–

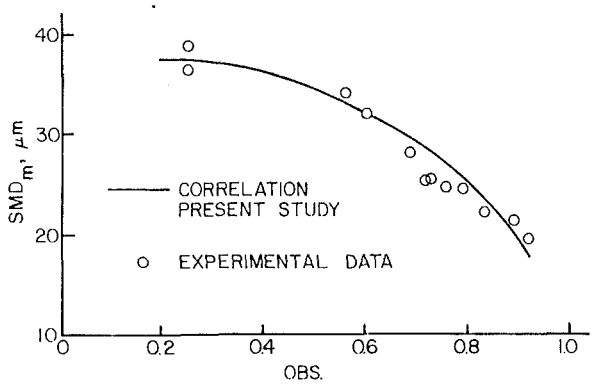

Fig. 6 SMD_m versus OBS

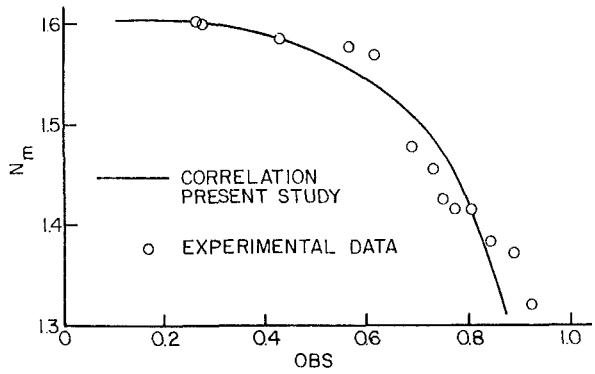

Fig. 7 N_m versus OBS

every atomizer shall have its own control; thus the air pressure and water flow rate will be different for different atomizers to obtain the same (within very narrow range) SMD_0 and N_0.

A Malvern drop sizer 2200 was used to measure spray characteristics.

Results

It is important to check whether different atomizers will produce the same spray characteristics. A typical set of results is shown in Table 1.

From Table 1, it can be seen that with separate control over atomizer air pressure drop and liquid flow rate, we are able to obtain the same spray characteristics from different atomizers.

A typical set of experimental results for the measured SMD and N changing with obscuration is shown in Figs. 6 and 7. It is clear that at OBS < 0.4, there is little change of SMD and N with obscuration, while for OBS > 0.6, the spray characteristics change dramatically with the increase of OBS. For this particular case, at OBS ≈ 0.8, $SMD_m/SMD_0 = 0.63$, $N_m/N_0 = 0.81$. A typical set of experimental data obtained is shown in Table 2, where $\dot{m}_w$ is the water flow rate and ΔP_a is the air pressure drop across the atomizer.

The effect of SMD_0 on the measurement of drop size under dense spray conditions is clearly shown in Figs. 8 and 9. When

Table 2 Spray characteristics changing with obscuration

Test	Combination of atomizers	$\dot{m}_w$ g/s	ΔP_a bar	SMD μm	N	OBS
1	1#	3.6	0.8	38.94	1.62	0.248
2	2#	3.6	0.8	37.22	1.63	0.246
3	3#	3.7	0.8	36.80	1.60	0.252
4	4#	5.4	1.1	38.37	1.59	0.418
5	5#	5.6	1.1	38.84	1.59	0.421
6	1#, 2#			33.47	1.58	0.561
7	2#, 4#			31.61	1.57	0.601
8	1#, 2#, 3#			27.80	1.48	0.683
9	4#, 5#			25.19	1.46	0.704
10	1#, 2#, 5#			25.30	1.43	0.730
11	2#, 3#, 5#			24.87	1.42	0.757
12	3#, 4#, 5#			24.56	1.42	0.792
13	1#, 2#, 3#, 4#			22.20	1.39	0.833
14	2#, 3#, 4#, 5#			21.64	1.38	0.887
15	1#, 2#, 3#, 4#, 5#			19.41	1.33	0.920

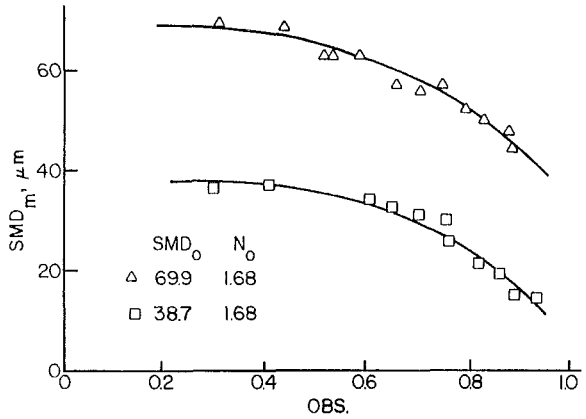

Fig. 8 SMD_m changing with OBS under the condition N_0 = const, showing the effect of SMD_0

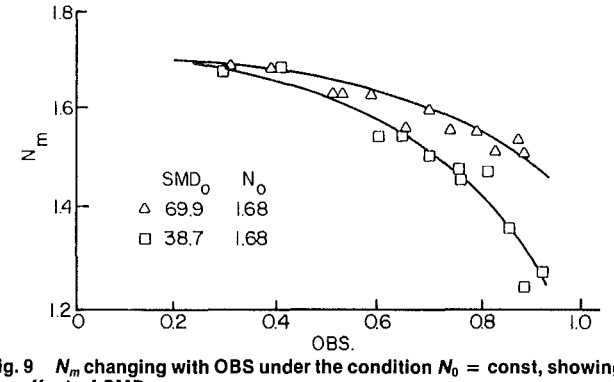

Fig. 9 N_m changing with OBS under the condition N_0 = const, showing the effect of SMD_0

SMD_0 is small the change of measured values with increase of obscuration is sharper.

These experimental data were analyzed by regression analysis. They show definitely that correction factor should be a function of obscuration, SMD_0, and N_0. The data-fitting error for such correlations is often less than 5 percent. We obtain equations in the following forms:

$$\frac{SMD_m}{SMD_0} = (CF)_{SMD} = f_1(\text{OBS}, SMD_0, N_0) \quad (6)$$

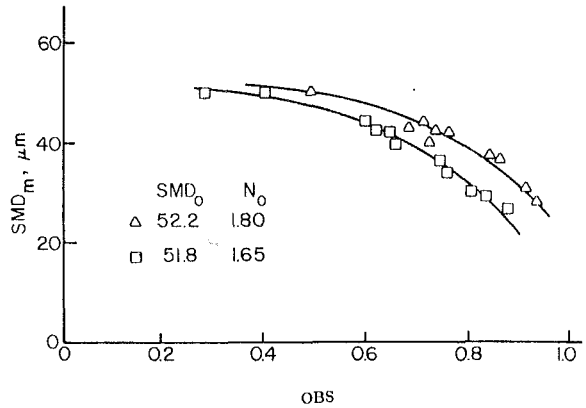

Fig. 10 SMD_m changing with OBS under the condition SMD_0 = const, showing the effect of N_0

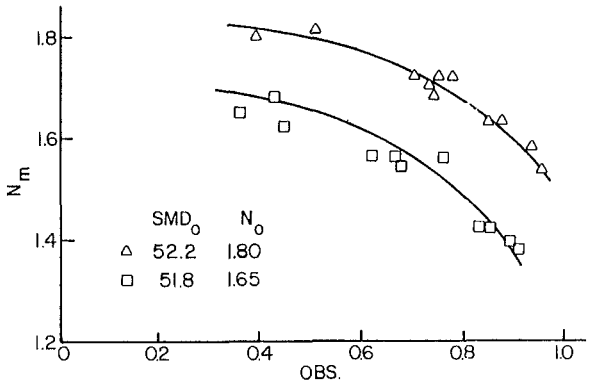

Fig. 11 N_m changing with OBS under the condition SMD_0 = const, showing the effect of N_0

$$\frac{N_m}{N_0} = (CF)_N = f_2(\text{OBS}, SMD_0, N_0) \quad (7)$$

In order to have some comparison with Dodge's correlation, we choose the following equation:

$$CF = 1 - a\exp[-b(1-\text{OBS}) - C SMD_0 - dN_0] \quad (8)$$

where a, b, c, d are constants obtained by the regression analysis of the experimental data.

Taking the logarithm for both sides of Eq. (8) we have

$$\ln(1-CF) = \ln a - b(1-\text{OBS}) - C SMD_0 - dN_0 \quad (9)$$

Suppose

$$y = \ln(-1-CF)$$
$$X_1 = 1-\text{OBS}$$
$$X_2 = SMD_0$$
$$X_3 = N_0$$
$$b_0 = \ln a$$
$$b_1 = -b$$
$$b_2 = -c$$
$$b_3 = -d$$

We have

$$y = b_0 + b_1X_1 + b_2X_2 + b_3X_3 \quad (10)$$

Using multiple variable linear regression analysis methods, with all experimental data obtained, b_0, b_1, b_2, b_3 can be determined. Finally we have the following two correlation equations for correction factors of SMD and N under high obscuration conditions:

$$\frac{SMD_m}{SMD_0} = (CF)_{SMD} = 1 - 1.2739\exp[5.1028(1-\text{OBS}) - 8.5087\cdot10^{-3}SMD_0 - 0.1642N_0] \quad (11)$$

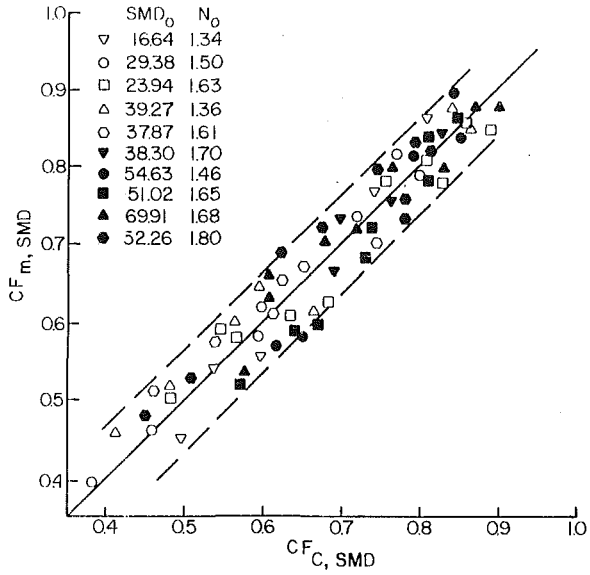

Fig. 12 Data correlation for CF_{SMD}; $CF_{m,SMD}$ obtained by measurement; $CF_{c,SMD}$ obtained by Eq. (11); dotted lines represent the limit of Δ_{max} = 8 percent

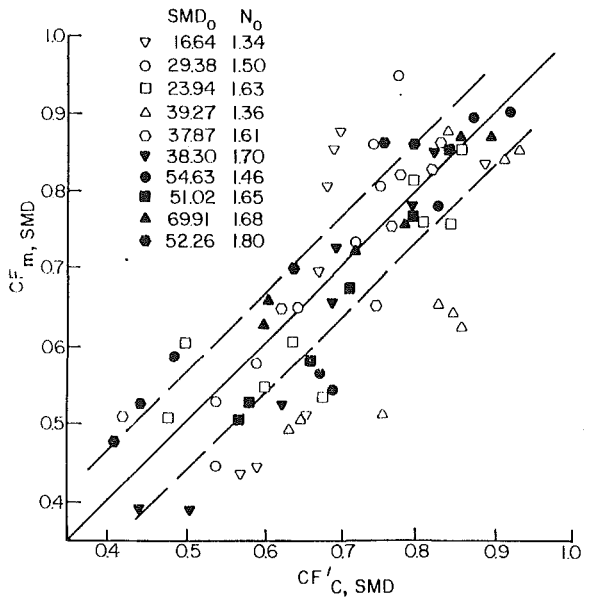

Fig. 14 Data correlation for CF'_{SMD}; $CF_{m,SMD}$ obtained by measurement; $CF'_{c,SMD}$ obtained by Eq. (15); dotted lines represent the limit of Δ_{max} = 8 percent

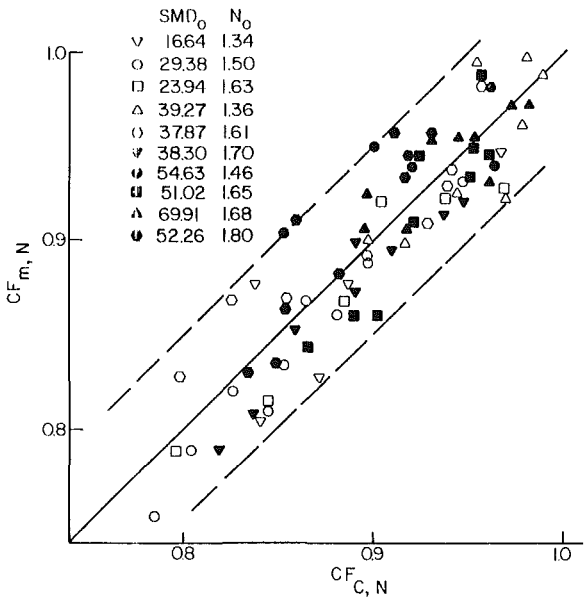

Fig. 13 Data correlation for CF_N; $CF_{m,N}$ obtained by measurement; $CF_{c,N}$ obtained by Eq. (12); dotted lines represent the limit of Δ_{max} = 5 percent

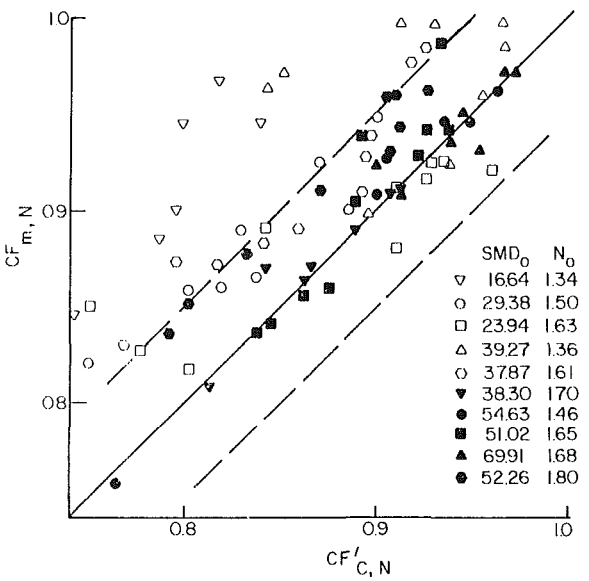

Fig. 15 Data correlation for CF'_N; $CF_{m,n}$ obtained by measurement; $CF'_{c,N}$ obtained by Eq. (16); dotted lines represent the limit of Δ_{max} = 5 percent

$$\frac{N_m}{N_0} = (CF)_N = 1 - 0.08769\exp[-4.5803(1-\text{OBS}) - 0.01626\text{SMD}_0 + 1.1280N_0] \quad (12)$$

where SMD is in μm.

The comparison between the measured correction factor, $CF_{m,SMD}$, $CF_{m,N}$ and calculated correction factor by Eqs. (11) and (12), $CF_{c,SMD}$ and $CF_{c,N}$, is shown in Figs. 12 and 13. The correlation for CF_{SMD} will offer a data-fitting error within ± 8 percent and the correlation for CF_N will offer a data fitting error within ± 5 percent.

Discussion

It would be interesting to investigate that if instead of Eqs. (6), (7) or Eqs. (11), (12) are used, we use the following equations to correlate the same experimental data:

$$(CF)'_{SMD} = f'_1(\text{OBS}, \text{SMD}_0) \quad (13)$$

$$(CF)'_N = f'_2(\text{OBS}, \text{SMD}_0) \quad (14)$$

What will the data-fitting error be?

By the same approach, we have the following correlation equations:

$$(CF)'_{SMD} = 1 - 0.9445\exp[-3.4639(1-\text{OBS}) - 6.9418\cdot 10^{-3}\text{SMD}_0] \quad (15)$$

$$(CF)'_N = 1 - 0.7262\exp[-3.3064(1-\text{OBS}) - 0.02285\text{SMD}_0] \quad (16)$$

The comparison between experimental data and $CF_{c,SMD}$, $CF_{c,N}$ by Eqs. (15) and (16) is shown in Figs. 14 and 15. The correlation for CF'_{SMD}, Eq. (15), will have a data-fitting error within 26 percent. The correlation for CF'_N, Eq. (16), will have a data-fitting error within 15 percent. Obviously using Eqs. (13), (14) or (15), (16) to have correction factor will be much

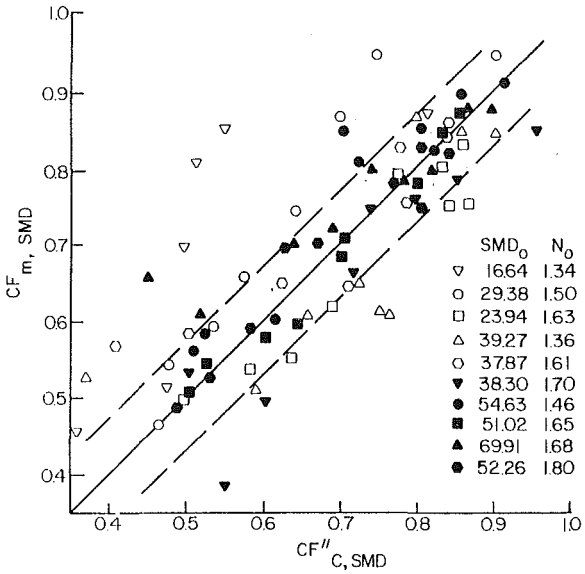

Fig. 16 Data correlation for CF''_{SMD}; $CF_{m,SMD}$ obtained by measurement; $CF''_{c,SMD}$ obtained by Eq. (19); dotted lines represent the limit of Δ_{max} = 8 percent

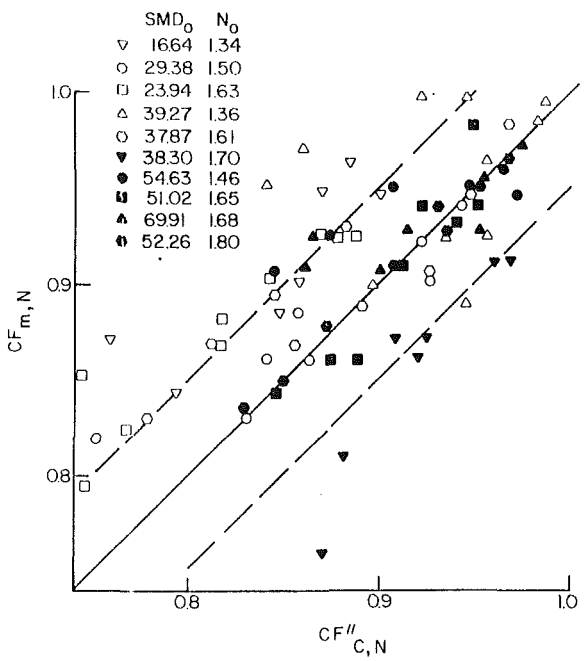

Fig. 17 Data correlation for CF''_N; $CF_{m,N}$ obtained by measurement; $CF''_{c,N}$ obtained by Eq. (20); dotted lines represent the limit of Δ_{max} = 5 percent

poorer than using Eqs. (6), (7) or (11), (12). That is, the effect of N_0 on correction factor cannot be neglected.

If instead of Eqs. (6), (7) or (11), (12), we use the following equations to correlate the same experimental data:

$$(CF)''_{SMD} = f_1''(\text{OBS}, N_0) \tag{17}$$

$$(CF)''_N = f_2''(\text{OBS}, N_0) \tag{18}$$

what will the data-fitting error be?

Using regression analysis and all experimental data obtained, we have the following correlation equations:

$$(CF)''_{SMD} = 1 - 27.1732\exp[-4.0866(1-\text{OBS}) - 2.1419N_0] \tag{19}$$

$$(CF)''_N = 1 - 14.8844\exp[-5.3214(1-\text{OBS}) - 2.3860N_0] \tag{20}$$

The comparison between experimental data and Eqs. (19) and (20) is shown in Figs. 16 and 17. The correlation for CF''_{SMD}, Eq. (19), will have a data-fitting error within 31 percent. The correlation for CF''_N, Eq. (20), will have a data-fitting error within 18 percent. Definitely using Eqs. (19), (20) to have the correction factor is also much poorer than using Eqs. (11), (12). That is, the effect of SMD on correction factor, also, can not be ignored.

Another problem we would like to discuss is that during our experiments, we keep the droplet number density nearly constant and increase the beam length to increase the obscuration, but for atomizer drop size measurements, the high obscuration is usually caused by high liquid flow rate.

At nearly the same SMD value, the flow rate is proportional to the number density; thus the high obscuration is actually caused by high number density. From Beer's law

$$\text{Obscuration} = 1 - \frac{I}{I_0} = 1 - \exp[-c(\Sigma n_i A_i)\cdot l] \tag{21}$$

where I, I_0 = light intensity and initial light intensity
n_i = droplet number density
A_i = cross-sectional area of droplets
l = light beam length (scattered by droplets)
c = constant

Thus, the change of obscuration can be caused either by change of droplet number density n_i or the light beam length affected by droplet particles. The question can be expressed as follows, whether the correlation factor should be the same, if obscuration is the same, no matter whether it is caused by high droplet number density or by longer light beam length.

In the present study we designed and manufactured the same type atomizers. They offer the same SMD and N values, but when they work alone, they will offer different obscurations (see Table 1 and Table 2). For one group, the obscuration is 25 percent; for another group, the obscuration is 42 percent. We used different combinations of atomizers to obtain a high obscuration level. Here the obscuration may be increased by: (1) increase of light beam length, such as No. 6, 8, 9, etc., in Table 2; (2) combination of increase of light beam length and increase of droplet number density, such as No. 7, 10, 11, 12, 15, etc., in Table 2.

We can see no difference between the measurements obtained at higher obscuration caused by these two ways. We have the confidence to believe that once obscuration is the same (also SMD_0, N_0), it does not matter which is the cause for high OBS. That means the results from the present study can be used for atomizer drop size measurement by Malvern with high liquid flow rate.

Conclusions

1 The correction factor for drop size measurement by laser light scattering under high obscuration condition is a function of obscuration, Sauter mean diameter at dilute spray condition, and drop size distribution parameter in Rosin–Rammler distribution at dilute spray condition. Neglecting any one of them will cause serious error. The equations provided require an iterative solution for practical use.

2 The correlations for the correction factor obtained by the present authors are as follows ($15 < SMD_0 < 80$; $1.2 < N_0 < 1.9$):

$$\frac{SMD_m}{SMD_0} = (CF)_{SMD} = 1 - 1.2739\exp[-5.1028(1-\text{OBS}) - 8.5087\cdot 10^{-3}SMD_0 - 0.1642N_0]$$

$$\frac{N_m}{N_0} = (CF)_N = 1 - 0.08767\exp[-4.5803(1 - \text{OBS}) - 0.01626\text{SMD}_0 + 1.1280N_0]$$

3 The correction factor correlation obtained in this study by increasing the light beam length affected by scattering to increase the obscuration can be used for atomization drop size measurement where the high obscuration is caused by high liquid flow rate.

4 An internal mixing air blast atomizer, which can be controlled by its air pressure drop and liquid flow rate to offer desired spray characteristics, is very suitable for such atomization studies.

5 There is a need to extend the range of the correlation to $\text{SMD}_0 \approx 120$–150 μm, $N_0 \approx 2.5 \sim 3$.

References

Dodge, L. G., 1984, "Change of Calibration of Diffraction-Based Particle Sizers in Dense Spray," *Optical Engineering*, pp. 626–630.

Felton, P. G., Hamidi, A. A., and Aigal, A. K., 1985, "Measurement of Drop Size Distribution in Dense Spray by Laser Diffraction," ICLASS-85.

Energy Considerations in Twin-Fluid Atomization

A. H. Lefebvre
Atomization and Spray Laboratory,
Thermal Science and Propulsion Center,
School of Mechanical Engineering,
Purdue University,
West Lafayette, IN 47907

With certain types of prefilming airblast atomizers, the manner in which the atomizing air impinges on the liquid sheet prohibits the wave formation that normally precedes the breakup of a liquid sheet into drops. Instead, the liquid is shattered almost instantaneously into drops of various sizes. This prompt atomization process is characterized by a broad range of drop sizes in the spray and by a lack of sensitivity of mean drop size to variations in liquid viscosity, atomizing air pressure, and initial liquid sheet thickness. Evidence is presented to show that which of these two different modes of atomization will occur in any given flow situation is largely dependent on the angle at which the atomizing air impinges on the liquid sheet. An equation for mean drop size, derived from the assumption that the main factor controlling prompt atomization is the ratio of the energy required for atomization to the kinetic energy of the atomizing air, is shown to provide a good fit to experimental data acquired from atomization studies on water and heating oil, carried out over wide ranges of air velocity, air/liquid ratio, and ambient air pressure.

Introduction

The concept of prefilming airblast atomization was developed into a practical atomizing device more than twenty years ago (Lefebvre and Miller, 1966). This development was accelerated by the growing recognition that conventional pressure-swirl atomizers would inevitably produce excessive amounts of exhaust smoke if applied to the new generation of high compression ratio turbojet engines. Since that time, prefilming airblast atomizers have become widely employed as fuel injectors for aero and industrial gas turbines.

In all practical forms of prefilming airblast atomizers, a conical liquid sheet is sandwiched between two coflowing streams of air. Normal design practice is to introduce a swirl component into both air streams so that the expanding liquid sheet and the coflowing air streams all have radial and tangential as well as axial components of velocity.

As airblast atomizers became more widely used in both aircraft and industrial applications, much interest was aroused in the contribution made by prefilming of the fuel to its subsequent atomization. In order to shed more light on the role of the prefilming process, Rizk and Lefebvre (1980) initiated an experimental program to investigate the influence of initial liquid sheet thickness on the mean drop sizes produced in the spray. To avoid the problems associated with trying to measure the thickness of a conical expanding sheet, they employed a specially designed airblast atomizer that injected a flat liquid sheet into the interface between two coflowing streams of high-velocity air. The construction of this atomizer was such as to allow the initial thickness of the liquid sheet to be varied and controlled over a wide range. The air passages were made clean and smooth to avoid any disturbance to the flow, with minimum area at the atomizing edge to attain maximum velocity in the plane of the initial disintegration of the liquid sheet. The two separate air streams that enclosed the liquid sheet issued from the atomizer *in a direction parallel to the sheet.*

The results of this research showed that thinner liquid films produce smaller drops, according to the relationship SMD $\propto t^{0.4}$. This result was considered to be supportive of the classical "wavy-sheet" mechanism for liquid sheet disintegration, as postulated theoretically by Squire (1953), Fraser et al. (1962), and Dombrowski and Johns (1963), which leads to the relationship SMD $\propto t^{0.5}$.

The experiments of Rizk and Lefebvre were carried out using atomizing air velocities in excess of 50 m/s in order to cover the range of air velocities of relevance to gas turbines under normal operating conditions. Subsequently, it was realized that at certain important off-design conditions the atomizing air velocity could fall to values appreciably less than 50 m/s. This led to a second research program, which was intended merely to repeat the work of Rizk and Lefebvre, but at lower levels of atomizing air velocity. As the atomizer used by these workers was no longer available, a new airblast atomizer was designed to replicate all its essential features. This it did, apart from one aspect that subsequently turned out to be of great importance.

This second program was conducted by Beck et al. (1989a, 1989b). These workers found, in contradiction to the Rizk–Lefebvre results (1980), that initial liquid sheet thickness exercised only a minor influence on the drop sizes produced in the spray. After much deliberation, they attributed the difference between the two sets of results to the fact that in the earlier nozzle design the atomizing air flowed parallel to the liquid sheet, as shown in Fig. 1(*a*), whereas in the later design the two atomizing air streams impinged on the liquid sheet at an angle of 30 deg, as illustrated in Fig. 1(*b*). They suggested

Contributed by the International Gas Turbine Institute and presented at the 35th International Gas Turbine and Aeroengine Congress and Exposition, Brussels, Belgium, June 11-14, 1990. Manuscript received by the International Gas Turbine Institute December 13, 1989. Paper No. 90-GT-3.

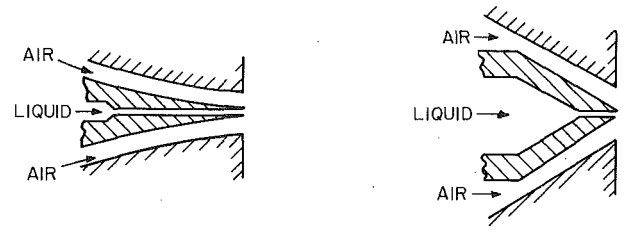

Fig. 1 Flat-sheet airblast atomizers

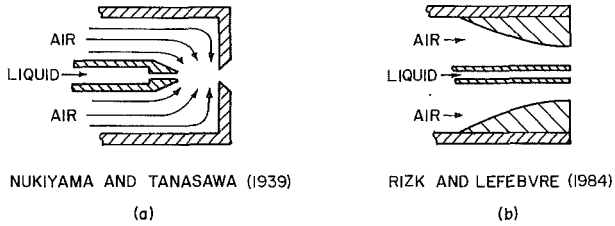

Fig. 2 Plain-jet airblast atomizers

that in the latter case the liquid was being "extruded" before breakup occurred, thereby reducing the thickness of the liquid sheet and, in some cases, eliminating all vestiges of the original sheet thickness. The process whereby the extruded sheet is converted into drops was not specified, but it was presumed that when breakup did occur it did so according to the classical wavy-sheet mechanism.

Another interesting facet of the research of Beck et al. (1988) was their observation that mean drop size is diminished only slightly by an increase in atomizing air pressure. As Rizk and Lefebvre (1980) confined their experiments to normal atmospheric pressure, a direct comparison with other flat sheet data is not possible, but it is of interest to note that all previous studies on the effect of ambient air pressure on the drop sizes produced in prefilming airblast atomization (conical sheet) have revealed a strong pressure dependence. Generally it is found (see, for example, Jasuja, 1979, and Lefebvre, 1980) that SMD $\propto P_A^{-n}$, with values of n ranging from 0.5 to 1.0.

So far the discussion has centered on prefilming airblast atomizers. The other important type of airblast nozzle is the "plain-jet" airblast atomizer, in which a round liquid jet is surrounded by a coflowing, high-velocity air stream. This type of atomizer was, in fact, the first to receive systematic study. It is exactly fifty years since Nukiyamo and Tanasawa (1939) published their classical treatise on plain-jet airblast atomization. Their comprehensive study resulted in an equation for predicting mean drop size. A surprising feature of this equation, and one that has provided a source of discussion ever since, is that mean drop size is completely independent of the initial liquid jet diameter. Another significant feature of this equation is that mean drop size is independent of ambient air pressure.

These surprising results encouraged Rizk and Lefebvre in 1984 to repeat the work of Nukiyamo and Tanasawa. The results of this second study showed, in contradiction to those of Nukiyamo and Tanasawa, that mean drop size is strongly dependent on initial liquid jet diameter (SMD $\propto d_o^{0.5}$) and ambient air pressure (for liquids of low viscosity, SMD $\propto \rho_A^{-0.5}$).

Rizk and Lefebvre (1984) offered no explanation for the marked differences between their results and those of Nukiyamo and Tanasawa, but it is of interest to examine these differences in the light of the explanation given above for similar differences in the results obtained with flat-sheet atomizers. The atomizers used by Nukiyamo and Tanasawa and by Rizk and Lefebvre are shown schematically in Figs. 2(*a*) and 2(*b*), respectively. It is apparent from inspection of these figures that in one case (2*a*) the air impinges on the liquid jet at an appreciable angle, whereas in the other case (2*b*) the atomizing air flows in essentially the same direction as the liquid stream.

The conclusion to be drawn from these various studies on both plain-jet and prefilming airblast atomizers is that the marked differences exhibited by different atomizers of ostensibly the same design are not necessarily due to experimental error. For both types of airblast atomizer, the dependence of mean drop size on initial jet diameter (or sheet thickness) and ambient air pressure is governed by the angle at which the atomizing air impinges on the liquid stream. If the atomizing air impacts the liquid at an appreciable angle, the ensuing atomization process is characterized by a lack of sensitivity of mean drop size to both the initial diameter (or thickness) of the liquid stream and to ambient air pressure. If, however, the atomizing air and liquid are flowing in essentially the same direction, the mean drop size becomes very dependent on the physical dimensions of the liquid stream and the ambient air pressure.

It is postulated that although both of the flat-sheet airblast atomizers shown in Fig. 1 employ high velocity air to shatter the liquid into drops, the difference between these two systems in regard to the manner in which the atomizing air is arranged to impact on the liquid sheet gives rise to two different mechanisms of sheet disintegration. In a similar manner, the occurrence of two different modes of atomization, caused by differences in the angle at which the atomizing air impinges on the liquid jet, is responsible for the markedly dissimilar spray characteristics exhibited by the two plain-jet airblast atomizers shown in Fig. 2.

For reasons of brevity, the following discussion is confined mainly to mechanisms of sheet disintegration, but consideration is also given to the disintegration of liquid jets by high-velocity air streams.

Mechanisms of Sheet Disintegration

Although the atomization of a liquid sheet in a flowing air stream might appear at first sight to be a fairly simple process, it is complicated by the fact that, in the disintegration of a liquid sheet into drops, several different mechanisms may be

Nomenclature

A = surface area, m^2
ALR = air/liquid ratio by mass
C = constant in Eq. (8)
C' = constant in Eq. (9)
C^* = constant in Eq. (14)
D = drop diameter, m
D_g = globule diameter, m
d_o = initial jet diameter, m
E = energy, Nm
m = mass, kg
$\dot{m}$ = mass flow rate, kg/s
n = number of drops in spray
P = pressure, Pa
SMD = Sauter mean diameter, m
t = initial sheet thickness, m
t_b = globule breakup time, s
U = velocity, m/s
w = width of liquid sheet, m
μ = viscosity, kg/ms
ρ = density, kg/m^3
σ = surface tension, kg/s^2

Subscripts

A = air
L = liquid
1 = before atomization
2 = after atomization

involved. The relative importance of the contributions to sheet breakup made by these different mechanisms will vary widely between one flow regime and another, depending on the physical properties, thickness, velocity, velocity profile, and turbulence characteristics of the liquid sheet, the velocity, density, and mass flow rate of the atomizing air, and the manner in which the atomizing air impinges on the liquid sheet. Also of prime importance are the atomizer design features that influence the extent to which the kinetic energies and turbulence properties of the air and liquid streams are effectively harnessed to achieve optimum flow conditions (from an atomization viewpoint) in the liquid sheet and maximum interaction between the liquid sheet and the surrounding air.

When a high liquid injection pressure is used to achieve atomization, as in plain-orifice and pressure-swirl atomizers, the velocity of the liquid jet or sheet produced at the nozzle exit greatly exceeds that of the surrounding air. Interaction between liquid and air is still of prime importance but, in this case, the impetus for this interaction stems from the kinetic energy of the liquid stream, with the air playing a more passive role. However, with twin-fluid atomizers of the airblast or air-assist type, the air into which the liquid jet or sheet is injected is by no means quiescent or slow moving, but has a velocity that is considerably higher than that of the liquid stream. The relative velocity required to promote the interaction between the liquid surface and the coflowing air is now furnished by the high-velocity air. To complete the reversal of roles played by the air and the liquid in pressure and airblast atomization, the liquid is injected into the atomizing air at low velocity. In fact, it is highly desirable that the liquid velocity should be kept as low as possible in order to maximize the relative velocity between the liquid and the atomizing air.

It is sometimes asserted that the fundamental difference between pressure and airblast atomizers is that the high relative velocity between the air and the liquid, which is essential for good atomization, is achieved in one case by injecting high-velocity liquid into slow-moving air and in the other case by injecting slow-moving liquid into a high-velocity air stream. However, this difference between the two methods of atomization, despite its tremendous practical importance, has no fundamental significance. The breakup mechanisms, which are dependent on the relative velocity between air and liquid, are essentially the same for both pressure and airblast atomization. In reality, the only fundamental difference between these two modes of atomization stems from their vastly different liquid injection velocities. In pressure atomizers, the various flow phenomena such as turbulence and cavitation, which, by promoting the self-destruction of the liquid jet or sheet, greatly enhance atomization, are highly velocity dependent. As airblast atomizers are necessarily characterized by low liquid injection velocities, they are deprived of these important aids to atomization, which consequently becomes almost solely dependent on the air/liquid ratio and the momentum of the atomizing air. As some of the complex mechanisms of liquid jet and sheet disintegration that are an integral part of pressure atomization are almost entirely absent in coflowing airblast atomization, the latter may justifiably be regarded as being basically simpler and far more amenable to analysis. This is evidenced by the fact that a number of reliable and consistent semi-empirical equations for estimating the mean drop sizes produced by plain-jet and prefilming airblast atomizers are available in the literature (see, for example, the review by Lefebvre, 1980), whereas no similar, widely accepted equations exist for pressure-swirl atomizers.

In most prefilming airblast atomizers, the liquid sheet and the surrounding atomizing air both flow in essentially the same direction, as illustrated in Fig. 1(*a*). A key feature of this type of flow situation is that the atomizing air has no velocity component in a direction normal to the liquid sheet. Its disruptive effect on the liquid sheet is thereby greatly reduced, and the initial interaction between the liquid and the coflowing air is lethargic enough to allow ample time and opportunity for the sheet to become wavy and for these waves to increase in amplitude until disintegration occurs according to the classical wavy-sheet mechanism. According to this mechanism, which applies only to liquids of low viscosity, waves are formed that protrude into the coflowing air stream. These waves promote interaction between the air and the liquid, causing the crests of the waves to become detached and form ligaments, which subsequently break down into drops. The size of these drops is directly related to the diameters of the ligaments from which they are formed. The ligament diameters, in turn, are dependent on sheet thickness, so there is a very direct relationship between the mean drop size of the spray and the initial sheet thickness, as postulated theoretically by Fraser et al. (1962) and Dombrowski and Johns (1963) and demonstrated experimentally by Rizk and Lefebvre (1980).

Thus, a main prerequisite for wavy-sheet formation is the absence of any significant air velocity component in a direction normal to the liquid sheet. If, however, the atomizing air is arranged to impinge on the liquid sheet at an appreciable angle, as illustrated in Fig. 1(*b*), the air now has a sizable transverse component of velocity. In consequence, the interaction between the liquid and the atomizing air is both strong and immediate. The liquid sheet emerging from the nozzle has no time to develop a wavy structure but is rapidly torn into small fragments by the vigorous interaction created between the liquid and the colliding air jets. The maximum critical size of the liquid fragments produced in this *prompt* atomization process will be governed primarily by the magnitude of the air velocity component normal to the liquid sheet, the air/liquid mass flow ratio, and the liquid surface tension.

A unique feature of this mode of atomization is that the rapid and violent disruption of the liquid sheet into drops ensures that the ensuring drop sizes are largely independent of the initial sheet thickness. Moreover, due to the highly random nature of the sheet disintegration process, and also to the complex flow patterns created by the impinging air jets, which give rise to a wide range of air velocities in the atomization zone, it would seem reasonable to expect this type of atomization to be characterized by a broad range of drop sizes in the spray. In this context it is of interest to note that the results of Beck et al. (1980) exhibit an exceptionally wide range of drop sizes in the spray, values of the Rosin–Rammler (1933) drop-size distribution parameter, q, being in the range from 1.6 to 2.0 as opposed to values of 2.0 to 3.0, which are normally associated with prefilming types of airblast atomizers.

Analysis

From inspection of the Beck et al. atomizer in Fig. 1(*b*), it is clear that the angle of impingement of the atomizing air on the liquid sheet is such as to preclude the formation of a wavy sheet. Instead, the liquid sheet disintegrates into ligaments and drops immediately downstream of the atomizer. Under these conditions it is conceivable that a parameter of significance to mean drop size might be the ratio of the kinetic energy of the atomizing air to the energy required for atomization. Expressions to denote these two energies are readily derived, as shown below.

Consider an airblast atomizer of the type shown in Figs. 1(*a*) and 1(*b*), in which the liquid is discharged in the form of a flat sheet of uniform thickness, t. If t is very small in comparison to the width of the sheet, then the total surface area of the sheet (including both sides) is given by

$$A_{L_1} = \frac{2m_L}{\rho_L t} \tag{1}$$

If the atomization process converts this sheet into drops of diameter D, we have

$$m_L = n\rho_L(\pi/6)D^3 \tag{2}$$

where n is the number of drops in the spray.

The total liquid surface area after atomization is obtained as the sum of the surface areas of each individual drop, i.e.,

$$A_{L_2} = n\pi D^2 \tag{3}$$

By combining Eqs. (2) and (3), the total surface area of all the drops in the spray is obtained as

$$A_{L_2} = \frac{6m_L}{\rho_L D} \tag{4}$$

The energy required to atomize a liquid sheet is equal to the product of the liquid surface tension and the change in surface area, i.e.,

$$\begin{aligned} E_L &= \sigma\delta A \\ &= \sigma(A_{L_2} - A_{L_1}) \\ &= \sigma\left[\frac{6m_L}{\rho_L D} - \frac{2m_L}{\rho_L t}\right] \\ &= \frac{2\sigma m_L}{\rho_L}\left[\frac{3}{D} - \frac{1}{t}\right] \end{aligned} \tag{5}$$

In the above equation it is of interest to note that the sheet can disintegrate into drops without any external source of energy when $D > 3t$.

The energy of the atomizing air is given by

$$E_A = m_A U_A^2/2 \tag{6}$$

Equating the energy required for atomization to the available energy in the air stream, and introducing a coefficient C to represent the efficiency of the atomization process, gives

$$\frac{2\sigma m_L}{\rho_L}\left[\frac{3}{D} - \frac{1}{t}\right] = \frac{C m_A U_A^2}{2} \tag{7}$$

Rearranging this equation gives the following expression for the diameter of the monosize drops:

$$D = \frac{3}{\left[\frac{1}{t} + \frac{C\rho_L U_A^2 \mathrm{ALR}}{4\sigma}\right]} \tag{8}$$

where ALR is the ratio by mass of atomizing air to liquid.

Although, for reasons given below, no attempt has been made to determine the value of C in Eq. (8), it is recognized that it must be appreciably less than unity, because most of the kinetic energy in the atomizing air stream is consumed in overcoming viscous losses and in accelerating the drops formed in atomization up to the velocity of the atomizing air. However, this transfer of momentum from the air to the droplets occurs *after* the air has made its initial impact on the liquid sheet, i.e., after the drops have been formed. Thus, because the liquid sheet is exposed to the full kinetic energy of the atomizing air, before any viscous losses and momentum exchange have occurred, it is the initial kinetic energy of the atomizing air that governs this mode of atomization.

A problem created by the ALR term in Eq. (8) is that it embodies the assumption that all of the air is equally effective in atomizing the liquid. In practice, it is found that air that is physically far removed from the liquid sheet plays a lesser role in the atomization process. Experience with both plain jet and prefilming types of airblast atomizers has shown that the addition of more atomizing air is very effective in reducing mean drop size when the ALR is low (<2) but is much less effective when the ALR is high (>5). To surmount this problem, it is customary to replace the ALR term in semiempirical expressions for SMD with the parameter $(1 + 1/\mathrm{ALR})^{-1}$. This parameter is generally preferred because it allows the influence of ALR on mean drop size to diminish with increase in ALR. By making this substitution, and replacing D with SMD, Eq. (8) becomes

$$\mathrm{SMD} = \frac{3}{\left[\frac{1}{t} + \frac{C'\rho_L U_A^2}{4\sigma(1 + 1/\mathrm{ALR})}\right]} \tag{9}$$

Comparison With Experimental Data

It is of interest to compare the predictions of mean drop size from Eq. (9) with the experimental data acquired by Beck et al. (1989a, 1989b). In all figures the data shown are expressed in terms of *absolute* and not *relative* air velocity. This is because for coflowing airblast atomization, where the disintegration of the liquid jet or sheet into drops occurs via the wavy-sheet mechanism, it is the *relative* velocity between the atomizing air and the liquid stream that governs the drop sizes in the spray. If, however, the angle of impingement of the atomizing air on the liquid jet or sheet is sufficiently high to prohibit wavy-sheet formation, then it is the *absolute* velocity of the atomizing air that determines mean drop size.

Figure 3 shows a plot of Sauter mean diameter (SMD) against atomizing air velocity. The data presented in this figure were obtained at normal atmospheric pressure using water flow rates of 10 and 20 g/s. The initial sheet thickness was maintained constant at 102 μm. The lines drawn in this figure represent the predictions of Eq. (9), using a value for C' of 0.007. Insertion of this constant into Eq. (9) gives

$$\mathrm{SMD} = \frac{3}{\left[\frac{1}{t} + \frac{0.007\rho_L U_A^2}{4\sigma(1 + 1/\mathrm{ALR})}\right]} \tag{10}$$

Figure 3 shows good agreement between the experimental data and the lines drawn to represent Eq. (10). Generally good agreement is also exhibited between experiment and theory in Fig. 4, which contains similar data to those shown in Fig. 3 but for different water flow rates.

Figure 5 also demonstrates the influence of air velocity on mean drop size, but in this instance the liquid is heating oil whose physical properties are appreciably different from those of water (σ = 0.0307 kg/s^2, μ_L = 0.00275 kg/ms). Again, the agreement between the experimental data and the lines drawn to represent Eq. (10) is clearly very satisfactory.

In Fig. 6 the Sauter mean diameter of the spray is shown plotted against air/liquid ratio. The four lines drawn in this figure represent the predictions of Eq. (10) for four different values of water flow rate. Also contained in this figure are the experimental data obtained for these same values of liquid flow rate at five different velocities, ranging from 32.6 to 59.5 m/s. Figure 6 shows that Eq. (10) predicts the experimental data obtained at all air velocities quite accurately for liquid

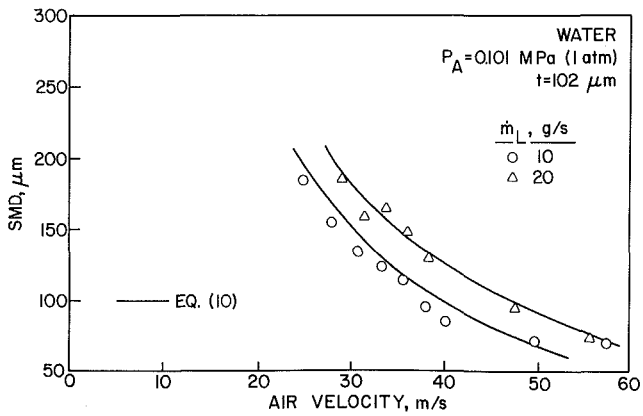

Fig. 3 Influence of air velocity on mean drop size for water

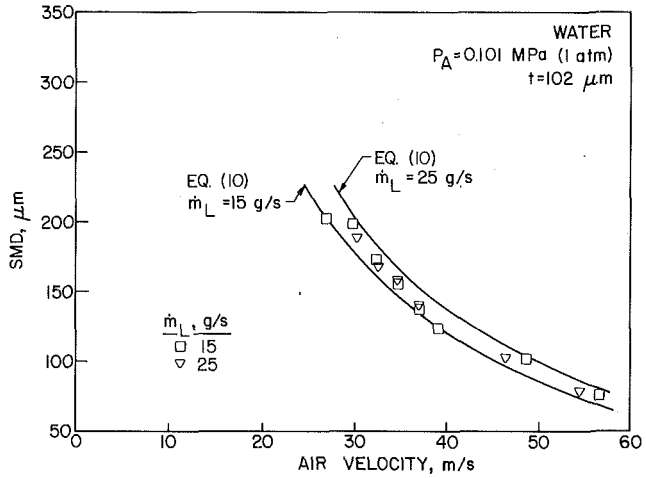

Fig. 4 Influence of air velocity on mean drop size for water

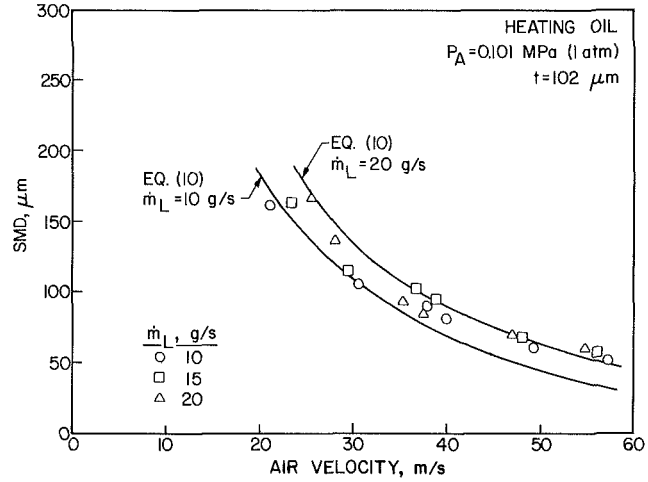

Fig. 5 Influence of air velocity on mean drop size for heating oil

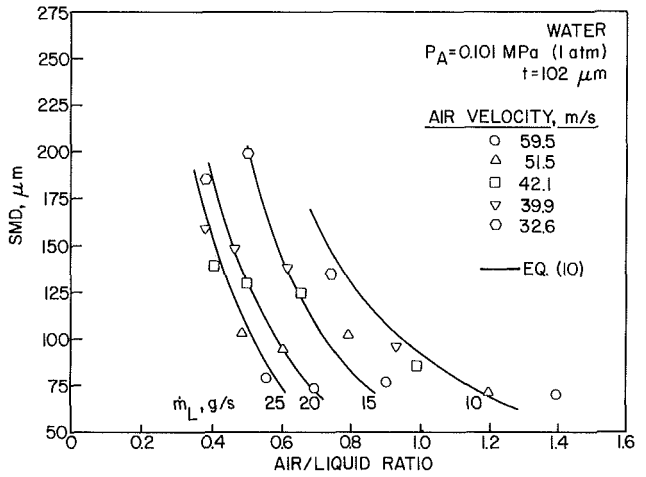

Fig. 6 Influence of air/liquid ratio and air velocity on mean drop size

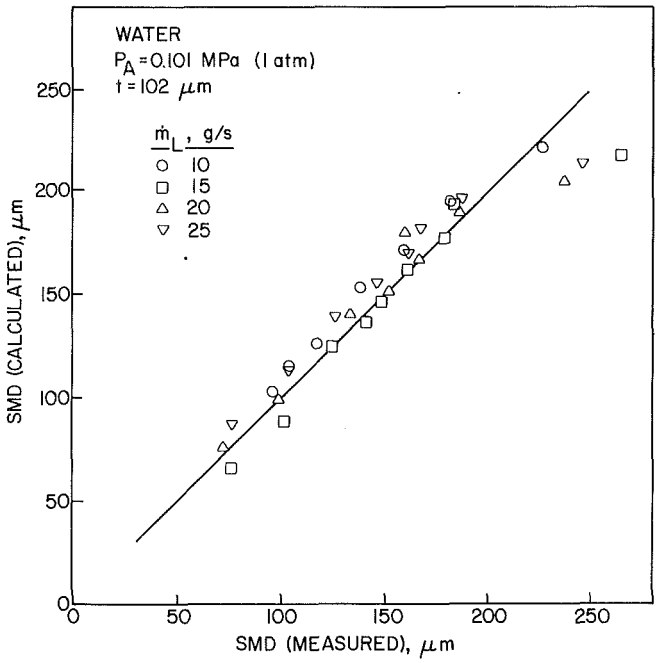

Fig. 7 Comparison of measured and calculated values of mean drop size

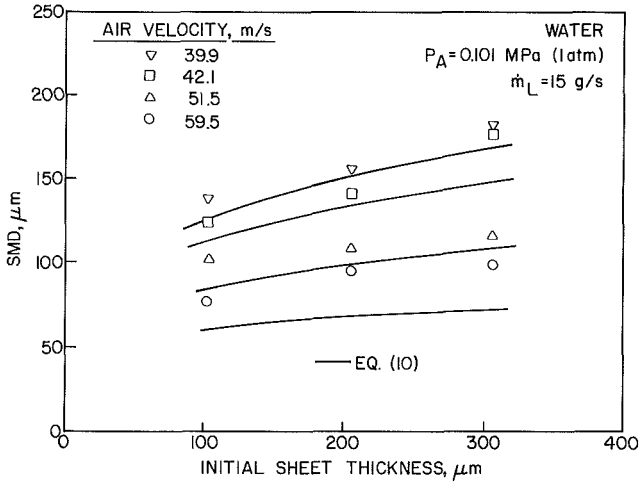

Fig. 8 Influence of initial liquid sheet thickness on mean drop size

flow rates of 20 and 25 g/s. Agreement between theory and experiment is also reasonably good for a liquid flow rate of 15 g/s, but is less satisfactory for the results obtained at a flow rate of 10 g/s, corresponding to the highest values of ALR.

Figure 7 contains all the experimental data on SMD obtained at normal atmospheric pressure for water flow rates of 10, 15, 20, and 25 g/s. In all tests, the initial liquid sheet thickness was kept constant at 102 μm. The purpose of Fig. 7 is to provide a comparison between measured values of SMD and the corresponding values calculated from Eq. (10). The level of agreement exhibited in Fig. 7 is good enough to lend credence to the notion that, for the method of air atomization under consideration, the ratio of the energy that is available for atomization to the energy required for atomization is a criterion of relevance to mean drop size.

The influence of initial sheet thickness on atomization quality is demonstrated in Fig. 8 in which SMD is shown plotted against t for air velocities of 39.9, 42.1, 51.5, and 59.5 m/s. The four lines drawn in this figure represent the predicted variations of mean drop size with initial liquid sheet thickness, as given by Eq. (10), for the same four air velocities. Although the absolute values of SMD are not well predicted by Eq. (10), Fig. 8 demonstrates a fairly good agreement between theory and experiment in regard to the general influence of variations in sheet thickness on mean drop size. It is evident in this figure that the effect of initial sheet thickness on mean drop size is quite small for the highest atomizing air velocity (59.5 m/s), but becomes increasingly significant with reduction in atom-

izing air velocity. For the highest air velocity (59.5 m/s), Eq. (10) predicts that SMD $\propto t^{0.125}$. For the lowest air velocity (39.9 m/s), the line drawn to represent Eq. (10) corresponds to SMD $\propto t^{0.29}$. These exponents of 0.125 and 0.29 should be compared with the theoretical value of 0.5 (Dombrowski and Johns, 1963) for wavy-sheet formation and the value of 0.4 obtained experimentally by Rizk and Lefebvre (1980). Consideration of these various exponents for initial sheet thickness suggests that, as the air velocity declines, the value of the exponent gradually increases toward the theoretical value of 0.5. This finding is consistent with the notion that reduction in air velocity normal to the liquid sheet is conducive to wave formation, until finally, for coflowing air and liquid streams, the classical wavy sheet formation becomes the dominant mechanism for atomization.

Figure 9 shows experimental data obtained with water at an ambient air pressure of 0.507 MPa (5 atm). The two lines drawn in this figure represent the predictions of Eq. (10) for the maximum and minimum liquid flow rates employed. Thus, ideally, all the data points in Fig. 9 should fall between these two lines. Inspection of Fig. 9 shows that the level of agreement between theory and experiment is generally satisfactory, at least in the velocity range from 25 to 60 m/s. As mentioned above, low air velocities are conducive to wave formation, and the discrepancy between theory and experiment exhibited in Fig. 9 for air velocities below 20 m/s is attributed to the intervention of the wavy sheet mechanism in the overall atomization process.

Figure 10 shows measured values of SMD along with the corresponding predicted values from Eq. (10). The data contained in this figure were obtained by injecting water through a slot of height 102 μm into atomizing air at pressures of 0.101, 0.305, and 0.507 MPa (1, 3, and 5 atm). Water flow rates were varied from 10 to 25 g/s. Figure 10 demonstrates generally good agreement between theory and experiment for all three levels of atomizing air pressure.

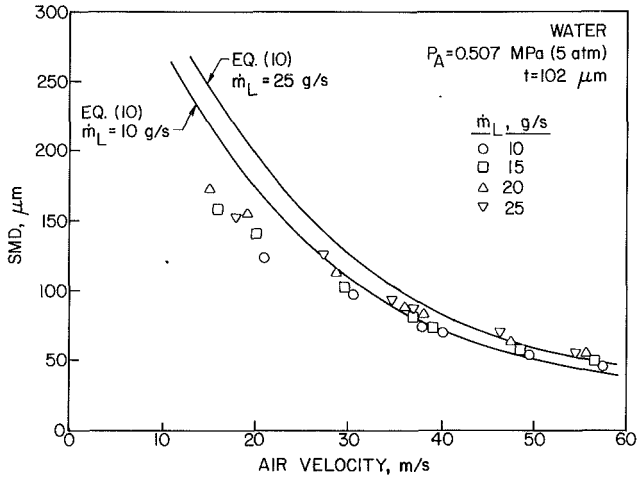

Fig. 9 Influence of air velocity on mean drop size

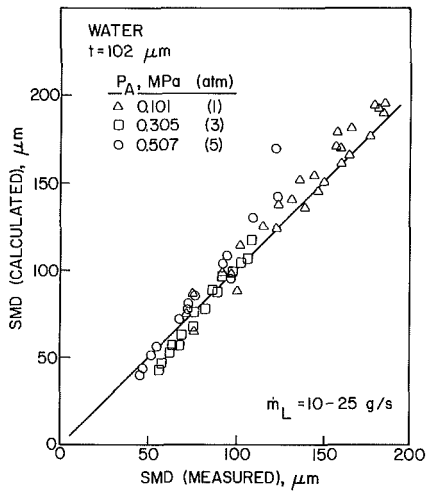

Fig. 10 Comparison of measured and calculated values of mean drop size

Discussion

Figures 3–9 allow comparisons to be made between values of mean drop size as calculated from Eq. (10) and the actual experimental data. From inspection of these figures it is clear that agreement between theory and experiment is generally satisfactory, especially for the results obtained using high atomizing air velocities at normal atmospheric pressure.

Of special interest is that Eq. (10) appears to provide a reasonably good prediction of the influence of ambient air pressure on mean drop size (see Fig. 10) even though it does not contain an air pressure term. However, it should be noted that all experiments were performed using the same set of values of liquid flow rate, namely 10, 15, 20, and 25 g/s, regardless of ambient air pressure. Thus, for any given liquid flow rate, increase in air pressure was always accompanied by a corresponding increase in air/liquid mass ratio. It is, of course, the effect of the concomitant variations in air/liquid ratio on mean drop size that is predicted by Eq. (10), not the change in air pressure. From analysis of the experimental data, Beck et al. (1989b) found that mean drop size does, in fact, diminish slightly with increase in air pressure. The effect is clearly quite small because the satisfactory correlation of data shown in Fig. 10 was obtained using Eq. (10), which takes no account of variations in air pressure. Nevertheless, the absence of a term to denote the influence of air pressure (or density) on mean drop size must be regarded as a deficiency of Eq. (10).

This drawback to Eq. (10) stems from the fact that it was derived solely in terms of the ratio of the energy required for atomization to the kinetic energy of the atomizing air. Now in most practical atomizers in which air is used as the driving force for atomization, the air attains its maximum velocity at the plane or region where it first makes contact with the liquid to be atomized; in fact, this is the hallmark of good atomizer design. Immediately downstream of this contact region is a potential core in which the air velocity remains sensibly constant (actually it declines somewhat as it imparts kinetic energy to the relatively slow moving liquid material), but downstream of the potential core the air velocity falls off fairly rapidly as it exchanges momentum with the ambient air or gas. This is an important point because it means that in addition to the liquid properties and gas properties that are normally included in all dropsize equations, consideration should also be given to the *time* available for droplets to be formed. In common with all other expressions for mean drop size, Eq. (10) takes no account of the time required for atomization. In this context, it should be borne in mind that the total atomization process actually comprises two separate processes, one of which, primary atomization, represents the initial breakup of the liquid sheet emerging from the nozzle into shreds and globules, while the subsequent process, secondary atomization, represents the conversion of the large drops and globules formed in primary atomization into droplets of various sizes. It is recognized that both processes must occupy a certain amount of time, with the time required for the conversion of globules into droplets being relatively long in comparison with the time required for the initial sheet breakup. The significance of time to mean drop size stems from the fact that if, for any reason, atomization is delayed, it will take place farther downstream from the nozzle in a region where the ligaments and globules

are being accelerated by a decelerating air stream. This momentum exchange between the liquid material and the atomizing air causes the relative velocity between the liquid and the surrounding air to decline with increase in downstream distance, so that when breakup finally occurs it does so in a region of lower relative velocity and the resulting drop sizes are larger.

According to Haas (1964) the breakup time of a liquid globule of diameter D_g is given by

$$t_b = 1.085 \frac{D_g}{U_A} \left(\frac{\rho_L}{\rho_A}\right)^{0.5} \tag{11}$$

Equation (11) is relevant to the present discussion because it raises the possibility that the influence of air density on mean drop size may be manifested not solely through its effect on air momentum ($\rho_A U_A^2$), but also through its influence on breakup time. Thus the observed small dependence of mean drop size on air density in the experiments of Beck et al. (1988) may be due in some measure to the influence of air density on breakup time, as indicated by Eq. (11).

Another possible explanation for the observed beneficial effect of an increase in air pressure on atomization quality is that it increases the effectiveness of the interaction between the atomizing air and the liquid sheet. As alluded to earlier in connection with the influence of air/liquid ratio on mean drop size, air that is physically far removed from the liquid sheet is much less effective from an atomization standpoint than air that is in close proximity to the liquid sheet. This means that an increase in air pressure, for constant values of air velocity and mass flow rate, would produce a more compact and, therefore, a more effective air jet, which would raise the value of C' in Eq. (9).

Conspicuous by its absence in Eq. (9) is a term to account for the effect of liquid viscosity on atomization. Although in the present theory this property should have no influence on atomization quality, in practice, by slowing down the atomization process and thereby causing it to extend into the regions of relatively low air velocity downstream of the initial impact zone, the effect of an increase in liquid viscosity is to raise the mean drop size of the spray.

Plain-Jet Airblast Atomization

Similar arguments to those employed above for flat-sheet atomizers may be used to explain the difference in atomizing performance between the two plain-jet airblast atomizers shown in Fig. 2. Equation (9), in which mean drop size is expressed in terms of liquid sheet thickness, is relevant only to prefilming airblast atomizers in which the liquid is converted into a thin sheet before being exposed on both sides to high-velocity air.

For a plain-jet airblast atomizer we have

$$A_{L_1} = \frac{4m_L}{\rho_L d_o} \tag{12}$$

where d_o is the initial diameter of the liquid jet

$$A_{L_2} = \frac{6m_L}{\rho_L D} \tag{4}$$

$$E_L = \frac{2\sigma m_L}{\rho_L}\left[\frac{3}{D} - \frac{2}{d_o}\right] \tag{13}$$

and

$$\text{SMD} = \frac{3}{\left[\dfrac{2}{d_o} + \dfrac{C^*\rho_L U_A^2}{4\sigma(1+1/\text{ALR})}\right]} \tag{14}$$

To the author's knowledge, no suitable experimental data are available against which to check the validity of this equation. [Note: The Rizk and Lefebvre data (1984) were obtained with an atomizer of the type shown in Fig. 2*b*, which features coflowing air and liquid streams.]

Summary and Conclusions

In common with many practical forms of airblast atomizers, the specially designed flat sheet atomizer used in the experimental program of Beck et al. employs a system of air and liquid flow passages that are so arranged that the atomizing air, instead of flowing parallel to the liquid sheet, impinges on it at an appreciable angle. This method of air impaction prevents the wavy-sheet formation that in classical theories of liquid sheet disintegration is generally regarded as an essential first step in the atomization process. Before any waves have time to develop, the liquid sheet emerging from the nozzle is completely disrupted by the atomizing air. Under these conditions, the mean drop size in the spray is controlled mainly by the ratio of the energy required for atomization to the kinetic energy of the atomizing air. These considerations lead to the following equation for mean drop size:

$$\text{SMD} = \frac{3}{\left[\dfrac{1}{t} + \dfrac{0.007\rho_L U_A^2}{4\sigma(1+1/\text{ALR})}\right]} \tag{10}$$

It is found that the values of mean drop size given by the above equation demonstrate reasonably good agreement with the corresponding measured values obtained using water and heating oil over wide ranges of air velocity, air/liquid ratio, and ambient air pressure.

The value of 0.007 for the constant in Eq. (10) was chosen to provide the best fit to the experimental data of Beck et al. who employed the atomizer shown schematically in Fig. 1(*b*). This atomizer is characterized by an angle of air impingement on the liquid sheet of 30 deg. Changes in the angle at which the atomizing air impacts the liquid sheet would be expected to affect the efficiency of the atomization process and thereby change the value of the constant in Eq. (10). This aspect calls for further investigation.

Although no suitable experimental data are available against which to check this hypothesis, it is postulated that the dissimilar spray characteristics exhibited by the two different designs of plain jet atomizer shown in Fig. 2 are also due to two different modes of atomization, the wavy-jet mechanisms in one case (2*b*) and prompt atomization in the other (2*a*). For the prompt atomization process, the mean drop size is given by

$$\text{SMD} = \frac{3}{\left[\dfrac{2}{d_o} + \dfrac{C^*\rho_L U_A^2}{4\sigma(1+1/\text{ALR})}\right]} \tag{14}$$

References

Beck, J. E., Lefebvre, A. H., and Koblish, T. R., 1991, "Airblast Atomization at Conditions of Low Air Velocity," *AIAA Journal of Propulsion and Power*, Vol. 7, No. 2, pp. 207–212.

Beck, J. E., Lefebvre, A. H., and Koblish, T. R., 1991, "Liquid Sheet Disintegration by Impinging Air Streams," *Atomization and Sprays*, Vol. 1, No. 2, pp. 155–170.

Dombrowski, N., and Johns, W. R., 1963, "The Aerodynamic Instability and Disintegration of Viscous Liquid Sheets," *Chemical Engineering Science*, Vol. 18, pp. 203–214.

Fraser, R. P., Eisenklam, P., Dombrowski, N., and Hasson, D., 1962, "Drop Formation From Rapidly Moving Sheets," *AIChE Journal*, Vol. 8, No. 5, pp. 672–680.

Haas, F. C., 1964, "Stability of Droplets Suddenly Exposed to a High Velocity Gas Stream," *AIChE Journal*, Vol. 10, pp. 920–924.

Jasuja, A. K., 1979, "Atomization of Oxide and Residual Fuel Oils," ASME JOURNAL OF ENGINEERING FOR POWER, Vol. 101, No. 2, pp. 250–258.

Lefebvre, A. H., and Miller, D., 1966, "The Development of an Airblast Atomizer for Gas Turbine Applications," College of Aeronautics Report Aero No. 193.

Lefebvre, A. H., 1980, "Airblast Atomization," *Prog. Energy Combust. Sci.*, Vol. 6, pp. 233–261.

Nukiyamo, S., and Tanasawa, Y., 1939, "Experiments on Atomization of Liquids," *JSME*, 6 parts, English translation by the Department of National Defence, Canada, pp. 1938–40.

Rizk, N. K., and Lefebvre, A. H., 1980, "Influence of Liquid Film Thickness on Airblast Atomization," ASME JOURNAL OF ENGINEERING FOR POWER, Vol. 102, pp. 706–710.

Rizk, N. K., and Lefebvre, A. H., 1984, "Spray Characteristics of Plain-Jet Airblast Atomizers," ASME JOURNAL OF ENGINEERING FOR POWER, Vol. 106, pp. 634–638.

Rosin, P., and Rammler, E., 1933, "The Laws Governing the Fineness of Powdered Coal," *Journal of the Institute of Fuel*, Vol. 7, No. 31, Oct., pp. 29–36.

Squire, H. B., 1953, "Investigation of the Instability of a Moving Liquid Film," *Brit. J. Appl. Phys.*, Vol. 4, pp. 167–169.

Factors Influencing the Effective Spray Cone Angle of Pressure-Swirl Atomizers

S. K. Chen

A. H. Lefebvre

Thermal Science and Propulsion Center,
Purdue University,
West Lafayette, IN 47907

J. Rollbuhler

NASA-Lewis Research Center,
Cleveland, OH 44135

The spray cone angles produced by several simplex pressure-swirl nozzles are examined using three liquids whose viscosities range from 0.001 to 0.012 kg/ms (1 to 12 cp). Measurements of both the visible spray cone angle and the effective spray cone angle are carried out over wide ranges of injection pressure and for five different values of the discharge orifice length/diameter ratio. The influence of the number of swirl chamber feed slots on spray cone angle is also examined. The results show that the spray cone angle widens with increase in injection pressure but is reduced by increases in liquid viscosity and/or discharge orifice length/diameter ratio. Variation in the number of swirl chamber feed slots between one and three has little effect on the effective spray cone angle.

Introduction

In most applications the function of the atomizer is not merely to disintegrate the liquid into small drops but also to discharge these drops into the surrounding gaseous medium in the form of a symmetric, uniform spray. With plain-orifice atomizers and certain types of pressure-swirl atomizers the drops are fairly evenly dispersed throughout the entire spray volume. Sprays of this type are often described as "solid." For many combustion applications a solid spray is considered undesirable because it can give rise to excessive concentrations of soot and particulates in the exhaust gases. In such situations a "hollow-cone" spray of wide cone angle is generally preferred, in which most of the fuel is contained in the larger drops that are concentrated at the periphery.

Hollow-cone, pressure-swirl atomizers are widely used as fuel injectors in gas turbine combustion chambers. The hollow conical structure of the spray incurs appreciable exposure to the influence of the surrounding air. Normally, an increase in spray cone angle increases the extent of this exposure, leading to improved atomization, better fuel-air mixing, and better dispersion of the fuel drops throughout the combustion volume. This is why the spray cone angle is such an important characteristic of a swirl atomizer. Experience with gas turbine combustors has shown that swirl atomizers with wide spray angles are usually characterized by a good "pattern factor," i.e., a fairly uniform distribution of temperature in the combustion products flowing into the turbine, and by relatively low concentrations of soot in the exhaust gases. However, reductions in spray cone angle can sometimes be beneficial in improving lean blowout and lean lightoff limits, and in reducing combustion inefficiency at low power conditions. For these reasons, considerable interest exists in the manner and extent to which spray cone angle is influenced by atomizer design features and liquid properties.

Contributed by the International Gas Turbine Institute and presented at the 1989 ASME COGEN-TURBO III, Nice, France, August 1989. Manuscript received at ASME Headquarters December, 1990.

Previous Work

According to Taylor's (1948) inviscid theory, the spray cone angle is determined solely by the swirl chamber geometry and is a unique function of the ratio of the inlet ports area to the product of swirl chamber diameter and orifice diameter, $A_p/D_s d_o$. This relationship is modified in practice by viscous effects, which depend on the form and area of the wetted surface. Agreement between theory and experiments carried out on nozzles of low l_o/d_o ratio is generally satisfactory for large cone angles, but the theoretical predictions are about 3 deg too low at a cone angle of 60 deg (Giffen and Massey, 1950; Carlisle, 1955).

Giffen and Muraszew's (1953) analysis of the flow in a swirl atomizer assumed a nonviscous liquid, which allowed the spray cone angle to be expressed as a function of nozzle dimensions only. It led to the following expression for the mean value of the spray cone half angle:

$$\sin \theta_m = \frac{(\pi/2)(1-X)^{1.5}}{K(1+\sqrt{X})(1+X)^{0.5}} \tag{1}$$

where $K = A_p/D_s d_o$ and $X = A_a/A_o$.

This equation gives a relationship between the atomizer dimensions, the size of the air core, and the mean spray cone angle. To eliminate one of these variables, Giffen and Muraszew (1953) derived the following expression for K in terms of X:

$$K = \frac{\pi(1-X)^{1.5}}{\sqrt{32X}} \tag{2}$$

Equations (1) and (2) allow the spray cone angle to be expressed in terms of either X or K. Rizk and Lefebvre (1985a) also derived the following equation for cone angle in terms of X:

$$\cos^2 \theta_{\max} = \frac{1-X}{1+X} \tag{3}$$

X is directly related to the liquid film thickness in the final discharge orifice, since the difference between the air core

diameter and the discharge orifice diameter is equal to twice the liquid film thickness. We have

$$X=\frac{(d_o-2t)^2}{d_o^2} \tag{4}$$

It should be noted that Eqs. (1) and (3) relate to the cone half-angle as measured close to the nozzle. Farther downstream of the nozzle the spray acquires curved boundaries owing to the effects of air entrainment on the spray. Furthermore, as the initial spray has a small but definite thickness, two different cone angles may be defined in this near-nozzle region: $2\theta_{\max}$ is the cone angle formed by the outer boundary of the spray, while $2\theta_{\max}$ represents the mean cone angle.

According to Eqs. (1)–(3), the spray cone angle is a function of atomizer dimensions only, as embodied in the relationship $K = A_p/D_s d_o$, and is independent of liquid properties, ambient air properties, and injection pressure. Rizk and Lefebvre's studies (1985b) on the effects of liquid properties, atomizer dimensions, and injection pressure on film thickness enabled them to derive the following equation for the mean spray angle:

$$2\theta_m = 6K^{-0.15}\left(\frac{\Delta P_L d_0^2 \rho_L}{\mu_L^2}\right)^{0.11} \tag{5}$$

According to this equation, the mean spray cone angle is increased by increases in discharge orifice diameter, liquid density, and injection pressure, and is diminished by an increase in liquid viscosity. A similar dependence of spray cone angle on liquid viscosity had been reported previously by Giffen and Massey (1950). From tests carried out on a swirl-plate atomizer over a range of viscosities from 2×10^{-6} to 50×10^{-6} m^2/s (2 to 50 cS), they found that the relation between the cone half-angle and viscosity could be expressed by the empirical equation

$$\tan \theta_{\max} = 0.169\nu_L^{-0.131} \tag{6}$$

According to Eqs. (5) and (6), surface tension should have no effect on spray cone angle, and this is generally confirmed by experiment (Giffen and Massey, 1950; Wang and Lefebvre, 1987).

In the present study attention is focused on the principal atomizer dimensions of relevance to spray cone angle, namely l_o, d_o, and l_o/d_o, and also on the influence of liquid viscosity.

Experimental

Seven simplex nozzles conforming to the basic design shown in Fig. 1 were specially manufactured for this program by the Delavan Company, all having the same flow number of 8×10^{-8} m^2. Five of these nozzles have the same discharge orifice diameter, d_o, of 0.457 mm, but the length/diameter ratio of the discharge orifice is different for each nozzle, the actual values being 0.5, 1.0, 2.0, 3.0, and 4.0. These five nozzles

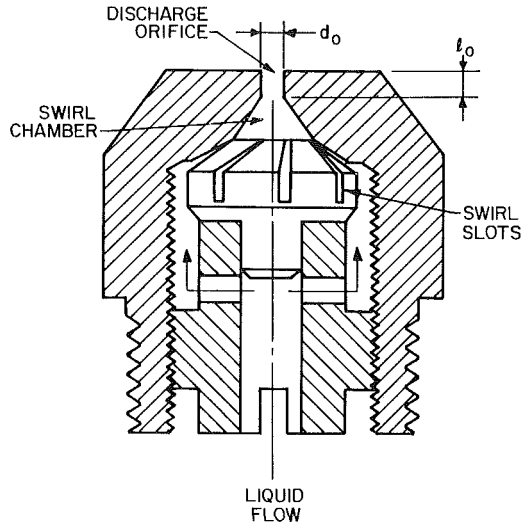

Fig. 1 Basic design of simplex atomizer

allow the effects of liquid viscosity and nozzle operating conditions to be examined for several values of d_o, l_o, and l_o/d_o, in a manner that permits the separate effects of these geometric parameters on atomization performance to be readily determined.

The nozzles described above employ three slots of rectangular cross section for feeding liquid into the swirl chamber. These tangentially cut slots are located 120 deg apart on the 360 deg circumference. In order to investigate the influence of number of feed slots on spray cone angle, two additional atomizers were made and tested. One nozzle features two diametrically opposite feed slots, while the other has a single feed slot. Both the single-slot and double-slot nozzles have the same total flow area as the three-slot nozzles, so the flow number should be about the same for all three nozzles.

The apparatus used to measure spray characteristics is shown schematically in Fig. 2. Liquid is supplied to the nozzle from a nitrogen-pressurized tank. The amount of liquid ejected from the nozzle is controlled by a hand-operated valve located in the bypass line. A number of valves, pressure gages, and flow meters are located in the nozzle feed line to provide the desired nozzle operating conditions in terms of liquid injection pressure and mass flow rate.

Two methods are used to determine the spray-cone angle. One method employs a Nikon F2, 35 mm single lens reflex camera in conjunction with a microflash of 0.5 μs duration to obtain high-speed snapshots of the spray. Some typical photographs are shown in Figs. 5 and 6. A major drawback to this technique is that the photographs indicate only the outer

Nomenclature

A_a = air core area, m^2
A_o = discharge orifice area, m^2
A_p = total cross-sectional area of swirl chamber feed slots, m^2
D_s = swirl chamber diameter, m
d_o = discharge orifice diameter, m
FN = flow number of atomizer = $\dot{m}_L/(\Delta P_L \rho_L)^{0.5}$, m^2
K = $A_p/D_s d_o$
l_o = length of discharge orifice, m
$\dot{m}_L$ = liquid flow rate, kg/s
ΔP_L = injection pressure, Pa
t = liquid film thickness in discharge orifice, m
X = A_a/A_o
y = liquid volume measured at the angle θ, m^3
θ = angular location of sampling tube center line, deg
$\theta_{\max}$ = maximum spray cone half-angle, deg
θ_m = mean spray cone half-angle, deg
θ_{eff} = effective mean spray cone angle, deg
μ_L = absolute liquid viscosity, kg/ms
ν_L = kinematic liquid viscosity, m^2/s
ρ_L = liquid density, kg/m^3

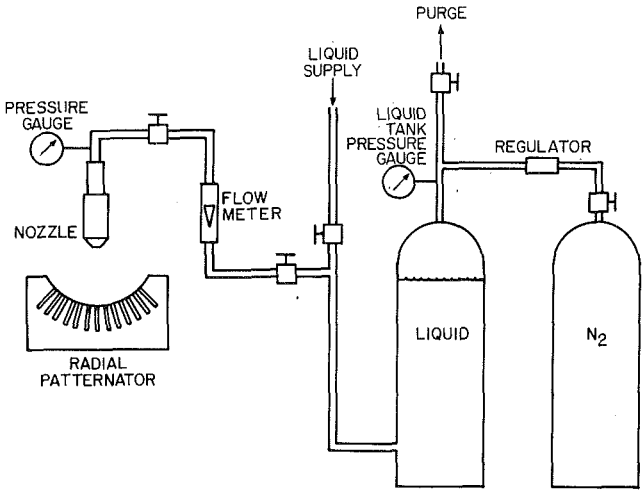

Fig. 2 Schematic layout of test rig

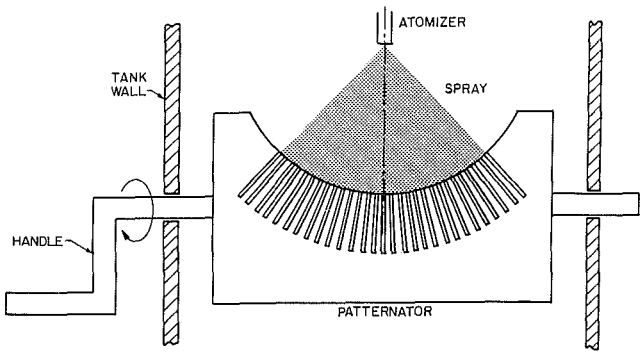

Fig. 3 Patternator for measurement of radial liquid distribution

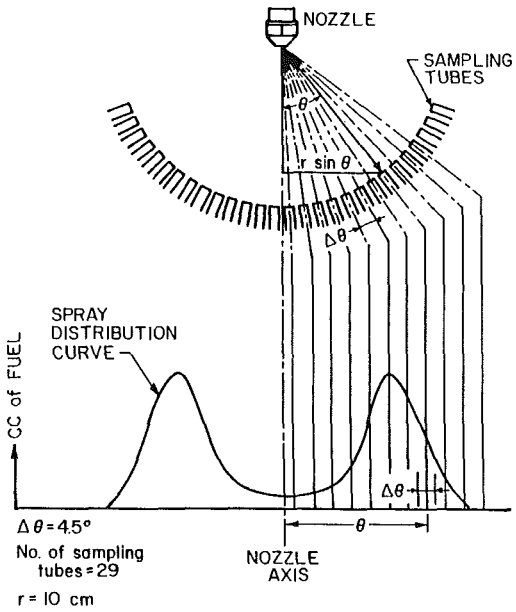

Fig. 4 Measurement of radial liquid distribution

boundaries of the spray and provide no information on the radial distribution of liquid within the spray. For these reasons, some workers prefer to measure the *effective* or *equivalent* cone angle of the spray. This technique, which is described below, provides a quantitative description of the radial distribution of liquid mass flux within the spray. The *effective* angle of the spray is measured using a patternator of the type illustrated in Fig. 3. This patternator is 1.27 cm deep and 31.75 cm wide. The sampling tubes were formed by cutting slots into the opaque white plastic base over which a clear thin sheet of plastic is glued. The outer edges that form the openings to the tubes are filed to sharp edges so that each tube has a well-defined sampling area. The tubes are almost square in cross section, each tube having an area of 0.504 cm^2. There are a total of 29 sampling tubes, spaced 4.5 deg apart along a radius of curvature of 10 cm. For each nozzle and each fluid the height of the nozzle above the patternator is determined by the need to ensure that the outer regions of the spray are always just inside the capture area of the patternator.

Before a spray sample is taken, the liquid flow rate is adjusted until the nozzle is operating at the desired conditions. At this point a container into which the liquid has been flowing is removed, and the sampling tubes begin to fill. When one of the tubes is nearly full, the liquid supply is turned off and the residual flow is diverted away from the patternator.

The volume of liquid in each tube is measured by visually locating the meniscus between lines scribed into the clear plastic of the patternator. Liquid distribution curves are made by plotting liquid volume as the ordinate and the corresponding angular location of the sampling tubes as the abscissa, as shown in Fig. 4. The method has been fully described by DeCorso and Kemeny (1957) and Ortman and Lefebvre (1985).

A problem arising in all radial patternation studies is that of deciding which portion of the spray should be sampled, bearing in mind that no practical atomizer produces a spray whose circumferential mass flux distribution is perfectly uniform. Ideally, radial patternation measurements should be carried out at a large number of angular locations in order to obtain an "average" value for the effective spray cone angle. In the present study the tedium associated with this procedure was avoided by measuring the circumferential liquid distribution of each individual nozzle. The technique employed has been described elsewhere (Lefebvre, 1989). The results obtained enabled an angular location to be identified that avoided any appreciable peaks or troughs in circumferential liquid distribution, and that could reasonably be considered as representative of the spray as a whole.

In order to describe more succinctly the effects of changes in operating parameters on radial liquid distribution, the curves of liquid volume versus angular position can be reduced to a single numerical value called the "effective spray cone angle." The effective spray angle is the sum of two angles, $\theta_{\text{eff}} = \theta_L + \theta_R$, which are calculated using the following equation:

$$\theta_L \text{ (or } \theta_R) = \frac{\Sigma y\theta\Delta\theta \sin\theta}{\Sigma y\Delta\theta \sin\theta} = \frac{\Sigma y\theta \sin\theta}{\Sigma y \sin\theta} \tag{7}$$

L and R represent the left and right lobes of the liquid distribution curve, respectively. θ is the angular location of the sampling tube centerline, $\Delta\theta$ the angle between the sampling tube centerlines, and y the liquid volume measured at the corresponding tube position. The physical meaning of the effective spray angle is that θ_L (or θ_R) is the value of θ that corresponds to the position of the center of the mass of a material system for the left- (or right-) hand lobe of the distribution curve.

The three liquids employed are water and two different mixtures of glycerine and water, to give viscosities of 0.001, 0.006, and 0.012 kg/ms. The addition of glycerine to water causes its surface tension to decline slightly (6 percent maximum) and its density to increase slightly (14 percent maximum) while increasing the viscosity by a factor of twelve. Thus, the results shown in Figs. 5–13 may be regarded as demonstrations of the influence of viscosity on spray-cone angle for essentially constant values of surface tension and density.

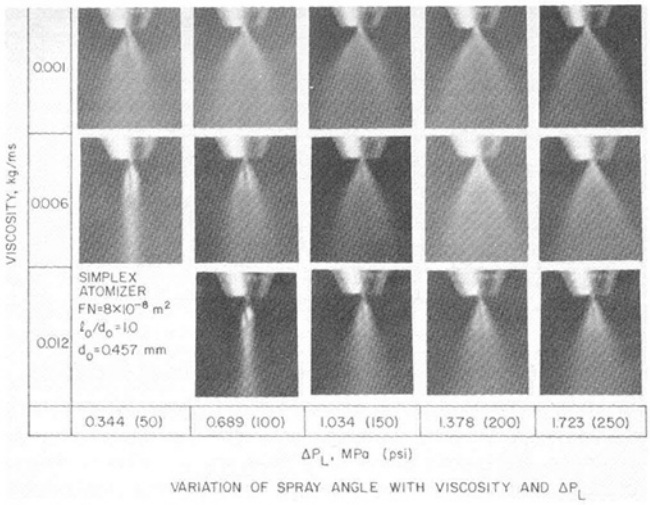

Fig. 5 Photographs illustrating the effects of liquid viscosity and injection pressure on visible spray angle

Results

In the course of this investigation a large amount of information was collected on the effects of liquid injection pressure, discharge orifice length/diameter ratio, and liquid viscosity on spray cone angle. The data obtained fall into two categories, those relating to the visible spray cone and those that describe the effective cone angle of the spray. These two aspects are discussed below in turn.

Visible Spray Cone Angle. The effects of injection pressure and liquid viscosity on the visible spray cone angle are shown in Fig. 5. The effect of an increase in ΔP_L on spray angle may be judged by viewing the individual snapshots in turn, moving from left to right. It is clear from these photographs that an increase in ΔP_L always serves to widen the spray angle. This effect is especially apparent for liquids of high viscosity. By inspecting any row of photographs from top to bottom the influence of liquid viscosity on spray angle may be discerned. In all cases an increase in μ_L causes this angle to decline. Figure 6 contains similar photographs to those in Fig. 5; their purpose is to demonstrate the effect of an increase in l_o/d_o on spray angle. The three horizontal rows of photographs in Fig. 6 represent three different levels of liquid viscosity. The pictures demonstrate that reductions in visible spray cone angle can be effected either by increasing the liquid viscosity or by increasing the length/diameter ratio of the final discharge orifice.

Effective Spray Cone Angle. Although the photographs contained in Figs. 5 and 6 enable some useful qualitative conclusions to be drawn on the effects of liquid properties and atomizer design features on spray cone angle, the edges of the spray are not sufficiently well defined to permit any kind of quantitative relationship between the relevant variables to be established. In any case, as discussed earlier, photographs such as Figs. 5 and 6 describe only the outer boundaries of the spray, and provide no information on the radial distribution of liquid mass flux within the spray boundary. For most practical purposes, the effective spray cone angle, as shown plotted in Figs. 7–13, not only provides a more useful description of the radial distribution of liquid mass flux in the spray, but can also be measured to a reasonable level of accuracy and expressed in quantitative terms.

The effects of injection pressure and discharge orifice length/diameter ratio on effective spray cone angle are illustrated in Fig. 7 for a liquid viscosity of 0.006 kg/ms. This figure shows that, over the range of injection pressures covered in these experiments, θ_{eff} increases with increase in ΔP_L. This same

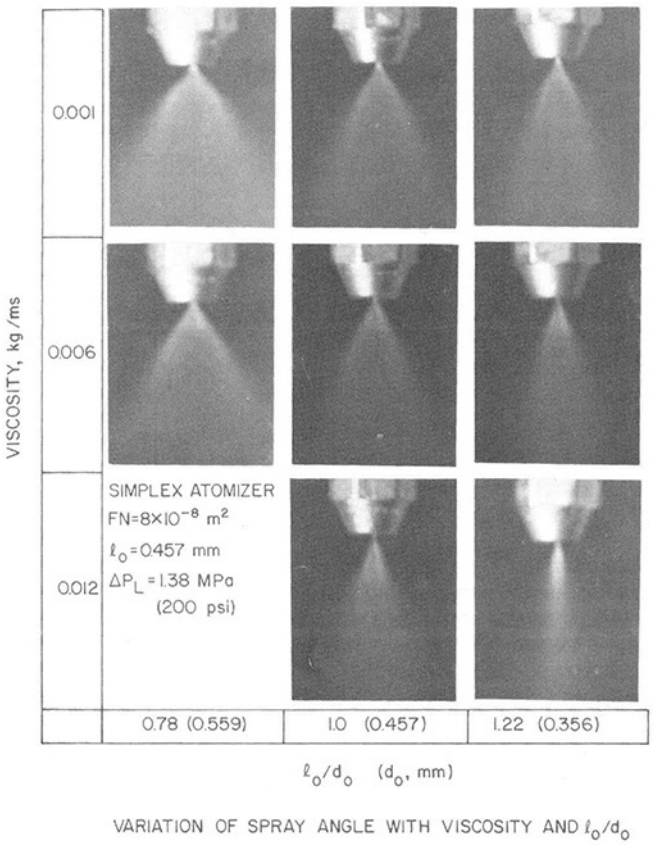

Fig. 6 Photographs illustrating the effects of liquid viscosity and discharge orifice length/diameter ratio on visible spray angle

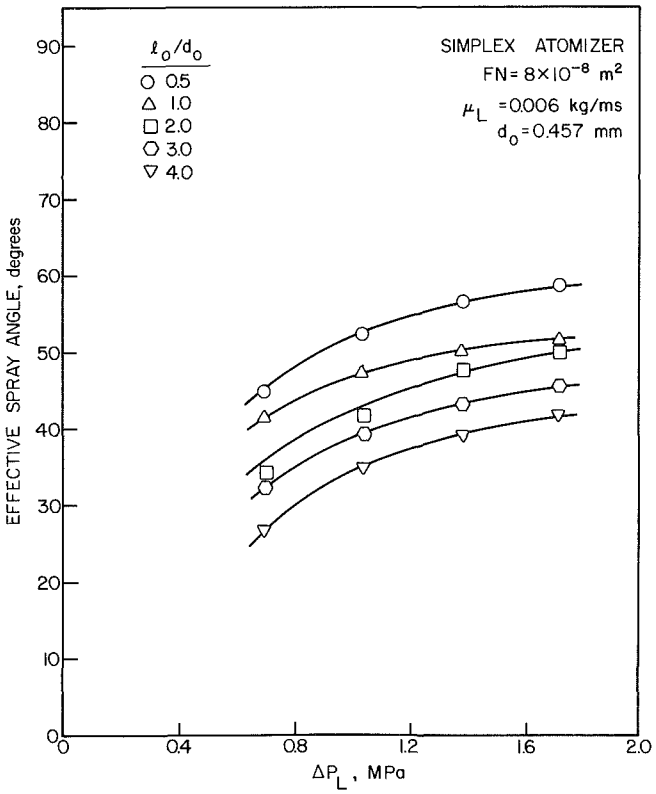

Fig. 7 Influence of injection pressure on effective spray angle

result was obtained at all other levels of liquid viscosity and for all values of discharge orifice length/diameter ratio. It is one of the reasons why the mean drop size declines with increase

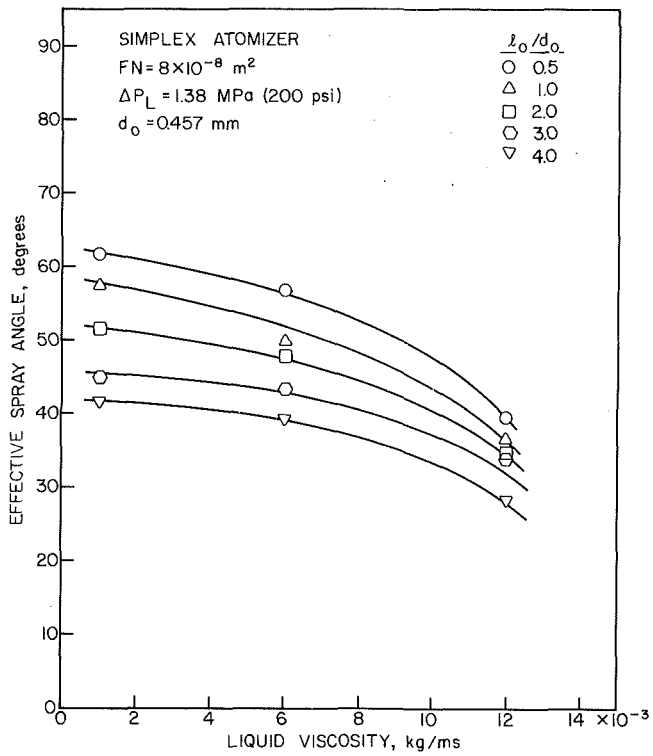

Fig. 8 Influence of liquid viscosity on effective spray angle

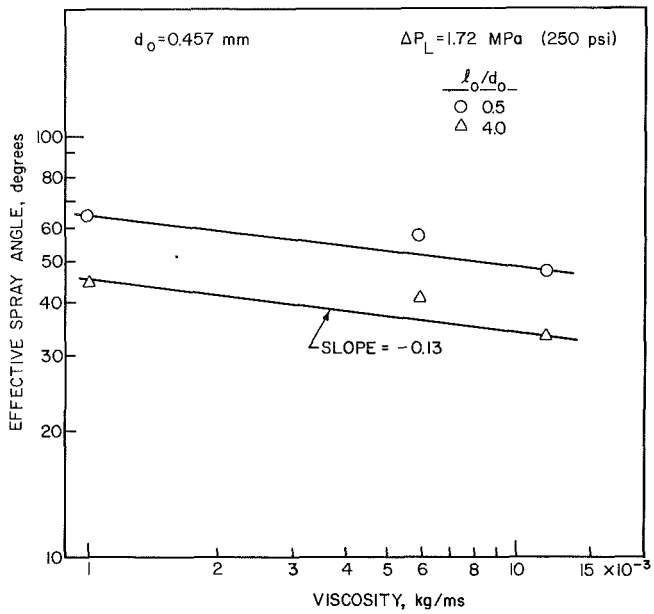

Fig. 9 Influence of liquid viscosity on effective spray angle

in ΔP_L (Lefebvre, 1987), since an increase in spray cone angle increases the interaction between the spray and the ambient air. However, θ_{eff} does not continue to increase indefinitely with increase in ΔP_L. Previous work, for example, Ortman and Lefebvre (1985), has shown that the effective spray angle widens as ΔP_L is raised until it attains a maximum value. Any further increase in ΔP_L beyond this point causes θ_{eff} to go down.

The influence of liquid viscosity on θ_{eff} is shown more directly in Figs. 8 and 9. Figure 8 illustrates how the spray cone angle diminishes with increase in viscosity, the effect becoming more pronounced at the highest level of viscosity. This figure contains experimental data obtained using five different nozzles to achieve wide variations in l_o/d_o, for a constant injection pressure of 1.38 MPa (200 psi). Similar data are plotted in logarithmic form in Fig. 9 for a higher level of injection pressure (1.72 MPa) and the two extreme values of l_o/d_o, namely 0.5 and 4.0. The lines drawn through the experimental points have a slope of -0.13, which is in exact agreement with the relationship between visible spray cone angle and liquid viscosity as measured by Giffen and Massey (1950) and expressed in Eq. (6). However, as one set of results relates to visible spray angle and the other to effective spray angle, the close agreement exhibited by these two sets of results must be regarded as somewhat fortuitous. Neither can a worthwhile comparison be made between the data acquired in the present study and the predictions of Eq. (5), since this equation applies only to the spray cone angle in the immediate vicinity of the nozzle and not to the effective spray cone angle as measured 10 cm downstream. Nevertheless, Eqs. (5) and (6) and Figs. 5, 6, and 8–11 are mutually consistent in showing that an increase in liquid viscosity always reduces the spray cone angle. This result is of considerable practical importance for continuous flow combustion systems, especially gas turbine combustors operating at high combustion pressures. It is well known (see, for example, Lefebvre, 1983) that an increase in fuel carbon/hydrogen ratio enhances flame radiation and raises the soot concentration in the combustor exhaust gases. However, for liquid hydrocarbons, an increase in carbon/hydrogen ratio is accompanied almost invariably by an increase in viscosity. Thus the higher rates of soot formation that characterize fuels of higher carbon/hydrogen ratio are not due solely to the change in fuel chemistry but also to the concomitant increase in viscosity which reduces the spray cone angle. This reduction in spray angle tends to raise the fuel concentration in the soot-forming zone, which normally lies on the combustor axis just downstream of the fuel nozzle.

The influence of discharge orifice length diameter ratio on effective spray cone angle is demonstrated in Figs. 10–12. Figure 10 shows θ_{eff} plotted against l_o/d_o for three different values of liquid viscosity. The data shown in this figure were obtained using a constant injection pressure of 1.03 MPa (150 psi). They demonstrate that increase in l_o/d_o reduces the effective spray cone angle. This finding can be explained on the grounds that spray cone angle is governed by the relative magnitudes of the axial and swirl components of velocity at the nozzle exit. For a constant liquid mass flow rate through the nozzle, the axial component of velocity remains constant and independent of liquid viscosity (assuming that Reynolds number remains high and neglecting the influence of viscosity on liquid film thickness) whereas the swirl component of velocity is greatly reduced by an increase in viscosity due to the higher frictional losses occurring along the walls of the final discharge orifice.

Figure 10 shows that the influence of orifice length/diameter ratio on spray angle diminishes with increase in liquid viscosity, and this is confirmed by the results presented in Fig. 11, which were obtained at a higher level of injection pressure (1.72 MPa, or 250 psi). The logarithmic plots of spray angle versus l_o/d_o in Fig. 11 show three straight lines for the three different values of liquid viscosity. The slopes of these lines conform to the relationship $\theta_{\text{eff}} \approx (l_o/d_o)^x$ where x varies from -0.20 for a liquid viscosity of 0.001 kg/ms to -0.125 for a viscosity of 0.012 kg/ms.

Generally it is found that the relationship between effective spray cone angle and l_o/d_o is not affected by changes in injection pressure. This is evident in Fig. 12, which shows the results of measurements made over a range of values of l_o/d_o for three different injection pressures. From inspection of this figure it is clear that, despite the strong influence of injection pressure on spray cone angle, it does not markedly affect the relationship between spray angle and l_o/d_o.

The simplex nozzles employed in this investigation conform to standard Delavan practice in their use of three equispaced slots for feeding the liquid into the swirl chamber. At the

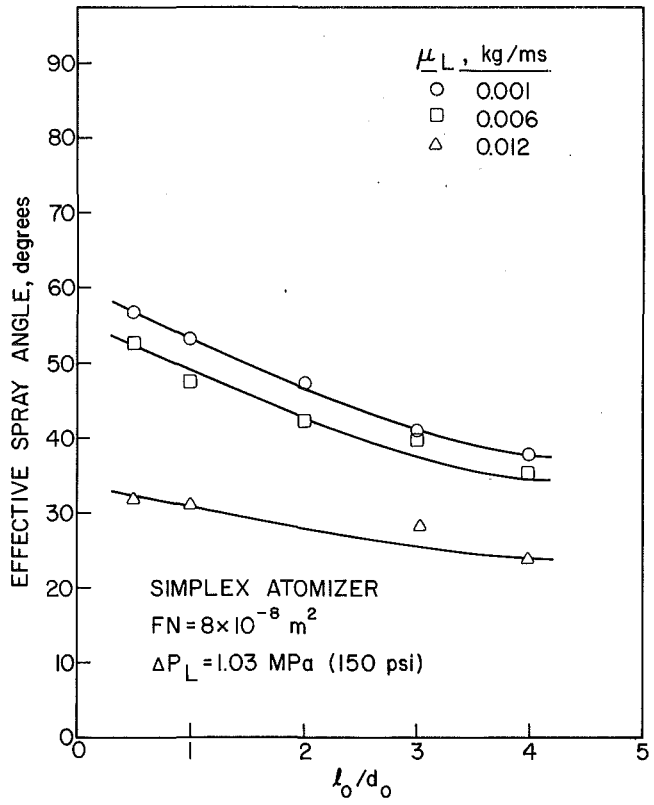

Fig. 10 Influence of l_o/d_o on effective spray angle for a ΔP_L of 1.03 MPa (150 psi)

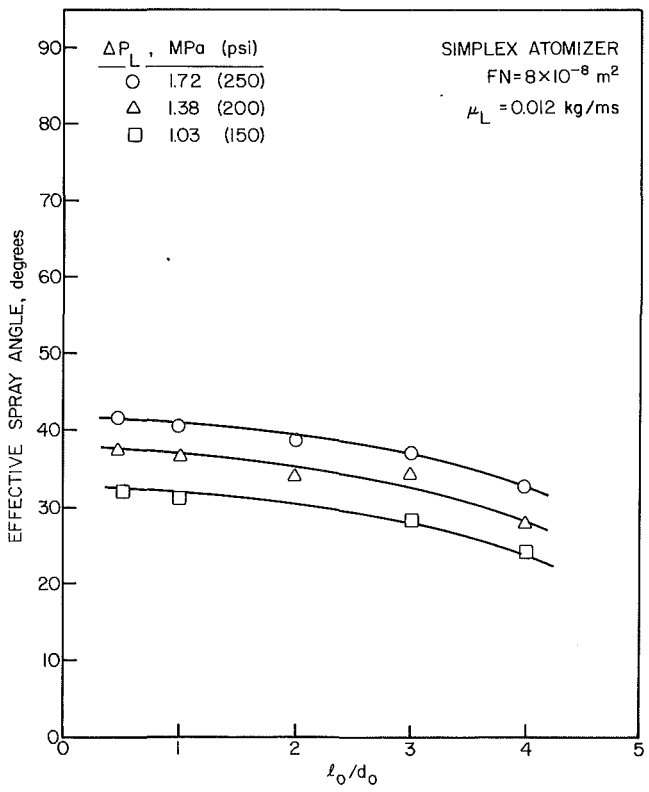

Fig. 12 Influence of l_o/d_o on effective spray angle for a constant liquid viscosity

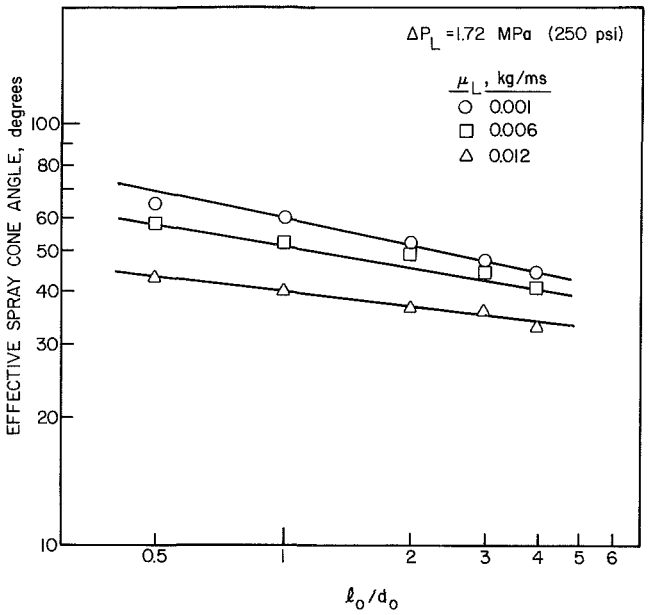

Fig. 11 Influence of l_o/d_o on effective spray angle for a constant injection pressure

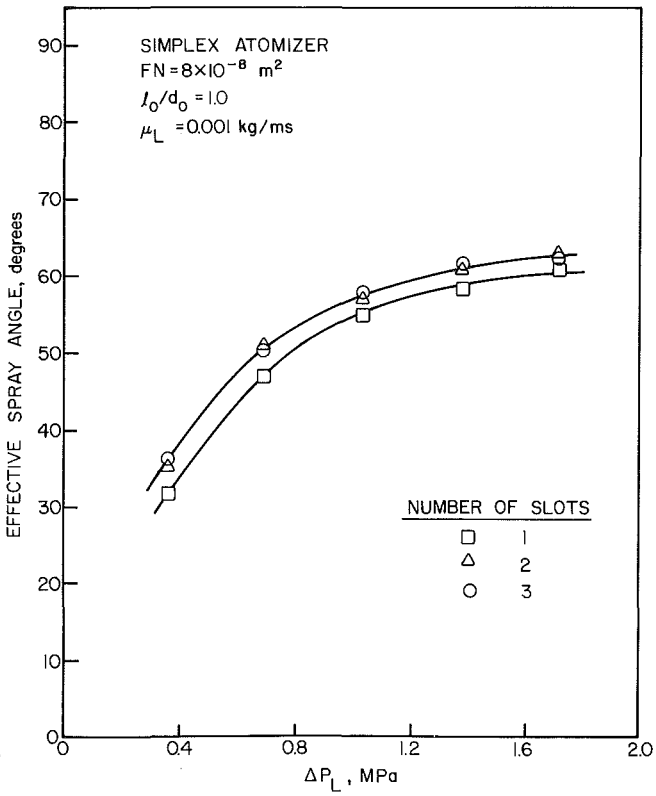

Fig. 13 Influence of number of swirl chamber feed slots on effective spray angle

present time there is considerable interest in reducing the number of feed slots in pressure-swirl fuel nozzles. This is because the elimination of one or more slots would allow the flow areas of the remaining slots to be increased, with consequent advantages in terms of reduced risk of blockage by contaminants in the fuel.

In order to investigate the influence of feed slot number on effective spray angle, two special nozzles were constructed. Both nozzles were designed to have the same total flow number as the standard three-slot nozzles, but one nozzle featured two equispaced feed slots and the other a single feed slot. The results of measurements of spray cone angle obtained with these two nozzles are shown in Fig. 13. Also included in this figure, for comparison, are corresponding results obtained

with a standard three-slot nozzle of the same discharge orifice length/diameter ratio. Figure 13 demonstrates that θ_{eff} is affected only slightly by variations in the number of swirl chamber feed slots. Reducing the number of slots from three to two caused no perceptable change in spray angle. Further reduction from two slots to one caused only a slight reduction in spray cone angle. The conclusion to be drawn from this figure is that spray cone angle is largely independent of the number of swirl chamber feed slots.

Conclusions

From measurements of effective spray cone angle carried out on the sprays produced by injecting liquids of different viscosities into air at normal atmospheric pressure, the following conclusions are drawn:

1 Over the range of injection pressures from 0.34 to 1.72 MPa (50 to 250 psi), the effective spray angle increases continuously with increase in liquid injection pressure. This result is generally true regardless of variations in liquid viscosity and atomizer geometry.

2 Increase in the length/diameter ratio of the final discharge orifice always leads to a reduction in spray cone angle.

3 Spray cone angle declines with increase in liquid viscosity.

4 Variations in the number of swirl chamber feed slots have little effect on spray cone angle.

Acknowledgments

The authors wish to express their gratitude to Delavan Incorporated, and in particular to Mr. Darrell Bobzin, for providing the specially manufactured nozzles employed in this investigation.

References

Carlisle, D. R., 1955, Communication on "The Performance of a Type of Swirl Atomizer," by A. Radcliffe, *Proc. IMechE*, Vol. 169, p. 101.

DeCorso, S. M., and Kemeny, G. A., 1957, "Effect of Ambient and Fuel Pressure on Nozzle Spray Angle," *Trans. ASME*, Vol. 79, No. 3, pp. 607–615.

Giffen, E., and Massey, B. S., 1950, Report 1950/5, Motor Industry Research Association, United Kingdom.

Giffen, E., and Muraszew, A., 1953, *Atomization of Liquid Fuels*, Chapman and Hall, London.

Lefebvre, A. H., 1983, *Gas Turbine Combustion*, Hemisphere Publishing Corporation, Washington, DC.

Lefebvre, A. H., 1987, "The Prediction of Sauter Mean Diameter for Simplex Pressure-Swirl Atomizers," *Atomization and Spray Technology*, Vol. 3, No. 1, pp. 37–51.

Lefebvre, A. H., 1989, *Atomization and Sprays*, Hemisphere Publishing Corporation, Washington, DC.

Ortman, J., and Lefebvre, A. H., 1985, "Fuel Distributions From Pressure-Swirl Atomizers," *AIAA Journal of Propulsion and Power*, Vol. 1, No. 1, pp. 11–15.

Rizk, N. K., and Lefebvre, A. H., 1985a, "Internal Flow Characteristics of Simplex Swirl Atomizers," *AIAA Journal of Propulsion and Power*, Vol. 1, No. 3, pp. 193–199.

Rizk, N. K., and Lefebvre, A. H., 1985b, "Prediction of Velocity Coefficient and Spray Cone Angle for Simplex Swirl Atomizers," *Proceedings of the 3rd International Conference on Liquid Atomization and Spray Systems*, London, pp. III C/2/1–16.

Taylor, G. I., 1948, "The Mechanics of Swirl Atomizers," *Seventh International Congress of Applied Mechanics*, Vol. 2, Part 1, pp. 280–285.

Wang, X. F., and Lefebvre, A. H., 1987, "Influence of Ambient Air Pressure on Pressure-Swirl Atomization," *Atomization and Spray Technology*, Vol. 3, pp. 209–226.

A Computational Fluid Dynamics and Chemistry Model for Jet Fuel Thermal Stability

J. L. Krazinski
Argonne National Laboratory,
Argonne, IL 60439

S. P. Vanka
University of Illinois at Urbana-Champaign,
Urbana, IL 61801

J. A. Pearce

W. M. Roquemore

Aero Propulsion and Power Laboratory,
Wright-Patterson AFB, OH 45433

This paper describes the development of a model for predicting the thermal decomposition rates of aviation fuels. A thermal deposition model was incorporated into FLANELS-2D, an existing computational fluid dynamics (CFD) code that solves the Reynolds-averaged conservation equations of mass, momentum, and energy. The decomposition chemistry is modeled by three global Arrhenius expressions in which the fuel decomposition was assumed to be due to an autoxidation reaction with dissolved oxygen. The deposition process was modeled by assuming that all deposit-forming species transported to the wall adhered and formed a deposit. Calibration of the model required the determination of the following parameters for a given fuel: (1) the pre-exponential constant and activation energy for the wall reaction, (2) the pre-exponential constant and activation energy for the bulk autoxidation reaction, and (3) the pre-exponential constant and activation energy for the precursor decomposition reaction. Values for these parameters were estimated using experimental data from published heated-tube experiments. Results show that the FLANELS-2D code performed well in estimating the fuel temperatures and that the three-equation chemistry model performed reasonably well in accounting for both the rate of deposition and the amount of dissolved oxygen present in the fuel at the end of the heated tube.

Introduction

The stability of an aviation fuel is a major consideration in the design of aircraft fuel systems. During both storage and exposure to elevated temperatures in the fuel system, aviation fuels can decompose to yield soluble gums, as well as insoluble materials that can deposit on heat transfer surfaces, obstruct valves and filters in the fuel lines, and degrade the performance of injection nozzles. Although the thermal stability of hydrocarbon fuels has been studied for a long period of time, the degradation process is complex and still poorly understood. Thermal decomposition and deposition reactions often involve unknown constituents that can vary from batch to batch of fuel and may include hundreds of reaction steps. Particles or particle precursors can form in the bulk fuel and can be transported by diffusion, turbulence, or surface forces to metal surfaces where they may stick or be repelled back into the bulk fuel. Particles can also form by chemical reactions taking place directly on metal or particulate-laden surfaces with possible catalytic effects being important (Roback et al., 1983). The relative importance and the details of these mechanisms are not understood. Furthermore, the coupling of the various chemical and physical processes masks the fundamental mechanisms taking place and this makes thermal deposition a very difficult problem to study.

Computational fluid dynamics and chemistry (CFDC) based models can, in a fundamental way, include the complex coupling between fluid dynamics, heat transfer, chemistry, and transport processes in thermal stability studies. Because of this, the CFDC based models offer the potential of being used as research tools to study thermal deposition processes of jet fuels and could eventually aid in the design of aircraft fuel system components. Kern and Seaton (1959) suggested that a theoretical analysis of thermal deposition processes offers the possibility of a more rational method of heat exchanger design. Since this idea was first proposed, many different empirically based models have been developed (Epstein, 1986). However, these models do not provide, in a fundamental way, the coupled effects necessary for predicting thermal deposition for radically different experimental apparatus and a wide range of operating conditions whereas CFDC models do. When used as a research tool, CFDC models can provide insights into the coupling between chemistry, fluid mechanics, and heat transfer and can be used to estimate the relative sensitivity of different parameters on thermal deposition. They can be used as organizational tools in which ideas about the thermal decomposition and deposition mechanisms can be postulated, predictions made, and experiments designed to evaluate and clarify the initial postulates. Because the CFDC models are not inherently constrained by test section geometry, they also have the potential of becoming aids to designers of heat exchangers and serving as tools for predicting the impact of thermal deposition on performance for different designs.

Contributed by the International Gas Turbine Institute and presented at the 35th International Gas Turbine and Aeroengine Congress and Exposition, Brussels, Belgium, June 11-14, 1990. Manuscript received by the International Gas Turbine Institute December 23, 1989. Paper No. 90-GT-33.

This paper describes the development of a second-generation CFDC thermal decomposition model. An initial CFDC based model with one-step global chemistry was developed in an attempt to account for the coupling between the deposition processes (Roquemore et al., 1989). This model was incorporated into an existing computer code (FLANELS-2D) that was originally developed for the calculation of multidimensional, reactive fluid flows. FLANELS-2D uses an efficient multigrid algorithm to solve the two-dimensional, Reynolds-averaged mass, momentum, and energy conservation equations (Vanka, 1988), as well as the k and ϵ equations for turbulent flows (Nallasamy, 1987). The one-step global chemistry model assumed that thermally stressed fuel reacted with dissolved oxygen to form deposit precursors. The precursors that were transported to the surface by convection and diffusion formed deposits. Although the results from this initial model were somewhat encouraging, the model did not sufficiently account for the deposition rates measured in the electrically heated-tube experiments of Marteney and Spadaccini (1984, 1986). An examination of their experimental data suggested the need for additional global chemistry expressions. This paper describes the second-generation deposition model, which attempts to correct some of the problems that were noted in the first model. Since global chemistry models are used, there are parameters that must be determined from experimental data. If the CFDC model with global chemistry provides a good representation of the thermal decomposition and deposition processes and the set of parameters have been determined from experiments for a given fuel, then the CFDC model should correctly predict the thermal stability characteristics of this fuel when thermally stressed in a different test apparatus at different operating conditions. The initial determination of the global chemistry parameters from experiments is referred to as the "calibration" procedure. In this paper, deposition data for a JP-5 fuel are used to calibrate the CFDC model and its predictive capabilities are then examined by a comparison with two additional sets of JP-5 data.

Development of the Thermal Decomposition Model

The formation and surface deposition of the decomposition products from aviation fuels are governed by a number of fluid dynamic and chemical processes. The fundamental process responsible for the thermal degradation of the fuel is the convective heat transfer from the wall to the fluid. When dissolved oxygen is present in the fuel, the increase in fuel temperature can result in autoxidation reactions and the formation of free radical species, which can lead to the eventual production of insoluble species that may deposit onto the walls. The rate of deposition can be a function of factors such as wall roughness, flow turbulence, sticking characteristics, and surface chemistry (Bowen and Epstein, 1979). Currently, there is no clear understanding of the role and significance of these factors on the deposition rate.

A simplified way to represent mathematically the formation, transport, and deposition of a given species onto a surface is to solve a general transport equation for the concentration of the species (C_i). Such an equation, which represents the convective and diffusive processes of transport, as well as the creation and destruction of a species through chemical reactions and deposition, can be written as

$$\nabla(\mathbf{G}C_i) = \nabla(\Gamma_c \nabla C_i) + S_f - S_d. \quad (1)$$

The mass flux $\mathbf{G}$ is a three-dimensional vector field that can convect the species from the bulk fluid to the wall; Γ_c represents the effective diffusion coefficient including both molecular and turbulent diffusion (Davies, 1966); and S_f and S_d are source terms representing the creation and destruction of a given species. Transport equations of the form of Eq. (1) are used to model processes involving both the deposit precursors and dissolved oxygen. The source term S_f, which represents the formation of precursors, is difficult to evaluate and is modeled by a single Arrhenius expression involving the local temperature and the concentrations of oxygen and fuel. The source term S_d represents the net loss of precursors due to chemical reactions and deposition processes (flow impaction, sticking, sedimentation, erosion, flaking, etc.) at the wall. Modeling of the source term S_d is also very difficult due to a lack of understanding of these processes and the absence of data from clearly defined experiments.

Marteney and Spadaccini (1984, 1986) conducted a series of thermal decomposition experiments in electrically heated tubes using JP-5 and found that their deposition data could be fitted with Arrhenius expressions throughout most of the temperature range. The low-temperature data ($T_{\text{wall}} < 533$K) were represented by an activation energy of 8–10 kcal/mole, suggesting a heterogeneous or wall-catalyzed reaction. Above 533 K, the data were fitted with a line corresponding to an activation energy of 40 kcal/mole, suggesting a homogeneous reaction in the bulk liquid. Presumably both types of reactions occurred at all times, but each was dominant in a different temperature regime.

Based on these results, the present model includes terms for both a wall reaction and a bulk fuel reaction. These initial reactions are modeled as global, one-step Arrhenius reactions occurring at all temperatures. The wall reaction is included in the model as a boundary condition in the oxygen equation having the form

$$D_{O_2}\left(\frac{\partial[O_2]}{\partial r}\right)_{\text{wall}} = -A_w \exp\left(\frac{-E_w}{RT_w}\right)[Fu]_w^{a_w}[O_2]_w^{b_w}. \quad (2)$$

Here D_{O_2} is the diffusion coefficient for dissolved oxygen in aviation fuel; E_w and A_w are the activation energy and pre-exponential constant for the wall reaction; and $[O_2]_w$ and $[Fu]_w$ are the oxygen and fuel concentrations at the fuel/wall interface. A value of 1.0 is currently used for a_w and b_w, while A_w and E_w for a particular fuel must be determined from experiments.

Nomenclature

a = exponent for the fuel concentration
A = pre-exponential constant
b = exponent for the dissolved oxygen concentration
C = concentration
D = diffusion coefficient
E = activation energy
Fu = fuel
$\mathbf{G}$ = mass flux vector
K = deposition coefficient
n = exponent on concentration C_w
O_2 = dissolved oxygen
Pre = deposit precursor
r = radial direction
R = universal gas constant
Re = Reynolds number
S = general source term
Sc = Schmidt number
T = temperature
Γ_c = effective diffusion coefficient
μ = dynamic viscosity
ρ = density

Subscripts

b = bulk reaction
d = destruction
dc = precursor decomposition reaction
f = formation
i = species i
w = wall reaction

For the homogeneous reaction in the bulk fuel, the initial model assumes a global reaction of the form

$$\text{Fuel} + \text{Dissolved Oxygen} \rightarrow \text{Deposit Precursor}$$

The source term for the homogeneous autoxidation reaction, S_f, is thus written as

$$S_f = A_b \exp\left(\frac{-E_b}{RT_b}\right)[Fu]^{a_b}[O_2]^{b_b} \tag{3}$$

where E_b and A_b are the activation energy and pre-exponential constant for the bulk liquid reaction, $[O_2]$ is the oxygen concentration, and $[Fu]$ is the concentration of the fuel. The values of a_b and b_b are set to 1.0. The values of A_b and E_b, in addition to A_w and E_w, must be determined from experiments. Note that the current chemistry models are restricted to temperatures where autoxidation reactions control the rate of fuel decomposition. Autoxidation reactions were found to control the decomposition rates below 533 K, whereas oxygenated products played an important role in the intermediate temperature regime of 533–755 K (Hazlett, 1980). At temperatures above 755 K, pyrolysis reactions become significant and result in fuel cracking in the absence of oxygen.

Deposits at a fuel/wall interface are assumed to form as a result of two different mechanisms: (1) the formation of deposits directly on the solid surface due to the heterogeneous reaction described by Eq. (2), and (2) the transport to the wall of deposit precursors produced in the bulk fluid. The total deposition rate is the sum of the rates from these two processes. The deposition rate due to the heterogeneous reaction is assumed to be proportional to the rate of transport of oxygen molecules to the surface, i.e., proportional to

$$D_{O_2}\left(\frac{\partial[O_2]}{\partial r}\right)_{\text{wall}} \tag{4}$$

For a fixed value of the activation energy E_w, calibration of the model involves adjusting the pre-exponential constant A_w until the predicted deposition rates match the experimental data.

The deposition rate due to the homogeneous bulk fuel reaction is assumed to be proportional to the mass flux of deposit precursors at the solid surface. The rate of deposition at the wall is described by the boundary condition

$$D_{C_i}\left(\frac{\partial C_i}{\partial r}\right)_{\text{wall}} = -KC_w^n \tag{5}$$

where C_w is the concentration of deposit precursors at the wall. For lack of better information, the precursor/wall interaction is assumed to be first order with respect to the wall concentration (i.e., $n=1$). The parameter K has units of velocity and may be interpreted as a deposition coefficient that incorporates the complex physicochemical processes occurring at the fuel/wall interface (Beal, 1970). K can be a function of the flow field, surface conditions, and temperature, but cannot be accurately predicted from first principles. The baseline model assumes that all of the precursor species arriving at the wall adhere and form a deposit, a condition enforced by setting K equal to a very large number (e.g., $K=10^{20}$). This ensures that C_w is effectively zero at the solid surface.

Initial attempts at calibrating the baseline model with the deposition data of Marteney and Spadaccini (1984, 1986) for JP-5 fuel indicated the need to introduce an additional parameter into the model. It was found that the peak predicted deposition rates were significantly higher (by factors of 50–100) than the data, and these differences could not be adequately explained by uncertainties in the diffusion coefficients or inaccuracies in the precursor transport model. It was believed that the differences resulted from the assumption that the deposit precursors that were formed in the bulk fluid were transported directly to the wall where they formed a deposit. However, Hazlett (1980) concluded that the deposit chemistry did not appear to be in the main reaction sequence that involved the formation and decomposition of the oxygenated products (e.g., hydroperoxides). Although hydroperoxides were found to be precursors to the formation of deposits, the actual deposit-forming chemistry appeared to be closely related side branch of the primary sequence of chemical reactions. For example, the maximum hydroperoxide concentration measured in Hazlett's (1980) decomposition experiments with *n*-dodecane was approximately 200 mg/L, whereas the typical deposit mass from a liter of fuel was only 0.01 to 0.1 mg.

A factor DPFRAC was originally introduced into the model to represent the fraction of the product species from the thermal decomposition reactions that became insoluble and formed a solid deposit. Although this modification reduced the peak predicted deposition rates, the model was still unable to account for the steep declines in deposition rates following the peak values in heated-tube experiments. These rapid decreases suggested that the phenomenon might be associated with a chemical process rather than a purely physical process such as diffusion. Consequently, a third reaction accounting for decomposition of the deposit precursors was added to the model. It was assumed that deposit precursors were "consumed" by this reaction and thereby removed from the chain reaction that leads to the formation of solid deposits on the tube wall. This third reaction was included in the precursor transport equation by a sink term of the form

$$S_d = -A_{dc}\exp\left(\frac{-E_{dc}}{RT_b}\right)[\text{Pre}] \tag{6}$$

where A_{dc} is the pre-exponential constant for the decomposition reaction, E_{dc} is the activation energy, and [Pre] is the precursor concentration. Some initial calculations were also performed with the alternate assumption of a second-order decomposition reaction between precursor and fuel molecules (Deshpande et al., 1989). Since the fuel concentration is essentially constant in the heated-tube tests, the results were similar to those obtained from the simple first-order reaction in Eq.(6).

Finally, the thermal decomposition model described above was incorporated into an existing computer code (FLANELS-2D). The transport equations for the dissolved oxygen and deposit precursors are solved simultaneously with the conservation equations of mass, momentum, and energy. Gas property equations in the original code were supplemented with property correlations for JP-5. The results obtained with the modified code are presented in following sections.

Calibration of The Model For JP-5 Fuel

The thermal decomposition model described above contains a number of unknown parameters that cannot be determined directly from the properties of a particular fuel. These parameters, related to both fuel chemistry and transport processes, must be obtained from well-controlled experiments that isolate the individual mechanisms of deposition. Although data from such experiments are not currently available, a large data base is available from heated-tube experiments, which can be used to obtain initial values for the unknown model parameters.

Because of the large temperature differences throughout the test section, there is a significant variation in the fluid properties, particularly the viscosity (Nixon et al., 1970). In order to account for these variable fluid properties, curve-fit equations for the fuel enthalpy, density, viscosity, and Prandtl number were included in the model. The transport equations for dissolved oxygen and the deposit precursors also require values for their respective Schmidt numbers

$$\text{Sc} = \frac{\mu}{\rho D}. \tag{7}$$

To calculate Sc for a particular species, corresponding values of the diffusion coefficient must be known. Accurate diffusion coefficients are particularly important for the precursor transport equation because they directly affect the predicted deposition rates. There is considerable uncertainty in the values of the diffusion coefficients because: (1) the theory for liquid-phase diffusion is not well developed (Reid et al., 1987), (2) tabulated values typically cover only a narrow range of temperature near room temperature, and (3) the actual species that are transported to the wall subsequently to form a deposit have not yet been identified. Since *n*-dodecane ($n-C_{12}H_{26}$) was deemed to be representative of a fuel molecule, self-diffusion coefficients for *n*-dodecane were used for the initial calculations (Ertl and Dullien, 1973).

Marteney and Spadaccini (1984, 1986) and Marteney (1989a) obtained thermal decomposition data for JP-5 fuel over a wide range of temperatures and flow rates. They conducted their experiments in long, thin, electrically heated tubes (constant heat flux boundary condition) and reported the deposition data as the mass of carbon deposited on the inside lateral surface area of each section during the test period (in units of $\mu g/cm^2-h$). The data for the model calibration were taken from two tests conducted by Marteney and Spadaccini (1984). The first test was conducted with an inlet fuel velocity of 0.076 m/s (Re = 70) and a maximum wall temperature of 589 K. The second test was conducted with an inlet fuel velocity of 2.13 m/s (Re = 3000) and a maximum wall temperature of 672 K. Printouts of measured fuel temperatures, wall temperatures, flow rates, and electrical power inputs were obtained from Marteney (1989b) for assembling input data files for the code and validating the predicted temperature profiles.

Because fuel decomposition involves chemical processes whose rates vary significantly with changes in temperature, it is important to predict temperature profiles accurately throughout the heated test section. Although the inlet Reynolds number corresponding to a fuel velocity of 2.13 m/s is in the transitional range, the Reynolds number increases rapidly along the heated test section as the fuel viscosity decreases. This test was thus modeled by assuming fully developed turbulent flow throughout the entire tube. Wall temperatures were calculated by assuming a constant heat flux boundary condition in conjunction with standard wall functions (Launder and Spalding, 1974). Figure 1 shows a comparison between the predicted and measured bulk fuel and wall temperatures for the calibration case, indicating good agreement with the data.

Prior to performing the model calibration, several input parameters for the model were fixed. The value of K in Eq. (5) was set equal to a large number (10^{20}) implying that all deposit precursors that reach the wall adhere and form a deposit. Based on reported oxygen concentrations of 45 wppm (Watt et al., 1968) and 55 wppm (Giovanetti and Szetela, 1986) for air-saturated Jet A fuel, a baseline value of 50 wppm (a mass fraction of 5.0×10^{-5}) was used for the inlet oxygen concentration of air saturated JP-5. Finally, the activation energy for the wall reaction was fixed at 8 kcal/mole, based on low-temperature deposition data for JP-5 (Marteney and Spadaccini, 1984).

With the above parameters fixed, calibration of the model requires a determination of the following parameters: (1) the pre-exponential constant for the wall reaction, A_w, (2) the pre-exponential constant, A_b, and activation energy, E_b, for the bulk autoxidation reaction, and (3) the pre-exponential constant, A_{dc}, and activation energy E_{dc} for the precursor decomposition reaction. In the low-temperature region ($T_{wall}<533$ K) the wall reaction dominates, so the model can be calibrated by adjusting only A_w. At higher temperatures where the deposition rate resulting from the bulk reaction becomes important, the parameters for the two homogeneous reactions are adjusted to calibrate the model.

The wall reaction model was calibrated with the turbulent

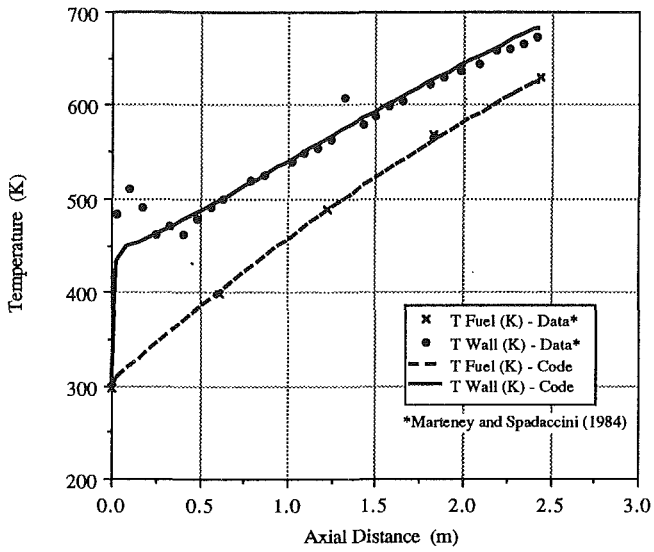

Fig. 1 Comparison of predicted temperature profiles with data of Marteney and Spadaccini (1984)

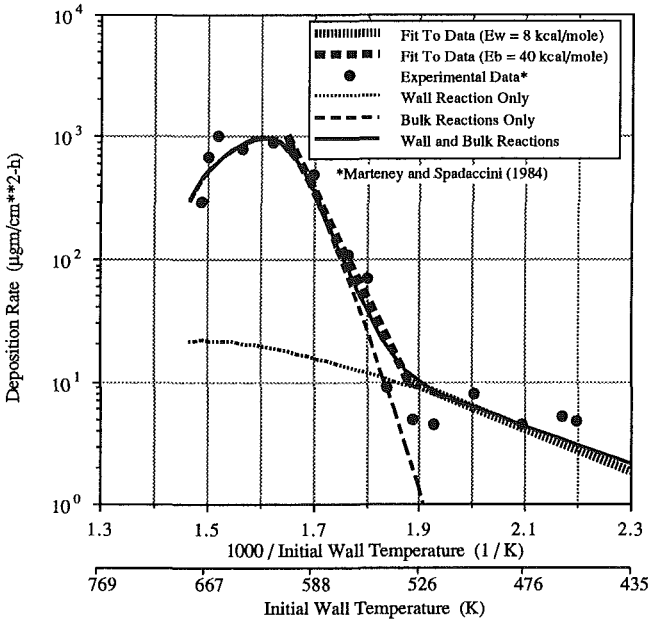

Fig. 2 Effect of wall and bulk reactions on predicted deposition rates for a fuel velocity of 2.13 m/s

flow data in Fig. 2. These data fall into a low-temperature regime and a high-temperature regime that were well fitted by lines corresponding to activation energies of 8–10 kcal/mole and 40 kcal/mole, respectively. Figure 2 shows calculated deposition rates for three cases: (1) deposits produced only from the heterogeneous wall reaction ($A_b=0$ and $A_{dc}=0$), (2) deposits produced only by precursors that are formed in the bulk fluid and subsequently transported to the wall by turbulent diffusion ($A_w=0$), and (3) deposits formed as a result of both wall and bulk reactions. For the low-temperature data below 533 K, the activation energy for the wall reaction was fixed at 8 kcal/mole and the pre-exponential constant was varied to match the data. A value of $A_w=4.0\times10^{1}$ cm^4/mole-s gave a good match to the data as shown in Fig. 2.

The autoxidation reaction was calibrated using the laminar flow data of Marteney (1989a) corresponding to an inlet fuel velocity of 0.076 m/s. This test included deposition data as well as measurements of the dissolved oxygen concentration at the exit of the heated tube. The data in Fig. 2 were well

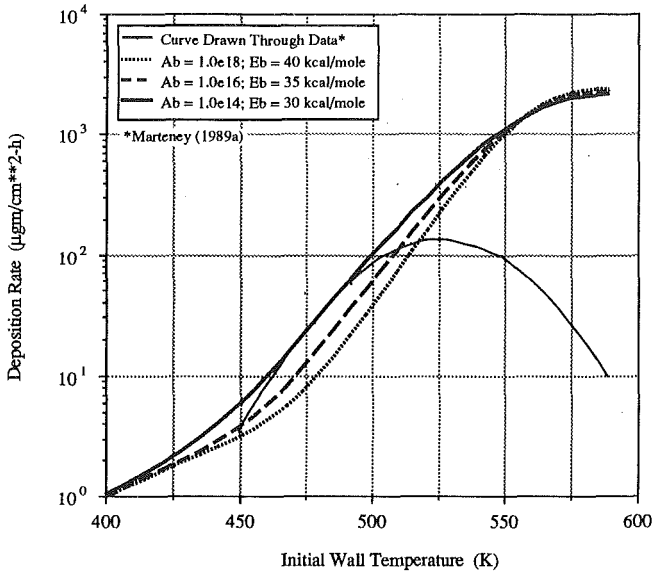

Fig. 3 Calibration of the autoxidation reaction for a fuel velocity of 0.076 m/s (no precursor decomposition)

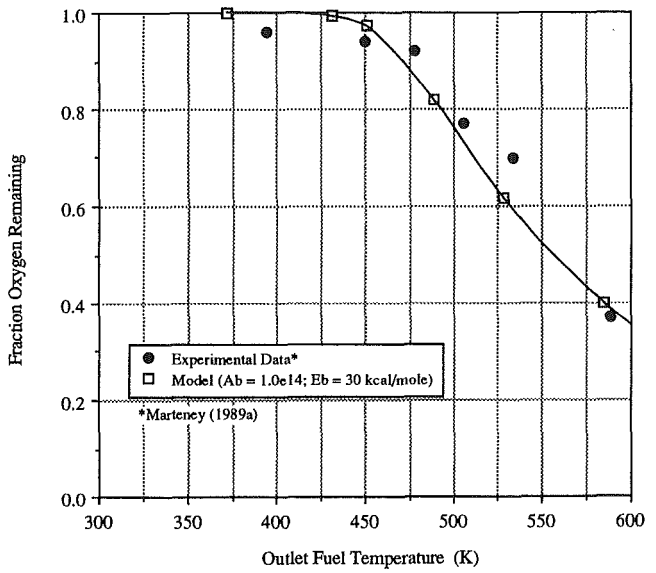

Fig. 4 Predictions of dissolved oxygen concentration at the tube exit for a fuel velocity of 0.076 m/s

fitted with an activation energy of 40 kcal/mole for initial wall temperatures above 533 K. However, the reaction rate of the homogeneous autoxidation reaction is governed by the local fluid temperature. When plotted against the corresponding fluid temperatures, the activation energy for this data appears to be lower, in the range of 25–30 kcal/mole. Calculated deposition rates for several values of the activation energy E_b are shown in Fig. 3. The precursor decomposition reaction was neglected in these calculations ($A_{dc}=0$). For an assumed value of E_b, the pre-exponential constant A_b was adjusted until the predicted oxygen concentration at the tube exit agreed with the data. All three combinations of parameters given in Fig. 3 thus result in good agreement with the oxygen consumption data. The parameters $A_b=1.0\times10^{14}$ cm^3/mole-s and $E_b=30$ kcal/mole also result in good agreement with the low-temperature deposition data shown. Consequently, these parameters were selected for the autoxidation reaction in the chemistry model. The corresponding oxygen concentrations predicted by the model are compared with the data in Fig. 4.

Using the selected parameters for the wall and autoxidation

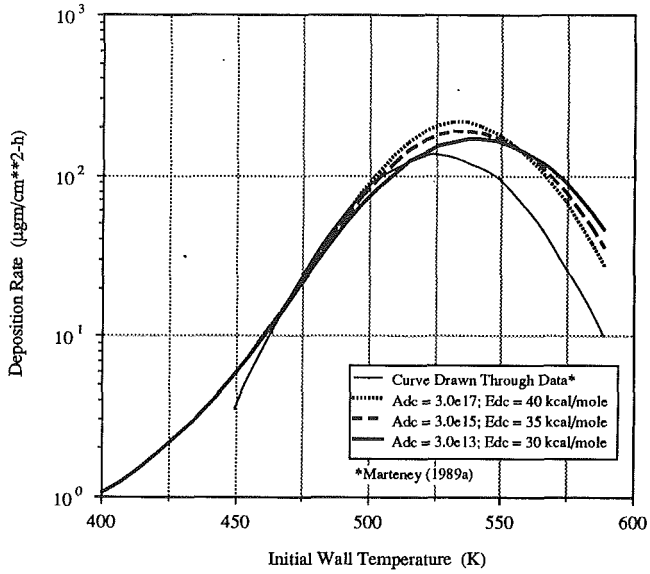

Fig. 5 Calibration of the precursor decomposition reaction for a fuel velocity of 0.076 m/s

reactions, the precursor decomposition reaction was calibrated by a comparison with the laminar and turbulent flow data. From Fig. 3 it appears that the rate of decrease of the measured deposition rates beyond the peak value is similar in magnitude to the rate of increase at lower temperatures. Therefore, the activation energy E_{dc} was also varied over the range of 30–40 kcal/mole. For each selected value of E_{dc}, the pre-exponential constant A_{dc} was adjusted in an attempt to match the peak deposition rates for laminar and turbulent flow. The results of this calibration procedure, presented in Fig. 5 for the laminar flow case, show that the calculated deposition rates are greater than the data at the higher temperatures, although the model does predict the rapid decrease in deposition rates following the peak value. The corresponding results for the turbulent flow case are shown in Fig. 2 for $A_{dc}=3.0\times10^{15}$ s^{-1} and $E_{dc}=35$ kcal/mole, the values selected for the calibrated precursor decomposition reaction. Using the calibrated values of the chemistry parameters, the model is able to reproduce three key qualitative features of the turbulent flow deposition data: (1) the lower temperature data fitted by an activation energy of 8 kcal/mole, (2) the higher temperature data fitted by an activation energy of 40 kcal/mole (both based on the initial wall temperature), and (3) the decrease in deposition rates that occurs following the peak value. Comparison of the calibrated model with additional deposition data is discussed in the following section.

Comparison of the Calibrated Model With Additional Data Sets

To test the predictive capabilities of the model, the model was compared with two additional sets of data for JP-5. For these comparisons, the model parameters were fixed at their calibrated values. The data were obtained at different flow rates and temperatures than those used to calibrate the model; thus, these comparisons serve to test the applicability of the model to different conditions, as well as suggest directions for further model development.

A test with a lower flow rate, corresponding to an inlet velocity of 0.3 m/s (Re = 400), was included in the test program of Marteney and Spadaccini (1984). The fuel inlet temperature for this test was 286 K and the test was modeled by assuming fully-developed turbulent flow in the test section. Predicted bulk fuel and wall temperatures at the exit of the test section

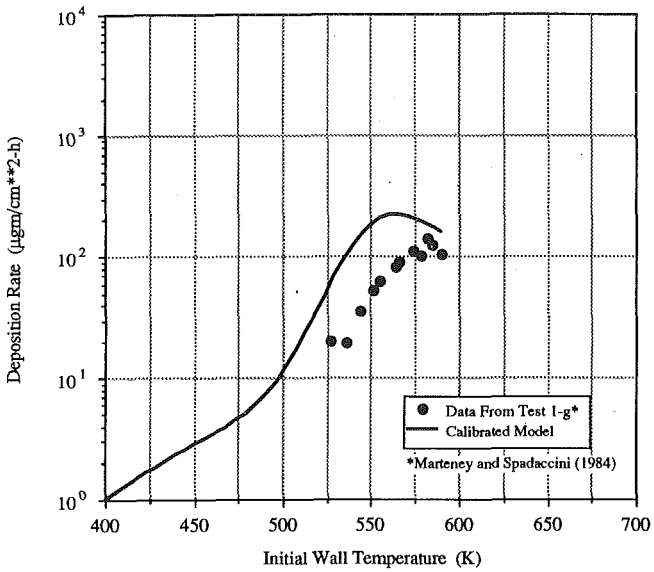

Fig. 6 Comparison of the calibrated model with deposition data for a fuel velocity of 0.3 m/s

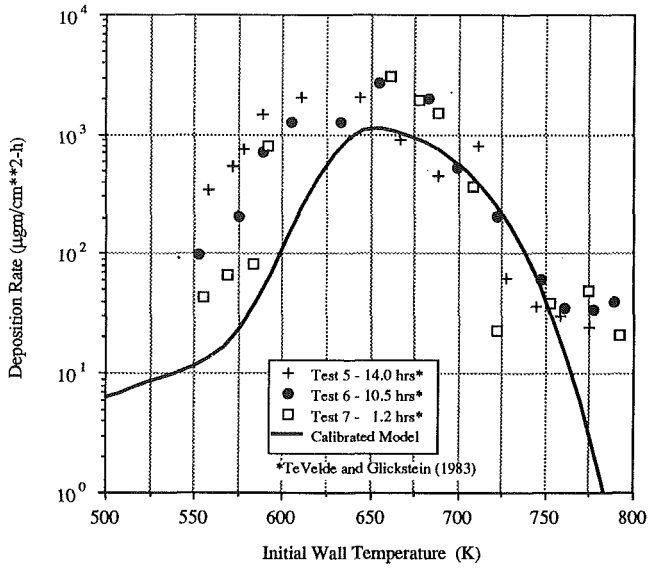

Fig. 7 Comparison of the calibrated model with deposition data for a fuel velocity of 2.57 m/s

were 552 K and 590 K, respectively. These values compared favorably with the experimental values of 533 K and 589 K.

The corresponding deposition rates predicted with the calibrated model are compared with the data in Fig. 6. The magnitude of the peak deposition rate predicted by the model is in good agreement with the data, although the calculated value occurs at a lower temperature. The temperature regimes in which the wall and the bulk reactions predominate are again evident in the calculated results; however, the peak predicted deposition rate occurs at a lower temperature than for the higher velocity case shown in Fig. 2. This may be a consequence of a greater depletion of dissolved oxygen in the fuel at lower temperatures due to the longer residence time in the heated tube. The discrepancy between the model predictions and the data may also be partly due to the assumption of fully developed turbulent flow in the test section. Because of the lower fuel velocity, the flow may have been in the laminar and transitional flow regimes throughout much of the test section.

The final set of JP-5 deposition data that was used for comparison with the calibrated model was a series of experiments conducted by TeVelde and Glickstein (1983). The high heat fluxes for these tests resulted in fuel exit temperatures of 755 K and initial surface temperatures up to 800 K. The temperature profiles predicted by the model were compared with the data and again were found to be in good agreement.

Figure 7 shows a comparison between the calibrated model and the deposition data for three test runs with JP-5 fuel. The model underpredicts the deposition rates at lower temperatures. At higher temperatures, the model shows better agreement with the data and predicts the sharp drop-off in deposition rates following the peak value. At initial wall temperatures above 750 K, the deposition rates appear to level off. Beyond this temperature, other data have shown an eventual increase in deposition rates with increasing wall temperatures. These increasing deposition rates could be due to fuel pyrolysis, which becomes significant at temperatures above 755 K (Hazlett, 1980). The current thermal decomposition model does not include the effects of fuel pyrolysis reactions.

Summary and Recommendations

Comparison of the calibrated model with experimental data indicated that the current model can characterize trends in fuel deposition rates and can serve to demonstrate the coupling between chemistry, fluid mechanics, and heat transfer processes that occurs during fuel decomposition. Much additional work is needed, however, before the model can be utilized to make reliable quantitative predictions of wall deposition rates under various flow conditions. Although the current global chemistry model appears to include many of the qualitative features of the JP-5 deposition data, further development and testing of the model should be coordinated with additional experiments that can be used to test proposed mechanisms of fuel decomposition and wall deposition. The model also needs to be upgraded to include the formation of solid particles in the bulk fuel and their transport to and from walls. In addition, the model must be modified to take into account the impact of wall deposits on the heat transfer characteristics and fluid dynamics of flowing systems.

The development of the model is hindered by a lack of data from well-controlled experiments that have isolated the various phenomena in the overall decomposition process. Additional experiments are needed to isolate the various factors and provide necessary input data for the model. These include experiments to better characterize the deposit-forming species and to acquire more reliable liquid diffusivity data, decomposition chemistry experiments to help decipher the decomposition kinetics, and wall deposition experiments conducted under isothermal conditions (without the decomposition chemistry) to understand further the transport processes and adhesion mechanisms of deposit-forming species. These experiments must be coordinated with further model development to ensure that the measurements provide the type of information needed to improve and validate the model.

Acknowledgments

This project was jointly supported by the U.S. Department of Energy, Pittsburgh Energy Technology Center, and the WRDC/Aero Propulsion and Power Laboratory, Wright-Patterson AFB. The authors wish to thank Dr. A. S. Nejad of the Advanced Propulsion Division of the WRDC/Aero Propulsion and Power Laboratory for providing the source code of FLANELS-2D, an unreleased CFD computer code that served as the base for the thermal deposition model. The authors also wish to thank Drs. P. J. Marteney and L. J. Spadaccini at United Technologies Research Center for providing data for the model calibration and for their many useful discussions.

References

Beal, S. K., 1970, "Deposition of Particles in Turbulent Flow on Channel or Pipe Walls," *Nuclear Science and Engineering*, Vol. 40, pp. 1–11.

Bowen, B. D., and Epstein, N., 1979, "Fine Particle Deposition in Smooth Parallel-Plate Channels," *Journal of Colloid and Interface Science*, Vol. 72, pp. 81–97.

Davies, C. N., 1966, "Deposition of Aerosols From Turbulent Flow Through Pipes," *Proceedings of the Royal Society A*, Vol. 289, pp. 235–246.

Deshpande, G. V., Serio, M. A., Solomon, P. R., and Malhotra, R., 1989, "Modelling of the Thermal Stability of Aviation Fuels," presented at the 198th ACS National Meeting, Symposium on the Chemical Aspects of Hypersonic Propulsion, Miami, FL.

Epstein, N., 1986, "Fouling of Heat Exchangers," *Heat Exchanger Sourcebook*, Hemisphere Publishing Company, Washington, DC, pp. 677–697.

Ertl, H., and Dullien, F. A. L., 1973, "Self-Diffusion and Viscosity of Some Liquids as a Function of Temperature," *AIChE Journal*, Vol. 19, pp. 1215–1223.

Giovanetti, A. J., and Szetela, E. J. 1986, "Long Term Deposit Formation in Aviation Turbine Fuel at Elevated Temperature," Paper No. AIAA-86-0525.

Hazlett, R. N., 1980, "Free Radical Reactions Related to Fuel Research," *Frontiers of Free Radical Chemistry*, W. A. Pryor, ed., Academic Press, New York, pp. 195–223.

Kern, D. Q., and Seaton, R. E., 1959, "A Theoretical Analysis of Thermal Surface Fouling," *British Chemical Engineering*, Vol. 4, pp. 258–262.

Launder, B. E., and Spalding, D. B., 1974, "The Numerical Computation of Turbulent Flows," *Computer Methods in Applied Mechanics and Engineering*, Vol. 3, pp. 269–289.

Marteney, P. J., and Spadaccini, L. J., 1984, "Thermal Decomposition of Aircraft Fuels," Technical Report NAPC-PE-143C, Naval Air Propulsion Center, Trenton, NJ.

Marteney, P. J., and Spadaccini, L. J., 1986, "Thermal Decomposition of Aircraft Fuel." ASME JOURNAL OF ENGINEERING FOR GAS TURBINES AND POWER, Vol. 108, pp. 648–653.

Marteney, P. J., 1989a, "Thermal Decomposition of JP-5 in Long Duration Tests," Technical Report NAPC-PE-201C, Naval Propulsion Center, Trenton, NJ.

Marteney, P. J., 1989b, Personal Communications, United Technologies Research Center, East Hartford, CT.

Nallasamy, M., 1987, "Turbulence Models and Their Applications to the Prediction of Internal Flows: A Review," *Computers & Fluids*, Vol. 15, pp. 151–194.

Nixon, A. C., Ackerman, G. H., Faith, L. E., Henderson, H. T., Ritchie, A. W., Ryland, L. B., and Shryne, T. M., 1970, "Vaporizing and Endothermic Fuels for Advanced Engine Application: Part III. Studies of Thermal and Catalytic Reactions, Thermal Stabilities, and Combustion Properties of Hydrocarbon Fuels," Technical Report AFAPL-TR-67-114, Part III, Vol. II, Air Force Aero Propulsion Laboratory, Wright-Patterson AFB, OH.

Reid, R. C., Prausnitz, J. M., and Poling, B. E., 1987, *The Properties of Gases and Liquids*, 4th ed., McGraw-Hill, Inc., New York, pp. 597–598.

Roback, R. E., Szetela, E. J., and Spadaccini, L. J., 1983, "Deposit Formation in Hydrocarbon Fuels," ASME JOURNAL OF ENGINEERING FOR POWER, Vol. 105, pp. 59–65.

Roquemore, W. M., Pearce, J. A., Harrison, W. E., III, Krazinski, J. L., and Vanka, S. P., 1989, "Fouling in Jet Fuels: A New Approach," *Preprints—Symposia on the Structure of Jet Fuels II*, W. E. Haines et al., eds., ACS Division of Petroleum Chemistry, Inc., Washington, DC, Vol. 34, pp. 841–849.

TeVelde, J. A., and Glickstein, M. R., 1983, "Heat Transfer and Thermal Stability of Alternative Aircraft Fuels, Vols. I and II," Technical Report NAPC-PE-87C, Naval Air Propulsion Center, Trenton, NJ.

Vanka, S. P., 1988, "Analytical Studies of Three-Dimensional Combustion Processes," Technical Report AFWAL-TR-88-2140, Air Force Aero Propulsion and Power Laboratory, Wright-Patterson AFB, OH.

Watt, J. J., Evans, A., Jr., and Hibbard, R. R., 1968, "Fouling Characteristics of ASTM Jet A Fuel When Heated to 700°F in a Simulated Heat Exchanger Tube," NASA Report TN D-4958.

C. W. Spicer

M. W. Holdren

D. L. Smith

Battelle,
Columbus, OH 43201-2693

D. P. Hughes
Tinker AFB,
Oklahoma City, OK 73145

M. D. Smith
Environics Division,
Tyndall AFB,
Panama City, FL 32403

Chemical Composition of Exhaust From Aircraft Turbine Engines

This paper reports measurements of the chemical composition of exhaust from two aircraft turbine engines. The two engines are the F101, used on the B-1B aircraft, and the F110, used on the F-16C and F-16D aircraft. Samples were collected from each engine using a probe positioned just behind the exhaust nozzle. The measurements reported here were made at four power settings from idle to intermediate power. Exhaust composition measurements included carbon monoxide, carbon dioxide, nitrogen oxides, total hydrocarbons, and individual organic species. The principal focus of this paper is on the detailed organic species results.

Introduction

Assessment of the environmental impact of aircraft operations is required by Air Force regulations, and by federal, state, and local authorities. Among the potential impacts in and around airports are exposure to toxic pollutants emitted by turbine engines, enhancement of atmospheric ozone pollution caused by emissions of reactive precursors in turbine engine exhaust, and reduction of visibility due to particle emissions. We have measured emissions from ten turbine engines over the past seven years, to address the environmental impact issues noted above (Spicer et al., 1984, 1987, 1988, 1989). This paper focuses on the organic emissions from two of these engines, the F101 and F110. These are both bypass turbine engines. The F101 is used on the B-1B aircraft, and the F110 is used on the F-16C and F-16D.

The environmental significance of organic emissions from aircraft turbine engines has not been established due to lack of data regarding the identities of emitted organic compounds and their emission rates. Earlier studies have been only partially successful in identifying and quantifying organic emissions (Lazano et al., 1968; Chase and Hurn, 1970; Groth and Robertson, 1974; Moses and Stavinoka, 1975; Brooks et al., 1978; Robertson et al., 1979; Conkle et al., 1980). The study reported here involved comprehensive measurements of the organic and inorganic gaseous emissions, and the particle emissions from two turbine engines. The particle emissions results are being reported separately (Kuhlman et al., 1990). Emissions measurements were made at five engine power settings, including idle, stage 1 augmentation (afterburner), intermediate (approximately 100 percent of rated thrust), and three other thrust settings. The measurements made under augmented power employed somewhat different procedures from those at other power settings (Spicer et al., 1989), and are not reported here. A detailed description of the measurement methods and protocols may be found from Spicer et al. (1989).

Contributed by the International Gas Turbine Institute and presented at the 35th International Gas Turbine and Aeroengine Congress and Exposition, Brussels, Belgium, June 11–14, 1990. Manuscript received by the International Gas Turbine Institute December 21, 1989. Paper No. 90-GT-34.

Experimental Methods

Exhaust Sampling. Emissions measurements were performed in an indoor test cell at the Production Engine Test Facility, Tinker AFB, Oklahoma City, OK. Both the F101 and F110 are bypass engines; the turbine exhaust and fan bypass air are mixed in the augmentor. All exhaust sampling was performed in the mixed stream using a 12-port sampling probe. The probe is of cruciform design, with three 1.59 mm orifices spaced along each of four 0.32 m arms. The probe was positioned 0.3–0.6 m behind the engine exhaust nozzle in the exhaust exit plane. The sampling ports are internally connected to a common manifold. The sampling probe and internal tubing are constructed of stainless steel. A stainless steel sample tube extends from the rear of the probe 2 m to the side (well out of the exhaust stream), where it connects to a heated, electrically grounded, flexible Teflon sample tube. This tube is used to transport the exhaust sample to the sampling and analysis systems shown schematically in Fig. 1. The temperature of all sampling system components downstream of the sampling probe was maintained at 150°C.

Sampling and Analysis Methods. This paper reports exhaust organic composition from measurements made using the "Organic Sampling System" noted in Fig. 1. The organic measurements utilized three different sampling and analysis pro-

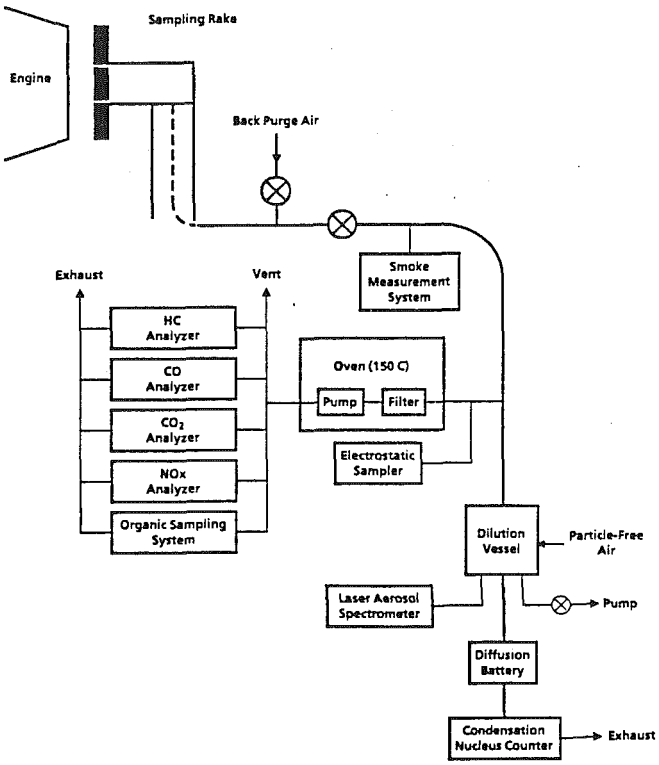

Fig. 1 Schematic diagram of exhaust sampling system and measurement apparatus

cedures to determine volatile organic compounds, carbonyl compounds, and polycyclic aromatic hydrocarbons in the exhaust. The methods are described in detail elsewhere (Spicer et al., 1989) and are noted briefly here.

Volatile Organic Compounds. Methane and C_2–C_{15} hydrocarbons were determined by cryogenic preconcentration and capillary column gas chromatographic analysis of whole air samples collected in surface-passivated canisters. Previous studies have demonstrated excellent stability of C_1–C_{15} hydrocarbons in these canisters. The canisters were evacuated at the start of each sampling period, and were filled at a constant rate over the 20-min test period. The sampling rate was controlled by a contamination-free Metal Bellows pump and Tylan mass flow controller. A Hewlett-Packard Model 5890 gas chromatograph with microprocessor control was used for analysis of canisters for C_1 to C_{15} hydrocarbons. The analysis procedure involved collection of a specific volume of air (usually 100 cc) through a cryogenic sample trap (15 cm long by 0.1 cm i.d. stainless steel tubing) filled with 60/80 mesh silanized glass beads. Two traps were used in this study, for separate analyses of C_2 to C_5 and C_4 to C_{15} hydrocarbons.

The gas chromatograph was equipped with two flame-ionization detectors. The C_2 through C_5 hydrocarbons were resolved with a 6-m by 0.2-cm i.d. column packed with phenylisocyanate on 80/100-mesh Porasil®C. Methane was determined without cryogenic preconcentration using this same column and detector. A 50-m OV-1 wide-bore fused-silica column (Hewlett-Packard) was used to separate the C_4 through C_{15} organic species. Calibration of the gas chromatographic systems made use of an external standard mixture, which was referenced to several NBS primary standard "propane and benzene in air" calibration mixtures. Selected canister samples were analyzed by gas chromatography/mass spectrometry to identify or confirm the identities of peaks observed in the normal chromatographic analysis.

Carbonyl Compounds. Carbonyl compounds were collected in liquid impingers containing 2,4-dinitrophenylhydrazine (DNPH). These compounds react with DNPH to form stable derivatives. The samples were analyzed by high-performance liquid chromatography (HPLC) using a UV detector. Two impinger samples were collected simultaneously over each 20-min test, to provide a backup sample.

The DNPH procedure employs a solution consisting of 2,4-dinitrophenylhydrazine and sulfuric acid dissolved in acetonitrile. During emissions testing, two impingers containing 10 ml of the reagent were placed in parallel in an ice bath and samples were collected for 20 min at 1 liter/minute. Prior to analysis, the volume of the sample was adjusted to 5 ml, and a 10-μl aliquot was analyzed by HPLC with UV detection at 360 nm. The amount of each aldehyde was determined from response factors for pure DNPH derivatives. A Zorbax® ODS (4.6 × 25 cm) column and 60/40 acetonitrile/water mobile phase were used for the HPLC separation.

Polycyclic Aromatic Hydrocarbons. Polycyclic aromatic hydrocarbons (PAH) in the exhaust were collected on a solid adsorbent (XAD-2 resin). Each test employed a 22-g portion of XAD-2 resin, which was prepurified by Soxhlet® extraction with dichloromethane for 16 h. During sampling, the XAD-2 resin was contained in a glass sampling module maintained at 54°C. Exhaust samples were collected from the sampling manifold at a rate of 0.028 m^3 min^{-1} for 20 min, for a total volume of 0.56 m^3. The XAD-2 resin samples were extracted for 16 hours with dichloromethane prior to analysis. The extracts were concentrated to 1 ml in a Kuderna-Danish apparatus and stored at −78°C in the dark until analysis.

The XAD-2 sample extracts were analyzed by gas chromatography/mass spectrometry (GC/MS) with conventional splitless injection, to determine selected PAH in the multiple-ion detection (MID) mode. A Finnigan TSQ GC/MS system interfaced with a Finnigan INCOS 2300 data system was used for these analyses. The gas chromatographic column was an Ultra 2 crosslinked phenylmethyl silicone column with the outlet of the column located at the inlet of the mass spectrometer ionization source.

The identification of the target PAH was based on both GC retention time and the molecular ion mass. The quantification of each target compound was based on comparisons of the respective integrated ion current response of the molecular ion to that of an internal standard.

Results

Engine emissions measurements were carried out in June, 1988, at Tinker AFB in Oklahoma City, OK. The two engines examined during these tests were an F110 engine (serial number 509153) and an F101 engine (serial number 470135). Both engines had been overhauled and performance tested just prior to these measurements. The environmental conditions and engine operating variables for these tests are given in Tables 1 and 2. The data on operating conditions represent the average of two measurements made at the beginning and end of each 20-min sampling period. All tests were run using JP-4 fuel.

Gaseous emissions were measured at four power settings for each engine by sampling at the exhaust nozzle exit. The nominal power settings used for the F101 engine were idle, 44 percent, 75 percent, and intermediate (approximately 100 percent of rated thrust). The F110 tests were run at nominal settings of idle, 30 percent, 63 percent, and intermediate power.

The gaseous organic species measured in the exhaust from the two engines are listed in Tables 3 and 4. Concentrations are given in parts per million carbon (ppmC) for all species. Concentrations in ppmC units can be converted to ppm by volume by dividing by the number of carbon atoms in the molecule.

The results of analysis of the XAD-2 samples for polycyclic aromatic hydrocarbons are shown in Tables 5 and 6 for the

Table 1 Engine operating conditions for F110 engine (S/N 509153)

Engine nominal power setting	Idle	30%	63%	Intermediate
Initial engine inlet temperature (C)	30	29.4	26.1	27.7
Final engine inlet temperature (C)	28.3	27.2	27.2	27.7
Initial barometric pressure (in. Hg)	28.87	28.83	28.80	28.77
Final barometric pressure (in. Hg)	28.87	28.83	28.80	28.77
Engine inlet total pressure (psia)	14.18	14.15	14.12	14.08
Engine inlet static pressure (psia)	13.99	13.6	12.76	11.4
Fuel	JP-4	JP-4	JP-4	JP-4
Rated thrust (lb) (Intermediate)	16007	16007	16007	16007
Measured thrust (lb)[1]	700	4095	9681	16778
Fuel flow (lb/hr)[1]	1104	2587	5793	10673
Air flow (lb/hr)[1]	86.6	132.8	194.9	260.4
Fuel/air ratio[1]	0.003541	0.005412	0.008257	0.0113831
Turbine blade temperature (C)[1]	--	--	--	806.667
Fan speed (rpm)[1]	3301	5223	7002	8184
Core speed (rpm)[1]	10651	12226	13710	14643
Actual thrust (% Intermediate)[1]	4.4	25.6	60.5	104.8

1 Corrected to standard day.

Table 2 Engine operating conditions for F101 engine (S/N 470135)

Engine nominal power setting	Idle	44%	75%	Intermediate
Initial engine inlet temperature (C)	25	27.2	28.3	28.9
Final engine inlet temperature (C)	25	27.8	28.9	29.4
Initial barometric pressure (in. Hg)	28.69	28.66	28.66	28.60
Final barometric pressure (in. Hg)	28.69	28.66	28.64	28.60
Engine inlet total pressure (psia)	14.09	14.055	14.025	14
Engine inlet static pressure (psia)	13.78	12.89	11.96	11.04
Fuel	JP-4	JP-4	JP-4	JP-4
Rated thrust (lb) (Intermediate)	17390	17390	17390	17390
Measured thrust (lb)	1033	7836	13432	18723
Fuel flow (lb/hr)[1]	1065	3726	6544	9976
Air flow (lb/sec)[1]	126	236	304	353
Fuel/air ratio[1]	0.002342	0.004386	0.005977	0.007833
Turbine blade temperature (C)[1]	--	--	743	878
Fan speed (rpm)[1]	3274	5913	6877	7370
Core speed (rpm)[1]	10372	12601	13597	14410
Actual thrust (% Intermediate)[1]	5.9	45.0	77.2	107.7

1 Corrected to standard day.

two engines. All concentrations in Table 5 and 6 are in units of $\mu g/m^3$. Total extractable organic mass for these samples is listed in Table 7.

The reliability of the exhaust sampling can be assessed by comparing the fuel/air ratio calculated from exhaust gas composition with the fuel/air ratio determined from measured fuel flow and air flow. The deviation in calculated and measured ratios ranged from 2 percent low to 35 percent high. On average, the calculated ratios were 19 percent higher than the measured ratios. This difference is greater than expected based on past studies. The difference in ratios could be due to nonrepresentative exhaust sampling, to measurement errors in gas composition results, or errors in measurement of fuel flow or air flow. We re-examined all of these data, but could find no explanation for the differences. The measured air flow is the variable that is perhaps the most sensitive to measurement error. As an example, an error of about 0.1 psia in the pressure transducer results would account for the average discrepancy in the calculated and measured fuel/air ratios. However, we have no data to support this or alternative explanations of the differences.

Discussion

The organic species identified in the exhaust of the F110 and F101 engines are listed in Tables 3–6. Other species were resolved by the gas chromatographic analysis and were characterized by the number of carbon atoms in the molecule (i.e., approximate molecular weight), but were not identified as specific chemical compounds. The sum of the concentrations of all resolved organic compounds is shown at the bottom of Tables 3 and 4. In assessing the environmental impact of turbine engine exhaust, it is useful to know what fraction of the total organic emissions is accounted for by the analysis scheme. If most of the organic emissions can be accounted for, assessment of the environmental impact of the exhaust will be more credible.

The accountability of organic species in turbine engine exhaust was determined in a recent study that utilized the same multiple sampling and analysis techniques employed in this

Table 3 Organic emissions from F110 engine with JP4 fuel (concentrations in ppmC)

Organic Species	Nominal Engine Power Setting: Idle	30%	63%	Intermediate[2]
Methane	1.766	1.462	1.098	0.674
Ethane	0.033	0.022	0.024	0.013
Ethene	0.497	0.089	0.127	0.230
Propane	0.026	0.023	0.009	0.005
Acetylene	0.208	0.020	0.011	0.007
Propene	0.082	0.017	0.022	0.048
1-Butene + 1,3-Butadiene	0.034	0.016	0.018	0.009
1-Pentene	0.006	0.002	0.003	0.001
C5-ene	0.001	<0.001	<0.001	<0.001
n-Pentane	0.011	0.012	0.005	0.001
C5-ene	<0.001	<0.001	<0.001	<0.001
C5-ene	<0.001	<0.001	<0.001	<0.001
2-Methylpentane	0.009	0.021	0.008	0.001
3-Methylpentane	0.008	0.012	0.004	0.001
1-Hexene	0.003	0.004	0.005	0.002
n-Hexane	0.018	0.032	0.008	0.004
Methylcyclopentane + unk	0.010	0.018	0.005	0.002
Benzene	0.079	0.023	0.017	0.011
2-Methylhexane	0.005	0.011	0.002	<0.001
3-Methylhexane	0.017	0.019	0.012	0.009
n-Heptane	0.013	0.028	0.005	0.002
Methylcyclohexane	0.016	0.034	0.006	0.002
Toluene	0.985	0.032	0.012	0.007
2-Methylheptane	0.008	0.011	0.001	<0.001
3-Methylheptane	0.009	0.009	0.008	0.007
n-Octane	0.010	0.023	0.004	<0.001
Ethylbenzene	0.024	0.006	0.002	0.001
m+p-Xylene	0.086	0.021	0.006	0.003
Styrene	0.005	0.009	0.002	<0.001
o-Xylene	0.030	0.007	0.002	0.001
n-Nonane	0.015	0.025	0.002	<0.001
p-Ethyltoluene	0.007	0.007	0.002	0.001
1,2,4-Trimethylbenzene	0.015	0.013	0.002	0.001
n-Decane	0.025	0.033	0.002	0.001
Methylbenzaldehyde+C10H14	0.006	0.007	0.001	<0.001
Undecane	0.021	0.022	0.002	0.001
Naphthalene	0.005	0.002	0.000	<0.001
Dodecane	0.019	0.015	0.002	0.001
Tridecane	0.037	0.017	0.004	0.001
Tetradecane	0.007	0.029	0.007	0.004
Formaldehyde	0.305	0.162	0.095	0.090
Acetaldehyde	0.140	0.080	0.042	0.032
Acrolein	0.015	<0.001	0.009	0.003
Propanaldehyde	0.066	0.012	<0.001	<0.001
Acetone	0.060	0.072	0.084	0.024
Benzaldehyde + unk	<0.001	<0.001	<0.001	<0.001
Glyoxal	0.064	<0.001	0.004	0.016
Methylglyoxal	0.051	0.003	0.012	0.018
Biacetyl	<0.001	<0.001	<0.001	<0.001
TOTAL IDENTIFIED SPECIES CONCENTRATION	4.848	2.485	1.695	1.235
TOTAL ORGANIC COMPOUND CONCENTRATION	6.840	3.440	2.090	1.500

2 At high Mach number; equivalent to 105 percent

work. The analysis techniques were able to account for 98 ± 10 percent of the total organic emissions (Spicer et al., 1984).

The fraction of total organic emissions accounted for in this study is estimated by comparing the sum of the concentrations of all resolved organic compounds with the total organic carbon concentration in the exhaust. The total organic carbon concentration was monitored using a heated probe, continuous flame ionization detector. This technique does not respond to oxygenated carbon, so the results must be adjusted for carbonyl compound response. Comparison of the total organic carbon concentrations with the adjusted sum of resolved species concentrations yields an average carbon balance of 75 percent. This accountability is based on the sum of the resolved volatile organic species that were quantified. The total organic carbon monitor also responds to lower volatility organic species that were not measured by the gas chromatographic procedure used in this study. The mass of these unresolved lower volatility compounds was determined by collection on, and subsequent extraction from XAD-2 resin. The measured amounts of "ex-

Table 4 Organic emissions from F101 engine with JP4 fuel (concentrations in ppmC)

Organic Species	Nominal Engine Power Setting: Idle	44%	75%	Intermediate[3]
Methane	1.865	1.542	1.302	1.231
Ethane	0.042	0.016	0.009	0.011
Ethene	0.671	0.058	0.078	0.103
Propane	0.023	0.021	0.015	0.014
Acetylene	0.242	0.005	0.003	0.008
Propene	0.172	0.005	0.013	0.019
1-Butene + 1,3-Butadiene	0.012	0.002	0.005	0.049
1-Pentene	0.013	0.001	0.001	0.002
C5-ene	0.001	<0.001	<0.001	<0.001
n-Pentane	0.025	0.005	0.003	0.005
C5-ene	<0.001	0.006	0.002	0.001
C5-ene	<0.001	<0.001	<0.001	<0.001
2-Methylpentane	0.039	0.011	0.005	0.009
3-Methylpentane	0.022	0.002	0.003	0.007
1-Hexene	0.009	0.003	0.002	0.002
n-Hexane	0.058	0.005	0.008	0.019
Methylcyclopentane + unk	0.030	0.003	0.005	0.010
Benzene	0.104	0.011	0.007	0.013
2-Methylhexane	0.014	0.001	0.004	0.006
3-Methylhexane	0.026	0.006	0.008	0.017
n-Heptane	0.030	0.006	0.008	0.018
Methylcyclohexane	0.038	0.004	0.008	0.021
Toluene	0.070	0.016	0.009	0.015
2-Methylheptane	0.010	0.003	0.002	0.005
3-Methylheptane	0.008	0.008	0.006	0.012
n-Octane	0.017	0.003	0.007	0.013
Ethylbenzene	0.008	(4)	0.002	0.003
m+p-Xylene	0.028	0.005	0.005	0.008
Styrene	0.005	0.018	0.002	0.004
o-Xylene	0.008	0.006	0.002	0.009
n-Nonane	0.009	0.003	0.004	0.007
p-Ethyltoluene	0.005	0.002	0.002	0.002
1,2,4-Trimethylbenzene	0.007	0.004	0.002	0.003
n-Decane	0.007	0.011	0.003	0.005
Methylbenzaldehyde+C10H14	0.002	0.003	0.001	0.001
Undecane	0.009	(4)	0.003	0.004
Naphthalene	<0.001	(4)	<0.001	<0.001
Dodecane	0.004	0.010	0.002	0.003
Tridecane	0.004	0.015	0.002	0.003
Tetradecane	0.007	0.010	0.001	0.002
Formaldehyde	0.328	0.044	0.044	0.050
Acetaldehyde	0.160	0.040	0.032	0.028
Acrolein	0.006	<0.001	<0.001	<0.001
Propanaldehyde	0.078	<0.001	<0.001	<0.001
Acetone	0.087	0.063	0.054	0.054
Benzaldehyde	<0.001	<0.001	<0.001	<0.001
Glyoxal	0.016	0.004	<0.001	<0.001
Methylglyoxal	0.012	<0.001	<0.001	<0.001
Biacetyl	0.008	<0.001	<0.001	<0.001
TOTAL IDENTIFIED SPECIES CONCENTRATION	4.336	1.981	1.673	1.796
TOTAL ORGANIC COMPOUND CONCENTRATION	5.160	3.150	2.190	2.460

3 At high Mach number; equivalent to 107 percent
4 Data missing due to sample contamination

Table 5 Polycyclic aromatic hydrocarbon (PAH) results for F110 engine (concentration in $\mu g/m^3$)

Compound	NOMINAL ENGINE POWER SETTING: Idle	30%	63%	Intermediate[5]
Naphthalene	4.7	2.9	1.4	1.1
1-Methylnaphthalene	6.0	4.2	1.1	0.60
2-Methylnaphthalene	4.3	2.9	0.75	0.38
1,2-Dimethylnaphthalene	3.5	2.4	0.56	0.31
Dimethylnapthalene	7.1	5.0	1.3	0.72
1,4&2,3-Dimethylnaphthalene	2.0	1.3	0.42	0.22
2,6-Dimethylnaphthalene	0.54	0.42	0.10	0.067
Acenaphthylene	0.31	0.28	0.077	0.045
Acenaphthene	0.21	0.13	0.077	0.050
Dibenzothiophene	0.089	0.045	0.052	0.036
Phenanthrene	1.3	0.70	0.80	0.55
Anthracene	0.12	0.047	0.049	0.041
Fluoranthene	0.51	0.40	0.22	0.19
Pyrene	0.61	0.40	0.22	0.15
Cyclopenta[c,d]pyrene	0	0	0	0
Benz[a]anthracene	0.038	0.019	0.022	0.019
Chrysene	0.064	0.056	0.035	0.026
Benzofluoranthenes	0.096	0.038	0.045	0.033
Benzo[e]pyrene	0.057	0.020	0.022	0.017
Benzo[a]pyrene	0.073	0.021	0.028	0.022
Indeno[1,2,3-c,d]pyrene	0.054	0.011	0.023	0.024
Dibenzo[a,h]anthracene	0.064	0.011	0.030	0.036
Benzo[g,h,i]perylene	0.045	0.011	0.023	0.026

5 At high Mach number.

Table 6 Polycyclic aromatic hydrocarbon (PAH) results for F101 engine (concentration in $\mu g/m^3$)

Compound	NOMINAL ENGINE POWER SETTING: Idle	44%	75%
Naphthalene	2.8	1.1	0.77
1-Methylnaphthalene	2.2	0.67	0.40
2-Methylnaphthalene	1.4	0.38	0.20
1,2-Dimethylnaphthalene	0.72	0.26	0.13
Dimethylnapthalene	1.5	0.50	0.38
1,4&2,3-Dimethylnaphthalene	0.51	0.20	0.13
2,6-Dimethylnaphthalene	0.099	0.065	0.016
Acenaphthylene	0.093	0.034	0.017
Acenaphthene	0.057	0.053	0.030
Dibenzothiophene	0.096	0.036	0.038
Phenanthrene	0.81	0.46	0.53
Anthracene	0.051	0.029	0.069
Fluoranthene	0.22	0.16	0.13
Pyrene	0.22	0.19	0.20
Cyclopenta[c,d]pyrene	0	0	0
Benz[a]anthracene	0.026	0.021	0.16
Chrysene	0.042	0.041	0.030
Benzofluoranthenes	0.051	0.046	0.028
Benzo[e]pyrene	0.030	0.031	0.024
Benzo[a]pyrene	0.033	0.036	0.032
Indeno[1,2,3-c,d]pyrene	0.033	0.031	0.020
Dibenzo[a,h]anthracene	0.045	0.041	0.024
Benzo[g,h,i]perylene	0.030	0.031	0.017

Table 7 Total extractable organic matter

Engine	Power Setting	Total Extractable Organic Mass, mg	Total Sampled Volume m^3 (STP)	Concentration of Extractable Organic Mass, mg/m^3
F110	Idle	0.24	0.3133	0.77
F110	30%	0.32	0.4259	0.75
F110	63%	0.20	0.4268	0.47
F110	Intermediate	0.36	0.4189	0.86
F101	Idle	0.20	0.3339	0.60
F101	44%	0.20	0.4175	0.48
F101	75%	0.20	0.4941	0.40

tractable organic mass'' are reported for each power level in Table 7. When the extractable organic mass concentration is added to the sum of resolved species concentration, the carbon balance is significantly improved. In this case, the analysis techniques account for 100 percent of the organic carbon emissions on average. For individual tests, the accountability ranges from 70 to 110 percent. This level of accountability for the organic carbon emissions gives credence to use of the data for environmental impact assessment.

Methane is the organic compound present at highest concentration in the exhaust from the F110 and F101 engines at all power levels reported here. Methane is an ubiquitous constituent of the atmosphere, with a typical concentration in the range of 1.7 to 1.9 ppm. At power levels above idle, the exhaust is depleted in methane compared with the incoming air used for combustion. The methane concentrations observed in the engine exhaust are consistent with partial combustion of the atmospheric methane present in the inlet air, although some methane production during combustion cannot be ruled out.

In previous studies (Spicer et al., 1984, 1987, 1988), four compounds (ethene, acetylene, propene, and formaldehyde) were found to account for 20–30 percent of turbine engine emissions at idle power. These four species account for about 16 percent of the volatile organic compound concentration in the exhaust from the F110 engine at idle, and 27 percent of the volatile organics at idle power for the F101 engine. Because methane is largely unreactive in terms of atmospheric reactions leading to photochemical air pollution, organic emissions are often categorized by nonmethane organic compound (NMOC) concentration. These same four species account for 22 percent of NMOC emissions for the F110 at idle, and 43 percent for the F101. At higher power settings up through intermediate power, the exhaust constituents present at the highest concentrations are methane, ethene, and formaldehyde.

Examination of the data in Tables 3 and 4 reveals that the

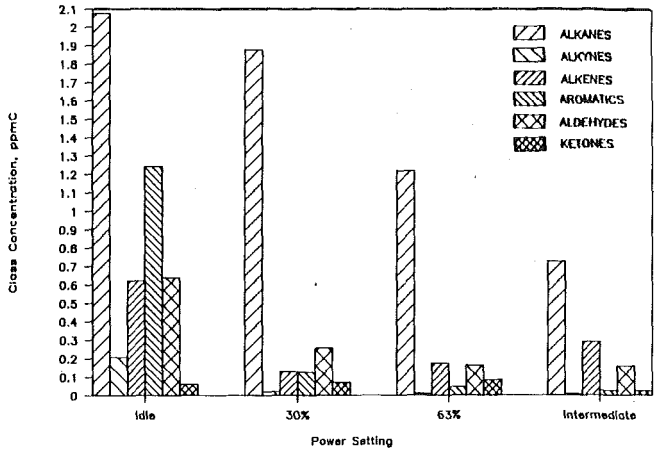

Fig. 2 Exhaust organic compound distribution by compound class for F110 engine for idle through intermediate power settings

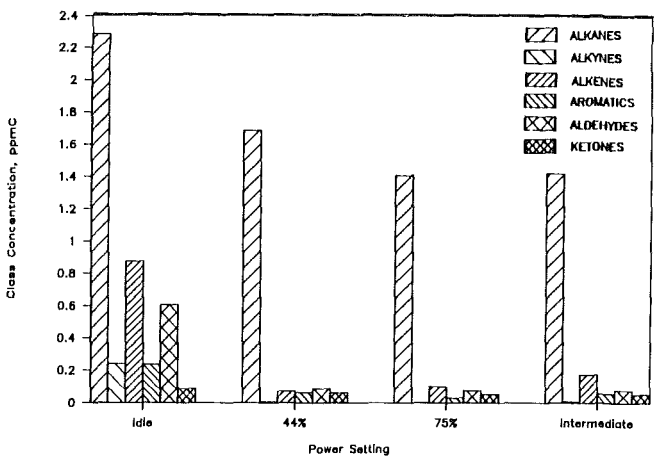

Fig. 3 Exhaust organic compound distribution by compound class for F101 engine for idle through intermediate power settings

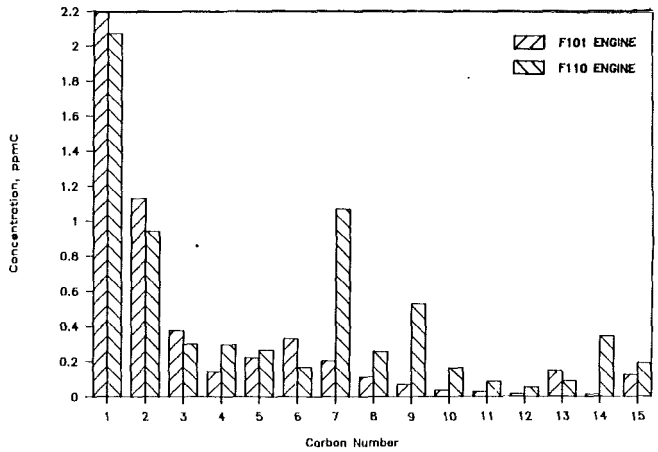

Fig. 4 Exhaust organic species concentrations by carbon number at idle

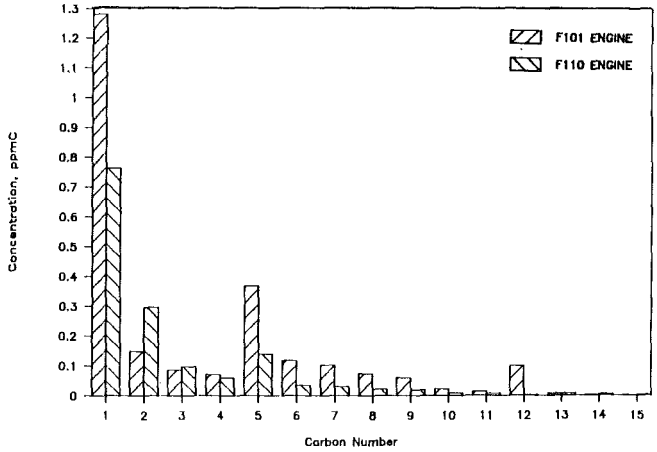

Fig. 5 Exhaust organic species concentrations by carbon number at intermediate power

organic emissions are reduced as the engine power is increased above idle. Exhaust organic concentrations for these two engines are significantly lower than for other engines examined using the same techniques (Spicer et al., 1984, 1987, 1988).

Distribution of Emissions by Compound Class. Different classes of chemicals often exhibit different environmental effects. For example, alkenes and aldehydes are more reactive than other compound classes in terms of photochemical air pollution. The distribution of organic emissions by compound class has been determined for the F110 and F101 engines based on the identified compounds in Tables 3–6. The class distribution for power settings from idle to intermediate is shown in Fig. 2 for the F110 engine and in Fig. 3 for the F101 engine. The most significant compound classes are alkanes, alkenes, aromatics, and aldehydes, with the relative contribution of these classes varying with power level. Alkanes dominate the class distribution at all power levels for both engines. The alkane class, in turn, is dominated by methane. Alkynes, represented by acetylene, are very low except at idle power. Alkenes, aldehydes, and ketones are generally products of incomplete combustion and, as such, are present at much higher concentrations at idle compared with higher power settings.

Distribution of Emissions by Carbon Number. Information regarding the distribution of emissions by volatility is important because such data most clearly distinguish the cracking and partial oxidation products from the unburned fuel. The number of carbon atoms in an organic molecule is highly correlated with volatility; the larger the molecule, the lower the volatility. Carbon number distributions for the F110 and F101 emissions were estimated from the gas chromatographic analysis results, and include all resolved compounds, whether identified or not. The chromatographic peaks for the *n*-alkanes were identified in the chromatograms, and unidentified peaks at retention times between two *n*-alkanes were assigned to the carbon number category of the lower carbon number *n*-alkane. For example, all unidentified chromatographic peaks with retention times between *n*-pentane and *n*-hexane were characterized as C_5 compounds.

The carbon number distribution of the JP-4 fuel used for these experiments shows C_7 and C_8 compounds are present at the highest percentage (Spicer et al., 1984, 1989). There is relatively little high-volatility material ($< C_5$) in the fuel. Therefore, the exhaust species found in the C_1 to C_4 categories are products of combustion, with the exception of methane, as noted earlier. Compounds in the C_1–C_4 classes are often referred to as "combustion-derived," and those materials C_5 and higher as "fuel-derived".

The carbon number distributions for emissions from the two engines operating at idle power are shown in Fig. 4. The distributions are fairly similar for the two engines, except for the C_7, C_9, and C_{14} categories, for which the F110 emissions are relatively higher. The high C_7 concentration for the F110 engine is due almost entirely to toluene emissions.

The carbon distribution of exhaust from engines operating at intermediate (~100 percent) power is shown graphically in Fig. 5. At this power level, where more complete combustion

is expected, the fuel-derived constituents are generally very low. The concentrations of combustion-derived exhaust constituents are also lower at intermediate power than at idle.

Emission Indices and Emission Rates. The emission index is defined as the mass of pollutant emitted per unit mass of fuel burned. The emission index has been calculated for the organic emissions from F110 and F101 engines for power levels from idle to intermediate (ICAO, 1981). The emission indices for the two engines were calculated based on the total hydrocarbon concentration measured by the continuous flame ionization detector. The emission indices are given in Table 8. Emission indices for CO, CO_2, NO_2, and NO_x are included in Table 8 for comparison (Spicer et al., 1989). As noted in the table, the emission index for NO_x was calculated using the molecular weight of NO_2. The data in Table 8 show that the emissions of organic compounds and carbon monoxide decrease as power is increased from idle to intermediate. A significant portion of the organic emission index is due to methane in the exhaust. As noted earlier, this species may not be produced by turbine engines, but may occur in the exhaust due to atmospheric methane in the combustion air. The emissions index for NO_x increases with increasing power from idle to intermediate. The emissions index for NO_2 shows no clear trend with engine power. The CO_2 emission index for the F110 engine shows little trend with power setting, while the index for the F101 increases with power level.

The emission indices for the engines may be used with the fuel flow data in Tables 1 and 2 to calculate emission rates. The emission rates are shown in Table 9 for power settings from idle through intermediate. These rates are given in units of kilograms per hour. The emission rates for CO are highest at idle, while the rates for CO_2, NO_2, and NO_x increase as engine power is increased from idle to intermediate. The rates for organic compounds are low at all power settings from idle to intermediate, and a large fraction of the organic emission rate may be attributed to methane present in the combustion air. The F110 and F101 engines exhibit significantly lower organic emissions rates at low power, compared with other engines we have tested (Spicer et al., 1984, 1987, 1988). These two engines appear to be substantially more efficient at fuel combustion at low power than engines tested earlier (Spicer et al., 1984, 1987, 1988).

Emissions of Polycyclic Aromatic Hydrocarbons (PAH). The class of compounds known as polycyclic aromatic hydrocarbons (PAH) contains numerous potent carcinogens (Sittig, 1985). Benzo(a)pyrene (BaP) is one of the most common and most hazardous members of this class of compounds, and is frequently used as a surrogate for PAH in general. BaP has been found in emissions from a variety of combustion sources, in urban air, cigarette smoke, and food sources. It has both a local and a systemic carcinogenic effect (Sittig, 1985).

The concentrations of BaP and other polycyclic hydrocarbons in F110 and F101 exhaust are reported in Tables 5 and 6. The exhaust concentrations of BaP are significantly lower than the OSHA standard for an eight hour time-weighted average concentration of 0.2 mg/m^3 (Sittig, 1985).

Table 8 Emission indices for F110 and F101 engines

	EMISSION INDEX (g/kg fuel)				
	Organic Compounds	CO	CO_2	NO_2	NO_x[6]
F110 Engine					
Idle	1.01	24.0	4352	1.2	6.6
30%	0.57	4.3	3638	0.63	9.4
63%	0.19	1.6	4473	1.0	20.1
Intermediate (105%)	0.16	1.3	4378	2.4	36.8
F101 Engine					
Idle	1.44	21.7	3408	1.4	5.0
44%	0.41	1.8	3511	1.2	11.0
75%	0.21	1.3	3982	1.7	19.2
Intermediate (108%)	0.20	1.4	4162	1.6	31.3

6 Calculated as NO_2 by convention.

Table 9 Emission rates for F110 and F101 engines

	EMISSION RATES (kg/hr)				
Power Setting	Organic Compounds	CO	$CO_2 (x10^3$	NO_2	NO_x[6]
F110 Engine					
Idle	0.51	12.0	2.18	0.60	3.3
30%	0.67	5.0	4.27	0.74	11
63%	0.50	4.2	11.8	2.6	53
Intermediate (105%)	0.78	6.3	21.2	11.6	178
F101 Engine					
Idle	0.69	10.5	1.65	0.68	2.4
44%	0.69	3.0	5.94	2.0	20
75%	0.62	3.8	11.8	5.0	57
Intermediate (107%)	0.91	6.4	18.8	7.3	142

6 Calculated as NO_2 by convention.

Conclusions

This study has characterized the organic chemical emissions from an F110 and an F101 turbine engine. The engines were operated in an indoor test cell using JP-4 fuel. Emission measurements were performed on exhaust generated at four power settings for each engine, ranging from idle to intermediate power. Engine operating parameters and environmental conditions were monitored during all emission tests. A battery of sampling and analysis techniques was used to identify and quantify individual organic species in the exhaust. Some chemicals were resolved by the analysis methods but were not identified; these species were quantified and characterized in terms of carbon number distribution.

This study has shown that the organic emissions from these two engines are very low compared with several other turbine engines. Methane is the dominant organic chemical in the exhaust at all power levels reported. Much of the methane in the exhaust may be due to atmospheric methane that was present in the ambient air used for combustion.

Other than methane, four compounds (ethane, formaldehyde, acetylene, and propene) account for 20–40 percent of the volatile organic emissions from these engines at idle. These four chemicals are products of combustion. Aldehydes, which also are products of the combustion process, were measured at significant concentrations in the exhaust. Several dicarbonyl compounds were observed in the exhaust. These chemicals are significant because they are photochemically reactive; they have not been reported by others who have studied turbine engine exhaust.

The distribution of emissions by compound class has been reported for four power settings. Alkanes are the most significant class of organic chemicals by concentration at all power levels. Alkenes, aldehydes, and ketones are generally products of incomplete combustion and are present at much higher concentrations at low power.

Emission indices and emission rates are reported at the various power settings for total volatile organic emissions. The emission index for volatile organic compounds decreases with increasing engine power from idle to intermediate. The emission rate shows a variable trend with engine power level. The emission indices and emission rates for CO, CO_2, NO_2, and NO_x are reported for comparison with the organic emission data.

References

Brooks, J. J., West, D. S., Strobel, J. E., and Stamper, L., 1978, "Jet Engine Exhaust Analysis by Subtractive Chromatography," Final Report SAM-TR-78-37, Dec.

Chase, J. O., and Hurn, R. W., 1970, "Measuring Gaseous Emissions From

an Aircraft Turbine Engine," *Proceedings of Society of Automotive Engineers Meeting*, New York, Apr., pp. 839–845.

Conkle, J. P., Lackey, W. W., Martin, C. L., and Richardson, A., 1980, "Organic Compounds in the Exhaust of a J-85-5 Turbine Engine," Final Report SAM-TR-80-29, Sept.

Groth, R. H., and Robertson, D. J., 1974, "Reactive and Nonreactive Hydrocarbon Emissions From Gas Turbine Engines," presented at the 67th Annual Meeting of the Air Pollution Control Association, Denver, June.

International Civil Aviation Organization, 1981, *International Standards and Recommended Practices, Environmental Protection, Vol. II, Aircraft Engine Emissions*.

Kuhlman, M. R., Sverdrup, G. M., Smith, D. L., Spicer, C. W., Hughes, D. P., Smith, M. D., and Seitchek, G. D., 1990, "Measurement of Primary Particles Emitted by Aircraft Turbine Engines," manuscript in preparation, Battelle, Columbus, OH.

Lazano, E. R., Melvin, W. W., and Hochheiser, S., 1968, "Air Pollution Emissions From Jet Engines," *J. Air Poll. Control Assoc.*, Vol. 18(6), pp. 392–394.

Moses, C. A., and Stavinoka, L. L., 1975, "Gas Chromatographic Analysis of Exhaust Hydrocarbons From a Gas Turbine Combustor," presented at the Western States Section/The Combustion Institute, Stanford Research Institute, Oct.

Robertson, D. J., Elwood, J. H., and Groth, R. J., 1979, "Chemical Composition of Exhaust Particles From Gas Turbine Engines," Final Report EPA 600/2-79-041, Feb.

Sittig, M., 1985, *Handbook of Toxic and Hazardous Chemicals and Carcinogens*, Noyes Publications, Park Ridge, NJ.

Spicer, C. W., Holdren, M. W., Lyon, T. F., and Riggin, R. M., 1984, "Composition and Photochemical Reactivity of Turbine Engine Exhaust," Report ESL-TR-84-28, Tyndall AFB, FL, Sept.

Spicer, C. W., Holdren, M. W., Miller, S. E., Smith, D. L., Smith, R. N., Kuhlman, M. R., and Hughes, D. P., 1987, "Aircraft Emissions Characterization: TF41-A2, TF30-P103, and TF30-P109 Engines," Report ESL-TR-87-27, Tyndall AFB, FL, June.

Spicer, C. W., Holdren, M. W., Miller, S. E., Smith, D. L., Smith, R. N., and Hughes, D. P., 1988, "Aircraft Emissions Characterization," Report ESL-TR-87-63, Tyndall AFB, FL, Mar.

Spicer, C. W., Holdren, M. W., Smith, D. L., Miller, S. E., Smith, R. N., and Hughes, D. P., 1989, "Aircraft Emissions Characterization: F101 and F110 Engines," Report ESL-TR-89-13, Tyndall AFB, FL, Mar.

Second-Generation Low-Emission Combustors for ABB Gas Turbines: Burner Development and Tests at Atmospheric Pressure

T. Sattelmayer

M. P. Felchlin

J. Haumann

J. Hellat

D. Styner

ABB Corporate Research Center,
Aerodynamics Department,
CH-5405 Baden, Switzerland

Based on fundamental research concerning swirling flows, including the vortex breakdown phenomenon, as well as on stability considerations of premixed flames, a second generation of low-emission burners has been developed. The lean premixing technique provides NO_x emissions below 25 ppmv for natural gas. For liquid fuels the oxides of nitrogen are limited to 42 ppmv (oil No. 2). The novel burner technology will be applied to the well-known ABB silo combustor. As a first step the Conical Premix Burner will be used to retrofit the ABB type 11N. For the ABB gas turbine type 8 the design of a novel fully annular combustor is in progress. Most of the conceptual work concerning burner aerodynamics and burner–burner interaction has been carried out on scaled-down burner and combustor models. For a second step a sector of the combustor in 1:1 scale has been tested at atmospheric pressure. Additional high-pressure tests provide information about the combustor performance at engine conditions. The present paper summarizes the results of the first two steps beginning with the early ideas in the conceptual phase up to the 1:1 tests, which prove the low-NO_x capability for both gaseous and liquid fuels under atmospheric pressure conditions.

Goal of the Continuing Combustor Development Program at ABB

In 1984 the first Dry-Low-NO_x combustor of ABB was put into service in Lausward (FRG). The cluster of burners is shown in Fig. 1. Combustion air and gaseous fuel are mixed in an array of tubes before the mixture enters a large tubular combustor via air swirlers. NO_x emissions below 40 ppmv have been measured at combustor pressures up to 14.5 bars and inlet temperatures up to 380°C. Due to the large residence times in the combustor, very high combustion efficiencies are obtained above approximately 40 percent load (Koch et al., 1985).

Using the experience gained from six units (total GT output 575 MW) with more than 63,000 hours of operation, the first goal of the investigation of low emission combustion is to improve the performance of ABB silo combustors by replacing the present burner including the mixing tubes (Fig. 2). For this purpose a novel dual-fuel burner of considerably simpler design has been developed. Additionally, several kinds of burner staging have been investigated to simplify the fuel supply and control system. In order to retain the reliability of the present silo combustor technology, only minor changes are made to parts of the hot gas path downstream of the burners.

Due to the NO_x limitation of 25 ppmv, the percentage of air required for combustion increases with increasing pressure ratio and air outlet temperature of the compressor. Simultaneously, more air is needed for wall cooling, as long as the basic combustor design and the wall cooling technique remain unchanged. The air consumption for wall cooling can be minimized by reducing the overall surface of the hot gas path from burner to turbine inlet. As a consequence, for gas turbines with very high pressure ratios (e.g., ABB type 8), the new combustor is of a fully annular design (Fig. 3) and will be equipped with 18 main burners and 18 alternately distributed smaller pilot burners. All burners are of the same type.

Premix Burner Development Using Scaled-Down Models

A unique property of the Conical Premix Burner (Fig. 4) is the flame stabilization in free space near the burner outlet utilizing the sudden breakdown of a swirling flow (Keller et al., 1988). The swirler of exceptionally simple design (Fig. 5) consists of two halves of a cone, which are shifted to form two air inlet slots of constant width. The premixing tube known from conventional burner designs has disappeared. Gaseous or liquid fuels can be burned. The operating principle for both cases is shown in Fig. 4. Gaseous fuels are injected into the combustion air by means of fuel distribution tubes comprising two rows of small holes perpendicular to the inlet ports of the swirler. Complete mixing of fuel and air is obtained shortly after injection. By distributing the holes along the inlet slots

Contributed by the International Gas Turbine Institute and presented at the 35th International Gas Turbine and Aeroengine Congress and Exposition, Brussels, Belgium, June 11–14, 1990. Manuscript received by the International Gas Turbine Institute January 27, 1990. Paper No. 90-GT-162.

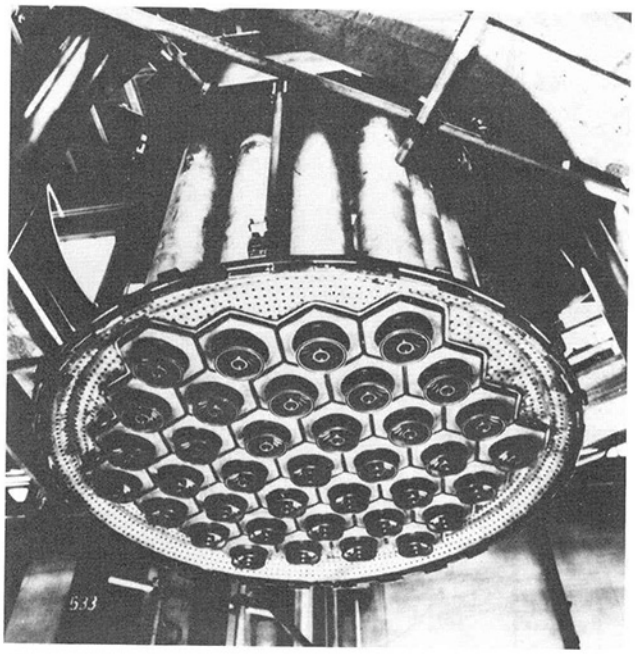

Fig. 1 First generation of low NO_x combustors (cluster of premix burners)

properly, the fuel concentration profile in the burner exit plane can be adjusted. Liquid fuels are injected at the burner tip using a pressurized or an air-assisted atomizer. Due to the flame stabilization in free space, premixing and combustion chambers can be combined. Droplet mixing and complete evaporation are achieved downstream of the air swirler before the recirculation zone is approached, where ignition of the mixture takes place near the flow stagnation point. As a result, a perfectly nonluminescent oil flame is obtained. In contrast to other more conventional premix burner designs, no diffusion or pilot stage is needed to improve the stability of the premixed flame. Combustors equipped with conical premix burners always operate in the pure premixed mode. Due to the fact that neither gaseous nor liquid fuel is present upstream of the swirler, exceptional reliability (flashback) is obtained. Since the zone of ignition is significantly displaced from the burner walls, the heat transfer to the burner section is minimized.

Frequently, severe stability problems occur with premixed flames in gas turbine combustors. An important property of the burner flow field is how strong the disturbances originating from combustion will influence the local position of the ignition zone near the stagnation point. A weak characteristic causes fluctuating local heat release and destabilizes the combustion process.

Vortex breakdown theory (Keller et al., 1988) clearly indicates that the most stable transition from a supercritical closed vortex flow into an annular form with recirculation on the axis is obtained only for swirling flows without a deficit in axial

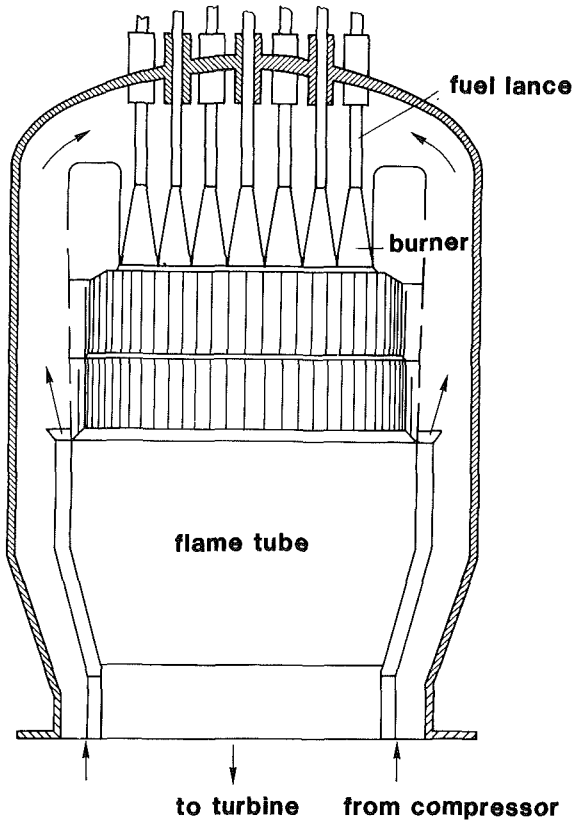

Fig. 2 Silo-combustor equipped with conical premix burners (e.g., GT11N)

velocity on the burner axis, as known from flows generated from, e.g., radial swirler configurations.

For the conical premix burner it can easily be shown that an analytical solution can be given for potential flow between the burner tip and the zone of vortex breakdown.

The solution does not depend on the axial burner coordinate:

$$u = f(u_{\text{ref}}, \beta, r);\ v(r) = 0;\ w(r) = f(u_{\text{ref}}, \beta, r)$$

The parameter β is a function of the cone angle and the width of the inlet slots:

$$\beta = \text{const} \cdot (\tan \alpha_c / b)$$

Figure 6 shows the theoretical velocity field for a prototype burner with an orifice diameter of 100 mm near the exit plane. The existence of an analytical solution leads to a high degree of understanding without using any elaborate numerical computer codes. Fuel concentration or spray penetration and evaporation calculations, for example, can be easily performed.

Theoretical considerations lead to the result that vortex breakdown near the burner exit plane will occur when parameter β exceeds a certain minimum value $\beta_{\min}$. Burners with lower values of β violate the vortex breakdown criterion and

Nomenclature

b = width of air inlet slot (conical premix burner)
c = air velocity
c_f = fuel concentration
D = burner diameter
$\dot{m}$ = mass flow rate
r = radius
T_{air} = air temperature upstream of burner
T_p = calculated primary zone temperature
T_{Burner} = burner temperature
T_c = gas temperature on burner centerline
u = axial air velocity
v = radial air velocity
w = tangential air velocity
x = axial coordinate
y = coordinate (combustor height)
z = coordinate (combustor width)
α_c = cone angle (Fig. 9)
α_w = angle of flow near burner wall (Fig. 9)
λ_{burner} = excess air coefficient of burner
λ_{comb} = excess air coefficient of combustor
Φ_{burner} = equivalence fuel/air ratio of burner
Φ_{main} = equivalence fuel/air ratio of main burner
Φ_{pilot} = equivalence fuel/air ratio of pilot burner

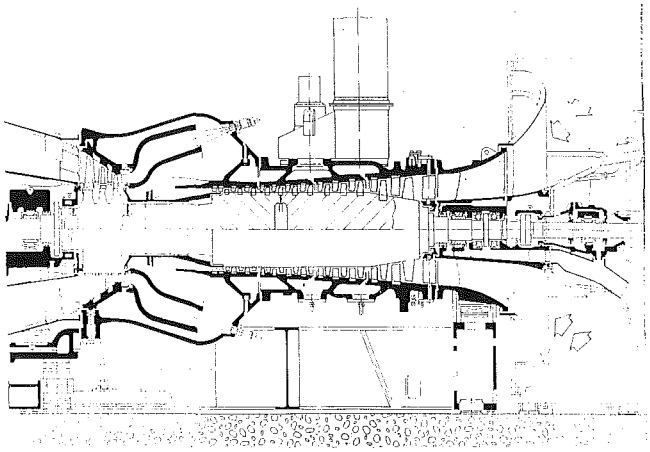

Fig. 3 Annular combustor-equipped with conical premix burners (e.g., GT8)

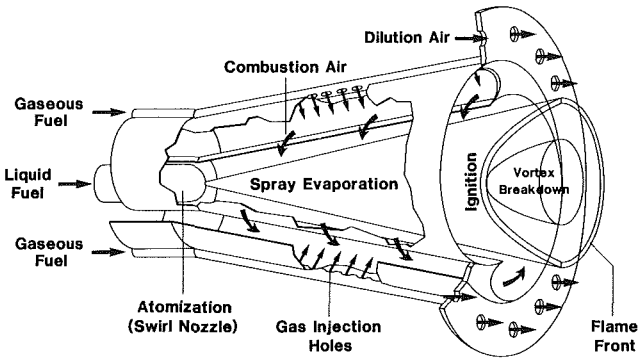

Fig. 4 Operating principle of the conical premix burner

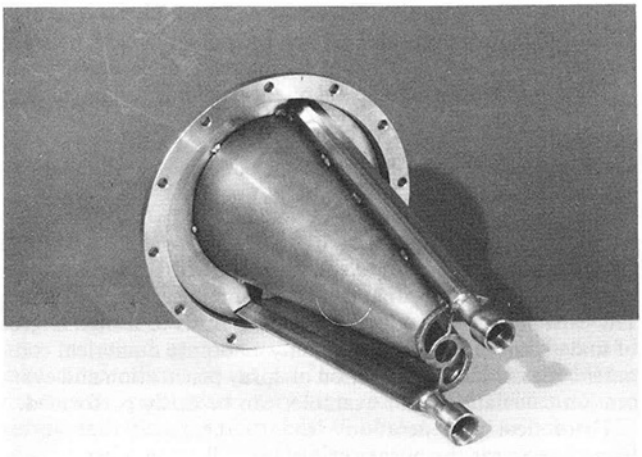

Fig. 5 Prototype burner for high-pressure tests

lead to flow fields completely unsuitable for combustion purposes.

Figure 7 shows laser-Doppler-anemometer measurements for a burner geometry fulfilling the theoretical criterion for vortex breakdown. The appropriate profiles within the burner are generated as predicted. The transition from a closed vortex flow with high velocities on the axis to its annular flow state with stagnation on the axis takes place within a short distance close to the burner outlet.

Satisfactory agreement between calculated (see Fig. 6) and measured velocity profiles is obtained in the region upstream of vortex breakdown (Fig. 8). The breakdown of the vortex flow occurs slightly upstream of the burner exit plane. As a

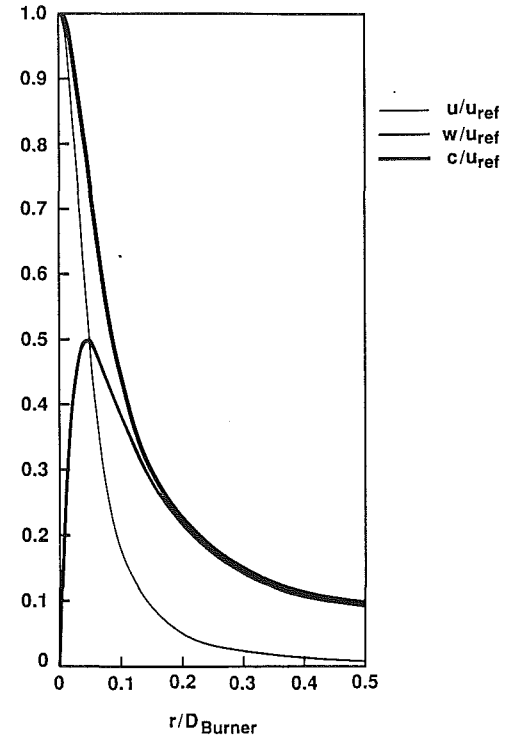

Fig. 6 Velocity distribution within burner (potential flow without breakdown)

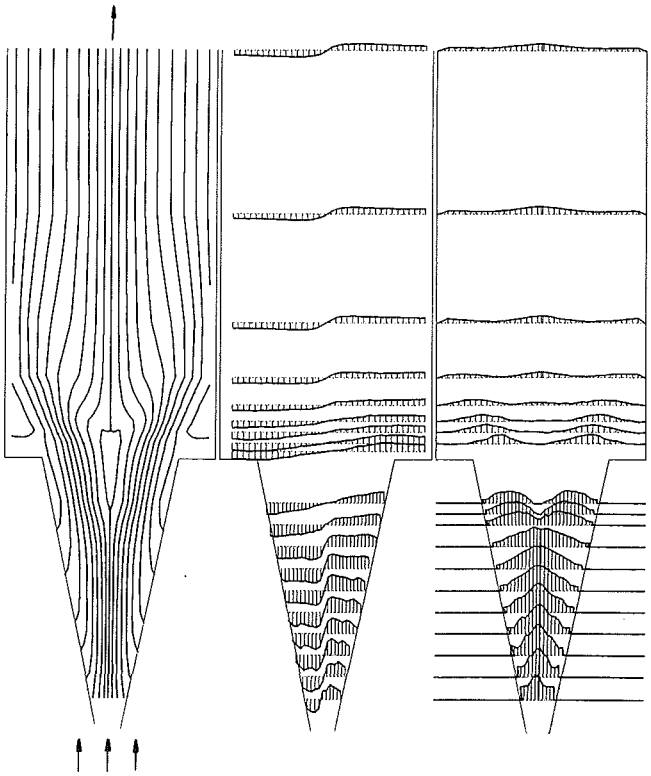

Fig. 7 Velocity distribution (LDA measurement, nonreacting flow)

consequence, only low swirl velocities are measured near the burner axis at the burner outlet due to the recirculation zone.

The flow direction near the burner wall depends on the distance between burner wall and burner centerline. Therefore, different curves are obtained for the three circumferential positions of measurement depicted in Fig. 9. Only in the region of vortex breakdown can major differences between prediction and measurement be seen.

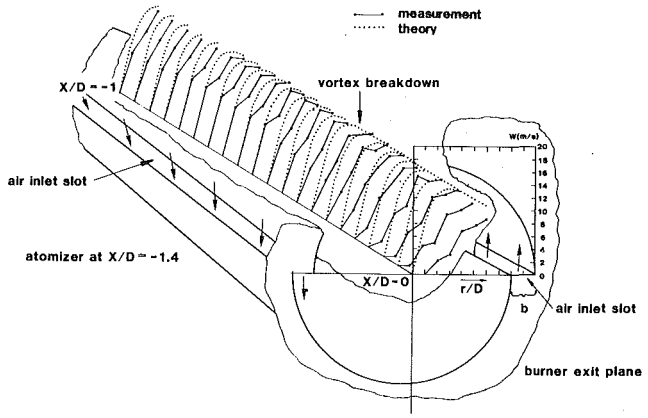

Fig. 8 Comparison of predicted and measured swirl profiles

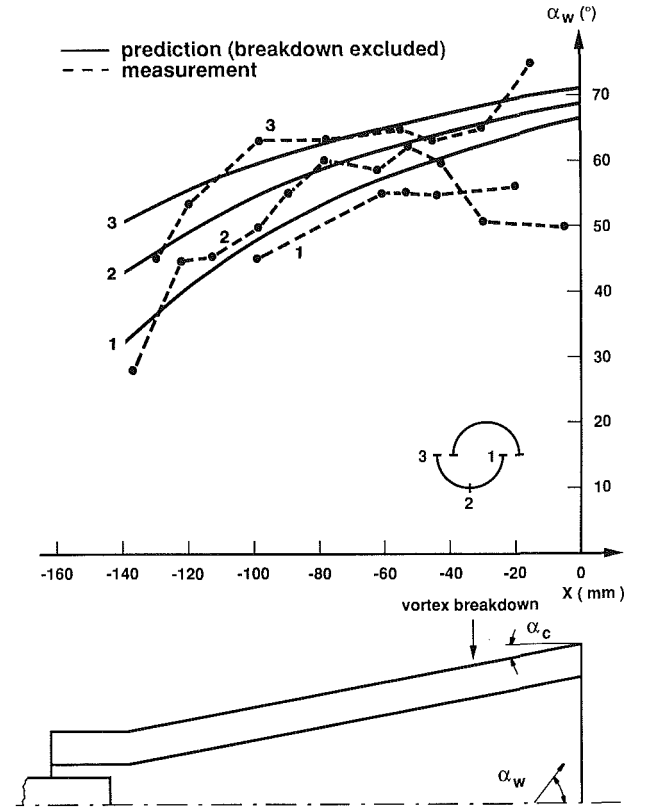

Fig. 9 Comparison of predicted and measured flow direction near the burner walls

Temperature profile measurements on the burner axis provide information about the flame position in the case of reacting flow. Figure 10 reveals that the air in the upstream part of the burner remains cold and that the temperature rise due to combustion takes place near the stagnation point found for cold flow. The beginning of the temperature rise depends weakly on the air preheat temperature.

In a first approach, completely homogeneous mixing of fuel and air is desirable to abate the formation of nitrogen oxides. Nevertheless, a profile with a slightly lower mixture strength in the central region of recirculation (Fig. 11) yields ultralow emission levels for the conical premix burner.

Typical results of emission measurements for propane performed at atmospheric pressure are shown in Fig. 12. The prototype burner used in the tests is rated to approximately 150 kW thermal output. A ceramic, almost adiabatic flame tube was used. As long as the fuel is injected along the inlet slots, very low NO_x, CO, and UHC emissions are obtained when the blowoff limit is approached ($\lambda \leq 2.3$). Since the

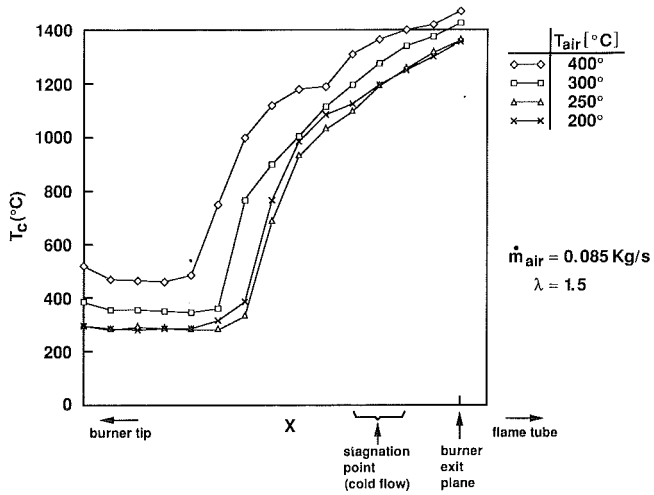

Fig. 10 Position of temperature rise on burner axis

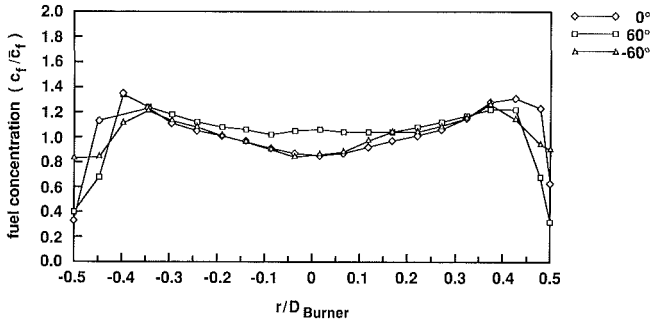

Fig. 11 Fuel distribution in burner exit plane (nonreacting gas flow, tracer measurement, tracer: CO)

average flame temperature remains above the limit where quenching of the reaction from CO to CO_2 occurs, an increase in carbon monoxide formation can hardly be detected and the premixed flame extinguishes without any significant intermediate stage of incomplete combustion. Similar results are obtained for clusters of burners, all operated with the same equivalence ratio, when quenching effects near cooled liner walls are not significantly strong.

Additionally, it can be concluded from Fig. 12 that the attempt to further simplify the conical premix burner using the oil nozzle for the injection of gaseous fuel (no fuel distribution tubes along the inlet slots required) leads to unsatisfactory NO_x emissions. Gas and air are not well mixed until combustion begins.

For liquid fuels better mixing is obtained due to spray penetration and droplet evaporation within the burner. Figure 13 shows the influence of nozzle position on burner performance for two pressurized nozzles, which differ slightly from each other in terms of flow number and spray angle. Generally, the nozzle position where minimum NO_x emissions are measured also yields minimum combustion noise.

Shifting the nozzle downstream leads to a deterioration of evaporation and results in luminescent flames from droplet combustion. For nozzle positions far upstream, nonuniform fuel concentration in the burner exit plane is obtained, which augments NO_x generation in the outer region of the flow. At the same time, combustion noise increases due to the lack of fuel in the recirculation zone on the burner axis. For air-assisted nozzles similar results were obtained. Figure 14 proves the low-NO_x capability of the conical premix burner at atmospheric pressure. The lowest NO_x emissions measured for oil ($\lambda_{Burner} \approx 2$) are approximately twice as high as those measured for propane if the data are compared on the basis of the burner equivalence ratio.

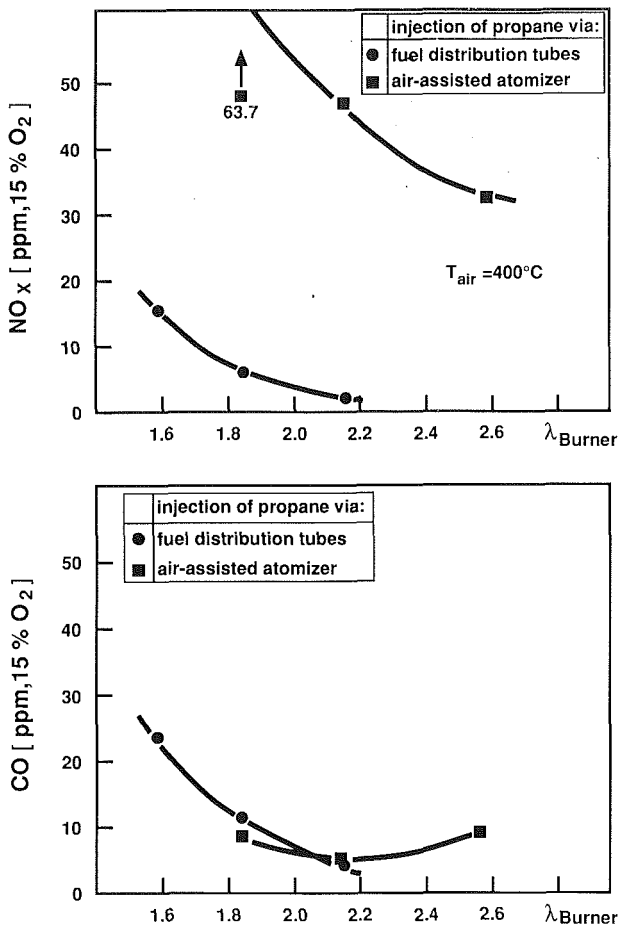

Fig. 12 NO_x and CO emissions of prototype burner (gaseous fuel)

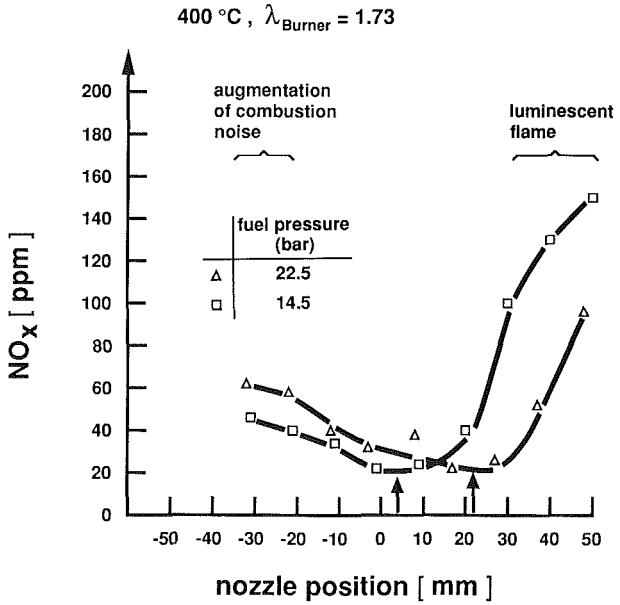

Fig. 13 Influence of nozzle position on NO_x emissions (pressurized nozzles)

In order to take the chemical composition of the fuel into consideration, the data are correlated to the primary zone temperature (Fig. 15) calculated on the basis of the total air mass flow including dilution air (see Fig. 4). Parameters are:

- kind of fuel (fuel bound nitrogen negligible)
- combustor inlet temperature
- burner (gaseous fuel, dual fuel)

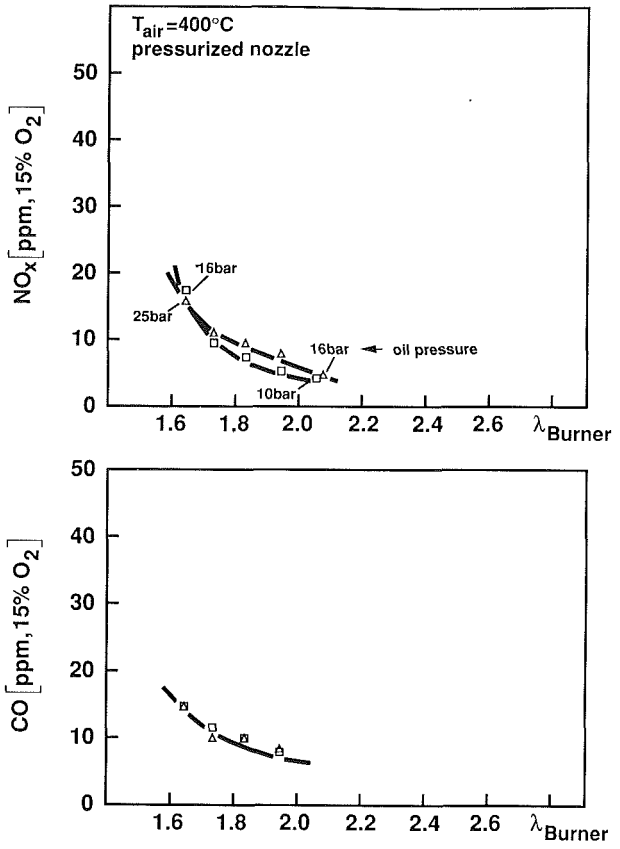

Fig. 14 NO_x and CO emissions of prototype burner (liquid fuel, fuel bound nitrogen negligible)

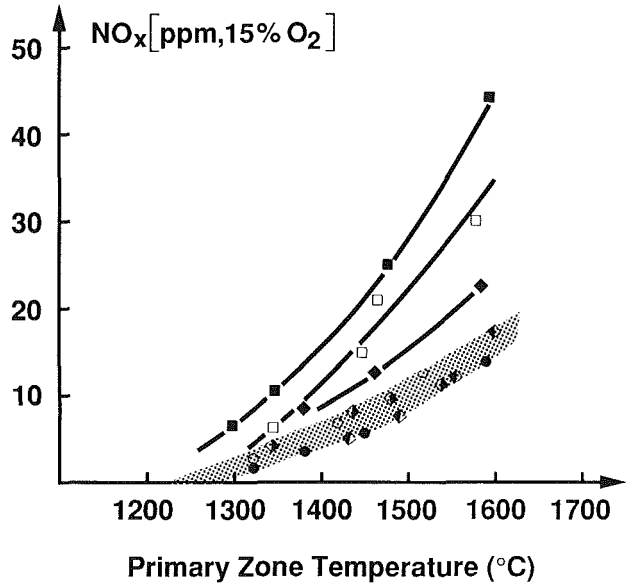

	burner type	fuel	spray angle	fuel or atomization air pressure (bar)	T_{air} (°C)	nozzle
○	prototype for gaseous fuel only	propane			20	
●	prototype for gaseous or liquid fuel	"			400	
◆		oil	30	10 - 16	"	pressurized
◆		"	30	16 - 25	"	
◆		"	60	10 - 16	"	
■		"	22	0.2	"	air-assisted
□		"	32	0.2	"	

Fig. 15 Influence of primary zone temperature on NO_x emissions

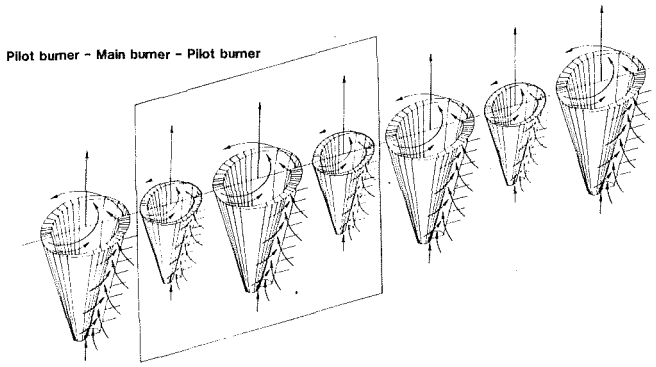

Fig. 16 Main- and pilot-burner configuration of the annular combustor

- kind of atomizer (pressurized, air-assisted)
- size of atomizer
- spray angle

Despite the wide scattering of the data, Fig. 15 clearly indicates that the optimum nozzle configuration for oil (pressurized nozzle, spray angle 30 deg) yields similar emissions to those measured for propane at different air inlet temperatures. Since the NO_x generation of premixed flames is mainly governed by the flame temperature, it can be concluded that a high degree of premixing is obtained even in the case of liquid fuels as long as the combustion air is strongly preheated. Tests using air-assisted atomizers reveal that the deterioration of droplet evaporation at lower air inlet temperatures leads to a remarkable increase in NO_x formation at constant flame temperature.

Burner Staging Principle

For single-shaft gas turbines running with constant speed, the fuel consumption changes by approximately a factor of three from idling to full load. Modern premix burners, however, must be operated at almost constant equivalence ratio if a certain NO_x limitation is not to be exceeded. An advantage of ABB silo combustors is that this is achieved by burner (fuel) staging: In principle, purely premixed combustion can be maintained down to very low load by concentrating the fuel flow on an appropriate number of burners in the center of the combustor.

Since the same procedure for can combustors will lead to unsatisfactory temperature profiles at the turbine inlet, additional diffusion stages are required, which exhibit an augmentation of NO_x emissions below full load.

A novel piloting technique has been realized in the ABB annular combustor (Fig. 16). Pilot and main burners are alternately distributed and have the same direction of swirl. Stable combustion from idling to full load is obtained as long as the pilot burners operate in self-stabilized mode. The fuel flow is split to obtain the desired equivalence ratios of the pilot burner independent of the thermal output of the combustor. Supplementary fuel is fed to the main burners. At low load the mixture obtained from the main burners is too lean to ignite at the burner outlet. Nevertheless, high combustion efficiencies and uniform temperature profiles at the turbine inlet are obtained due to the unstable arrangement of hot (pilot burners) and cold (main burners) vorticities, which generate intense mixing in the primary zone. Without any sudden transition in combustor performance, the self-stabilized mode of the main burners is reached near full load.

Figures 17 and 18 show two examples of the temperature field measured in a combustor model with a burner configuration consisting of two pilot burners and one main burner located between them. It can be understood easily that a very uniform temperature profile is obtained at high load (Fig. 17) due to equal equivalence ratios of all burners. More interesting is the result for pilot burner operation only (Fig. 18): Although

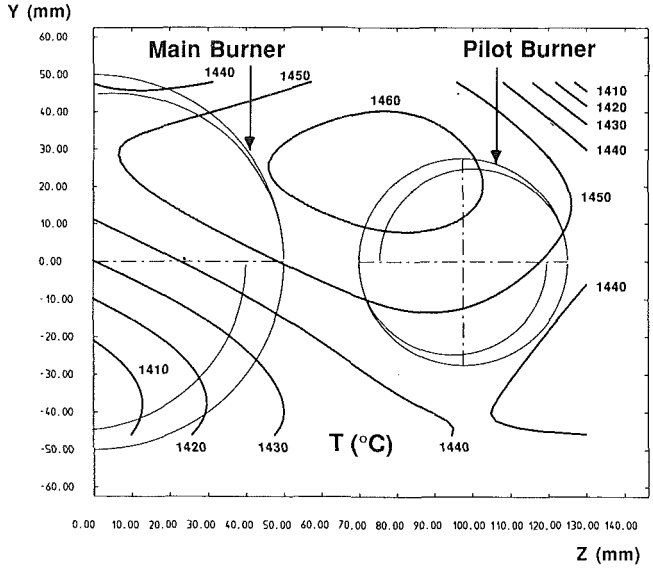

Fig. 17 Temperature distribution at high load (X = 400 mm, Φ_{pilot} = Φ_{main} = 0.56)

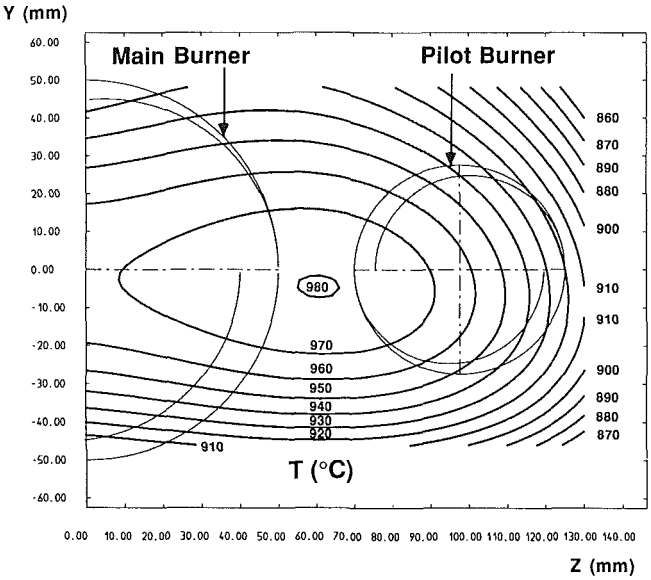

Fig. 18 Temperature distribution at low load (X = 400 mm, Φ_{pilot} = 0.56, Φ_{main} = 0)

77 percent of the combustion air passes through the main burners in the annular configuration, the temperature field quality remains very satisfactory even when all fuel is fed to the pilot burners.

In characterizing the temperature field by means of pattern factors for the whole cross section (OTDF) and for the profiles measured in the y direction (PTDF), an impression of the temperature uniformity can be gained (Table 1, coordinate Z: see Fig. 18)).

As long as adiabatic conditions are considered, very low values are calculated from the measurements. A combination of film cooling with convective cooling using a finned liner was found to be appropriate for the annular combustor with its low flame temperature and its well-defined flow direction near the wall. Including the effect of wall cooling causes pattern factors to increase slightly. Side wall effects of the test rig cause a deterioration in ODTF. For this reason the values given for ODTF in Table 1 are higher than those to be expected for the annular burner configuration. The measurements indicate, nevertheless, an adequate temperature uniformity at the turbine inlet section. An additional mixing section will not be

Table 1 Temperature pattern factors

Fuel	Mode	OTDF(%)	PTDF(%) (y-profile)
without wall cooling (≈adiabatic wall):			
Propane	$\phi p=\phi m$	4	2-4
	$\phi m=0$	10	6–8
Oil	$\phi p=\phi m$	7	2-7
	$\phi m=0$	12	4–7
wall cooling included:			
Propane	$\phi p=\phi m$	<12	<3 Z=0 <9 Z=100mm
	$\phi m=0$	<20	<6 Z=0 <10 Z=100mm

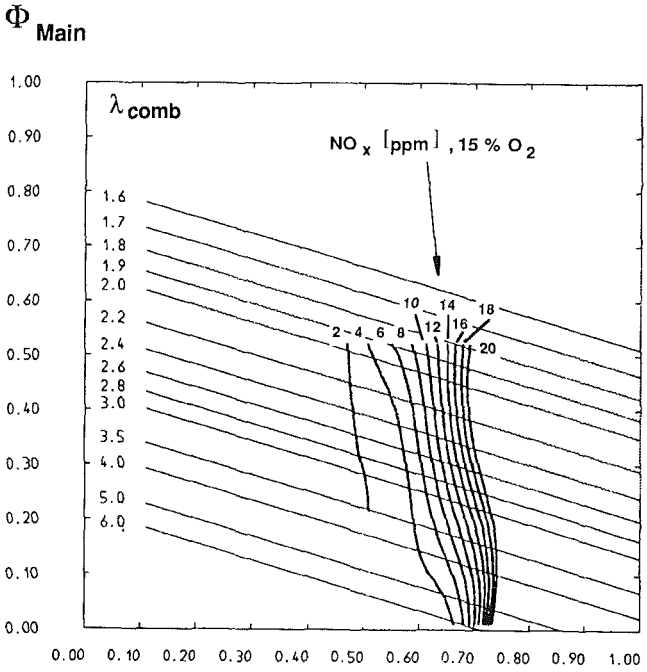

Fig. 19 NO_x emission chart (400°C, propane)

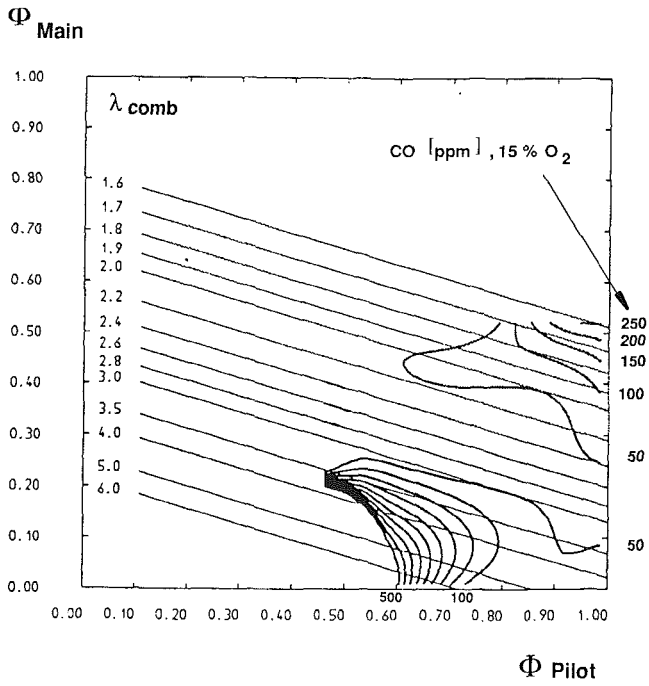

Fig. 20 Co-emission chart (400°C, propane)

required and the entire air flow can be used as burner or wall cooling air, respectively.

Emission measurements provide information about the burnout and the NO_x generation in the partial load regime, when the main burners do not operate in self-stabilized mode. In Fig. 19 the NO_x emissions are plotted versus the pilot burner and main burner equivalence ratios. Independently from how the fuel flow is split, the thermal output of the combustor remains constant along the straight λ_{comb} lines. NO_x emissions below 5 ppmv are obtained in a wide range of operation when the fuel flow to the pilot burner is properly chosen. When a uniform full load equivalence ratio for all burners of approximately $\phi = 0.44$ ($\lambda_{comb} = 2.3$) is fixed (see Fig. 14), idling is reached at $\lambda_{comb} \approx 6$. With regard to nitrogen oxides, the pilot burner equivalence ratio should be decreased from $\phi_p \approx 0.65$ to 0.44 while the main burner load is increased from $\phi \approx 0.03$ to 0.44. Almost complete burnout was measured for $\lambda_{comb} \leq 3.3$ (Fig. 20) or, in terms of gas turbine output, above 50 percent load. At lower loads the pilot burner equivalence ratio must be increased slightly to improve burnout. As long as NO_x generation at very low loads is not considered, almost complete burnout can be achieved even at idling.

Based on the tests at atmospheric pressure, it can be concluded that the technique of piloting proposed for the ABB annular combustor leads to very promising results in the partial load regime, comparable to those obtained for burner staging in silo combustors.

Validation of Results in 1:1 Scale at Ambient Pressure

Subsequent to the conceptual phase of the combustor project, various experiments were performed on 1:1 scale at atmospheric combustor pressure using natural gas and oil No. 2 as fuels. The program included single burner tests as well as tests of a combustor segment (test rig comprising two pairs of burners). The NO_x emissions in the high load regime (main burners) are shown in Fig. 21. Without any problems of flame stability, ultralow emissions are obtained for natural gas. For oil No. 2 the emissions obtained from the scaled-down models cannot be fully validated. Beside the effects originating from fuel bound nitrogen, which can clearly be detected, the poorer performance at 1:1 scale is due to the influence of burner size on droplet spray penetration. The calculation of the spin-up and evaporation of droplets for the three cases:

1 scaled-down burner operated at atmospheric pressure
2 burner of engine size operated at atmospheric pressure
3 burner of engine size under engine conditions

predicts the desired homogeneous fuel concentration only in cases 1 and 3. Tests at engine size but at atmospheric pressure (case 2) lead to a high concentration of the fuel vapor in the outer part of the burner exit plane, generated from the droplets with an initial droplet size greater than the mass median diameter of the spray. To prevent liquid fuel from igniting within the burner, the residence time must be minimized. For all test cases the calculated residence time does not exceed approximately 6 ms.

To answer the question whether the desired NO_x limitation can be reached under engine conditions, the influence of air pressure on NO_x formation must be known. Based on experimental data, various scaling laws can be found in the literature. Oversimplified kinetic approaches indicate an influence pro-

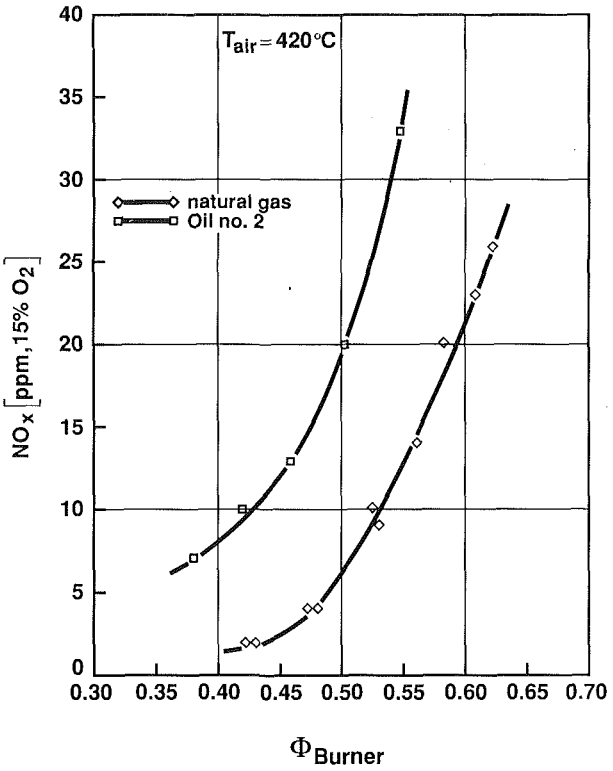

Fig. 21 Optimum performance of the main burner at engine size and atmospheric pressure (420°C)

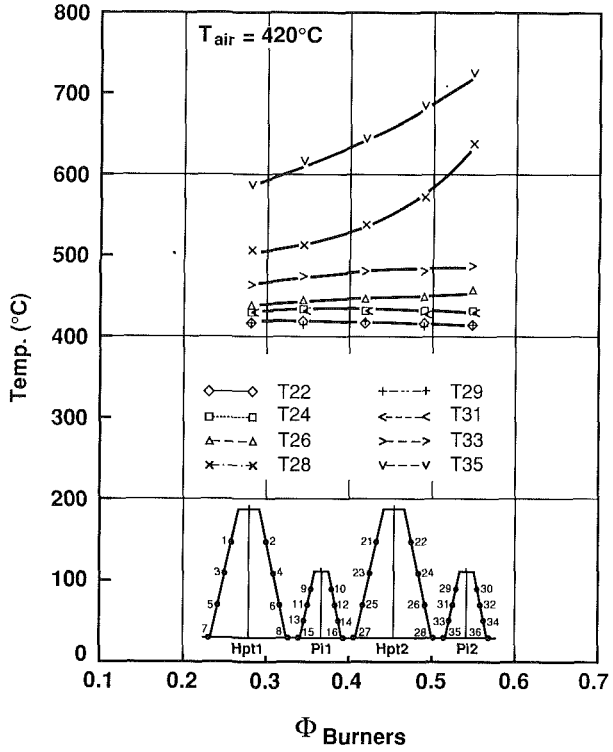

Fig. 22 Burner temperatures ($\phi_p \approx 2.2 \cdot \phi_{burner}$, $\phi_m \approx 0.65 \cdot \phi_{burner}$)

portional to the square root of combustor pressure. If the equivalence ratio at full load is adjusted to $\Phi_{Burner} = 0.44$, full-load emissions for natural gas will not exceed the NO_x target even in the case of a scaling law $NO_x \sim p_{combustor}$ (Aigner et al., 1990). By stabilizing the flame in free space, the heat transfer to the conical premix burner is minimized. Figure 22 proves that the burner temperature (thermocouples 22, 24, 26, 29, 31, and 33) does not significantly exceed the temperature of the air. Only the thermocouples at the burner exit plane (28 and 35) record elevated temperatures, since the impingement cooling of the combustor front panel was not present in the tests at atmospheric pressure.

Conclusions

Compared to the first generation of ABB low-NO_x burners, the conical premix burner exhibits several advantages:

- simple design
- no fuel upstream from burner (flashback impossible)
- no premixing tube
- simple oil injection technique

The following results have been obtained during the test program at ambient pressure:

(*a*) Burner models:

- zone of recirculation in free space (vortex breakdown), which acts as a flameholder
- excellent stability of premixed flame
- ignition near burner exit plane
- zone of reaction displaced from burner walls
- low-NO_x capability for gaseous as well as liquid fuel

(*b*) Partial load performance:

- simple piloting concept for the annular combustor
- only two burner groups (pilot burners and main burners)
- excellent temperature profile without mixing zone
- low NO_x emissions as well as complete burnout above 50 percent load

(*c*) Combustor segment (1:1 scale):

- natural gas: validation of results from model experiments
- natural gas: NO_x emissions extremely low: less than 25 ppmv at engine conditions
- oil No. 2: NO_x emissions somewhat higher than in model experiments
- low burner temperatures

References

Aigner, M., et al., 1990, "Second Generation Low Emission Combustors for ABB Gas Turbines: Tests at Full Engine Conditions," ASME Paper No. 90-GT-308.

Keller, J. J., et al., 1988, "Vortex Breakdown as a Fundamental Element of Vortex Dynamics," *ZAMP*, Vol. 39, No. 3, May.

Koch, H., et al., "Dry-NO_x Brennkammer, Entwicklung und erreichte Resultate," CIMAG, Oslo.

Status of Topping Combustor Development for Second-Generation Fluidized Bed Combined Cycles

R. V. Garland

P. W. Pillsbury

Westinghouse Electric Corp.,
Orlando, FL 32826

Addition of a fluidized bed combustor to a high-efficiency combined cycle plant enables direct firing of inexpensive run-of-the-mine coal in an environmentally acceptable manner. To attain high thermal efficiencies, coal pyrolysis is included. The low heating value fuel gas from the pyrolyzer is burned in a topping combustion system that boosts gas turbine inlet temperature to state of the art while the pyrolyzer-produced char is burned in the bed. The candidate topping combustor, the multi-annular swirl burner, based on a design by J. M. Beér, is presented and discussed. Design requirements differ from conventional gas turbine combustors. The use of hot, vitiated air for cooling and combustion, and the use of low heating value fuel containing ammonia, are two factors that make the design requirements unique. The multi-annular swirl burner contains rich-burn, quick-quench, and lean-burn zones formed aerodynamically rather than the physically separate volumes found in other rich-lean combustors. Although fuel is injected through a centrally located nozzle, the combustion air enters axially through a series of swirlers. Wall temperatures are controlled by relatively thick layers of air entering through the various swirler sections, which allows the combustor to be of all-metal construction rather than the ceramic often used in rich-lean concepts. This 12-in.-dia design utilizes some of the features of the previous 5-in. and 10-in. versions of the multi-annular swirl burner; test results from the previous projects were utilized in the formulation of the test for the present program. In the upcoming tests, vitiated air will be provided to simulate a pressurized fluidized bed effluent. Hot syngas seeded with ammonia will be used to simulate the low-Btu gas produced in the pyrolyzer.

Introduction

This paper presents the design considerations and features of a low-emissions, low heating value gas-fueled laboratory test topping combustor that is being prepared for tests under the sponsorship of the Department of Energy's Morgantown Energy Technology Center (DOE/METC). The test program is part of Phase 2 of a three-phase ongoing METC program, "Second-Generation Pressurized Fluidized Bed (PFB) Combustion Systems R&D." Phase 1 involved the conceptual design and economic study of the second-generation PFB combined cycle plant (Robertson et al., 1988); Phase 2 addresses individual subscale testing of the plant's major components; Phase 3 will cover the testing of these components integrated into one combustion system: a coal pyrolyzer, a circulating PFB, a gas cleanup system, and a topping combustor.

Cycle Description

The advantages of the combined cycle over conventional steam plants or simple cycle gas turbines are well known. Many oil and gas-fired combined cycles are in service and more are being built. This program deals with evaluating the feasibility and economics of a Second-Generation Pressurized Fluidized Bed Combustion Combined Cycle. The plant is fueled with coal but can achieve thermal efficiencies closely approaching those of the oil-fired combined cycles being marketed today (Garland and Robertson, 1988). Figure 1 is a schematic representation of the plant.

Coal is fed to a pyrolyzer unit that operates at 1600°F (871°C) and produces a low heating value fuel gas and combustible char. The char is burned in the PFB that is pressurized by the gas turbine compressor air. The bed produces steam and operates at 1600°F (871°C); the hot gases leaving the PFB are filtered; the cleaned hot gases are then piped back to the gas turbine.

Before entering the turbine, the 1600°F (871°C) gases, still rich in oxygen content, are raised to 2100°F (1149°C) by burning the pyrolyzer-produced low heating value fuel gas in a topping combustion system. Thus turbine inlet temperature is a full 500°F (280°C) higher than the bed temperature, and this is the primary reason that the plant thermal efficiency is 5 to

Contributed by the International Gas Turbine Institute and presented at the 35th International Gas Turbine and Aeroengine Congress and Exposition, Brussels, Belgium, June 11–14, 1990. Manuscript received by the International Gas Turbine Institute December 23, 1989. Paper No. 90-GT-30.

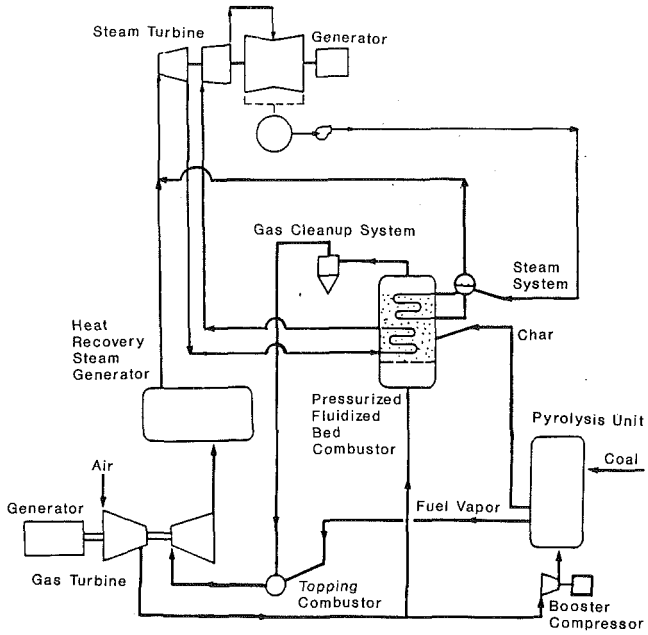

Fig. 1 Schematic representation of a second-generation PFB combined cycle

7 percentage points higher than comparably sized first-generation PFB combined cycles.

Combustor Design

Because the air entering the combustor is 1600°F (871°C) rather than the usual 700°F (370°C) for gas turbines, the conventional type of combustor is not suitable. Both emissions and wall cooling problems preclude the use of the conventional design.

In selecting a combustor design that will withstand the conditions expected in the topping application, the effective utilization of the 1600°F (871°C) air mentioned above could satisfy the wall cooling challenge by maintaining a cooling air layer of substantial thickness. The creation of thick layers of cooling air at the leading edge of each inlet section is easily achieved if the combustor is made up of concentric annular passages. The Multi-Annular Swirl Burner (MASB), based on a design by J. M. Beér (1989) (Fig. 2), introduces the entire combustion air quantity into the combustor by means of annuli of substantial radial thickness. This feature of the MASB alone made it the prime choice for a previous DOE-sponsored program (Vermes et al., 1986), and the choice for further development in this program.

The previous DOE-sponsored topping combustor test program tested a 10-in. (25-cm) MASB fired with methane. The engineering design and combustor development were carried out by a team at Westinghouse in Concordville, PA, led by Mr. Géza Vermes. In that program wall temperatures were the major concern just as they are in this current effort. To investigate thoroughly the potential problem of excessive wall temperature, a two-phase test program was conducted. The first phase of the program fired the test MASB with methane using 850°F (454°C) combustion air. Radiometers were placed in the rich zone of the MASB to measure flame radiation. Data from this first test confirmed the analysis performed during the design phase. The measured wall temperatures were actually somewhat lower than those predicted before the test. Assumptions were adjusted accordingly, and wall temperature predictions were made for the second test that would fire methane with 1400°F (760°C) combustion air.

The test utilizing 1400°F (760°C) combustion air yielded most encouraging results and corroborated the wall temperature predictions. The measured wall temperatures were less than 100°F (55°C) higher than the combustion air temperature and the condition of the combustor after test was excellent even though the calculated adiabatic flame temperature in the rich zone was 3964°F (2180°C).

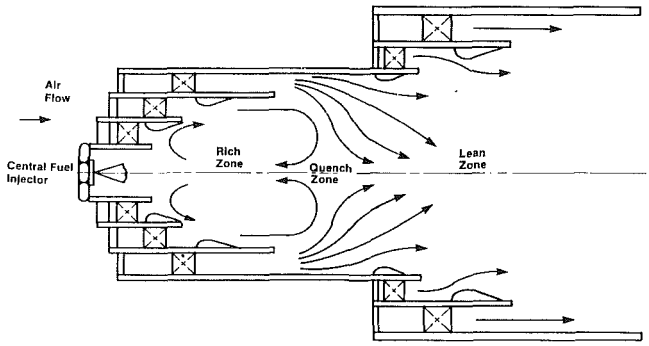

Fig. 2 Conceptual arrangement of the multi-annular swirl burner based on J. M. Beér's patented design

In addition to the requirements based on wall cooling, there are three further considerations. One is the fact that the high inlet air temperature could increase oxides of nitrogen (NO_x) generation in the combustor. Second, NO_x potential from fuel bound nitrogen must be considered, and therefore, an inherently low NO_x design is preferable. Third, the combustor, if possible, should be able to function *without* the air having been preheated to 1600°F (871°C); otherwise, the turbine could not be operated without the fluidized bed ("black-plant start"). To meet this third consideration, the design of choice has to have a recirculation zone where hot gases will maintain the reaction process even in the absence of high air inlet temperature. The MASB possesses the characteristics to meet these considerations, as well.

Aerothermal Design

A thorough analysis and discussion of the aerothermal design aspects of the MASB are contained in the previous project report by Vermes et al.; therefore, only the appropriate descriptions and findings will be repeated here.

The Combustion Process in the MASB

The conceptual arrangement of the MASB in Fig. 2 shows the salient feature of the combustor: The entire combustion air flow is admitted through axial flow, concentric vane rows. These vane rows impart a tangential component (swirl) to the axial approach air. The amount of swirl is different in each vane row, or swirler. Depending on the radial distribution of the swirl, the flow pattern will break down at some axial distance into the burner and a recirculation zone will develop.

Injection of the fuel takes place in this recirculation zone and this zone will be considered as the primary reaction zone of the MASB. The primary zone is surrounded by colder, unreacted air from swirlers adjacent to the primary zone and, thus, a rapid quenching of the reaction takes place roughly at the downstream end of the primary zone.

The mixture of unburned fuel and quench air progresses to the secondary reaction zone of the burner where combustion reactions will be completed at generally low temperatures because of the large surplus of air in this zone. A relatively small fraction of the total air flow, say 10 percent, can be introduced further downstream, either axially or in the form of radial jets, to adjust the exit temperature profile. This profile air does not take part in the combustion process.

Burner Aerodynamics

A key feature of the MASB design is the lack of need for

film cooling air, as a result of which the total amount of air entering the combustor is available for the effective management of the flow and mixing process. For the radial distribution of the swirl velocity distribution of the air entering the combustor the designer may consider two bounding cases:

(*a*) free vortex flow, in which the magnitude of the swirl velocity varies inversely proportionally with the radial distance from the combustor axis (W = const/r); or

(*b*) forced vortex flow (solid body type rotation), in which the swirl velocity is directly proportional to the radial distance (W = const•r).

In the present design, free vortex flow was chosen for several reasons. First, free vortex flow provides a more uniform radial profile of the axial velocity, which means that air supplied from a constant pressure area is ready to enter the combustor without need to establish some radial pressure distribution upstream of the combustor in order to control the flow rate in the individual annuli of the MASB.

Second, free vortex flow gives lower pressure drop across the combustor. The MASB's pressure drop is lower than that of conventional combustors by more than 50 percent. Third, the free vortex flow was shown in previous experiments to provide better wall cooling, and fourth, it concentrates the fuel rich mixture ratio on the flame axis in the primary combustion zone by delayed mixing, thereby making the combustion air staging for NO_x reduction more effective. This latter effect occurs due to a combination of highly swirling flow near the flame axis on the one hand, and a positive radial density gradient, on the other (Beér et al., 1971).

It should be noted, however, that in reality the free vortex flow transforms in the central core of the flow into solid body rotation due to the viscosity of the gas, which does not permit infinite rotational velocity to be attained in the center of the rotation. The resulting combination of free and forced vortex flows, referred to as a Rankine vortex, is illustrated in Fig. 3.

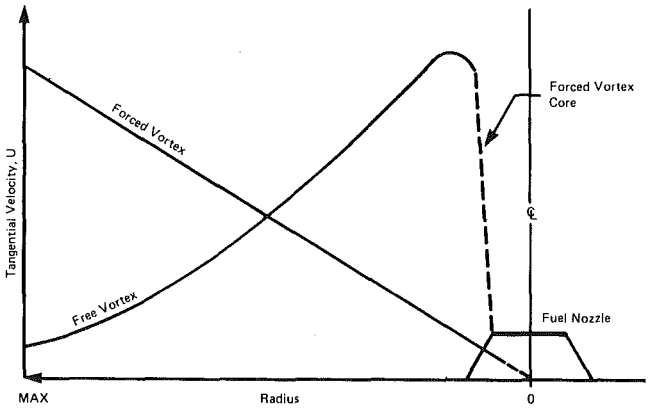

Fig. 3 Velocity characteristics for free and forced vortex flows

Fuel Injection. Low jet velocity for the fuel is desirable to keep the turbulence level low at the flame boundary. Fuel flow at maximum test conditions is 5.78 ft^3/sec (0.16 m^3/s), about 6 times the fuel volumetric flow of the previous program, which employed natural gas as a fuel. This required the fuel injector and flow passages to be much larger in this new design. Figure 4 shows the test combustor.

Note the fuel flow passage at the exit of the fuel nozzle. It is 4 in. (10 cm) in diameter. The equivalent diameter of the natural gas-fueled MASB was less than half of that.

A different injection method is employed in this new design, as well. Rather than have the fuel injected through an axially oriented nozzle as before, a series of orifices angled at 40 deg is used that imparts a rotation to the fuel in the same direction as the swirling air to encourage uniform mixing while maintaining a cooling air layer at the walls of the recirculation (rich) zone.

A completely new feature is employed in this fuel nozzle to aid in the control of NO_x emissions. About 10 percent of the 1600°F (871°C) combustion air enters the upstream end of the fuel nozzle assembly, travels through an inner annulus, and is directed through an orifice in the fuel injector to mix with the fuel as shown in Fig. 4. Its purpose is to help control NO_x as will be described below. (See next to last paragraph of the section "Emissions.") The effects of varying primary zone air quantity will be investigated by means of an oxygen injector located at the upstream end of the fuel nozzle assembly. Injecting oxygen will have the effect of increasing the mixing air quantity at the fuel injector. Nitrogen will be injected during one test point. This will have the effect of eliminating the mixing air at the fuel injector and will yield meaningful data regarding decreasing mixing air through the fuel injector. The center section of the fuel nozzle assembly provides the means for natural gas firing at lightoff.

Metallurgy. The 200°F (110°C) increase in combustion air temperature caused concern that the combustor material, Hastelloy X, used in the previous test program, might not be suitable for this new design. A new material, Haynes 230, was used, which is reported to exhibit better thermal stability, greater tensile strength, and greater impact strength at 1600°F (871°C) (Haynes International, 1987). In addition, Haynes 230 shows greater resistance to grain growth than Hastelloy X. Taken altogether, it is felt that this new material's properties are such that a 100°F (55°C) increase in average metal temperature can be tolerated, while retaining long-term creep resistance (Haynes International, 1987).

Adiabatic Flame Temperature. The use of low heating value fuel provides an advantage as regards flame temperature. As reported in the previous program, the adiabatic flame temperature in the rich zone using methane and 1400°F (760°C) combustion air was 3964°F (2184°C). The use of this syngas, which contains a high percentage of an inert constituent, will

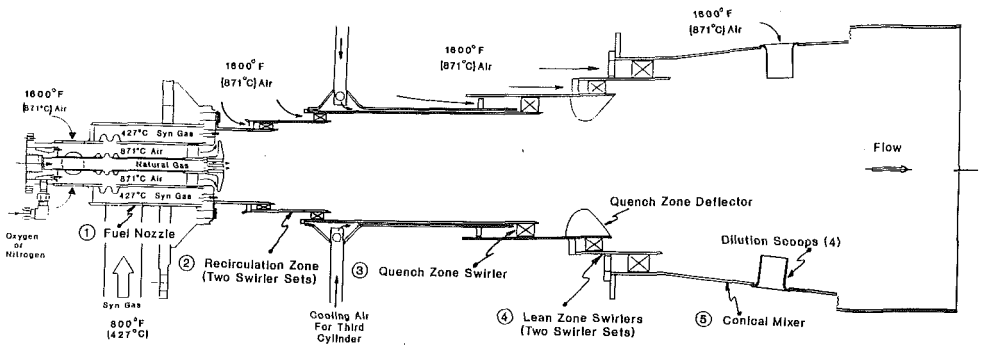

Fig. 4 Fuel nozzle/swirler arrangement for the test combustor

produce a flame temperature of 2850°F (1566°C) even though the combustion air temperature is 200°F (110°C) higher in this case. Thus, other factors remaining equal, radiation to the walls will be lower. Since radiation is a function of absolute temperature to the fourth power, the radiation in this case will be on the order of $[(1566 + 273)/(2184 + 273)]^4 = 0.31$ times the natural gas value.

Emissions. NO_x emissions from the previous methane-fired combustor were greater than expected. It was thought that rich-lean combustion had not quite been achieved in that case and so it was decided to provide more residence time in the rich zone for this low heating value fuel. Also, it was decided to try to fine-tune the stoichiometry of that zone, so means were provided to introduce small quantities of air, oxygen, or nitrogen at will, into it. This is intended to stimulate quick initiation of combustion to proceed through specific processes that preclude the formation of NO_x due to fuel-bound nitrogen.

The MASB is designed to operate under staged combustion conditions so as to reduce NO_x emissions to a minimum. Nitrogen oxides are formed in three main processes:

1 fixation of atmospheric nitrogen at high temperature and lean combustion according to the so-called atom shuttle Zeldovich reactions;

2 fixation of atmospheric nitrogen by hydrocarbon fragments in the fuel-rich initial stages of a hydrocarbon fuel-air flame (called prompt NO_x);

3 oxidation of organically bound nitrogen compounds to NO in lean flames.

In the rich-lean concept of the MASB there is sufficient oxygen to sustain the reactions for the first process listed above.

In Process Two above, it is inevitable that NO will be formed; therefore it is important to initiate pyrolysis of the fuel early, so that the prompt NO can go through the reduction-reaction paths, and then the final steps necessary to be destroyed and to produce molecular nitrogen. The fixation of atmospheric nitrogen, N_2, by hydrocarbon radicals such as CH and CH_2 leads to the formation of cyanides, mainly HCN. The cyanides then react with OH and O radicals to form amines by hydrogen abstraction reactions, and NO by their further oxidation. The process is illustrated by reactions R1 through R8 below:

"Prompt NO" Formation Reactions

Hydrocarbon Fragments Generate Cyanide (HCN)	
(R1)	$CH_2 + N_2 = HCN + NH$
(R2)	$CH + N_2 = HCN + N$
Hydrogen Abstraction Generates Ammonia Radicals (NH, NH_2)	
(R3)	$HCN + OH = CN + H_2O$
(R4)	$HCN + OH = HNCO + H$
(R5)	$HNCO + H = NCO + H_2$
(R6)	$HNCO + H = NH_2 + CO$
(R7)	$NCO + H = NH + CO$
Ammonia Radical Generates NO	
(R8)	$NH + O = NO + H$

Following the NO formation reaction, two destruction routes are possible. NO can be reduced either by reacting with ammonia (NH_j, N) species to form molecular nitrogen (reactions (R9) through (R11) below); or by reacting with hydrocarbon radicals such as CH and CH_2 to provide hydrogen cyanide (reactions (R12) through (R15)) that in turn is converted to NH_j through reactions R3 through R7 above. The ammonia species thus formed are subsequently destroyed through Eqs. (R16) through (R20).

Destruction Paths for NO

Reduction with Ammonia (Not Significant at Conditions of MASB)	
(R9)	$NO + NH_2 = N_2H + OH$
(R10)	$NO + NH_2 = N_2 + H_2O$
(R11)	$NO + NH = N_2 + OH$
Reaction with Hydrocarbon Fragments to give Cyanide (HCN), which feeds Eq. (R3) through (R7)	
(R12)	$CH + NO = HCN + O$
(R13)	$CH_2 + NO = HCN + OH$
(R14)	$CH_2 + NO = CH_2O + N$
(R15)	$CH_3 + NO = HCN + H_2O$

The paths through which the NO reduction passes are influenced by temperature, fuel equivalence ratio, and reaction time. Maintaining a rich zone temperature above 2600°F (1425°C) but below 3100°F (1700°C) is essential. Maintaining the primary zone rich, along with keeping it at a high temperature, promotes reactions (R12) through (R15). These reactions then proceed through reactions (R3) through (R8), as mentioned earlier. It has been found that NO reduction through its reaction with NH_j (R9)–(R11) is not significant at the rich zone conditions of the MASB. Consequently, the route in which CH_j reacts with NO provides the means for producing ammonia species (R3)–(R7) that can be reduced directly to molecular nitrogen by reactions (R16) through (R20).

Final Steps of the NO_x Reduction Path at Lower Temperature (2600°)

(R16)	$NH + N = N_2 + H$
(R17)	$NH + NH = N_2 + H + H$
(R18)	$NH + NH_2 = N_2H_2 + H$
(R19)	$N_2H_2 + H = N_2H + H_2$
(R20)	$N_2H + H = N_2 + H_2$

Fuel-bound nitrogen, newly formed NO, and organic nitrogen compounds from Process Two can be converted to N_2 in *fuel-rich* flame regions if the temperature is sufficiently high and the residence time sufficiently long for these reactions.

The above discussion centered on the formation of "prompt NO_x" and how it is destroyed through the control of temperature and fuel–air mixture in the rich zone. Process Three, the formation of NO in the lean zone due to fuel ammonia, is also suppressed. A high percentage of the fuel ammonia will be converted to N_2 and H_2 in the rich zone through (R16)–(R20) before it enters the lean zone.

The MASB design provides the means to achieve low NO_x through (R16)–(R20) by incorporating two features:

1 Air is bled through the fuel distribution plate at the front of the fuel nozzle assembly (described earlier).

2 The third combustor cylinder is lengthened.

The 0.42 lb/s (0.19 kg/s) of air at 1600°F (871°C) bled through the fuel distribution plate is insufficient to produce ignition, but its temperature is high enough to start fuel pyrolysis. The pyrolyzed fuel will then be mixed with more air as it moves out of the fuel injection area and into the zone where air from Swirlers 1 and 2 is entering. The final mixture will still be fuel rich with an equivalence ratio of 1.5, and, it will also be hot. (Equivalence ratio is defined as the actual fuel–air ratio to the stoichiometric fuel–air ratio.)

High temperature is important for the chemical reactions that convert NO and other nitrogen species to N_2 in the fuel-rich region. For effective reaction, the temperature should be above 2600°F (1426°C) and this has been accomplished by the steps taken to maintain a 1.5 equivalence ratio.

The Configuration Effect of a Longer Residence Time. For effective reaction it is not enough to provide the desired mixture of oxidizer and reactants. Sufficient residence time must be provided for the reactions to take place, as well. The lengthening of the fuel-rich first part of the MASB serves this purpose. It is necessary that the air introduced through Swirlers 1 and 2 be uniformly mixed with the fuel before quench zone air from Swirler 3 is added. The increased length of the third combustor cylinder (shown in Fig. 4) serves this additional purpose.

As mentioned above, less flame radiation is expected with the syngas, which simulates the pyrolyzer fuel, than with the methane used previously. Nevertheless, the lengthened third

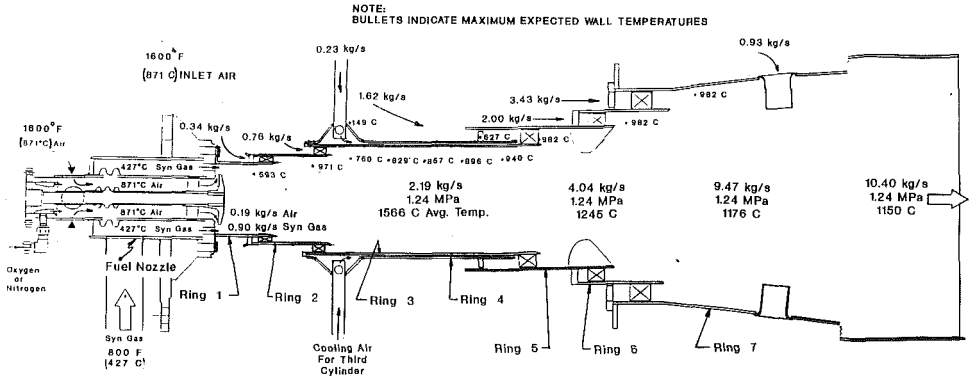

Fig. 5 Flow conditions and predicted maximum wall temperatures for the test combustor

cylinder may present an additional heat transfer problem relative to the other swirlers because the boundary layer formed on its walls by the air injected through Swirler 2 may dissipate. This would result from its great length. The air might be unable to provide effective wall cooling. Extra cooling of this wall element has been provided to take care of this potential problem as addressed below.

Topping Combustion Heat Transfer. The projected combustor conditions while operating at a burner outlet temperature (BOT) of 2100°F (1150°C) are shown in Fig. 5, and include the following:

1 Predicted average combustion gas temperatures at various sections.

2 Predicted average combustion internal pressures.

3 Expected coolant temperature surrounding the combustor: 1600°F (871°C).

4 Design mixing and cooling flows, section by section.

5 Estimated maximum combustor metal cylinder temperatures (rings 1 through 7, Fig. 5).

As indicated, except for the third cylinder, which employs a special cooling jacket, the individual cylinder temperatures were determined by considering the combined effects of external convection within the swirler annulus, hot gas side convection, and film cooling along the surfaces downstream of the swirler annulus. Internal combustor radiation is relatively low in the third cylinder, for the reasons explained above in the "Adiabatic Flame Temperature" paragraph. However, to allow for the effect of radiation, a very conservative approach was taken when estimating gas side film coefficients and adiabatic wall temperatures. Allowances were made to account for variations in geometry such as the internal surface of the first cylinder and the cooling jacket used for the third cylinder. Cylinder No. 3 is expected to operate at the lowest temperature of all the cylinders, due to its cooling jacket. Heatup of the air within the jacket, end to end, is expected to be 300°F (167°C).

In Fig. 5 it is seen that some metal temperatures are labeled in the 1600°F (871°C) to 1800°F (982°C) range. These temperatures are higher than those predicted and measured in the previous Topping Combustor Feasibility Test Program. In that program, the analysis and assumptions used in estimating wall temperatures took a very conservative approach. Figure 6 displays the results of the previous topping combustion test conducted in 1985 (Pillsbury and Garland, 1987). Of particular interest is what it might reveal as regards wall temperatures for this test. The data points form a straight line for all practical purposes and show the wall temperatures are less than 100°F (55°C) higher than the combustion air temperature in the primary zone. Keeping in mind that the data in this figure are based on a methane-fired test where the adiabatic flame temperature was about (3960°F) 2200°C in this zone, it is possible

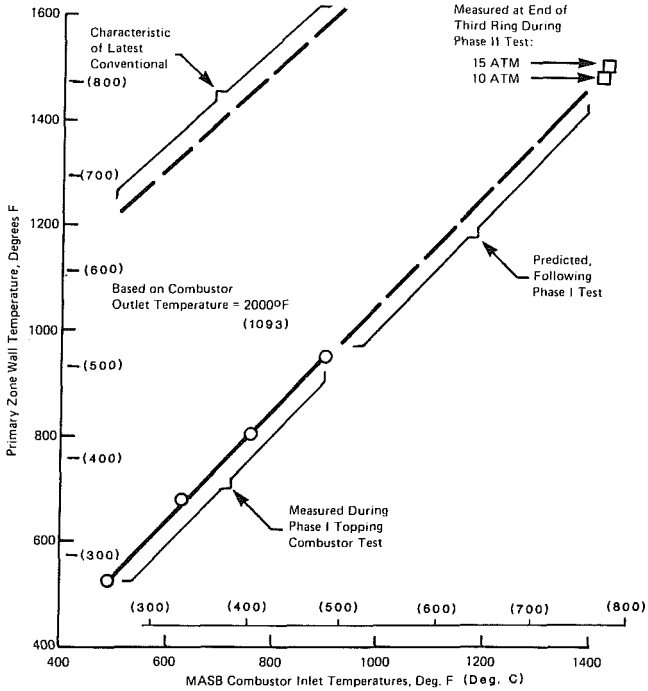

Fig. 6 Primary zone third ring wall temperature versus combustor inlet temperature for methane-fired MASB

to extrapolate the data to estimate the wall temperature that might exist in the previous design with (1600°F) 871°C combustion air. Extrapolation reveals that the wall temperature would be about 1690°F (921°C). Thus, for the upcoming test using 1600°F (871°C) combustion air and 2100°F (1150°C) burner outlet temperature, the very conservatively estimated wall temperature shown in Fig. 5 could be considerably lower. Because the burner outlet temperature for this test is 100°F (55°C) higher than the previous test, wall temperatures in some regions will probably be greater than 1690°F (921°C). The higher trends were anticipated as described in the paragraph labeled "Metallurgy" above, and brought about the recommended change in material for this program.

Because of the short duration of the test program, and because there are existing applications where Haynes 230 is exposed to temperatures as high as 2150°F (1180°C), the increase in predicted wall temperature is not expected to affect structural integrity of the test combustor.

Topping Combustor Evaluation. The topping combustor described above has been fabricated and is in the process of being instrumented and installed in the same test rig used for the methane-fueled tests described previously. The test rig is

being installed at the University of Tennessee Space Institute, Tullahoma, TN. This facility is capable of providing the high-pressure, high mass flow combustion air necessary for MASB experimental evaluation. The simulated pyrolysis gas will be blended in high-pressure tube trailers by an industrial specialty gas supplier, and heated before injection into the combustor.

Acknowledgments

The topping combustor development work being performed by Westinghouse through the Department of Energy's Morgantown Energy Technology Center is managed by Mr. Don Bonk, Project Manager, Office of Technical Management. The design work for the combustor was performed in consultation with Dr. János Beér, Professor of Chemical Fuel Engineering, at MIT. The heat transfer within the combustor was analyzed by Mr. Jan Smed of Combustion Turbine Engineering, Westinghouse Power Generation Operations Division. Special thanks are extended to these gentlemen for their help and guidance both in the preparation of this paper and the overall execution of the project.

The Project

This DOE/METC project is being carried out through the efforts of several contractors. The prime contractor is the Foster Wheeler Development Corporation and four subcontractors are working in conjunction. The five companies and their prime contact personnel are listed below:

- Foster Wheeler Development Corporation
  Archie Robertson, Program Manager
- Gilbert/Commonwealth, Inc.
  Lynn Rubow, Project Manager
- Institute of Gas Technology
  Amir Rehmat, Project Leader
- Westinghouse Power Generation Project Division
  Richard Garland, Project Manager
- Westinghouse Science and Technology Center
  Richard Newby, Project Manager

References

Beér, J. M., 1965, British Patent No. 45652/65.

Beér, J. M., Chigier, N., Davies, T., and Bassnidale, K., 1971, "Laminarization of Turbulent Flames in Rotating Environments," *Combustion and Flame*, Vol. 16, pp. 39–45.

Beér, J. M., 1989, U.S. Patent No. 4845940.

Garland, R., and Robertson, A., 1988, "Operating Envelopes for Second Generation PFBC Combined Cycle Plants," ASME Paper No. 88-JPGC/GT-5.

Haynes International, 1987, "Haynes® Alloy No. 230," Booklet H-3000B.

Pillsbury, P., and Garland, R., 1987, "Feasibility Test for a Low Emissions Topping Combustor for Fluidized Bed Applications," ASME Paper No. 87-GT-272.

Robertson, A., Garland, R., Newby, R., Patel, J., and Rubow, L., 1988, "Second-Generation PFB Combustion Plant Performance and Economics," EPRI Seminar on Fluidized Bed Combustion Technology for Utility Applications.

Vermes, G., Pillsbury, P., and Garland, R., 1986, "Generic Studies of Advanced Fluid Bed Air Heater Technology: Topical Report No. 5, Energy Distribution and Combustor Development," DOE/CE/40543-5, U.S. Technical Information Center, U.S. Department of Energy, Springfield, VA, pp. 5–94.

G. A. Richards

R. G. Logan

C. T. Meyer

R. J. Anderson

U. S. Department of Energy,
Morgantown Energy Technology Center,
Morgantown, WV 26505

Ash Deposition at Coal-Fired Gas Turbine Conditions: Surface and Combustion Temperature Effects

A study of ash deposition from a cleaned bituminous and conventional bituminous coal is presented. An electrically heated drop tube furnace is used to burn the coal and provide deposition conditions representative of proposed coal-fired gas turbines. Variations in the combustion temperature and deposit surface temperature demonstrate that surface cooling may significantly reduce ash deposition, or may provide little benefit, depending on the combustion conditions. Lower temperature combustion produced larger ash particles, with a greater fraction of ash adhering to the deposition test surface. Although the sticking coefficient was higher at the lower combustion temperature, the deposits were readily removed. A modest numerical simulation suggests that the smallest ash particles can experience significant boundary layer cooling and may account for the reduction in sticking observed at some conditions.

Introduction

The U.S. Department of Energy is currently sponsoring the development of coal-fired gas turbines, with supporting research being conducted at a number of government, private, and university laboratories (Kothari and Rekos, 1988). While significant progress has been made, a major issue to be resolved is how to reduce the detrimental effects of coal mineral ash on turbine hardware. Erosion from particulate ash may be a problem if ash residues exceed 5 μm in size, but it is believed that this problem can be controlled by limiting the size of included fines (France et al., 1984). Hot corrosion by alkali sulfates may be aggravated by the erosive loss of protective coatings, but oxidation problems are currently receiving less attention than the immediate barrier associated with reducing the deposition of ash on the turbine hardware. The deposition problem is particularly severe on the fixed turbine stators, where ash may adhere in a manner that could force engine shutdown.

The problem of ash deposition in proposed coal-fired turbines has some connection to the established problem of ash fouling in industrial boilers. However, a number of distinctions should be made between the two applications. First, in the gas turbine, ash particles arrive at the turbine blade with a high velocity, typically greater than 100 m/s. This is very different from the situation in a boiler, where particle arrival occurs at speeds on the order of 10 m/s. A second difference concerns the temperature history of arriving ash particles. In the turbine, a finely divided coal aerosol will be burned in a relatively short residence time, followed by a rapid quench with dilution air, and possibly further cooling in the boundary layer surrounding cooled airfoils. The boiler environment is relatively uneventful by comparison, with fewer abrupt changes in temperature and (typically) a lower temperature for the deposit-metal interface. The difference in temperature history means that ash morphology and composition may differ between the boiler and the turbine. Thus, earlier experience with methods to reduce boiler deposition may not meet the more stringent demands of turbine applications. The ash deposition in a gas turbine is characterized by the following mechanisms. Particles arrive at the surface with high velocity gas flow (or by particle diffusion on the suction side of the blade). Referring to Fig. 1, three mechanisms are involved in the deposition process:

- **Particle/Surface Molten Phase Adhesion.** Particles will stick to the surface if the adhesive force is sufficiently strong to overcome the energy remaining from impact, which would otherwise allow the particle to rebound.
- **Deposit Erosion.** Particles may have sufficient energy to rebound and, in addition, erode part of the existing deposit.
- **Deposit Spalling.** Particles may adhere to the deposit surface, but the deposit strength is so low that part of the deposit may occasionally spall off the surface because of aerodynamic forces, vibration, or abrasive injection cleaning (nutshelling).

Selective control of these three mechanisms may reduce ash deposition. For example, the ratio of adhering mass (particles that fail to rebound) to the total mass of particles that impact the surface, is called the sticking coefficient and has been the subject of many studies (Ross et al., 1988; Rosner and Na-

Contributed by the International Gas Turbine Institute for publication in the JOURNAL OF ENGINEERING FOR GAS TURBINES AND POWER. Manuscript received at ASME Headquarters January 1991.

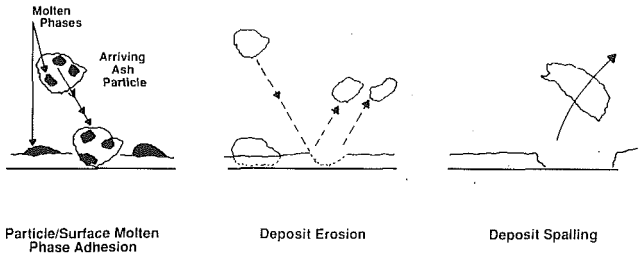

Fig. 1 Mechanisms in ash deposition

garajan, 1987; Benson et al., 1985; Ahluwalia et al., 1989). Reductions in the sticking coefficient will clearly provide an advantage to turbine operation, since a smaller proportion of the impacting ash particles will actually deposit on the hardware.

Aside from reducing the sticking coefficient, deposition control may also be accomplished by promoting deposit spalling of weakly bound ash layers. Boiler experience has included some attempts to reduce the deposit strength by intermittent injections of various additives (Raask, 1985). Spiro et al. (1989) have recently proposed that kaolin clay will act to reduce deposit strength through chemical reactions that are suspected to devitrify the deposit melt. An accompanying increase in viscosity and reduction in molar volume were thought to cause spontaneous deposit spalling. Initial tests with kaolin in a simulated turbine environment provided remarkable evidence that kaolin is effective at reducing the deposition problem (Spiro et al., 1989).

To expedite the ongoing development of coal-burning gas turbines, continued work is needed to quantify the nature of the ash deposition and potential deposition reduction schemes. While useful data have been obtained from turbine simulators (Ahluwalia et al., 1989; Spiro et al., 1989), the cost and complexity of such experiments hinder the rapid assessment of deposition changes resulting from fuel additives, different operating conditions, and coal type. This paper reports results from a drop-tube combustor specially developed to quantify the sticking coefficient as a function of operating conditions with fuel additives, for example. The present results identify temperature conditions that produce a low sticking coefficient and a low deposit strength. In addition, a modest computer simulation of the ash transport process confirms the experimental evidence, showing that large ash particles are relatively unaffected by surface cooling, while smaller particles may be cooled significantly in the thermal boundary layer above cooled hardware surfaces.

Experimental Procedure

Deposition experiments were performed in the combustion/deposition entrained reactor (CDER). A detailed description of the CDER and experimental procedure is given elsewhere (Anderson et al., 1988). The CDER is essentially an electrically heated drop-tube furnace with an exit nozzle designed to produce a high-velocity jet of combustion gases (Fig. 2). The CDER is capable of operating at pressures up to 12 atm, but the current results were obtained at 1 atm.

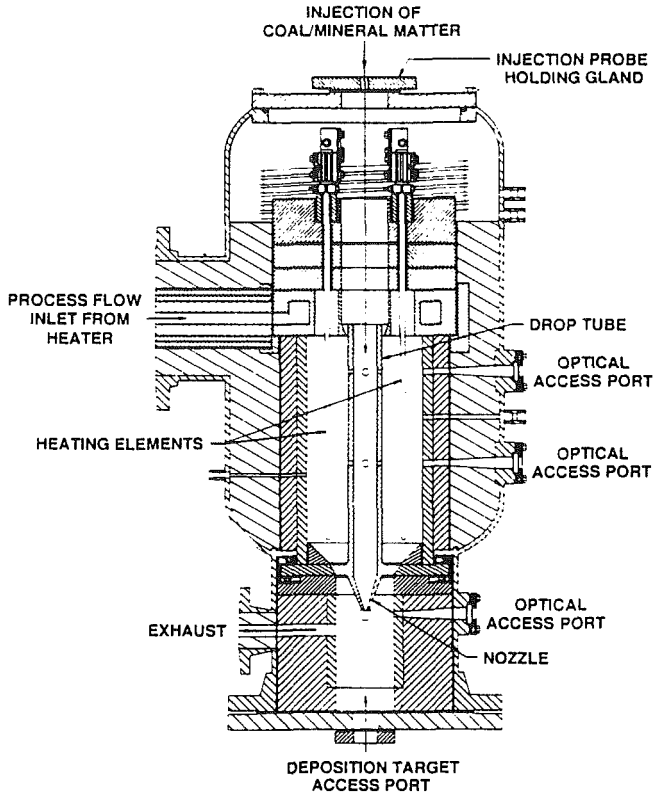

Fig. 2 Combustion/deposition entrained reactor (CDER)

Dry coal is injected into the top of the reactor and passes through the drop-tube region, where electric heaters allow careful control of the combustion temperature. Combustion temperatures reported here are measured with a type-K thermocouple, which contacts the drop tube exterior just above the optical access port. The process flow entering the reactor is heated to the temperature indicated by this thermocouple so that the drop tube interior is essentially isothermal, except for a short mixing region near the top. Coal/mineral matter is conveyed into the top of the drop tube with ambient temperature air amounting to less than 10 percent of the total drop tube flow. Temperature traverses conducted just 5 cm below this point showed a small 50 K drop in the centerline temperature, which was subsequently flattened by the mixing and heat input from the hot drop-tube walls. Residence time in the drop tube is more than 400 ms.

At the exit of the combustion zone, the products of combustion are accelerated through a 3.2-mm-dia nozzle, creating a jet with a mean velocity of 300 m/s. This is similar to the velocity expected in the first stage of an operating gas turbine. The high-velocity jet is directed perpendicular to a deposition target located 6 mm below the nozzle exit (Fig. 3). The target is a removable 12.7-mm platinum disk, 0.254 mm thick. Platinum was chosen as an inert target material to eliminate specific surface reactions peculiar to any particular blade material. The target and nozzle configuration was developed according to the procedures recommended by Marple and Willeke (1976)

Nomenclature

C = particle specific heat, J/kg-°K
C_D = particle drag coefficient
d_p = particle diameter, m
h = convection coefficient, W/m^2-°K
Re = particle Reynolds number, diameter
T_g = gas temperature, °K
T_p = particle temperature, °K
u = radial gas velocity
V = vertical gas velocity
x = radial coordinate
y = vertical coordinate
μ = dynamic gas viscosity, N•S/m^2
ρ = gas density
ρ_p = particle density, kg/m^3

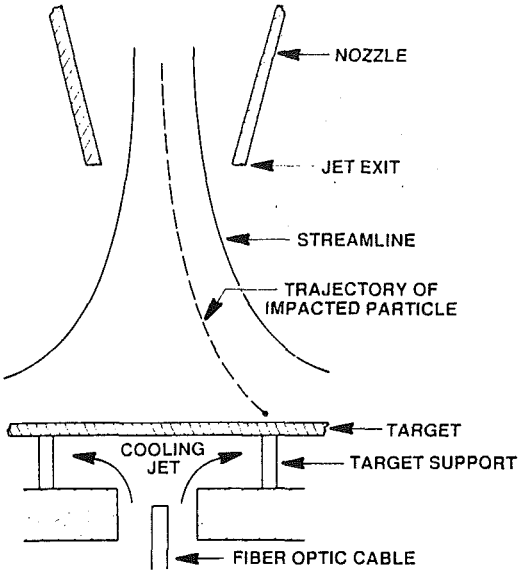

Fig. 3 CDER nozzle/target assembly

Table 1 Ash characteristics

	Arkwright Pittsburgh Bituminous	Blue Gem (Cleaned) Bituminous
% ASTM Ash	6.93	0.56
Ash Comp. (Wt%)		
SiO_2	48.09	16.86
Al_2O_3	25.07	22.75
Fe_2O_3	10.95	29.57
TiO_2	1.27	1.95
P_2O_5	0.18	0.48
CaO	5.78	7.03
MgO	1.25	2.46
K_2O	1.16	0.53
Na_2O	0.90	1.54
SO_2	5.34	8.07
Ash Fusion Temp. (K) (± 40)		
(Reducing Conditions)		
Initial Deformation	1,465	1,511
Softening	1,589	1,581
Hemispherical	1,629	1,644
Fluid	1,656	1,700

to ensure that all particles larger than 0.5 μm would be forced by inertia to impact the target rather than follow the gas streamlines. Figure 3 also shows that an opposing jet of cooling air can be supplied from an annular passage below the target. The center of the annulus is a sapphire rod in series with a fiber optic cable that monitors the target temperature through two-color pyrometry. The target temperatures reported here represent the temperature of the bottom of a clean target without the coal feed. Coal feed (and associated heat release) changed the measured temperature by less than 50 K, because the coal is deliberately supplied at a rate that is approximately 20 times more dilute than in an operating turbine. The dilute coal stream was chosen to allow long sampling times during deposition tests to improve the time resolution of ash deposit growth. A modest investigation of variations in the feed rate demonstrated little change in the measured sticking coefficient with higher coal feed rates.

Table 1 provides the ash composition for the two coals studied in the current investigation. The Arkwright bituminous is an uncleaned coal with almost 7 percent ash. The Blue Gem coal is a beneficiated bituminous coal with 0.56 percent ash. The major difference in composition between the two ashes is in the oxides of iron and silicon, with Arkwright having more silicon dioxide and less iron oxide than the Blue Gem coal. Despite these differences, the softening temperatures of the two coals are similar.

The Arkwright coal was used as a baseline fuel. The sticking fraction was measured by first quantifying the coal feed from quenched filter samples obtained at the nozzle exit. Quenching was accomplished by replacing the target assembly with a 47-mm, open-faced filter holder. Air injection at the periphery of the holder was used in conjunction with a vacuum pump to draw gasses through the filter. The cold air injection served to extinguish combustion of any unburned carbon. Samples collected in this manner showed that the resulting ash contained anywhere from 0.5 to 25 percent carbon, depending on the combustion temperature. As discussed elsewhere (Ahluwalia et al., 1989), the unburned carbon that survives low-temperature combustion can adhere to the deposit where it will have sufficient time to complete burning. The sticking fraction, S, is then computed from the ratio of ash (excluding unburned carbon), which is collected on the filter, versus the ash that adheres to the target during the same time interval:

$$S = \frac{\text{mass of ash adhering to target}}{\text{mass of ash (excluding unburned carbon) on filter sample}}.$$

Initial tests were conducted to establish the behavior of sticking coefficient versus time. Sticking data were obtained at times from 2 to 20 min for Arkwright coal, at reactor temperatures of 1373 and 1573 K. Results shown in Fig. 4 demonstrate that the sticking coefficient was approximately constant after 10 min, but was either larger or smaller after only 2 min, depending on the reactor temperature. Error bars included on this plot demonstrate that excellent data reproducibility was achieved in the CDER tests for times longer than 5 min. Thus, the study of sticking coefficient versus time suggested that 10-min test intervals would provide the most representative data for this investigation, and subsequent sticking data will refer to the 10-min test. While the sticking behavior could admittedly change for operation over many hours, it is not meaningful to consider longer tests until means are found to reduce the sticking coefficient below current levels.

As previously mentioned, the deposition tests were conducted with the coal feed deliberately supplied in a dilute form. Operating gas turbines could be expected to burn fuel at an overall (i.e., postdilution) equivalence ratio of 0.3. The current investigation was conducted at an equivalence ratio of 0.015. These dilute conditions were studied so that the reactor temperature could be easily characterized, controlled only by the electric heaters, and (almost) unaffected by the coal heat release. It is also noted that most proposed coal-fired turbine systems (Kothari and Rekos, 1988) include some form of particulate control (filters or cyclones), so that the product stream would have a very low particle concentration. While it was suspected that dilute conditions would merely slow the particle arrival rate (and thus not affect the fraction that stuck), it was noted that concomitant changes in the partial pressure of gaseous species might alter the sticking data by promoting condensation of gases responsible for liquid-phase adhesion. Figure 5 presents the measured sticking coefficient for Blue Gem coal and suggests that the fraction of adhering ash is approximately independent of the equivalence ratio, except at the highest feed rate for the 1373 K data, where the sticking coefficient is modestly reduced. However, the scatter in the data shows that the sticking fraction was somewhat erratic at the highest feed rates. Equivalence ratios higher than those shown in Fig. 5 were attempted but abandoned because of problems in feeding and mixing the fuel in the drop tube. The higher feed rates produced a jet of coal dust from the fuel injection probe, which resisted rapid mixing and, therefore, produced more

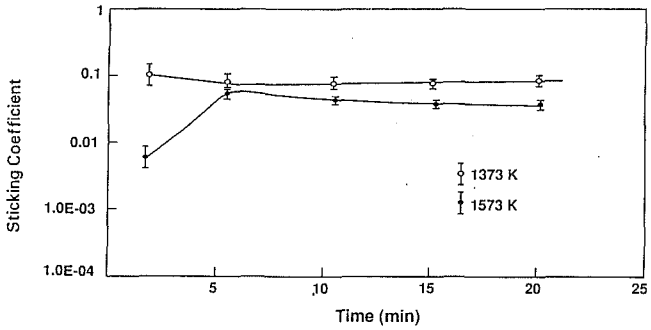

Fig. 4 Sticking coefficient versus time (Arkwright coal)

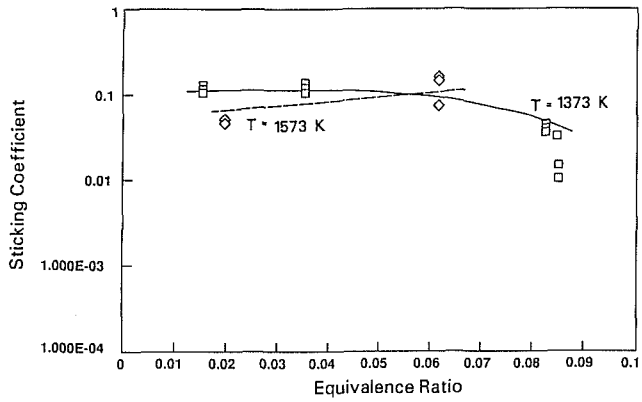

Fig. 5 Sticking versus equivalence ratio (Blue Gem coal)

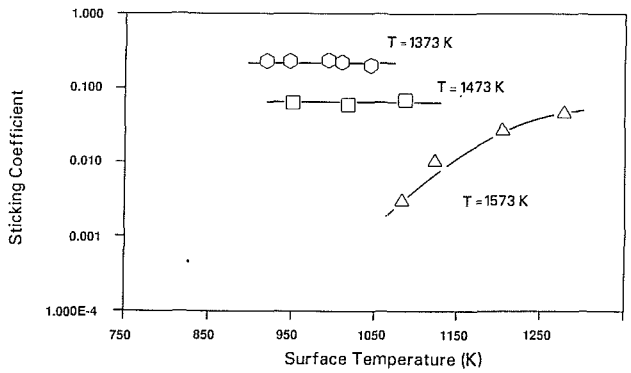

Fig. 6 Effect of surface temperature on sticking coefficient (Arkwright coal)

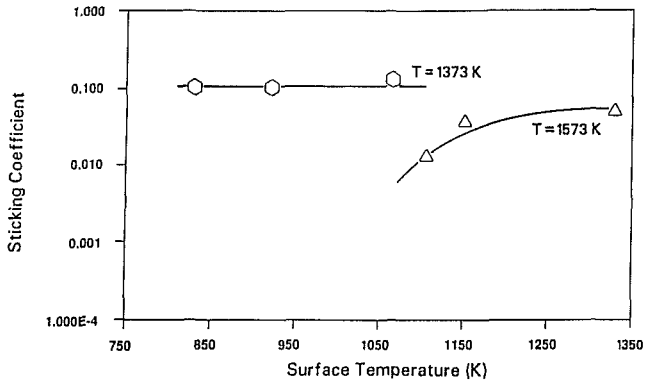

Fig. 7 Effect of surface temperature on sticking coefficient (Blue Gem coal)

unburned carbon in the depositing ash. The difficulties in feed rate and mixing were best avoided by operating the system in a dilute manner, and all subsequent discussion will be referenced to an equivalence ratio of 0.015.

Combined Effects of Surface Temperature and Combustion Temperature

Figures 6 and 7 present sticking coefficient data for the Arkwright and Blue Gem coals over a range of surface temperatures. The individual curves are referenced to the gas temperature in the drop tube (effectively the combustion temperature, since the dilute operation assures isothermal gas temperatures through the reaction region). Referring first to the data obtained at the low gas temperature of 1373 K, the sticking coefficient was unaffected by changes in the target surface temperature. Data for the Arkwright coal were also obtained at a gas temperature of 1473 K, and again the sticking coefficient was independent of the surface temperature but had a slightly smaller magnitude than at 1373 K gas temperature. Finally, at the highest gas temperature of 1573 K, both the Arkwright and Blue Gem coals showed a significant reduction in sticking coefficient as the surface temperature was cooled from 1250 K to 1050 K. This effect was more pronounced for the Arkwright coal than for the Blue Gem coal. However, the qualitative behavior of both coals was the same: at low combustion temperatures, the surface cooling had no effect on sticking coefficient; at higher combustion temperatures, surface cooling produced a significant reduction in the fraction of adhering ash. The reduction in sticking coefficient with surface temperature was expected from experience in boiler deposition (Raask, 1985), and also from recent deposition tests on gas turbine simulators (Ahluwalia et al., 1989). However, the data obtained at lower combustion temperatures (1373 K and 1473 K) were unexpected both because the sticking coefficient was independent of the surface temperature, and also because the magnitude of the sticking coefficient was smaller at higher combustion temperatures. It is possible that the higher combustion temperatures serve to vaporize molten species that would otherwise be present to promote adhesion. However, this would not explain why the low-temperature products of combustion were insensitive to surface cooling.

This distinctive behavior prompted further investigation. It was recognized that unlike the previous gas turbine simulator tests (Ahluwalia et al., 1989; Spiro et al., 1989), the depositing ash at each gas temperature experienced a unique combustion history and was, therefore, suspected to be physically and chemically disparate at the different gas temperatures. In fact, evidence for such a distinction was recognized early in the test program, where a noticeable difference in the appearance and character of the ash deposit was clearly evident at the various combustion temperatures. To investigate these differences, quenched ash samples were obtained on a standard filter with high (cold) air dilution and vacuum suction to quench and capture ash just after exiting the nozzle. Table 2 presents the fraction of unburned carbon for the Arkwright and Blue Gem coals at various combustion temperatures. The table shows that the low-temperature ash (1373 K) contained up to 20.8 percent unburned carbon, while the carbon content of the high-temperature ash was much less. Further differences in the nature of the deposit were evident when attempting to clean the platinum deposition targets for subsequent trials. The deposits obtained from low-temperature combustion (1373 K) were easily removed and exhibited a granular character that was readily pulverized. Conversely, high-temperature combustion (1573 K) produced strongly bonded deposits that were somewhat glassy.

These differences in the character of the deposit raise some interesting issues. The data in Figs. 6 and 7 show that higher

Table 2 Carbon content of ash

	Combustion Temperature (K) 1373	1573
Arkwright	20.8%	0.9%
Blue Gem	16.7%	5.0%

temperature combustion and surface cooling can produce a lower sticking coefficient. However, as previously explained, the smaller fraction of ash that did stick was tightly bonded to the hardware. In practice, reductions in the sticking coefficient must be weighed against the ability to remove the deposit during turbine maintenance. Deposition control strategies would thus seem to benefit from consideration of both the sticking coefficient and the deposit adhesion strength. A preliminary paper from this laboratory (Richards et al., 1988) has reported initial efforts to characterize deposit strength concurrent with the sticking measurements now in progress. Again, although the current data demonstrate a reduction in sticking coefficient by higher combustion temperatures, the adhering ash is bonded tightly to the metal surface, perhaps offsetting the advantage of a reduced sticking coefficient.

To assess further the difference in ash properties at the different combustion temperatures, scanning electron micrographs of the quenched ash samples were obtained. The micrographs revealed some physical differences in the ash produced at different temperatures, but the most notable difference was recognized when the micrographs were used to produce particle-size distributions by digital image analysis. A mass distribution was produced from the image analysis by weighing the size distribution with the cube of the diameter. The mass size distribution thus obtained (for Arkwright coal) is plotted in Fig. 8 and clearly demonstrates a shift in mass size distribution at the two combustion temperatures. The high-temperature combustion produced ash with particle sizes all less than 20 μm in diameter, and with a peak in the mass distribution just above 5 μm. Conversely, much of the low-temperature ash was concentrated in the large particles between 10 and 40 μm. A very small fraction of the ash was contained in particles smaller than 5 μm.

In terms of the observed sticking data, these differences in mass size distribution suggest the following hypothesis. The sticking coefficient data obtained at low combustion temperatures were insensitive to surface cooling, because the relatively large particles could not be cooled before impacting on the deposit surface. On the other hand, the small particles associated with high-temperature combustion could be quenched as they passed through the thermal boundary layer adjacent to the cooled deposition surface. If, for example, the mechanism of particle adhesion is attributed to some molten phases, it is possible that cooling of the small particles would solidify molten phases and reduce the sticking coefficient at high combustion temperatures. Molten phases would not solidify at low combustion temperatures, because the majority of large particles could not adjust to the rapid temperature change as they pass through the boundary layer.

To explore these possibilities, an approximate model of both the flow and particle trajectories in the nozzle/target region was constructed. While a more detailed finite difference solution to the flow and thermal fields could be obtained as in Marple and Liu (1974), such refinement was not needed in the present calculations, where the goal was merely to confirm physical insight into the deposition process for small and large particles as previously described. Furthermore, uncertainties in particle shape and density make refined flow calculations of uncertain value in predicting particle trajectories. As such, the flow and thermal fields were modeled as an axisymmetric,

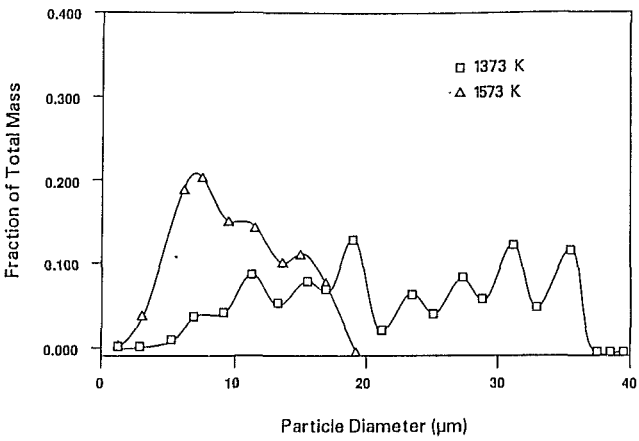

Fig. 8 Ash particle mass distribution (Arkwright coal)

potential stagnation flow coupled to a boundary layer stagnation flow. This approach allowed the flow field to be written as a direct function of location through the standard Blasius solution within the boundary layer (Schlichting, 1979), having boundary conditions imposed to meet the external potential flow solution. Having thus described the flow and thermal fields, the local gas velocity and temperature were used as inputs to the equations of particle motion and thermal energy:

$$\ddot{x}=\frac{3}{4}C_D\,\mathrm{Re}\,\frac{\mu}{\rho_p d_p^2}(u-\dot{x}), \tag{1}$$

$$\ddot{y}=\frac{3}{4}C_D\,\mathrm{Re}\,\frac{\mu}{\rho_p d_p^2}(v-\dot{y}), \text{ and} \tag{2}$$

$$T_p=\frac{6h}{\rho_p d_p C}(T_g-T_p). \tag{3}$$

The convection coefficient, h, was obtained from standard correlations for spheres (Bird et al., 1960). The equations of motion utilize a drag coefficient that was calculated from empirical expressions for C_D as in Morsi and Alexander (1972). Equations (1)–(3) were numerically integrated over time steps of 1 μs in the potential flow region, and 0.1 μs inside the boundary layer. Calculations were started with the particle gas velocity equal to characteristic velocities in the CDER experiments at the nozzle exit (300 m/s) and at the highest gas temperature studied (1573 K). The particle trajectories began at the same nozzle target separation as exists in the CDER experiments. Trajectories were started at 0.01 nozzle radii from the center line. The potential/boundary layer flow model used here is not an exact representation of the flow field in the CDER, but can be expected reasonably to mimic the behavior near the flow centerline where edge effects are minimal. Results of these calculations are shown in Fig. 9, where particle trajectories within the boundary layer are plotted for 1.25 and 2.50 μm (diameter) particles. The coordinate axes in this figure are made dimensionless with the nozzle/target separation. As the figure shows, particle trajectory is greatly affected by the particle diameter. The twofold increase in diameter represents an eightfold increase in particle mass. The trajectories reflect the increased inertia of the larger particle, which impacts the target essentially perpendicularly, while the smaller particle is diverted noticeably by the radial gas velocity. Similar distinctions are evident in the particle temperature history shown in Fig. 10. In this figure, the horizontal axis is the particle temperature as the particle drops through the vertical coordinate (dimensionless height). The deposition surface was maintained at 1050 K in these calculations, just as in the CDER experiments (i.e., the high combustion temperature, 1573 K) and cooled surface (1050 K). As seen in the figure, target cooling can effectively cool the smaller particle, but not the larger particle.

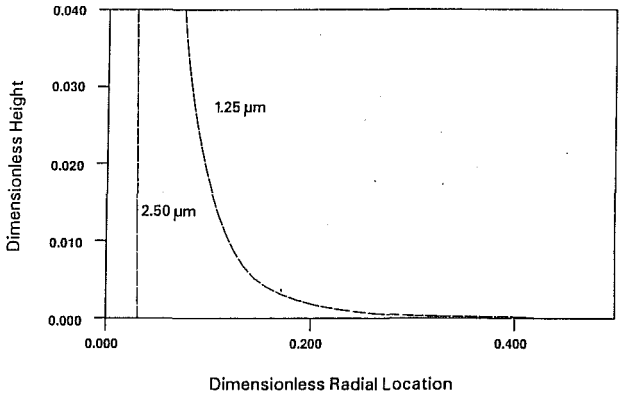

Fig. 9 Ash particle trajectory for 1.25 and 2.5-μm-dia particles

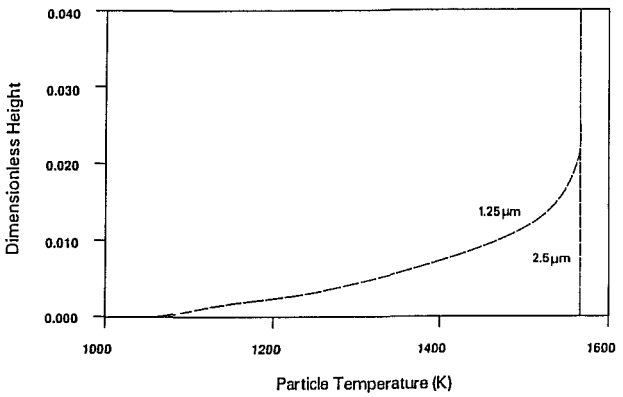

Fig. 10 Ash particle temperature history for 1.25 and 2.5-μm-dia particles

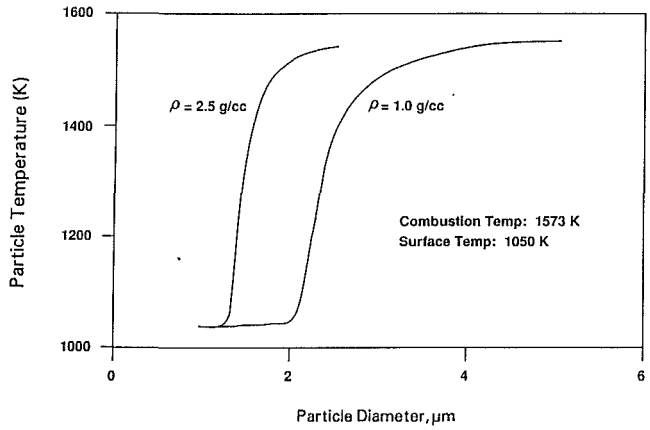

Fig. 11 Ash particle temperature at impact

The 2.5 μm particle arrives at the surface unaffected by the surface cooling, while the 1.25 μm particle is cooled to the surface temperature before impacting.

The above calculations are dependent on a number of parameters that are difficult to characterize. For example, the particle drag coefficient is undoubtedly affected by the irregular particle shape, while the particle density and specific heat may be complicated by the mineral ash composition and structure. These differences will contribute to a quantitative change in the results of the calculation, but the qualitative behavior is unchanged. For example, Fig. 11 shows the temperature of impacting ash particles of different sizes when they impact the deposition surface. Conditions are as shown on the figure, with results plotted for two different particle densities. Referring first to the smaller density of 1 g/cc, the results show that all particles smaller than 2 μm will arrive at the surface cooled to the surface temperature. Particles larger than 4 μm will be thermally unaffected by the transit through the cool boundary layer. Similar behavior is observed at the larger density of 2.5 g/cc, but the relative sizes are reduced.

With regard to the experimental data, it is interesting to note that the above calculations demonstrate that small particles can be quenched in the thermal boundary layer adjacent to hardware surfaces. However, because of the high velocities associated with turbine applications, it is likely that the larger particles cannot be cooled in the relatively brief passage through the thermal boundary layers. No specific critical size for particle cooling is stated in the present investigation, because the critical size will obviously change in different flow geometries and flow velocities. While it is difficult to characterize a critical size for cooling, even with a generous choice for all unknown parameters in the current tests, large particles (i.e., larger than 10 μm) will arrive at the surface essentially uncooled. Referring again to the experimental mass distribution for low-temperature combustion (Fig. 8), it is evident that most of the impacting ash will arrive at the deposition surface unaffected by surface cooling. Assuming that ash adhesion is promoted by soft or molten material constituting the ash, the calculations may explain why the sticking coefficient was independent of surface temperature at the low combustion temperature (Figs. 6 and 7). Because the majority of the mass occurs in large particles, the molten components responsible for adhesion cannot be frozen in the transition through the boundary layer. Conversely, the high-temperature combustion products are characterized by many particles smaller than 5 μm (Fig. 8), and molten phases associated with these small particles could be effectively frozen during transition through the thermal boundary layer. This behavior may explain the reduction in deposition observed experimentally for the high-temperature combustion products where surface cooling was observed to reduce the sticking coefficient.

Conclusions

The data and calculations suggest that a proper combination of combustion history and hardware surface temperature can contribute to effective deposition mitigation in coal-burning turbines. If the combustion history is such that most of the remaining ash is in large particles, surface cooling will be unable to quench arriving ash particles, and the sticking coefficient could be unaffected by surface cooling. However, if the combustion process is tailored to produce fine ash particles, the surface cooling can be very effective at reducing deposition. A critical size for effective cooling is not presented in the present analysis, because this size is dependent on a number of parameters that are difficult to characterize and will vary with flow geometry and coal ash type. It is also observed that the combustion temperature plays a role in determining the strength of the ash deposit. Although the low-temperature combustion produces a greater sticking coefficient, the ash deposits are weakly bonded and can be easily removed. This suggests that a trade-off between sticking coefficient and deposit strength may be needed to ensure that a minimal quantity of ash adheres to hardware, and also that the ash, which does stick, can be removed by on- or off-line cleaning.

References

Ahluwalia, R. K., Im, K. H., and Wenglarz, R. A., 1989, "Flyash Adhesion in Simulated Coal-Fired Gas Turbine Environment," ASME JOURNAL OF ENGINEERING FOR GAS TURBINES AND POWER, Vol. 111, pp. 672–678.

Anderson, R. J., Meyer, C. T., and Dennis, R. A., 1988, "A Combustion/Deposition Entrained Reactor for High Temperature/Pressure Studies of Coal

and Coal Minerals," presented at the 1988 Annual AIChE Meeting, Washington, DC, Nov. 27–Dec. 2.

Benson, S. A., Tangsathitkulchai, M., and Austin, L. G., 1985, "Studies of Ash Deposit Formation Using a Laboratory Furnace," *Proceedings of the Second Annual Pittsburgh Coal Conference*, p. 689.

Bird, R. B., Stewart, W. E., and Lightfoot, E. N., 1960, *Transport Phenomena*, Wiley, New York.

France, J. E., Grimm, U., Anderson, R. J., and Kovach, J. J., 1984, *Deposition and Corrosion in Gas Turbines Utilizing Coal or Coal-Derived Fuel*, DOE/METC/84-17 (DE84009290).

Kothari, V., and Rekos, N., 1988, *Proceedings of the Annual Coal-Fuel Heat Engines and Gas Stream Cleanup System Contractors Review Meeting*, DOE/METC-88/6094, NTIS/DE88001088, CONF-880656.

Marple, V. A., and Liu, Y. H., 1974, "Characteristics of Laminar Jet Impactors," *Environmental Science and Technology*, Vol. 8, pp. 648–654.

Marple, V. A., and Willeke, K., 1976, "Impactor Design," *Atmospheric Environment*, Vol. 10, pp. 891–896.

Morsi, S. A., and Alexander, A. J., 1972, "Theoretical Low Speed Particles Collision With Symmetrical and Cambered Aerofoils," ASME Paper No. 72-WA/FE-35.

Raask, E., 1985, *Mineral Impurities in Coal Combustion*, Hemisphere Publishing, Washington, DC.

Richards, G., Logan, R., Meyer, C., and Anderson, R. J., 1988, "Deposition Effects in Pressurized Combustion of Coal-Derived Fuels," *Proceedings of the AR&TD Direct Utilization and Instrumentation and Diagnostics Contractors Review Meeting*, sponsored by U.S. Department of Energy, Pittsburgh Energy Technology Center, Sept. 6–9, Pittsburgh, PA.

Rosner, D. E., and Nagarajan, R., 1987, "Toward a Mechanistic Theory of Net Deposit Growth From Ash-Laden Flowing Combustion Gasses: Self-Regulated Sticking of Impacting Particles and Deposit Erosion in the Presence of Vapor Glue," *24th National Heat Transfer Conference*, AIChE Symposium Series, Vol. 3, No. 257, pp 289–296.

Ross, J. S., Anderson, R. J., and Nagarajan, R., 1988, "Effect of Sodium Deposition in a Simulated Combustion Gas Turbine Environment," *J. Energy and Fuels*, Vol. 2, pp. 282–289.

Schlichting, H., 1979, *Boundary Layer Theory*, McGraw-Hill, New York.

Spiro, C. L., Chen, C. C., Kimura, S. G., Lavigne, R. G., and Schields, P. W., 1989, "Deposit Remediation in Coal-Fired Gas Turbines Through the Use of Additives," ACS Division of Fuel Chemistry, preprints of papers presented at the ACS National Meeting in Dallas, TX, Vol. 34, No. 2.

Self-Tuning Control of a Coal-Fired Fluidized Bed Combustor

K. W. Junk

R. R. Fullmer

R. C. Brown

Department of Mechanical Engineering,
Iowa State University,
Ames, IA 50010

This paper investigates the temperature control of a two-bed fluidized combustor using a self-tuning control algorithm to vary secondary air flow rate. The controller consists of a recursive least-squares parameter estimator, an observer, and a linear optimal control design procedure. This combination enables the controller to estimate the system parameters and update the feedback gains when necessary. Further, this study addresses the tracking form of optimal control, accomplished by augmenting the state vector with an integrator. The self-tuning control algorithm was compared with a simple PI controller, which was tuned using the Ziegler–Nichols method. In this study, self-tuning control provided improved performance over classical control. Compared with conventional, constant-gain control, self-tuning control reduced steady-state variance by a factor of 6.67 while maintaining good tracking characteristics.

Introduction

In recent years, fluidized bed combustors (FBCs) have become an attractive means for meeting future power generation and process heat requirements in an environmentally acceptable manner. Among many favorable characteristics, fluidized bed combustors are capable of burning low-grade, variable quality fuels at low combustion temperatures. Coal-fired FBCs, for example, typically operate in the range of 760°C to 980°C, to be compared with temperatures of 1650°C for boilers that utilize cyclone furnaces. The lower combustion temperatures result in lower NO_x emissions, elimination of ash clinkering, and elimination of slag fouling. In addition, an acceptor stone, such as dolomite or limestone, is often used in the bed material to reduce the sulfur content of the product gases. However, due to inherent nonlinear dynamics arising from fluidization, radiation, and chemical kinetics, classical linear control schemes may be inappropriate. Consequently, new algorithms to control temperature in FBCs should be examined.

Traditionally, many dynamic systems are controlled using simple linear feedback controllers. From step inputs, a linear model can be formulated, a root locus constructed, and a proportional-integral-derivative (PID) controller designed. Alternatively, PID control may be designed through heuristic techniques, such as the Ziegler-Nichols method (Doebelen, 1985). Although predicated on linear system theory and design, PID controllers have a robust nature such that the system will usually remain stable even though weakly nonlinear dynamics may be present. Fluidized beds, on the other hand, are highly nonlinear systems and have transient natures that are not well understood. When controlled using linear techniques, highly nonlinear systems may be poorly tuned in the desired operating range as nonlinear behavior is often compensated through excessively conservative design (Hunt, 1989). To improve system performance, several strategies have been developed that attempt to contend with nonlinear system dynamics. One particularly successful approach has been the use of adaptive control design techniques. Controllers built upon these techniques not only promise to improve system performance, but also lend themselves well to applications in process control.

Contributed by the Power Division for publication in the JOURNAL OF ENGINEERING FOR GAS TURBINES AND POWER. Manuscript received by the Power Division February 15, 1990.

Process Description

Nonlinear and nonstationary behavior is inherent in virtually all aspects of bubbling bed combustors, and nowhere is this more apparent than in the temperature of the bed. Wide variations in temperature can be attributed to a nonlinear heat transfer coefficient as well as to highly variable (and unpredictable) composition of coal. However, slight fluctuations in temperature significantly reduce sorbent effectiveness, adversely affect NO_x emissions, and diminish combustion efficiency. Therefore, constant and uniform bed temperature is essential for optimal combustor performance.

Control of bed temperature must be accomplished without extensive equipment modifications during combustor operation. For a fixed coal feed rate, bed temperature can be controlled through methods such as varying fluidization velocity, discharging bed material, or slumping sections of the bed. However, load turndown ratios obtained with these procedures rarely exceed four (Brown and Foley, 1988). An alternative approach to conventional temperature control techniques utilizes a two-bed design. This approach has attained turndown ratios greater than ten (Brown et al., 1989).

A schematic of a two-bed combustor is shown in Fig. 1. The combustor is comprised of a central, fluidized combustion bed and an annular, fluidized heat transfer bed. For this investigation, a laboratory-scale test rig was built: The combustion bed contained approximately 15 cm of sand whereas the heat transfer bed contained approximately 23 cm of sand. Each bed has an independent air plenum in which air flow rates could be adjusted separately so that combustion and heat transfer processes were decoupled.

Temperature control is achieved by changing the air velocity in the annular bed. When no air is supplied to the annular

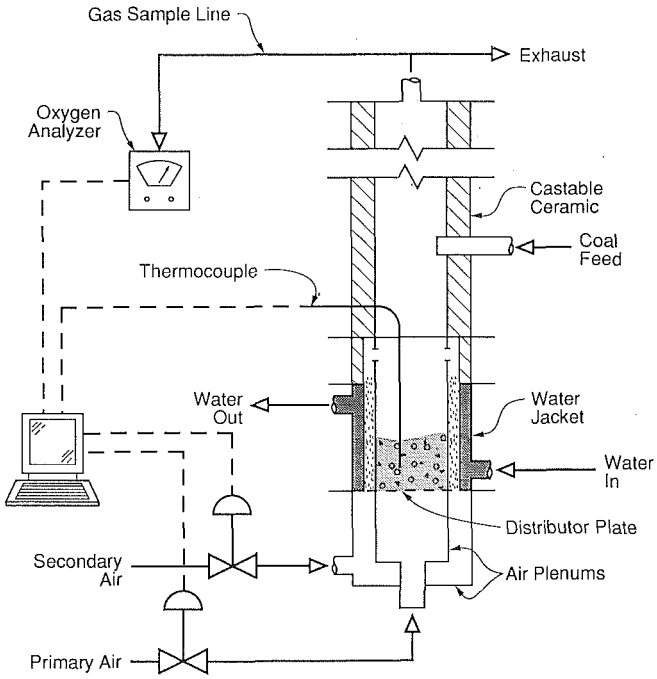

Fig. 1 Schematic of a two-bed fluidized combustor

bed, heat transfer from the central bed to the water jacket is by conduction through the bed material. As the air velocity increases to a point just before incipient fluidization, heat transfer is augmented by gas convection. A further increase in air velocity will fluidize the annular bed, adding particulate convection to the entire heat transfer process. The result is a dramatic increase in the rate at which heat is removed from the central bed and a corresponding decrease in the temperature of the central bed.

Combustion bed temperatures were measured with thermocouples and the annular bed air flow rate was adjusted accordingly. Because a single-input, single-output control objective was specified, primary air flow and coal feed rates were maintained at constant values during combustor operation. Although many control parameters were available, adjusting the secondary air flow rate was found to be the most effective method by which temperature could be altered in the two-bed design under investigation.

Temperature and flow rate data were acquired and digital control was executed with an Intel 8088-based microcomputer (4.77 MHz). The unit was configured with an Intel 8087 math coprocessor, 640 K of addressable memory, and a 20 Mb hard drive. The data interface consisted of a Metrabyte DAS-8 A/D converter and a Metrabyte DDA-06 D/A converter. The DAS-8 is an 8-channel, 12-bit, successive approximation A/D converter with conversion times of 25 μs. The DDA-06 is a 6-channel, 12-bit analog output interface with 24 parallel digital I/O lines. Both data acquisition and digital control codes were written and compiled with Microsoft QuickBASIC 4.0.

Temperature data were obtained from three type-K (chromel/alumel) thermocouple probes in the central bed, and one type-K thermocouple probe in the annular bed. To protect them from the abrasive bed environment, the thermocouples were enshrouded in a 304 stainless steel casing. The probes were connected to a Metrabyte sub-multiplexer board (model EXP-16), which amplified thermoelectric voltages and provided cold junction compensation. Analog signals from the sub-multiplexer board were sent to the DAS-8 A/D interface board.

Experiments were performed using bituminous coals of variable quality and composition, including Illinois No. 6 and Iowa "Cherokee" seam coals as well as various weathered Iowa coals. The coals are crushed and screened to a top size of 0.953 cm, meeting feeder clearance requirements, and screened to a bottom size of 0.318 cm, thereby reducing the quantity of elutriable fines in the fuel supply. Neither proximate nor ultimate analyses were performed to characterize the coals as such information was not required for proper controller performance.

Self-Tuning Control Algorithm

One type of self-tuning control, as described by Åström and Wittenmark (1989) and Goodwin and Sin (1984), consists of three components: (1) a recursive least-squares (RLS) parameter identification procedure, (2) an observer, and (3) a linear optimal control law. A linear optimal control design was chosen because closed-loop stability is guaranteed, provided the system is either (*a*) uniformly completely controllable and uniformly completely reconstructible or (*b*) exponentially stable (Kwakernaak and Sivan, 1972). A schematic of the self-tuning controller is shown in Fig. 2. Note that the controller consists of two loops: an outer feedback loop and an inner controller adjustment loop. An overview of the self-tuning control algorithm is presented for a second-order model; extensions to higher order models are straightforward.

1 System Model. In the discrete-time domain, systems are described through a difference operator representation. The forward shift operator and backward shift operator are written as q and q^{-1}, respectively. For a function $y(t)$, where t is a sequential time index, $qy(t)$ references the function y at time $(t+1)$; similarly, $q^{-1}y(t)$ references the function y at time $(t-1)$. Using left difference operator representation, systems are modeled through linear combinations of past outputs, $y(t)$, and past inputs, $u(t)$. Following the notation of Goodwin and Sin (1984), systems are expressed in the discrete-time domain through a deterministic autoregressive moving-average (DARMA) model of the form

$$A(q^{-1})y(t) = B(q^{-1})u(t) + d \qquad t \in [0, 1, 2, 3, \cdots,] \tag{1}$$

where A and B are the scalar polynomials

$$A(q^{-1}) = 1 + a_1 q^{-1} + \cdots + a_n q^{-n}$$

$$B(q^{-1}) = b_1 q^{-1} + \cdots + b_m q^{-m}$$

and d is an offset parameter. For a second-order system, Eq. (1) may be expanded and rearranged to obtain

Nomenclature

K = gain vector of observer
L = gain vector of controller
P = covariance matrix
R_u = weighting matrix (system input)
R_x = weighting matrix (system output)
T = temperature, °C
t = discrete time index
u = system input (secondary air flow rate), m^3/min
x = state vector
y = system output (temperature), °C
y^* = system set point (temperature), °C
z = integrator variable
δ = Kronecker delta
θ = coefficient vector of DARMA model
λ = forgetting factor
ϕ = variate vector of DARMA model
σ = standard deviation

Superscripts

$\hat{}$ = denotes an estimate

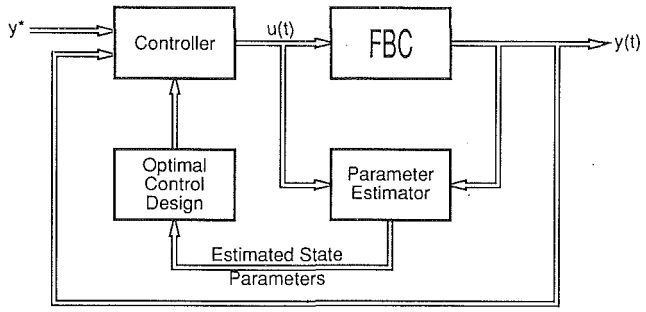

Fig. 2 Self-tuning control loops

$$y(t) = -a_1 y(t-1) - a_2 y(t-2) + b_1 u(t-1) + b_2 u(t-2) + d$$
$$t \in [0, 1, 2, 3, \cdots] \tag{2}$$

where, for the FBC, $y(t)$ denotes a deviation central bed temperature and $u(t)$ denotes a deviation annular bed air flow rate. Deviations were taken about initial conditions, e.g., $y(t) = T(t) - T(t_o)$, to enforce zero initial conditions. The offset parameter d has been incorporated in the DARMA model to account for nonsteady-state initial conditions.

Alternatively, the DARMA model may be written in state-space form. Using left difference operator representation, the DARMA modal may be described through the set of linear difference equations

$$\begin{bmatrix} x_1(t+1) \\ x_2(t+1) \end{bmatrix} = \begin{bmatrix} -a_1 & 1 \\ -a_2 & 0 \end{bmatrix} \begin{bmatrix} x_1(t) \\ x_2(t) \end{bmatrix} + \begin{bmatrix} b_1 \\ b_2 \end{bmatrix} u(t) + \begin{bmatrix} d \\ 0 \end{bmatrix} \tag{3}$$

in which $y(t)$ is described through an output equation, a linear combination of state variables $x_1(t)$ and $x_2(t)$. In this case, the output equation takes the form

$$y(t) = [1, 0] \begin{bmatrix} x_1(t) \\ x_2(t) \end{bmatrix} \tag{4}$$

This particular state variable representation (SVR) is in an observer form since the system is uniformly completely observable (Goodwin and Sin, 1984). In matrix notation, Eqs. (3) and (4) can be abbreviated as

$$x(t+1) = Ax(t) + Bu(t) + D$$
$$y(t) = Cx(t) \tag{5}$$

where

$$A = \begin{bmatrix} -a_1 & 1 \\ -a_2 & 0 \end{bmatrix} \qquad B = \begin{bmatrix} b_1 \\ b_2 \end{bmatrix} \qquad D = \begin{bmatrix} d \\ 0 \end{bmatrix}$$
$$C = [1, 0]$$
$$x(t) = [x_1(t), x_2(t)]^T \tag{6}$$

Additional considerations concerning SVRs, including discussions pertaining to necessary and sufficient conditions for system controllability and observability, are presented by Goodwin and Sin (1984) and Kwakernaak and Sivan (1972).

2 Recursive Least Squares. Coefficients of the DARMA model—a_1, a_2, b_1, b_2, and d—can be estimated through off-line identification procedures, such as least squares. However, for a fluidized bed, the coefficients of the DARMA model tend to drift since the model is a linear approximation of the nonlinear system about the current operating point. That is, as the temperature changes, the coefficients of the DARMA model also change. In addition, coefficients from one run may not match the coefficients of another run, especially if different types of fuel or bed material are used between runs. Hence, better coefficient estimates may be obtained through on-line procedures, such as a recursive least-squares algorithm with exponential data weighting.

Recursive least squares is built upon dividing the DARMA model between variates and coefficients in the manner

$$y(t) = \phi(t-1)^T \theta \tag{7}$$

where

$$\phi(t-1) = [-y(t-1), -y(t-2), u(t-1), u(t-2), 1]^T \tag{8}$$

and

$$\theta = [a_1, a_2, b_1, b_2, d]^T \tag{9}$$

Given $\phi(t-1)$, the recursive least-squares algorithm has been arranged so as to estimate θ through the sequential equations (Goodwin and Sin, 1984; Ljung and Wittenmark, 1982)

$$\hat{\theta}(t) = \hat{\theta}(t-1) + \frac{P(t-2)\phi(t-1)}{\lambda(t-1) + \phi(t-1)^T P(t-2)\phi(t-1)} [y(t) - \phi(t-1)^T \hat{\theta}(t-1)] \tag{10}$$

in which

$$P(t-1) = \frac{1}{\lambda(t-1)} \left[P(t-2) - \frac{P(t-2)\phi(t-1)\phi(t-1)^T P(t-2)}{\lambda(t-1) + \phi(t-1)^T P(t-2)\phi(t-1)} \right] \tag{11}$$

Here, $P(t-1)$ is a covariance matrix and $\lambda(t-1)$ is an exponential weighting ("forgetting") factor. Typically, values for λ range from 0.95 to 1.00, where a value of 1.00 retains all data. Caution must be exercised when specifying λ. If λ is much less than 1.00, old data are discarded too quickly, and system noise becomes a problem. On the other hand, if λ is very close to 1.00, old data, and corresponding old coefficients, diminish the ability of the algorithm to track new, changing coefficients. In this study, a constant forgetting factor of 0.99 was found to be satisfactory.

In addition to weighting data, consideration was given to initial values for θ and P. Initial values for θ were obtained through an off-line analysis of an early test run. Initial parameter coefficients were specified as

$$\hat{\theta}(0) = [-1.19, 0.228, -0.05, -0.30, 1.4]^T \tag{12}$$

The P matrix, on the other hand, was initially set to 15 I. Large values were specified along the diagonal of the covariance matrix to reflect the uncertainty of the off-line estimates. Because the initial P matrix was set so large, initial covergence dynamics often results in large, spurious variations in parameter estimates. Difficulties stemmed from convergence problems associated with the characteristic equation

$$A(q^{-1})y(t) = 0;$$
$$A(q^{-1}) = (1 + a_1 q^{-1} + a_2 q^{-2}) \tag{13}$$

Occasionally, $A(q^{-1})$ was estimated as unstable (i.e., roots outside the unit disk in the complex plane). To prevent such results, Eq. (13) was analyzed with Jury's stability test. If the roots were estimated as unstable, θ was not updated. By using Jury's stability test, parameters converged quickly and smoothly as absurd estimates were discarded. Typically, $A(q^{-1})$ was estimated as unstable two to fifteen times during initial parameter convergence.

3 System Reconstruction. The underlying assumption regarding the state-space model is that the state vector $x(t)$ is completely known or measurable. In this case, the state is partially measurable insofar as the central bed temperature $x_1(t)$ is measurable. In contrast, the state variable $x_2(t)$ is an internal system state and cannot be measured directly. Hence, the state vector must be approximated (i.e., reconstructed) through a function of the observed variable, $x_1(t)$.

The state vector can be approximated through a full-order observer, a dynamic system whose output exponentially converges to the state to be reconstructed. A full-order observer can be expressed through the equation

$$\hat{x}(t+1) = A\hat{x}(t) + Bu(t) + D + K[y(t) - C\hat{x}(t)]$$
$$K = [k_1, k_2]^T \tag{14}$$

For self-tuning control, SVR observer coefficients are replaced by estimates obtained from the recursive least-squares algorithm. Dynamics of the observer are characterized by a difference equation of the reconstruction error (Kwakernaak and Sivan, 1972)

$$e(t) = (A - KC)e(t-1);$$
$$e(t) = x(t) - \hat{x}(t) \tag{15}$$

Eigenvalues of Eq. (15) are specified through an approximate choice of values for the gain vector, K. For the fluid bed used in this investigation, eigenvalues placed at 0.3 (z-domain) produced an adequate observer response.

4 Optimal Control. The estimated state matrix along with the corresponding state observer can be incorporated directly into an optimal control design, which is a regulator form of optimal control. Since a variable set point is often required, the regulator problem is converted to a tracking problem through integral action. Integral action was chosen over precompensation to enforce zero steady-state error conditions. The conversion is accomplished by augmenting the SVR with a function $z(t)$ that integrates the difference between the set point, $y^*(t)$, and system output, $y(t)$. The integral (i.e., sum) of the differences

$$z(t) = \sum_{i=0}^{t-1} (y^*(i) - y(i)) \tag{16}$$

can be expressed recursively as

$$z(t+1) = z(t) + y^*(t) - y(t);$$
$$z(0) = 0 \tag{17}$$

By augmenting Eq. (5) with Eq. (17), the new third-order state can be written as (Goodwin and Sin, 1984)

$$\begin{bmatrix} x(t+1) \\ x(t+1) \end{bmatrix} = \begin{bmatrix} A & 0 \\ -C & I \end{bmatrix} \begin{bmatrix} x(t) \\ z(t) \end{bmatrix} + \begin{bmatrix} B \\ 0 \end{bmatrix} u(t) + \begin{bmatrix} D \\ y^* \end{bmatrix}$$
$$\begin{bmatrix} y(t) \\ z(t) \end{bmatrix} = \begin{bmatrix} C & 0 \\ 0 & I \end{bmatrix} \begin{bmatrix} x(t) \\ z(t) \end{bmatrix} \tag{18}$$

In abbreviated form,

$$\bar{x}(t+1) = \bar{A}\bar{x}(t) + \bar{B}u(t) + \bar{D}$$
$$\bar{y}(t) = \bar{C}\bar{x}(t) \tag{19}$$

where $\bar{x}(t)$ is the column vector $[x_1(t), x_2(t), z(t)]^T$ and $\bar{y}(t)$ is the column vector $[y(t), z(t)]^T$. A block diagram of the augmented state-space model is given in Fig. 3. To ensure asymptotic stability of the augmented closed-loop system under feedback control, $(\bar{A}, \bar{B})$ must be stabilizable. The pair $(\bar{A}, \bar{B})$ is stabilizable if (1) the pair $(\bar{A}, \bar{B})$ is reachable, (2) A is nonsingular, and (3) the rank of B is equal to the number of outputs (Goodwin and Sin, 1984). All three conditions are satisfied with the two-bed combustor used in this investigation.

Feedback gains for the augmented state, $L(t)$, are obtained from a third-order algorithm, which minimizes the performance index

$$J = \bar{x}(N)^T R_N \bar{x}(N) + \sum_{t=0}^{N-1} (\bar{x}(t)^T R_x \bar{x}(t) + u(t)^T R_u u(t)) \tag{20}$$

subject to

$$\bar{x}(t+1) = \bar{A}\bar{x}(t) + \bar{B}u(t) + \bar{D}$$
$$\bar{y}(t) = \bar{C}\bar{x}(t)$$
$$u(t) = -L(t)\bar{x}(t)$$
$$\bar{x}(t_o) = \bar{x}_o$$

The feedback gain vector $L(t)$ is optimized by minimizing

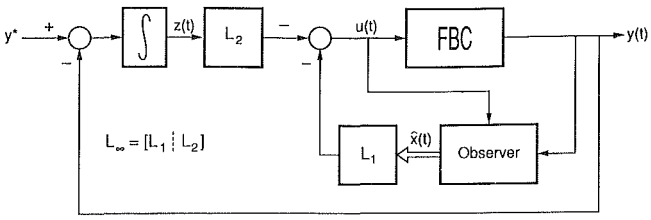

Fig. 3 Augmented closed-loop controller

Eq. (20), which is weighted by the symmetric, positive definite matrices R_x, R_u, and R_N. Solution of the linear optimal control problem requires (Goodwin and Sin, 1984)

$$L(t) = [R_u + \bar{B}^T S(t+1)\bar{B}]^{-1} \bar{B}^T S(t+1)\bar{A} \tag{21}$$

where $S(t)$ satisfies the Joseph stabilized version of the matrix Riccati equation:

$$S(t) = R_x + L(t)^T R_u L(t) + (\bar{A} - \bar{B}L(t))^T S(t+1)(\bar{A} - \bar{B}L(t)) \tag{22}$$

Sufficient conditions for a local minimum are discussed by Bryson and Ho (1975). A steady-state solution of the feedback gain vector, L_∞, is obtained by iterating Eqs. (21) and (22) backward in time. Provided $(\bar{A}, \bar{B})$ is stabilizable and $(\bar{A}, \sqrt{R_x})$ is observable, $L(t)$ converges uniquely to L_∞ (Lewis, 1986); convergence is usually achieved within five to ten iterations. Note that, because the optimization horizon is made sufficiently large, steady-state feedback gains are independent of the terminal condition $\bar{x}(N)^T R_N \bar{x}(N)$. Furthermore, if $(\bar{A}, \bar{B})$ is stabilizable and $(\bar{A}, \sqrt{R_x})$ is observable, the closed-loop system with feedback gain L_∞ is asymptotically stable (Lewis, 1986). Finally, by replacing the state vector $\bar{x}(t)$ with stable estimates obtained from the observer, the secondary air flow rate can be calculated from the equation

$$u(t) = -L_\infty[\hat{x}_1(t), \hat{x}_2(t), z(t)]^T \tag{23}$$

Experimental Results

Several experiments were run on the two-bed combustor. However, for brevity, only one test will be examined in detail; results from this run sufficiently characterize the performance of the self-tuning controller.

For the test runs, the time interval between control signal updates was set to 20 seconds, one-tenth of the dominant time constant. Sampling intervals much smaller than 20 seconds resulted in parameter identification difficulties. Specifically, to avoid estimating system parameters on measurements predominated by noise, a sufficient change in temperature had to occur between data samples. On the other hand, sampling intervals much larger than 20 seconds resulted in poor regulation as bed temperatures tended to stray between control updates.

Weighting matrices R_x and R_u were specified as

$$R_x = \begin{bmatrix} 100 & 0 & 0 \\ 0 & 1 & 0 \\ 0 & 0 & 1 \end{bmatrix}$$
$$R_u = [8000] \tag{24}$$

Temperature data are illustrated in Fig. 4 and corresponding annular bed air flow rate data are illustrated in Fig. 5. RLS coefficient estimates and feedback gains are graphed in Figs. 6–9.

The initial transient temperature response of this run was typical of most self-tuning control tests on the fluidized bed. Initial coefficient estimates and initial feedback gains fluctuated as both the covariance matrix and the partial regression coefficient vector converged. Parameter convergence during the initial tuning process is apparent by the temperature re-

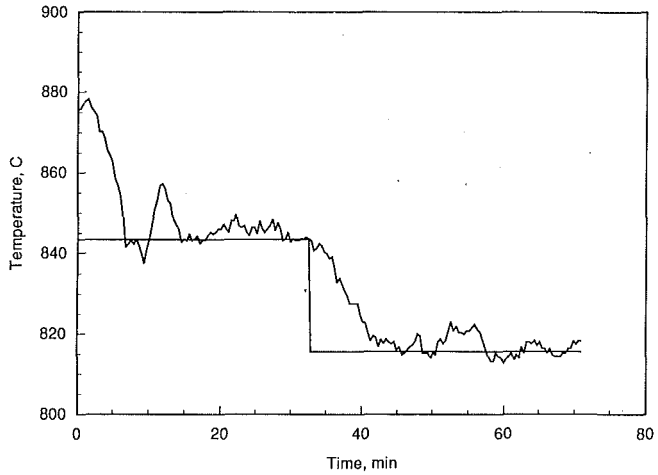

Fig. 4 Temperature response with self-tuning control

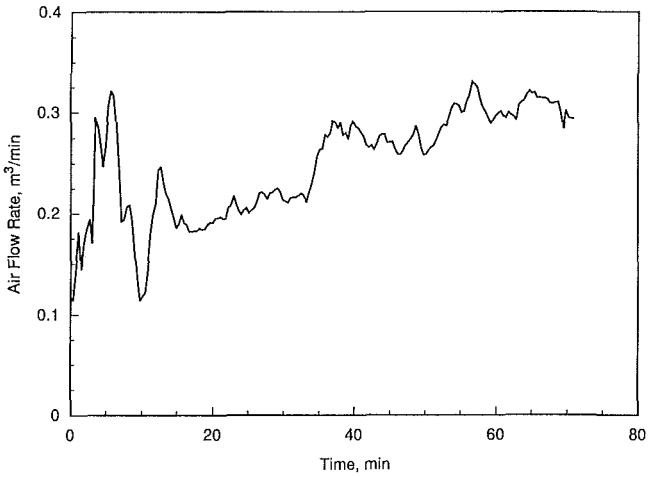

Fig. 5 Secondary air flow command

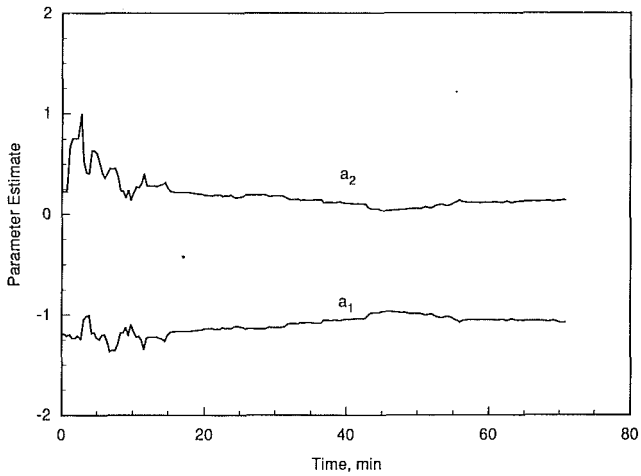

Fig. 6 Estimates of a_1 and a_2

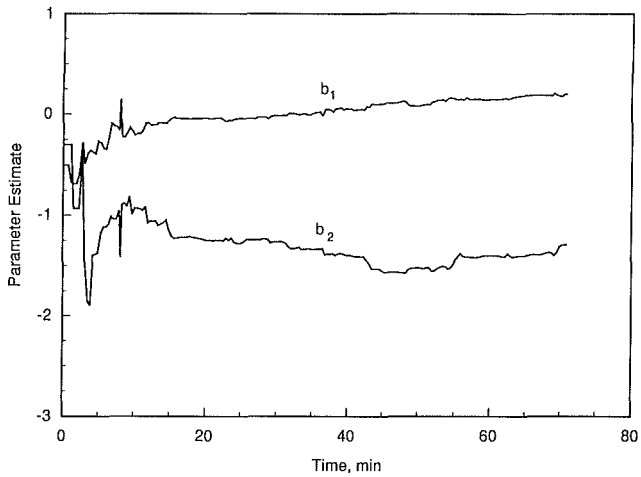

Fig. 7 Estimates of b_1 and b_2

sponse at 11 minutes into the run. After coefficients and feedback gains converged, the bed temperature asymptotically approached the set point temperature. At steady-state conditions, the bed temperature had an rms error of 1.04°C and a pooled variance of 2.88°C^2 (120 df).

Coefficient trajectories of a_1 and a_2 are graphed in Fig. 6. Both coefficients converged quickly and varied only slightly during the test run. During the initial tuning period, a few flats are present on both the a_1 and a_2 trajectories. At these places, Jury's stability test detected roots outside the unit disk, and plateaus were created as RLS estimates were not revised.

Similar patterns are present in the b_1 and b_2 trajectories (Fig. 7). As with the a_1 and a_2 coefficients, initial convergence of b_1 and b_2 was tumultuous. In contrast to the a and b trajectories, the offset parameter, d (Fig. 8), converged in a relatively quick and smooth manner. Originally, the offset parameter was intended to account for nonsteady initial conditions; however, during combustor operation, the RLS procedure incorporated nonlinear system dynamics in the estimate of d. Therefore, as the fluidized bed evolved over time, the estimate of d changed accordingly.

In this run as well as all other runs, parameter estimates varied about mean values. Some concern arose over whether estimate "noise" would adversely affect feedback gains and system performance. For the most part, though, slight deviations present in the parameter estimates were not mapped onto the feedback gains, as illustrated in Fig. 9. In other words, after the tuning transient, coefficient estimates fluctuated slightly, but feedback gains, l_1, l_2, and l_3 (corresponding to state variables $\hat{x}_1(t)$, $\hat{x}_2(t)$, and $z(t)$, respectively) remained approximately constant.

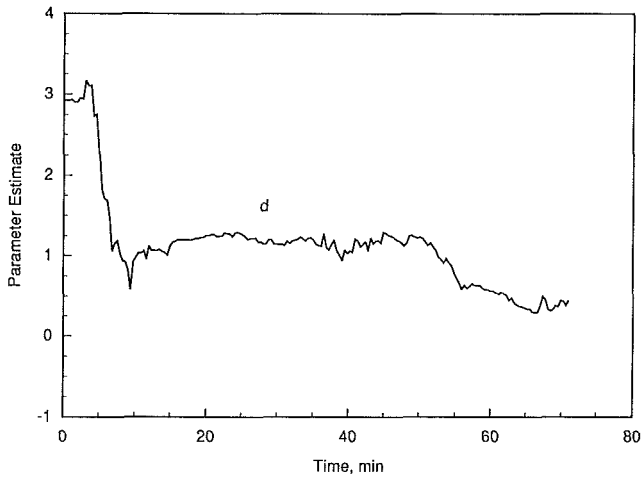

Fig. 8 Estimate of d

Two unknown disturbances were introduced into the system: one at 18 minutes and another at 50 minutes. The nature and magnitude of the disturbances are presently unknown although variable properties of the coal are suspected. Note that, even for these disturbances, the controller was capable of bringing the system back to the set point temperatures with minimal overshoot.

As a reference, the self-tuning algorithm was compared with a PI controller tuned by the Ziegler–Nichols method. The control law

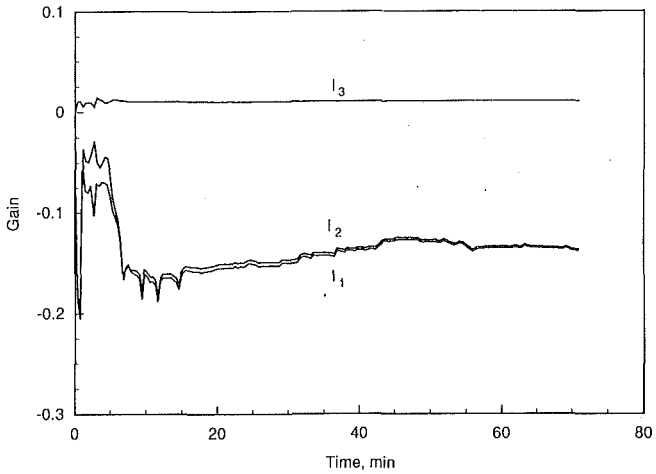

Fig. 9 Feedback gains

$$u(t) = -0.078\left[e(t) + \frac{1}{114}\int_0^t e(t)dt\right]$$

$$e(t) = y^*(t) - y(t) \tag{25}$$

was implemented with a time interval of 20 seconds between control signals.

Temperature response under PI control is graphed in Fig. 10 and corresponding annular air flow rates are graphed in Fig. 11. Note that both transient and steady-state behavior are considerably worse with PI control than with self-tuning control. For example, substantial overshoot was present at 10 minutes into the run. Poor performance is further evidenced by a steady-state rms error of 4.37°C and a pooled, steady-state variance of 19.2°C^2 (155 df). Although system performance was not extraordinary, no system instabilities were observed during controller operation.

Poor performance of PI control is due, in part, to an off-line parameter estimation procedure. With variable characteristics of coal and bed sand, system estimation from a step input did not accurately describe future operations. In itself, the self-tuning control algorithm used in this investigation is a PI controller; however, for an FBC, on-line parameter estimation allows for better tuning of the system than off-line parameter estimation.

Conclusion

The two-bed fluidized combustor in this study highlights both the benefits and limitations of self-tuning control. Perhaps the greatest advantage of self-tuning control is the ability of the controller to identify system parameters, tune itself to optimal settings, and retune itself should process dynamics change. The adaptive tuning process worked well with the two-bed fluidized combustor, and after an initial tuning period, the controller could track the set point temperature and respond to system disturbances. Further, because the controller could estimate parameters on-line, system response was better than that with classical PI control.

Although system performance was improved, the self-tuning controller had some restrictions. For example, the controller required supervision logic in the form of Jury's stability test to ensure proper parameter convergence. In addition, the parameter estimation scheme could not effectively separate nonstationary, colored noise from system dynamics; hence, to increase the signal-to-noise ratio, the sampling rate had to be increased. A longer sampling interval resulted in a larger steady-state temperature variance as the controller could not immediately correct temperature deviations.

Clearly, self-tuning control is not a panacea; rather, self-tuning control is an effective design option that contends with

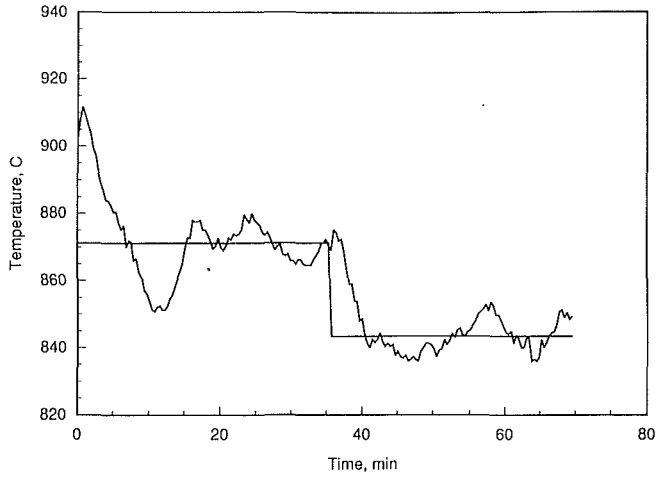

Fig. 10 Temperature response with PI control

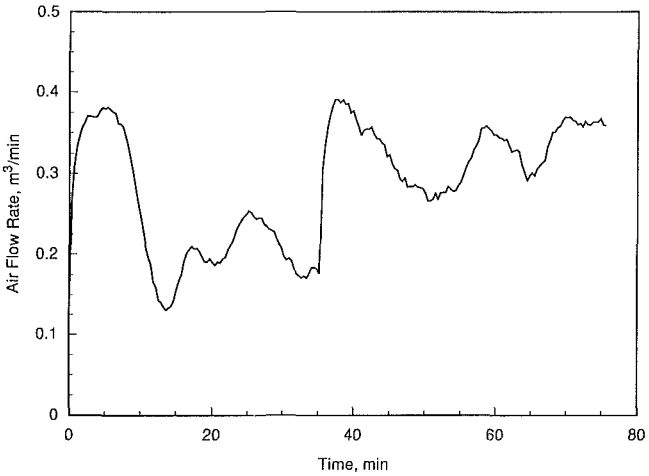

Fig. 11 Secondary air flow command

nonlinear system dynamics through a linearized, time-varying model. Although self-tuning control worked well for the SISO case, a fluidized bed combustor is inherently a multiple-input, multiple-output (MIMO) system with coupled, nonlinear dynamics. However, the self-tuning algorithm used in this study can be generalized to a MIMO control objective. For example, both bed temperature and combustion efficiency can be regulated through simultaneous adjustments of primary and secondary air flow rates. Since self-tuning control seems to be particularly well suited for MIMO objectives, future work should address the characteristics and limitations of self-tuning MIMO control on fluidized bed combustors using the same principles developed for the SISO case.

References

Åström, K. J., and Wittenmark, B., 1989, *Adaptive Control*, Addison-Wesley, New York.

Brown, R. C., and Foley, J. E., 1988, "Load Turndown in a Two-Bed Fluidized Combustor," *Industrial and Engineering Chemistry Research*, Vol. 27, pp. 24–30.

Brown, R. C., Foley, J. E., and Buttermore, W., 1989, "Heat Transfer in a Two-Bed Fluidized Combustor," *American Institute of Chemical Engineers Symposium Series*, Vol. 85, No. 269, pp. 153–158.

Bryson, A. E., and Ho, Y., 1975, *Applied Optimal Control*, Hemisphere Publishing Corp., Washington, DC.

Doebelen, E. O., 1985, *Control System Principles and Design*, Wiley, New York.

Goodwin, G. C., and Sin, K. S., 1984, *Adaptive Filtering, Prediction, and Control*, Prentice-Hall, Englewood Cliffs, NJ.

Hunt, K. J., 1989, *Stochastic Optimal Control Theory With Application in Self-Tuning Control*, Springer-Verlag, New York.

Kwakernaak, H., and Sivan, R., 1972, *Linear Optimal Control Systems*, Wiley-Interscience, New York.

Lewis, F., 1986, *Optimal Control*, Wiley-Interscience, New York.

Ljung, L., and Wittenmark, B., 1982, *Theory and Practice of Recursive Identification*, MIT Press, Cambridge, MA.

Relationship Between Feedstock Characteristics and Erosivity of FBC Bed Materials

A. V. Levy
Lawrence Berkeley Laboratory,
University of California,
Berkeley, CA 94720

B. Q. Wang

G. Q. Geng

Xian Institute of Highways,
Xian, Shaanxi,
The People's Republic of China

The erosion-corrosion (E-C) metal wastage mechanisms and rates that occur in 1018 plain carbon steel used in tubular heat exchangers of fluid bed combustors (FBC) are discussed. The characteristics of FBC bed material erodent particles such as composition, shape, size, and strength were found to have a major effect on the surface degradation mechanisms and rates that occurred. A total of 16 different bed material particles from ten different FBCs were tested. It was determined that when the particles were strong enough not to shatter when they impacted the steel's surface, their shape and composition were the most important factors in determining their erosivity. The relative amounts of SiO_2, CaO, $CaCO_3$, $CaSO_4$, and alkali compounds in the bed materials were related to the metal wastage by using laboratory mixtures of the compounds as erodents. The ratio of SiO_2 to CaO and $CaCO_3$ was especially important in determining the erosivity of the bed materials. It was found that increasing this ratio increased the metal wastage. A sharp transition ratio occurred on either side of which the metal wastages were linear. The slope of the linear curve was low for the lower sand content mixtures and higher for higher sand content mixtures. The transition ratio required a higher CaO content for higher velocity particles.

Introduction

Fluidized bed combustors (FBC) are of continuously increasing interest, worldwide, as an attractive alternative to conventional, stoker-type boilers for the generation of electricity because of their attractive operation efficiencies and clean exhaust gases. The metal wastage of heat exchanger tubes in FBCs by erosion-corrosion (E-C) mechanisms has become a problem of significant importance. A recent review [1] of the experiences at several FBC operating units showed that, in some cases, the wastage was severe enough to limit tube lifetimes to only a few thousand hours, while in other, apparently similar units, little or no wastage occurred. Therefore, the need to determine what kinds of metal loss rates and mechanisms occur when tubing steels are eroded-corroded by the various types of particles in FBCs is an important aspect in the development of this type of power generation equipment.

The erosivity of fluidized bed combustor bed material particles is dependent upon a combination of the nature of the particles and the conditions under which they strike the surface of heat exchanger tubes. These tubes are located in the bed, along the water walls, or in the convection pass of the FBC. Each area in which tubes are located has a different local, service environment, i.e., temperature, gas composition and particle velocity, impact angle, or solids loading, that directly relates to the metal wastage that the tubes experience. An equally important factor that determines the metal loss that occurs is the character of the bed material particles themselves [2, 3, 4]. Their composition, shape, and size are major factors in establishing metal wastage rates of FBC heat exchanger tubing materials. The bed material particle characteristics are strongly influenced by the nature of the feedstock material, i.e., coal, woodchips, limestone, sand, and what becomes of them in the combustion process.

In this paper the erosivity of various bed material and feedstock particles will be established. They were determined in laboratory erosion-corrosion tests using particles of various compositions, shapes, and sizes that were obtained from several commercial FBCs. The effects of individual characteristics of the particles on their erosivity were obtained in a laboratory, standard elevated temperature erosion-corrosion test on 1018 plain carbon steel. It is hoped that the knowledge that is presented will be of value to FBC operators in their efforts to balance feedstocks to achieve as low a metal wastage condition on heat exchanger tubes as is possible.

Test Conditions

The tests were carried out in the elevated temperature blast nozzle type of tester described in [5]. Air was utilized as the carrier fluid for the particles, creating a generally oxidizing atmosphere. A standard set of test conditions was used to compare the erosivities of the various particles.

Contributed by the International Gas Turbine Institute and presented at the 35th International Gas Turbine and Aeroengine Congress and Exposition, Brussels, Belgium, June 11–14, 1990. Manuscript received by the International Gas Turbine Institute January 14, 1990. Paper No. 90-GT-249.

Standard Test Conditions	
Metal	= 1018 steel
T	= 450°C
V	= 20 m/s
α	= 30 deg
t	= 5 hr
Solid loading	= 375 g

These test conditions approximately simulated the E-C environment in the convection pass, superheater region of a circulating fluidized bed combustor. Particle velocity was determined using a computer program [6].

The tests used to determine the effects of various sand–limestone mixtures were carried out at a temperature of 450°C, an impingement angle of $\alpha = 30$ deg, a particle velocity of 20 m/s for sand–limestone mixture tests, and particle velocities of 10, 20, and 30 m/s for sand–calcined limestone mixtures. Two test times were used at two particle loadings, 5 h for 375 g (at $V = 20$, 30 m/s) and 8 hours for 600 g (at $V = 10$ m/s).

The particle loadings resulted in a steady-state metal loss condition [2]. The metal wastage of the specimens was determined by microscopic dimensional measurements of cross sections through the area of greatest metal loss to determine the thickness of the remaining sound metal.

Materials

The target material for all of the erosion-corrosion tests was 1018, plain carbon steel, which is commonly used in both bubbling fluidized bed combustors (BFBC) for in-bed evaporator tubes and circulating fluidized bed combustors (CFBC) for convection pass primary superheater tubes. Sixteen different erodent particles from ten FBCs as well as five different sand and limestone particles used in two of the FBCs were tested. Several of the as-received bed materials are shown in Fig. 1 and sand and limestone particles are shown in Fig. 2. The 16 different bed materials have been designated Nos. 1 through 16. Their sources (Units A through J), size and type (BFBC, CFBC, and PFBC) are listed in Table 1. The particles from the CFBFs were taken at a location in the convection pass below the superheater tube banks. It is not known where the particles from the BFBCs and PFBCs were taken, but it is assumed that they were taken from bed drains.

The particles have a wide range of particle sizes with those from the BFBCs having a much wider size range than those from the CFBCs, including particles considerably over 1 mm in diameter. To be able to compare the erosivity of different bed material particles, an average particle size of 250 μm was screened out and used as a standard test size. By screening the actual bed material to obtain one size of particle, an unknown degree of particle selection occurred as the characteristics of larger and smaller particles in a total bed material can differ somewhat. To account for this, the actual, as-received, particle sizes of the different bed materials were also used as erodent particles.

The sand–limestone and sand–calcined limestone mixtures were prepared in the laboratory from feedstock of CFBC Unit B. Limestone was calcined in a static air furnace at 950°C for 12 h. Figure 3 shows the appearance of the sand, limestone, and calcined limestone used in the mixtures. The white appearing particles are the result of charging in the scanning electron microscope (SEM) (a gold flash was used to minimize this). The EDX silver peak is from the adhesive used to bond the particles to the SEM pedestal. An average particle size of 250 μm was used in the mixture tests. The particles were generally quite angular in shape.

Results and Discussion

Erosion-Corrosion Rates. The metal wastage of specimens

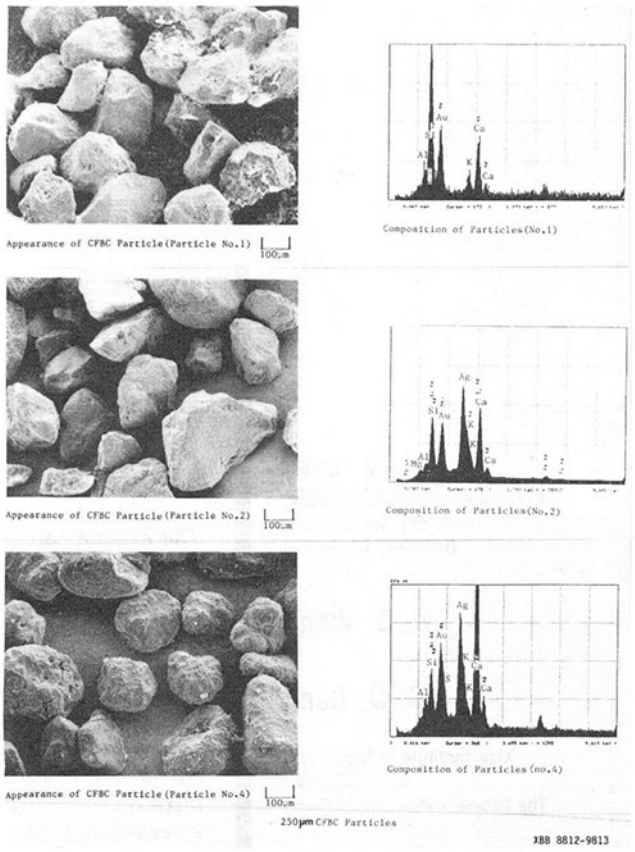

Fig. 1 As-received CFBC bed material particles

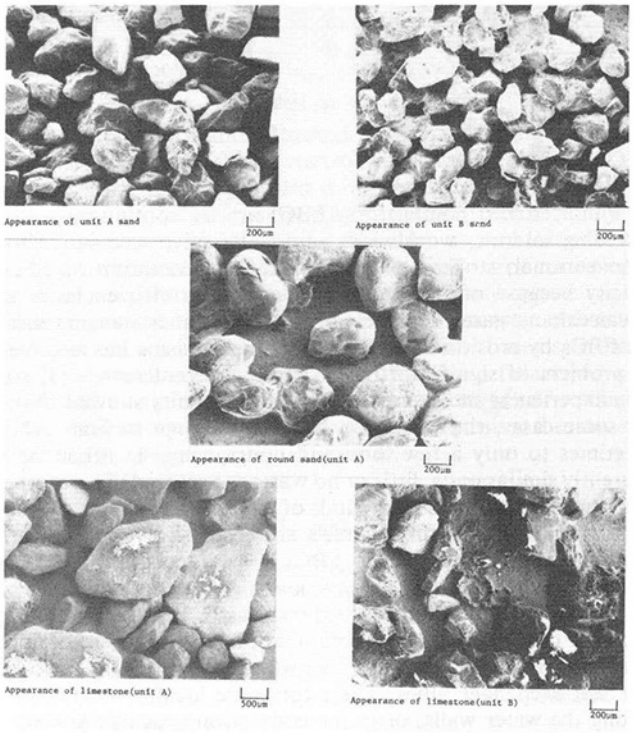

Fig. 2 As-received CFBC sand and limestone particles

E-C by the different erodent particles in order of erosivity ranking are listed in Table 2. The particles that caused the greatest metal loss in the 5-h tests had the most angular shape, the highest amount of SiO_2 and the lowest amount of CaO or $CaSO_4$. The effects of these characteristics will be discussed. When the as-received size particles were used as erodents, gen-

Table 1 Source, size, and type of bed materials and metal wastage

Erodent Particle No.	Type	Unit	Average Size μm dia	Thickness Loss* μm
1	CFBC	A	250	7.9
2	CFBC	A	250	6.6
3	CFBC	C	365	5.1
4	CFBC	B	300	5.8
5	BFBC (0.03% Cl)	D	250	3.2
6	BFBC (0.3% Cl)	D	250	2.3
7	BFBC	E	250	3.1
8	CFBC	A	250	4.0
9	CFBC	F	250	2.8
10	CFBC	G	250	3.9
11	BFBC	H	770	2.1
12	PFBC	I	670	6.7
13	BFBC	J	570	3.4
14	BFBC	J	720	5.8
15	BFBC	D	800	2.6
16	CFBC	A	370	4.7
Angular Sand		A	450	12.5
Round Sand		A	400	3.3
Angular Sand		B	230	5.5
Limestone		A	800	5.8
Limestone		B	300	4.5

*Test Conditions

Material = 1018 steel
T = 450°C
α = 30°
V = 20 m/s
t = 5 hrs. (375 g loading)
Air

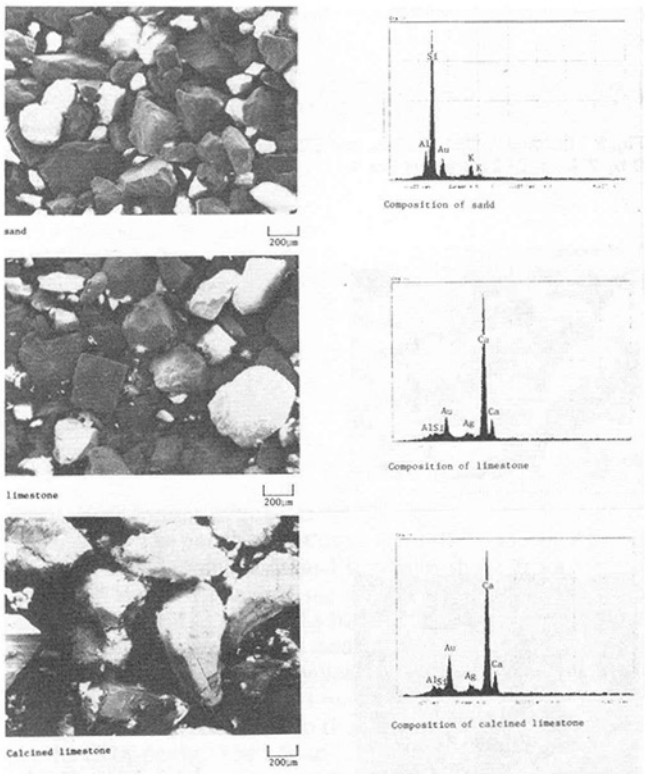

Fig. 3 Sand and limestone particles used to prepare mixtures

Table 2 Ranking of erosivity of bed material particles

Bed Material Particle No.	Unit	Type	Metal Loss, μm 250μm Particle Size	Metal Loss, μm Other Particle Size	Erosivity Ranking
1	A	CFBC	7.9		1
2	A	CFBC	6.6		2
4	B	CFBC	5.4		3
3	C	CFBC	4.8	5.1(1)	4
8	A	CFBC	4.0		5
16	A	CFBC	3.95	4.7(2)	6
10	G	CFBC	3.9		7
5	D	BFBC	3.2		8
7	E	BFBC	3.1		9
9	F	CFBC	2.8		10
12	I	PFBC	2.5	6.7(3)	11
6	D	BFBC	2.3		12
14	J	BFBC	2.3	5.8(4)	12
13	J	BFBC	1.9	3.4(5)	13
15	D	BFBC	---	2.6(6)	14
11	H	BFBC	1.9,	2.1(7)	15

Test Conditions:

Material = 1018 steel

T = 450°C
α = 30°
V = 20 m/s
t = 5 hrs. (375 g loading)
air
Particle size = 250μm
Other particle sizes:
(1) 365μm (4) 720μm
(2) 370μm (5) 570μm
(3) 670μm (6) 800μm
(7) 770μm

erally the larger size particles were more erosive than the smaller ones. However, this effect varied considerably, as can be seen in Table 2. The smaller size CFBC particles were generally more erosive than the larger size BFBC particles. The largest size particle, No. 15, at 800 μm dia, had a lower erosivity than several of the 250 μm-dia bed material particles because of its other characteristics. Where the same type of particle was tested at two different sizes, for example, particle Nos. 13 and 14, the larger size particle was more erosive, although other characteristics also contributed to the difference. On the other hand, an increase in particle No. 11's size from 250 μm to 770 μm caused almost no change in erosivity. Also, the same size particle from the same FBC, particle Nos. 1 and 2, had different erosivities because of their other characteristics. In Table 1, it can be seen that round sand was much less erosive than the angular sand at nearly the same particle size because of the difference in their shapes.

Table 2 shows that, with one exception, CFBC bed material particles had higher erosivity than BFBC or PFBC bed material particles. This difference was primarily due to the fact that the CFBC bed materials had a higher SiO_2 content as the result of purposeful sand additions to the combustor's charge. The BFBC and PFBCs only contained SiO_2 from the coal fuel. The reason for the one exception (CFBC particles No. 9) is related to particle shape and composition, as will be discussed later.

In Table 2 it can also be seen that among the different CFBC bed materials, particle Nos. 1 and 2 had the highest erosivity. Particle Nos. 8 and 16 had much lower erosivity than particle Nos. 1 and 2 even though they were all from the same unit A. BFBC bed material particles Nos. 13, 15, and 11 had the lowest erosivity of all of the particles tested.

Surface Layer Characteristics. *CFBC.* The microstructures of the surfaces of the E-C specimens correlated with their metal loss rates. As the layer on the target surfaces changed its character, i.e., thickness, composition, morphology, and continuity, the substrate metal wastage rate changed. Figure 4 shows the thin, intermittent layer that formed on the 1018 steel as the result of impacts by the most erosive particle, No. 1. From the EDX peak analyses, it can be seen that there was a low Ca content and a relatively high Si content in the mixed iron oxide–bed material scale segments.

When the bed material consisted of rounder particles with higher $CaSO_4$, CaO contents, Particle No. 4, the metal loss in the 5-h laboratory test decreased. The phases contained in the erodent particles are listed in Table 3. The highest content phase is listed first. Table 3 also lists the microhardnesses of the principal constituents of the bed materials, SiO_2 and CaO–$CaSO_4$–$CaCO_3$.

The surface and cross section of the scale layer on the 1018 steel impacted by particle No. 4 are shown in Fig. 5. The cross section was similar in thickness and morphology to that caused by particle No. 2. However, since the fuel contained sulfur and a greater amount of limestone was used in the charge, the principal constituent of the outer part of the scale layer was

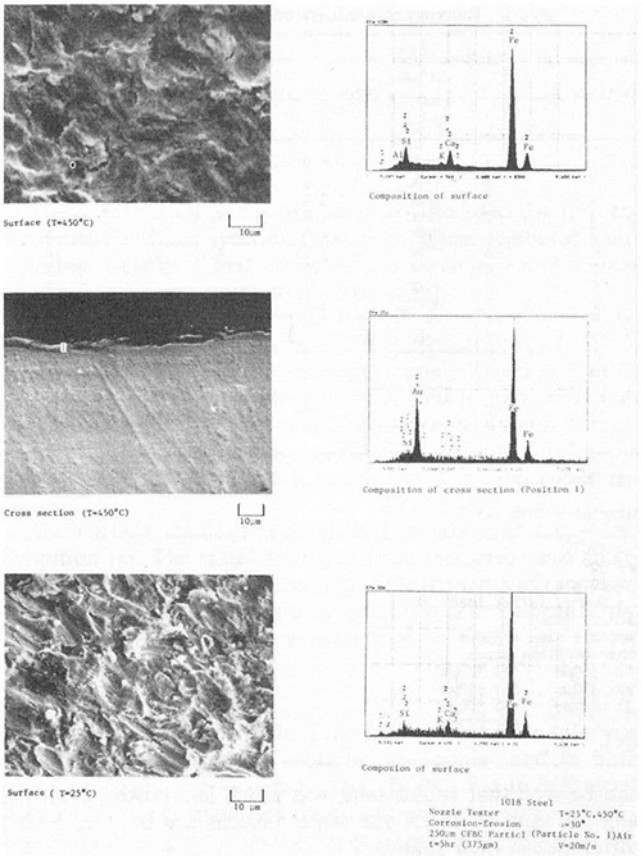

Fig. 4 Surface, cross section, and EDX peak analyses of 1018 steel E-C by 250-μm CFBC particle No. 1

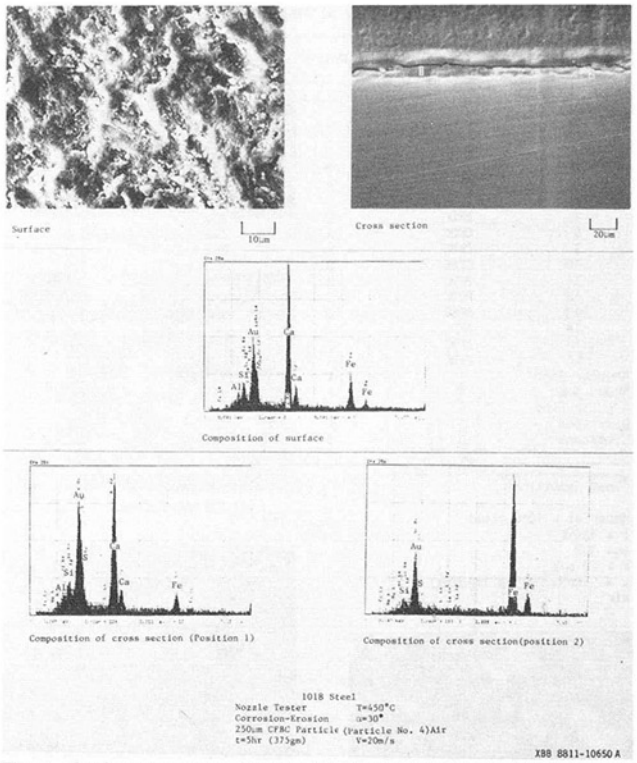

Fig. 5 Surface, cross section, and EDX peak analyses of 1018 steel E-C by 250 μm-CFBC particle No. 4

Table 3 Microhardness and phases of particles

Erodent Particle No. (Unit No.)	Microhardness (Hv 100) (From 10 determinations)		X-Ray diffraction Analyses, Phase (Larger quantities listed first)
	SiO_2	$CaO/CaSO_4$, $CaCO_3$	
No. 1 (Unit A)	1232	112	SiO_2, CaO
No. 2 (Unit A)	881	110	SiO_2, CaO
No. 3 (Unit C)	1074	59	SiO_2, CaO, $CaCO_3$
No. 4 (Unit B)	878	98	$CaSO_4$ (more), SiO_2, CaO, Al_2O_3, $CaCO_3$
No. 5 (Unit D)	470	99	$CaSO_4$, CaO, SiO_2, Al_2O_3
No. 7 (Unit E)	777	99	$CaSO_4$, CaO, SiO_2
No. 8 (Unit A)	1067	63, 331	CaC, $CaCO_3$, SiO_2
No. 9 (Unit F)	589	114, 208	$CaSO_4$, CaO, $CaCO_3$, SiO_2, MgO
No. 11 (Unit H)	----	138, 251	$CaSO_4$, CaC, $CaCO_3$, SiO_2
No. 15 (Unit D)	545	166, 236	$CaSO_4$, SiO_2, Al_2O_3, MgO
Sand (Unit A)	1329		SiO_2
Sand (Unit B)	981		SiO_2
Round Sand (Unit A)	1273		SiO_2
Limestone (Unit A)		288	$CaCO_3$
Limestone (Unit B)		192	$CaCO_3$

$CaSO_4$; see Table 3. The $CaSO_4$ and the CaO appear to have acted as a cement to bond the layer together and make it more protective. The rounder shapes of the particles were also responsible for the lower metal loss.

The least erosive bed material particles from a CFBC, particle No. 9, are shown in Fig. 6. Table 2 shows that they caused a metal loss that was 65 percent less than that caused by particle No. 1. The top micrograph shows that the particles were quite round, the particle characteristic that has the greatest effect on its erosivity [4]. The morphology of the layer was continuous

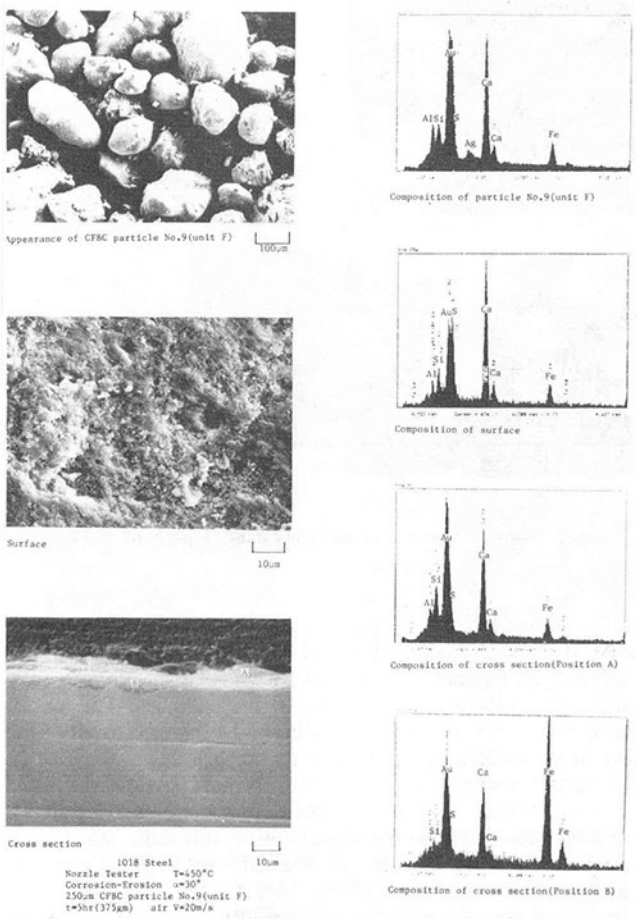

Fig. 6 Surface, cross section, and EDX peak analyses of 1018 steel E-C by 250-μm CFBC particle No. 9 and the appearance of the particles

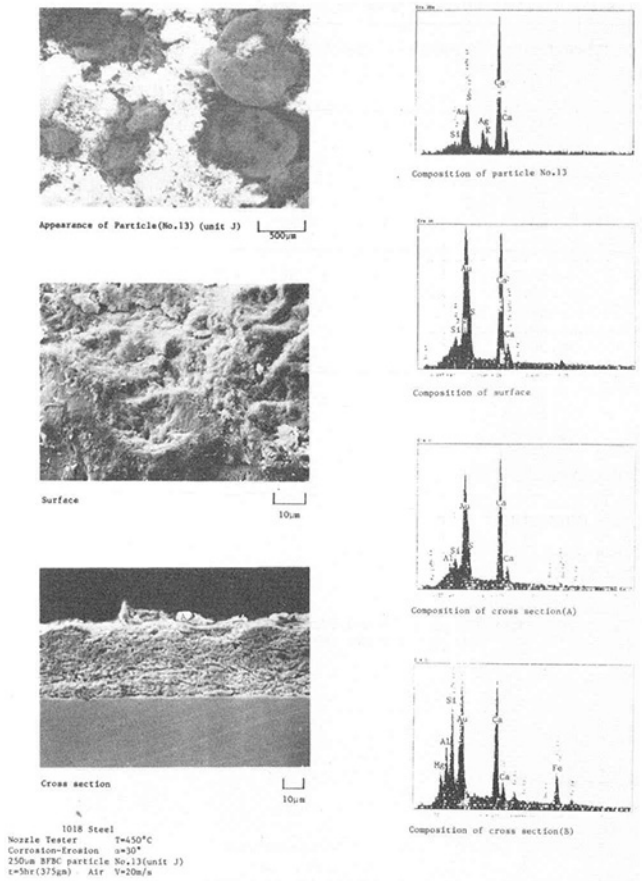

Fig. 7 Surface, cross section, and EDX peak analyses of 1018 steel E-C by 250-μm BFBC particle No. 13

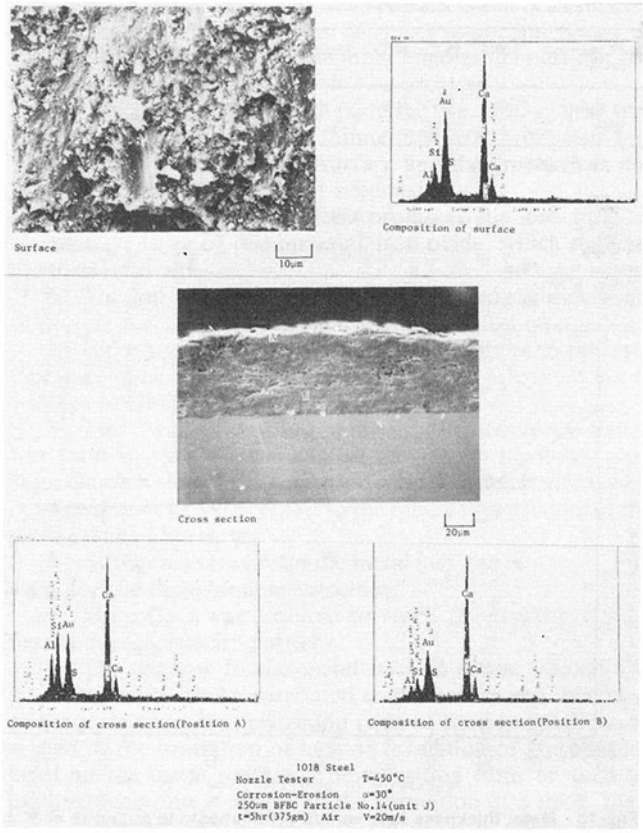

Fig. 8 Surface, cross section, and EDX peak analyses of 1018 steel E-C by 250-μm BFBC particle No. 14

and, therefore, protective and it had a high $CaSO_4$, CaO content throughout (Table 3). It contained more Ca near the scale–metal interface than the layers formed by other CFBC particles, as can be seen in the EDX peaks. All of these positive factors contributed to the low erosivity. The CFBC from which this particle came is known to have a benign environment and has experienced minimal tube metal wastage.

BFBC. The particles that came from BFBCs formed thicker surface layers in the standard test than those from CFBCs. Figure 7 shows the layer from BFBC particle No. 13, which was quite round in shape. As in all other tests, the scale layer developed early in the test and then maintained a constant thickness. The layer was typical of those formed by BFBC particles by having only bed material with essentially no iron oxide in it until quite near to the scale metal interface, as seen in the EDX peaks. The 1.9 μm metal loss listed in Table 2 was the lowest for any particle tested.

BFBC particle No. 14 caused the surface layer to form on the 1018 steel that is shown in Fig. 8 when the 250-μm size was used in the standard test. It is somewhat layered and contains only bed material down to very near the substrate metal. It is only when the interface area is viewed at a higher magnification in Fig. 9 that the presence of the iron oxide layer can be discerned. A thin, continuous, iron oxide scale with a small amount of calcium in it occurred near the scale–metal interface.

Sand–Limestone Mixtures. The relationship between the erosive SiO_2 and the softer calcium compounds that became a part of the scale layer on E-C steel surfaces was investigated by making a series of mechanical mixtures of silica and limestone as well as silica and calcined limestone in the laboratory, ranging from 100 percent SiO_2 to 100 percent calcium compound, and determining the erosivity of the resulting mixtures.

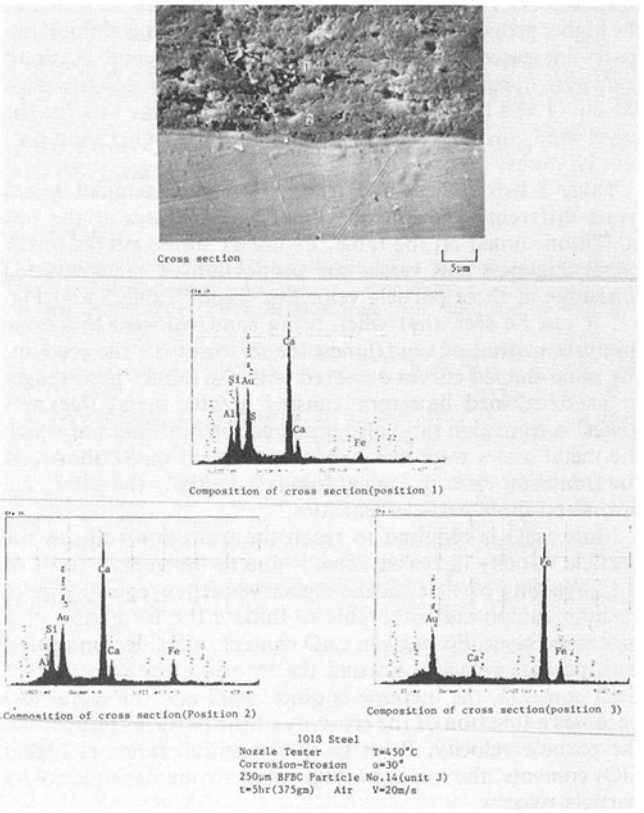

Fig. 9 Interface area of 1018 steel E-C by particle No. 14

Table 4 lists the metal thickness losses of samples tested using the different sand–limestone mixtures. Figure 10 shows the curve of the metal thickness loss versus the proportions of sand

Table 4 Metal thickness loss for sand/limestone mixtures

Sand/Limestone (wt %)	100/0	95/5	90/10	80/20	70/30	50/50	30/70	10/90	0/100
Metal Loss (μm)	6.0	5.7	5.2	4.7	4.4	4.3	4.2	4.2	4.1

TEST CONDITIONS:

1018 steel
T = 450°C
V = 20 m/s
α = 30°
t = 5 hrs
Particle size: 250μm
Loading: 375gm

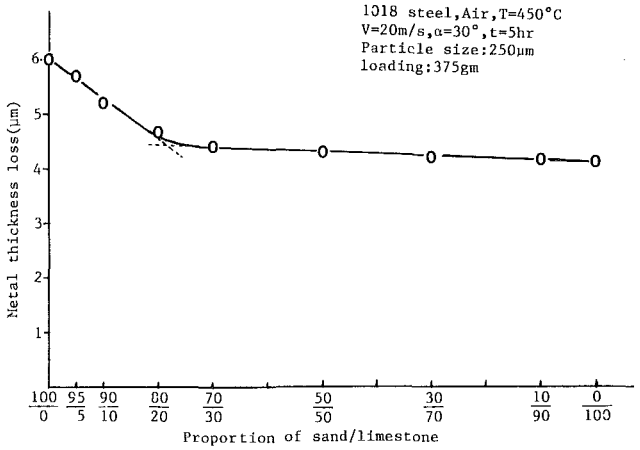

Fig. 10 Metal thickness loss versus sand/limestone mixtures at V = 10, 20, 30 m/s

to limestone. From Table 4 and Fig. 10 it can be seen that at the higher proportions of sand to limestone, the metal thickness losses increased with increasing amounts of sand. A sharp transition occurred at the 80/20 ratio, on either side of which the curve was linear. The slope of the curve was low for the lower sand content mixtures compared to the higher sand content mixtures.

Table 5 lists the metal thickness losses of samples tested using different sand-calcined limestone mixtures at the test conditions noted on the table. Figure 11 shows curves of the metal thickness loss versus the proportion of sand/calcined limestone at three particle velocities. From Table 5 and Fig. 11, it can be seen that when using sand/calcined limestone mixtures instead of sand/limestone mixtures for the erodent, the same shaped curves occurred with the higher percentages of sand/calcined limestone causing greater metal thickness losses. A transition ratio also occurred, on both sides of which the metal losses were linear. Moreover, as Fig. 11 shows, at the transition ratio the metal loss is essentially the same, 2.3 μm, at all three particle velocities.

More CaO is required to reach the transition ratio as the particle velocity increases. This is due to the greater force of the impacting particles at the higher velocities requiring more calcium compound to be able to initiate the formation of a protective layer. For a given CaO content, metal loss increased with particle velocity. Beyond the transition ratio, at higher CaO contents, the increase is quite small and the metal loss becomes a function of the erosivity of the particles rather than the particle velocity. Prior to the transition ratio, at higher SiO_2 contents, the metal wastage has a strong dependency on particle velocity.

The difference in the effect of particle velocity on metal wastage strongly relates to the formation of the protective layer. At the higher, angular shaped SiO_2 contents, the metal itself is participating in a high metal wastage, elevated temperature erosion process [7]. When the CaO content exceeds

Table 5 Metal thickness loss for sand/calcined limestone mixtures

Sand/Calcined Limestone Proportion (wt. %)	Particle Velocity (m/s)	Thickness Loss (μm)
0/100	20	1.0
30/70	20	1.5
50/50	20	1.9
70/30	20	2.6
80/20	20	3.4
90/10	20	5.0
100/0	20	6.0
50/50	10	1.7
70/30	10	2.2
80/20	10	2.5
90/10	10	3.6
100/0	10	3.9
30/70	30	1.7
50/50	30	2.0
60/40	30	2.3
70/30	30	4.0
100/0	30	8.5

TEST CONDITIONS:

1018 steel
T = 450°C
α = 30°
Particle Size:250μm
Particle Loading 375 gm t = 5 hrs (for 20, 30 m/s)
600 gm t = 8 hrs (for 10 m/s)

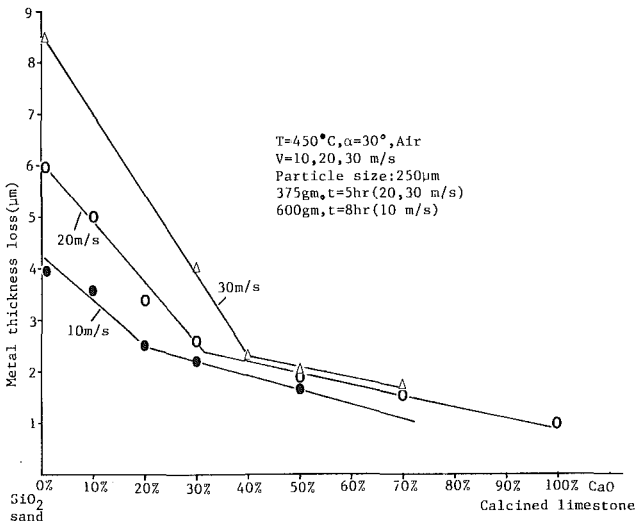

Fig. 11 Metal thickness loss versus sand-calcined limestone mixtures at V = 10, 20, 30 m/s

that of the transition ratio, a protective layer forms that prevents direct participation by the base metal in the metal loss process. The protective layer is being eroded and the metal wastage rate decreases. The loss of the layer is a function of the erosivity of the erodent, which slowly decreases with increasing CaO content. Comparing Table 4 with Table 5, it can be seen that the calcined limestone particles have a much lower erosivity than the limestone particles. At a CaO particle velocity of 20 m/s the metal thickness loss was only 1 μm, which is one quarter of that caused by limestone, 4.1 μm.

Figure 12 shows the cross section of specimens E-C by different sand–limestone mixtures, along with their EDX analyses. It can be seen that when the 95/5 sand–limestone ratio mixture was used, no protective layer containing calcium formed on the surface. The metal was directly deformed and eroded by the impacting particles. Some evidence of metal platelet formation can be seen.

At the transition ratio of 80/20, a protective layer that contained some calcium had formed on the metal. The calcium compound appears to act as a form of binding cement that

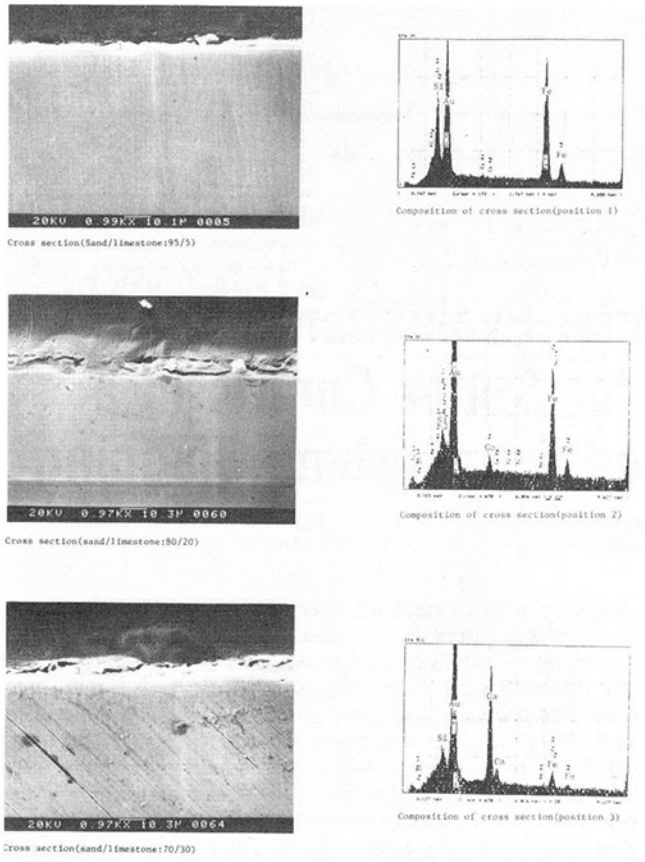

Fig. 12 Cross sections of 1018 steel surfaces eroded by $SiO_2/CaCO_3$ erodent mixtures

permits an adherent, protective layer of mixed calcium compound–iron oxide to form. Beyond the transition ratio of 80/20 a protective layer with a high calcium content formed (bottom micrograph), which resulted in lower metal wastage. Combining Fig. 12 with Fig. 10, it can be seen that the transition ratio is related to the formation or lack of formation of a protective layer on the metal surface. Once there was enough calcium in the erodent to form a protective layer, further increases in the amount of limestone had only a minor effect on the amount of metal loss. The small but continued decrease in the metal loss in this region of the curve resulted from the decreasing amount of sand that was in the erodent mixtures.

Conclusions

1 The basic mechanism of E-C metal wastage was the formation of a multilayer deposit/scale of bed material and iron oxide, the erosion of the brittle outer surface by a cracking and chipping mechanism, and the continual replacement of the layers by oxidation of the base metal and deposition of bed material to maintain a constant thickness of deposit/scale.

2 The CFBC bed material particles caused more metal wastage than BFBC bed material did at the same test conditions.

3 When the particles were strong enough not to shatter upon impact, their shape was the most important factor in determining their erosivity: the more angular the particle, the greater its erosivity.

4 The more strong/hard material, i.e., SiO_2, that was present in a bed material, the thinner and less continuous was the scale that formed on the surface and the greater was the amount of metal wastage that occurred.

5 The Ca compound content promoted the formation of a protective layer of bed material–iron oxide, which reduced the metal wastage.

6 The bed materials' particle size affected their erosivity to varying degrees, but did not have a major effect on erosivity.

7 Increasing the ratio of sand to limestone or to calcined limestone in an erodent mixture caused an increase in the metal wastage in elevated temperature tests at $V = 10$–30 m/s.

8 There was a transition in the sand/Ca compound mixture ratio where a marked change occurred in the metal wastage. On each side of the transition ratio, the metal loss varied in a linear manner with respect to the ratio of sand to limestone or to calcined limestone.

9 At the transition ratio the metal loss was essentially the same for the three erodent velocities.

10 More CaO was required to reach the transition ratio for the higher velocity particles.

11 The changes in the metal loss on either side of the transition ratio can be correlated to the nature and thickness of the scale layer. The transition ratio of sand to limestone is related to the formation or lack of formation of a protective layer on the metal surface. The transition ratio of sand to calcined limestone is related to the formation of a thick, protective layer or a thin, less protective layer on the metal surface.

12 In the scale layer, calcium compounds are mechanically mixed with iron oxide.

Acknowledgments

Research sponsored by the Department of Energy under DOE/FEAA 10 10 0, Advanced Research and Technical Development, Fossil Energy Materials Program Work Breakdown Structure Element LBL-3, under Contract No. DE-ACO3SF00098.

References

1 Stringer, J., Stallings, J. F., and Wheelden, J. M., "Wastage in Bubbling Fluidized-Bed Combustors: An Up-date," *Proceedings of ASME 1989 International Conference on Fluidized Bed Combustion*, San Francisco, CA, May 1889, pp. 857–862.

2 Levy, A. V., Wang, B. Q., Geng, G. Q., and Mack, W., "Erosivity of Particles in Circulating Fluidized Bed Combustors," NACE Corrosion 89, Paper No. 543, 1989.

3 Kalmanovithe, D. P., Hajicek, D. R., and Mann, D., M., "Corrosion and Erosion in a Fluidized Bed Combustor: Effect of Bed Chemistry," NACE Corrosion 89, Paper No. 547, 1989.

4 Wang, B. Q., Geng, G. Q., and Levy, A. V., "Surface Behavior of Heat Exchanger Tubes in Fluidized Bed Combustors," *Proceedings of ICMC*, San Diego, CA, 1999.

5 Levy, A. V., Yan, J., and Patterson, J., "Elevated Temperature Erosion of Steels," *WEAR 108*, No. 1, 1986, pp. 43–60.

6 Kleist, D. M., "One Dimensional Two Phase Particulate Flow," M.S. Thesis, Report LBL 6967, Lawrence Berkeley Laboratory, University of California, Berkeley, CA, 1977.

7 Levy, A. V., and Man, Y. F., "Effect of Test Variables on the Erosion-Corrosion of Chromium Steel," NACE Corrosion 87, Paper No. 17, San Francisco, CA, Mar. 1987.

Experimental Evaluation of Sorbents for Sulfur Control in a Coal-Fueled Gas Turbine Slagging Combustor

L. H. Cowell

C. S. Wen

R. T. LeCren

Solar Turbines Incorporated,
San Diego, CA 92138

A slagging combustor has been used to evaluate three calcium-based sorbents for sulfur capture efficiency in order to assess their applicability for use in a coal-fueled gas turbine. Testing is completed in a bench-scale combustor with one-tenth the heat input needed for the full-scale gas turbine. The bench-scale rig is a two-stage combustor featuring a fuel-rich primary zone and a fuel-lean secondary zone. The combustor is operated at 6.5 bars with inlet air preheated to 600 K. Gas temperatures of 1840 K are generated in the primary zone and 1280 K in the secondary zone. Sorbents are either fed into the secondary zone or mixed with the coal–water mixture and fed into the primary zone. Dry powdered sorbents are fed into the secondary zone by an auger into one of six secondary air inlet ports. The three sorbents tested in the secondary zone include dolomite, pressure-hydrated dolomitic lime, and hydrated lime. Sorbents have been tested while burning coal–water mixtures with coal sulfur loadings of 0.56 to 3.13 weight percent sulfur. Sorbents are injected into the secondary zone at varying flow rates such that the calcium/sulfur ratio varies from 0.5 to 10.0. Hydrated lime exhibits the highest sulfur dioxide reductions in the exhaust of 90 percent. Pressure-hydrated dolomitic lime and dolomite reduce SO_2 concentrations by 82 and 55 percent, respectively. Coal sulfur loading is found to have a small influence on sorbent sulfur capture efficiency. Pressure-hydrated dolomitic lime ground with the coal during coal–water mixture preparation and injected into the primary zone is found to lower the sulfur dioxide concentration by an insignificant amount.

Introduction

Solar Turbines Incorporated is currently sponsored by DOE Morgantown Energy Technology Center to develop a coal-fueled version of its 3.8 MW Centaur Type H gas turbine for industrial cogeneration applications. This six-year program will culminate in a 100-hour run of a coal-fueled gas turbine engine. The need to use indigenous fuels for energy generation and cogeneration has been recognized by both government and industry. Mixtures of pulverized coal and water (CWM) have the potential of being burned directly in gas turbines using injection and fuel-handling methods similar to those used for heavy petroleum fuels.

In order for the coal-fueled turbine to be environmentally viable, a successful approach for sulfur control must be demonstrated. Sulfur emissions must be controlled for two reasons: First, sulfur is an ambient pollutant, and second, sulfur combines with alkalis that can act corrosively on the turbine hot-end. A study has been completed to examine different options for sulfur control. This paper is a discussion of an experimental evaluation of one control technique that has high potential to resolve the sulfur emissions issue satisfactorily for the coal-fueled turbine.

Contributed by the International Gas Turbine Institute and presented at the 35th International Gas Turbine and Aeroengine Congress and Exposition, Brussels, Belgium, June 11–14, 1990. Manuscript received by the International Gas Turbine Institute January 6, 1990. Paper No. 90-GT-7.

Coal-Fueled Turbine Description

The coal-fueled gas turbine consists of an existing compressor and turbine package fitted with a coal-fueled combustor island. A block diagram of the gas turbine package is included in Fig. 1 and the combustor island is illustrated in Fig. 2. The system has been described in detail by Cowell et al. (1989), Cowell and LeCren (1989), Roberts et al. (1988), and LeCren and White (1987).

As an overview, the combustion island system consists of a Two-Stage Slagging Combustor (TSSC), a Particulate Rejection Impact Separator (PRIS), and a Secondary Filter. The TSSC is a rich-lean staged combustor designed for NO_x control. Air and fuel are introduced in the primary zone and additional air is added in the secondary zone. The primary zone is operated fuel rich (equivalence ratio of 1.3) at a temperature of 1840 K and the secondary zone operates fuel lean (equivalence ratio of 0.4) at an outlet temperature of 1280 K. All components in the combustion island are refractory lined. Coal ash is removed

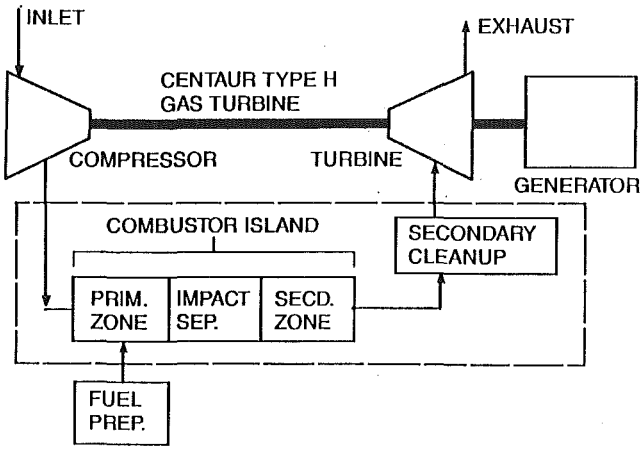

Fig. 1 Coal-fueled gas turbine

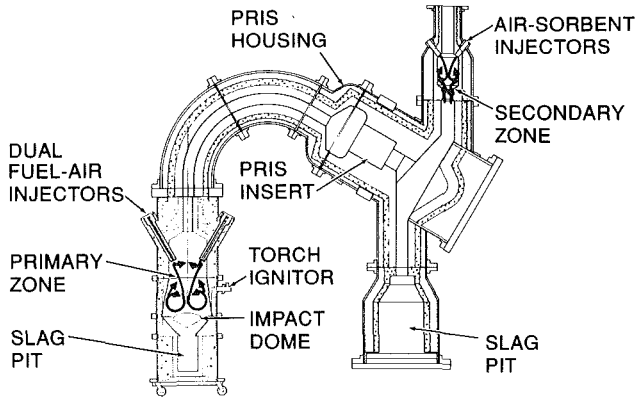

Fig. 2 TSSC description

in the slagging primary zone and in the PRIS, which is situated in the rich zone between the primary and secondary combustion zones. In both ash removal locations, inertial separation is used to remove 90 to 95 percent of the ash. The secondary filter is a high-temperature barrier filter designed to remove the remaining ash and sulfur sorbents.

Fate of Sulfur in the Slagging Combustor

Upon injecting a CWM into the primary combustion zone, the slurry is atomized and undergoes a rapid devolatization followed by a burnout of the char. Figure 3 illustrates a simplified scheme involved in the combustion of a coal particle. The volatile organic and inorganic sulfur species are vaporized from the burning coal particles and are transported to the surface by molecular diffusion. The reducing atmosphere surrounding a burning particle allows the reduction to take place on volatile species, but as soon as the vapors diffuse away from the burning particle, the oxidizing nature of the bulk gas stream would oxidize sulfur species to their highest oxidation state. The rate of sulfur release from coal is very fast from both sulfur bound in the organic matrix and sulfur in discrete minerals even under the local reducing condition.

Under primary zone reducing conditions, pyritic sulfur decomposes to sulfur (S_2), hydrogen sulfide (H_2S), and carbonyl sulfide (COS) (Malte, 1983; Robinson, 1978). The rich zone devolatization of organic sulfur is not well understood; however, it is believed that H_2S is the principal product, accounting for 90 percent of the evolved sulfur, with contributions of COS, CS_2, and S_2. In a slagging combustor the formation of sulfur species can also be significantly influenced by the sulfur slag interactions, such as the creation of iron sulfite intermediaries. These species will turn to higher oxidized states,

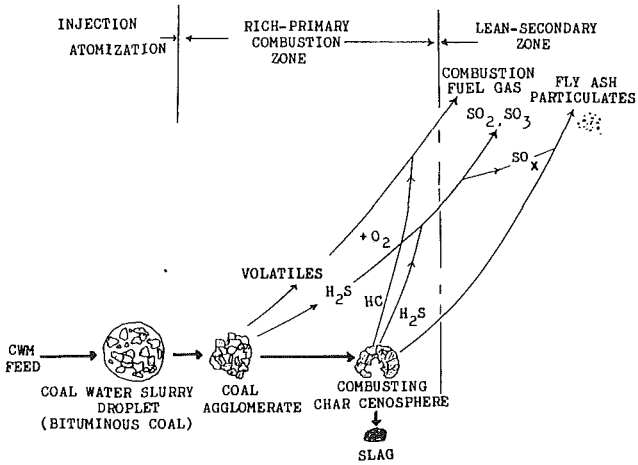

Fig. 3 CWM burnout and sulfur routes in combustion

SO_x, as they are exposed to the primary air stream. In the slagging combustor as these species enter the fuel lean secondary zone, over 90 percent of the sulfur is converted to SO_2 while the remaining several percent exist as SO_3; see Garman et al. (1984).

Sulfur Control Strategy

While no emissions regulations exist for coal-fueled gas turbines, SO_2 emission limits will be based on existing regulations for coal-burning boilers and gas turbines burning conventional fuels. For coal-burning boilers NSPS regulations limit SO_2 emissions to 1.2 lb SO_2/MMBtu, which converts to 150 ppmv @ 15 percent O_2. Proposed NSPS sulfur regulations for small industrial units are imposing an additional requirement of 90 percent sulfur reduction and the 1.2 lb/MMBtu limit (see "Steam Generating Units"). Stricter regional standards such as imposed in Southern California by the SCAQMD limit emissions to 0.54 lb SO_2/MMBtu (75 ppmv @ 15 percent O_2). The design control goal selected for the coal-fueled Centaur is the more strict regional regulation of 75 ppmv @ 15 percent O_2.

A conservative design approach has been used to select the sulfur control strategy used in this developmental work. A detailed study of the literature has provided a list of design approaches that can be broadly categorized into in-situ sulfur removal and exhaust scrubbing. The latter approach is an existing technology commercially available. The cost of exhaust scrubbing, however, would have a serious impact on the marketability of the coal-fueled turbine. An in-situ design was selected because of lower cost.

In-situ sulfur removal has received a great deal of attention in recent years. A recent review of this work can be found from Newby (1989). In-situ sulfur capture techniques include: coal physical cleaning, synthesized coal-sorbent particles, sorbent contacting the combustion gases, and advance methods (e.g., electrochemical or membranes). The latter was not considered because the technologies are not proven. The three remaining sulfur control strategies are all considered viable. Coal cleaning is used to bring sulfur levels down as low as possible within critical cost constraints. Coal cleaning by itself will not meet anticipated sulfur control levels for the coal-fueled turbine. The remaining techniques are both evaluated in this study.

Techniques in which sorbent contacts the combustion gases include entrained sorbent, fluidized beds, and fixed beds. Both fluidized and fixed sorbent beds would impose the addition of another vessel and the associated cost to the system, whereas entrained sorbents could be introduced at any location upstream of the secondary filter. The sorbents entrained in the

gas stream are removed from the exhaust flow by the secondary filter.

The location of sorbent injection is a test variable. The location of sorbent injection is dependent to a large extent on the type of sorbent selected. Based on a thermodynamic equilibrium study, assuming the use of calcia-based sorbents, the most suitable location for sorbent injection would be the secondary combustion zone. Another location that has great benefits in terms of reduced material handling costs is to grind the sorbent with the coal during the preparation of the coal slurry and inject this coal–sorbent slurry into the primary zone. While the thermodynamics suggest that the temperature in the primary zone is too high for high sulfur capture, the potential advantages warrant experimental investigation of this option.

In order to maximize the potential for successful sulfur removal, the type of sorbent was quickly narrowed to include only calcia-based materials. Efforts continue to be made to evaluate other potential sorbents, but thus far these sorbents' cost and novelty preclude their use in this program. Based on previous studies, the sorbents selected for evaluation include dolomite, pressure-hydrated dolomitic lime, and hydrated lime.

The strategy selected for sulfur control in the coal-fueled turbine consists of a dry powdered calcia-based sorbent injected into the slagging combustor upstream of the secondary filter. The sorbent is entrained by the gas flow where sulfur–calcia reactions occur. The spent sorbent is removed from the gas stream at the secondary filter by the barrier filter. The test program has been devised to evaluate three sorbents injected at two possible sites. Sorbents are evaluated based on sulfur removal effectiveness and cost.

Test Description

Sulfur removal evaluations are made in a bench scale slagging combustor consisting of only the primary and secondary combustion zones. On top of the secondary zone is attached an extension piece to lengthen the residence time for sorbent–sulfur reactions. Bulk residence times in the primary zone are approximately 150 ms. The secondary combustion zone provides 50 ms residence time with an additional 150 ms available in the residence time test section. The test rig is illustrated in Fig. 4.

Locations for sorbent injection, indicated in Fig. 4, include the secondary zone through one of the six secondary air inlet ports and into the primary zone as a sorbent–coal slurry. Injecting sorbents into the primary zone is accomplished using the standard fuel feed system. Sorbents are fed into the secondary zone via a 5-cm auger system illustrated in Fig. 5. The auger feeds sorbent into the air supply line going to one of the secondary air inlet ports. The sorbent is entrained with the secondary air flow. The auger can convey dry powdered sorbents at continuous flow rates varying from 4.5 to 54.5 kg/h. The sorbent flow rate is linearly related to auger speed. The sorbent flow rate is measured by tank weight difference over time and checked by a predetermined auger speed versus flow rate relation. Typically, these two flow rate determinations agree within 2 percent of each other.

Sulfur being discharged from the bench scale combustor is assumed to be exclusively in the form of SO_2. A water-cooled gaseous sampling probe is located at the exhaust of the residence time test section. The gaseous sample is connected to a Western Research UV SO_2 meter for continuous monitoring. The sample is also analyzed for O_2, CO_2, CO, and NO_x using conventional instrumentation. A particulate sampling probe is also located at the exit of the residence time test section and is used to collect batch particulate samples, which are analyzed primarily for carbon and ash content to determine coal utilization. The combustor is instrumented extensively with thermocouples and pressure taps to monitor combustor performance.

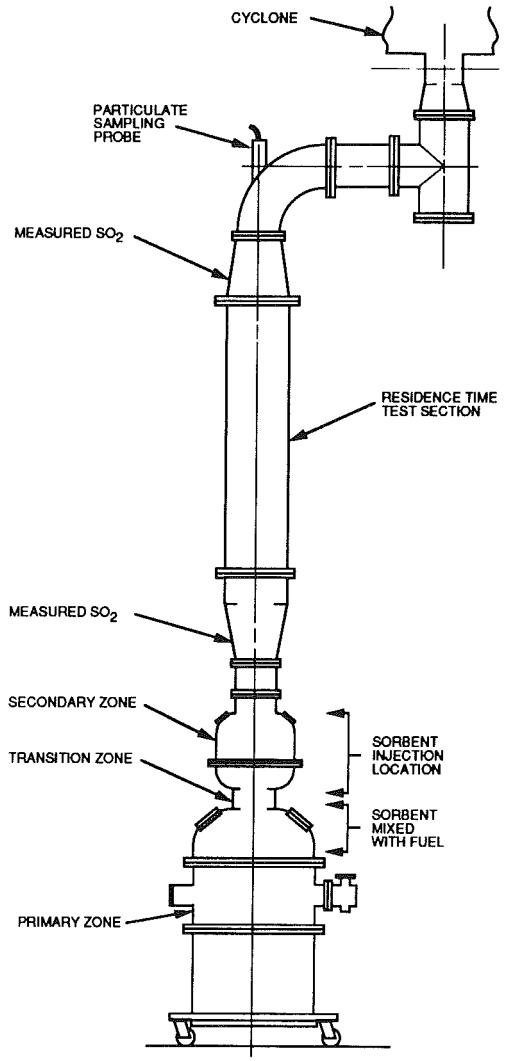

Fig. 4 Bench-scale two-stage slagging combustor for sorbent evaluation

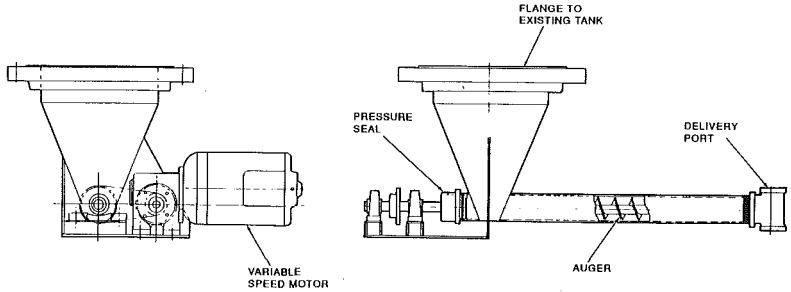

Fig. 5 Sorbent screw feeder

Table 1 Chemical and physical analyses of calcium-based sorbents used in recent tests

	Dolomite	PHDL	HL
Supplier	National Minerals	ChemStar	ChemStar
Brand Name	Dolomite #100	Type S Hydrated Lime	High Calcium Hydrated Lime
Bulk			
Density (lbs/ft^3)	60	25	86
Specific Gravity	2.86	2.24	2.23
Cost ($/ton)	20.00	119.00	119.00
Chemical Analysis			
Acid Insoluble	--	0.40	1.5
Fe_2O_3	0.12	0.10	0.10
SiO_2	0.47	--	--
Al_2O_3	0.08	0.50	0.50
$MgCO_3$	42.57	--	--
$CaCO_3$	57.20	1.50	1.50
CaO	--	--	Trace
MgO	--	0.60	1.00
$Mg(OH)_2$	--	40.00	--
$Ca(OH)_2$	--	55.00	95.00
H_2O	0.1	0.4	0.50
ASTM Lime % Available	--	--	
Sieve Analysis (% Less) (microns)			
297	99.3	99.0	100
149	90.0	96.0	100
105	76.0	90.1	99
74	57.0	86.0	97
44	40	79.0	88
30	35.0	--	--
20	27.0	--	--
10	15.0	--	--
5	9.0	--	--
2	3.0	--	--
1	7.0	--	--
Surface Area (M^2/gm)	--	20-30	20-30

The procedure for evaluating sorbents injected into the secondary zone is as follows. The combustor is heated on diesel fuel for 2 to 3 hours before switching to CWM. After switching to CWM the diesel flow is stopped and the rig is operated at the desired test setting for 45 to 60 minutes. Pollutant concentrations, including SO_2, are recorded prior to sorbent injection. At this time the auger is turned on and set to the desired flow rate so that sorbent is introduced to the secondary combustor. The sorbent tank weight and the SO_2 concentration are recorded every 30 seconds over a ten-minute injection period. The sorbent flow rate is a weight average over the entire injection period. The sorbent flow rate is stopped for about ten minutes so that the SO_2 concentrations rebound to approximately the initial value. The sorbent flow rate is set to a new value and the cycle is repeated.

Results

A series of sorbent evaluation tests have been completed in the bench scale combustor studying sorbent type, coal sulfur loading, and sorbent injection location.

Sorbent Type. Three sorbents have been evaluated in the bench scale combustors, including dolomite, pressure-hydrated dolomitic lime (PHDL), and hydrated lime (HL). The properties of these three sorbents are summarized in Table 1. The sorbents are all commercially available in the Western United States. Sorbents like coal may differ in type, and often similar types from various mines and seams can vary substantially. The goal of this study was to ascertain as well as possible the gross difference in sorbent sulfur removal effectiveness for three readily available types of calcium sorbent. Another independent variable between the three sorbents tested is the particle size. The three test sorbents were selected based on a literature survey and consultations with experts in this area. Dolomite was selected as the cheapest alternative that may meet the sulfur control levels. Pressure-hydrated dolomitic lime and hydrated lime should have a substantially higher effectiveness than dolomite but at a significant cost penalty.

The three test sorbents were fed into the secondary combustion zone while burning the coal-water mixture (CWM) described in Table 2. This CWM has a medium sulfur content (1.4 wt% in the coal). The combustor was operated under similar conditions for each day of testing. Only one type of sorbent is tested during each test period. Combustor operating parameters and results for tests evaluating the three types of sorbents are shown in Table 3. The inlet temperature and pressure are typical operating points for the bench-scale rig. The equivalence ratio in the primary zone is averaged over the test, as is the outlet temperature, which is measured at the downstream end of the residence time test section. Design point equivalence ratio is 1.3 and outlet temperature is 1280 K. The emissions shown in Table 3 are also averaged over the entire run. The data shown are typical results for the combustor with NO_x generally below 125 ppmv @ 15 percent O_2, showing a strong relation to primary zone equivalence ratio. Carbon monoxide emissions are less than 50 ppmv and carbon conversion is typically greater than 98 percent. In general, the combustor operating parameters were not influenced by sorbent addition with the obvious exception of SO_2 emissions.

The sulfur capture data are summarized in the bottom half

Table 2 Coal-water slurry fuel characteristics

Coal Content of Fuel (wt%)	54.6
Ash Content of Fuel (wt%)	2.2
Coal particle Top Size (micron)	45
Gross Heating Value of Fuel (Btu/lb)	8024
Viscosity of Fuel @ 100 sec^{-1}	300
Coal particle Mean Size (micron)	8.0
Dispersant (wt%)	1.4
Proximate Analysis of Coal (wt%)	
Ash	3.93
Volatiles	38.01
Fixed Carbon	58.06
Ultimate Analysis of Coal (wt%)	
Carbon	82.23
Oxygen (by difference)	8.85
Hydrogen	5.63
Nitrogen	1.80
Sulfur	1.44

Table 3 Slagging combustor performance with three sorbents injected into secondary zone

	Dolomite	Pressure Hydrated Dolomitic Lime	Hydrated Lime
Test Conditions			
Coal Sulfur (wt%)	0.56 - 1.4	1.4	1.4
Inlet Air			
Temperature (K)	597	604	609
Pressure (bars)	6.1	6.1	6.0
Primary Zone Equivalence Ratio	1.19	1.27	1.42
Outlet Temperature (K)	1217	1221	1247
Results			
Emissions @ 15% O_2 (ppmv)			
NO_x	117	92	79
CO	9	7	16
Carbon Conversion (%)	99.8	98.9	97.6
Sorbent Injection Range (kg/hr)	11-66	3-21	6-16
(Ca/S)	0.94-5.7	0.55-4.1	1.15-2.91
SO_2 Reductions (%) @ Ca/S of 3	55	82	90
Ca/S @ SO_2 of 75 ppmv	3.4	2.4	1.5

of Table 3 and included in greater detail in Figs. 6–11. Included in the table are the sorbent injection rate, the SO_2 reduction at a normalized sorbent input, and the required sorbent input to meet 75 ppmv SO_2 emissions. The SO_2 reduction is calculated using only measured values of SO_2 concentration, and is simply the SO_2 without sorbent injection minus the SO_2 with sorbent injection, that quantity divided by the SO_2 without sorbent injection. From Table 3 the most effective sorbent is hydrated lime, followed by pressure-hydrated dolomitic lime and dolomite, respectively. This information is summarized in Figs. 6–10.

In Fig. 6 the SO_2 reduction is plotted against the Ca/S molar ratio for dolomite injection into the secondary zone. The same data are plotted in Fig. 7 but in the form of SO_2 concentration versus Ca/S ratio. Both these figures contain data from a series of different tests in which different CWMs were used. All the CWMs had properties similar to those listed in Table 3, with the exception of coal sulfur loading as indicated in the figures. The curves in Fig. 7 reflect the difference in coal sulfur, as is evident at the points taken without sorbent injection (Ca/S equals 0) where the SO_2 concentrations measured in the exhaust increase proportionally with coal sulfur loading. In order to compare the three sorbents, a practical sorbent input as reflected by Ca/S ratio has been set at 3. Referring to the curve in Fig. 6, the corresponding SO_2 reduction is 55 percent at a Ca/S ratio of 3. Referring to Fig. 7, in order to meet a SO_2 emission limit of 75 ppmv, the required Ca/S input varies with coal sulfur loading over the range of 2.6 to 3.4.

Data taken injecting the other two sorbents are shown in Figs. 8, 9, and 10. In Figs. 8 and 9 SO_2 reductions versus Ca/S ratio are shown for pressure-hydrated dolomitic lime and hydrated lime, respectively. The curve labeled as dolomite is taken from Fig. 6, which is generated from a range of CWMs with varying coal sulfur loadings. The curves for both PHDL and HL are from data taken in the tests reported in Table 3 in which one slurry was used with a coal sulfur loading of 1.4 wt%. As suggested in Table 3, a lower Ca/S ratio is required to meet the same SO_2 reduction as the sorbent type is switched from dolomite to PHDL to HL. The SO_2 reduction at a Ca/S ratio of 3, as taken through a polynomial regression from the curves shown in Figs. 8 and 9, is 82 percent for PHDL and 90 percent for HL. Figure 10 is a graph of the SO_2 exhaust concentration versus Ca/S relation for the same data. The difference in initial values of measured SO_2 concentration should be noted, particularly in assessing the difference in sulfur capture efficiency of PHDL and HL. The performance criteria listed in Table 4 for these sorbents do have measurement error bands that overlap.

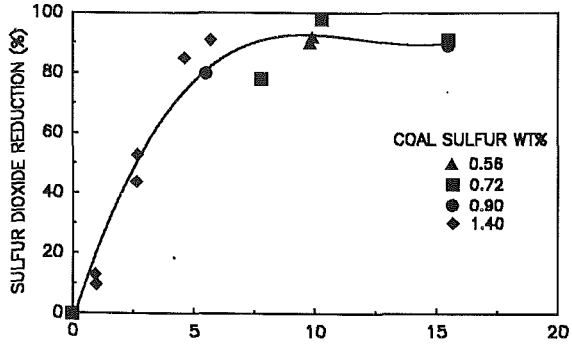

Fig. 6 SO_2 reduction of dolomite injection into the secondary zone

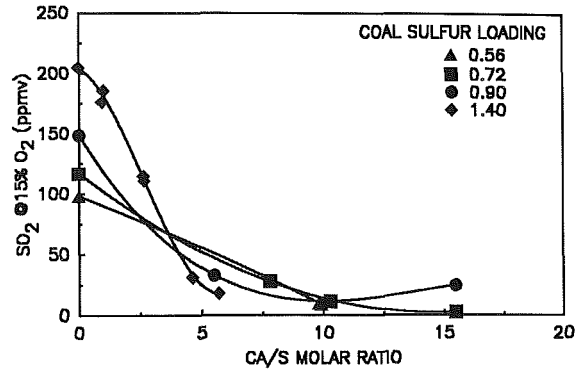

Fig. 7 SO_2 concentration in the exhaust of the slagging combustor injecting dolomite into the secondary zone

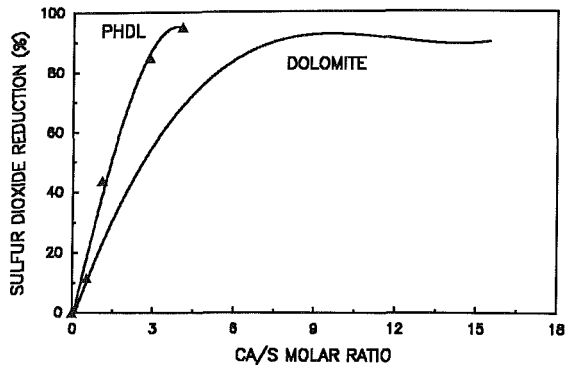

Fig. 8 SO_2 reductions of pressure-hydrated dolomite lime and dolomite injected into the secondary zone

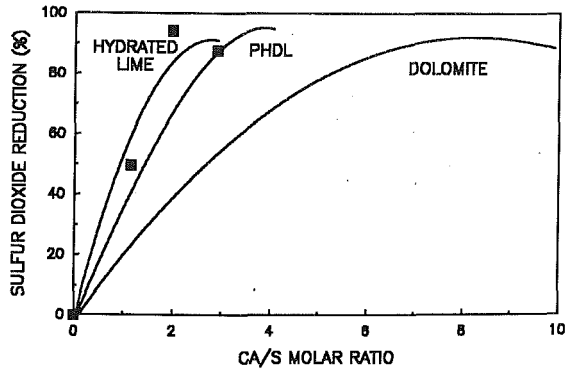

Fig. 9 A comparison of the SO_2 reduction of three sorbents injected into the secondary zone

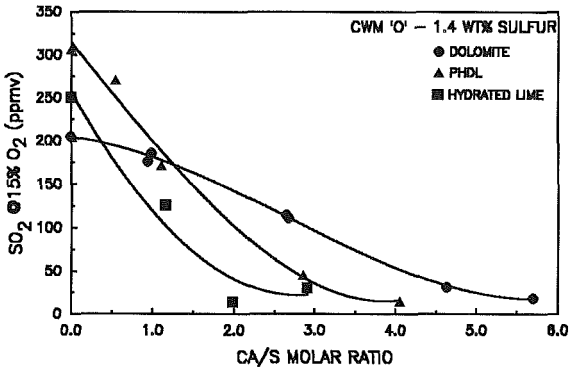

Fig. 10 A comparison of the SO_2 concentration for three sorbents injected into the secondary zone

Coal Sulfur Loading. The data shown in Fig. 6 indicate that coal sulfur loading has little if any influence on the sulfur removal effectiveness of dolomite injected into the secondary combustion zone. A test was concluded with a CWM made with a coal containing more than double the sulfur loading at 3.1 wt%. The data taken are shown graphically in Fig. 11. As presented earlier, all the data taken with coals with sulfur loadings that vary from 0.56 to 1.4 wt% are included in one curve. The data taken with the higher sulfur coal indicate that there is an improvement in sulfur capture effectiveness as the coal sulfur loading is increased. The influence is not strong, and supports the earlier conclusion that the sulfur loading has little influence on sulfur capture. The data scatter in Fig. 6 prevents observing the small effect that is more clearly observed in Fig. 11.

Sorbent Injection Location. As a means of investigating the effectiveness of injection of sorbent in the primary zone, a CWM was made with 5.3 wt% PHDL ground in with the coal during slurry preparation. The coal-sorbent slurry was fed into the primary zone as a standard fuel. The base coal used to prepare this slurry had higher sulfur content than the slurry listed in Table 3 at 3.3 wt%. Two batches of CWM were made with this coal, one with sorbent and one without. The two CWMs have similar properties with the exception of ash content, coal content, and heating value. All of these differences are a direct result of the sorbent in the fuel. A test with the CWM without the sorbent operating at conditions similar to those listed in Table 4 yielded an average SO_2 emission concentration of 658 ppmv @ 15 percent O_2. The next test conducted with sorbent in the fuel yielded SO_2 emissions of 649 ppmv, a reduction of only 2 percent. The sorbent-enriched slurry operated in the combustor like a standard fuel except for a lower outlet temperature and lower slag removal in the primary combustion zone. The sorbent also reacted with the alumina-silica refractory lined primary zone walls, creating a lower melting point eutectic that resulted in significant refractory damage.

Table 4 Summary of secondary zone sorbent injection performance and cost for coal with 1.4 percent sulfur

	Dolomite	Pressure Hydrated Dolomitic Lime	Hydrated Lime
SO_2 Reductions (%) @ Ca/S of 3	55	82	90
Ca/S @ SO_2 of 75 ppmv	3.4	2.4	1.5
Sorbent Cost ($) per pound Sulfur removed to meet SO_2 of 75 ppmv	0.24	0.41	0.28
Maximum Sulfur Loading @ Ca/S of 3 to Meet 75 ppmv	0.72	1.81	3.26

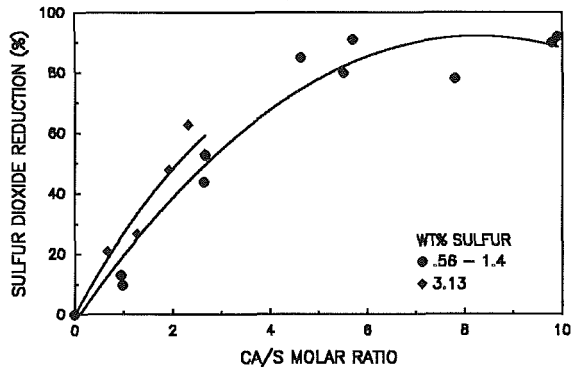

Fig. 11 Influence of coal sulfur loading on sulfur capture of dolomite injected into the secondary zone

For high sulfur capture to be demonstrated in the primary combustion zone through the addition of calcia-based sorbents, both thermodynamics and chemical equilibria show that the sorbent must be at a substantially lower temperature than the surrounding gas streams (Bettleheim and Billenge, 1978). In a primary zone with an available residence time of 150 ms ample time exists for the sorbent to attain thermal equilibrium with the gas stream. Thus, while high sulfur capture may occur in the early stages of the coal-sorbent combustion process, the sulfur-calcia compounds decompose, emitting the sulfur to the gas stream again. The design possibility of injecting the sorbent with the fuel and eliminating a sorbent feed system is very attractive; however, based on the data this approach is not a suitable selection for this combustion system.

Discussion

Based on the data collected in this study, the primary SO_2 control approach of injecting a dry calcia-based sorbent into the secondary combustion zone will successfully meet sulfur emission limits. The three sorbent types all provide significant SO_2 reductions. The choice of sorbent type becomes a trade-off between sulfur capture effectiveness and cost.

Table 4 summarizes the important factors in this design choice for the three sorbents tested. The first two quantities listed in Table 4 are taken from the test rig data and indicate that, all things being equal, the effectiveness of the sorbents increases in the order of dolomite, PHDL, and HL. The tests were conducted such that the number of unwanted variables

were reduced; however, as noted earlier, the sieve analyses of the three sorbents vary significantly. Based on these data, the sorbent costs per pound of sulfur removed to meet an SO_2 limit of 75 ppmv with a coal of 1.4 wt% sulfur loading value were calculated for each sorbent and are shown in Table 4. These values indicate that while more dolomite is required to meet the same SO_2 emissions limit, the cost overrides the sorbent effectiveness, and dolomite is the most attractive choice followed closely by HL and more distantly by PHDL. Note that this analysis is based entirely on sorbent cost and does not include other factors such as storage and disposal.

The last value appearing in Table 4 is the maximum sulfur level of the coal that could be burned, controlling the SO_2 emissions to 75 ppmv @ 15 percent O_2 by injecting the sorbent listed at a Ca/S ratio of 3. Dolomite has the lowest value and HL has the highest at 3.26 wt% sulfur. Although the selection of the cut-off Ca/S ratio of 3 is arbitrary, it must be acknowledged that a practical maximum sorbent input does exist. The limiting Ca/S ratio will be set by a number of variables, including the maximum particulate loading the secondary barrier filter can withstand, the maximum sorbent input the combustor can withstand before its performance is compromised, and the actual sulfur emissions limit regulated for the coal-fueled turbine.

The values listed in Table 4 suggest a control strategy employing two types of sorbent based on the coal sulfur loading. Clearly, dolomite has a cost advantage over the other types of sorbents and is an appropriate choice for coals of low sulfur loading. Hydrated lime is not much more costly than dolomite and could effectively lower SO_2 emission from the burning of coals containing a wide range of sulfur loadings. Pressure-hydrated lime does not offer advantages in cost or effectiveness and is no longer being considered.

Conclusions

An experimental study of a sulfur-removal design for a slagging combustor for a coal-fueled gas turbine has been completed. The program has included an evaluation of three types of calcia-based sorbent injected into a lean secondary combustion zone and a calcia sorbent ground with the coal during slurry preparation and injected into the primary combustion zone as a sorbent slurry fuel.

The three types of sorbent injected into the secondary combustion zone include dry pulverized dolomite, hydrated lime, and pressure-hydrated dolomitic lime. The hydrated lime demonstrated the highest sulfur dioxide reduction, up to 90 percent. Pressure-hydrated dolomitic lime and dolomite produced reductions of 82 and 55 percent, respectively. Dolomite was tested while burning CWMs with a wide range of coal sulfur loadings and indicate only a slight increase in sulfur removal effectiveness with increasing coal sulfur loading.

Pressure-hydrated dolomitic lime ground with the coal during slurry preparation was burned in the primary combustion zone. These tests conducted with a coal containing greater than 3.1 percent sulfur have demonstrated SO_2 reductions of 2 percent.

Based on the sorbent effectiveness and cost, a control approach of injecting either dolomite or hydrated lime into the secondary combustion zone of the slagging combustor has been selected. The choice between dolomite and hydrated lime is contingent upon the coal sulfur loading of the slurry used. Another issue that is being resolved concerning this sulfur-control approach is the impact the sorbent has on the secondary barrier filter. This issue will be examined in subscale rig testing.

Acknowledgments

The work described in this paper was performed by Solar Turbines Incorporated under contract No. DE-AC21-86MC23166 from DOE-Morgantown Energy Technology Center, with Mr. Donald Geiling as Program Manager.

References

Bettleheim, L., and Billenge, B. H. M., 1978, *Industrial Air Pollution Handbook*, McGraw-Hill, London.

Cowell, L. H., Hasen, A. M., LeCren, R. T., and Stephenson, M. D., 1989, "Coal-Fueled Two-Stage Slagging Combustor Island and Cleanup System for Gas Turbine Application," *Proceedings Sixth Annual International Pittsburgh Coal Conference*, pp. 1040–1049.

Cowell, L. H., and LeCren, R. T., 1989, "Development of a Coal-Fueled Gas Turbine Slagging Combustor," ASME Paper No. 89-GT-115.

Garman, A. R., Simons, G. A., and Boni, A. A., 1984, "Surrogate Fuel Exploratory Tests," DOE/MC/20486-1711.

LeCren, R. T., and White, D. J., 1987, "The Burning of a Coal-Water Slurry Fuel in a Two-Stage Slagging Combustor," ASME Paper No. 87-GT-270.

Malte, P. C., 1983, "Mechanisms and Kinetics of Pollutant Formation During Combustion," Washington State, Thermal Energy Laboratory, Report No. 77-24.

Newby, R. A., 1989, "Review of In-Situ Desulfurization Phenomena and Performance in Coal-Based Power Generation Systems," *Proceedings Sixth Annual International Pittsburgh Coal Conference*, pp. 255–266.

Roberts, P. B., LeCren, R. T., Cowell, L. H., Hasen, A. M., and Noble, M., 1988, "Coal-Fueled Gas Turbine Combustor Island Development," ASME Paper No. 88-GT-89.

Robinson, L., 1978, "Coal Minerals Affect Sulfur in Processing," *Hydrocarbon Processing*, Nov., p. 213.

"Steam Generating Units," 1989, *Air and Water Pollution Control*, Vol. 2, No. 12, June 14.

Journal of Engineering for Gas Turbines and Power

Technical Briefs

Effects of Input Variables on the Thermal Efficiency of a Multisolid Fluidized Bed Combustor (20 MW(e))

T. R. Marrero[1] and C. H. Hansford[2]

Introduction

A 20 MW(e) multisolid fluidized bed combustion boiler (MSFBC) was recently put into operation at the University of Missouri—Columbia Campus Power Plant. This MSFBC, manufactured by Riley-Stoker, is designed to burn high-sulfur coal (4 percent sulfur) with a heating value of 25,570 kJ/kg (11,000 Btu/lb) by means of limestone addition and low combustion temperatures of about 845°C (1550°F). The maximum continuous steam rating (MCR) is 90.72×10^3 kg/h (200,000 lb/h) at a pressure of 6.55 MPa gage (950 psig) and a temperature of 454°C (850°F).

To evaluate the new boiler's thermal efficiency, a Fortran-77 computer program was written for use on a Digital Equipment Corporation VAX 8650. The basis of the program is the ASME Power Test Code (PTC) 4.1 (McLean and Murdock, 1969), which incorporates both the input-output and heat loss methods. However, neither calculation method explicitly accounts for the addition of limestone for sulfur capture. The standard PTC calculations were modified to account for sulfation (heat credit) and calcination (heat loss) due to the presence of limestone (Georgetown, 1982; Alliston and Garcia-Malloi, 1983; Bersani et al., 1985; Combustion Engineering, 1986; Longmire, 1986). A sensitivity analysis was conducted to determine which of the two computational methods for determining thermal efficiency is the most sensitive to input data at different load conditions and what input variables need to be measured with particular care.

Results indicate that the input-output method is more sensitive to variations in the input values, especially coal and steam flow rates and coal heating value.

Methodology

Input data from a series of startup tests were used in the sensitivity analysis to determine base values of the thermal efficiency at different loads for both the input-output and heat loss methods. The steam generator load levels were 51, 72, and 91 percent of the MCR. At each of these power levels, the magnitude of each input variable was changed, one variable at a time, from a −1 percent (a decrease of 1 percent in magnitude) to 2 percent at 1/2 percent increments. The gross thermal efficiency was computed for each input variable incremental change. From these computations, the effect on thermal efficiency was determined.

The operating data for flow rates, temperatures, and flue gas composition were collected by a Bailey Network 90. Additional inputs included chemical analyses and thermodynamic properties.

Results and Discussion

Table 1 presents the results of the sensitivity analysis of the MSFBC thermal efficiency at 91 percent MCR. This table corresponds to inputs for both efficiency calculation methods with a 1 percent reduction in the reference input values. The results are divided into six different categories and presented on a percentage basis.

The fuel parameters, heating value, and coal flow rate had the most significant effect on thermal efficiency calculations. Of the two methods, the input-output method was more sensitive to input parameters than the heat loss method. The input-output method resulted in a change of efficiency of approximately the same magnitude as the change in the value of the input variable, whereas in the heat loss method only a fraction of a percent change occurred. A 1 percent reduction in heating value resulted in a 0.722 percent increase in thermal efficiency

Table 1 Sensitivity analysis of the UMC multisolid fluidized bed combustor thermal efficiency: 91 percent MCR and a deviation of −1 percent

		Method Used	
		Heat Loss, %	Input-Output, %
A.	**Fuel Parameters:**		
	Heating Value	-0.184	+0.722
	Coal Flow Rate	-0.099	+0.739
	Carbon Content	+0.052	+0.001
	Hydrogen Content	+0.040	+0.001
	Sulfur Content	-0.021	+0.015
	Moisture Content	+0.014	*
B.	**Steam Parameters:**		
	Flow Rate	*	-0.700
	Final Steam Temperature	*	-0.157
	Feedwater Temperature	*	+0.199
	Spray Water Temperature	*	+0.002
	Spray Water Flow Rate	*	-0.028
	Blowdown	*	-0.005
	Main Steam Pressure	*	+0.031
C.	**Ash Parameters:**		
	Carbon Content	+0.079	**
	Flow Rate	+0.079	**
	Calcium Carbonate	-0.001	**
D.	**Flue Gas Parameters:**		
	Specific Heat	+0.047	*
	CO_2	-0.045	-0.001
	SO_2	+0.012	-0.009
	CO	+0.002	**
	O_2	**	**
	Temperature	+0.083	*
E.	**Limestone Parameters:**		
	Flow Rate	+0.020	**
	Calcium Carbonate	+0.016	**
F.	**Combustion Air Parameters:**		
	Flow Rate	+0.022	-0.001
	Specific Heat	-0.001	+0.001
	Humidity	+0.001	**
	Ambient Temperature	-0.022	-0.006

* Not Applicable.
**Negligible value of less than + 0.001%.

[1]Associate Professor, University of Missouri—Columbia, Columbia, MO 65211.
[2]Graduate Student, University of Missouri—Columbia, Columbia, MO 65211.
Contributed by the Power Division of the AMERICAN SOCIETY OF MECHANICAL ENGINEERS. Manuscript received by the Power Division May 9, 1990.

at 91 percent load for the input-output method. The heat loss method resulted in a smaller effect of a 0.184 percent reduction in efficiency. A similar reduction of 1 percent in the coal flow rate for the input-output method resulted in a 0.739 percent increase in efficiency and a 0.099 percent reduction in efficiency by the heat loss method. There was a 5 percent variation in coal heating value from sample to sample during the test series; this indicates that it is important to have accurate coal heating values, especially when the input-output method is used. The coal sulfur content was of minor significance to both methods. A -1 percent deviation in value resulted in a -0.021 percent change in the efficiency by the heat loss method, and a $+0.015$ percent change by the input-output method. Carbon content ($+0.052$ percent), hydrogen ($+0.04$ percent), and moisture content ($+0.014$ percent) also affected the heat loss efficiency to a similar degree, but had little or no influence on the efficiency calculated by the input-output method.

Steam parameters were also important to the input-output method. The steam flow rate was almost as significant as the coal heating value and flow rate. A 1 percent reduction in the flow rate of steam resulted in 0.7 percent reduction in the input-output efficiency. The final steam temperature and feedwater temperature were also of some importance, resulting in a -0.156 and $+0.199$ percent change in efficiency, respectively. The superheater spray water flow rate (-0.028 percent), main steam pressure ($+0.031$ percent), spray water temperature ($+0.002$ percent), and blowdown flow rate (-0.005 percent) were much less significant. The remaining input parameters had very little effect on the input-output method.

In the heat loss method of calculation, the carbon content and flow rate of the ash were also important. A $+0.079$ percent change in efficiency resulted from a -1 percent change in both of these parameters. Flue gas parameters were of similar magnitude in the heat loss method, with the exit gas temperature being especially important. A -1 percent deviation in its input value resulted in a $+0.083$ percent change in efficiency. Of somewhat less significance were the specific heat of the flue gas ($+0.047$ percent change) and the CO_2 content (-0.045 percent). The SO_2 and CO contents were much less influential on the calculated results.

The limestone and combustion air parameters had little effect on the heat loss efficiency. The limestone flow rate resulted in a $+0.02$ percent change; limestone calcium carbonate content resulted in a $+0.016$ percent change in efficiency. Ambient air temperature had a similarly small effect, -0.022 percent.

The effect of load on the sensitivity of thermal efficiency calculations to input variation is shown in Table 2. These results show that it is difficult to generalize about the influence of load. A decrease in some variables resulted in an increase in efficiency, while others resulted in decreased efficiency. For example, a 1 percent reduction in coal flow rate resulted in a reduction in efficiency, but a similar reduction in the ash carbon content resulted in an increase in efficiency. Also, the change in efficiency is not always proportional to the change in load. That is, the effect at 51 percent is not always roughly half the effect at 91 percent. Sometimes there is little, if any, change with a change in load. Coal carbon content, for example, did not change significantly with load.

Table 2 Load effects on sensitivity analysis of thermal efficiency calculations for an MSFBC: 51, 72, 91 percent MCR and a deviation of -1 percent

	Heat Loss Method, %			Input-Output Method, %		
Variable	51%	72%	91%	51%	72%	91%
Coal Heating Value	-0.148	-0.144	-0.184	+0.762	+0.710	+0.722
Coal Flow Rate	-0.058	-0.067	-0.099	+0.781	+0.729	+0.739
Exit Gas Temperature	+0.101	+0.087	+0.083	*	*	*
Steam Flow Rate	*	*	*	-0.741	-0.687	-0.699
Ash Carbon Content	+0.039	+0.048	+0.079	**	**	**
Ash Flow Rate	+0.038	+0.047	+0.079	**	**	**
Coal Carbon Content	+0.059	+0.049	+0.052	+0.002	+0.002	+0.001
Flue Gas Specific Heat	+0.057	+0.047	+0.047	*	*	*
Flue Gas CO_2 Content	-0.055	-0.045	-0.045	-0.002	-0.002	-0.001
Coal Hydrogen Content	+0.036	+0.038	+0.040	**	**	**

*Not Applicable.
**Negligible value of less than +0.001%.

Conclusions

The input-output method was more sensitive to variations in the input values tested than was the heat loss method. It was most affected by the coal flow rate, coal heating value, and steam flow rate. Steam temperature and feedwater temperature were important, but less so. Therefore, it is important that these values be as accurate as practicable. All the other inputs had a minor or negligible effect on the input-output method.

The heat loss method was affected by more parameters, but was much less sensitive to variations in their values. It was also most sensitive to heating value and coal flow, but much less so than in the input-output method. The flue gas exit temperature, specific heat, and CO_2 content were significant factors, as were the carbon content, flow rate of ash, and the carbon and hydrogen content of the coal. Accurate measurements of these are essential.

Acknowledgments

The authors appreciate the interest and support from many personnel at the University of Missouri—Columbia Campus Power Plant.

References

Alliston, M. G., and Garcia-Malloi, J. A., 1983, "Efficiency of the Georgetown University Atmospheric Fluidized-Bed Boiler," *Proc. Seventh International Conference on Fluidized-Bed Combustion*, Vol. 2, pp. 886-901.

Bersani, A. A., Garver, D. L., and Sinn, B. T., 1985, "Determination of Boiler Efficiency for Fluidized-Bed Steam Generators," *Proc. Eighth International Conference on Fluidized-Bed Combustion*, Vol. 3, pp. 1333-1340.

Combustion Engineering, 1986, "Great Lakes Fluidized-Bed Combustion," United States Department of Energy, Final Report DOE/ET/10389-1986.

Georgetown University, 1982, "Great Lakes Fluidized-Bed Combustion," United States Department of Energy, Final Report DOE/ET/10381-1192.

Longmire, E., 1986, "Performance Calculations for Colorado-Ute Electric Association's Atmospheric Fluidized Bed Combustion Demonstration Project," First Draft, Electric Power Research Institute, Vol. 4.

McLean, W. G., and Murdock, J. W., 1969, *ASME Power Test Code Steam Generating Units PTC 4.1*, ASME, New York.